



## City Research Online

### City, University of London Institutional Repository

---

**Citation:** Tonini, S. (2006). Fuel spray modelling in direct-injection diesel and gasoline engines. (Unpublished Doctoral thesis, City University London)

This is the accepted version of the paper.

This version of the publication may differ from the final published version.

---

**Permanent repository link:** <https://openaccess.city.ac.uk/id/eprint/8486/>

**Link to published version:**

**Copyright:** City Research Online aims to make research outputs of City, University of London available to a wider audience. Copyright and Moral Rights remain with the author(s) and/or copyright holders. URLs from City Research Online may be freely distributed and linked to.

**Reuse:** Copies of full items can be used for personal research or study, educational, or not-for-profit purposes without prior permission or charge. Provided that the authors, title and full bibliographic details are credited, a hyperlink and/or URL is given for the original metadata page and the content is not changed in any way.



**School of Engineering and Mathematical Sciences**

# **Fuel Spray Modelling in Direct-Injection Diesel and Gasoline Engines**

**Ing. Simona Tonini**

**This thesis is submitted for the fulfilment of the requirements for the  
Degree of Doctor of Philosophy**

**July 2006**



*“ciò che cerchi è sempre vicino a te,  
nella misura in cui ti adoperi  
per scoprirne il vero e assoluto fine”  
G.T.*



# TABLE OF CONTENTS

LIST OF TABLES	6
LIST OF FIGURES	7
ACKNOWLEDGEMENTS	17
DECLARATION	18
ABSTRACT	19
NOMENCLATURE	20
CHAPTER 1 INTRODUCTION	23
1.1 Background	23
1.2 Motivation	24
1.3 Present contribution	25
1.4 Thesis outline	27
CHAPTER 2 LITERARY REVIEW	29
2.1 Introduction	29
2.2 Numerical developments of dense spray calculations under high pressure and temperature conditions	30
2.3 Liquid droplet vaporisation modelling	35
2.3.1 Ideal equilibrium droplet vaporisation modelling	37
2.3.2 Multi-component droplet vaporisation modelling	45
2.3.3 Super-critical droplet vaporisation modelling	48
2.4 Experimental and computational investigations on high-pressure fuel injection systems for direct injection gasoline engines	58
2.5 Conclusions	63
CHAPTER 3 MATHEMATICAL FORMULATION	66
3.1 Introduction	66
3.2 Continuous phase modelling	66
3.2.1 Finite volume discretisation method	66
3.2.2 Generic transport equation	68
3.2.3 Face interpolation	70
3.2.4 Temporal discretisation	73



3.3 Eulerian-Lagrangian solution algorithm	74
3.4 Dispersed phase modelling	77
3.4.1 Lagrangian model formulation	77
3.4.2 Injection modelling	79
3.4.3 Parcel atomisation modelling	82
3.4.4 Liquid droplet secondary break-up	89
3.4.5 Liquid droplet evaporation	93
3.4.6 Forces acting on a moving parcel	93
3.4.7 Parcel to parcel interaction	96
3.4.8 Parcel turbulent dispersion	97
3.4.9 Parcel impingement	100
3.5 Coupling of continuous and dispersed phases	102
3.6 Summary	111
CHAPTER 4 MODELLING, VALIDATION AND PARAMETRIC INVESTIGATION OF SINGLE DROPLET VAPORISATION PROCESSES	113
4.1 Introduction	113
4.2 Mathematical formulation of single droplet vaporisation modelling	116
4.2.1 Single-component vaporisation modelling	118
4.2.2 Multi-component vaporisation modelling	128
4.3 Model validation and parametric investigation	132
4.4 Conclusions	162
CHAPTER 5 VALIDATION AND NUMERICAL INVESTIGATION OF DIESEL SPRAY MODELLING	163
5.1 Introduction	163
5.2 Results from multi-hole cavitating nozzles	165
5.2.1 Overview of the test cases	167
5.2.2 Spray velocity and size prediction	170
5.3 Results from the 2-D axis-symmetric single-hole nozzles	173
5.3.1 Overview of the test cases	173
5.3.2 Validation under non-evaporating conditions	180
5.3.3 Validation under evaporating conditions	182
5.3.4 Spray physical sub-models investigation	194
5.3.5 Numerical parameters investigation	206



5.4 Results from the Sandia experimental measurements (Siebers [218])	227
5.4.1 Overview of the test cases	227
5.4.2 Effect of physical and geometrical parameters	228
5.5 Conclusions	234
CHAPTER 6 APPLICATIONS TO HIGH-PRESSURE INJECTION SYSTEMS FOR GDI ENGINES	236
6.1 Introduction	236
6.2 Swirl-pressure atomiser	238
6.2.1 Multi-component fuel vaporization in a constant volume chamber	239
6.2.2 Spray development in a GDI engine	241
6.3 Multi-hole gasoline injector	251
6.3.1 Spray model validation results	253
6.3.2 Parametrical investigation	257
6.4 Outwards-opening pintle-type injector	263
6.4.1 Internal nozzle flow investigation	263
6.4.2 Near-nozzle flow and spray simulations	269
6.5 Conclusions	273
CHAPTER 7 CONCLUSIONS AND RECOMMENDATIONS FOR FUTURE WORK	275
7.1 Overview	275
7.2 Conclusions	276
7.3 Recommendations for further work	279
REFERENCES	282



# LIST OF TABLES

Table 4-I: Scheme of the evaporation model assumptions investigated.	117
Table 4-II: Molecular weight, boiling temperature at atmospheric pressure, critical temperature and pressure for six hydrocarbons.	133
Table 4-III: Operating conditions for the parametric investigation on single droplet evaporation modelling.	146
Table 5-I: Table with operating conditions for the PLN injection system and schematic showing the PDA measurement points where droplet velocity has been obtained at 10, 20, 30 and 40mm from the nozzle hole exit on the centreline.	168
Table 5-II: Table with operating conditions for injection inside the high-pressure/temperature chamber from a VCO injector.	169
Table 5-III: Injector geometric and flow parameters and operating conditions.	175
Table 5-IV: 'Standard' settings for the spray sub-models used for non-evaporating sprays from cavitating <sup>(1)</sup> and non-cavitating <sup>(2)</sup> nozzles.	182
Table 5-V: Summary of the effect of spray physical sub-models on the predicted liquid and vapor penetration under non-evaporating and evaporating conditions for the sharp-inlet nozzle. [ $P_{INJ}=1200\text{bar}$ ].	205
Table 5-VI: Table with operating conditions for two cases of liquid droplet injection in a constant volume domain with variable cell density.	208
Table 5-VII: Description of the computational grids used for the numerical investigation on the modelling of non-evaporating and evaporating diesel sprays from the cavitating nozzle design presented in section 5.3.	213
Table 5-VIII: Summary of the numerical parameters effect on the predicted liquid and vapour penetration under non-evaporating and evaporating conditions for the sharp-inlet nozzle. [ $P_{INJ}=1200\text{bar}$ ].	226
Table 5-IX: Summary of variation of the various parameters investigated. Those include the injector nozzle hole geometric and flow characteristics, the ambient pressure and temperature, the fuel temperature, the injection pressure and fuel physical properties.	227
Table 5-X: Fuel boiling temperatures and distillation curves.	227
Table 6-I: Optical multi-valve engine characteristics.	241
Table 6-II: List of the engine operating conditions, the injection starting time and duration and the fuel composition for the four cases proposed as part of the parametric investigation.	243
Table 6-III: Computational domain used for internal nozzle flow simulations for the outwards-opening injector and list of the geometric and operating conditions investigated.	264
Table 6-IV: List of the geometric and operating conditions for the Eulerian-Lagrangian spray simulations.	271

# LIST OF FIGURES

Figure 3-1: Scheme of the control volume discretisation method.	67
Figure 3-2: Scheme of the temporal and spatial variation of the generic flow variable $\phi$ over the control volume, according to the finite volume discretisation method.	68
Figure 3-3: Scheme of the control volume for the convection terms differencing schemes.	71
Figure 3-4: Continuous and dispersed phase solution algorithm.	75
Figure 3-5: Scheme of the different spray regions in proximity of the nozzle hole exit. Figure adapted from Taskinen [168].	83
Figure 3-6: Illustration of a droplet experiencing bag break-up, taken from Bayvel et al. [182].	90
Figure 3-7: Stripping break-up [183].	90
Figure 3-8: Stages of simple drop division [182].	90
Figure 3-9: Possible particle collision outcomes. Figure adapted from Orme [193].	97
Figure 3-10: Schematic of different impact regimes, Bai et al. [200].	100
Figure 3-11: Spatial and temporal discretisation length scales for fuel injection system modelling: (a) air flow, (b) internal nozzle flow, (c) fuel injection, (d) liquid atomisation, (e) spray development.	102
Figure 3-12: Dynamic grid refinement in the region around the parcel location, at three time steps after start of injection, for (a) multi-hole injector and (b) hollow cone spray injector.	104
Figure 3-13: Schematic showing how the continuous phase variables seen by the parcel are interpolated among the cells around the parcel.	105
Figure 4-1: Scheme of the main parameters in the single droplet vaporisation modelling.	116
Figure 4-2: Scheme of single-droplet vaporisation algorithm.	131
Figure 4-3: Droplet surface (a) non-dimensional area and (b) liquid temperature profiles for four different fuels; $P_G=1\text{bar}$ , $T_G=600\text{K}$ , $T_{d,0}=300\text{K}$ , $D_{d,0}=50\mu\text{m}$ and $\Delta U_0=100\text{m/s}$ .	133
Figure 4-4: (a) Vaporisation rate and (b) vapour mass fraction at the liquid/gas interface profiles for four different fuels; $P_G=1\text{bar}$ , $T_G=600\text{K}$ , $T_{d,0}=300\text{K}$ , $D_{d,0}=50\mu\text{m}$ and $\Delta U_0=100\text{m/s}$ .	133
Figure 4-5: Gas-phase (a) Lewis and (b) Reynolds number profiles for four different fuels; $P_G=1\text{bar}$ , $T_G=600\text{K}$ , $T_{d,0}=300\text{K}$ , $D_{d,0}=50\mu\text{m}$ and $\Delta U_0=100\text{m/s}$ .	134
Figure 4-6: (a) Mass and (b) heat transfer Spalding number profiles as function of the operating conditions and the vaporisation model correlation; n-decane, $P_G=1/10\text{bar}$ , $T_G=500/1000\text{K}$ , $T_{d,0}=300\text{K}$ , $D_{d,0}=50\mu\text{m}$ and $\Delta U_0=100\text{m/s}$ .	135
Figure 4-7: Effect of calculation of heat transfer Spalding number on the droplet (a) non-dimensional surface area and (b) temperature profiles; n-decane, $P_G=1/10\text{bar}$ , $T_G=500/1000\text{K}$ , $T_{d,0}=300\text{K}$ , $D_{d,0}=50\mu\text{m}$ and $\Delta U_0=100\text{m/s}$ .	136
Figure 4-8: Zero droplet vaporisation rate: effect of back temperature on droplet (a) non-dimensional surface area and (b) liquid temperature profiles; n-heptane, $P_G=1\text{bar}$ , $T_G=290/400/500/800\text{K}$ , $T_{d,0}=300\text{K}$ , $D_{d,0}=50\mu\text{m}$ and $\Delta U_0=100\text{m/s}$ .	137
Figure 4-9: Zero temperature gradient at the gas-liquid interface: effect of back temperature on droplet lifetime under low-medium-high back pressure conditions; n-heptane, $P_G=1/10/30\text{bar}$ , $T_{d,0}=T_G$ , $D_{d,0}=50\mu\text{m}$ and $\Delta U_0=100\text{m/s}$ .	138
Figure 4-10: Positive gas-liquid temperature gradient at the interface: effect of back temperature on droplet (a) non-dimensional surface area and (b) liquid temperature profiles; n-heptane, $P_G=1\text{bar}$ , $T_{G,0}=500\text{K}$ , $T_{d,0}=300\text{K}$ , $D_{d,0}=50\mu\text{m}$ and $\Delta U_0=100\text{m/s}$ .	138



- Figure 4-11: Negative gas-liquid temperature gradient at the interface: effect of back temperature on droplet lifetime and liquid bulk temperature; n-decane,  $P_G=1\text{bar}$ ,  $T_{d,0}=500\text{K}$ ,  $D_{d,0}=50\mu\text{m}$  and  $\Delta U_0=100\text{m/s}$ . 139
- Figure 4-12: Temporal evolution of the (a) non-dimensional droplet diameter squared for water. The experimental results are from Ranz et al. [51] and the operating conditions are:  $P_G=1\text{bar}$ ,  $T_G=298\text{K}$ ,  $T_{d,0}=282\text{K}$ ,  $D_{d,0}=1.1\text{mm}$  and  $Re_d=0$ . 140
- Figure 4-13: Comparison of steady state droplet temperatures (measured when  $m_d=0.1\text{ m}_{d,0}$ ) as a function of the free stream temperature predicted by the models with the experimentally measured wet bulb temperatures for: n- heptane [57]. The conditions are:  $P_G=1\text{bar}$ ,  $T_{d,0}=300\text{K}$ ,  $D_{d,0}=1\text{mm}$  and  $Re_d=0$ . 141
- Figure 4-14: Droplet (a) lifetime and (b) liquid bulk temperature as a function of back temperature for n-heptane and n-tridecane fuels;  $P_G=1\text{bar}$ ,  $T_{d,0}=300\text{K}$ ,  $D_{d,0}=50\mu\text{m}$  and  $Re_d=0$ . 141
- Figure 4-15: Effect of droplet vaporisation model on the droplet non-dimensional surface area profiles for (a) n-heptane and (b) n-tridecane fuels;  $P_G=1\text{bar}$ ,  $T_G=600\text{K}$ ,  $T_{d,0}=300\text{K}$ ,  $D_{d,0}=50\mu\text{m}$  and  $Re_d=0$ . 142
- Figure 4-16: Effect of droplet vaporisation model on the liquid temperature profiles for (a) n-heptane and (b) n-tridecane fuels;  $P_G=1\text{bar}$ ,  $T_G=600\text{K}$ ,  $T_{d,0}=300\text{K}$ ,  $D_{d,0}=50\mu\text{m}$  and  $Re_d=0$ . 142
- Figure 4-17: Temporal evolution of the droplet diameter squared for hexane. The experimental results are from Downing [52] and the operating conditions are:  $P_G=1\text{bar}$ ,  $T_G=298\text{K}$ ,  $T_{d,0}=282\text{K}$ ,  $D_{d,0}=1.1\text{mm}$  and  $Re_d=110$ . 143
- Figure 4-18: Effect of liquid temperature distribution model on the temporal evolution of the droplet (a) non-dimensional surface area and (b) temperature profiles. The experimental results are from Wong at al. [211] and the operating conditions are: n-decane,  $P_G=1\text{bar}$ ,  $T_G=1000\text{K}$ ,  $T_{d,0}=315\text{K}$ ,  $D_{d,0}=2\text{mm}$  and  $Re_{d,0}=17$ . 144
- Figure 4-19: Temperature radial profiles at 0.4, 0.8, 1.2 and 2.4ms after start of injection for n-decane fuel droplet. The operating conditions are:  $P_G=1\text{bar}$ ,  $T_G=1000\text{K}$ ,  $T_{d,0}=315\text{K}$ ,  $D_{d,0}=2\text{mm}$  and  $Re_{d,0}=17$ . The computational results are from the 'effective conductivity model' and experiments from Wong at al. [211]. 145
- Figure 4-20: (a) droplet surface area regression and temperature profiles and (b) liquid phase spatial temperature distributions predicted by the 'infinite conductivity model', ICM, the 'finite conductivity model', FCM, and the 'effective conductivity model'; n-octane  $T_{\text{back}}=450\text{K}$ ,  $P_{\text{back}}=13\text{bar}$ ,  $D_0=20\mu\text{m}$ ,  $T_0=300\text{K}$ ,  $\Delta U_0=100\text{m/s}$ . 146
- Figure 4-21: Effect of liquid temperature distribution model on the predicted droplet life time under different back conditions, for (a)  $20\mu\text{m}$  and (b)  $100\mu\text{m}$  droplet. The operating conditions are: n-octane,  $T_{d,0}=300\text{K}$ ,  $\Delta U_0=100\text{m/s}$ ; LPEqM for liquid-gas interface equilibrium. 147
- Figure 4-22: Phase equilibrium of n-hexane/nitrogen system predicted by the Peng-Robinson equation of state; comparison with data of Poston et al. [212]. 148
- Figure 4-23: (a) n-C<sub>8</sub>H<sub>18</sub> and (b) N<sub>2</sub> liquid/vapour fugacity coefficients predicted by the P-R EOS for n-C<sub>10</sub>H<sub>22</sub>/N<sub>2</sub> system in thermodynamic equilibrium at low and high pressure conditions. 149
- Figure 4-24: Liquid/vapour (a) compressibility factors and (b) N<sub>2</sub> mole fractions predicted by the P-R EOS for n-C<sub>8</sub>H<sub>18</sub>/N<sub>2</sub> system in thermodynamic equilibrium at low and high pressure conditions. 149
- Figure 4-25: Effect of back pressure and temperature on the enthalpy of vaporisation profiles for (a) n-heptane, (b) n-octane, (c) n-decane and (d) n-tridecane fuel in thermodynamic equilibrium with N<sub>2</sub>, as predicted by the ideal correlation function of temperature and the Peng-Robinson equation of state (PR-EOS). 150
- Figure 4-26: Effect of liquid temperature distribution model on the predicted droplet (a) non-dimensional surface area and (b) mean liquid temperature using the HPM for liquid-gas interface equilibrium. The operating conditions are: n-octane,  $P_G=13\text{bar}$ ,  $T_G=450\text{K}$ ,  $D_{d,0}=100\mu\text{m}$ ,  $T_{d,0}=300\text{K}$ ,  $\Delta U_0=100\text{m/s}$ . 151
- Figure 4-27: Effect of liquid temperature distribution model on the predicted liquid temperature radial profiles at four time steps after start of injection, using the HPM for liquid-gas interface equilibrium. The operating conditions are: n-octane,  $P_G=13\text{bar}$ ,  $T_G=450\text{K}$ ,  $D_{d,0}=100\mu\text{m}$ ,  $T_{d,0}=300\text{K}$ ,  $\Delta U_0=100\text{m/s}$ . 151



- Figure 4-28: Effect of liquid temperature distribution model on the predicted droplet life time under different back conditions, for (a) 20 $\mu$ m and (b) 100 $\mu$ m droplet. The operating conditions are: n-octane,  $T_{d,0}=300$  K,  $\Delta U_0=100$ m/s; HPM for liquid-gas interface equilibrium. 152
- Figure 4-29: Gas pressure effect on the droplet diameter profile over the evaporation distance for n-heptane fuel droplet predicted by the uniform temperature distribution model considering (a) high-pressure effect (HPM) and (b) ideal equilibrium conditions (LPEqM) at the liquid/gas interface; the experimental results are from Stengele et al. [213] and the operating conditions are:  $P_G=20/30/40$ bar,  $T_G=550$ K,  $D_{d,0}=0.78$ mm,  $T_{d,0}=340/350/360$ K,  $\Delta U_0=0.5$ m/s. 153
- Figure 4-30: Temporal evolution of the non-equilibrium contribution to the surface mole fraction for Langmuir-Knudsen model; unless specified the operating conditions are: n-decane fuel,  $P_G=1$ bar,  $T_G=1000$  K,  $T_{d,0}=315$  K,  $D_0=2$  mm and  $Re_{d,0}=17$ ; calculations end when  $m_d=0.01m_{d,0}$ ; effect of (a) initial droplet Reynolds numbers; gas temperatures, and (c) initial droplet diameters. 154
- Figure 4-31: Effect of evaporation model at the liquid-gas interface on the predicted droplet life time under different back conditions, for (a) 20 $\mu$ m and (b) 100 $\mu$ m droplet. The operating conditions are: n-octane fuel,  $T_{d,0}=300$ K,  $\Delta U_0=100$ m/s; uniform liquid temperature distribution. 155
- Figure 4-32: Droplet lifetime function of ambient temperature and pressure for n-heptane droplet.  $D_{d,0}=50\mu$ m,  $T_{d,0}=300$ K,  $Re_d=0$ . 155
- Figure 4-33: n-decane (a) droplet surface area regression, (b) mean temperature, (c) n-octane liquid concentration and (d) n-octane/n-decane total vaporized mass profiles, predicted by the 'infinite diffusivity model', IDM, the 'finite diffusivity model', FDM, and the 'effective diffusivity model', EDM; initial fuel composition 50%n-octane-50%n-decane,  $T_G=1000$ K,  $P_G=1$ bar,  $D_{d,0}=2$ mm,  $T_{d,0}=300$ K,  $Re=110$ . 157
- Figure 4-34: n-octane liquid phase spatial concentration distributions at four time steps after start of injection predicted by the 'finite diffusivity model', FDM, and the 'effective diffusivity model', EDM; initial fuel composition 50%n-octane-50%n-decane,  $T_G=1000$ K,  $P_G=1$ bar,  $D_{d,0}=2$ mm,  $T_{d,0}=300$ K,  $Re=110$ . 157
- Figure 4-35: n-octane/n-dodecane vaporised mass profiles, assuming not interaction (a) and uniform mixing (b) between the two species;  $T_{back}=1000$ K,  $P_{back}=5$ bar,  $m_0(C_8H_{18}/C_{12}H_{26})=3.65E-5$ Kg,  $T_{d,0}=300$ K,  $Re=0$ . 158
- Figure 4-36: Effect of fuel composition on the predicted droplet life time under different back conditions, for (a) 20mm and (b) 100mm droplet. n-octane,  $T_{d,0}=300$  K,  $\Delta U_0=100$ m/s, uniform liquid temperature distribution, and HPM to solve the liquid-gas interface equilibrium. 159
- Figure 4-37: Gas pressure effect on the droplet diameter profile over the evaporation distance for two-components fuel droplet predicted by the multi-component model considering (a) ideal equilibrium conditions (LPEqM) and (b) high-pressure effect (HPM) at the liquid/gas interface; the experimental results are from Stengele et al. [109] and the operating conditions are:  $P_G=20/30/40$ bar,  $T_G=550$ K, fuel initial composition 30% pentane and 70% nonane,  $D_{d,0}=0.7/0.65$ mm,  $T_{d,0}=370/380/400$ K,  $\Delta U_0=0.5$ m/s. 160
- Figure 4-38: Gas pressure effect on the droplet velocity profile over the evaporation distance for two-components fuel droplet predicted by the multi-component model considering (a) ideal equilibrium conditions (LPEqM) and (b) high-pressure effect (HPM) at the liquid/gas interface; the experimental results are from Stengele et al. [109] and the operating conditions are:  $P_G=20/30/40$ bar,  $T_G=550$ K, fuel initial composition 30% pentane and 70% nonane,  $D_{d,0}=0.7/0.65$ mm,  $T_{d,0}=370/380/400$ K,  $\Delta U_0=0.5$ m/s. 160
- Figure 4-39: Gas temperature effect on the droplet (a) diameter and (b) velocity profiles over the evaporation distance for two-components fuel droplet predicted by the multi-component model considering high-pressure effect (HPM) at the liquid/gas interface; the experimental results are from Stengele et al. [109] and the operating conditions are:  $P_G=30$ bar,  $T_G=550/650$ K, fuel initial composition 70% pentane and 30% nonane,  $D_{d,0}=0.8/0.82$ mm,  $T_{d,0}=370/380$ K,  $\Delta U_0=0.5$ m/s. 161
- Figure 4-40: Initial droplet size effect on the droplet (a) diameter and (b) velocity profiles over the evaporation distance for two-components fuel droplet predicted by the multi-component model considering high-pressure effect (HPM) at the liquid/gas interface; the experimental results are from Stengele et al. [109] and the operating conditions are:  $P_G=30$ bar,  $T_G=550$ K, fuel initial composition 70% pentane and 30% nonane,  $D_{d,0}=0.72/0.80$ mm,  $T_{d,0}=370$ K,  $\Delta U_0=0.5$ m/s. 161



- Figure 4-41: Fuel composition effect on the droplet diameter profiles over the evaporation distance for single and two-components fuel droplets predicted by the multi-component model considering high-pressure effect (HPM) at the liquid/gas interface; the experimental results are from Stengele et al. [109] and the operating conditions are:  $P_G=30\text{bar}$ ,  $T_G=550\text{K}$ ,  $D_{d0}=0.63/0.70/0.71/0.74\text{mm}$ ,  $T_{d0}=380\text{K}$ ,  $\Delta U_0=0.5\text{m/s}$ . 162
- Figure 5-1: Sub-domain of the computational grids used, 2D-s1, 2D-s2 and 2D-s3. The minimum cell length on the axial direction is also indicated. 164
- Figure 5-2: Tip geometry of (a) the conical mini-sac type and (b) VCO type injectors [219]. 166
- Figure 5-3: Predicted internal nozzle flow structure for (a) the sac volume and the injection hole of a conical mini-sac type 6-hole nozzle and for (b) the 6-hole VCO nozzle operating at 1200bar at 350 $\mu\text{m}$  needle lift, as predicted using the two-phase cavitating model of Giannadakis [148]. 167
- Figure 5-4: Predicted (a) injection pressure, (b) hole exit contraction area and (c) nozzle discharge coefficient as function of the measured needle lift signal for nominal rail pressure of 300bar, for the VE distributor-type pump, connected to Stanadyne pencil-type nozzle; injection of diesel spray under atmospheric conditions. 168
- Figure 5-5: Predicted (a) injection (sac volume) pressure (b) hole exit effective area and (c) nozzle discharge coefficient as function of the measured needle lift signal for nominal rail pressure of 800 and 1200 bar for the 6-hole VCO nozzle. 169
- Figure 5-6: Comparison between PDA droplet velocity measurements and model predictions using one and two levels of cell refinement at (a)10, (b) 20, (c) 30 and (d) 40mm from the nozzle exit for non-evaporating spray under atmospheric conditions and nominal rail pressure of 300bar. 170
- Figure 5-7: Comparison between PDA droplet diameter measurements [216] and model predictions at different points across the spray, located 2 and 3mm from the centreline and at 12.5mm from the nozzle hole exit for evaporating spray, with nominal rail pressure of 800bar, 500K back temperature and 17.2bar back pressure. 171
- Figure 5-8: CCD spray images [216] and model predictions at (a) 0.3 and (b) 0.5ms after start of injection using one and two levels of local refinement [ $T_{\text{AIR}}=300\text{K}$ ,  $P_{\text{BACK}}=17.2\text{bar}$ ,  $P_{\text{INJ}}=1200\text{bar}$ ]. 172
- Figure 5-9: Comparison between experimental data [216] and model predictions obtained using grids with one and two levels of dynamic local refinement for the liquid penetration temporal profiles [ $T_{\text{AIR}}=300\text{K}$ ,  $P_{\text{BACK}}=17.2\text{bar}$ ,  $P_{\text{INJ}}=1200\text{bar}$ ]. 172
- Figure 5-10: Numerical grid of the (a) sharp-inlet (cavitating) nozzle and (b) rounded-inlet (non-cavitating) nozzle [148]. 173
- Figure 5-11: Fuel injection rate of the (a) sharp-inlet nozzle and (b) rounded-inlet nozzle and (c) predicted effective area of the sharp-inlet nozzle used as input to the spray model for the three nominal rail pressures investigated. 174
- Figure 5-12: Predicted effective and geometric injection velocity for the cavitating and the non-cavitating nozzle for nominal rail pressures of (a) 500bar and (b) 1200bar. The non-cavitating and the cavitating nozzles have the same volumetric capacity. 176
- Figure 5-13: Predicted near-nozzle spray cone angle for the cavitating and the non-cavitating nozzle during the injection period for rail pressures of (a) 500bar and (b) 1200bar. 176
- Figure 5-14: Effect of initial conditions and atomisation model on predicted droplet SMD for the three nominal rail pressures investigated (a) cavitating nozzle and (b) non-cavitating nozzle. 178
- Figure 5-15: Predicted non-evaporating spray development at 0.2, 0.4, 0.6 and 0.8ms after start of injection. Liquid penetration and induced flow field are shown [ $P_{\text{INJ}}=1200\text{bar}$ ,  $P_{\text{BACK}}=54\text{bar}$ ,  $T=900\text{K}$ ]. Scatter plots and air flow vectors are coloured according to their total velocity. 179
- Figure 5-16: Predicted evaporating spray development at 0.2, 0.4, 0.6 and 0.8ms after start of injection. Liquid penetration (right), vapour penetration (left) and induced flow field (right) are shown [ $P_{\text{INJ}}=1200\text{bar}$ ,  $P_{\text{BACK}}=54\text{bar}$ ,  $T=900\text{K}$ ]. The colour scales for the vapour concentration and the flow velocity vector distributions are normalised with their maximum values. 179
- Figure 5-17: Comparison between CCD images and predicted spray structures at 1ms ASOI for the (a,b) cavitating and the (c,d) non-cavitating nozzles for rail pressures of 500bar and 1200bar, under non-evaporating conditions. 181



- Figure 5-18: Effect of initial conditions and atomisation model on predicted non-evaporating spray tip penetration for the three nominal rail pressures investigated of the (a) sharp-inlet nozzle and (b) rounded-inlet nozzle. 181
- Figure 5-19: Grid effect on predicted non-evaporating spray tip penetration of the sharp-inlet nozzle for nozzle for nominal rail pressures of (a) 500bar and (b) 1200bar. Minimum cell lengths are 0.6, 0.3 and 0.15mm for grid 2D-s1, 2D-s2 and 2D-s3 respectively. 182
- Figure 5-20: (a) Comparison between experimental data and model predictions for the temporal variation of liquid penetration and (b) predicted spray SMD, using the 'Standard' spray model settings, defined in Table 5-IV, with the high-pressure droplet evaporation model, for the three nominal rail pressures tested. 183
- Figure 5-21: Effect of numerical grid on temporal variation of (a) liquid penetration and (b) non-dimensional evaporation rate, using the 'Standard' spray model settings [ $P_{INJ}=1200\text{bar}$ ]. Minimum cell lengths are 0.6, 0.3 and 0.15mm for grid 2D-s1, 2D-s2 and 2D-s3 respectively. 184
- Figure 5-22: Effect of evaporation model on temporal variation of (a) liquid penetration, (b) non-dimensional vaporization rate, (c) spray SMD and spray temperature using the 'Standard' spray model settings [ $P_{INJ}=1200\text{bar}$ ]. 185
- Figure 5-23: Effect of drag coefficient model on temporal variation of liquid penetration, using the 'Standard' spray model settings [ $P_{INJ}=1200\text{bar}$ ]. 186
- Figure 5-24: Effect of injected droplet size on temporal variation of (a) liquid penetration and (b) non-dimensional vaporization rate. (c) Spray tip total velocity for  $5\mu\text{m}$  droplet case. Liquid core atomisation, droplet secondary break-up and droplet collisions models are de-activated [ $P_{INJ}=1200\text{bar}$ ]. 187
- Figure 5-25: Effect of initial droplet size on temporal variation of (a) mean droplet heat transfer number, (b) normalised mean temperature difference between liquid and gaseous phases, (c) total spray surface area and (d) normalised energy exchange between liquid and gaseous phases. Liquid core atomisation, droplet secondary break-up and droplet collisions models are de-activated [ $P_{INJ}=1200\text{bar}$ ]. 188
- Figure 5-26: Effect of fuel physical properties on temporal variation of (a) liquid penetration and (b) non-dimensional vaporization rate. Liquid core atomisation, droplet secondary break-up and droplet collisions models are de-activated [ $P_{INJ}=1200\text{bar}$ ]. 189
- Figure 5-27: Effect of fuel physical properties on temporal variation of (a) liquid penetration and (b) spray SMD, using the 'Standard' spray model settings [ $P_{INJ}=1200\text{bar}$ ]. 190
- Figure 5-28: Predicted arithmetic mean diameter of the whole spray using different fuels and activating/de-activating droplet secondary break-up [ $P_{INJ}=1200\text{bar}$ ]. 190
- Figure 5-29: Predicted (a) mean droplet deformation and (b) liquid penetration temporal profile, using the 'Standard' spray model settings and including the droplet deformation effect [ $P_{INJ}=1200\text{bar}$ ]. 191
- Figure 5-30: Predicted liquid penetration (right), vapour penetration (left) and induced flow field (right) at 1ms ASOI (a) using the 'Standard' spray model settings and (b) including the droplet deformation effect [ $P_{INJ}=1200\text{bar}$ ]. 191
- Figure 5-31: Effect of initial conditions and atomisation model on predicted evaporating spray tip penetration for the three nominal rail pressures investigated of the (a) sharp-inlet nozzle and (b) rounded-inlet nozzle. 192
- Figure 5-32: Comparison between CCD images and predicted spray structures at 1.6ms ASOI for the (a,b,c) cavitating and the (d,e,f) non-cavitating nozzles for rail pressures of 500bar, 800bar and 1200bar under evaporating conditions. 193
- Figure 5-33: Effect of atomisation model on liquid and vapour penetration for non-evaporating sprays with (a)  $P_{INJ}=500\text{bar}$  and (b)  $P_{INJ}=1200\text{bar}$  and for evaporating sprays with (c)  $P_{INJ}=500\text{bar}$  and (d)  $P_{INJ}=1200\text{bar}$ . 195
- Figure 5-34: Effect of atomisation model on the spray SMD predicted by the droplet secondary break-up for (a)  $P_{INJ}=500\text{bar}$  and (b)  $P_{INJ}=1200\text{bar}$ . 195
- Figure 5-35: Effect of atomisation model and atomisation angle on temporal variation of liquid and vapor penetration of (a) non-evaporating and (b) evaporating spray from the sharp-inlet nozzle [ $P_{INJ}=1200\text{bar}$ ]. 196



- Figure 5-36: Effect of atomisation model and atomization angle on temporal variation of (a) non-dimensional vaporization rate and (b) spray SMD of evaporating spray from the sharp-inlet nozzle [ $P_{INJ}=1200\text{bar}$ ]. 197
- Figure 5-37: Predicted liquid penetration (right), (a/b) flow field axial velocity or (c/d) vapour penetration (left) and induced flow field (right) (a/c) at 1ms ASOI, deactivating and (b/d) including the droplet secondary break-up model of Arcoumanis et al. [76], for (a/b) non-evaporating and (c/d) evaporating spray [ $P_{INJ}=1200\text{bar}$ ]. 198
- Figure 5-38: Effect of break-up model on temporal variation of liquid and vapour penetration of (a) non-evaporating and (b) evaporating spray of the sharp-inlet nozzle [ $P_{INJ}=1200\text{bar}$ ]. 199
- Figure 5-39: Effect of break-up model on (a) spray SMD and (b) vaporisation rate for evaporating spray of the sharp-inlet nozzle [ $P_{INJ}=1200\text{bar}$ ]. 199
- Figure 5-40: (left) Percentage of occurring of different secondary droplet break-up events and (right) droplet Weber number distribution along the injection period for non-evaporating and evaporating sprays with nominal rail pressure of 500 and 1200 bar. 200
- Figure 5-41: Percentage of break-up event as function of the distance from the injector (a) for non-evaporating and evaporating sprays and (b) for different break-up mode and evaporating conditions [ $P_{INJ}=1200\text{bar}$ ]. 201
- Figure 5-42: Effect of drag coefficient model on liquid and vapor penetration profiles of (a) non-evaporating and (b) evaporating spray of the sharp-inlet nozzle [ $P_{INJ}=1200\text{bar}$ ]. 201
- Figure 5-43: Effect of droplet turbulent dispersion model on temporal variation of liquid and vapour penetration of the sharp-inlet nozzle [ $P_{INJ}=1200\text{bar}$ ]. 202
- Figure 5-44: Temporal variation of parcel deformation, for evaporating sprays with two nominal injection pressures injected from the sharp-inlet nozzle. 203
- Figure 5-45: Effect of droplet shape on the temporal variation of liquid and vapour penetration with (a)  $P_{INJ}=500\text{bar}$  and (b)  $P_{INJ}=1200\text{bar}$ , and corresponding non-dimensional evaporation rate for (c)  $P_{INJ}=500\text{bar}$  and (d)  $P_{INJ}=1200\text{bar}$ . 203
- Figure 5-46: Effect of evaporation model on (a) temporal variation of liquid and vapour penetration and (b) non-dimensional evaporation rate for the sharp-inlet nozzle [ $P_{INJ}=1200\text{bar}$ ]. 204
- Figure 5-47: Summary of the effect of spray physical sub-models on the predicted liquid and vapour penetration under non-evaporating and evaporating conditions for the sharp-inlet nozzle. [ $P_{INJ}=1200\text{bar}$ ]. 206
- Figure 5-48: Effect of grid cell size on predicted spray structure at 0.6ms ASOI in homogeneous grids with (a) 2mm, (b) 1mm (c) 0.5mm cell size and (d) in a grid with variable cell size. Source terms are given to the cell-of-parcel. [Injection of liquid droplets according to the operating conditions described in Table 5-VI, Case I]. 208
- Figure 5-49: Schematic showing how source terms are distributed to the cells around the parcel and the continuous phase variables at the parcel location are interpolated; (a) standard method and (b) solution method. 209
- Figure 5-50: Effect of source term distribution and continuous phase variable interpolation on calculated spray structure on a plane perpendicular to the injection axis at 15mm from the injection hole, at 0.6ms ASOI. (a) 'Method 1': cell of parcel and (b) 'Method 2': within a region of 0.4mm. [Injection of liquid droplets according to the operating conditions described in Table 5-III, Case I]. 210
- Figure 5-51: Effect of dynamic grid refinement on predicted (a) liquid penetration and (b) spray development, using five 2-D axis-symmetric grids with minimum cell size from 2.4mm down to 0.15mm, obtained with four successive levels of dynamic grid refinement from the coarse grid (b.1) [Injection of liquid droplets according to the operating conditions described in Table 5-VI, Case II]. 212
- Figure 5-52: 3-D static and adaptive numerical grids used for the simulation of the spray development (a)  $50 \times 10^3$  cells, (b)  $240 \times 10^3$  cells, (c)  $50 \times 10^3$  cells with automatic local refinement at the spray tip. 212
- Figure 5-53: 2-D axis-symmetric adaptive numerical grid at three time instances calculated during the spray development at (a) 0.2ms, (b) 0.5ms and (c) 1.0ms. 213



- Figure 5-54: Effect of numerical grid on the predicted liquid and vapor spray penetration of the (a) non-evaporating and (b) evaporating sprays for nominal rail pressure of 500bar, using 2-D static grids. 215
- Figure 5-55: Effect of numerical grid on the predicted liquid and vapor spray of the (a) non-evaporating and (b) evaporating sprays for nominal rail pressure of 1200bar, using static and adaptive 2-D grids. 215
- Figure 5-56: Effect of numerical grid on the predicted liquid and vapour spray penetration of the (a) non-evaporating and (b) evaporating sprays for nominal rail pressure of 1200bar, using static and adaptive 3-D grids. 216
- Figure 5-57: Computational domain effect on the standard deviation of the predicted liquid and vapour penetration from the experimental measurements, using static and adaptive 2D and 3D numerical grids with nominal rail pressure of 1200bar, for (a) non-evaporating and (b) evaporating sprays. 216
- Figure 5-58: Computational domain effect on the normalised calculation time relative to the reference-case, using static and adaptive 2D and 3D numerical grids with nominal rail pressure of 1200bar, for (a) non-evaporating and (b) evaporating sprays. 217
- Figure 5-59: Effect of interpolation/distribution distance on predicted liquid and vapour spray penetration of the (a) non-evaporating and (b) evaporating spray (fixed distance, proportional to the 'equivalent' parcel diameter). [ $P_{INJ}=1200\text{bar}$ ]. 219
- Figure 5-60: Effect of constant factor, in the interpolation/distribution distance proportional to the 'equivalent' parcel diameter, on predicted liquid and vapour spray penetration for the evaporating spray [ $P_{INJ}=1200\text{bar}$ ]. 219
- Figure 5-61: Effect of initial injector hole size on predicted (a) 'equivalent' parcel size percentage distribution and (a) droplet SMD for the evaporating spray (interpolation/distribution distance proportional to the 'equivalent' parcel diameter). [ $P_{INJ}=1200\text{bar}$ ]. 220
- Figure 5-62: Effect of initial injector hole size on predicted (a) liquid (black lines) and vapour (red lines) penetrations and (b) non-dimensional vaporisation rate of the evaporating spray (interpolation/distribution distance proportional to the 'equivalent' parcel diameter). [ $P_{INJ}=1200\text{bar}$ ]. 220
- Figure 5-63: Effect of total number of parcels injected on predicted liquid and vapour penetration profiles for the evaporating spray (interpolation/distribution distance proportional to the 'equivalent' parcel diameter). [ $P_{INJ}=1200\text{bar}$ ]. 221
- Figure 5-64: Effect of 'cell' virtual' velocity calculation on the prediction of the continuous phase (Cont-phase(p)) and mean flow field (a) velocity and (b) temperature; evaporating spray  $P_{INJ}=1200\text{bar}$ . 222
- Figure 5-65: Effect of virtual properties on predicted liquid and vapour spray penetration of (a) non-evaporating and (b) evaporating spray. [ $P_{INJ}=1200\text{bar}$ ]. 223
- Figure 5-66: Effect of time step on liquid and vapour spray penetration of (a) non-evaporating and (b) evaporating spray. [ $P_{INJ}=1200\text{bar}$ ]. 224
- Figure 5-67: Effect of discretisation method of the gas-phase equations on spray tip penetration of (a) non-evaporating and (b) evaporating spray (HYBRID, JASAC, BSUO for space, EULER, CRANK NICOLSON for time) [ $P_{INJ}=1200\text{bar}$ ]. 225
- Figure 5-68: Summary of the numerical parameters effect on the predicted liquid and vapour penetration under non-evaporating and evaporating conditions for the sharp-inlet nozzle. [ $P_{INJ}=1200\text{bar}$ ]. 226
- Figure 5-69: Effect of injection pressure on predicted spray structure 1.0ms after start of injection for four nominal rail pressures [ $T_{BACK}=1000\text{K}$ ,  $\rho_{BACK}=14.8\text{kg/m}^3$ ]. The colour scale of the vapour penetration is normalised with its maximum value. 228
- Figure 5-70: Effect of back density on predicted spray structure 1.0ms after start of injection for four nominal rail pressures [ $T_{BACK}=1000\text{K}$ ,  $P_{INJ}=1350\text{bar}$ ]. The color scale of the vapour penetration is normalised with its maximum value. 229
- Figure 5-71: (a) Liquid length and (b) spray SMD versus orifice diameter for different ambient gas temperature (T) and density ( $\rho_a$ ) and nozzle orifice pressure drop ( $\Delta P_f$ ). [Fuel used: HMN, initial fuel temperature 438K]. 229
- Figure 5-72: Liquid length versus pressure drop across the nozzle hole orifice as function of ambient gas temperature (T). [Fuel used: HMN, initial fuel temperature 438K]. 230



- Figure 5-73: (a) Liquid length as a function of gas density for different gas temperatures. [Nozzle hole diameter 0.246mm, HMN fuel, initial fuel temperature 438K, pressure drop 136MPa]. 231
- Figure 5-74: Effect of fuel on liquid length (HMN/ $n\text{-C}_{14}\text{H}_{30}$  versus Cetane/ $n\text{-C}_{16}\text{H}_{34}$ ). [Nozzle hole diameter 0.246mm, HMN fuel, initial fuel temperature 438K, pressure drop 136MPa]. 232
- Figure 5-75: Liquid length as function of initial fuel temperature for different ambient conditions. [Nozzle hole diameter 0.246mm, HMN fuel, pressure drop 135MPa]. 232
- Figure 5-76: (a) Non-dimensional vaporization rate and (b) liquid and vapour penetration temporal profiles for a mixture of 50% dodecane and 50% hexadecane [Nozzle hole diameter 0.246mm, HMN fuel, pressure drop 135MPa, 1295K gas temperature,  $30.3\text{kg/m}^3$  gas density]. 233
- Figure 5-77: Liquid mixture and vapor distribution of (left) dodecane and (right) hexadecane fuels at (a) 0.5ms and (b) 1.0ms after start of injection [Nozzle hole diameter 0.246mm, HMN fuel, pressure drop 135MPa, 1295K gas temperature,  $30.3\text{kg/m}^3$  gas density]. 233
- Figure 6-1: GDI combustion systems [2]. 236
- Figure 6-2: Three different injector designs for spray-guided concept with central-mounted injector: swirl atomizer, multi-hole nozzle and outward opening injector [2]. 237
- Figure 6-3: (a) Schematic of the pressure swirl atomiser. (b) Calculated and measured temporal variation of the spatially averaged (mean) nozzle flow exit conditions: axial velocity, swirl velocity and film thickness [117]. 238
- Figure 6-4: Effect of fuel composition on the liquid dispersed phase (a) size and (b) temperature distributions at 0.5, 2.5 and 4.5ms ASOI. Scatter plots are coloured according to the droplet (a) diameter and (b) temperature.  $P_{\text{back}}=10\text{bar}$  and  $T_{\text{back}}=600\text{K}$ . 240
- Figure 6-5: Effect of fuel composition on the continuous phase (a) temperature and (b) octane concentration distributions at 0.5, 2.5 and 4.5ms ASOI.  $P_{\text{back}}=10\text{bar}$  and  $T_{\text{back}}=600\text{K}$ . 240
- Figure 6-6: Outline of the numerical grids of the five blocks constructed for meshing the DI gasoline engine; a combination of tetrahedrals and hexahedrals cells has been used. 242
- Figure 6-7: Predicted flow field inside the engine cylinder on the symmetry plane at three crank angles ATDC for WOT conditions, with engine rotational speed of 1500rpm. 242
- Figure 6-8: Comparison between CCD spray images [225] and model predictions during the injection period; multi-component fuel injected from a high pressure swirl atomiser during induction into the moving cylinder of the multi-valve GDI engine. 243
- Figure 6-9: Scatter plots at three crank-angles ATDC of liquid droplet coloured according to the liquid temperature and flow field streamlines coloured according to the gas axial velocity from two different views; operating conditions correspond to the WOT 3-components case. 245
- Figure 6-10: Droplet size distribution and percentage of vaporized fuel according to the droplet diameter for (a) single and (b) multi-component fuel cases at three crank angles ATDC. 246
- Figure 6-11: Liquid temperature distribution single and multi-component fuel cases at three crank angles ATDC. 246
- Figure 6-12: Scatter plots at three crank angles during the compression stroke of the droplet size as a function of droplet velocity and temperature for (a) single- and (b) multi-component fuel case; operating conditions correspond to the WOT. 247
- Figure 6-13: Droplet scatter plots at three crank angles during the compression stroke of the droplet size as a function of droplet temperature and fuel mass fraction of (a)  $\text{C}_6\text{H}_{14}$ , (b)  $\text{C}_8\text{H}_{18}$  and (c)  $\text{C}_{10}\text{H}_{22}$ ; operating conditions correspond to the WOT and 3-components fuel. 248
- Figure 6-14: (a) Fuel composition during the induction and the compression strokes for the WOT 3-components case. (b) Calculated fuel evaporation rate for all four injection cases investigated. 249
- Figure 6-15: Predicted percentage of fuel evaporated relative to total fuel injected for the WOT cases investigated for (a) one-component and (b) 3-component fuels. The percentage of fuel remaining on the wall is also shown, while the percentage value of fuel remaining in liquid form both inside the engine cylinder as well as on the cylinder walls at the end of the compression stroke is specified. 250



- Figure 6-16: Comparison between (left) LIF [225] and (right) model predictions for the vapour fuel concentration distribution in terms of air fuel mass ratio (AFR) at three crank angles during the compression stroke. 251
- Figure 6-17: (a) Numerical grid used for flow simulations inside the six-hole injector nozzle (b) temporal development of volumetric flow-rate for 120 and 200bar nominal rail pressure, estimated from an 1-D fuel injection system model, (b) predicted volumetric flow-rate transient profile under atmospheric conditions for 120 and 200 bar injection pressure and (c) volume fraction inside the injection holes due to onset and development of cavitation, at 200bar nominal rail pressure [129]. 252
- Figure 6-18: PDA measurement grid points. 252
- Figure 6-19: (a) Half numerical grid of the 60° sector representing 1/6 of the constant volume chamber and (b) fuel spray droplet distribution and air-flow ribbons 1.0ms after ASOI, coloured according to their total velocity magnitude. Nominal rail pressure 200bar, back-pressure 1bar. 253
- Figure 6-20: Effect of grid dynamic refinement on the spray penetration; coarse grid ~100,000 cells, fine grid ~250,000 cells. 254
- Figure 6-21: Comparison between model predictions and experimental data of spray tip penetration for two different nominal injection and back pressure conditions. 254
- Figure 6-22: Comparison between CCD images [129] and model predictions from the multi-hole injector at 0.5ms ASOI, revealing (a)  $P_{in}=120\text{bar}$ ,  $P_{back}=1\text{bar}$ , (b)  $P_{in}=200\text{bar}$ ,  $P_{back}=1\text{bar}$  and (c)  $P_{in}=200\text{bar}$ ,  $P_{back}=12\text{bar}$ . 255
- Figure 6-23: Temporal variation of droplet (a) droplet AMD (b) mean and rms axial velocity component and (c) mean and rms radial velocity component, 10mm below the nozzle exit under atmospheric conditions. 256
- Figure 6-24: Temporal variation of droplet (a) droplet AMD (b) mean and rms axial velocity component and (c) mean and rms radial velocity component, 30mm below the nozzle exit under atmospheric conditions. 256
- Figure 6-25: Temporal variation of droplet (a) AMD, (b) mean and rms axial velocity component and (c) mean and rms radial velocity component, for nominal injection pressures of 200bar, chamber pressures of 1 and 12bar, at 30mm below the nozzle exit. 257
- Figure 6-26: (a) Fuel spray distribution and air-flow ribbons from the '6+1' central hole nozzle configuration showing the over-penetration of the central hole spray relative to the side ones. Droplets and air-flow ribbons are coloured according to their total velocity magnitude. (b) Atomisation cone angle effect on the temporal profile of liquid penetration for the central spray under non-evaporating conditions. 259
- Figure 6-27: (a) Fuel spray distribution and air-flow ribbons coloured according to their total velocity magnitude, (b) fuel vapour mass fraction iso-surfaces for evaporating ( $T_{back}=388\text{K}$ ) conditions superimposed to liquid droplets distribution and air-flow ribbons coloured according to their total velocity magnitude, at 1.0ms ASOI, and (c) liquid and vapour spray penetration for non-evaporating and evaporating cases;  $P_{back}=1\text{bar}$ . 260
- Figure 6-28: Grid effect on the temporal profiles of liquid and vapour penetration for (a) atmospheric back-pressure conditions under room temperature and (b) high-back pressure and temperature conditions. Grid 1, Grid 2 and Grid 3 correspond to the computational domains described in Figure 5-3. 260
- Figure 6-29: (a) Nominal rail pressure and (b) back conditions effect on the temporal profiles of liquid and vapour penetration. 261
- Figure 6-30: (a) Initial fuel temperature and (b) hole size effect on the temporal profiles of liquid and vapour penetration. 262
- Figure 6-31: Temporal variation of (a) liquid and vapour penetrations and of (b) vapour penetration for each species present in the single component (100%  $\text{C}_8\text{H}_{18}$ ) and in the multi-component (20%  $\text{C}_6\text{H}_{14}$ -50%  $\text{C}_8\text{H}_{18}$ -30%  $\text{C}_{10}\text{H}_{22}$ ) fuels. 262
- Figure 6-32: Parcel scatter plots colored according the total velocity and vapour fuel concentration iso-surfaces corresponding to 1% vapour mass fraction for the (a) single component (100%  $\text{C}_8\text{H}_{18}$ ) and the (b) multi-component (20%  $\text{C}_6\text{H}_{14}$ -50%  $\text{C}_8\text{H}_{18}$ -30%  $\text{C}_{10}\text{H}_{22}$ ) fuels at 1ms ASOI. 263

Figure 6-33: (a) Main flow path inside the nozzle and (b) recirculation zones formed below the needle guides (in colour scale); on the black-white scale the stream lines of the main flow path are superimposed. 265

Figure 6-34: (a) Schematic showing the definition of axial and circumferential velocity components and the corresponding deviation angles. (b) Circumferential and axial velocity component distributions at the nozzle exit gap around the 360° circumference at the nozzle exit plane [Standard design, 50µm needle lift,  $m_{FR} = 0.048$  kg/s]. 266

Figure 6-35: Spatially averaged along the needle lift gap (a) axial (b) circumferential velocity component and resulting deviation angles on the (c) X-Y and (d) X-Z planes around the 360° circumference of the nozzle exit plane for the designs listed in Table 6-III [50µm needle lift,  $m_{FR} = 0.036$  kg/s]. 268

Figure 6-36: Predicted temporal profiles (a) flow rate and (b) mean injection velocity for two nominal injection pulse widths of 0.3 and 0.5 ms. 268

Figure 6-37: (a) VOF and velocity distribution near the nozzle exit, revealing the mechanism of flow detachment from the surfaces of the needle and the cartridge near the nozzle exit plane, as a result of the induced air velocity (b) CCD image taken from a non-cavitating large-scale transparent nozzle [140], showing flow separation at the nozzle exit along the nozzle circumference. The formation of the liquid strings is connected to those air pockets formed at the nozzle exit. 269

Figure 6-38: (a) Mie spray image taken at the end of injection and (b) calculated sample droplet scatter plots coloured according to their velocity, for nominal rail pressure of 200bar, at  $P_{back}=4$ bar and room temperature. 270

Figure 6-39: (a) Numerical grid used for the Lagrangian spray calculations. Sample droplet scatter plots along two planes corresponding to (b) the middle of the flow passage ( $\Phi=0^\circ$ ) and (c) below the lower guides ( $\Phi=45^\circ$ ) at 0.4ms ASOI. Droplets are coloured according to their axial velocity component [Standard design]. 272



# ACKNOWLEDGEMENTS

I am grateful to many people, but I wish to express my sincere gratitude first to my supervisor Dr. Manolis Gavaises, for being my teacher and a generous friend.

Ευχαριστώ παρα πολλοί!

A special acknowledgment for my second supervisor Prof. C. Arcoumanis, for his human and professional support in some crucial moments since I started this adventure at City University as a member of his research group.

I would like to thank Prof. G.E. Cossali, from the University of Bergamo, who has encouraged me with wise advices from the beginning.

I can't imagine which contribution I could bring without the collaboration with Dr. A. Theodorakakos, the 'mind' of the 'GFS group' I have the honour to work with.

I'm very grateful to Dr. J.M. Nouri, for his always jovial and helpful recommendations, and I'm also extremely glad for the opportunity of sharing dreams, crisis and fun with the 'worldwide' PhD students who 'have been living' in the office in the last few years. In particular, I'd like to express special thanks to Manos and Nikos, my CFD and experimental 'angels'.

Since I spent long time of the writing-up in the office at UniBg, I'm grateful to all my colleagues there and especially to Prof. G.E. Cossali and Prof. M. Marengo, who gave me the opportunity to collaborate with them.

I also wish to mention and thank Dr. D. Bouris, Prof. G. Bergeles and the PhD students from NTUA, who always made me feeling welcome during the long periods I spent studying in Athens.

I would like to acknowledge Siemens Automotive VDO, Yamaha Motor Corporation of Japan and BMW for their financial support and their direct contribution to the research programs presented in this thesis.

Last, but certainly not least, I would like to thank my family, for their continuous loving encourage to look at things from the positive point of view and to take anytime the opportunity to learn something more, and Ale for standing by me these last years, for his understanding and for always showing me how life can be so great!



# DECLARATION

I hereby declare that the investigation presented in this thesis is my own work excepted where otherwise indicated.

I grant powers of discretion to the University Librarian to allow this thesis to be copied in whole or in part without further reference to me. This permission covers only single copies made for study purposes, subject to normal conditions of acknowledgement.

London, 13 July 2006

Simona Tonini  
(Simona Tonini)

# ABSTRACT

Computational fluid dynamics methodologies have been achieving in the last decades remarkable progresses in predicting the complex physical process in internal combustion engines, which need to be continuously optimised to get the best compromise between fuel economy, emissions and power output/drivability. Among the variety of computational tools developed by researchers to investigate the multi-phase flow development from high-pressure fuel injection systems for modern diesel and gasoline direct injection engines, the Eulerian-Lagrangian stochastic methodology, which models the air/vapour mixture as continuous phase and the liquid droplets as the dispersed one, has become standard among the developers of commercial or in-house university CFD codes due to its intuitive assumptions and simple implementation. It is generally recognised that this method is specifically suitable for dilute sprays, but it has shortcomings with respect to modelling of the dense sprays present in the crucial region close to the nozzle exit of fuel injection systems. Moreover, the mathematical formulation of the Eulerian-Lagrangian models is intrinsically related to critical numerical issues, like the difficulty of correctly estimating the initial conditions at the nozzle hole exit required by spray modelling calculations and, furthermore, the dependency of the results on the spatial and temporal discretisation schemes used to solve the governing flow equations. To overcome some of these difficulties, a modified Lagrangian methodology has been developed in this study. The interaction between the Eulerian and the Lagrangian phases is not treated on the cell-to-parcel basis, but using spatial distribution functions, which allow for distribution of the spray source terms on a number of cells located within a distance from the droplet centre. The end result is a numerical methodology which can handle numerical grids irrespective of the volume of the Lagrangian phase introduced. These improvements have been found to offer significant advances on Lagrangian spray calculations without the need to switch to Eulerian models in the near nozzle region. Besides these fundamental numerical issues, the present study offers some new insights on the physical processes involved in evaporating sprays under a wide range of operating conditions typical of advanced diesel and gasoline direct injection engines. Attention has been directed on the topic of liquid droplet vaporisation modelling, which has been addressed by implementing and discussing different models published in the literature. Topics of particular emphasis include phase equilibrium, quasi-steadiness assumption, fuel composition, physical properties correlation, droplet shape and energy and mass transfer in the liquid and gas phases. The models have been implemented and validated against an extensive data base of experimental results for single and multi-component droplets vaporising under sub- and super-critical surrounding conditions and then implemented in the in-house GFS code, the multi-phase CFD solver developed within the research group over the last decade. A variety of physical sub-models have been assessed against comprehensive experimental data, which include the effect of thermodynamic, operating and physical parameters on the liquid and vapour penetration of diesel sprays. In particular, the effect of liquid atomisation, evaporation, aerodynamic drag, droplet secondary break-up and fuel physical properties has been thoroughly tested. The sensitivity of the predictions on the numerical treatment of the multi-phase interaction has been investigated by identifying and properly modelling the numerical parameters playing the most crucial role in the simulations. Finally the validated code has been used to investigate the flow processes from three high-pressure injection systems for direct injection spark-ignition engines. These have included the pressure swirl atomiser, the multi-hole injector and the outward-opening pintle nozzle. These investigations have enlightened the crucial role of the accurate modelling of the link between the internal nozzle flow prediction and the characteristics of the forming sprays in term of the successive multi-phase flow interaction, as function of the design of the fuel injection system used.



# NOMENCLATURE

## Abbreviations

1-D	One-dimensional
2-D	Two-dimensional
3-D	Three-dimensional
3-D	Three-dimensional
ASOI	After start of injection
BD	Blended differencing
CA	Crank Angle
CAD	Computer aided design
CD	Central differencing
CCD	Charge coupled device
CFD	Computational fluid dynamics
CPU	Central processing unit
CV	Control volume
ECM	Effective conductivity model
ECM	Effective diffusivity model
FCM	Finite conductivity model
FDM	Finite diffusivity model
FV	Finite volume
GDI	Gasoline direct injection
GFS	General Fluid Solver
HPM	High Pressure Model
ICM	Infinite conductivity model
I-Level	Injector Flow – Low Emission levels by engine modelling
LDV	Laser Doppler velocimetry
LPEqM	Low-pressure ideal equilibrium model
l.h.s.	Left-hand-side
NON-EqM	NON-equilibrium model
PDA	Phase Doppler Anemometry
PDE	Partial differential equation
pdf	Probability density function
PFI	Port fuel injection
UD	Upwind differencing
r.h.s.	Right-hand-side
RMS	Root mean square
STD	Standard
TKE	Turbulent kinetic energy
VCO	Valve covering orifice
VOF	Volume of fluid

## Roman Symbols

A	Area
a	EOS coefficient

---

$b$	EOS coefficient
$B$	Spalding mass transfer number
$C_D$	Drag coefficient
$C_{DEF}$	Deformation coefficient
$d$	Interpolation cell distance
$D$	Diameter
$\vec{F}$	Flux
$g$	Gravitational acceleration
$\vec{i}$	Unit tensor
$m$	Mass
$\dot{m}$	Evaporation rate
$N_c$	Number of cells in interpolation region
$N_f$	Number of species in the mixture
$MW$	Molecular weight
$p$	Static pressure
$partn$	Number of particles in a parcel
$r$	Interpolation region dimension
$R$	Universal gas constant
$R_{CAV}$	Equivalent bubble radius
$\vec{q}$	Flux vector
$s$	Source term
$T$	Temperature
$t$	Time
$t^*$	Inherent fragmentation time
$t_{END}$	Fragmentation over break-up time
$\vec{T}$	Stress tensor
$\vec{u}$	Velocity vector
$V$	Volume
$x$	Mole fraction
$y$	Mass fraction
$Z$	Compressibility factor

### Greek Symbols

$\alpha$	Void fraction
$\beta$	Non-dimensional evaporation parameter
$\beta_t$	Volumetric thermal expansion coefficient
$\delta$	Interpolation cell weighting factor, Dirac function
$\Delta h$	latent heat of vaporisation
$\Delta x$	Distance
$\varepsilon$	Turbulence dissipation rate
$\Phi$	Arbitrary scalar
$\phi$	Fugacity coefficient
$\kappa$	Turbulent kinetic energy
$\Lambda_K$	Knudsen layer thickness
$\lambda_{ci}$	Interpolation region parameter
$\mu$	Dynamic viscosity
$\psi_e$	Molecular accommodation coefficient
$\rho$	Density



$\xi$	Constant
$\theta$	Angle
$\tau$	Time
$\Gamma$	Diffusion factor

**Subscript**

atm	Atmospheric
B	Boiling
c	Continuous phase
C	Convection
CONV	Convective
D	Diffusion
DEF	Deformed
DISS	Dissipation
DROP	Droplet
EFF	Effective
Eq	Equilibrium
f	face
i	Variable index
G	Gas
L	Liquid
NON-Eq	Non-equilibrium
P	Parcel
rad	Radiation
ref	Reference
REL	Relative
S	Surface
tot	Total
TURB	Turbulent
vap	vapour
$\infty$	Surrounding

**Non-dimensional numbers**

Le	Lewis number
Nu	Nusselt number
Oh	Ohnesorge number
Pe	Peclet number
Pr	Prandtl number
Re	Reynolds number
Sc	Schmidt number
We	Weber number

# Chapter 1

You see things and you say 'Why?' But I dream things that never were; and I say, 'Why not?'

George Bernard Shaw

## INTRODUCTION

### 1.1 Background

The development of 'Computational Fluid Dynamics' (CFD) methodologies for prediction of the physical processes in internal combustion engines is a challenging task due to the complex features and phenomena involved [1]. Internal combustion engines are used in every automobile and are the driving force for many electric generators and other industrial and household machines. The main target for scientists and manufacturers of small- and mid-size displacement engines remains the best compromise between fuel economy, exhaust emissions and power output/drivability. Improving the fuel economy of diesel and gasoline engines for automotive applications has a higher priority this decade than at any time since the oil crisis in the 1970's, due to the global warming phenomenon and the correlation between fuel consumption and greenhouse gases, carbon dioxide and particulate emissions. The recent stringent emission legislations have forced the scientific and industrial community to collaborate in the discovery of innovative solutions for modern passenger car engines [2].

The complex nature of the physical and chemical processes occurring within internal combustion engines has motivated researchers to develop sophisticated experimental and theoretical tools for detailed investigations of the relevant phenomena. Due to the increasing maturity of refined computational models and the recent advanced performance of computer hardware, CFD has become a powerful tool to explore the multi-phase flow characteristics in fuel injection systems for modern direct injection engines, investigating the link between the internal nozzle flow distribution and the subsequent spray formation, the interaction of the flow with the developing spray and the successive combustion and pollutant formation processes. These phenomena form a composite system of time and length scales ranging over a wide spectrum, which requires physical processes to be correctly understood.



The precision of CFD simulations is determined by a combination of different factors, which have to take into account the adequacy of the physical models used to mathematically describe the phenomena, the dependency of the predictions on the discretisation techniques implemented and finally the computational time required to obtain a solution. These crucial issues are receiving increasing consideration by the scientific community, which is continuously putting an enormous effort in providing sophisticated and efficient computational modelling solutions.

## 1.2 Motivation

Modelling of the flow processes inside the fuel injection system and the injection nozzle of diesel and gasoline direct injection engines has recently provided better understanding of the near-nozzle spray formation, showing that fuel atomisation process is controlled by the nozzle geometry, the characteristics of the fuel supply system, and the liquid-gas aerodynamic interaction. For these reasons, efforts are currently concentrated in using both experiments and calculations in an attempt to gain better understanding of these phenomena and their effect on performance and durability of emerging diesel and gasoline high-pressure fuel injection systems and their application to direct injection internal combustion engines.

The detailed characteristics of the physical processes taking place inside the nozzle and the combustion chamber have been theoretically investigated using a variety of computational tools. In particular, the vaporisation process of real fuels under the wide range of operating conditions occurring during the engine cycle has been found to significantly affect combustion, encouraging special attention among the researchers with the support of theoretical analysis and computational modelling.

Moreover, the improved performance of computational fluid dynamics have provided sophisticated tools, which can predict complex phenomena in a flexible, accurate, fast and economical fashion [1]. Eulerian-Lagrangian multi-phase flow methodologies, by which the air/vapour mixture is modeled as continuous phase and the liquid droplets as the dispersed one, have been developed over the last decades and implemented in commercial and in-house CFD codes, providing sophisticated solution to thermo-fluid-dynamic problems. The stochastic particle method of Dukowicz [3] is usually

implemented to account for the dispersed phase on a Lagrangian frame of reference, where the properties of the representative droplets are randomly chosen from calculated distribution functions. Many of the fundamental physical processes assumed to take place during the spray development need to be incorporated in the modelling. These include link with the internal nozzle flow conditions, liquid droplet aerodynamic break-up, turbulent dispersion, vaporisation, droplet-to-droplet interaction and wall impingement. With this methodology, phenomenological sub-models are required to account for the various physical processes taking place in the sub-grid time and length scales. The mathematical formulation of the models implemented is intrinsically related to crucial numerical issues, like the dependency of the results on the spatial and temporal discretisation schemes used to solve the equations governing the flow field, the difficulty to correctly estimate the initial conditions at the nozzle hole exit required by spray modelling calculations and the inability of the conventional Lagrangian methodology to compute the dense spray close to the injector region. These factors have an effect on the stability and accuracy of the methods. Special effort needs to be dedicated to address these topics in order to provide efficient tools, which should be developed in parallel with modern experimental techniques for the progress of innovative fuel injection systems for future internal combustion engines.

### 1.3 Present contribution

A modified Lagrangian methodology has been investigated and implemented in the current work with the scope to overcome some of the numerical difficulties arisen by the conventional Lagrangian or Eulerian spray models. In this study, the interaction between the Eulerian and the Lagrangian phases is not treated on the cell-to-parcel basis, but using spatial distribution functions. These allow for distribution of the spray source terms on a number of cells located within a distance from the droplet centre. This distance and the distribution weighing factor may be based on more fundamental spray and single droplet studies. The end result is a numerical methodology which can handle numerical grids as small as possible, irrespective of the volume of the Lagrangian phase introduced. Moreover, mass, momentum and energy source terms, expressing the multi-phase flow interaction, are controlled within their physical limits using semi-implicit procedures during the parcel iterations. At the same time, the model uses variable time steps for the various sub-processes involved, while considering the residence time of



each Lagrangian parcel in every cell of the continuous phase and the corresponding contribution to the source terms left behind. Moreover, Lagrangian parcels of different physical state (i.e. liquid droplet in air and vapour/air bubbles in liquid) may coexist, thus allowing for simultaneous simulation of the internal nozzle flow and the injected spray. At the same time, fully transient as well as ‘pseudo’ steady-state events are simulated, in order to identify similarities and differences due to the various parameters affecting the two-phase flow.

Furthermore, the present study offers some new insights on the physical processes involved in evaporating sprays under a wide range of operating conditions typical of modern diesel and gasoline direct injection engines. Focus has been made to the topic of liquid droplet vaporisation modelling, which has been addressed implementing and discussing different models published in literature, with particular emphasis on the subjects of phase equilibrium, quasi-steadiness assumption, fuel composition, physical properties, droplet shape, surrounding conditions effect and energy and mass transfer modelling in the liquid and gas phases. The models have been implemented and validated against extensive data base of experimental results under a wide range of operating conditions.

The droplet vaporisation modelling has been successively implemented in the GFS code, the unstructured multi-phase in-house CFD code supporting transient flow cases with moving boundaries. This code has been developed by the research group over the last decade and it has been used for the purposes of the present investigation. A variety of physical sub-models are assessed against comprehensive experimental data bases, which include the effect of thermodynamic, operating and physical parameters on the liquid and vapour penetration of diesel sprays. In particular, the effect of liquid atomisation, evaporation, aerodynamic drag, droplet secondary break-up and fuel physical properties is thoroughly tested. Based on the findings, the physical mechanism allowing enhanced predictions of evaporating fuel sprays is identified. Successively, possible errors resulting from the numerical treatment of the interaction of the liquid and the gas phases have been minimised, by implementing static and dynamic grid refinement techniques, imposing specific criteria for source terms distribution expressing the coupling between the two phases and introducing ‘virtual’ local flow

field variables in order to moderate the source terms during the tracking of the parcels and to guarantee that the continuous phase properties will not take non-physical values.

Finally the validated code has been used to investigate the flow processes from three high-pressure spray-guided injection systems for direct injection spark-ignition engines, the pressure swirl atomiser, the multi-hole injector and the outward-opening pintle nozzle. Special attention is given to the link between internal nozzle flow characteristics and the subsequent spray development for a variety of nozzle designs and physical operating conditions. The computational results have been validated against experimental data, including high resolution CCD and high-speed spray images and phase Doppler anemometry measurements, available for fuel injection into ambient air, a constant volume chamber operating at elevated pressures and temperatures and the cylinder of a transparent multi-valve direct injection engine.

The good agreement between computational and experimental results confirms that the developed GFS code is a powerful tool, which can provide accurate predictions of multi-phase flow phenomena.

## 1.4 Thesis outline

The present thesis is structured in seven chapters.

The introductory Chapter 1 briefly illustrates the theoretical background of the current investigation, followed by the outline of the motivations and the main contributions of the present work.

Chapter 2 reviews the most relevant publications on the main topics of research covered by this thesis, focusing on the numerical development of dense spray calculations under high pressure and temperature conditions, on the theoretical and computational implementation of liquid droplet vaporisation modelling and finally on the experimental and computational investigation on high-pressure fuel injection systems for direct injection gasoline engines.

The mathematical formulation of the continuous and dispersed phase modelling is described in Chapter 3 according to the Eulerian-Lagrangian methodology implemented



in the ‘GFS’ code. Successively, the discussion focuses on the numerical implementation of the multi-phase coupling developed for the purposes of this thesis.

Chapter 4 focuses on the mathematical formulation, validation and successive parametrical investigation of single droplet vaporisation modelling, covering the main topics of the subject, which includes fuel composition, phase equilibrium assumptions, heat and mass transfer diffusion in the liquid and gas phase and surrounding conditions effect.

The validated single droplet vaporisation model has been incorporated in the ‘GFS’ code, which is used to predict the spray development from different high pressure diesel injection systems. Chapter 5 enlightens the spray modelling validation against extensive data bases of experimental measurements. Successively the detailed investigation on the physical and numerical parameters of the various sub-models implemented in the code is presented and discussed.

In Chapter 6 the discussion focuses on the investigation of the internal nozzle flow and subsequent spray development from three innovative high-pressure injection systems for direct injection gasoline engines, the pressure swirl atomiser, the multi-hole injector and the outwards-opening nozzle. The computational results have been compared with high resolution CCD and high-speed spray images and phase Doppler anemometry measurements obtained as part of the experimental programme of the research performed in parallel by other members of the research group.

The main conclusions from the current investigation are summarised in Chapter 7, followed by the most important recommendations for future work.

# Chapter 2

Trust one who has gone through it...  
Virgil [The Aeneid]

## LITERARY REVIEW

### 2.1 Introduction

This chapter focuses on the brief discussion of published research on various topics that are relevant to the subjects of the current work. The first section is dedicated to the literary review on the numerical development of dense spray calculations under high pressure and temperature conditions. The focus has been given to the spatial and temporal discretisation issues related to the Eulerian-Lagrangian approximations adopted to predict the physical phenomena.

One of the main contributions made in the current work is the implementation of different liquid droplet vaporisation models from the literature in the GFS code developed to predict the spray characteristics under a wide range of vaporisation rate conditions. Therefore, the second section deals with the extensive literary review on the subject of single droplet vaporisation modelling, starting from the simplest ‘ $d^2$ -law’ and step by step relaxing the more severe assumptions in order to more accurately predict the process.

Finally the main aspects concerning the experimental and computational investigation on high-pressure fuel injection systems for direct injection spark-ignition engines, recently performed by the researchers with the scope to simultaneously increase the engine performance and reduce its emissions, are presented and discussed in the last section of the chapter.

This represents, in synthesis, the fundamental background for the theoretical and computational investigations presented in the following chapters of the thesis. The author refers to Gavaises [4] as the main source for literary review essential to work on spray modelling using the GFS code, co-developed within the research group in the last years.



## 2.2 Numerical developments of dense spray calculations under high pressure and temperature conditions

The performance of direct injection diesel and gasoline engines is highly dependent on the quality of the air-fuel mixture preparation, the injection strategy and the minimisation of cycle-to-cycle and spray-to-spray variations [5, 6]. Penetration of fuel sprays in direct-injection (DI) engines promotes fuel-air mixing, but impingement of liquid-phase fuel on in-cylinder surfaces can lead to increased emissions. As a result, understanding how various parameters affects penetration and which processes control fuel vaporisation in diesel and gasoline sprays are important, both to the engine designer and to those developing multidimensional computational models. Computational fluid dynamics has become an integral part of the analysis and design of automotive products. Recent advances in computer software and particularly in computer hardware enable time-dependent flows within complex geometries to be calculated on readily available computers [7]. Effective models, which provide cost efficient ways of studying different engine geometries, operating conditions and injection strategies are essential tools in modern engine design since they reduce the number of experimental test cases required for product development [8].

The accuracy of CFD simulations is determined not only by the adequacy of the physical models but also from the dependency of the results on the discretisation techniques implemented, as pointed out by Bauman [9]. The interaction of flow with the spray and the subsequent combustion and pollutant formation processes form a complex system of physical phenomena whose time and length scale ranges over a wide spectrum. Its numerical description relies on spatial and temporal averaging and discretisation of the relevant differential equations, which may suffer of accuracy and stability problems. In literature, extensive investigations on adequate scaling factors in order to compensate for the mesh influence have been presented, emphasising the necessity to empirically ‘tune’ coefficients or other inputs to the models by reference to experimental data to obtain satisfactory predictions [1, 10]. It is generally accepted that accurate modelling of the interaction of flows with sprays is a key factor in simulating the whole engine flow and combustion process. The stochastic particle method proposed by Dukowicz [3] is usually implemented to account for the dispersed phase on a Lagrangian frame of reference, where the properties of the representative droplets are



randomly chosen from calculated distribution functions. With this methodology, phenomenological sub-models are required to account the various physical processes taking place in the sub-grid time and length scales. Lippert et al. [11] recently concluded that the physical sub-models related to spray processes employed in in-cylinder CFD calculations are still a long way from being fully predictive and necessarily empirical to some extent. This has multiple causes, not least of which is the tremendous range of scales in space and time that would be required for fully resolving the physical phenomena such as droplet formation from ligament or liquid film atomisation. This crucial process is controlled by a variety of parameters like the nozzle geometry, the characteristics of the fuel supply system, and the liquid-gas aerodynamic interaction. Modelling of the flow processes inside the fuel injection system and the injection nozzle has provided better understanding of the near-nozzle spray formation. Moreover, for evaporating sprays, the initial droplet size distribution influences the fuel-air mixture formation. Recent modelling effort has lead to the successful coupling of the local flow conditions at the injector exit with advanced primary break-up models that account for injector flow induced turbulence as well as cavitation effects on the primary spray break-up processes. Primary and secondary break-up modelling, which accounts for the competing effects of turbulence, cavitation and aerodynamic induced fragmentation processes, is based upon the spatially and temporally resolved injector flow data at the nozzle exit. The turbulence and cavitation induced break-up competes with the aerodynamic one until at a certain distance downstream of the nozzle exit the aerodynamic break-up processes become dominant [12]. Modelling of evaporating spray shows that the gas phase penetration can be strongly dependant on turbulence scales, according to Versaevel et al. [13], and the momentum exchange between the injected liquid and the surrounding air. However, better atomisation achieved by increasing injection pressure alone, is not promoting liquid penetration.

Particular emphasis has been given in the last decade to the influence of the temporal and spatial resolution of the continuous air motion on the computational spray sub-models. Many studies have demonstrated the strong dependence of the method on the grid resolution, as remarked by Subramaniam et al. [14]. Lippert et al. [11] suggested that it is important to distinguish two related but distinct usages of the term ‘grid dependency’. The first relates to the fact that if the resolution of the grid is coarse, the solution may change as the grid is made finer, which is function of the basic



discretisation error. However, if a convergent numerical scheme is employed, the solution will asymptotically cease changing as the grid is made finer and finer, approaching a grid-independent solution. The second implied meaning of the term of ‘grid dependency’ is that as the grid is modified, such as by changing the topology of the grid, a different solution may be predicted. This issue seriously undermines the ability to predict sprays consistently and accurately. The reason for such grid-dependence is that, on one hand, the cell volumes used for the solution of the gas phase equations should be bigger than the volume of the droplets they contain, as imposed by the Eulerian-Lagrangian formulation for two-phase flows, on the other hand, the grid size should be small enough to resolve the gas phase development near the nozzle. These contradictory requirements are not easily satisfied at operating conditions of diesel and gasoline sprays.

Aneja et al. [15] concluded that grid dependency is mainly because of the various sub-models involved and inadequate spatial resolution hindering the coupling between the gas and liquid phases. Lippert et al. [11] distinguished the phase coupling into ‘gas-to-liquid’ and ‘liquid-to-gas’ effects. The first comprises the interpolation process, whereby gas quantities known at Eulerian nodes are estimated at the parcel location. Liquid-to-gas coupling refers to the agglomeration of particle source terms in the Eulerian conservation laws. Beard et al. [16] developed a new Lagrangian-Eulerian coupling method (CLE), introducing a sphere of momentum influence along the parcel trajectories, which improves the phase coupling. Nordin [17] suggested a weighting scheme for the distribution of the liquid/gas source terms that is based on the reciprocal of the distance between the parcel and the eight nearest nodes (in a hexahedral mesh) raised to an integer power, observing that it helps in reducing grid dependency.

Lippert et al. [11] proposed a methodology for momentum coupling that can be applied to meshes of arbitrarily structure, shape and topology, utilising a ‘least-squares based’ interpolation scheme for gas-to-liquid coupling and a kernel smoothing scheme for liquid-to-gas coupling. Break-up, collision and evaporation models were turned off to clarify the effect of the momentum coupling. They concluded that the proposed model is effective, even for coarse meshes, in eliminating grid artifacts in the spray shape. The model also predicts the monotonic behaviour of tip penetration, calculated according to the 98 percent of the liquid mass as a well-known measure of the spray characteristics,



which should increase as the mesh density approaches finer resolution. This cannot be guaranteed with the standard method of phase coupling, which calculates the gas-to-liquid and the liquid-to-gas transfers according to the cell hosting the parcels.

Further complications are realised in the modelling of droplet-to-droplet interactions. Barroso et al. [18] and Larimi et al. [19] found that liquid penetration result to be highly dependent on grid-resolution if coalescence is taken into account. The Void Fraction Compensation method (VFC) by Hieber [20] compensates the lack of spatial resolution by correcting the droplet density in each cell according to a predetermined average liquid void fraction. This methodology has been proved to be effective in spray computations where the mesh resolution is very low. Therefore, the VFC method might be useful in simulations of large bore diesel engines, but it is not offering improvements in the near nozzle flow field where atomisation, secondary break-up, vaporisation and momentum exchange are far more important processes.

To overcome the above numerical problems, some authors have computed the spray atomisation and vaporisation processes not using a fully 3-D CFD model but using a simpler 1-D one, which provides add-hoc source terms (from mass, momentum and energy exchanges) as input to multi-dimensional CFD codes. With this approach, grid-independent results can be obtained because the source terms coming from the 1-D model are not at all dependant on the multi-dimensional mesh resolution. On the other hand, the results of the 1-D model are highly dependant on the initial droplet diameter, which can be considered as an adjustable constant [13].

Recent studies remarked that real sprays show mesh dependence, mainly attributable to the insufficient resolution of the liquid-gas momentum transfer, as a consequence of the inadequate space resolution of the strong velocity and vapour concentration gradients. The liquid phase is injected typically with a velocity of hundreds of meters per second into an almost quiescent environment, thereby creating strong velocity gradients, especially at the nozzle exit [20]. Liquid phase penetration is sensitive to the cell size especially for small droplets and increased gas density. Hence, if the computational cells are small enough to capture the velocity gradients close to the injector, this will result in a gaseous jet with velocity close to the liquid and, thus, a low relative velocity. When the grid is too coarse, the numerical diffusion, together with the fact that the



momentum increase yields a lower increase in velocity, results in a much higher relative velocity [17]. Local mesh refinement can be utilised for the resolution of small-scale flow structures near boundaries and in regions of high gradients [21]. Other studies give evidence that simulations in a constant volume chamber are more sensitive to spatial and temporal resolution and to injection profile than in the engine combustion chamber [18]. For the time being, comparative studies between different operating conditions are still possible as long as the same mesh is used and the operating conditions are not too different [22]. The integration of fully automatic adaptive mesh refinement into the solution process, the generation of meshes and their new boundaries, the transfer of history-dependent field variables from the old mesh to the new one and the definition of the proper criteria for refinement as a function of the phenomena taking place suggest the main steps to be followed for further investigations, as described in Tristano et al. [23], Wan et al. [24] and Malik [25]. Finally, Steiner [26] recommended that the demand for CFD models for industrial applications, with a high degree of predictability and low computational cost, should require “intelligent meshing strategies” making crucial the resolution of relevant length-scales, the definition of realistic boundary conditions, with a proper coupling between cavitating nozzle flow and spray calculations, and the validation of physical sub-models predicting the spray processes near the nozzle orifice.

Although fuel sprays are usually modelled using a Lagrangian treatment of representative parcels of droplets, it is generally recognised that this method is especially suitable for dilute sprays, but it has shortcomings with respect to modelling of dense sprays [12]. Further problems are reported, connected with bad statistical convergence [27] and also with dependence of the propagation of the spray on grid size [28]. An alternative approach has been proposed by v. Berg et al. [29] and Tomiyama [30], who implemented a modified two-fluid Eulerian/Eulerian method treating different size classes of the spray droplets as separate, interpenetrating phases and solving conservation equations for each of them. The model is based on an Eulerian multiphase approach that has been derived from ensemble averaging of the conservation equations [31]. For each phase, mass, momentum and energy conservation equations are solved as well as corresponding equations for the turbulent kinetic energy and its dissipation rate. Within each computational cell the droplet phases are characterised by a certain volume fraction. The model has been applied to Diesel injection test cases



using simplified but typical spray conditions. Effects of inlet conditions, various drag formulations and basic functionality of the secondary breakup, evaporation and collision models have been tested successfully. A disadvantage of this method is that the number of equations to be solved dramatically increases when the droplet size distribution becomes wider and therefore the number of droplet size classes increases. This is the reason why Platzner et al. [32] suggested to predict the particle size distribution using a maximum entropy formalism. The droplet size distribution, their volume fraction and velocities will be eventually used as input conditions for a Lagrangian method which allows a reliable prediction of sprays by accounting for all the relevant physical effects.

Recently, Lebas et al. [33] and Beau et al. [34] proposed a 3-D model for atomisation based on a Eulerian single-phase approach, which improves the treatment of the interaction between the liquid and the gas phases in the very dense spray region, close to the injector nozzle. This approach considers the liquid and the gas phases as a mixture of a single flow with variable density. The method switches to Lagrangian calculations when the spray is considered to be diluted enough based on a dilution criterion, such as a critical value of the liquid volume fraction. The work suggests the innovative implementation of hybrid Eulerian-Eulerian and Eulerian-Lagrangian methodologies, which represent a promising solution to the discussed numerical issues related to multi-phase flow modelling.

### **2.3 Liquid droplet vaporisation modelling**

The vaporisation process taking place in a liquid droplet immersed in a gaseous environment involves simultaneous heat and mass transfer. The heat for vaporisation is transferred to the droplet surface by conduction, convection or radiation from the surrounding gases and the vapour is transferred by convection and diffusion back into the gas flow field. The overall flow rate of vaporisation depends on the pressure, temperature and transport properties of the gas, the temperature, volatility, size of the droplet and the velocity of the droplet relative to that of the surroundings. The droplet evaporation process includes the detachment of fuel molecules from the surface of the droplet into gas in the immediate vicinity of droplets (evaporation proper) and the diffusion of fuel vapour from the surface of the droplet into the ambient gas [35]. Due to



the complexity of the mathematical formulation of the first processes, the researchers, in most practical applications, have focused only on the prediction of the second one. The most common models, known as ‘hydrodynamic models’ of droplet evaporation, are based on the assumption that fuel vapour in the vicinity of the droplet surface is always saturated implying that the rate of fuel evaporation is equal to the rate of fuel diffusion from the droplet surface to the ambient gas. Parallel to these, some researchers have focused on the details of detachment of fuel molecules developing models, which are based on the kinetic Boltzmann equation, ‘kinetic models’, or on the modelling of the dynamics of individual molecules, ‘molecular dynamics models’. In this review only the main contributions on hydrodynamics modelling are presented and discussed.

The theory of fuel droplet vaporisation has been intensively developed during the past several decades. Schrage [36] and Fuchs [37] presented theoretical discussions on the subject of droplet vaporisation in the early fifties. Since then, a large number of monographs and review papers have been published, trying to cover all the aspects of the phenomena of droplet heating and vaporisation. The most representative are those of Spalding [38], Clift et al. [39], Faeth [40], Givler et al. [41], Sirignano [42], Bellan [43], Bird et al. [44] and Sazhin [35].

A variety of different models have been proposed in order to capture the physical phenomena involved in the process. It is possible to classify these models into two categories: (a) extended models studying the physics of a single vaporising droplet, deriving simplified correlations and validating simpler models; (b) models to be implemented in more complex whole-spray simulations. Other classifications of these models are related to the spatial resolution of the heat and mass diffusions in the droplet interior, the nature of the droplet composition (either single- or multi-component), the definition of the property estimation methods including high-pressure effect and the validity of the assumption of ‘in-equilibrium conditions’ at the liquid/vapour interface. In the following section the main contributions on the subject of droplet vaporisation are presented and discussed, focusing on the ideal equilibrium, multi-component and high pressure vaporisation modelling.

### 2.3.1 Ideal equilibrium droplet vaporisation modelling

The simplest model for droplet evaporation was suggested by Maxwell back in 1877 [37]. According to this model, the rate of droplet evaporation is controlled exclusively by the diffusion process. Godsave [45] and Spalding [46] proposed what is universally recognised as the first contribution on single droplet vaporisation modelling, known as the ‘classical  $d^2$ -law’. It was derived for an isolated, pure-component droplet burning in a quiescent, oxidising environment; it neglects the liquid heating assuming the droplet temperature to be uniform and constant at its wet-bulb state and it forces Lewis number to unity in the gas phase near the droplet. The direct proportionality of the square of the droplet size function of time suggests its name. Its limitation lies in the fact that it takes into account only the diffusion process, but ignores the effect of convective flow of the mixture of gas and fuel vapour away from the surface of the droplet (Stefan flow).

The majority of the models present in literature assume that the Soret and Dufour effects, which can occur simultaneously, can be neglected. The first one describes the flow of matter caused by a temperature gradient (thermal diffusion), while Dufour effect describes the flow of heat caused by concentration gradients [47]. Both effects are believed to be small in most cases although sometimes their contribution may be significant [48]. Moreover, in most models of droplet evaporation the ambient gas is assumed ideal. This hypothesis becomes questionable when the pressures are high enough, as observed in internal combustion engines. Another simplification widely used in droplet heating models is the assumption that the temperature over the whole droplet surface is the same (although it can vary with time). This assumption effectively allows the separation of the analysis of heat transfer in gaseous and liquid phases. The errors introduced by this assumption in intermediate conditions are generally assumed to be acceptable [35].

Accurate prediction of the thermo-transport properties is an essential part of modelling droplet evaporation phenomena, as the evolution of the vapour-gas mixture directly influences the liquid mixture’s response to the ambient, and subsequently the evaporation, mixing and combustion process. Most of the methods proposed in literature solve the crucial issue of the ‘property estimation method’, PEM, by using polynomials as strong functions of temperature composition, and in some instances of



pressure. Many researchers found that when constant liquid thermo-physical properties are assumed, large deviation of the results are predicted compared to the more detailed variable properties approach, especially in the second half of the droplet lifetime, due to the increase of the mass diffusion coefficient, up to five times higher than the initial value, while the liquid thermal diffusivity decreases only to half of its initial value. In particular, the assumption of unity Lewis number, result of the constant property calculation of Schmidt and Prandtl numbers, implies equal mass and heat diffusion in a flow field less dominated by convective effects. On the contrary, in most convective conditions, the mass diffusion is most likely two-orders of magnitude slower than the thermal diffusion, and the unity Lewis number assumption may not be justified. Moreover, the uncertainty in the prediction of the droplet lifetimes seems to be due to the accuracy in the estimation of gas-phase properties, since the liquid-internal transport has a less pronounced effect on droplet lifetime. Hubbard et al. [49] investigated the effect of transient and variable properties for a single droplet vaporising into an infinite stagnant gas environment, implementing different reference property schemes and finally concluding that for the purposes of engineering calculations, the most appropriate scheme for property estimation is the well known '1/3 rule'. They also enlightened the important fact that the transient evaporation of single droplets into an infinite stagnant gas is independent of initial size, provided time is scaled with respect to the initial radius squared, suggesting non-dimensional lifetime as one of main parameters for the characterisation of the droplet vaporisation phenomena.

In the case of moving droplets, convection heat transfer takes place, which incorporates bulk fluid motion (advection) and diffusion (conduction) effects. Fundamental experimental studies on liquid droplet evaporation under convective environment were performed by Frössling [50]. On the basis of a dimensionless analysis, he derived the well-known relationship for the Sherwood number as a function of Reynolds and Schmidt numbers. For the determination of the correlation constant, he investigated the evaporation of water, nitrobenzene, and aniline droplets suspended in air. Ranz et al. [51] conducted experiments on the evaporation of pure-component droplets suspended from a feed capillary with a diameter of about 80 $\mu$ m. In the capillary they put a thermocouple for droplet temperature measurements. The droplet was observed through a microscope and its image was recorded on a motion picture film. The droplet diameters were measured frame by frame on a microfilm viewer. From their



experiments, they determined evaporation rates at different ambient conditions and used their results to modify the coefficient of Frössling's correlation. Their relationships for Nusselt and Sherwood numbers are still used today in numerical models in order to account for convection. Downing [52] continued the work of Ranz et al. [51] using the same experimental techniques and investigating millimetre size droplets of pure liquids (n-hexane) at temperatures from 300 up to 613K for Reynolds numbers from 24 up to 325. In the analysis of the data obtained in all these experiments, the drop surface temperature was not estimated but assumed to be the temperature of adiabatic saturation. Their analysis also suffered from inaccuracies in determining the values of water vapour diffusivity and terminal velocities of the water drops. Beard et al. [53] performed measurements of small water drops falling freely at terminal velocity in a wind tunnel. The air stream was directed upwards and controlled by a valve so that the droplet was kept stationary. The initial droplet size ranged from 70 up to 375 $\mu\text{m}$ . A minimum size of 27 $\mu\text{m}$  was investigated. For the determination of the evaporation rate, they used drag correlations for droplets and their measurements of the terminal velocity. For low Reynolds numbers, they found that the Sherwood number smoothly approached a value equal to 2, as commonly assumed under low convective environment conditions.

Computational investigations concluded that for stationary droplets the thickness of the boundary layer around droplets can be infinitely large. In the case of moving droplets, however, this thickness is always finite. All these differences between the heat transfer processes in the case of stationary and moving droplets required the development of different methods of analysis. Sirignano et al. [54], through a combination of stagnation-point and flat-plate analysis, concluded that the convective cases cannot be treated by a correction on the spherically symmetric case and Prakash et al. [55] first introduced a gas-phase boundary layer outside the droplet and a Hill's vortex in the droplet core with thin viscous and thermal boundary layers near the droplet surface and in-viscid internal wake near the axis of symmetry. This model, although quite detailed, is too cumbersome to be included in a complete combustion analysis. Tong et al. [56] proposed a simplified model, the so-called 'film theory', which assumes that the resistance to heat and mass exchange between a surface and a gas flow may be modelled introducing the concept of gas film of constant thickness, whose values can be influenced by the Stefan flow.



Yuen et al. [57] showed that particle drag is affected by droplet evaporation in two different ways. First, the temperature and concentration gradients, between the droplet surface and the ambient, cause substantial reduction in the absolute gas viscosity, which decreases friction drag. Second, evaporation affects the boundary layer surrounding the droplet. This blowing effect reduces friction-drag and increases form-drag. At low Reynolds number, the droplet drag coefficient is close to that for a solid sphere of the same diameter. However, at high convective flows heat, mass and momentum transfers of a vaporising droplet manifest much more complex phenomena than its solid counterpart. For example, a decrease in viscous drag (due to blowing effect) is accompanied by an increase in pressure drag of similar magnitude. In order to account for both variable properties and blowing effects, large numbers of steady-state correlations for drag as well as heat and mass transfers have been proposed [57, 58, 59]. The appropriate Reynolds number that is used to compute the drag coefficient from the standard curve for a sphere is then based on the '1/3-rule' for viscosity.

Aggarwal et al. [60] proposed a critical comparison of different gas and liquid phase models used to predict the heating process of a single-component isolated droplet for both stagnant and convection situations in a high-temperature environment. They compare the 'd<sup>2</sup>-law', which neglects the liquid heating assuming the droplet temperature to be uniform and constant at its wet-bulb state, with the 'infinite conductivity' model, which predicts a uniform, but time-varying droplet temperature and the 'conduction limit' model, which studies the droplet heat transfer mainly controlled by thermal diffusion. They concluded that the 'd<sup>2</sup>-law' gives poor agreement with the other models, and therefore it should be discarded in practical cases. The 'infinite conductivity model', on the other hand, may be useful in the low ambient temperature case, when the droplet lifetime is long compared to the heating-up time, while the 'conduction limit model' should be used for detailed liquid temperature distribution profiles. The results also pointed out that the 'conduction limit' model initially predicts higher droplet surface temperature and therefore faster vaporisation rate compared to the 'infinite conductivity' model, while this trend is reversed at later times. They also found that when the droplet vaporises in a convective environment, the gasification rate increases compared to the stagnant case, and the liquid circulation generated in the droplet interior enhances the liquid-transfer rate. In order to simulate the effect of a convective vaporisation, they proposed the Ranz et al. [51] and the Tong



et al. [56] correlations, which correct the equations describing the stagnant case with empirical or purely theoretical relationships. The results suggested that the Ranz et al. [51] correlation over-predicts the vaporisation rate, while the Tong et al. [56] model results to be valid only when the Reynolds number is large compared to unity, remarking that a proper calculation of the convective effect contribution on droplet heating and vaporisation is crucial in practical applications. They also used the droplet heating models for spray vaporisation predictions, concluding that the prediction of liquid heating has an effect on the calculated vapour distributions, especially during the early stages of the vaporisation period, with considerable consequence on successive combustion calculations.

The classical model was substantially refined by Abramzon et al. [61] including variable physical properties, non-unitary Lewis number in the gas phase, Stefan flow (blowing) effect on heat and mass transfers, transient liquid heating inside the internally circulating droplet. Gas phase calculations are based on the 1-D ‘stagnant film theory’, which introduces the blowing effect on film thickness of the thermal and diffusional films. Some of the main oversimplified assumptions of the classical vaporisation model have been relaxed: the Lewis number may vary considerably during the vaporisation period, the Stefan flow effect may depend on the droplet Reynolds number and the transient liquid heating represents a controlling factor of the droplet vaporisation rate. Liquid circulation inside the droplet is found to considerably change the time scale of internal heating processes. A detailed step-by-step procedure to analyse the gas-phase vaporizing phenomena was proposed. The liquid phase analysis suggested four models to describe the droplet heating history: the ‘infinite conductivity’ or ‘rapid mixing limit’ model, which is based on the assumption that there are no temperature gradients inside the droplet, the ‘conduction limit model’, which takes into account finite liquid thermal conductivity, but not the liquid re-circulation, the ‘extended liquid heating’ or ‘Hill’s vortex model’, which describes the recirculation inside the droplet in terms of vortex dynamics, and finally the ‘effective conductivity model’, which takes into account both finite liquid thermal conductivity and re-circulation inside the droplet via the introduction of a correction factor to the liquid thermal conductivity function of the instantaneous liquid Peclet number. The first two represents the two extremes bounding the possible wide range of real conditions. The multi-dimensional ‘extended model’ predicts the vaporisation process in a more precise way, but its complexity may not be



suitable for spray calculations. The ‘effective conductivity’ model agrees very well with the results predicted by the ‘extended model’; since it requires a reasonably limit amount of computational time per single droplet life story, it is recommended by the author in performing spray combustion calculations. Sirignano [42] proposed a similar classification of the models of droplet heating in order of ascending complexity suggested by Abramzon et al. [61]. Comparing the heat-up time with the droplet lifetime, he distinguished three cases. (i) The droplet heat-up time is very small compared with its lifetime. Then the interior liquid is heated quickly and a uniform liquid temperature equal to the wet-bulb temperature at the surface can be assumed. In this case the assumption of steady-state evaporation is valid and the ‘classical  $d^2$ -law’ approximates the vaporisation process in a good way. (ii) The droplet heat-up time is of the same order of magnitude of its lifetime. Then the heat-up process has to be taken in consideration and the use of transient but averaged liquid temperature, according to the ‘infinite liquid-conductivity model’, ICM, predicts the correct vaporisation phenomena. (iii) The heat-up time is much larger than the droplet lifetime and needs special investigation. This case occurs with large temperature gradients between the two phases, small liquid thermal conductivity, or large liquid heat capacity, which create a quasi-steady thermal thin layer close to the liquid surface region. Consequently, the droplet vaporisation in stagnant or convective environments is modelled by the ‘conduction limit model’, FCM, or the ‘effective conductivity model’, ECM, respectively. He also included as last class the models based on the full solution of the Navier–Stokes equations. This model is identified to be too complicated for application in most CFD codes, whereas it is widely used for validation of more basic models of droplet heating, or for in-depth understanding of the underlying physical processes.

Very few researchers have studied the effect of ambient turbulence on the droplet vaporisation in forced convection conditions. Wu et al. [62] conducted an experimental investigation on the effect of ambient turbulence and fuel properties on the evaporation rate of single droplets at room temperature, with the aim to correlate the laminar and turbulent evaporation rates through the effective vaporisation Damkohler number, defined as the ratio between the turbulence eddy timescale based on the initial droplet size and the vaporisation timescale based on the film theory proposed by Abramzon et al. [61], as first introduced by Gokalp et al. [63]. They concluded that the ambient turbulence effect is more pronounced as the droplet becomes smaller. The results show



that the time history of droplet diameter follows the ‘ $d^2$ -law’ in turbulent environments with generally higher evaporation rates as compared with those in quasi-laminar cases; they also proposed a correlation between the droplet evaporation rate in laminar environment and the total evaporation rate due to ambient turbulence. Other recent studies focused on the analysis of the effects of turbulence on droplet evaporation have been proposed by Birouk et al. [64] and Wu et al. [65].

The effect of radiation absorption on heating and evaporation in a single droplet has been studied in Harpole [66], Lage et al. [67, 68], Dombrovsky [69], Dombrovsky et al. [70, 71], Sazhin et al. [72] and Abramzon et al. [73]. Lage et al. [67] based their analysis on the solution of Maxwell equations with the boundary conditions at the droplet surfaces (Mie theory), predicting the distribution of the radiation absorption inside a liquid water and n-decane droplet due to external blackbody radiation. The results suggested that the effect of radiation absorption for n-decane droplet is relatively small, around 2 percent, and it can be equivalent to the selection between different liquid-phase models, such as the ‘conduction-limit’ or ‘infinite-conductivity’ assumptions [73]. Their model is certainly very accurate, although it is inadequate for practical applications in CFD codes. Dombrovsky et al. [70] proposed a simpler model, which introduces an average absorption efficiency factor, which represents the fraction of incident radiation absorbed by droplets. The model ignores the effects of differential absorption of thermal radiation inside then droplets, which have been successively taken into account in Dombrovsky et al. [71]. It was found that thermal radiation has a pronounced effect on the vaporisation rate of diesel fuels. Within the available range of spectral absorption data, the effect of thermal radiation on the vaporisation rate of diesel is considerably stronger than for n-decane, especially in the regions of semi-transparency, attributable to the contribution of additives in diesel fuel. Due to its quite simple formulation, this model offers a realistic solution for computational spray applications [73].

When highly accurate calculations are not required, but CPU time economy is essential, then the effect of finite thermal conductivity and recirculation in droplets can be taken into account using the ‘parabolic temperature profile’ model proposed by Dombrovsky et al. [74], which shows good accuracy at large times, but can differ considerably from



the numerical results for small times. The implementation of this generalised model into CFD codes has not yet been investigated [35].

In most of the computational investigations published over the last decades on single droplet vaporisation the drop shape has been assumed to remain unchanged in time. However, Dai et al. [75] observed that droplets in real combustion applications are subjected to significant turbulent dispersion. Eddies accelerate droplets, likely causing significant droplet distortion. This distortion may have implications on droplet heating-up. The details of this acceleration and the coupling with droplet distortion are currently very difficult to calculate. However, simplified models are available. A numerical model has been used to investigate the effect of droplet oscillation on internal heat transfer. The working hypothesis was that droplet oscillation would make the temperature within oscillating droplets more uniform. This trend was observed, however the magnitude of the effect was very small. Consequently, the effect of droplet distortion on internal heat transfer can be neglected for Biot number less than 0.25 and initial distortions less than 35 percent. It should be noted that the case investigated in this work was for a droplet subject to an initial perturbation and then allowed to stabilise. The effect of oscillations might be greater in a drop subject to continuous perturbations, such as in turbulent flow. Unfortunately, most of the vaporisation models in the literature, including those that account for liquid core circulation do not include the effects of distortion, which was found to increase the effective surface area available for evaporation [76]. A detailed numerical study of an evaporating and deforming droplet by Haywood et al. [77] suggests that the internal circulation tends to form the drop into a prolate spheroid, and not an oblate spheroid as would be expected. These authors, however, didn't investigate the distortion effect on the Reynolds number, although their numerical study agrees well with the experimental observation of Renksizbulut et al. [78]. Arcoumanis et al. [76] included the distortion effects on vaporisation on the non-dimensional heat and mass transfer coefficients. The modification on the Reynolds number is based on the equivalent diameter of a spheroid corresponding to highly convective spray flow conditions. The results showed that the inclusion of the distortion in the evaporation model has a far more dramatic effect on vaporisation than, for example, accurate calculation for the internal temperature distribution. Finally, Mashayek [79] concluded that the rate of evaporation is increased if the amplitude of deformation varies significantly along the surface of a drop. These

preliminary conclusions suggest that the subject of droplet deformation requires further investigation, which will certainly add new insights to the complex topic of droplet vaporisation.

### 2.3.2 Multi-component droplet vaporisation modelling

The droplet evaporation models described in the previous section have been based on the assumption that liquid consists of one component only. In most practical applications, real fuels are blends of more than hundreds of compounds with a wide variety of thermo-physical properties. The behaviour of an isolated droplet changes significantly according to the nature of its composition, in particular the transient thermal and especially mass transport may be the rate-controlling factor and must be included in the vaporisation modelling. Multi-component fuel droplets exhibit certain features like micro-explosion not found in single component droplets [80]. This phenomenon may occur when the volatile component is trapped inside the droplet due to the high mass diffusion resistance in case it is heated beyond its boiling point. Moreover, multi-component effect have been found to play a crucial role, especially during ‘cold-starting’ engine conditions, when the ambient gas temperature is low and the highly volatile components play an important role for ignition and burning engine processes.

Law [81] first studied the combustion phenomenon of a multi-component droplet assuming vapour phase to be quasi-steady and modelling the liquid-phase processes with the ‘infinite diffusivity’ model. Law [82] investigated multi-component droplet vaporisation using the ‘diffusion-limit’ model for both energy and species transports in the liquid phase. He also explored the possibility of micro-explosion in the droplets, limiting the study to pure vaporisation only. Successively, Law et al. [83] developed a ‘ $d^2$ -law’ for multi-component droplets analogous to that for single component droplets using steady-state transport equations for the liquid phase.

The multi-component nature of liquid fuels was investigated in Aggarwal [84], focusing on the sensitivity of the liquid and gas-phase models on the liquid vaporisation behaviour. ‘Infinite-diffusion’, ‘diffusion-limit’ and ‘vortex’ models have been compared for the liquid phase, while two correlations have been discussed for the gas



phase. The first conclusion they derived is that the assumption of quasi-steadiness of gas-phase processes in the film surrounding the droplets is valid for cases with pressure much lower than the critical value and for ratio of initial gas density to liquid density much smaller than unity. The comparison between the models predicting the liquid phase diffusion suggested that the ‘infinite-diffusion’ assumption grossly over-predicts and under-predicts the vaporisation of the volatile and non-volatile components, respectively. Moreover the predictions of ‘diffusion-limit’ and ‘vortex’ models are in a good agreement, due to the fact that the internal circulation does not affect the transport rates inside the droplet in any significant way and it causes uniformity of temperature and concentration only along the streamlines. At high Lewis number, the internal circulation results in almost uniform temperature distribution, but not uniform concentration distributions. In analogy with the heat transfer process modelling, the authors suggested that the effect of liquid motion may be incorporate in the ‘diffusion-limit’ model by introducing an effective diffusivity, function of Reynolds number and the initial composition. Generally the multi-component nature of a fuel should be taken into account for accurate predictions, when the initial liquid composition of each constituent is more than 10 percent. The Ranz et al. [51] correlation for the gas-phase modelling was compared to the simplified axis-symmetric model proposed by Abramzon et al. [61]. Since the first one over-predicts the fuel mass fractions of both volatile and non-volatile components, while the second one results valid only with significant Reynolds numbers, the authors suggested to switch from one model to the other according to the specific operating conditions.

Megaridis et al. [85] proposed a numerical investigation on the processes governing the vaporisation of a multi-component isolated liquid droplet in a convective environment, accounting for variable thermo-physical properties, surface blowing effect, internal liquid heat and mass circulation. The results show the preferential vaporisation of the more volatile species, which leads to the gradual reduction of its concentration, having its maximum value in regions close the center of the internal liquid vortex formed inside the droplet. Under the assumption of equal binary diffusion coefficients for all the species, the non-Fickian terms in the diffusion equation result to be equal to zero. The assumption of Fickian gaseous diffusion results not to affect the time-wise variation of Sherwood number for the heaviest component, but it has a more important effect on the corresponding values for the more volatile species. The authors remarked that the wide



range of time scales involved in the single-component droplet vaporisation becomes even wider for multi-component vaporisation since the liquid-phase mass diffusion characteristic time is at least one order of magnitude larger than the droplet lifetime. On the other hand, the gas-phase time scales are much smaller. The potential of micro-explosion was also investigated, calculating the equilibrium vapour pressure distribution in the droplet interior through the droplet lifetime using the Raoult's law in conjunction with the Clausius-Clapeyron equation. The results reveal that the calculated vapour pressure remains at least 10 percent lower than the ambient pressure, indicating no possibility for catastrophic fragmentation.

The importance of variable liquid properties on droplet evaporation was investigated by Kneer et al. [86] who found that the predictions are highly affected by the dependence of liquid properties on temperature and composition. In particular, they concluded that variable liquid diffusion coefficient controls the relative thermal and mass diffusion, and in turn, the rate of evaporation. They employed a 'diffusion-limit' model, using a uniform mesh for the non-dimensional spatial (radial) coordinate of 100 grid points, although detailed studies revealed that the number of grid points can be reduced down to 20 resulting only in minor deviations of the solution. The predictions assuming constant liquid thermo-physical properties produced large deviation in the results compared to the more detailed variable properties approach, particularly in the second half of the droplet lifetime. This is caused by the considerably increase of the mass diffusion coefficient, which raise to a value about five-times higher than its initial value. The authors also proposed a different approach, with a quasi-constant properties formulation that updates the liquid properties after each time step is executed. Since it requires approximately the same amount of computing time of the variable properties formulation, they concluded that the constant properties approach should be preferred once improved with the introduction of proper temperature and composition reference values. They suggested a reference value dependent on the gas temperature, which leads to higher temperatures, implying higher diffusion coefficient and consequently better results, closer to the variable-property model predictions.

The models presented in this section are based on the discrete description of the species contained in the mixture. This is applicable only in the case when the number of components in the droplets is small. In realistic cases, such as diesel or gasoline fuels,



when the number of components in a droplet is measured in hundreds, this approach ceases to be practical [35]. An alternative approach is based on so called ‘continuous thermodynamics’ concept, which characterises some macroscopic aspects of the components in the mixture, such as the molar mass, the boiling point, the degree of aromaticity or Lewis basicity, with a continuous distribution function. The main advantage of this model is that it adds only two equations to the computational algorithm, one describing the variation of the mixture mean molecular weight and the second one expressing the change of the distribution function variance. As in the conventional approach, it is assumed that the diffusion coefficients for all the components are the same. The theoretical study and the derivation of the model equations are given in Tamim et al. [87], Lippert [88] and Harstad et al. [89]. A continuous distribution function is able to describe the fuel composition of a homologous group with similar boiling points. Moreover, in order to investigate fuels with additives or components with significantly differing vaporisation properties, Abdel-Qader et al. [90] proposed multiple continuous distribution functions, which add more details to the fuel modelling, suggesting also that the ‘well-mixed’ liquid diffusion assumption (infinite-diffusivity limit) is a reasonable hypothesis for spray application modelling.

Lately, Burger et al. [91] introduces a new computationally effective model for multi-component droplet evaporation, the ‘Distillation Curve Model’ (DC model), which implements the distillation curve of actual multi-component fuels, like kerosene, diesel or gasoline. The model calculates the fractional boiling during the droplet evaporation process as a function of a single variable, expressing the actual mean molar mass of fuel inside the droplet. Pre-computed physical properties and lookup tables have been generated in order to improve the efficiency of the model. The numerical algorithm is based on algebraic equations, which brings clear advantages from the point of view of CPU efficiency [35], suggesting innovative solutions for droplet vaporisation modelling.

### **2.3.3 Super-critical droplet vaporisation modelling**

Investigations of the droplet vaporisation behaviour at high pressure and temperature conditions typical of modern diesel and gasoline engines lead to further great interest

and engineering challenges. In such environments, the phenomenon of trans-critical and super-critical vaporisation is likely to occur, arguing on the validity of common assumptions of low-pressure vaporisation models. Under high pressure and temperature conditions the gas-phase non-idealities and the liquid-phase solubility of gases, which are negligible at low pressures, become essential considerations. Furthermore, a single-component fuel droplet assumes a multi-component behaviour and liquid mass transports in the droplet interior become central processes. Secondly, as the droplet surface approaches the trans-critical state, the latent heat reduces to zero, the gas and liquid densities become equal at the droplet surface and the transient effects in the gas phase assume crucial role as those in the liquid phase, since the characteristic times for transport processes in the two phases become comparable. Furthermore, the dependence of liquid and gas-phase thermo-physical properties on temperature, composition and pressure [92] cannot be ignored. Under these conditions, the researchers have proposed a new methodology to predict the thermodynamic equilibrium for each species in the mixture introducing the phase fugacity coefficients, which are calculated implementing a virial equation of state (EOS). The most commonly used equations of state are the cubic Peng-Robinson EOS [93], the Redlich-Kwong EOS [94] and the Soave-Redlich-Kwong EOS [95]. Relevant publications on the subject of fluid-phase equilibrium can be found in Prausnitz et al. [96], while detailed descriptions on the computational implementation of the numerical algorithms used for high-pressure vaporisation modelling are proposed in Patankar [97], Cotterman et al. [98] and Wei et al. [99].

Jin et al. [100] proposed an analysis of multi-component fuel droplet vaporisation under elevated pressures and temperatures, with emphasis on the liquid heat and mass transfers and high-pressure phenomena. Gas is assumed to be dissolved only in a very thin layer of the liquid surface, neglecting their diffusion inside the droplet. They found that high-pressure environment significantly increases the transient effects. Under these conditions, it is necessary to implement temperature, composition and pressure dependent transport properties. They estimate the contribution of radiation heat on liquid phase heat-up to be about 2%, therefore it can be neglected in the calculations. For multi-component droplet vaporisation, the parameter more sensitive to liquid internal circulation seems to be the residual percentage of the more volatile component mass, while as the pressure increases, it is more difficult for a volatile component to vaporise preferentially. The phenomenon of micro-explosion under high-pressure



droplet vaporisation was also examined. Multi-component droplet seems to less likely reach its thermo-dynamically critical points, because the more volatile species have higher critical pressures. At elevated pressure the potentiality for micro-explosion occurring seems to be low, because the volatility difference among the constituents decreases and the local equilibrium is not enough to maintain build-up and development of vapour bubbles.

Unsteady vaporisation of a droplet in a high-pressure quiescent environment was investigated by Delplanque et al. [101], who argued on the validity of classical laws and approximations and highlighted the necessity to introduce super-critical effect in the vaporisation models. The results suggested that the quasi-steady theory is not valid for reduced pressures above 0.1. Moreover, the ideal gas assumption does not correctly model the liquid-vapor equilibrium under high pressure and temperature conditions, since it significantly under-predicts the vaporisation rate. Moreover they stated that the approximation of the enthalpy of vaporisation, which is the energy required to vaporise one mole of component 'i' from the liquid mixture to the gaseous mixture at a specific temperature and pressure, with the latent heat, which they defined equal to the energy required to vaporise one mole of the pure liquid 'i' in its own vapour at the saturation conditions, results to be quite inaccurate. According to their definition the latent would result in an overestimation of the energy required by the phase change, and consequently it would underestimates the droplet heating. The authors also suggested that near the critical point a small change in pressure could lead to violent boiling and possibly micro-explosion, implying that this subject would require further investigation to be correctly understood.

Jia et al. [102] proposed an investigation on high-pressure droplet vaporisation, focusing on the issues of liquid-phase gas solubility, droplet lifetime, thermo-physical properties, fuel vapour condensation, validity of isobaric assumption, bulk-flow and liquid-phase heat-up transient processes. They concluded that the Peng-Robinson EOS and the Soave-Redlich-Kwong EOS seem to better represent the vapour-liquid equilibrium over a wide pressure range compared to the Redlich-Kwong EOS. Moreover, the higher the ambient temperature, the shorter is the ambient pressure range over which the assumption of not consider gas solubility in the liquid phase can be employed. Under high-pressure vaporisation, no wet-bulb temperature is reached and

the droplet heat-up time increases as a proportion of the total vaporisation time. The authors investigated the influence of the fuel vapour mass fraction on the vaporisation characteristics, showing that it plays a significant role particularly at lower temperature and higher pressure conditions, when it may induce condensation to occur at the droplet surface during the early part of the droplet lifetime.

An important result emerging from experimental investigations of Nomura et al. [103] was that a droplet does not immediately attain the critical mixing state as it is introduced into an ambient where pressure and temperature exceed the thermodynamic critical point of the liquid fuel. Moreover, while most studies indicated that the droplet surface generally reaches the critical mixing state at pressure conditions, which are much higher than the fuel critical pressure, they reported a wide scatter in the minimum ambient pressure required to reach the critical state. This observation was successively supported by computational investigation [92, 104]. Givler et al. [41] added a more detailed investigation on this topic, concluding that a vaporizing droplet of paraffin fuel can reach the critical state for ambient pressures greater than approximately twice the fuel's critical pressure and for ambient temperatures approximately twice the fuel's critical temperature, while combusting droplets can reach this state when ambient pressure is approximately two and half times that of the fuel's critical pressure.

A numerical simulation of the spray formation and vaporisation of an unsteady fuel spray under diesel-like conditions, implementing an extended vaporisation model, which accounts for heat and species diffusion within the droplets, was proposed by Hohmann et al. [105]. The model assumes that the surface tension and the enthalpy of vaporisation vanish at the critical state; however the calculations showed that all the droplets are completely evaporated prior to this point. Under high temperature and low-pressure conditions the influence of the 'effective-diffusivity model', which takes into account the enhanced temperature and concentration distributions inside the droplet due to liquid circulation, seems to be significant. Moreover the prediction revealed that with high pressure the real gas effects become more predominant, especially at low temperatures, and they can be properly predicted only by the high-pressure model, since the ideal gas model calculates excessively low vaporisation rates.



Grading et al. [106] proposed a ‘zero-dimensional’ multi-component droplet vaporisation model, focusing on the comparison between low-pressure and high-pressure property-estimation methods (PEM). The model neglects the solubility of any ambient species in the liquid even using high-pressure PEM, reducing the number of unknowns and equations to be solved, since at diesel-engine pressures, during most of a droplet’s lifetime, nitrogen mass fraction in the liquid at the surface is found to remain below 10 percent. This percentage value increases once the droplet approaches the critical state, but at this condition, since the liquid and gas phase densities approach each other, the assumption of quasi-steady gas-boundary layer surrounding the droplet is expected to fail in any case. The results show that this methodology allows a number of physical phenomena to be captured, such as the influence of forced convection and surface blowing on heat and mass transfer, droplet heat-up, droplet internal-motion and temperature-pressure-concentration dependent properties. Under low droplet temperature conditions, liquid Prandtl and Schmidt numbers are large, thus the time scale for momentum diffusion is comparatively short and a spherical vortex (Hill’s vortex) is quickly established. The model is found to account for droplet internal transport with a sufficient high level of accuracy, even though only mass-averaged and surface properties are used. The authors remarked the uncertainty in the prediction of the droplet lifetimes due to the accuracy in the estimation of gas-phase properties, concluding that the liquid-internal transport has a less pronounced effect on droplet lifetime. They also stated that the influence of the reference state in calculating the liquid/gas thermo-physical properties increases with increasing ambient temperature. A comparison between the predictions obtained implementing low-pressure and high-pressure multi-component droplet vaporisation models reveals that the ideal Raoult’s law under-estimates the vaporisation rate especially of the heavier components.

Miller et al. [107] proposed an extensive evaluation of eight liquid droplet evaporation models: two versions of the classical “ $d^2$ -law”, assuming infinite liquid conductivity and considering Stefan flow effects, four versions of the simple heat-mass transfer analogy model, and two non-equilibrium Langmuir-Knudsen evaporation flow formulations based on the ‘infinite liquid conductivity’ and ‘finite liquid conductivity’ models, respectively. The importance of choosing proper reference temperature and composition values in evaluating physical transport properties has been also investigated. Bellan et

al. [108] first introduced the non-equilibrium Langmuir-Knudsen evaporation law for use in droplet combustion models, revealing that non-equilibrium effects play an important role in practical spray calculations, with droplet size in the order of few micrometers. Under low vaporisation rate conditions, all the proposed models nearly predict identical evaporation histories, showing reasonable agreement with experiments. The non-equilibrium effects seem to become significant when the initial droplet diameter is less than  $50\mu\text{m}$  and they result to be enhanced with increasing slip velocity, while the ambient gas temperature seems to have negligible influence on non-equilibrium effects. Several combinations of property reference assumptions for both the vapour and gas phase species have been proposed, based on the wet-bulb, the boiling or the ambient gas temperatures and the '1/3-rule' according to Hubbard et al. [49]. The authors remarked that the use of reference temperature larger than the droplet surface temperature results in a considerable over-prediction of the experimental evaporation rate measurements. On the other hand, the implementation of a reference state based on the wet-bulb and the boiling temperature gives better predictions at the early stage of the process, while the '1/3-rule' appears to be more correct at later times. Moreover the results suggested that for large droplets a significant improvement is achieved introducing an analytic form of the heat transfer reduction due to evaporation, calculated from the solution of the quasi-steady gas-phase equations, when compared to standard empirical relation. Finally the authors recommended that Langmuir-Knudsen law should be used for general gas-liquid flow calculations, because not only it incorporates realistic non-equilibrium evaporation behaviour prevailing in many practical situations, but it also does not require additional computational effort compared to the other proposed ideal equilibrium models.

Experimental results from vaporizing free-falling, non-interacting mono and multi-component droplets have been compared with computational predictions using the high-pressure evaporation model based on the 'conduction limit' and the 'diffusion limit' assumptions in Stengele et al. [109]. The free falling droplets used in the experiments are one order of magnitude larger in comparison with combustor spray, although, since their velocities are much lower, the Reynolds number is comparable to conditions of combustion chambers and the non-dimensional number analogy is justified. The authors remarked that spray modelling strongly depends on the correct prediction of droplet motion and evaporation, observing that, especially during cold starting engine



conditions, when the ambient gas temperature is relatively low, the highly volatile components of the fuel play a significant role for ignition and burning engine processes. Since the droplet temperature rises with pressures, the unsteady heating of the droplet significantly affects the droplet evaporation process and steady state evaporation cannot be obtained. The results give evidence to the fact that with elevating pressures the evaporation distance and the velocity of the droplets decreases, due to increased aerodynamic force. Towards the end of the evaporation process, the droplet velocity profiles reveal steep gradients, due to significant deceleration of the droplet in combination of enhanced vaporisation and negligible influence of gravity. The results also show that the evaporation distance shortens elevating the gas temperature, reducing the initial droplet diameter or increasing the fuel volatility.

A comprehensive investigation of the trans-critical droplet vaporisation phenomena was proposed in Zhu et al. [104] with a detailed treatment of the liquid-vapour phase equilibrium at the droplet surface, using three equations of state, namely Peng-Robinson (PR), Redlich-Kwong (RK) and Soave-Redlich-Kwong (SRK) EOS. The results from the computational work have been validated against experimental data over a wide range of operating conditions. For n-heptane-nitrogen system, the phase equilibrium predictions using RK-EOS show significant differences from those using PR and SRK-EOS, since the RK-EOS yields higher fuel-vapour concentration, higher solubility of nitrogen into liquid, lower critical-mixing-state temperature and lower latent heat of vaporisation. Under low and moderate ambient temperature conditions, RK-EOS over-predicts the droplet vaporisation rate, under-predicting its lifetime. These differences become less noticeable at higher ambient temperatures typical of combusting droplets. Furthermore, the droplet lifetime predictions using the PR-EOS result in excellent agreement with measurements over a wide range of ambient pressures, while the results using the RK-EOS show significant differences and those based on SRK-EOS are in reasonable agreement with the experiments. The computational results also reveal that at low to moderate temperatures, the droplet lifetime first increases reaching a maximum value and then decreases as the pressure increases. Successively, under high ambient temperature environments the droplet lifetime decreases monotonically with increasing pressure. These conclusions result in good agreement with the reported experimental data.

The option to represent a vaporising multi-component droplet as a surrogate pure fuel droplet has been investigated in Aggarwal et al. [110] comparing the ‘infinite-diffusion’ and the ‘diffusion-limit’ vaporisation models, over a range of parameters relevant to gas turbine combustors. Three typical operating conditions have been considered: (1) lean blowout for ground-idle operation; (2) premixing, pre-vaporizing system at high-power conditions; (3) start-up (ignition and flame propagation) conditions. The validity of quasi-steady high-pressure droplet vaporisation assumption is examined, considering non-ideal gas behaviour, liquid-phase solubility of gases, variable thermo-transport properties temperature, pressure and composition dependent. The predictions highlight that under high-power conditions, the vaporisation behaviour of a gas turbine fuel can be well represented by an equivalent single component fuel, which boiling point corresponds to 50 percent of the multi-component fuel boiling point. Using the ‘diffusion-limit’ model the composition of the fuel seems not to play any relevant role, while the use of the ‘infinite-diffusion’ model indicates discrepancies between the vaporisation rates of bi-component and single-component fuel droplets. Since the total vaporisation rate is a better indicator of how well a single-component fuel can represent the vaporisation behaviour of a multi-component fuel, it is recommended that a ‘diffusion-limit’ model or an ‘effective-diffusivity’ model, in case of forced convection, would be employed, particularly in CFD code predicting the development of real fuel vaporizing sprays. The authors remarked that liquid and gas-phase properties change considerably during the droplet lifetime, which, on the other hand, seems to be relatively insensitive to pressure, under the conditions investigated. However the droplet heat-up time becomes a more significant fraction of the droplet lifetime under high-pressure conditions. As a result, differences between the ‘infinite-diffusion’ and the ‘diffusion-limit’ models are increasingly more noticeable at elevated pressures independently on the fuel composition, since the former model over-predicts the vaporisation rate for both single and multi-component fuel droplets. Moreover, the representation of a bi-component fuel droplet with an equivalent single-component yields to increasingly better results at high pressures, concluding that under these conditions the vaporisation rate seems to be more sensitive to the droplet heating model rather than to the liquid fuel composition. This can be attributed to a significant increase in droplet heat-up time and a reduction in the relative volatility differential between the constituent fuels. On the other hand, for ignition, LBO, and idle operation conditions, the multi-component fuel effects become relatively important. The use of an equivalent



single-component fuel produces unacceptable results, especially when the ‘infinite-diffusion’ model is implemented. They showed that the predicted vaporisation histories of n-heptane droplets using a quasi-steady high-pressure model, that incorporates the non-ideal gas behaviour, the dissolution of gases into the liquid, and the dependence of thermo-transport properties on pressure, show good agreement with the experimental data over a wide range of pressures. At ambient pressure equal to 40atm, the model under-predicts the vaporisation rate, which is perhaps indicative of the high-pressure limit of the quasi-steady vaporisation model assumption.

Hohmann et al. [111] investigated the fuel vaporisation behaviour under high-pressure conditions, focusing on the sensitivity of the results on the different models that predict the real gas effects and their solubility in the liquid phase. Particular emphasis is given to the influence of droplet vaporisation modelling on the spatial temperature and vapour concentration distributions in the gas phase. The mass fraction of the dissolved gas in the liquid has been calculated in the order of 5 percent, nearly independent of temperature, suggesting that it can be neglected in order to simplify the numerical algorithm. The enthalpy for phase change estimated by the high-pressure model is smaller compared to the ideal case, while higher mole fractions of the vaporizing species are calculated, predicting higher vaporisation rates. The authors remarked that under high pressure and temperature conditions, the droplet internal transport processes become more significant, compared to the low pressure and temperature conditions. This can be explained by the fact that gaseous thermal conductivity usually increases with temperature, while opposite behaviour is expected for liquid thermal conductivity, thus enhancing the heat transport effect inside the droplet under high temperature conditions. The authors focused their investigation also on the issue where it is possible for an evaporating droplet to reach a pseudo-critical state at first in its interior, leading to a splashing from the inside. Calculations cannot predict this effect since they are based on the assumption that droplets are heated-up from their surface to the interior and the concentration of the dissolved gases follow an equivalent behaviour. High-pressure vaporizing spray calculations have been also performed, showing a good agreement against experimental data. The heat and mass transfer models seem not to significantly influence the spray behaviour, due to the fact that many different physical processes occur during the spray development (primary and secondary break-up, collision, coagulation, mass-momentum and heat transfer coupling with the

surroundings) having a strong effect particularly on the droplet size, and consequently making the details from complex vaporisation modelling rather superfluous. Their main conclusion is that for spray simulations the simpler ‘well-mixed’ model for the liquid heat transfer analysis should be implemented, with the support of ready tables, generated from single droplet investigation under high-pressure vaporizing conditions, in order to take into account the contribution of high-pressure effect on the vaporisation rates.

A general conclusion on droplet vaporisation was drawn by Kim et al. [112], who stated that droplet's lifetime increases with pressure at a low ambient temperature conditions, but it decreased at high temperatures. Moreover, they remarked that the latent heat of vaporisation is reduced increasing both the droplet's temperature and the ambient pressure; in particular during the final stages of droplet evaporation, the main factor determining the phase equilibrium switches from the ambient pressure to the droplet's temperature. The results show that these effects are amplified under high ambient temperature conditions.

Recently Sazhin [113] has presented the latest progresses in the development of a combined analytical, asymptotic and numerical approach, which models heating and evaporation of fuel droplets and ignition of fuel vapor/air mixture based on a new zero-dimensional code. The effect of temperature gradient inside the droplets was investigated by comparing the ‘effective thermal conductivity’ and the ‘infinite thermal conductivity’ models. The results pointed out that in the absence of break-up, the influence of the temperature gradients in the liquid phase on the droplet evaporation, under realistic diesel engine environment, is minor. In the presence of the break-up process, however, the liquid temperature gradients can lead to a significant decrease in the predicted droplet evaporation time. Even in the absence of break-up, the effect of the temperature gradient inside the droplets was shown to lead to a noticeable decrease in the calculated total ignition delay, while in the presence of break-up this effect was shown to be substantially enhanced. Finally the authors concluded with the recommendation that the effect of the temperature gradients inside the vaporizing droplets should be taken into account in CFD codes describing droplet break-up and evaporation processes, and successively ignition of the evaporated fuel/air mixture.



The proposed literary review on the droplet vaporisation modelling remarks the complexity of the physical and computational issues involved and the extensive investigation made by the researchers to cover the wide range of operating conditions present in real single droplet and spray applications. One of the main aspects to be taken into account is the compromise between the requested accuracy and the necessary computational effort, which suggest the preferable modelling to be used.

## **2.4 Experimental and computational investigations on high-pressure fuel injection systems for direct injection gasoline engines**

The worldwide concern over global warming and the quantitative relationship between fuel consumption and carbon dioxide emissions have started recently to attract the attention of the automotive manufacturers. The European Commission and the European Automotive Manufacturers Association (ACEA) in 1998 agreed that the average CO<sub>2</sub> emissions for new cars has to be reduced to 140g/km by 2008, implying a reduction of fuel consumption of more than 25 percent from the 1995 baseline, and a more stringent target of CO<sub>2</sub> to 120g/km by 2012 is under discussion [2]. This legislation combined with the increased customer demand for fuel efficient vehicles is leading to further research and development of gasoline injection concepts to improve fuel economy.

In recent years a number of automotive manufactures have introduced gasoline direct injection (GDI) into the European and Japanese markets, since it's proving to offer advantages compared to the port-fuel injection (PFI) strategy [114, 115, 116]. Injecting fuel directly into the engine cylinder totally avoids the problems associated with fuel wall wetting in the port, while providing enhanced control of the metered fuel for each combustion event, satisfying the conflicting requirements of mixture preparation during high-load (homogeneous stoichiometric/lean) and part-load (stratified overall lean) conditions [117] as well as a reduction in fuel transport time. The GDI engine offers the potential for leaner combustion, less cylinder-to-cylinder air-fuel mixing variation and lower unburned hydrocarbon emissions even during the cold start. Gasoline direct injection has demonstrated its ability to satisfy existing and future emission legislation; moreover it also has sufficient technical development potential to meet successive emission standards in all global markets, like the extremely stringent California SULEV

restrictions [118]. Due to the higher pressure operating conditions in the GDI system, the fuel entering the cylinder is much better atomised than that of the PFI system, enhancing the fuel vaporisation rate.

The fuel injection system in a gasoline direct injection engine is a key component that must be carefully matched with the in cylinder flow field to provide the desired mixture cloud over the entire operating range of the engine, producing a well-atomised fuel spray [114]. The combustion system designs for gasoline direct injection can be divided into three main types, classified according to the relative position of the injector towards the spark plug and the piston crown and according to the mixture preparation approach, as suggested by Mitroglou et al. [119]. The first production solutions have adopted either wall guided or air guided concepts, in which the fuel spray is directed from a side-mounted fuel injector towards a contoured piston surface and then upward towards the spark plug. According to Wirth et al. [2] wall or air guided concepts are inherently limited in their thermodynamic potential as stratified mixture formation is directly linked to the piston motion. Heat loss under homogeneous operation is also increased due to increased surface to volume ratio of the combustion chamber caused by the piston bowl required for stratified operation. Additionally, due to the interaction of the piston wall, the stratified operating window is limited by smoke emissions. The second generation of direct injection gasoline engines suggests that the spray guided concept, with a centrally mounted fuel injector spraying along the cylinder axis towards a spark plug with electrodes located near the edge of the spray, has the capability to offer a potential improvement in terms of substantial fuel economy, high pressure cycle efficiency and reduced HC and CO<sub>2</sub> emissions [120]. Spark location, fuel injection quantity and timing represent crucial factors for this family of high pressure injection systems for GDI. There are presently three different mixture preparation principles under development for spray-guided systems based on the swirl-pressure atomiser, the multi-hole and the outward-opening pintle nozzles. Research programmes using both experimental techniques and calculations have been performed in the last decades and they are still currently running, in order to gain understanding of the nozzle flow, spray characteristics, performance and durability of emerging gasoline high-pressure fuel injection systems as well as their application to direct injection spark-ignition engines.



Pressure swirl atomizers represents the first and most widely utilised designs in the market because of their relatively cheap manufacturing costs and simple and efficient atomisation characteristics that suit both early and late injection strategies [121]. Several investigations have focused on pressure swirl atomisers [122, 123, 124]. In general, this type of injector can produce very finely atomised droplets with diameters in the range of 15-25 $\mu\text{m}$  over a moderate range of injection pressures from 50 up to 120bar. Abo-Serie et al. [125] found that following a delay period between signal initiation and first appearance of fuel at the nozzle exit, four stages have been identified during the spray development: a very early asymmetric poorly atomised jet penetrating in the central part of the nozzle hole with a tip velocity proportional to injection pressure, an asymmetric non-hollow spray, a swirl-developing hollow-cone spray with a multi-layer structure, and a fully-developed and well atomised hollow-cone spray with a cone angle nearly independent of injection pressure. Arcoumanis et al. [126] and Abo-Serie et al. [127] revealed from spatial distribution analysis that larger droplets are located near the outer edge of the spray and this trend becomes more pronounced for sprays injected against higher back pressure and temperature. In addition to the injection pressure controlling the degree of fuel atomisation, the back pressure was found to exert an influence on the droplet velocities leading to lower Weber numbers and enhanced droplet agglomeration. Gavaises et al. [128] used a combination of single and multi-dimensional computational fluid dynamics models implemented in a RANS flow solver to investigate the temporal and spatial variation of droplet size and velocity, concluding that accurate estimation of the nozzle flow exit conditions is very important for the accurate prediction of sprays injected from pressure swirl atomisers, with the proposed sub-models offering significant improvements in terms of the calculated spray structure.

Another high-pressure injector, the multi-hole nozzle, has been recently introduced by fuel injection manufacturers, aiming to overcome the dependence of the spray characteristics on thermodynamic and operating conditions revealed in pressure swirl atomisers. This type of injector offers the flexibility of combining a variety of configurations, positioning the holes throughout the injector nozzle cap, similarly to diesel injectors [129]. The authors also found, from multi-phase internal nozzle flow simulations, that cavitation is the main flow factor that determines injection velocity and initial droplet size. Moreover, PDA measurements of the spray characteristics

revealed that droplet velocities increase sharply at the start of injection to a maximum value and then remain unchanged during the main part of injection before decreasing rapidly towards the end of injection. The spatial velocity profiles were found to be jet-like at all axial locations with the local velocity maximum found on the spray axis. AboSerie et al. [130] confirmed from spray images that penetration decreases with increasing chamber pressure or decreasing injection pressure, that higher droplet velocities are present at the spray centre and that a multi layer structure is formed along the spray axis. They also observed a stronger interaction between the six sprays as the chamber pressure increases. Lippert et al. [115] concluded that multi-hole injectors allow ultra-lean stratification for a wide range of part-load operating conditions, without compromising smoke and hydrocarbon emissions because of enhanced vaporisation, resulting in a shortened liquid length. This was found to be attributable to the increased air entrainment available because the spray does not collapse under elevated cylinder pressures typical of late injection. Pontoppidan et al. [131] revealed a particular behaviour of the multi-hole atomiser, which is related to its space-penetration characteristics. Unlike the swirl-atomiser, where spray is typically divided in a dense or pilot spray and a main spray with a lower penetration velocity, the sprays ejected from the multi-hole atomiser behave all as unitary pilot sprays, which suffer far less from aerodynamic drag and therefore their mean penetration velocity remain high for a long period. However the researchers found that the multi-hole atomiser presents a high risk of nozzle contamination by high temperature carbonisation due to the relatively small nozzle hole size. It is therefore essential that the injector position within the combustion chamber layout have been optimised not only for the mixture preparation, but also to limit the average injector tip temperature. Overall the performed investigations suggest that high-pressure multi-hole injectors for GDI engines should be preferred to pressure swirl atomisers, due to their superior spray structure stability under varying chamber thermodynamic and injector operating conditions [132, 133, 134, 135].

Finally, investigation on outward opening injectors for GDI automotive combustion systems is currently in progress. The research findings suggest that the outwardly opening design offers several advantages avoiding the initial purely atomised spray generated by pressure-swirl atomisers and most inwardly opening GDI injectors. Since under all operating conditions the initial liquid sheet thickness formed at the nozzle exit is defined primarily by the needle lift (pintle stroke), this provides a flexible design that



allows the spray angle, penetration and droplet size to be more efficiently controlled. Swirling flow may also be used in the outwardly opening pintle injector for reducing the spray penetration, and for increasing the spray cone angle. Moreover, the initial sheet thickness exiting from the nozzle is smaller during the valve opening and closing events, resulting in better fuel atomisation and consequently promoting the vaporisation process. According to manufacturing requirements, the absence of nozzle holes directly exposed to the combustion chamber environment makes the outwardly opening design more robust [114] and cocking-free, which may be a significant problem with multi-hole nozzles. As suggested in Das et al. [136] a high variation in the spray characteristics is observed for small changes in the injector design and operating conditions, underlying the importance of understanding its behaviour for a proper functioning over a wide range of working variables. Particular emphasis has been given to the effect of nozzle seat-angle, injection velocity and needle lift on spray penetration and droplet size distribution. Other attempts to investigate the injection performance and the spray characteristics in GDI systems with outward opening injectors have been presented over the last few years. For example, a promising study on injection rate modulation and injector geometric parameters using regenerated fuels has been presented in Stan et al. [137]. Implementation of wall film and spray models in commercial CFD codes, accounting for the contribution of swirl velocity on the calculation of the spray cone angle and resolving some numerical grid dependence issues at the impingement locations is shown in Zeng et al. [138]. Additionally, the effect of film formation and air fuel mixing on spray development and engine emissions was simulated leading to the conclusion that leaner mixture around the spark-plug tends to yield higher engine-out unburned hydrocarbon production. Recent numerical investigations suggest the main advantages of an innovative spray-guided combustion system, the Vortex Induced Stratification Combustion (VISC), which, combining the effect of central injector location and wide cone angle with the air-vortex normally present in the engine cylinder, provides a significantly wider injection time window, robust combustion and efficient smoke emission control [139]. Recently, Nouri et al. [140], investigated the internal and near nozzle flow characteristics from an enlarge scale transparent model of an outward opening injector using high resolution CCD camera, high speed video camera and LDV methods. The images of internal flow between the valve seat and square cross section end of the needle guide showed the presence of four separated jet flows and four pairs of highly unstable counter-rotating

vortices with each pair bounded in between of two adjacent jets. Magnified images of flow just outside the nozzle exit showed clearly a stream-wise interconnecting filaments type spray structure as the liquid film emerges from exit passage and exposes into air. The interspacing between the strings was found to be linearly related to injection velocity and almost independent on the needle lift. The same conclusion was drawn by Nouri et al. [141] who investigate the spray characteristics from a high-pressure piezo pintle-type injector into a constant volume chamber. They also concluded that the locations of the strings remained the same from one injection to the next and that its structure was unaffected by elevated back-pressure from 1bar up to 12bar. Overall, the effect of back pressure was to reduce the spray tip penetration due to the increased drag and the spray cone angle was found to be stable and independent of back-pressure, confirming the considerable advantage relative to pressure swirl atomisers.

These preliminary conclusions open an interesting field for future research on the flow processes inside the fuel injection system, in order to provide better understanding of the near-nozzle spray formation, investigating how fuel atomisation process is controlled by the nozzle geometry, the characteristics of the fuel supply system and the liquid-gas aerodynamic interactions. For these reasons, efforts are concentrated in using both experiments and calculations in an attempt to gain better understanding of these phenomena and their effect on performance and durability of emerging gasoline high-pressure fuel injection systems and their application to direct injection spark-ignition engines.

## 2.5 Conclusions

The chapter has focused on the presentation and discussion of the main topics of research investigated for the purposes of the current work. A few important conclusions can be drawn from this review.

The interaction of flow with the spray and the subsequent combustion and pollutant formation processes form a complex system of physical phenomena whose time and length scale ranges over a wide spectrum. The accuracy of CFD simulations is determined not only by the adequacy of the physical models, but also from the dependency of the results on the discretisation techniques implemented.



Two possible reasons for grid dependent computational results are that, on one hand, the cell volumes used for the solution of the gas phase equations should be bigger than the volume of the droplets they contain, as imposed by the Eulerian-Lagrangian formulation for two-phase flows, on the other hand, the grid size should be small enough to resolve the gas phase development near the nozzle.

Different methodologies for liquid/gas phase coupling, which can be applied to meshes of arbitrarily structure, shape and topology, have been proposed in order to reduce the grid-dependent issue. Furthermore, local mesh refinement, in combination with ‘intelligent meshing strategies’, can be utilised for the resolution of small-scale flow structures near boundaries and in regions of high gradients. Finally, the implementation of hybrid Eulerian-Eulerian and Eulerian-Lagrangian methodologies represents a promising solution to the numerical issues related to multi-phase flow modelling.

The proposed literary review on droplet vaporisation modelling remarks the complexity of the physical and computational issues involved and the extensive investigation made by the researchers to cover the wide range of operating conditions present in real single droplet and spray applications. Liquid/gas phase thermodynamic equilibrium conditions, liquid composition, heat and mass transfer assumptions represent the main topics investigated.

One of the crucial aspects to be taken into account is the compromise between the requested accuracy and the necessary computational effort, which suggest the preferable modelling to be used.

During the last decades, investigation on the flow processes inside the high pressure fuel injection systems for GDI engines have been performed, in order to provide better understanding of the near-nozzle spray formation, investigating how fuel atomisation process is controlled by the nozzle geometry, the characteristics of the fuel supply system and the liquid-gas aerodynamic interactions.

Relevant efforts are concentrated in using both experiments and calculations in an attempt to gain better understanding of complex physical phenomena occurring in emerging gasoline high-pressure fuel injection systems, focusing on their effect on

performance and durability and their application in direct injection spark-ignition engines.



# Chapter 3

The mathematical sciences particularly exhibit order, symmetry, and limitation; and these are the greatest forms of the beautiful.  
Aristotle [Metaphysica]

## MATHEMATICAL FORMULATION

### 3.1 Introduction

In this chapter the discussion will focus on the mathematical modelling of the continuous and dispersed phases, in order to illustrate the fluid flow thermodynamics characteristics. The traditional model of fluids used in physics is based on a set of partial differential equations known as the Navier-Stokes equations. The equations are derived by considering the mass, momentum, and energy balances for an infinitesimal control volume. They need to be augmented by an equation of state for compressible flows. The GFS code, used for the purposes of the current study, initially structured by Theodorakakos [142] and Gavaises [4] and developed in the last decade within their research group, solves the time-averaged forms of the continuity, momentum and conservation equations for scalar variables using collocated Cartesian velocity components on a Cartesian non-uniform, curvilinear, non-orthogonal numerical grid. It is based on the finite volume discretisation method, which will be briefly illustrated in the next section of this chapter, followed by the description of the governing continuous phase equations. Subsequently the spray model, which describes the dispersed phase according to the Eulerian-Lagrangian methodology, will be presented. The chapter will close with the discussion on some numerical issues related to the modelling of multi-phase fluid flows, which represent the main contributions made by the author to the GFS solver.

### 3.2 Continuous phase modelling

#### 3.2.1 Finite volume discretisation method

As already mentioned, flows and related phenomena can be described by set of partial differential (or integro-differential) equations. They can be numerically solved using discretisation methods, which approximate the differential equations by a system of algebraic equations [143]. The ‘Finite Volume’ (FV) method represents one of the most

used approaches in CFD, sub-dividing the solution domain into a finite number of contiguous control volumes (CV), and assigning all the dependent variables to the CV centers, according to the so-called ‘collocated approach’. Interpolation is used to express variable values at the CV surface in terms of the nodal values. Surface and volume integrals are approximated using appropriate quadrature formulae. The equations for all CVs are summed to obtain the desired solutions.

One advantage of the finite volume method over the other discretisation approaches is that it does not require a structured mesh and, furthermore, the boundary conditions can be applied non-invasively. This is true because the values of the conserved variables are located within the volume element, and not at nodes or surfaces. Finite volume methods are especially powerful on coarse non uniform grids and in calculations where the mesh moves to track interfaces or shocks. In the finite volume method, the volume integrals in a partial differential equation that contains a divergence term are converted to surface integrals, using the divergence theorem. These terms are then evaluated as fluxes at the surfaces of each finite volume. Because the flux entering a given volume is identical to that leaving the adjacent volume, these methods are conservative.

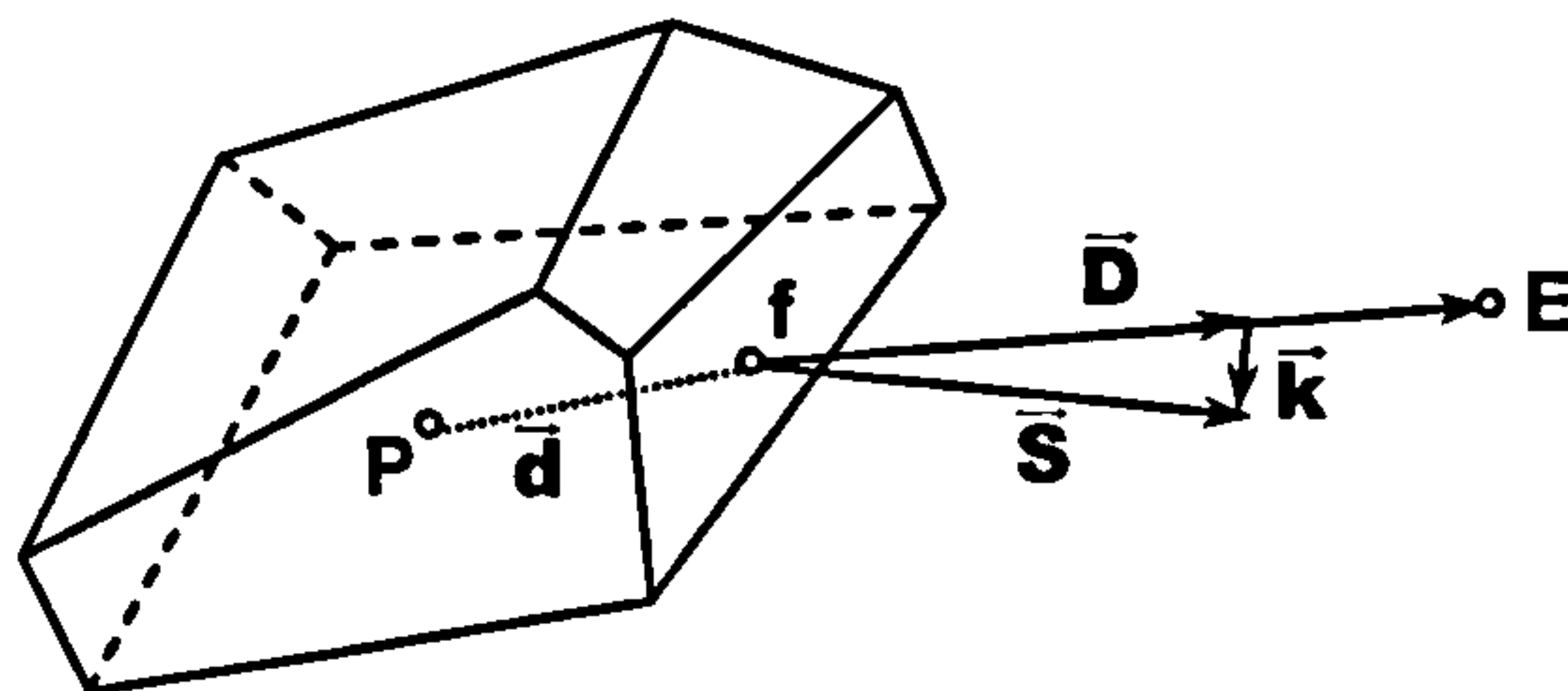


Figure 3-1: Scheme of the control volume discretisation method.

Figure 3-1 represents a typical control volume (cell) with an arbitrary number of faces. ‘P’ is the center of the cell, while ‘E’ is the center of an adjacent cell. The cells ‘P’ and ‘E’ have ‘f’ as a common face. The vector  $\vec{d} = \overline{PE}$  connects point ‘P’ with its neighbour ‘E’. Vector  $\vec{S}$  is the outward pointing face area vector normal to the face. The mesh is defined as non-orthogonal if the angle between  $\vec{S}$  and  $\vec{d}$  is not zero. Vectors  $\vec{D}$  and  $\vec{k}$  are defined according to the following equations in order to account for the orthogonal and non-orthogonal contributions to the face gradients, according to the notation of Jasak [144]:

$$\vec{D} = \frac{\vec{d}}{\vec{d} \cdot \vec{S}} |\vec{S}|^2 \quad (3-1)$$



$$\vec{k} = \vec{S} - \vec{D} \quad (3-2)$$

### 3.2.2 Generic transport equation

The purpose of the control-volume-based technique is to solve the integral equations governing the fluid flows once they are converted to algebraic equations. The general form of the conservation equation for a flow quantity  $\phi$  with reference to the control volume, shown in Figure 3-2, is defined as:

$$\frac{\partial}{\partial t} \int_V \phi \rho dV + \oint_{\partial V} \vec{F}_C \cdot d\vec{S} - \oint_{\partial V} \vec{F}_D \cdot d\vec{S} = \int_V Q_V dV + \oint_{\partial V} \vec{Q}_S \cdot d\vec{S} \quad (3-3)$$

where  $t$  is time,  $\vec{F}_C = \rho \vec{u} \phi$  the flux over the boundary due to convection (or motion of the fluid),  $\vec{u}$  the fluid velocity vector,  $\rho$  the density of the fluid,  $\vec{F}_D$  the flux vector over the boundary due to diffusion,  $Q_V$  the internal source,  $\vec{Q}_S$  the source vector at the boundary,  $V$  the volume of the control volume,  $\partial V$  its boundary and  $d\vec{S}$  the outward pointing surface element vector.

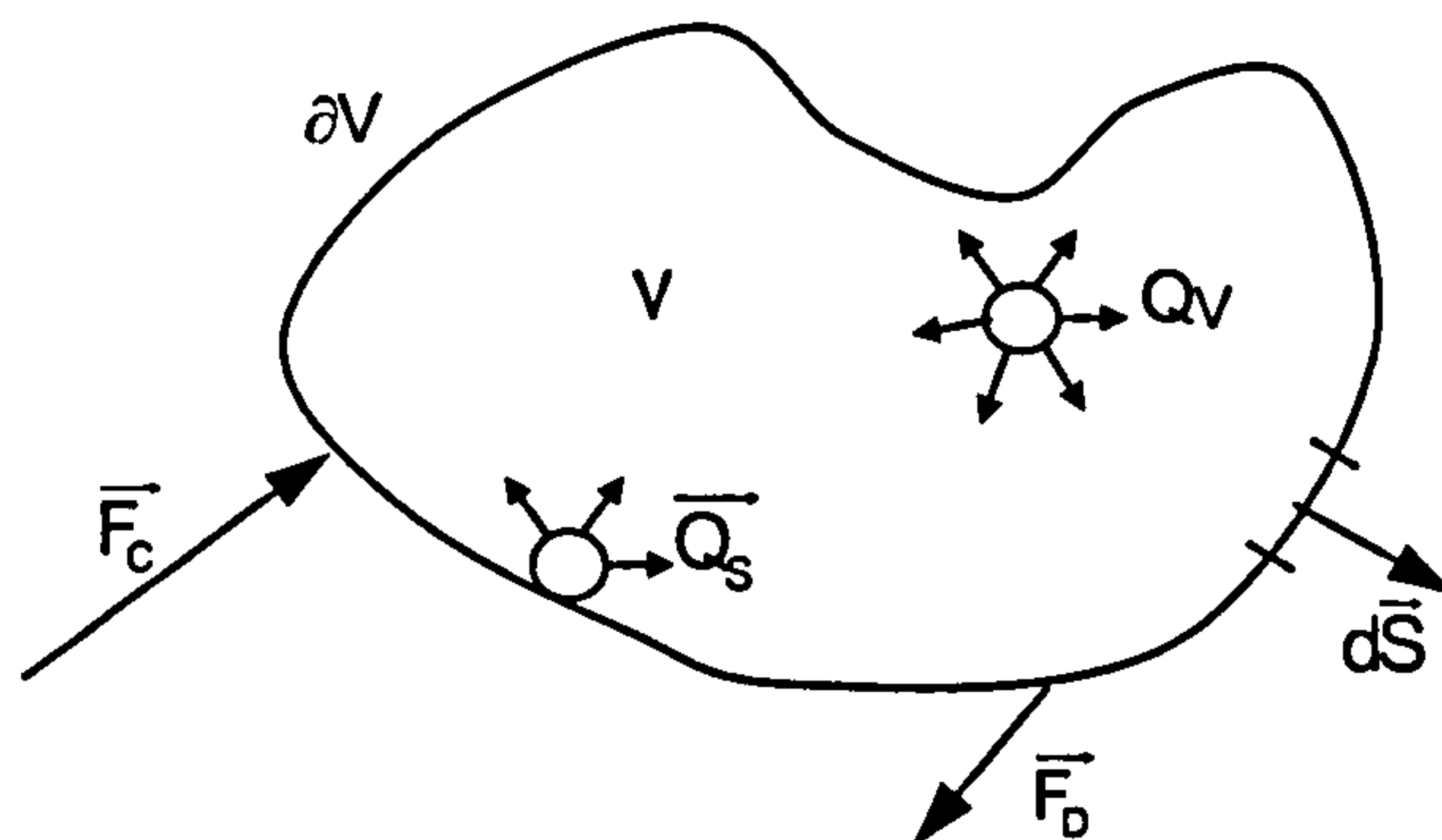


Figure 3-2: Scheme of the temporal and spatial variation of the generic flow variable  $\phi$  over the control volume, according to the finite volume discretisation method.

For continuous fluxes and surface sources, Gauss's theorem can be applied, thus giving:

$$\frac{\partial}{\partial t} \int_V \phi \rho dV + \int_V \nabla \cdot \vec{F}_C dV - \int_V \nabla \cdot \vec{F}_D dV = \int_V Q_V dV + \int_V \nabla \cdot \vec{Q}_S dV \quad (3-4)$$

If the volume is contracted to a single point, then the above equation reduces to the general conservative differential form:

$$\frac{\partial \phi \rho}{\partial t} + \nabla \cdot \vec{F}_C - \nabla \cdot \vec{F}_D = Q_V + \nabla \cdot \vec{Q}_S \quad (3-5)$$

The time-averaged form of the compressible Navier-Stokes equations describing the continuity, momentum and conservation equations for any scalar variables is expressed as follows:

$$\begin{aligned}
 \frac{\partial}{\partial t}(\alpha_c \rho_c) + \nabla \cdot (\alpha_c \rho_c \vec{u}) &= \dot{s}_{\text{mass}} \\
 \frac{\partial}{\partial t}(\alpha_c \rho_c \vec{u}) + \nabla \cdot (\alpha_c \rho_c \vec{u} \otimes \vec{u} - \alpha_c \vec{T}) &= \vec{\dot{s}}_{\text{momentum}} \\
 \frac{\partial}{\partial t}(\alpha_c \rho_c \varphi) + \nabla \cdot (\alpha_c \rho_c \varphi \vec{u} - \alpha_c \vec{q}) &= \dot{s}_{\text{scalar}} \\
 \alpha_c &= 1 - \frac{V_{\text{parcel},c}}{V_c}
 \end{aligned}
 \tag{3-6}$$

here  $\rho_c$  is the continuous-phase density in the cell with volume  $V_c$ ,  $V_{\text{parcel},c}$  the total volume of the dispersed phase in the cell,  $\alpha_c$  its void volume fraction,  $\varphi$  any scalar variable (i.e. temperature, concentration, turbulent kinetic energy),  $\vec{q}$  its flux vector,  $\vec{u}$  the velocity vector and  $\vec{T}$  the stress tensor defined as:

$$\vec{T} = -\left(P + \frac{2}{3}\mu_c \nabla \cdot \vec{u}\right)\vec{I} + \mu_c \left[\nabla \otimes \vec{u} + (\nabla \otimes \vec{u})^T\right]
 \tag{3-7}$$

where  $\vec{I}$  is the unit tensor,  $\mu_c$  the continuous phase dynamic viscosity and  $P$  the static pressure calculated using a pressure correction method, which has been implemented in the GFS code according to the SIMPLE [145] and PISO [146, 147] algorithms. For further details refer to Giannadakis [148]. All the numerical investigations proposed in the next chapters have been obtained using the PISO model.

For the generic scalar variable  $\varphi$  the diffusion flux vector  $\vec{q}$  is calculated as:

$$\vec{q} = \Gamma_\varphi \nabla \varphi
 \tag{3-8}$$

where  $\Gamma_\varphi$  is the diffusion factor:

$$\Gamma_\varphi = \frac{\mu_c}{Pr_\varphi}
 \tag{3-9}$$

$Pr_\varphi$  is the Prandtl number for the scalar variable  $\varphi$ .

The source terms on the right-hand side of the above equations are due to mass, momentum and energy exchange between the two phases, and they require appropriate modelling. The physical models are equally important as the numerical treatment of those source terms and they will be discussed in a successive section of the chapter. As far as the effect of turbulence on the fluid flow, although different models have been



implemented in the code, the conventional ‘k-ε’ model, developed by Launder et al. [149], has been used in the simulations presented in the next chapters of this thesis.

The GFS code implements an iterative algorithm, using a combination of solvers from the extensive SLAP library [150], to solve the transport equations previously described, on a collocated curvilinear non-orthogonal computational grid using Cartesian velocity components. The mathematical model requires the discretisation of the equations according to the finite volume approach and the definition of the appropriate boundary conditions implementing either constant values or fixed gradients at the boundary.

A review of the main differential operators used to discretise the governing equations for multi-phase fluid flows is presented in details in Giannadakis [148].

In the next sections the calculation of the generic variable  $\phi$  on the center of the face ‘f’, from the corresponding cell-centred values, is described according to five different interpolation schemes, followed by a brief discussion on the temporal discretisation methods implemented in the code.

### 3.2.3 Face interpolation

The calculation of the generic variable  $\phi$  on the center of the face ‘f’ depends on the type of numerical interpolation scheme adopted, which has a dramatic effect on the accuracy and stability of the method. The desired properties of the selected interpolation scheme should be: transportiveness, when convection becomes more dominant than diffusion, upstream nodes have more influences than downstream ones; conservativeness, when the flux across any cell face is uniquely determined for the two adjacent control volumes; boundedness, when in the absence of any source term, the grid node values remain between the minimum and the maximum boundary values and finally accuracy. The combination of these properties is not an easy task, since they might be contradictory to each other [151]. In order to illustrate the different numerical schemes, the equation for the generic variable  $\phi$ , equation (3-3), assuming only the convection term is reduced to:

$$\int_V \nabla \cdot \bar{F}_c dV = \int_{\delta V} \nabla \cdot (\rho \bar{u} \phi) dV = 0 \quad (3-10)$$

where the fluid density and the velocity vector are both interpolated on the center of the face using geometrical weighting factors. Applying the Gauss’ theorem and the differential operators, the following expression is obtained:

$$\sum_{f=1}^n C_f \varphi_f = 0 \quad (3-11)$$

The mass flux  $C_f$  through face 'f' is defined as:

$$C_f = \rho_f \vec{S}_f \cdot \vec{u}_f \quad (3-12)$$

where  $\vec{S}_f$  is the outward pointing surface vector.

The control volume shown in Figure 3-3 is used to illustrate the different face interpolation schemes for the variable  $\varphi$ . Its cell center is represented by the point 'P', while 'E' and 'W' are the cell centers of the two adjacent control volumes.  $\vec{u}_w$  and  $\vec{u}_e$  are the velocity vectors of the fluid entering in the control volume from the face 'g' and exiting from the face 'f', respectively. The five face interpolation schemes implemented in the GFS code and used for the numerical investigation presented in Chapter 5 are described below. They all assume that the values of the generic variables  $\varphi$  at the cell center of the computational domain are all known from the previous time step or solution iteration.

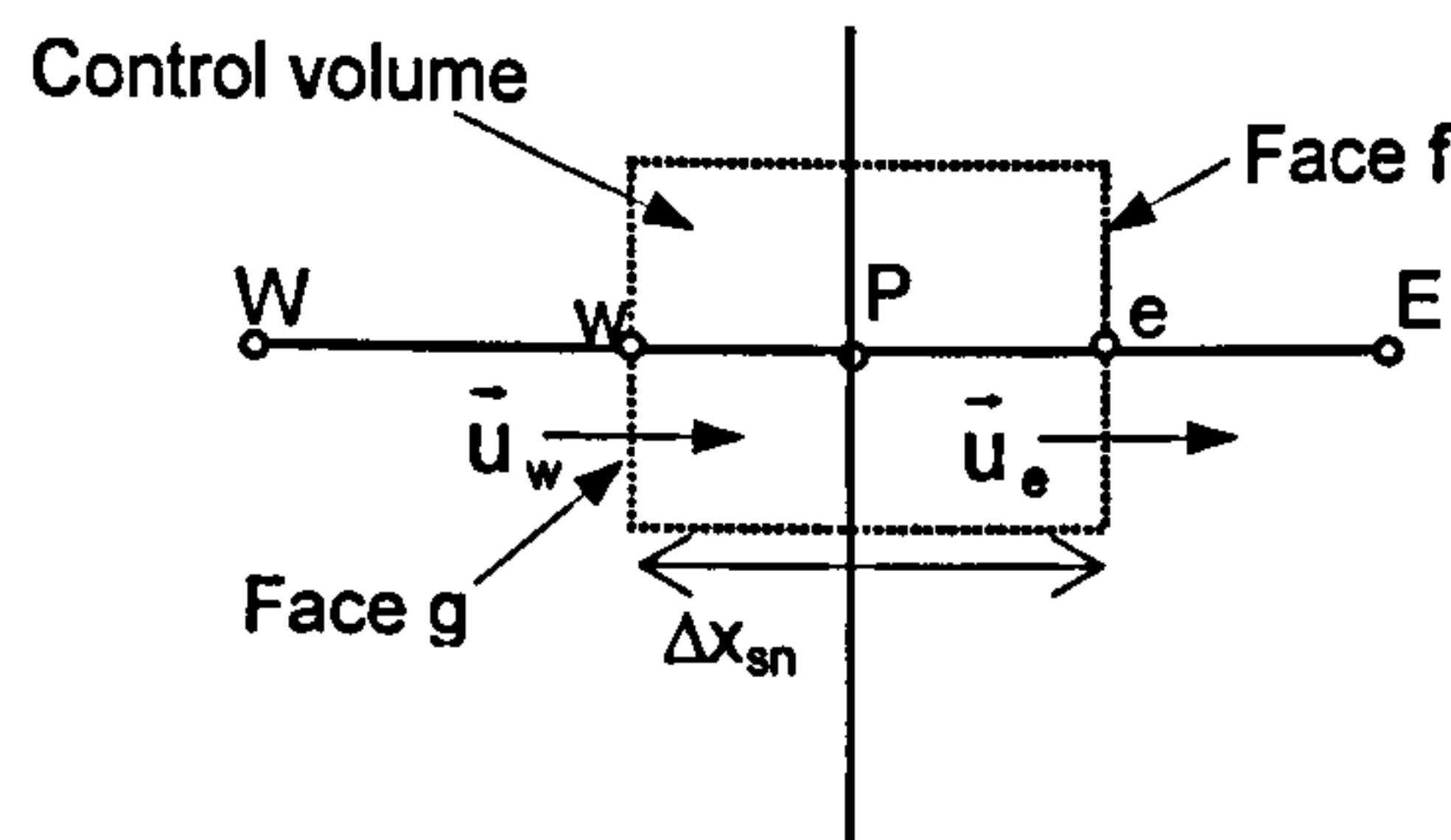


Figure 3-3: Scheme of the control volume for the convection terms differencing schemes.

#### 'First order upwind', FOU

$$\varphi_f = \begin{cases} \varphi_P & \text{for } \vec{u}_e \geq 0 \\ \varphi_E & \text{for } \vec{u}_e < 0 \end{cases} \quad (3-13)$$

where  $\varphi_P$  and  $\varphi_E$  are the values of the variable assigned to the nodes 'P' and 'E'. It is directly correlated to the nature of the fluid convection, considering the direction of the flow from the selected face. It is only first order accurate, although the boundedness property is always satisfied.

#### 'Central differencing', CD

$$\varphi_f = \Delta x_{eE} / \Delta x_{PE} (\varphi_P \cdot \varphi_E) + \varphi_E \quad (3-14)$$



where  $\Delta x$  represents the distance between two points. It is second-order accurate, even though it can produce unbounded results and numerical instability.

#### 'Hybrid scheme', HYBRID

It is a combination of the previous two schemes, in order to satisfy accuracy and boundedness requests.

$$\varphi_f = \begin{cases} \varphi_P & \text{for } Pe_f > \frac{1}{1 + \Delta x_{eE} / \Delta x_{PE}} \\ \Delta x_{eE} / \Delta x_{PE} (\varphi_P - \varphi_E) + \varphi_E & \text{for } -\frac{1}{\Delta x_{eE} / \Delta x_{PE}} \leq Pe_f \leq \frac{1}{1 + \Delta x_{eE} / \Delta x_{PE}} \\ \varphi_E & \text{for } -\frac{1}{\Delta x_{eE} / \Delta x_{PE}} > Pe_f \end{cases} \quad (3-15)$$

The local Peclet number on the face 'f',  $Pe_f$ , is defined as the ratio of the convective,  $C_f$ , to the diffusive,  $D_f$ , fluxes through face 'f':

$$Pe_f = \frac{C_f}{D_f} \quad (3-16)$$

#### 'Gamma differencing scheme', JASAK

Jasak et al. [152] proposed the Gamma differencing scheme, which introduces a blending factor to switch from FOU to CD schemes in order to achieve boundedness, minimize artificial diffusion and enhance accuracy. Other references to the Gamma differencing model can be found in Ubbink [153] and Ubbink et al. [154].

$$\varphi_f = \begin{cases} \varphi_P & \text{for } \tilde{\varphi}_P \leq 0 \text{ or } \tilde{\varphi}_P \geq 1 \\ \frac{1}{2}(\varphi_P + \varphi_E) & \text{for } \xi \leq \tilde{\varphi}_P < 1 \\ (1 - \frac{\tilde{\varphi}_P}{2\xi}) \varphi_P + \frac{\tilde{\varphi}_P}{2\xi} \varphi_E & \text{for } 0 \leq \tilde{\varphi}_P < \xi \end{cases} \quad (3-17)$$

where  $\tilde{\varphi}_P$  is defined as:

$$\tilde{\varphi}_P = 1 - \frac{\varphi_P - \varphi_E}{2\nabla\varphi_f \cdot \vec{d}} \quad (3-18)$$

$\xi$  is a constant of the differencing scheme, which usually takes a value around 1/6,  $\vec{d}$  represents the vector connecting 'P' with 'E' and  $\nabla\varphi_f$  is the gradient of the function  $\varphi$  in 'e', evaluated using the discretised form of Gauss' theorem.

### ‘Bounded second order upwind scheme’, BSOU

The BSOU scheme has been proposed by Papadakis et al. [151] employing a flux blending technique between first and second order upwind schemes. It is transportive, conservative, bounded, stable and accurate, leading to its implementation in the GFS code as a suitable solution algorithm for general problems.

$$\varphi_f = \begin{cases} \varphi_P & \text{for } \hat{\varphi}_P < 0 \\ \varphi_W + (1 - \Delta X_{Pe}/\Delta X_{WP})(\varphi_P - \varphi_W) & \text{for } 0 \leq \hat{\varphi}_P \leq (\Delta X_{WP}/\Delta X_{We}) \\ \varphi_W + (1 - \gamma_e \Delta X_{Pe}/\Delta X_{WP})(\varphi_P - \varphi_W) & \text{for } (\Delta X_{WP}/\Delta X_{We}) < \hat{\varphi}_P < 1 \\ \varphi_P & \text{for } \hat{\varphi}_P > 1 \end{cases} \quad (3-19)$$

where the normalized variable  $\hat{\varphi}_P$  and the blending factor  $\gamma_e$  are expressed as:

$$\hat{\varphi}_P = \frac{(\varphi_P - \varphi_W)}{(\varphi_E - \varphi_W)}, \quad \gamma_e = \frac{(\varphi_E - \varphi_P)/(\varphi_P - \varphi_W)}{\Delta X_{Pe}/\Delta X_{WP}} \quad (3-20)$$

### 3.2.4 Temporal discretisation

When a time dependant problem is simulated, the first term in the general form of the conservation equation (3-3) is also present, representing the time derivative of the generic transport variable over the control volume. Using a first order accurate discretization scheme for the control volume with center ‘P’ and assuming a linear variation of  $\varphi$  within the time step, the above term can be approximated as:

$$\int_{V_P} \frac{\partial \rho \varphi}{\partial t} dV \approx \frac{(\rho \varphi V)_P^{t+\Delta t} - (\rho \varphi V)_P^t}{\Delta t} \quad (3-21)$$

where ‘t’ denotes the current time step, while ‘t+Δt’ indicates the following one. The terms in the above equation are all time-dependent, leading to their approximation in the interval between t and Δt. Assuming that the integral of  $\frac{\partial \rho \varphi}{\partial t}$  over the control volume

can be defined as a generic function  $g(\rho, \varphi, \bar{u}, \Gamma, S_\varphi)$ , it’s crucial to specify how this function varies in the time interval. A weighting factor  $\beta$  is introduced to model this variation and the final expression for equation (3-21) is proposed:

$$\frac{(\rho \varphi V)_P^{t+\Delta t} - (\rho \varphi V)_P^t}{\Delta t} = (1 - \beta) \left[ g(\rho, \varphi, \bar{u}, \Gamma, S_\varphi) \right]^t + \beta \left[ g(\rho, \varphi, \bar{u}, \Gamma, S_\varphi) \right]^{t+\Delta t} \quad (3-22)$$



The different temporal discretisation schemes correspond to the specific value selected for  $\beta$ . The explicit and implicit Euler schemes are defined by  $\beta$  equal to 0 and 1 respectively, while the implicit Crank-Nicolson scheme corresponds to  $\beta$  equal to 0.5. Both the implicit schemes are fully unconditionally stable, while the accuracy of the Euler methods is enhanced by the second-order accurate Crank-Nicolson scheme.

### 3.3 Eulerian-Lagrangian solution algorithm

The solution algorithm implemented in the CFD code to solve the spray phenomena according to the Eulerian-Lagrangian frame of reference is schematically illustrated in Figure 3-4. The process starts with the acquisition of the input information about the grid, the necessary boundary and operating conditions and the computational parameters. Once all the solution variables are initialised, the iterative procedure initiates. The transient process is predicted sub-dividing the total time interval into several fractions, corresponding to the continuous phase time steps.

First the dispersed phase is solved. The continuous phase time step is successively sub-divided into smaller intervals, which determine the number of sub-cycles performed for the discrete phase solution. During each Lagrangian tracking time step, the parcels are injected according to the operating conditions calculated by internal nozzle flow simulations. The spray code has been implemented with the scope to allow the simultaneous modelling of the physical processes and the numerical treatment of different parcel states: liquid droplet, ligament, bubbles, solid particles, liquid film and liquid wall film. The modelling of the spray processes requires the estimation of the continuous phase variables at the parcel location, which are interpolated implementing a numerical algorithm presented and discussed in the following section 3.5. The peculiarity of this method is the definition of a specific region of interaction between the parcel and its surroundings, according to particular criteria for each interaction process and each parcel state. The spray development is predicted, estimating the effect on the particle characteristics of the parcel tracking, liquid film and ligament atomisation, droplet evaporation, forces exerting upon the parcel, droplet secondary break-up, parcel-to-parcel interaction, turbulent dispersion and impingement. For each process different sub-models have been implemented using iterative procedures.

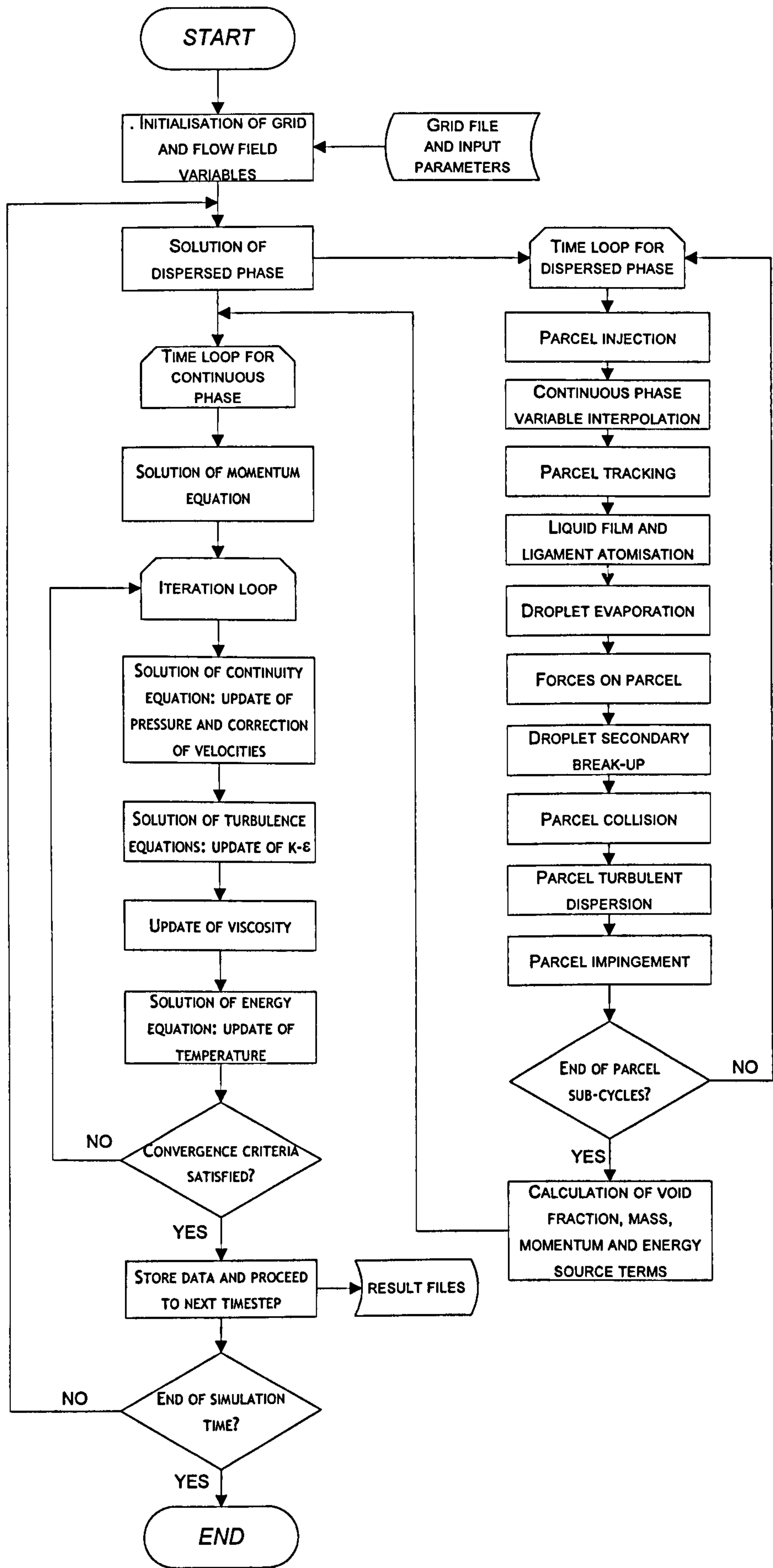


Figure 3-4: Continuous and dispersed phase solution algorithm.



The source terms derived by the mass, momentum, energy and void fraction exchanges between the dispersed and continuous phases are calculated and distributed among the cells identified within the region of influence, according to the procedure described in section 3.5. The code has been structured in a way that allows the computational domain to be dynamically refined as the simulation proceeds. Different options have been implemented in order to refine the grid only where and where it's needed. The cells that respond to the particular criterion selected (pre-defined area, region of spray development or spray tip) are identified and they are splitted in order to create the new grid, starting from the original one, at the beginning of the successive simulation time step. At the end of the dispersed phase iterative procedure, the source terms from the parcel interaction with the surroundings are added to the continuous phase governing equations. First the momentum conservation equations are calculated estimating the new fluid velocity fields. Then, through an iterative algorithm, the continuity, turbulence and energy equations are solved, updating the density, pressure, viscosity, corrected velocity and temperature fields. Once the convergence criteria are satisfied, the continuous and discrete phase characteristics are recorded in result files and the algorithm proceeds to the following time step. The liquid and gas thermo-physical properties for a wide range of hydrocarbons fuels, water and air, used for the simulations of diesel and gasoline direct injection engines, are calculated according to the extensive library implemented in the GFS code, which contains empirical correlations, function of temperature, pressure and composition, taken from [155, 156].

A particular feature of the GFS code consists in the implementation of an algorithm, which calculates, as the simulation proceeds, the main post-processing parameters useful to describe the spray phenomena. A considerable effort has been put in order to make this procedure as more complete and efficient as possible, defining transient profiles and spatial distributions of the dispersed and the continuous phase properties. The program calculates the properties (velocity, size, temperature, Reynolds and Weber numbers) for each parcel and for the continuous phase variables at the parcel locations instantaneously present in the computational domain and the transient profiles of the same variables averaged among the particles in the whole spray. Moreover, it estimates the cell mean property spatial distributions, defining the average velocity, size, volume, mass and temperature of the particles inside each cell of the computational domain, and the principal spray parameters (liquid penetration, defined according to the 95% of the

total mass or the average location of the 10 most remote parcels from the injection point; vapour penetration for each species present in the mixture, defined as the maximum distance from the injection point of the cell which vapour concentration is bigger than a threshold value, fixed equal to 1%). Finally, the program records the principal spray events, like the atomisation time, the break-up distance, the evaporation rate and the spray mean deformation.

The next section of the chapter focuses on the mathematical description of the main sub-models implemented in the dispersed phase Lagrangian modelling for spray investigations.

### **3.4 Dispersed phase modelling**

In this section the mathematical formulation of the dispersed phase modelling for spray applications is presented and discussed, illustrating the numerical approach and the various sub-models implemented in the GFS code in order to describe the complex physical phenomena occurring. The Eulerian-Lagrangian numerical approximation to predict the multi-phase flow processes in internal combustion engines has been extensively discussed in the past, for example by O'Rourke et al. [157], Amsden et al. [158], Lee et al. [159], Han [160] and Arcoumanis et [76]. It is based on the assumption that the transport of the dispersed phase can be predicted by tracking the trajectories of a certain number of representative parcels flowing in the carrier gas, which is modeled as continuous phase according to the standard Eulerian methodology presented in the previous section.

#### **3.4.1 Lagrangian model formulation**

The Lagrangian-type formulation is based on a fluid-particle model introduced by Dukowicz [3]. The spray is represented by a collection of computational particles, each containing a large number of identical non-interacting droplets. The model assumes that the inter-phase transport of mass, momentum and energy is quasi-steady and their transfer coefficients to and from the droplets are independent on the proximity of neighbouring droplets and can be represented by empirical correlations. The properties of the representative parcels are randomly chosen from calculated distribution functions



using a Monte-Carlo approximation. This formulation is often referred to as the ‘discrete droplet model’, DDM, or stochastic particle model. If appropriately chosen probability distributions are used to define the particle properties and a sufficiently large number of computational particles is introduced, an adequate statistical representation of realistic sprays may be obtained. The model assumes that the spray can be statistically described by a distribution function  $f(\bar{x}, \bar{u}, m, T)$ , which states at any time  $t$  the probability to find in a unit volume a number of particles with the same chemical composition, located in the spatial range  $(\bar{x}, \bar{x}+d\bar{x})$ , having velocities in the range  $(\bar{u}, \bar{u}+d\bar{u})$ , mass in the range  $(m, m+dm)$ , and temperature in the range  $(T, T+dT)$ . According to this assumption, the following equation expresses the conservation of the total number of particles in any volume of  $(\bar{x}, \bar{u}, m, T)$  [161, 162]:

$$\frac{d}{dt} \int \int \int \int f(\bar{x}, \bar{u}, m, T) d\bar{x} d\bar{u} dm dT = \frac{d}{dt} f_{\text{SOURCE}}(\bar{x}, \bar{u}, m, T) = \dot{f}_{\text{SOURCE}}(\bar{x}, \bar{u}, m, T) \quad (3-23)$$

where the effect of all processes that could alter the number of droplets are included in the source term, at the r.h.s. of equation (3-23).

The differential form of this conservation equation can be defined as:

$$\frac{\partial f}{\partial t} + \nabla_{\bar{x}}(f \cdot \bar{u}) + \nabla_{\bar{u}}\left(f \cdot \frac{d\bar{u}}{dt}\right) + \frac{\partial}{\partial T}\left(f \cdot \frac{dT}{dt}\right) + \frac{\partial}{\partial m}\left(f \cdot \frac{dm}{dt}\right) = \dot{f}_{\text{SOURCE}}(\bar{x}, \bar{u}, m, T) \quad (3-24)$$

The equation (3-24) is usually called the ‘spray equation’ and describes the dynamics of the single-parcel distribution function. No assumption has been imposed for the particle shape or for its state (solid or liquid), and thus, it is valid for any particulate flow. The source terms of equation (3-24) can be approximated as:

$$\dot{f}_{\text{SOURCE}} = \dot{f}_{\text{Injection}} + \dot{f}_{\text{Atomisation}} + \dot{f}_{\text{Break-up}} + \dot{f}_{\text{Collision-Coalescence}} + \dot{f}_{\text{Impingement}} + \dot{f}_{\text{Turbulence}} \quad (3-25)$$

where the various terms at the r.h.s. of this equation represent the temporal variations in the liquid particle size distribution function due to fuel injection, liquid core disintegration at the injector exit, droplet secondary break-up, particle collision or coalescence, particle-wall interactions and liquid-gas turbulence dispersion, respectively. The continuum distribution function  $f(\bar{x}, \bar{u}, m, T)$  is approximated by a number of discrete particles, according to the following expression:

$$dN = \dot{f}(\bar{x}, \bar{u}, m, T) d\bar{x} d\bar{u} dm dT \quad (3-26)$$

which represents the average number of droplets at any time  $t$  with mass in the interval  $(m, m+dm)$ , temperature in the interval  $(T, T+dT)$ , located in the volume interval

$(\bar{x}, \bar{x}+d\bar{x})$  and with velocity in the interval  $(\bar{u}, \bar{u}+d\bar{u})$ . The ensemble average for the number of particles in a small interval  $\Delta m \cdot \Delta T \cdot \Delta \bar{x} \cdot \Delta \bar{u}$  can be expressed as:

$$\begin{aligned} \Delta N &= \int_{\Delta m, \Delta T, \Delta \bar{x}, \Delta \bar{u}} \left\langle \sum_k \delta(m-m_k) \delta(T-T_k) \delta(\bar{x}-\bar{x}_k) \delta(\bar{u}-\bar{u}_k) \right\rangle dm dT d\bar{x} d\bar{u} = \\ &= \left\langle \sum_k \delta(m-m_k) \delta(T-T_k) \delta(\bar{x}-\bar{x}_k) \delta(\bar{u}-\bar{u}_k) \right\rangle \Delta m \Delta T \Delta \bar{x} \Delta \bar{u} \end{aligned} \quad (3-27)$$

where  $\delta$  is the Dirac function, and the term  $\Delta m \cdot \Delta T \cdot \Delta \bar{x} \cdot \Delta \bar{u}$  is taken outside the integration, assuming that the ensemble average is constant over this small interval. The comparison between equation (3-26) and equation (3-27) leads to the following expression:

$$f(\bar{x}, \bar{u}, m, T) = \left\langle \sum_k \delta(m-m_k) \delta(T-T_k) \delta(\bar{x}-\bar{x}_k) \delta(\bar{u}-\bar{u}_k) \right\rangle \quad (3-28)$$

which defines the relationship between the continuum statistical description embodied in the spray equation and the discrete particle modelling. Due to computational issues, it is not possible to account for the actual large number of particles present in a spray, thus a sampling technique is usually employed. It assumes that each single computational parcel represents a characteristic group of identical particles, imposing the total mass conservation,  $M_{TOTAL}$ :

$$\sum_k N_{pk} \cdot m_k = M_{TOTAL} \quad (3-29)$$

where  $N_{pk}$  is the number of identical particles represented by the parcel  $k$ , with mass  $m_k$ . The estimation of the particle initial conditions (position, velocity, mass and temperature) represents one of the most crucial issues of any Lagrangian spray models, since it requires the knowledge of the flow characteristics at the exit of the injector nozzle. That information can be provided by complicated experimental measurements or internal nozzle flow predictions, employing a variety of multi-phase CFD methodologies. The next sections focus on the discussion of the numerical sub-models implemented in the GFS code and used for the computational investigations presented in the following chapters with the target to characterize the injection and further development of diesel and gasoline sprays for direct injection engine applications.

### 3.4.2 Injection modelling

The Lagrangian methodology implemented for the numerical approximation of the spray equation (3-24) requires that the initial parcel characteristics, velocity, size, temperature, composition and number of particles per parcel, are known variables. Most



of the spray models implemented in CFD codes calculate the injection parcel properties using as input to the model the fuel injection rate, although other information are required, particularly under cavitating hole flow conditions. They are mainly represented by the percentage of the hole exit cross-sectional area occupied by cavitation bubbles, which leads to the increased injection velocity, and the variable hole discharge coefficient, which affects both the fuel injection rate and the hole turbulence characteristics. This information is determined by the flow conditions at the exit of the injector nozzle and it can be numerically predicted by the GFS code implementing two different methodologies. The first one consists of a one-dimensional, transient and compressible flow model accounting for the pressure wave dynamics in the injection system and justified in view of the length of the pipes being much longer than their diameters. Assuming mass and momentum conservation, the pressure and the flow rate in the pipe are estimated together with the mean pressure in the volumes of the system.

A complete review of all the geometric and operating parameters that characterise the flow behaviour inside the injection system and have a strong influence on the nozzle exit conditions and the subsequent spray development can be found in Gavaises [4] and Arcoumanis et al. [163]. In order to properly characterise the nozzle flow under cavitating conditions, a phenomenological 1-D hole-cavitation model has been implemented. It uses an empirical correlation for estimating the reduction of the hole-discharge coefficient as a function of the cavitation number. The average hole turbulent kinetic energy and its dissipation rate as a function of operating and geometric parameters are then estimated [76, 164, 165]. The second methodology implemented to predict the transient flow rate and the injection pressure boundary conditions upstream of the injector is represented by the two-phase nozzle hole cavitation model developed by Giannadakis [148]. It predicts the amount of vapour reaching the nozzle exit, transiently resolved during the injection period. This is closely associated with an increase of the injection velocity relative to the non-cavitating flow, and a decrease in the mass flow rate.

Generally, in most the spray models, the flow characteristics at the exit of the injection holes are given as a function of time from the solution of the flow in the fuel injection system and in the injection holes. An effort has been made in the present investigation to estimate the spray injection conditions, guided by the consideration that in various

modern fuel injection systems the spray development is crucially affected by the spatial distribution of the fluid flow characteristics at the nozzle exit. A numerical algorithm has been implemented, which spatially and temporally remaps the flow characteristic distributions at the hole exit, obtained from two-phase internal nozzle flow simulations; at each computational time step the model randomly selects for each injected parcel its initial position inside the hole exit area and successively it interpolates the parcel injection properties (velocity, temperature, turbulence variables) from the remapped flow distributions at the hole exit.

In the simpler case of spatially averaged injection conditions, only function of time, the mass of the injected parcel is calculated from the transient fuel injection rate from each individual hole, while the injection velocity, assumed to be uniform along the injection hole cross sectional area, is equal to the effective injection velocity estimated from the geometric velocity and the area contraction coefficient due to the presence of cavitation bubbles, according to the following expression:

$$u_{JET} = \frac{\dot{Q}}{A_{HOLE} C_{EFF}} \quad (3-30)$$

where  $u_{JET}$  is the spray velocity at the nozzle exit calculated according to the effective injection-hole area,  $\dot{Q}$  the instantaneous volume flow rate,  $A_{HOLE}$  the hole geometric area and  $C_{EFF}$  the hole area contraction coefficient, defined as the ratio between the cross sectional area effectively occupied by the liquid and the geometric area. The position of the injected parcels coincides to the coordinates of the hole center, while its direction corresponds to the hole axis. The initial parcel dimension is estimated assuming that it corresponds to the effective hole area occupied by the liquid fuel. The number of parcels injected at each computational time step is calculated according to the total fuel volume and the total parcel number to be injected, as mathematically expressed by the following equation:

$$N_{PAT} = \frac{\dot{Q} \Delta t N_{Ptot}}{V_{Ptot}} \quad (3-31)$$

where  $N_{PAT}$  represents the number of parcels injected during the time step  $\Delta t$ ,  $N_{Ptot}$  the total injected parcel number and  $V_{Ptot}$  and total volume of the liquid fuel to be injected. The number of particles contained in each parcel during the time step  $\Delta t$  is calculated according to the next expression:



$$N_{\text{particle}\Delta t} = \frac{\dot{Q}\Delta t}{\sum_{i=1, N_{p\Delta t}} V_{\text{particle}\Delta t, i}} \quad (3-32)$$

where  $V_{\text{particle}\Delta t, i}$  represents the volume of one particle in the parcel  $i$  and the sum is extended to the total number of parcels injected during the time step  $\Delta t$ .

The initial droplet deformation is assumed to be zero, while the temperature of the injected parcel is set equal to the temperature of the fuel, given as input condition.

A crucial parameter characterising the spray structure is represented by the parcel size distribution, which is affected by the different physical processes taking place during the spray development, as supported by experimental measurements. Although empirical correlation have been derived to calculate the maximum parcel stable diameter and the Sauter mean diameter of the new formed particles, in the literature there are no fundamental models on the theory of parcel size distributions [4]. The spray model developed in the GFS code implements a set of mathematical functions, which include normal,  $\chi^2$ , log-normal, Nukiyama-Tanasawa, Rosin-Rammler, upper-limit, hyperbolic and log-hyperbolic distributions to calculate the parcel size distribution according to the so-called ‘maximum entropy formalism’ [166]. The detailed derivation of the most common mean diameters used to define the parcel size is described in Gavaises [4].

Following the start of injection, various spray sub-models are implemented for the calculation of the physical processes taking place in the sub-grid time and length scales. They are presented and discussed in the following sections of the chapter, focusing on the models used for the purposes of the present investigations, and suggesting the main references for all the remaining spray models implemented in the GFS code.

### 3.4.3 Parcel atomisation modelling

The break-up phenomenon follows the so-called ‘cascade process’, where the parcel break-up can take place many times during the injection period until they reach a stable form [167]. If the primary break-up, named as ‘liquid jet atomisation’, takes place in the region close to the nozzle exit, due to laminar, turbulent and cavitation collapse mechanisms, the droplet secondary-break-up occurs in the dilute region of the spray development (Figure 3-5), mainly induced by aerodynamic forces.



The term ‘atomisation’ expresses the physical process by which the continuous liquid jet gradually disintegrates into a large number of small droplets and ligaments [4]. It is generally accepted to play a crucial role in determining the successive spray development. Although extensively explored by experimental and computational investigations, it remains a phenomenon difficult to comprehend, since it requires the understanding of the link between the internal nozzle flow characteristics and the subsequent spray formation from the hole exit. The main conclusions from these studies reveal that the atomisation mechanism is determined by a combination of different parameters, which include the liquid physical properties, the surrounding gas conditions, the velocity profile at the exit of the injection hole and the type of the atomiser. The disintegration of the liquid jet emerging from the injector holes is mainly due to aerodynamic effect, internal jet turbulence or presence of cavitating bubbles in the injector holes, although the latter effect is found to play the more significant role. The next sections focus on the description of the mathematical formulation of the jet turbulence induced and the cavitation induced atomisation models, which have been implemented in the GFS code and used for the spray simulations presented in the following chapters. As far as the aerodynamic induced atomisation model, developed by Reitz et al. [169], which has been also implemented in the code, the author refers to the detailed explanation proposed in Gavaises [4] and in Gavaises et al. [117].

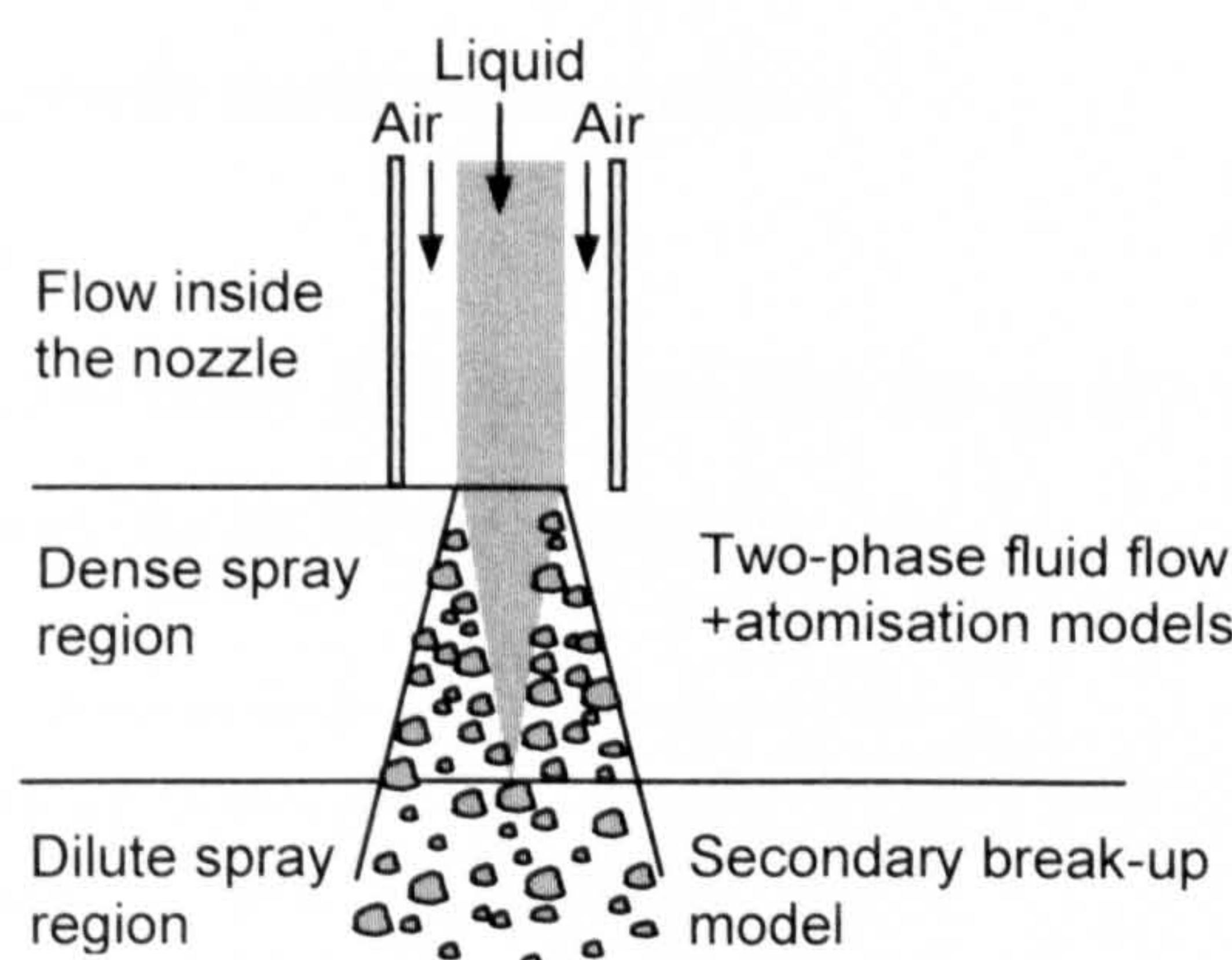


**Figure 3-5: Scheme of the different spray regions in proximity of the nozzle hole exit. Figure adapted from Taskinen [168].**



### Jet turbulence-induced atomisation model

The jet turbulence-induced atomisation model, developed by Huh et al. [170], assumes that perturbations on the spray surface, exiting from the injector hole, are induced by the jet turbulence and once these fluctuations have reached a certain level, they grow exponentially according to the Kelvin-Helmholtz instability mechanism until they detach from the liquid core and they form new droplets. The emerging liquid jet turbulence time and length scales are assumed to be correlated with the turbulence kinetic energy and its dissipation rate, according to the following expressions:

$$\begin{aligned} L_{\text{TURB}} &= C_{\mu} \frac{K_{\text{TURB}}^{3/2}}{\epsilon_{\text{DISS}}} \\ \tau_{\text{TURB}} &= C_{\mu} \frac{K_{\text{TURB}}}{\epsilon_{\text{DISS}}} \end{aligned} \quad (3-33)$$

where  $K_{\text{TURB}}$  and  $\epsilon_{\text{DISS}}$  represent the turbulent kinetic energy and its dissipation rate calculated by the 'k- $\epsilon$ ' turbulence model [149] and  $C_{\mu}=0.09$  is a model constant. The turbulence-induced atomisation model states that the length scale of turbulence determines the atomisation scale:

$$L_{\text{ATOM}} = C_1 L_{\text{TURB}} = C_2 L_{\text{WAVE}} \quad (3-34)$$

where  $L_{\text{ATOM}}$  is the length scale of atomisation and  $L_{\text{WAVE}}$  is the wavelength of the jet surface fluctuations. The time scale of atomisation is assumed to be a linear function of the turbulence and the Kelvin-Helmholtz surface wave time scales, which represent the initial and exponential growth times respectively:

$$\tau_{\text{ATOM}} = C_3 \tau_{\text{TURB}} + C_4 \tau_{\text{WAVE}} \quad (3-35)$$

The Kelvin-Helmholtz instability theory states that for an in-viscid liquid on an infinite plane the time scale of waves can be expressed as:

$$\tau_{\text{WAVE}} = \frac{1}{\left[ \frac{\rho_L \rho_G}{(\rho_L + \rho_G)^2} \left( \frac{u_{\text{REL}}}{L_{\text{WAVE}}} \right)^2 - \frac{\sigma}{(\rho_L + \rho_G) L_{\text{WAVE}}^3} \right]^{0.5}} \quad (3-36)$$

where  $\rho_L$  and  $\rho_G$  are the liquid density and gas pressure respectively and  $u_{\text{REL}}$  is the liquid-gas relative velocity at the nozzle hole exit.

The atomisation constant  $C_1$ ,  $C_2$ ,  $C_3$ ,  $C_4$  are set equal to 2, 0.5, 1 and 1.5 respectively, in order to assure that the secondary droplet diameter equals the dominant eddy diameter, which is twice the integral length scale of turbulence, and that half of the surface wave area is detached from the jet forming a droplet. Successively, the spray cone angle and the atomisation break-up rate are calculated as:

$$\tan \frac{\theta_{\text{SPRAY}}}{2} = \frac{L_{\text{ATOM}}/\tau_{\text{ATOM}}}{u_{\text{REL}}} \quad (3-37)$$

$$\frac{dD}{dt} = 2 \frac{L_{\text{ATOM}}}{\tau_{\text{ATOM}}} \quad (3-38)$$

The transition criterion for this regime is arbitrarily chosen when the initial growth time equals the exponential one, which corresponds to the time when the internal spray turbulence reduces to a level that does not affect atomisation any longer, as predicted by the 'k-ε' model. The transient profiles of the length and time turbulence scales are expressed by the following correlations, derived by the hypothesis of isotropic turbulence without the turbulence generation term:

$$\begin{aligned} L_{\text{TURB}}(t) &= L_{\text{TURB}}(0) \cdot \left[ 1 + (C_5 - 1) \frac{t}{\tau_{\text{TURB}}(0)} \right]^n \\ \tau_{\text{TURB}}(t) &= \tau_{\text{TURB}}(0) + (C_5 - 1)t \\ n &= 1 - \frac{1}{2(C_5 - 1)} \end{aligned} \quad (3-39)$$

where the constant  $C_5$  is set equal to 1.92 according to the 'k-ε' model, and the time  $t$  is recorded for each fluid ligament exiting from the injection hole. The size of the new formed droplets detached from the liquid jet is randomly chosen from a specified logarithmic distribution function, assuming that the number of droplets with size  $D$  is inversely proportional to the atomisation time scale  $\tau_{\text{ATOM}}(t)$ , directly proportional to the surface area ratio  $(D_{\text{JET}}/D)^2$  and to the turbulence energy spectrum  $\Phi(D)$  and that the number of droplets with size  $D$  per unit interval of  $D$  is proportional to  $1/D$ . This probability distribution function can be mathematically expressed as follows:

$$\text{pdf}(D) = \zeta \frac{\Phi(D)}{\tau_{\text{ATOM}}(D)} \quad (3-40)$$

where  $\zeta$  represents the normalization constant and the turbulence energy spectrum is calculated by the equation:

$$\Phi(D) = \zeta \frac{(k/k_e)^2}{\left[ 1 + (k/k_e)^2 \right]^{11/6}} \quad (3-41)$$

where:

$$k = \frac{1}{D}, \quad k_e = \frac{1}{L_e}, \quad L_e = \frac{\Lambda}{0.75} \quad (3-42)$$



$\Lambda$  is an integral length scale assumed as the average size of the energy-containing eddies. Finally the droplet size is randomly selected from the distribution function  $\text{pdf}(D)$  defined as the volume fraction of droplets with size  $D$  per unit interval of  $D$  around  $D$ :

$$\text{pdf}(d) = \frac{1}{V} \frac{\partial V}{\partial d} \quad (3-43)$$

imposing the mathematical constrain:

$$\int_0^{D_{\max}} \text{pdf}(D) dD = 1 \quad (3-44)$$

$D_{\max}$  is the maximum possible droplet size, defined according to the effective cross section area of the nozzle holes.

### Cavitation-induced atomisation model

Recent researches on the nozzle flow characteristics under practical diesel and gasoline injection applications for internal combustion engines reveal that two-phase cavitating flow generally describes the fluid regime. Gavaises [4] and Arcoumanis et al. [164] developed a cavitation-induced atomisation model, which considers the effect of cavitation on the disintegration of the liquid jet. The model assumes that the collapsing of the cavitation bubbles emerging from the injection hole, due to the pressure gradient between the internal bubble and the surrounding pressures, induces the liquid jet fragmentation. Additionally, due to turbulence effect in the spray, bubbles may burst on the surface of the liquid jet before they totally collapse. In order to model the atomisation process, the characteristic time and length scales of the perturbations caused on the jet surface by these effects should be defined. First the total area at the exit of the injection hole occupied by bubbles is estimated, defining an equivalent bubble radius having the same area as the whole cavitating bubbles:

$$R_{\text{CAV}} = \sqrt{r_{\text{HOLE}}^2 - r_{\text{EFF}}^2} \quad (3-45)$$

where  $r_{\text{HOLE}}$  is the hole radius and  $r_{\text{EFF}}$  is calculated from the effective hole area  $A_{\text{EFF}}$  due to the onset of cavitation:

$$r_{\text{EFF}} = (A_{\text{EFF}} / \pi)^{0.5} \quad (3-46)$$

Successively, from the Rayleigh theory of bubble dynamics [171], the collapsing time for a bubble with radius  $R_{\text{CAV}}$  is calculated according to the following equation:

$$\tau_{\text{COLLAPSE}} = 0.9145 R_{\text{CAV}} \sqrt{\frac{\rho_L}{P_G}} \quad (3-47)$$

The model states that the bubbles move in the radial direction within the liquid jet with liquid turbulent velocity  $u_{\text{TURB}}$ , which is estimated from the turbulent kinetic energy theory, assuming isotropic turbulence:

$$u_{\text{TURB}} = \sqrt{\frac{2}{3} K_{\text{TURB}}} \quad (3-48)$$

Successively, the average time required for a bubble of radius  $R_{\text{CAV}}$  to reach the periphery of the jet is calculated by the following expression:

$$\tau_{\text{EXIT}} = \frac{r_{\text{HOLE}} - R_{\text{CAV}}}{u_{\text{TURB}}} \quad (3-49)$$

The minimum between the bubble collapsing and exiting times defines the characteristic time scale of atomisation:

$$\tau_{\text{ATOM}} = \min \{ \tau_{\text{COLLAPSE}}, \tau_{\text{EXIT}} \} \quad (3-50)$$

Several studies have been done to investigate the effect of geometric and operating condition parameters on the relative role of bubble collapsing and exit times, to understand which of the two phenomena controls the atomisation process. Another important aspect that should be taken into account is related to the ideal assumption of spherical bubbles implemented by the model. Due to the significant tension forces acting on the collapsing bubbles, deformation effect cannot be neglected. Empirical coefficients have been introduced in the previous correlations defining the atomisation time scales [4].

The atomisation length scale of the perturbations on the jet surface due to cavitation phenomena is mathematically expressed as a function of the equivalent cavitating bubble radius:

$$L_{\text{ATOM}} = 2\pi R_{\text{CAV}} \quad (3-51)$$

The model assumes that the liquid jet fragmentation is caused by the deformation of its surface ( $L_{\text{ATOM}}$ ) during the atomisation time ( $\tau_{\text{ATOM}}$ ) due to the cavitation-induced force:

$$F_{\text{TOTAL}} = \xi \cdot C N_{\text{dyn}} \cdot M_{\text{JET}} \frac{L_{\text{ATOM}}}{\tau_{\text{ATOM}}^2} \quad (3-52)$$

where  $\xi$  is an empirical constant whose value is set equal to 0.007, from the comparison between model predictions and experimental data for the droplet SMD at the closest



point to the injection hole exit where measurements could be obtained [164],  $M_{JET}$  is the mass of the liquid jet element to be atomized and  $CN_{dyn}$  represents the dynamic cavitation number, which is introduced to define the degree of bubble cavitation:

$$CN_{dyn} = \frac{P_{SAC} - P_{BACK}}{\frac{1}{2} \rho_{JET} u_{JET}^2} \quad (3-53)$$

$P_{SAC}$  and  $P_{BACK}$  represent the nozzle sac and surrounding gas pressures respectively. The balance between the jet atomisation force and the surface tension force, which is calculated as:

$$F_{SURFACE} = 2\pi r_{JET} \sigma. \quad (3-54)$$

can be mathematically expressed by the following equation:

$$F_{SURFACE} = F_{TOTAL}. \quad (3-55)$$

This leads to the estimation of the maximum stable diameter of a droplet in the dense spray region. The actual droplet size is calculated implementing a probability distribution function, as described in the section 3.3.3, while the spray cone angle is defined as:

$$\tan \frac{\theta_{SPRAY}}{2} = \frac{L_{ATOM}}{\tau_{ATOM} u_{JET}} \quad (3-56)$$

where  $\theta_{SPRAY}$  states for the spray cone angle. Many experimental investigations reveal that the liquid droplets are not uniformly distributed in the spray cone angle, however larger particles are found close to the spray axis and smaller ones at the spray periphery. At present there are not theoretical studies describing the droplet dispersion in the radial direction, thus the model only assumes that the particles are distributed within the cone angle according to a correlation function of their mass:

$$\theta_i = C_{PROFILE} \cdot \theta_{SPRAY} \left( 1 - \frac{m_i}{m_{max}} \right) \quad (3-57)$$

where the angle  $\theta_i$  defines the position of the atomized droplet  $i$  from the spray axis,  $m_i$  represents the droplet mass,  $m_{max}$  is the mass of the droplet with the maximum possible size and  $C_{PROFILE}$  is a coefficient depending on the exit velocity profile, according to Hiroyasu et al. [172] and Su et al. [173]:

$$C_{PROFILE} = \psi \frac{Q(\theta_i)}{Q_{total}} \quad (3-58)$$

where  $\psi$  is a random number uniformly distributed in the range (0,1),  $Q(\theta_i)$  is the flow rate at the angle  $\theta_i$  and  $Q_{total}$  is the total flow rate.

### 3.4.4 Liquid droplet secondary break-up

Once spherical droplets are created, after primary atomisation has been completed, secondary break-up starts and its governing mechanisms are common for any type of spray [174, 175]. It only depends on the initial droplet sizes, relative velocity between the drop and ambient gas and the physical properties of the system (e.g., pressure, temperature, viscosity, surface tension, etc.). These parameters determine the break-up mechanism under which a droplet will further disintegrate [176].

Droplet aerodynamic break-up plays an important role on the predictions of the droplet size population. Different correlations estimating the post break-up droplet characteristics have been reported in Arcoumanis et al. [76]. The models implemented in the GFS code and used for the purposes of the present investigations combines correlations from various literature findings [157, 175, 177, 178, 179, 180, 181] in order to predict the droplet mean diameter, its deformation and break-up time over a wide range of Weber number, which is defined as:

$$We = \frac{\rho_G \cdot D_{HOLE} \cdot U_{INJ}^2}{\sigma_L} \quad (3-59)$$

where  $U_{INJ}$  is the mean injection velocity,  $D_{HOLE}$  is the diameter of the injection hole,  $\rho_G$  is the density of the surrounding gas and  $\sigma_L$  is the liquid surface tension.

The model assumes that the liquid droplets, formed from the atomisation process of the jet emerging from the injection nozzle, may experience deformation and further disintegration as they move into the surrounding gas, due to the non-uniform pressure distribution developing around them, which results from the relative velocity between the droplets and the gas and the enhanced motion within the droplet. Extensive research on the the droplet break-up reveals that it is not an instantaneous process and the inherent time of fragmentation plays a relevant role:

$$t^* = \frac{D_{DROP}}{U_{REL}} (\rho_L / \rho_G)^{0.5} \quad (3-60)$$

This time characterises the rate of the perturbation amplitude growth on the droplet surface, while the dimensionless break-up time is defined as:

$$\tau = t/t^* \quad (3-61)$$

The model distinguishes among the vibrational, bag and bag-and-stamen, chaotic, sheet stripping, wave crest stripping and catastrophic break-up regimes depending on the droplet Weber number [178, 179]:



$We < 12$	Vibrational	
$12 < We < 18$	Bag	
$18 < We < 45$	Bag and steamen	
$45 < We < 100$	Chaotic	(3-62)
$100 < We < 350$	Sheet stripping	
$350 < We < 1000$	Wave crest stripping	
$1000 < We$	Catastrophic	

The following figures illustrate some examples of droplet break-up. Figure 3-6 shows the bag break-up mechanism, where the unstable droplet moving into a cross flow is deformed before disintegrating into many smaller droplets [182].

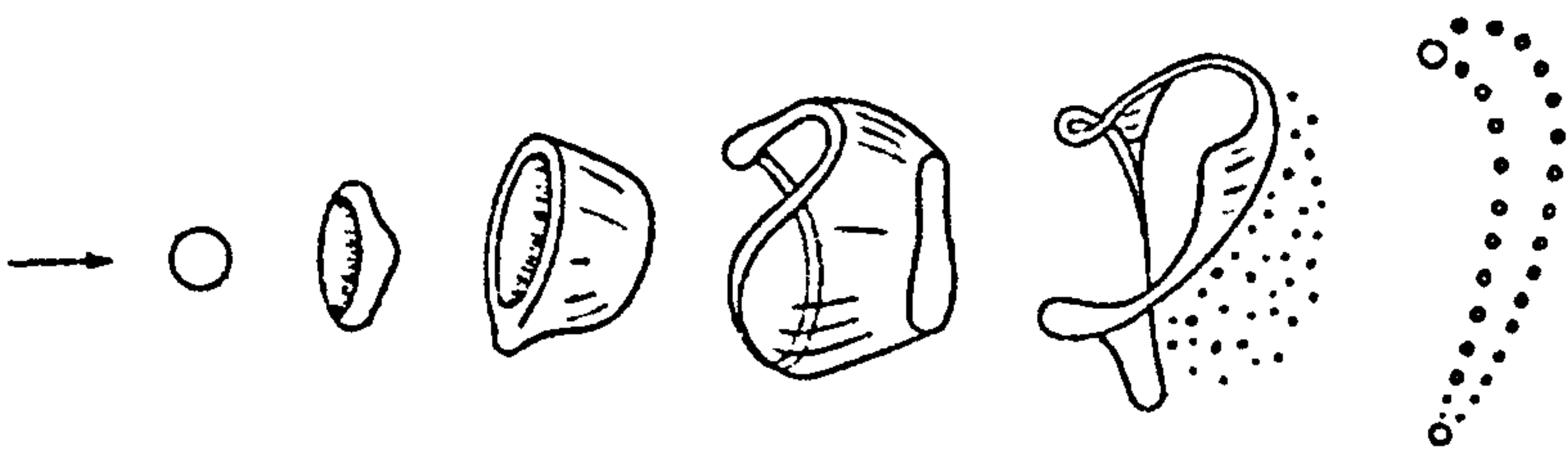


Figure 3-6: Illustration of a droplet experiencing bag break-up, taken from Bayvel et al. [182].

The stripping break-up, also called ligament break-up, is presented in Figure 3-7 [183], which shows a droplet travelling in a cross flow and forming ligaments, in the direction of the airflow, which eventually disintegrates into smaller droplets.



Figure 3-7: Stripping break-up [183].

Another type of stripping break-up was recorded by Bayvel et al. [182] and shown in Figure 3-8, in which the initial droplet is distorted by the air travelling in the opposite direction, leading to the formation of two ligaments that eventually form two droplets of identical size.

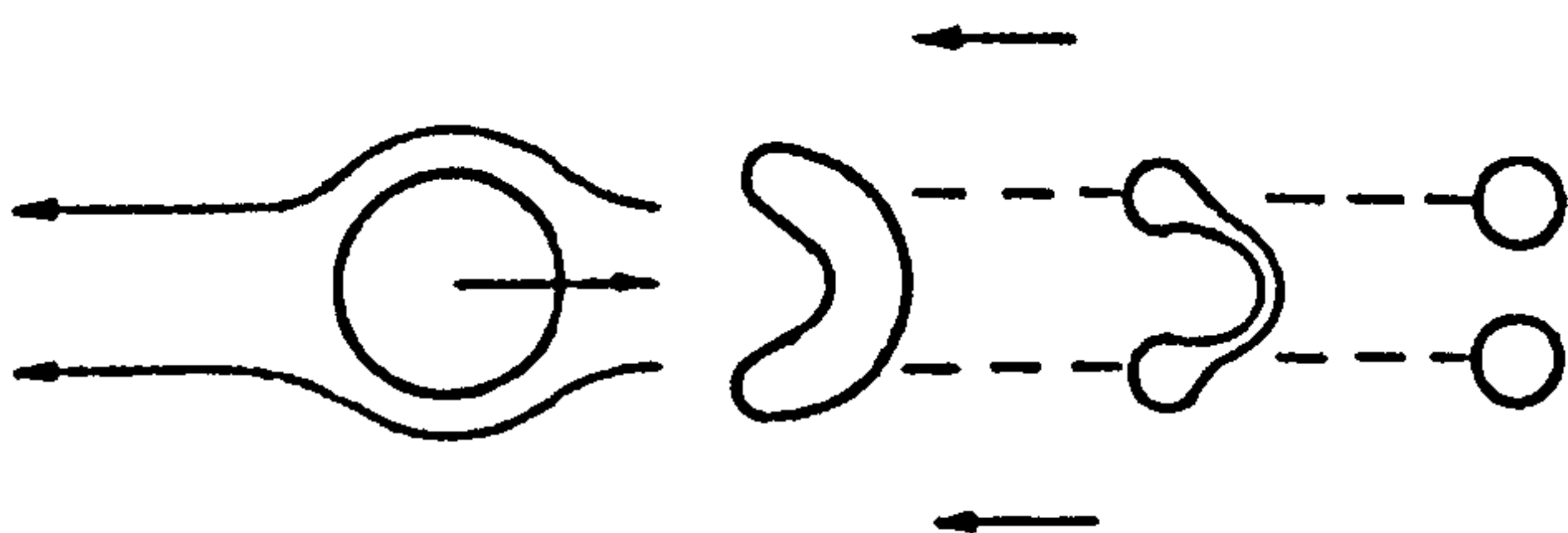


Figure 3-8: Stages of simple drop division [182].

Analysis of the experimental data leads to some conclusions about the order of inherent induction times and time of complete break-up, and also to conclusions about the maximum deformation of a droplet and the spectrum of secondary droplets. In the first fragmentation mode, the droplet breaks into 2-4 fragments, and to the maximum point in time  $\tau=2-3$ , the droplet deformation reaches its maximum deformation. In the bag-chaotic fragmentation modes at time  $\tau =1-2$  the maximum lateral deformation of the droplet is  $D_{DEF}/D_{DROP}=3-6$ , and the balloon inflation begins. The fragmentation is completed at  $\tau=5$  and until then, the displacement of the liquid is about  $D_{DEF}/D_{DROP}=10$ . In the stripping mode, fragmentation initiates approximately at a time close to the point of attaining the maximum deformation of  $D_{DEF}/D_{DROP}=2-3$  at  $\tau =1-2$ , and ends at  $\tau =5$ . Tiny droplets of  $D=0.1 \cdot D_{DROP}$  begin to prevail, and their amount grows with the increase of the Weber number. Various correlations exist for the calculation of the break-up time, according to the different regime defined by equation 3-62:

$$\begin{aligned}
 We_{CRIT} < We < 12 \quad \tau_{END} &= 0.25\pi \left[ \frac{\sigma}{\rho_L D_{DROP}^3} - 6.25 \frac{\mu_L}{\rho_L D_{DROP}^2} \right]^{0.5} \\
 12 \leq We < 18 \quad \tau_{END} &= 6(We - 12)^{-0.25} \\
 18 < We \leq 45 \quad \tau_{END} &= 2.45(We - 12)^{0.25} \\
 45 < We \leq 350 \quad \tau_{END} &= 14.1(We - 12)^{-0.25} \\
 350 < We \leq 1000 \quad \tau_{END} &= 0.766(We - 12)^{0.25} \\
 We > 1000 \quad \tau_{END} &= 5.5
 \end{aligned} \tag{3-63}$$

The viscosity effects are introduced with the contribution of the Ohnesorge number:

$$\tau_{END} = \frac{\tau_{END}}{1 - Oh/7} \tag{3-64}$$

where the Ohnesorge number (or viscosity group) is defined as:

$$Oh = \frac{\mu_{LIQUID}}{(\rho_{LIQUID} D_{HOLE} \sigma)^{1/2}} \tag{3-65}$$

During that break-up time, the droplet experiences deformation and it is assumed that its shape can be approximated by that of a spheroid having an instantaneous diameter on the elongated axis  $D_{DEF}$  which can take a maximum value of  $D_{DEF,MAX}$ ; according to Hsiang et al. [180, 181] and Faeth et al. [174,175] these parameters can be calculated from the following correlations:

$$D_{DEF,MAX}/D_{DROP} = 1 + 0.19We^{0.5} : Oh < 0.1 \tag{3-66}$$



$$\frac{D_{\text{DEF}} - D_{\text{DROP}}}{D_{\text{DEF,MAX}} - D_{\text{DROP}}} = 0.8 \frac{t}{\tau_{\text{END}}} \quad (3-67)$$

After the pass of the total break-up time, three group cases are considered for calculating the SMD of the formed droplets. In the vibrational, bag and bag-and-stamen modes ( $We < 45$ ), the SMD of the formed droplets is given by:

$$\text{SMD} = \frac{4D_{\text{DROP}}}{4 + 0.5(1 + f(\text{Oh}) We^{0.5})} \quad (3-68)$$

where  $f(\text{Oh})$  is generally function of the Ohnesorge number  $\text{Oh}$  and it can be taken equal to 0.19. For these regimes, the maximum possible droplet size  $D_{\text{MAX}}$  required for the calculation of the droplet size distribution is assumed to be equal to the initial droplet size. For the chaotic and catastrophic regimes:

$$\frac{\rho_G \cdot \text{SMD} \cdot U_{\text{REL}}^2}{\sigma} = C \left( \frac{\rho_L}{\rho_G} \right)^{1/4} \left( \frac{\mu_L}{\rho_L \cdot D_{\text{DROP}} \cdot U_{\text{REL}}} \right)^{1/2} We \quad (3-69)$$

where  $C=6.2$  is an empirical coefficient introduced to fit the experimental data [174,175]. The maximum possible droplet size  $D_{\text{MAX}}$  is assumed to be equal to the initial droplet size for the chaotic regime, and equal to the maximum stable diameter for the catastrophic break-up regime, which, according to Pilch et al. [178], can be estimated from the following correlation:

$$D_{\text{STABLE}} = We_{\text{CRIT}} \frac{\sigma}{\rho_L U_{\text{REL}}^2} \left( 1 - \frac{V_F}{U_{\text{REL}}} \right)^{-2} \quad (3-70)$$

where  $V_F$  is the velocity of the fragment cloud when the droplet breaks, calculated as:

$$V_F = U_{\text{REL}} \left( \frac{\rho_L}{\rho_G} \right)^{0.5} (B_1 \tau_{\text{END}} + B_2 \tau_{\text{END}}^2) \quad (3-71)$$

where  $B_1=0.375$  and  $B_2=0.236$  are empirical constants chosen to fit the experimental data. The associated loss of droplet kinetic energy is assumed to be dissipated within the droplet during its deformation; since this represents only a very small fraction of the total droplet kinetic energy (of the order of 0.5% in the most extreme cases), it is not added as source term to the energy exchange between the liquid and gas phases.

A different approximation is introduced for the calculation of the droplet size in the stripping regime ( $100 < We < 1000$ ). The mass flux leaving the droplet is estimated from the correlation:

$$\frac{dM_{\text{STRIP}}}{dt} = C \cdot \rho_L \left( \frac{\rho_G}{\rho_L} \right)^{1/3} \left( \frac{\mu_G}{\mu_L} \right)^{1/6} \mu_L^{1/2} U_{\text{REL}}^{1/2} D_{\text{DROP}}^{3/2} \quad (3-72)$$

where  $C$  is another empirical constant set equal to 12; details can be found in Ranger et al. [184].

The model assumes that the maximum possible droplet size  $D_{MAX}$  equals the droplet diameter before break-up and that only one droplet is formed, then the maximum entropy formalism algorithm described in section 3.3.3 is implemented to calculate the actual size of the small droplets, knowing their SMD and the  $D_{MAX}$ . Finally the number of particles per parcel is updated imposing the mass conservation:

$$N_{particle,p}^{after\ break-up} = N_{particle,p}^{before\ break-up} \frac{V_{drop,p}^{before\ break-up}}{\sum_k^{N_{p,tot}} V_{drop,k}^{after\ break-up}} \quad (3-73)$$

where  $N_{particle,p}^{before\ break-up}$  and  $N_{particle,p}^{after\ break-up}$  state for the number of particles in the parcel  $p$  before and after break-up respectively,  $V_{drop,p}^{before\ break-up}$  the volume of the droplet contained in the particle  $p$  before break-up,  $V_{drop,k}^{after\ break-up}$  the volume of the droplet contained in the parcel  $k$  after break-up and  $N_{p,tot}$  the total number of parcels present in the spray.

### 3.4.5 Liquid droplet evaporation

The droplet vaporisation process represents one of the main subjects investigated in the present work, thus its modelling is presented in details in the next chapter. The discussion focuses on the mathematical formulation of the wide range of single droplet vaporisation models selected from the extensive literature about this field of research, followed by the modelling validation against experimental data and the parametrical investigation on numerical and operating parameters. The results from the single droplet vaporisation modelling have been transferred to the spray code and implemented in the simulations presented in Chapter 5 and 6 for diesel and gasoline spray applications under a wide range of operating conditions.

### 3.4.6 Forces acting on a moving parcel

The Newton's second law states that the momentum transfer between each individual particle and its surrounding can be expressed as:

$$\frac{d(m_p \vec{u}_p)}{dt} = \sum F_i = F_{TOTAL} \quad (3-74)$$



where  $m_p$  and  $\vec{u}_p$  represent the particle mass and velocity vector respectively, and  $F_{\text{TOTAL}}$  the sum of all the forces  $F_i$  exerting upon the particle itself, which can be distinguished in the following components:

$$F_{\text{TOTAL}} = F_{\text{AEROD}} + F_M + F_{\text{BASSET}} + F_A + F_G + F_{\text{THERM}} + F_{\text{MAGNUS}} + F_{\text{SHAFMAN}} + F_{\text{PRES}} + F_{\text{CERT}} \quad (3-75)$$

$F_{\text{AEROD}}$  is the aerodynamic force,  $F_M$  is the ‘added mass’ or ‘virtual mass’ force,  $F_{\text{BASSET}}$  is the ‘Basset history integral’ force,  $F_A$  is the Archimides force,  $F_G$  is the gravitational force,  $F_{\text{THERM}}$  is the thermoforesis force,  $F_{\text{MAGNUS}}$  is the Magnus,  $F_{\text{SHAFMAN}}$  is the Shafman force,  $F_{\text{PRES}}$  is the surrounding fluid pressure gradient force and  $F_{\text{CENTR}}$  are centrifugal forces. The mathematical expressions of all these forces are given in Gavaises [4]. Here only the details of the aerodynamic force modelling is discussed, since it is the one actually playing a role in the simulations presented in this thesis.

### Aerodynamic force

The aerodynamic force comprises skin friction and form drag; it is mathematically expressed according to the following form:

$$\vec{F}_{\text{AEROD}} = C_D \frac{\rho_L A_p}{2} \vec{u}_{\text{rel}} |\vec{u}_{\text{rel}}| \quad (3-76)$$

where  $C_D$  is the aerodynamic drag coefficient and  $A_p$  is the cross sectional area of the particle exposed to the relative flow direction. Numerous investigations have focused on the definition of the drag coefficient, since it determines to a large extend the momentum exchange between the gas and the liquid phases. The well-known Stokes law states that:

$$C_D = \frac{24}{\text{Re}} \quad (3-77)$$

It holds only for flows that are entirely dominated by viscous forces, that is to say for low Reynolds numbers. For higher Reynolds numbers, the inertial forces become significantly larger and most of the correlations for droplet drag coefficient in common use are based on the analysis of experimental data. In diesel engines the droplets usually experience a drag that differs from that of spherical solid particles, since the flow pattern around the droplet is considerably different. Since there is no single expression for droplet drag coefficient that applies to all conditions, the following correlation is adopted for a spherical undistorted droplet moving in a low temperature environment, taking into account the flow circulation inside the liquid droplet, according to Feng et al. [185]:

$Re < 5$  :

$$C_D = \frac{8.}{Re} \frac{3.\lambda+2.}{\lambda+1.} \left( 1. + 0.05 \frac{3.\lambda+2.}{\lambda+1.} Re \right) - 0.01 \frac{3.\lambda+2.}{Re+1.} Re \log(Re)$$

$Re \geq 5$ .,  $Re \geq 1000$ .  $\Rightarrow Re = 1000$  .:

$$C_{D,0} = \frac{48.}{Re} \left( 1. + \frac{2.21}{\sqrt{Re}} - \frac{2.14}{Re} \right)$$

$$C_{D,1} = 17.Re^{-2/3.}$$

(3-78)

$$C_{D,\infty} = \frac{24.}{Re} \left( 1. + \frac{1.}{6.} Re^{2/3.} \right)$$

$$\lambda > 0. \text{ AND } \lambda < 2: C_D = \frac{\lambda - 2.}{2.} C_{D,0} + 4. \frac{\lambda}{\lambda + 6.} C_{D,\infty}$$

$$\lambda > 2.: C_D = \frac{4.}{\lambda + 2.} C_{D,1} + \frac{\lambda - 2.}{\lambda + 2.} C_{D,\infty}$$

$$\lambda = \mu_L / \mu_G$$

where  $Re$  is the Reynolds number.

Yuen et al. [57] found that evaporation affects droplet drag in two different ways; firstly, the temperature and concentration gradients between the particle surface and the ambient gas cause substantial reductions in the viscosity of the gas, which reduces drag coefficient. Secondly, the mass transfer associated with droplet evaporation induces the so called ‘blowing’ effect, which reduces friction drag and increases form drag. These effects can be taken into the calculation of the drag coefficient through empirical correlations, for example those reported by Lefebvre [186].

For movement in an evaporating environment, temperature and concentration gradients and ‘blowing’ effect due to mass transfer influence the drag coefficient, according to the Eisenklam’s empirical correlation [187]:

$$C_{D,EVAP} = C_D / (1. + B) \quad (3-79)$$

where  $B_M$  is the Spalding mass transfer number, defined as:

$$B_M = \left( \sum_{i=1}^{N_f} y_{i,G,S} - \sum_{i=1}^{N_f} y_{i,G,\infty} \right) / \left( 1. - \sum_{i=1}^{N_f} y_{i,G,S} \right) \quad (3-80)$$

With  $y_{i,G,S}$  and  $y_{i,G,\infty}$  the vapour mass fraction of the species  $i$  at the droplet surface and in the surrounding ambient, respectively.

The correlation (3-79) was found to be valid for droplets with in the range of 25-500 $\mu$ m and for mass transfer number from 0.06 up to 12.3 [186].

In case of movement in the presence of other droplets, the expression for the drag coefficient takes the following form, according to Rusche et al. [188]:



$$C_{D,\theta} = C_D \cdot \left( \exp^{2.1(1-\alpha_L)} + (1-\alpha_L)^{0.249} \right) \quad (3-81)$$

where  $\alpha_L$  is the local liquid volume fraction.

The relatively high velocity between the liquid particle and the surrounding gas induces particle deformation [184, 180], which considerably affects the drag coefficient according to the following expression:

$$C_{D,DEF} = C_D \left[ 0.85 + 0.15 D_{DEF}/D_p \right] \quad (3-82)$$

where  $C_D$  is the drag coefficient of the spherical particle, calculated from the previous equations, and the ratio  $D_{DEF}/D_p$  represents the droplet deformation estimated by the break-up model, equation (3-67).

Among all the forces exerting upon a moving parcel and presented in this section, the aerodynamic and gravity forces have been found to play a more significant role on both the single parcel dynamics and the whole spray development so their effect has been always included in the simulations presented in this investigation. Once defined all the forces acting on the parcel, the Newton's second law expressed by equation (3-74) is solved; successively the trajectory equation is integrated in time to calculate the new parcel position:

$$\vec{x}_p^{new} = \vec{x}_p^{old} + \int_t^{t+\Delta t} \vec{u}_p dt \quad (3-83)$$

Where  $\vec{x}_p^{old}$  and  $\vec{x}_p^{new}$  stand for the old and new parcel position vectors respectively,  $\vec{u}_p$  its velocity vector, calculated from the Newton's second law (3-74) and  $\Delta t$  the tracking time

### 3.4.7 Parcel to parcel interaction

Stochastic collision models are commonly used in Lagrangian simulations of particulate and spray flows. Numerical results suggest that collision processes in sprays have a great influence on the average drop size. Unfortunately, droplet collisions can be very expensive to calculate [189]. Droplet collisions in dense spray are modeled by statistical rather than deterministic approach [190]. The phenomenon, caused by differences in the velocities of the two colliding particles, has remarkably effect on the spray development particularly in the regions with high particle density, such as close to the spray axis [191] and during spray impingement close to the wall, due to the opposite direction of



incoming and outgoing droplets. The particle-to-particle interaction model implemented in the GFS code refers to the O'Rourke's collision algorithm [192], where three types of collision mode are taken into account: permanent coalescence, separation, and bouncing (Figure 3-9).

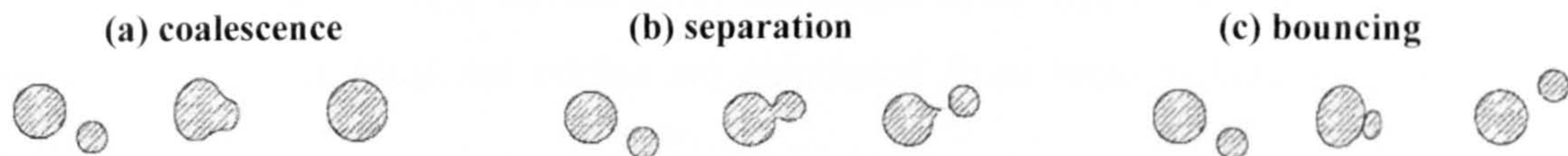


**Figure 3-9: Possible particle collision outcomes. Figure adapted from Orme [193].**

Coalescence occurs when the energy is not only big enough to overcome the gas film, but also to overcome the surface tension of the individual particles; moreover the energy is not sufficient to re-break the surface tension of the newly-formed surface; consequently the mass, energy and momentum in the new larger particle are conserved. Separation after collision takes place when the energy is large enough to overcome the surface tension of the newly formed parcel, this leads the two parcels to temporarily coalesce, and then to break apart into the two original parcels. Therefore, their size and the number of particles they contain remain unchanged, and only a small amount of momentum is lost during the process. Finally bouncing occurs if the energy of collision is not enough to expel the gas film between the droplets. The parcel characteristics remain unchanged except for the droplet velocities. The detailed mathematical expressions of the different models implemented in the GFS code is given in Gavaises [4], although they have not been used in the simulations proposed for the purposes of this thesis.

### 3.4.8 Parcel turbulent dispersion

In technological applications the interaction of the particles with the turbulent structure of the flow is an extremely complex problem. The major governing factors in the motion of spherical particles in a turbulent flow field are the particle inertia and drag, the fluid turbulence and the crossing trajectory effects. Several studies have been done with the scope to include the effect of turbulent dispersion on the parcel motion. Gosman et al. [195] suggested the so-called 'eddy interaction model' for homogeneous isotropic turbulent flows, which complete description is given in Graham [196]. The model states that the instantaneous velocity of the fluid phase should be calculated by



adding to the mean fluid velocity,  $\bar{u}_{\text{MEAN}}$ , a random fluctuating component,  $\bar{u}'$ , which is sampled from an assumed distribution function:

$$\bar{u} = \bar{u}_{\text{MEAN}} + \bar{u}' \quad (3-84)$$

In this concept, characteristic quantities of the turbulence structure are determined from mean gas flow properties. Specifically, the length scale  $l_{\text{EDDY}}$  and the dissipation time scale  $t_{\text{EDDY}}$  of the idealized eddies are calculated from local turbulence properties as follows:

$$l_{\text{EDDY}} = c_{\mu}^{3/4} \frac{k^{2/3}}{\varepsilon} \quad (3-85)$$

$$t_{\text{EDDY}} = \frac{k}{\varepsilon} \quad (3-86)$$

where  $k$  and  $\varepsilon$  represent the turbulent kinetic energy and its dissipation rate calculated by the turbulent model and  $C_{ps}=0.145$  is an empirical constant. The time it takes the drop to travel through the eddy,  $t_{\text{TRAV}}$ , is defined by the following expression, obtained from the solution of a simplified and linearized form of the drop motion equation:

$$t_{\text{TRAV}} = C_{ps} \frac{k^{3/2}}{\varepsilon} \frac{1}{|\bar{u}_{\text{rel}}|} \quad (3-87)$$

where  $\bar{u}_{\text{rel}}$  is defined as a function of the fluid and parcel velocities:

$$\bar{u}_{\text{rel}} = \bar{u}_{\text{MEAN}} + \bar{u}' - \bar{u}_p \quad (3-88)$$

When the smaller of these time scales has elapsed, the droplet is deemed to enter a new eddy, and the interaction time period is defined as:

$$t_{\text{TURB}} = \min\{t_{\text{EDDY}}, t_{\text{TRAV}}\} \quad (3-89)$$

Consequently, the random process generates a new velocity fluctuation from a Gaussian distribution function determined by:

$$G(\bar{u}') = \frac{1}{\sqrt{2\pi} s} \exp\left(-\frac{\bar{u}'^2}{2s^2}\right) \quad (3-90)$$

where  $s$  represents its standard deviation, according to the following equation:

$$s = \sqrt{\frac{2}{3} k} \quad (3-91)$$

The determination of the eddy length scale and the velocity scale is crucial for the performance of the eddy lifetime models.

The previous model is according to Gosman et al. [195] algorithm. Other two parcel turbulence dispersion mathematical formulations have been implemented in the GFS code and proposed in the present investigation. They refer to O'Rourke et al. [197] and the Langevin [198] models, briefly described as follows.

### **O'Rourke et al. [197] model**

O'Rourke et al. [197] turbulent dispersion model is an extension of Gosman et al. [195] model. The main algorithm to calculate the fluctuating component of the fluid velocity that the parcel 'sees' at its location is kept un-changed, with the only exception of the coefficient  $C_{ps}$  in equation (3-87), which is set equal to 0.16432. Moreover, the model calculates the turbulent component of the parcel velocity when the turbulence interaction period, defined by equation (3-89), results to be greater than the parcel tracking time. In this case the new parcel fluctuating velocity is estimated from a Gaussian distribution function with standard deviation mathematically expressed as follows:

$$s_{\text{parcel}} = \sqrt{\frac{1 - \exp(-C_D t_{\text{TURB}})}{1 + \exp(-C_D t_{\text{TURB}})} 1 - \exp(-C_D \Delta t) s^2} \quad (3-92)$$

where  $C_D$  represents the parcel drag coefficient calculated according to the equation (3-78), and  $\Delta t$  the parcel tracking time.

### **Langevin model [198]**

The Langevin model proposes a different algorithm to estimate the fluctuating fluid velocity. First, it defines the lagrangian time scale, function of the turbulence kinetic energy dissipation rate,  $\varepsilon$ , and the standard deviation,  $s$ , which is calculated according to equation (3-91):

$$t_{\text{LAGRANGIAN}} = \frac{2}{\mu_{\text{Langevin}}} \frac{s^2}{\varepsilon} \quad (3-93)$$

where the constant  $\mu_{\text{LANGEVIN}}$  is set equal to 2.1. Then, the interaction time period is assumed equal to the parcel tracking time:

$$t_{\text{TURB}} = \Delta t \quad (3-94)$$

The diffusion and the correlation function terms,  $\chi$  and  $\xi$  respectively, are defined by the following expression:



$$\chi = S \sqrt{\frac{2}{t_{\text{LAGRANGIAN}}}} \quad (3-95)$$

$$\xi = 1 - \frac{t_{\text{TURB}}}{t_{\text{LAGRANGIAN}}} \quad (3-96)$$

Finally the fluctuating velocity  $\bar{u}'$  is updated according to a correlation, function of the old fluctuating velocity,  $\bar{u}'^{\text{old}}$ , the correlation function,  $\xi$ , the diffusion term,  $\chi$ , and the value obtained implementing a Gaussian distribution function,  $\bar{u}'^{\text{pdf}}$ , with standard deviation equal to  $\sqrt{t_{\text{TURB}}}$  :

$$\bar{u}'^{\text{new}} = \xi \bar{u}'^{\text{old}} + \chi \bar{u}'^{\text{pdf}} \quad (3-97)$$

### 3.4.9 Parcel impingement

Interest in spray-wall interactions has recently intensified because of the development of direct injection spark ignition engines. In this type of engine, impingement of the spray on the piston and the cylinder walls leads to increased emissions of hydrocarbons and soot. Experiments described in the literature indicate that the outcome of spray impingement is controlled by varying parameters like parcel velocity, size, temperature, incidence angle, fluid properties (i.e. density, viscosity and surface tension), wall temperature, surface roughness, wall film thickness and gas boundary layer characteristics in the near wall region, leading to a wide spectrum of possible droplet outcomes [199]. The model of Bai et al. [200] was formulated using a combination of simple theoretical analysis and experimental data from an extensive variety of sources [201, 203, 204]. It suggests that the impingement process can be distinguished in a total of seven regimes, as shown in Figure 3-10:

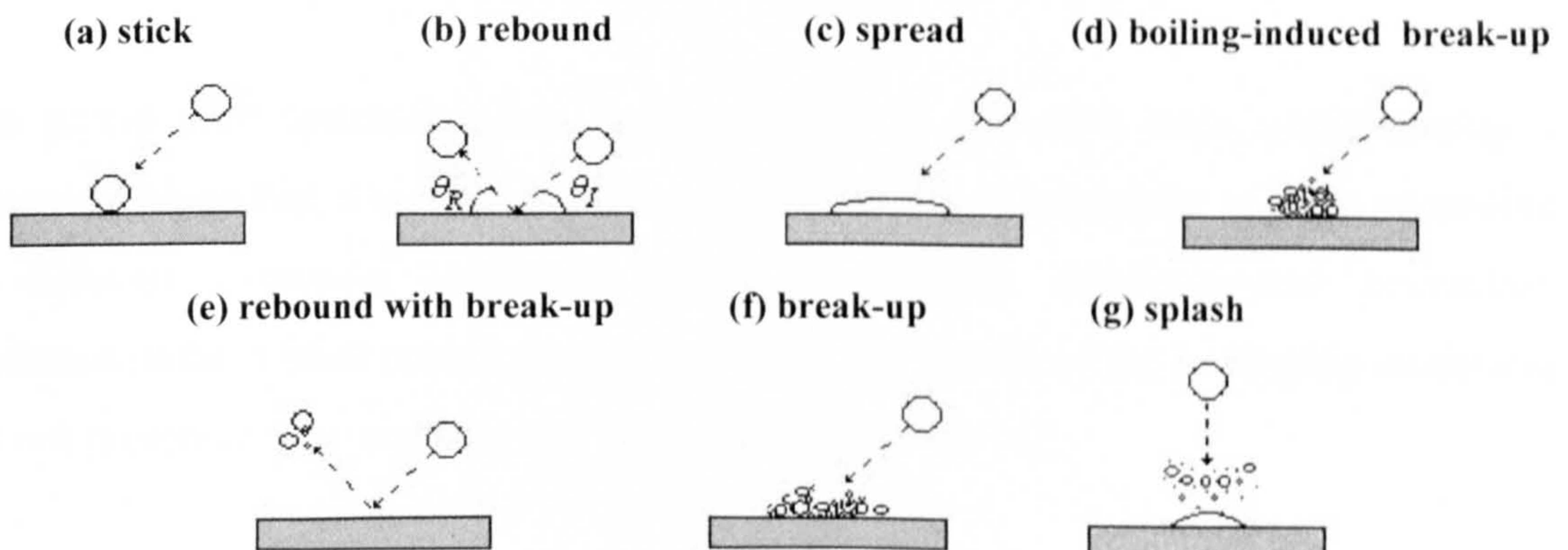


Figure 3-10: Schematic of different impact regimes, Bai et al. [200].



**Stick:** The particle attaches to the wall approaching a spherical form. The particle kinetic energy must be low as well as the wall temperature for this regime to occur (below the ‘pure adhesion temperature’,  $T_{PA}$ ).

**Rebound:** The particle bounces off the wall after impact. This regime takes place under two conditions: (i) on dry walls, with the wall temperature being higher than a ‘pure rebound’ characteristic temperature ( $T_{PR}$ ) at which contact between the liquid particle and the hot surface is prevented by the intervening vapour film; (ii) on a wetted wall, where the air film between the droplet and the liquid film prevents the energy lost to be large, which results in the particle to bounce.

**Spread:** The kinetic energy of the particle is higher than those that ‘stick’, which allows it to spread out on the wall, forming a liquid film.

**Boiling-induced break-up:** When the wall temperature is near to the Nakayama temperature (i.e. temperature at which a particle reaches its maximum evaporation rate), the particle disintegrates due to rapid liquid boiling. The kinetic energy of the impinging particle does not need to be large.

**Rebound with break-up:** In this mode the particle bounces off a hot surface, which temperature is lower than the pure rebound temperature, with break-up into two or three particles taking place at the same time.

**Break-up:** The particle undergoes a large deformation on the hot surface, which temperature is higher than the pure rebound temperature; a thermo-induced instability causes the liquid film to randomly break.

**Splash:** When the impinging particle carries a high amount of kinetic energy, a crown is formed, followed by the formation of ligaments which eventually break into secondary particles.

The parcel wall interaction has been modelled in the GFS code implementing a numerical algorithm, which takes into account a variety of impinging regimes according to different impaction conditions. Since no specific droplet-to-wall interaction mechanisms have been investigated in this work, the details of the impinging modelling are not presented here and they can be found in Gavaises [4].



### 3.5 Coupling of continuous and dispersed phases

This paragraph focuses on the interaction between the continuous and dispersed phases, which physical modelling has been illustrated in the previous sections of the chapter. It is based on the consideration that the Eulerian-Lagrangian frame of reference, implemented in the GFS code, is sensitive to the spatial and temporal discretisation methodology adopted. This is due to the fact that the various phenomena taking place are characterised by different space and time length scales, which require appropriate modelling. Figure 3-11 illustrates the schematic of the flow development inside a direct injection combustion engine, showing the commonly used cell sizes and time steps implemented to resolve the physical processing occurring.

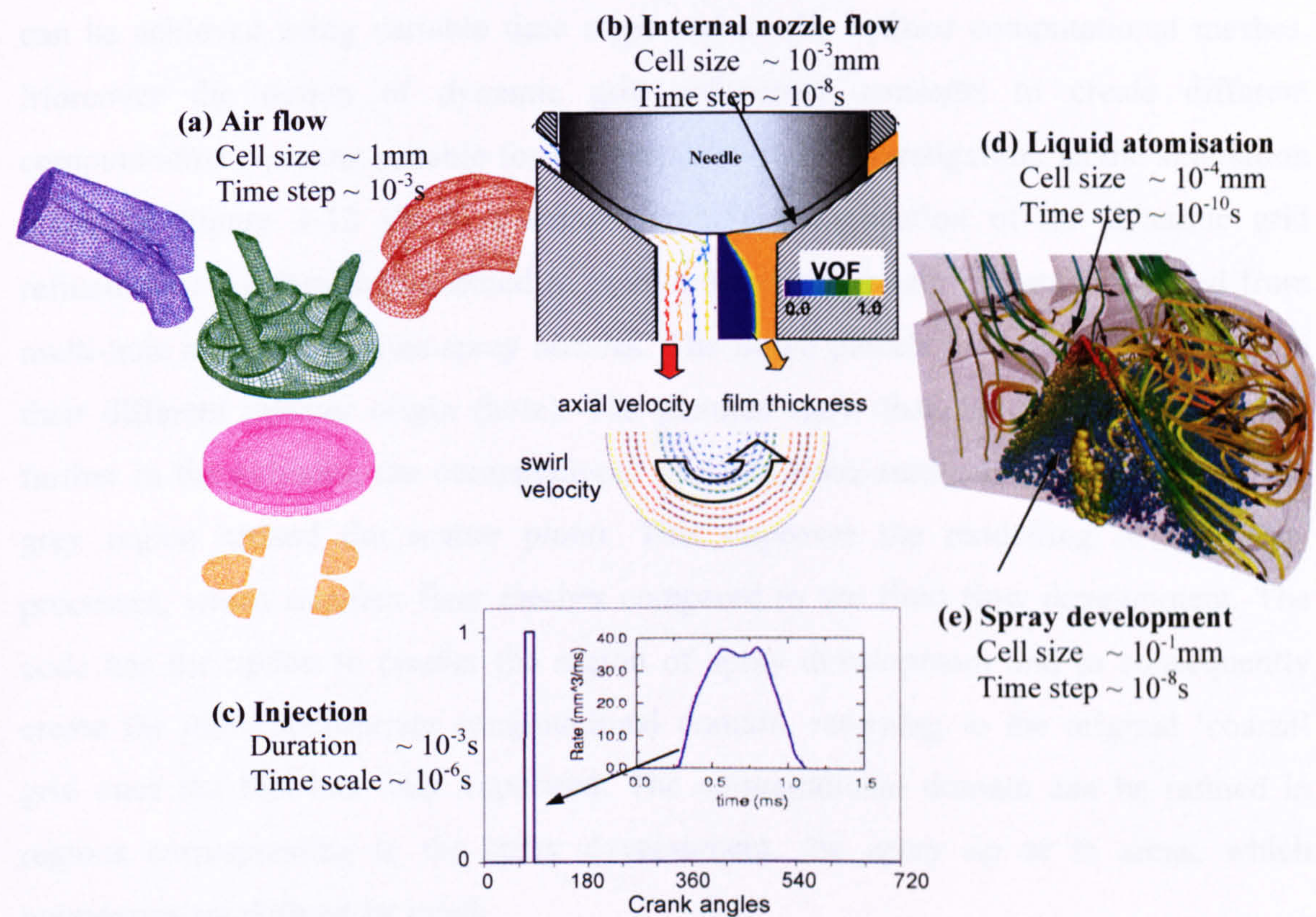


**Figure 3-11: Spatial and temporal discretisation length scales for fuel injection system modelling: (a) air flow, (b) internal nozzle flow, (c) fuel injection, (d) liquid atomisation, (e) spray development.**

It clearly highlights the variety of spatial and temporal discretisation lengths predicting the flow fields in the various regions and periods during the engine cycle. The modelling of the air flow development inside the engine ports and in the cylinder bore requires a mesh with cell size of the order of 1mm and time step of about 1ms. On the



other hand, the processes governing the fuel injection system should be predicted using smaller time steps of the order of  $10^{-8}$ s and finer computational grids, which cell size varies from  $10^{-1}$ mm for in-cylinder spray development investigation, up to  $10^{-3}$ mm and  $10^{-4}$ mm for internal nozzle flow and liquid atomisation predictions, respectively. Furthermore, Figure 3-11(c) shows that the fuel injection interval of time corresponds to a small fraction of the total engine cycle period. Its duration is few milliseconds and it is usually modelled using a time step of the order of the microsecond. The successive atomisation process of the fuel emerging from the nozzle hole also interests a small fraction of the total engine period and a confined region of space.

This suggests the idea to implement specific spatial and temporal discretisation length scales during the simulation, according to the different phenomena taking place. This can be achieved using variable time steps and locally refined computational meshes. Moreover the option of dynamic grid refinement consents to create different computational domains suitable for the purposes of the investigation, as the simulation proceeds. Figure 3-12 shows a sample from the application of the dynamic grid refinement algorithm implemented to predict the development of sprays injected from multi-hole and hollow cone-spray nozzles. The liquid parcels are colored according to their different injector origin (hole). The pictures show that, as the sprays penetrate further in the cylinder, the computational grid has been automatically refined (darker grey region around the scatter plots). This improves the modelling of the spray processes, which requires finer meshes compared to the fluid flow development. The code has the option to predict the region of spray development and to consequently create the more appropriate computational domain, returning to the original 'coarse' grid once the fuel has fully vaporised. The computational domain can be refined in regions corresponding to the spray development, the spray tip or in areas, which boundaries are defined by input.

The spatial and temporal discretisation length scales affect the estimation of the flow variables of the continuous phase 'seen' by the discrete parcels as they move in the surrounding fluid. Moreover, they have a strong influence on the mathematical treatment of the source terms expressing the mass, momentum and energy exchanges between the liquid and the gas phases. The author developed and implemented in the CFD code a combination of different interpolation/distribution methods. They are based



on the assumption that the region of influence between the two phases should be independent on the cell size and, and it should be defined according to some physical criteria.

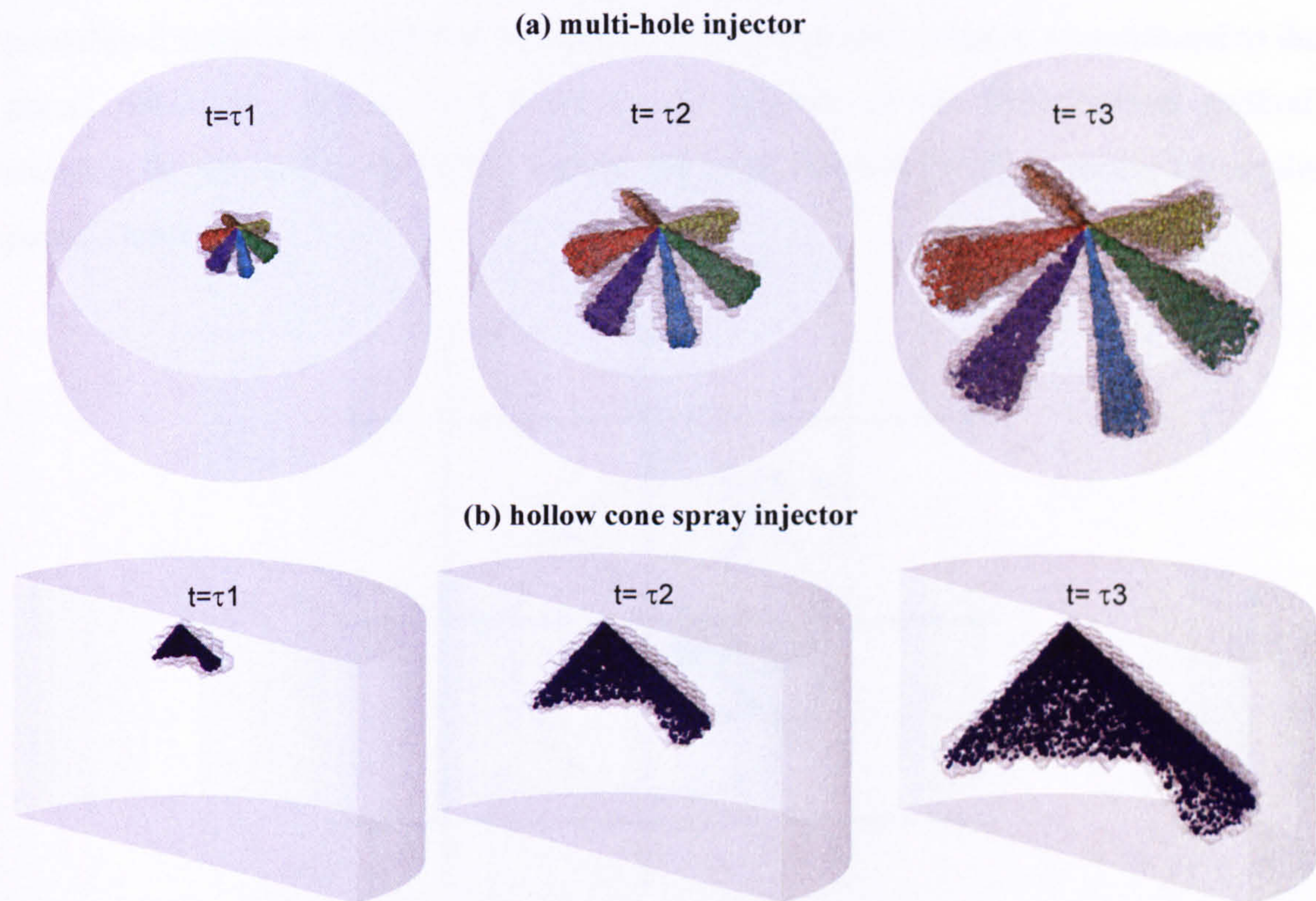


**Figure 3-12: Dynamic grid refinement in the region around the parcel location, at three time steps after start of injection, for (a) multi-hole injector and (b) hollow cone spray injector.**

In order to simulate the physical phenomena taking place from the start of fuel injection to the subsequent spray development and the multi-phase interaction, the model requires the knowledge of the transient fluid characteristics ‘seen’ by the parcels. The values of the continuous phase properties (temperature, pressure, velocity, density, viscosity, heat capacity, turbulence variables and void fraction) at the parcel location can be estimated using four different interpolation algorithms.

The first method states that the continuous phase scalar and vector variables should take the values of the fluid flow characteristics at the cell of the parcel location, as mathematically expressed by the following equation:

$$\varphi(\vec{x} = \vec{x}_p) = \varphi(\vec{x} = \vec{x}_{C_i}) \quad (3-98)$$

where  $\varphi$  is the requested scalar/vector quantity to be interpolated,  $\vec{x}_p$  and  $\vec{x}_{C_i}$  are the locations of the parcel centre and host cell centre respectively. Applications of this



algorithm show that it is sensitive to the computational grid volume, and thus, more accurate interpolation schemes are required.

The second method is based on the assumption that the region of influence between the two phases should be independent on the cell size but should be rather based on a predefined distance  $r$ , which can be equal to a fixed constant value or proportional to the parcel dimension. Figure 3-13 describes the scheme of the implemented method, showing the parcel  $P$  in the cell  $C_i$  and the region of influence within a radius  $r$  from the parcel centre.

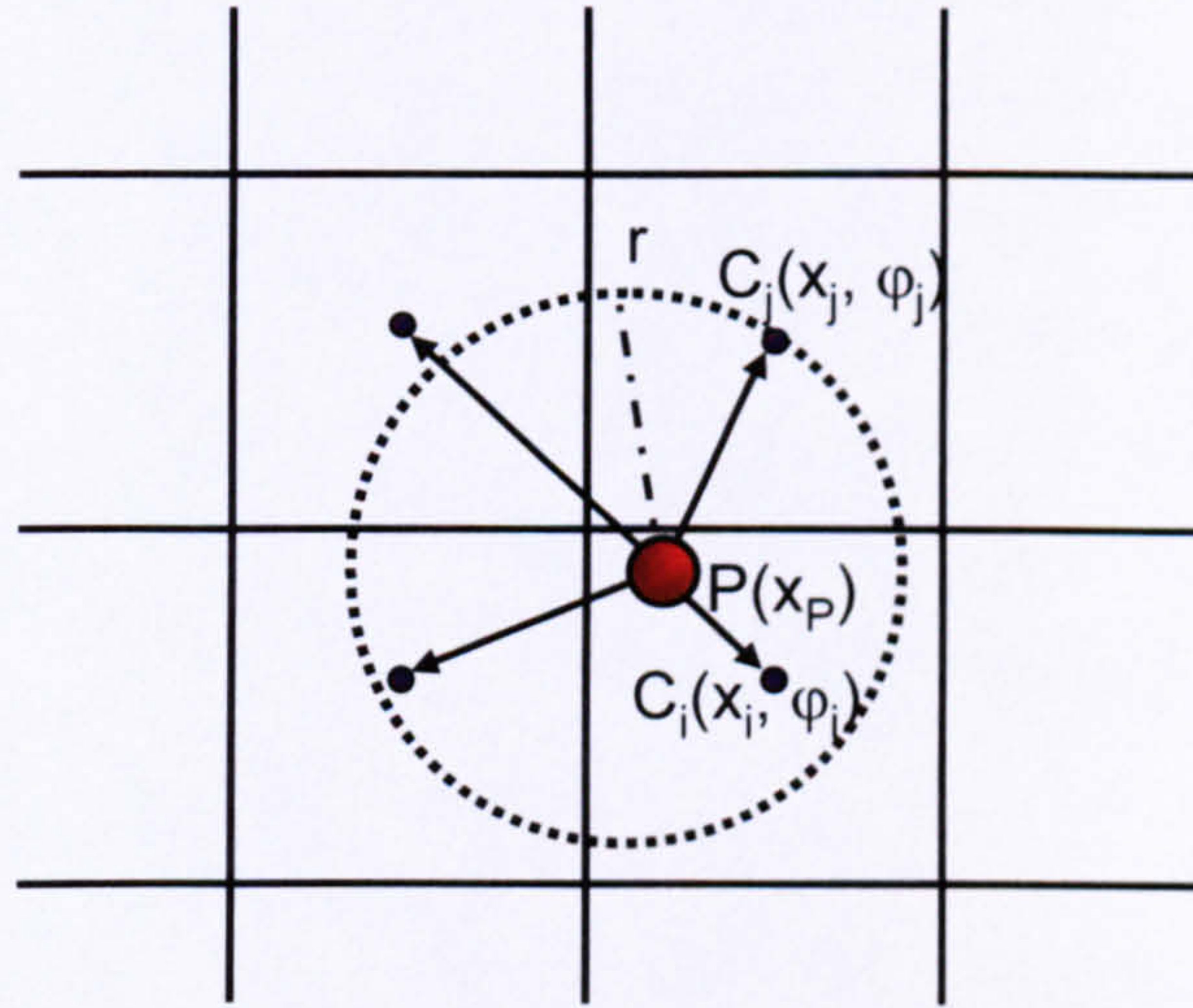


**Figure 3-13:** Schematic showing how the continuous phase variables seen by the parcel are interpolated among the cells around the parcel.

The cells found within this distance are identified and a weighting factor,  $\delta_i$ , function of this distance, rather than the cell volume, is used for the interpolation of the continuous phase variable, according to the following equations:

$$\varphi(\vec{x} = \vec{x}_p) = \sum_{i=1}^{N_c} \varphi(\vec{x} = \vec{x}_{C_i}) \delta_i \quad (3-99)$$

The weighting factor  $\delta_i$  is expressed as follows:

$$\delta_i = \frac{\lambda_{C_i} / (\gamma d_i / r + 1)}{\sum_{i=1}^{N_c} \lambda_{C_i} / (\gamma d_i / r + 1)}, \quad i = 1, N_c \quad (3-100)$$

where  $\lambda_{C_i}$  represents either a proportionality factor or the cell volume,  $\gamma$  is a user-defined constant increasing the relative weight of the closer cells and  $N_c$  is the total number of cells found within this region. The parcel-to-cell relative distance is defined as:

$$d_i = |\vec{x}_{C_i} - \vec{x}_p|, \quad i = 1, N_c \quad (3-101)$$



The third method is based on the gradient-approach. The variables are interpolated according to the Taylor theorem, as illustrated in the following expression:

$$\varphi(\vec{x} = \vec{x}_p) = \varphi(\vec{x} = \vec{x}_{C_i}) + (\nabla \varphi)_{\vec{x}=\vec{x}_{C_i}} \cdot \Delta \vec{x}_{C_i,p} \quad (3-102)$$

where  $(\nabla \varphi)_{\vec{x}=\vec{x}_{C_i}}$  represents the gradient of the quantity  $\varphi$ , calculated at the parcel cell centre,  $C_i$ , with use of the Gauss' divergence theorem and  $\Delta \vec{x}_{C_i,p} = \vec{x}_{C_i} - \vec{x}_p$  is the distance vector between the cell and the parcel centres.

The fourth method, developed by Giannadakis [148], represents the multi-point interpolation technique, which averages the continuous phase variables calculated at a number of points on the parcel surface using the gradient-approach method. Several investigations show that this scheme achieves better approximation of the continuous phase properties at the parcel location in case of discrete parcels whose diameter is comparable to the size of the host cells, as in case of growing bubbles in cavitating flows, although it is prohibitively expensive in terms of computational times, thus requiring further development before its implementation for standard spray model applications.

The second important aspect of the multi-phase flow interaction modelling is related to the numerical treatment of the source terms, which express the mass, momentum and energy multi-phase exchange, in the fluid flow conservation equations. They are mathematically correlated with the Lagrangian approximation of the spray distribution function  $f(\vec{x}, \vec{u}, m, T, t)$  defined in equation (3-23).

The mass source term resulting from the droplet evaporation process is defined by the following expression:

$$\dot{S}_{MASS,i} = \int f(\vec{x}, \vec{u}, m, T, t) \frac{dm_i}{dt} d\vec{x} d\vec{u} dm dT \quad (3-103)$$

where  $\frac{dm_i}{dt} = \dot{m}_i$  represents the liquid vaporisation rate for each species in the liquid mixture.

The temporal variation of the relative momentum between the two phases is due to the relative velocity and mass changes, as a consequence of the forces exerting upon the moving parcel and the evaporation process respectively:

$$\dot{S}_{MOMENTUM} = \int f(\vec{x}, \vec{u}, m, T, t) \left[ m \frac{d\vec{u}}{dt} + \vec{u} \frac{dm}{dt} \right] d\vec{x} d\vec{u} dm dT \quad (3-104)$$

Finally the energy coupling term takes into account the heat flux between the two phases and the kinetic energy variations, due to the acceleration or deceleration of the parcel flowing in the continuum surrounding, according to the following expression:

$$\dot{S}_{\text{ENERGY}} = \int f(\bar{x}, \bar{u}, m, T) \left[ \frac{dm}{dt} \left( \frac{\bar{u}^2}{2} + C_{p_L} T \right) + m \left( \left| \bar{u} \frac{d\bar{u}}{dt} \right| + C_{p_L} \frac{dT}{dt} \right) \right] d\bar{x} d\bar{u} dm dT \quad (3-105)$$

The finite volume methodology implemented to solve the fluid flow conservation equations allows estimation of the source terms expressing the multi-phase interaction during the sub-cycles of the discrete phase. The source terms are then added explicitly to the continuous phase solution. Source terms are distributed among the cells of the computational domain, according to specific physical and numerical criteria. The standard method, used by the majority of commercial CFD codes, gives all source terms to the cell of the parcel location, independently of the vicinity of neighbour cells. The author developed a method, which is based on the assumption that the interaction between the Eulerian and the Lagrangian phases should be not treated on the cell-to-parcel basis, but using spatial distribution functions. These allow for distribution of the spray source terms on a number of cells found within a distance from the droplet centre. This method is similar to the algorithm described for the second interpolation scheme, equations (3-99) and (3-101). The total source term exchanged by the parcel P with its surrounding,  $\dot{S}_p$ , calculated from equations (3-103), (3-104) and (3-105), is distributed among the cells found in the region of influence:

$$\dot{S}_{p,i} = \dot{S}_p \delta_i, \quad i = 1, N_c \quad (3-106)$$

where  $\dot{S}_{p,i}$  represents the contribution of the source term to the cell  $i$ ,  $N_c$  the total number of cells affected by the distribution and  $\delta_i$  the weighting factor, which is equal to 1 in case of source terms added to the cell of the parcel location, or is based on a combination of distance, cell volume and internal energy when a spatial distribution method is implemented.

The first method proposed defines the spatial distribution weighting factor according to the cell volume:

$$\delta_i = \frac{\text{Vol}_{C_i}}{\sum_{i=1}^{N_c} \text{Vol}_{C_i}}, \quad i = 1, N_c \quad (3-107)$$



where  $\text{Vol}_{C_i}$  represents the volume of the cell  $i$ . This represents a criterion based on the assumption that bigger cells should exchange bigger source terms with the dispersed phase.

Another spatial distribution approach is based on the physical and geometric criterion stating that the phase interaction is proportional to the distance of the parcel from the different cells inside the region of influence, with closest cells having a bigger contribution, as expressed by the following equation:

$$\delta_i = \frac{1/(\gamma d_i/r + 1)}{\sum_{i=1}^{N_c} 1/(\gamma d_i/r + 1)}, \quad i = 1, N_c \quad (3-108)$$

where  $d$ ,  $r$  and  $\gamma$  correspond to the distribution variables defined in equation (3-100).

A different way to define the parcel-to-cell distance (equation 3-101) is proposed for the momentum source term distribution, taking into account the tracking of the parcel during the dispersed phase sub-cycles. The final parcel location,  $\vec{x}_p$ , is replaced by an average point corresponding to the middle distance travelled by the parcel during its tracking time, according to the following expression:

$$\vec{x}_p^{\text{middle}} = 0.5 \left( \vec{x}_p^{\text{old}} + \vec{x}_p^{\text{new}} \right) \quad (3-109)$$

where  $\vec{x}_p^{\text{old}}$  and  $\vec{x}_p^{\text{new}}$  state for the parcel location at start and at the end of the dispersed phase time step, respectively.

In this case the distribution region has been defined as proportional to the covered distance by the parcel within the dispersed phase tracking time:

$$r = A_1 0.5 \sqrt{\left( \vec{x}_p^{\text{new}} - \vec{x}_p^{\text{old}} \right) \cdot \left( \vec{x}_p^{\text{new}} - \vec{x}_p^{\text{old}} \right)} \quad (3-110)$$

$A_1$  is a constant of proportionality selected equal to 1.1, derived by the assumption that the region of influence for the momentum exchange between the two phases corresponds to a circular region, around the middle parcel location, which size is 10% bigger than the distance travelled by the parcel during its tracking time step.

The third distribution method results from the combination of the cell volume and the distance of each cell from the parcel location:

$$\delta_i = \frac{\text{Vol}_{C_i} / (\gamma d_i/r + 1)}{\sum_{i=1}^{N_c} \text{Vol}_{C_i} / (\gamma d_i/r + 1)}, \quad i = 1, N_c \quad (3-111)$$

Finally, a distribution method, taking into account the internal energy of the cells inside the interaction region between the parcel and the surroundings, is defined according to following expression:

$$\delta_i = \frac{\text{Vol}_{c_i} \rho_{c_i} C_{p_{c_i}} T_{c_i} / (\gamma d_i / r + 1)}{\sum_{i=1}^{N_c} \text{Vol}_{c_i} \rho_{c_i} C_{p_{c_i}} T_{c_i} / (\gamma d_i / r + 1)}, \quad i = 1, N_c \quad (3-112)$$

This method results particularly useful in case of distribution of mass and energy source terms due to the liquid droplet vaporisation, since the gas phase internal energy available represents the limiting factor governing the physical phenomenon.

As far as the void fraction integration during the parcel sub-cycles, the model considers the residence time of the parcels within a computational cell. Additionally, the excess volume that may result computationally if a cell is fully filled by liquid parcels is again distributed to the surrounding cells. Further details can be found in Giannadakis [148].

Finally, another contribution to the computational methodology, with the scope to guarantee numerical stability and more realistic results, consists in the introduction of ‘virtual’ local flow field variables. This method has an effect in moderating the source terms during the parcel tracking time step, assuring that the continuous phase properties will not take non-physical values during the parcel sub-cycles. It has a significant consequence in the case of very dense sprays, predicted using Eulerian grids with cell size comparable to that of the discrete parcels. The cell ‘virtual’ values for velocity, temperature, species concentration and void fraction are calculated according to the following expression:

$$\phi_c^{\text{new}} = \phi_c^{\text{old}} + \frac{S_c}{\Psi_c} \quad (3-113)$$

where  $\phi_c$  represents the old/new value of the ‘virtual’ cell variable to be estimated,  $S_c$  the source term from mass, momentum, energy and ‘void’ exchanges between the discrete and the continuous phases and  $\Psi_c$  a parameter representing the cell mass or the product between the cell mass and heat capacity at constant pressure, according to the different variables to be estimated. In particular for the calculation of ‘virtual’ cell velocities, the equation (3-113) assumes the form:

$$\vec{u}_c^{\text{new}} = \vec{u}_c^{\text{old}} + \frac{\dot{S}_{\text{MOMENTUM},c}}{m_c} \quad (3-114)$$



Where the  $\dot{S}_{\text{MOMENTUM},c}$  represents the momentum source term calculated by equation (3-104) and added to the continuous phase using the distribution methods described in equation (3-106). A numerical algorithm has been implemented in order to check the value calculated by equation (3-114), according to the physical criteria stating that, during the parcel tracking time, each component of the surrounding velocities should not become higher than the corresponding parcel value if it was initially lower. In case the equation (3-114) estimates a non-physical value, the ‘virtual’ cell velocities are forced to be equal to the parcel velocity values. The same check is done for surrounding velocity initially higher than the parcel ones. This has an effect on the momentum exchange experienced by the following parcel travelling in the same cell, or by the same parcel during the successive sub-cycles, since the gas phase velocity approaches the parcel velocities and vice-versa, preventing their values from diverging, due to considerable momentum transfers. This method plays a significant role particularly in the dense spray region at the exit of the injector hole, where the number of particles and the liquid/gas relative velocities are considerable high.

The ‘virtual’ cell species concentrations are calculated according to the following expression:

$$\phi_{ic}^{\text{new}} = \phi_{ic}^{\text{old}} + \frac{\dot{S}_{\text{MASS},i,c}}{m_c} \quad (3-115)$$

Since they represent the ratio between the vapour mass of each species present in the cell and its total mass, their values are limited to 1. Their estimation limits the vaporisation process, since the vapour mass fraction surrounding the liquid droplet controls the evaporation mass transfer, as described in details in the following chapter.

Finally the ‘virtual’ cell temperature is calculated as follows:

$$T_c^{\text{new}} = T_c^{\text{old}} + \frac{\dot{S}_{\text{ENERGY},c}}{m_c C_{p,c}} \quad (3-116)$$

Its value is limited by the internal energy available inside the cell, estimated by the product between the cell mass, heat capacity and temperature. The physical criterion behind this method is based on the assumption that the surrounding gas cannot become colder than the parcel within the evaporation sub-cycle, if the energy is transfer from the gas to the liquid. In this case the ‘virtual’ cell temperature is numerically limited to take the parcel temperature value. A similar approach is implemented in case of energy

transferred from the parcel to the surrounding gas, when the gas temperature cannot become higher than the liquid one within the vaporisation time step.

The structure of the code has been built in order to take into account the contribution of the different source terms within the sub-cycles of momentum transfer and vaporisation, which are the main processes responsible of the multi-phase interaction investigated in this work. The computational effort required for the source term spatial distribution may prohibitively increase the CPU time, since for all the parcels at the beginning of each process sub-cycle the cells within the region of influence should be identified and the distribution procedure described above has to be implemented. It has been found that the most expensive part, in terms of computational time, is the selection of the cells within the region of influence. This suggests to implement an algorithm to calculate once, at the beginning of the simulation, the cells within a specified distance from each cell centre of the computational domain. This procedure, although it reduces the CPU time, it does not allow to interpolate the continuous phase variables at the parcel location and distribute the source terms from liquid/gas phase interaction among a dynamic region of influence, which interaction distance  $r$  in Figure 3-13 is assumed to be proportional to the parcel dimension.

### 3.6 Summary

This chapter has described the numerical algorithm implemented in the GFS code and used in the present investigation, predicting the fuel spray development. It is based on the Eulerian-Lagrangian approach, by which air/vapour mixture is modelled as continuous phase and the liquid particles as the dispersed one. Initially the finite volume methodology was briefly presented and discussed. This method has been applied for the numerical solution of the partial differential equations which govern the air flow. Then, the Lagrangian model was presented, focusing initially on the fundamental physical processes assumed to take place during the spray development. These include link with the internal nozzle flow conditions, fuel atomisation, liquid droplet secondary break-up, vaporisation, aerodynamic forces, turbulent dispersion, droplet-to-droplet and droplet-to-wall interactions. Successively, the computational parameters, which control the multi-phase interaction, were discussed. The contribution of the author to the general structure of the spray code and to the implementation of



different methods for the numerical treatment of the continuous phase variable interpolation and the source term distribution has been discussed. It is based on the assumption that the region of influence between the two phases should be independent of the cell size and it should be rather defined according to some physical and numerical criteria. In addition, the developed code allows local dynamic grid refinement of the computational domain where and when is needed in order to resolve better the flow development in the spray development region.

# Chapter 4

In all affairs it's a healthy thing now and then to hang a question mark on the things you have long taken for granted.  
Bertrand Russell

## MODELLING, VALIDATION AND PARAMETRIC INVESTIGATION OF SINGLE DROPLET VAPORISATION PROCESSES

### 4.1 Introduction

The vaporisation process taking place in a liquid droplet immersed in a gaseous environment involves simultaneous heat and mass transfers. The heat for vaporisation is transferred to the droplet surface by conduction, convection or radiation from the surrounding gases and the vapour is transferred by convection and diffusion back into the gas flow field. The overall rate of vaporisation depends on one hand on the pressure, temperature and transport properties of the gas and on the other hand on the temperature, volatility and size of the droplet. Moreover the relative motion between the liquid droplet and the surrounding gas affects the vaporisation process. In the last two decades, considerable effort has been made by researchers to add new physical insight to all aspects of fuel evaporation. In liquid fuel combustors, for example, the evaporation process becomes a rate-controlling factor and, in particular in direct-injection spark-ignition engines, the spatial and temporal distribution of the fuel vapour influences the choice of the location of the spark plug. The classical fuel evaporation theory, exhaustively treated in textbooks by Williams [205], Chigier [206], Sirignano [42], deals with spherically-symmetric, quasi-steady, single-component isolated droplets. In order to address the requirements of real combustor modelling, the multi-dimensionality and transient effects have been successively considered together with a proper characterisation of the fuel composition and the interaction among the parcels that define dense sprays typically present in real operating conditions. A variety of different models have been proposed in order to capture the physical phenomena involved in the process. It is possible to classify these models into two categories: (i) extended models studying the physics of a single vaporising droplet, deriving simplified correlations and validating simpler models; (ii) models to be implemented in more



complex whole-spray simulations. This chapter focuses on the review of single droplet vaporisation modelling, describing its mathematical formulation according to the different assumptions imposed by the models. Initially the multi-component nature of the droplet has been neglected and the fuel composition has been described by one ‘pseudo-species’. The classification of droplet vaporisation model in order of increasing complexity, proposed by Sirignano [42], has been followed: (i) the ‘classical  $d^2$ -law’, which neglects the liquid heating, assuming the droplet temperature to be uniform and constant at its wet-bulb state; the (ii) the ‘infinite liquid-conductivity model’, ICM, which predicts uniform, transient liquid temperature profiles; (iii) the ‘conduction limit model’, or ‘finite liquid-conductivity model’, FCM, which provides radial temperature profiles inside the droplet as vaporisation takes place, neglecting convective effect; (iv) the ‘effective conductivity model’, ECM, which includes convective effect in the previous ‘conduction limit model’. As far as the ‘vortex model’, which captures the droplet internal circulation due to the relative motion between the liquid and gas phases, and the models based on the full solution of the Navier–Stokes equations, they have not been proposed in the present investigation. The effect of convective transport caused by the droplet motion relative to the gas has been modelled according to the so-called ‘film theory’ proposed by Tong et al. [56], which assumes that the resistance to heat and mass exchange between a surface and a gas flow may be investigated introducing the concept of gas film of constant thickness. The effect of transient and variable thermo-physical properties in the gas and liquid phases is addressed, suggesting to calculate them at a reference value. The vaporisation models result to be very sensitive to their estimation. Furthermore, investigations of the droplet vaporisation behaviour at high pressure and temperature conditions typical of modern diesel and gasoline engines have brought further interest and engineering challenges. In such environments, the phenomenon of super-critical vaporisation is likely to occur, arguing on the validity of common assumptions like the gas-phase quasi-steadiness, the ideal gas behaviour and the solubility of gases in the liquid-phase. Moreover the enthalpy of vaporisation is markedly different at low and high pressure conditions. The calculation of the fuel vapour concentration at the droplet surface, due to the transient vaporisation process, represents one of the main features of the models implemented. In the present investigation, three different models are used to describe the liquid/gas interface conditions. The first one assumes ideal phase equilibrium at the interface and it uses the Clausius-Clapeyron equation to evaluate the vapour pressure at the droplet surface. The



non-equilibrium Langmuir-Knudsen evaporation law has been investigated in Miller et al. [107] showing that non-equilibrium effects are significant for droplet sizes in the typical range of practical spray simulations. The concentration of the vaporising species is corrected with a correlation function of the gas and phase properties, the liquid density and the vaporisation rate. Under high-pressure conditions the assumption of ideal mixing is no longer valid. Gas solubility in the liquid-phase and variable thermo-physical properties depending on pressure, temperature and composition can be estimated modelling the thermodynamic equilibrium for each species in the mixture in terms of fugacity coefficients. The liquid and gas phase concentration and the enthalpy of vaporisation are calculated through an iterative algorithm, implementing a viral equation of state. Typical diesel and gasoline fuels consist of more than a hundred components and exhaust emissions, cold-starting and warming-up performances are affected by the distillation characteristic of the fuel. Furthermore, the nature of the fuel in diesel and gasoline engines determines the dependence of flame propagation on the laminar flame speed, which is a function of both fuel composition and the vapour fuel/air mixture ratio. Consequently, the prediction of the fuel vapour concentration, the equivalence ratio and the correct initial composition of the fuel to be injected have to be correctly estimated. In this investigation the fuel has been described as a mixture of discrete known species. Following a procedure similar to the one adopted for internal liquid temperature investigation, the liquid phase mass transfer is predicted by the ‘infinite mass diffusion model’, IDM, which provides uniform transient species concentration profiles as vaporisation takes place, and by the ‘finite mass diffusion model’, FDM, or the ‘effective mass diffusion model’, EDM, which describe the liquid concentration radial distributions in stagnant or convective environments, respectively. Figure 4-1 describes the single droplet vaporisation phenomenon, focusing on the main parameters described by the modelling.

The next sections describe first the mathematical formulation of the droplet vaporisation models implemented in the CFD code and used for the purposes of the present investigation. Successively the results from the modelling have been validated against extensive experimental data-bases under a variety of operating conditions.



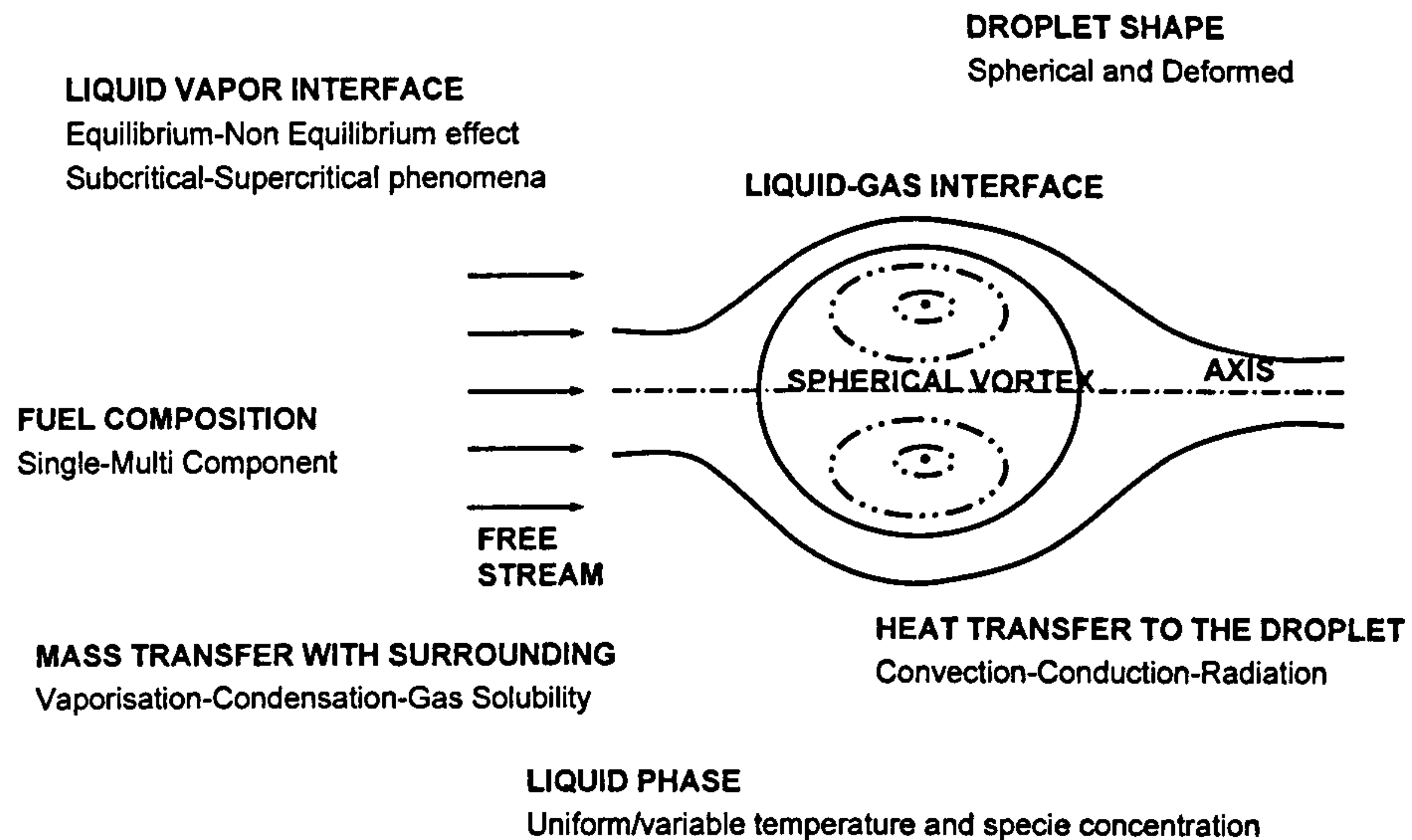


Figure 4-1: Scheme of the main parameters in the single droplet vaporisation modelling.

## 4.2 Mathematical formulation of single droplet vaporisation modelling

The conservation equations governing the temporal evolution of global droplet quantities during the evaporation process are the conservation of total droplet mass:

$$\frac{dm_L}{dt_L} = \dot{m}_L \quad (4-1)$$

with the vaporisation rate  $\dot{m}_L$  defined to be positive when the droplet losses mass, and the conservation of energy for the droplet:

$$\frac{d}{dt}(m_L C_{pL} T_L) + \Delta h_{\text{vap}} \frac{dm_L}{dt} = 4\pi R_d^2 h (T_\infty - T_L) + 4\pi R_d^2 \sigma \epsilon (T_{\text{rad}}^4 - T_L^4) \quad (4-2)$$

which states that the energy to heat-up the droplet plus the energy for droplet vaporisation equal the contributions of energy by convection and radiation transfer from the surrounding ambient to the droplet surface. If radiation effects are neglected, the second term on the right side of equation (4-2), representing the irradiative heat flux from a blackbody coming from infinite, is not present. When the contribution of heat radiation is included, the radiation source temperature,  $T_{\text{rad}}$ , is set equal to the ambient gas,  $T_\infty$ , or to a specific value, assuming the presence of a flame front. Different models have been introduced to capture the change of droplet size/temperature/composition due to the vaporisation processes. Moreover, the contribution of mass/energy source terms due to mass/heat transfers between the liquid and gas phases is estimated, according to the different operating conditions and numerical assumptions considered.

Initially the single-component vaporisation models are presented, with the mathematical formulation of the ‘infinite conductivity model’ (ICM), which predicts uniform liquid-phase transient temperature profiles, the ‘finite conductivity model’ (FCM) and the ‘effective conductivity model’ (ECM), which investigate the spatial temperature distribution inside the droplet in stagnant and convective surroundings, respectively.

As far as the definition of the interface vaporisation conditions, the initial assumption of ideal equilibrium at the liquid/gas interface is relaxed introducing non-equilibrium effects and investigating the physical processes under high-pressure conditions, involving solubility of gases in the liquid phase and pressure dependent physical properties. The modelling of multi-component fuel vaporisation requires a more complex algorithm, which formulation is described in a separate section. According to the literature, particular attention has to be given to the definition of the physical property correlations for the liquid and the gas phase, function of pressure, temperature and mixture composition. The author refers to Poling et al. [155] and Perris et al. [156] for the detailed description of the relationships used. Table 4-I summaries the main assumptions adopted in the different droplet vaporisation models presented and discussed in the following sections.

Number of droplets in the parcel	1 / N (part <sub>n<sub>p</sub></sub> )
Fuel composition	Single / Multi-component
Droplet shape	Spherical / Deformed
Liquid-gas interface conditions	Low-pressure ideal equilibrium (LPEqM) / NON-equilibrium (NON-EqM) / High-pressure effect (HPM)
Liquid-phase temperature distribution	Uniform (ICM) / Radial in stagnant flow (FCM) / Radial in convective flow (ECM)
Liquid-phase composition distribution	Uniform (IDM) / Radial in stagnant flow (FDM) / Radial in convective flow (EDM)
Flow field	Convective/ Stagnant
Radiation effect	Neglected / Considered
Liquid/gas relative velocity	Constant / Variable (Drag coefficient model)

**Table 4-I: Scheme of the evaporation model assumptions investigated.**



### 4.2.1 Single-component vaporisation modelling

#### Uniform temperature distribution within the droplet: ‘infinite conductivity model’, ICM

The model assumes that the thermal diffusivity in the liquid phase is much faster than the droplet lifetime, predicting uniform droplet temperature profiles. The procedure starts with the definition of the input variables and the initial conditions parameters, represented by the ambient pressure and temperature, the liquid/gas phase relative velocity, the initial droplet size and temperature and the fuel vapour concentration, the vaporisation time step and the gas phase domain.

The effect of convective transport due to the droplet motion relative to the gas is taken into account adopting the so-called ‘film theory’ [56]. According to Hubbard et al. [49] the film temperature and composition are an average of the conditions at the droplet surface and the ambient gas. The ‘1/3 rule’ is implemented, as suggested by the following expressions:

$$\begin{aligned} T_{F,ref} &= \frac{(T_{\infty} + 2 \cdot T_{L,S})}{3} \\ Y_{F,ref} &= \frac{(Y_{F,\infty} + 2 \cdot Y_{F,S})}{3} \end{aligned} \quad (4-3)$$

A first estimation of the vapour mass fraction at the droplet surface is defined according to the physical conditions at the gas/liquid interface of the previous time step.

The thermo-physical properties (density, thermal conductivity, heat capacity at constant pressure, viscosity and binary diffusion coefficients) of pure ambient air, fuel vapour and gas phase mixture are calculated as function of pressure, temperature and composition at conditions far away from the droplet and according to the film reference conditions, estimated by the equations (4-3).

The gas-phase non-dimensional numbers, Reynolds, Schmidt and Prandtl, are expressed as follows:

$$Re = \frac{2 \cdot \rho_a \cdot \Delta U \cdot R_d}{\mu_{G,ref}}, \quad Sc = \frac{\mu_{G,ref}}{\rho_{G,ref} \cdot Diff_G}, \quad Pr = \frac{\mu_{G,ref} \cdot Cp_{G,ref}}{\lambda_{G,ref}} \quad (4-4)$$

where the subscript ‘a’ refers to the pure ambient air, ‘G’ to the gas-phase mixture and ‘ref’ to the film reference conditions.

An iterative procedure has been implemented to calculate the droplet heating-up and the vaporisation processes. The liquid-phase thermo-physical properties are calculated at the beginning of each vaporisation sub-cycle, as function of ambient pressure and liquid temperature. The calculation of the fuel vapour concentration at the droplet surface, due to the transient vaporisation phenomenon, represents one of the main features characterising the particular model implemented. Three different approaches are suggested to investigate the liquid/gas interface conditions.

#### Ideal phase equilibrium, LPEqM

Under the hypothesis of ideal phase equilibrium at the interface, the Clausius-Clapeyron equation is used to evaluate the vapour pressure at droplet interface,  $P_{V_s} = f(T_L)$ , function of the liquid temperature. Once  $P_{V_s}$  is determined, the equilibrium mole and mass fractions at the surface,  $X_{F,S}$  and  $Y_{F,S}$ , can be evaluated as follows:

$$X_{F,S} = \frac{P_{V_s}}{P_{\infty}}, \quad Y_{F,S} = \frac{X_{F,S} \cdot MW_F}{X_{F,S} \cdot MW_F + (1 - X_{F,S}) \cdot MW_A} \quad (4-5)$$

Assuming constant latent heat of vaporisation, the surface vapour mole fraction is related to the saturation pressure  $P_{sat}$  through the following correlation:

$$X_{F,S} = \frac{P_{sat}}{P_{\infty}} = \frac{P_{atm}}{P_{\infty}} \exp \left[ \frac{\Delta H_{vap}}{\bar{R}/MW_f} \left( \frac{1}{T_B} - \frac{1}{T_L} \right) \right] \quad (4-6)$$

where  $T_B$  is the liquid phase normal boiling temperature (corresponding to atmospheric pressure,  $P_{atm}$ , conditions),  $\bar{R}$  the universal gas constant,  $MW_f$  the molecular weight of the fuel and  $\Delta h_{vap}$  the latent heat of vaporisation.

#### Non-equilibrium conditions at the interface (Langmuir-Knudsen evaporation law), NONEqM:

Bellan et al. [108] first introduced the non-equilibrium Langmuir-Knudsen evaporation law, showing that non-equilibrium effects are significant for droplet sizes in the typical range of practical spray simulations. The non-equilibrium law reflects in the calculation of the vapour mole fraction at the droplet surface:

$$X_{F,S, \text{NON-Eq}} = X_{F,S, \text{Eq}} - \left( \frac{L_K}{R_d} \right) \beta \quad (4-7)$$



where  $X_{F,S,Eq}$  is the vapour mass fraction at the droplet surface calculated assuming equilibrium conditions, equation (4-6),  $R_d$  the droplet radius and  $L_K$  the Knudsen layer thickness:

$$L_K = \frac{\mu_G \sqrt{2\pi T_L \bar{R} / MW_f}}{\alpha_e Sc P_\infty} \quad (4-8)$$

$\alpha_e$  is the molecular accommodation coefficient (assumed equal to unity),  $Sc$  the gas phase Schmidt number, while the non-dimensional evaporation parameter  $\beta$  is defined as:

$$\beta = -\left(\frac{3 Pr \tau_d}{2}\right) \frac{\dot{m}_L}{m_L} \quad (4-9)$$

$Pr$  is the non-dimensional gas phase Prandtl number,  $\dot{m}_L$  the evaporation rate, and  $\tau_d$  is the particle time constant for Stokes flow defined as:

$$\tau_d = \rho_L D^2 / (18 \mu_G) \quad (4-10)$$

#### High-pressure conditions at the interface (fugacity coefficients method), HPM:

For high-pressure conditions, the assumption of ideal mixing behaviour is no longer valid and the Raoult's law for the calculation of the vapour mass fractions at the droplet surface is not appropriate. Effects like non-ideal gas behaviour, liquid-phase solubility of gases, variable thermo-physical pressure dependent properties are usually modelled using viral equations of states for the calculation of the liquid-vapour mole fractions at the interface and the enthalpy for vaporisation. The criteria for phase equilibrium at the droplet surface can be expressed using liquid and vapour fugacity coefficients, which can be calculated by an equation of state. The cubic equation of state of Peng-Robinson EOS has been implemented here:

$$P = \frac{\bar{R}T}{V-b} - \frac{a(T)}{V(V+b)+b(V-b)} \quad (4-11)$$

the coefficients  $a$  and  $b$  for the pure components are function of temperature, and the coefficients  $a_m$  and  $b_m$  are calculated using mixing rules [155].

The EOS can be transformed into a cubic equation:

$$z^3 - (1 - B^*)z^2 + (A^* - 2B^* - 3B^{*2})z - A^*B^* + B^{*2} + B^{*3} = 0 \quad (4-12)$$

with

$$A^* = \frac{a_m P}{\bar{R}^2 T^2} \text{ and } B^* = \frac{b_m P}{\bar{R} T} \quad (4-13)$$

The compressibility factor can be expressed as follows:

$$Z = \frac{PV}{\bar{R}T} = f_p(T, P) \quad (4-14)$$

The thermodynamic equilibrium for each component in the (gas/liquid) mixture is expressed in terms of fugacity coefficients:

$$\phi_i^l x_i^l = \phi_i^v y_i^v \quad i = 1, n \quad (4-15)$$

where  $x_i^v$  is the mole fraction of species  $i$  in the liquid phase and  $y_i^v$  is the corresponding mole fraction in the vapour phase.

The fugacity coefficients are pressure, temperature and composition dependent. For an equation of state that is explicit in pressure, they can be evaluated by:

$$\ln \phi_i = - \int_{\infty}^V \left[ \left( \frac{\partial P}{\partial N_i} \right)_{T, V, N_{j \neq i}} - \frac{\bar{R}T}{V} \right] dV - \bar{R}T \ln Z \quad (4-16)$$

Using the Peng-Robinson EOS, the integration leads to the following equations, valid for each species in the mixture:

$$\ln \phi_i = \frac{b_i}{b} (Z - 1) - \ln(Z - B^*) + \frac{A^*}{2\sqrt{2}B^*} \left( \frac{b_i}{b} - \frac{2}{a} \sum_j y_j (a_i a_j)^{1/2} \right) \ln \left( \frac{z + B^*(1 + \sqrt{2})}{z + B^*(1 - \sqrt{2})} \right) \quad (4-17)$$

An iterative method is required to obtain the equilibrium mole fraction defined in the matrix (4-15), once the compressibility factor is calculated from equation (4-14) and the fugacity coefficients from equation (4-17).

The calculation of the heat required to vaporise the droplet at each time step depends of the particular assumption imposed. Three correlations have been found in literature and implemented here. The first one calculates the heat of vaporisation function only of liquid temperature:

$$\Delta h_{\text{vap}} = \Delta h_{\text{vap}}(T_L) = A1 \cdot (1 - T_R)^{A2} + A3 \cdot T_R + A4 \cdot T_R^2 \quad (4-18)$$

where  $A1$ ,  $A2$ ,  $A3$  and  $A4$  are correlation constants, according to Perry et al. [156] and  $T_R$  is the reduced liquid temperature:

$$T_R = \frac{T_L}{T_C} \quad (4-19)$$

The second correlation calculates the heat of vaporisation as function of surface, critical and normal boiling fuel temperatures, according to Aggarwal et al. [207]:



$$\Delta h_{\text{vap}} = \left( \frac{T_c - T_L}{T_c - T_{Bn}} \right)^{0.38} \Delta h_{\text{vap}}(T_{Bn}) \quad (4-20)$$

where  $T_c$  is the fuel critical temperature,  $T_{Bn}$  the normal boiling temperature and  $\Delta h_{\text{vap}}(T_{Bn})$  the latent heat of vaporisation, calculated according to the temperature-dependent correlation (4-18).

Finally the third correlation includes the pressure effect at the gas/liquid interface (real gas behaviour, solubility of gases into the liquid and pressure effect on thermo-physical properties) in the calculation of the heat of vaporisation, according to the fugacity coefficients method:

$$\Delta h_v = -\frac{\bar{R}T^2}{MW_i} \frac{\partial}{\partial T} \left( \ln \frac{\phi_{i,v}}{\phi_{i,l}} \right) \quad (4-21)$$

where the fugacity coefficients are calculated from the algorithm described by equations (4-11) to (4-17).

Once the vaporised fuel concentration at the droplet surface has been estimated, the mass transfer Spalding number is calculated:

$$B_M = \frac{Y_{F,S} - Y_{F,\infty}}{1 - Y_{F,S}} \quad (4-22)$$

For an evaporating droplet, a correction factor has to be introduced to take into account the presence of Stefan flow, which influences the ‘film’ thickness [208]:

$$F(B_M) = (1 + B_M)^{0.7} \frac{\log(B_M)}{B_M} \quad (4-23)$$

Successively, the heat transfer Spalding number can be estimated. The theoretical definition of the heat transfer Spalding number states that:

$$B_T = \frac{Cp_{G,\text{ref}} (T_\infty - T_L)}{\Delta h_v} \left( 1 - \frac{\dot{Q}_{\text{heat}}}{\dot{Q}_c} \right) = \frac{\dot{m}_L Cp_{G,\text{ref}} (T_\infty - T_L)}{\dot{Q}_c} \quad (4-24)$$

where  $\dot{Q}_{\text{heat}}$  represents the energy flux for droplet heating, and  $\dot{Q}_c$  is the total convective energy flux from the surroundings, defined as function of the gas phase Nusselt number, the gas viscosity at reference conditions, the droplet size and the temperature gradient:

$$\dot{Q}_c = 2\pi R_d Nu \lambda_{G,\text{ref}} (T_\infty - T_L) \quad (4-25)$$

Abramzon et al. [61] suggested another correlation for the heat transfer Spalding number:

$$B_T = (1. + B_M)^{f_{\text{corr}}} - 1. \quad (4-26)$$

$f_{\text{corr}}$  is a correction factor, defined as:

$$f_{\text{corr}} = \frac{C_{p_{g,\text{ref}}}}{C_{p_{f,\text{ref}}}} \frac{1.}{Le} \frac{1. + \frac{kRM}{2.} \frac{Re^{1/2}}{F(B_M)}}{1. + \frac{kRM}{2.} \frac{Re^{1/2}}{F(B_T)}} \quad (4-27)$$

$$F(B_T) = (1. + B_T)^{0.7} \frac{\log(B_T)}{B_T} \quad (4-28)$$

where  $Le$  is the non-dimensional Lewis number, defined as:

$$Le = \frac{Sc}{Pr} \quad (4-29)$$

$kRM$  is an empirical factor, equal to 0.6 according to Ranz et al. [51] or equal to 0.555 according to Frössling [50]. An iterative procedure is implemented for the calculation of the heat transfer Spalding number and its correction factor. When the Prandtl and the Schmidt numbers equal one, the mass and the heat transfer Spalding numbers result to be coincident.

The mass and thermal transfer rates defined by Sherwood and Nusselt numbers are expressed according to the following correlations:

$$Sh = \left(2. + \frac{kRM \cdot Re^{1/2} \cdot Sc^{1/3}}{F(B_M)}\right) \frac{\log(B_M)}{B_M} \quad (4-30)$$

$$Nu = \left(2. + \frac{kRM \cdot Re^{1/2} \cdot Pr^{1/3}}{F(B_T)}\right) \frac{\log(B_T)}{B_T} = \frac{2 \cdot h \cdot R_d}{\lambda_{G,\text{ref}}} \quad (4-31)$$

The droplet mass and energy equations are solved implementing an adaptive time step, function of the transient liquid and gas local properties, according to the following equation:

$$\delta t_{\text{evap}} = \left( \frac{\rho_L^{\text{new}} Vol_L^{\text{new}} C_{p_L}^{\text{new}} (T_L^{\text{new}} - T_L^{\text{old}})}{h A_L^{\text{new}} (T_G^{\text{new}} - T_L^{\text{new}}) - \Delta h_{\text{vap}} \dot{m}_L} \right) \quad (4-32)$$

where  $\delta t_{\text{evap}}$  is the adaptive evaporation time step,  $Vol$  and  $A$  are the droplet volume and surface area, respectively, the superscript 'old' and 'new' state for the previous and current time steps, respectively and  $h$  is the convective heat transfer variable, function



of the droplet diameter, the Nusselt number and the gas phase thermal conductivity (equation (4-31)).

The differential equation defining the vaporisation rate, according to the correlation proposed by Ranz et al. [51], is discretised and numerically solved:

$$\frac{dm_L}{dt} = 2 \cdot \pi \cdot R_d \cdot \rho_{G,ref} \cdot Diff_{G,ref} \cdot Sh \cdot \log(B_M) \quad (4-33)$$

then the amount of liquid vaporized at each time step,  $m_{vap}$ , is calculated:

$$m_{vap} = m_L^{old} - m_L^{new} \quad (4-34)$$

Due to the droplet deformation, the area of the droplet in contact with the gas is larger than that of a spherical droplet and, thus, it is expected that this will affect the heat flux. In order to account for this effect, it has been assumed that this inter-phase area  $A_{DEF}$  is equal to that of a spheroid having its maximum and minimum diameters equal to those of the deformed droplet, as calculated from the break-up model:

$$A_{DEF} = C_{DEF} \left( \frac{D_{DEF,MAX}}{D_{SPH}} \right)^2 A_{SPH} \quad (4-35)$$

where  $D_{DEF,MAX}$  states for the maximum diameter assumed by the deformed droplet, calculated from equation (3-67), the subscript 'SPH' refers to the spherical droplet and the empirical coefficient  $C_{DEF}$  has to be calibrated from experiments; in the present investigation, its value has been taken equal to 0.3. The vaporisation rate, defined in equation (4-33), has to be multiplied by the ratio between the deformed and the spherical surface area.

The energy equation (4-2) is solved numerically by an implicit method. The new liquid temperature, the contribution of the energy source term due to the heat transfer between the two phases, and the first estimation of the new gas 'virtual' temperature affected by heating and vaporisation processes are calculated implementing an iterative algorithm. First the new liquid temperature is estimated:

$$T_L^{new} = \frac{\sum_{i=1}^3 n_i}{\sum_{j=1}^5 d_j} \quad (4-36)$$

where the parameters  $n_i$  and  $d_i$  are defined as:

$$\begin{aligned}
n_1 &= h \cdot A_L^{\text{new}} \cdot T_\infty \\
n_2 &= \rho_L^{\text{new}} \cdot \text{Vol}_L^{\text{new}} \cdot C_{p_L}^{\text{new}} \cdot T_L^{\text{old}} / \delta t_{\text{evap}} \\
n_3 &= -m_{\text{vap}} \cdot \text{partn}_p \cdot \Delta h_{\text{vap}} / \delta t_{\text{evap}} \\
d_1 &= (\rho_L^{\text{new}} - \rho_L^{\text{old}}) \cdot \text{Vol}_L^{\text{new}} \cdot C_{p_L}^{\text{new}} \cdot T_L^{\text{old}} / \delta t_{\text{evap}} \\
d_2 &= (\text{Vol}_L^{\text{new}} - \text{Vol}_L^{\text{old}}) \cdot \rho_L^{\text{new}} \cdot C_{p_L}^{\text{new}} \cdot T_L^{\text{old}} / \delta t_{\text{evap}} \\
d_3 &= (C_{p_L}^{\text{new}} - C_{p_L}^{\text{old}}) \cdot \text{Vol}_L^{\text{new}} \cdot \rho_L^{\text{new}} \cdot T_L^{\text{old}} / \delta t_{\text{evap}} \\
d_4 &= \rho_L^{\text{new}} \cdot \text{Vol}_L^{\text{new}} \cdot C_{p_L}^{\text{new}} \cdot T_L^{\text{old}} / \delta t_{\text{evap}} \\
d_5 &= h \cdot A_L^{\text{new}}
\end{aligned} \tag{4-37}$$

$\text{partn}_p$  represents the number of droplets per parcel (equal to one in case of single droplet modelling).

The energy source term is calculated according to the following expression:

$$\begin{aligned}
ST_{\text{ENERGY}} &= - \left[ h \cdot A_d^{\text{new}} \cdot (T_\infty^{\text{old}} - T_L^{\text{new}}) + \dot{Q}_{\text{rad}} \right] \cdot dt + \\
&\quad m_{\text{vap}} \cdot (C_{p_{\text{vap},L}}^{\text{new}} \cdot T_L^{\text{new}} - C_{p_{\text{vap},G}}^{\text{old}} \cdot T_\infty^{\text{old}}) \cdot \text{partn}_p
\end{aligned} \tag{4-38}$$

Finally, the new value of the ‘virtual’ gas temperature, affected by the vaporisation process, is calculated implementing a Newton-Rampson method:

$$\begin{aligned}
F(T) &= T_{\text{GAS}}^{\text{new}^0} \cdot C_{p_{\text{GAS}}}^{\text{new}^0} - C_1 = 0. \\
C_1 &= (m_{\text{GAS}}^{\text{old}} \cdot T_{\text{GAS}}^{\text{old}} \cdot C_{p_{\text{GAS}}}^{\text{old}} - ST_{\text{ENERGY}}) / m_{\text{GAS}}^{\text{old}} \\
F_1(T) &= \frac{dF(T)}{dT} = C_{p_{\text{GAS}}}^{\text{new}^0} + T_{\text{GAS}}^{\text{new}^0} \cdot \frac{dC_{p_{\text{GAS}}}(T)}{dT} \\
T_{\text{GAS}}^{\text{new}^1} &= T_{\text{GAS}}^{\text{new}^0} - \frac{F(T)}{F_1(T)}
\end{aligned} \tag{4-39}$$

Once the new liquid mass and temperature are defined, the droplet size can be updated, together with the values of the mass source term and the concentration of the vapour species at conditions far away from the droplet, according to:

$$Y_{F,\infty}^{\text{new}} = \frac{m_{\text{vap}}^{\text{old}} + m_{\text{vap}}^{\text{new}}}{m_{\text{G,tot}}} \tag{4-40}$$

The vaporisation model assumes that the vaporisation rate and the Nusselt number are function of the gas phase Reynolds number. The liquid vaporisation under free-convection environments requires the proper definition of the Nusselt number (equation (4-31)), function of Grashof number according to the theoretical correlation of the Nusselt number for a sphere:



$$\text{Nu} = 2 + \frac{0.589\text{Ra}^{1/4}}{\left[1 + \left(\frac{0.469}{\text{Pr}}\right)^{9/16}\right]^{4/9}} \quad \text{Pr} \geq 0.7, \quad \text{Ra} \geq 10^{11} \quad (4-41)$$

$$\text{Ra} = \frac{g\beta_t(T_s - T_\infty)(2 \cdot R_d)^3}{\nu\alpha} \quad (4-42)$$

$$\beta_t = \left. \frac{1}{\rho} \frac{\partial \rho}{\partial T} \right|_p = \frac{1}{\rho_\infty} \frac{\rho_\infty - \rho_L}{T_\infty - T_L} \quad (4-43)$$

with  $\beta_t$  representing the volumetric thermal expansion coefficient.

The program stops when the droplet is completely evaporated or when its size becomes smaller than a user-defined value due to numerical issues.

#### Variable droplet temperature distribution: 'finite conductivity model, FCM

When the thermal diffusion time in the liquid-phase is of the order of magnitude of the droplet lifetime, the assumption of uniform liquid temperature inside the droplet is not valid any more. The 'finite conductivity model', FCM, predicts the instantaneous temperature distribution inside the droplet, in case of stagnant vaporisation. The equations defined in the previous model are still valid, up to equation (4-35), while the liquid phase temperature distribution should be analysed in details.

The droplet is arbitrarily discretised into a fixed number of intervals, with  $r$  representing the radial coordinate from the droplet centre. At each space-step the liquid properties are calculated as a function of the local temperature. In particular the heat transfer thermal conductivity is defined as follows:

$$\alpha_L(r) = \frac{\lambda_L}{\rho_L \cdot \text{Cp}_L} \quad (4-44)$$

The liquid temperature field  $T_L(t, r)$  is determined by solving the thermal diffusion equation:

$$\frac{\partial T_L(r, t)}{\partial t} = \frac{\alpha_L}{r^2} \frac{\partial}{\partial r} \left( r^2 \frac{\partial T_L}{\partial r} \right) \quad (4-45)$$

with the initial and boundary conditions:

$$\begin{aligned}
T_L(t=0) &= T_{L,0} \\
\kappa_{G,\text{ref}} r^2 \frac{\partial T_L}{\partial r} \bigg|_s &= \kappa_L r^2 \frac{\partial T_L}{\partial r} \bigg|_s + \frac{\dot{m}_L L}{4\pi} \\
\frac{\partial T_L}{\partial r} \bigg|_{r=0} &= 0.
\end{aligned} \tag{4-46}$$

According to Abramzon et al. [61], non-dimensional variables are introduced in order to deal with fixed boundaries, even if the droplet surface regresses. The system is solved implementing a TDMA method. The mean liquid temperature is calculated as an arithmetic mean value along the radial direction. The liquid phase transport properties (density, heat capacity, viscosity and thermal conductivity) are calculated as function of the mean liquid temperature. The number of discretisation points in the radial direction is usually set  $\sim 100$  and the time step  $\sim 10^{-6}/10^{-8}$  s.

Once the new liquid temperature profile is determined, the remaining vaporisation parameters are calculated, according to the procedure defined in the ‘infinite conductivity model’ (uniform liquid phase transient temperature profile).

#### Convection effect on the variable droplet temperature distribution: ‘effective conductivity model, ECM

This model includes the effect, due to the relative motion between the two phases, in the definition of the liquid temperature distribution, predicted by the ‘finite conductivity model’. According to Sirignano [209] the maximum velocity at the droplet surface derives from the balance between the total friction on the gas side and the total friction on the entire surface for the liquid side. The friction drag coefficient, CF, has to be introduced. For a solid non-vaporizing sphere the available numerical data on CF can be correlated as:

$$CF = 12.69 Re^{-2/3} \quad (10 \leq Re \leq 100) \tag{4-47}$$

Renksizbulut et al. [58] found that for an evaporating sphere, due to the Stephan flow, the friction factor coefficient is inversely proportional to the mass transfer number:

$$CF = \frac{12.69 \cdot Re^{-2/3}}{1 + B_M} \tag{4-48}$$

$$\Delta U_{\text{MAX}} = \frac{\mu_{G,\text{ref}}}{\mu_L} \frac{CF \cdot Re \cdot \Delta U}{6 \cdot \pi} \tag{4-49}$$



Once the liquid thermo-physical properties are defined, at each radial location inside the discretised droplet, the dimensionless Reynolds, Prandtl, Peclet numbers are defined as follows:

$$\text{Re}_L(r) = \frac{2 \cdot \rho_L \cdot \Delta U_{\text{MAX}} \cdot R_d}{\mu_L}, \quad \text{Pr}_L(r) = \frac{\mu_L \cdot C_{pL}}{\lambda_L}, \quad \text{Pe}_L(r) = \text{Re}_L \cdot \text{Pr}_L \quad (4-50)$$

The effect of internal circulation induced by the vaporisation process and the motion of the external immiscible flow is included in the model defining the effective liquid thermal conductivity:

$$\alpha_{L\text{eff}}(r) = \chi \cdot \alpha_L \quad (4-51)$$

where the empirical coefficient  $\chi$  is determined fitting numerical results according to Johns et al. [210]:

$$\chi = 1.86 + 0.86 \cdot \tanh[2.225 \cdot \text{Log}_{10}(\text{Pe}_L / 30)] \quad (4-52)$$

The liquid phase is solved according by the set of equations from (4-44) up to (4-46) of the FCM, where the liquid thermal diffusivity, equation (4-44), is replaced by the effective liquid thermal diffusivity, equation (4-51).

### 4.2.2 Multi-component vaporisation modelling

Single component fuels are not representative of practical applications since almost all conventional gasoline and diesel fuels consist of mixtures of hydrocarbons. The modelling of multi-component mixtures includes some additional complexities since different components have different vaporisation rates, which are responsible of liquid-phase mass diffusion due to the consequent concentration gradients. Findings in the literature have suggested the coupled solution of liquid and gas phase energy and species continuity equations. In the liquid phase, mass diffusion is commonly much slower than heat diffusion, the more volatile substances tend to vaporise faster until their surface-concentration values reach a limit, and further vaporisation of these components becomes liquid-phase mass diffusion controlled. The main complexities related to the multi-species composition of the liquid-gas phases refer to the accurate definition of the physical transport properties, the implementation of the algorithm to solve the equilibrium conditions at the interface, and the determination of the species-concentration profiles. The multi-component vaporisation algorithm is proposed as follows, describing in details the solution of liquid concentration spatial distributions, due to mass diffusion.

The mass conservation equation for the  $N_f$  species in the mixture, coupled with the total conservation of mass and the energy equations (4-1) and (4-2), respectively is defined as:

$$\frac{dm_{L,i}}{dt} = -\dot{m}_{L,i} \quad i = 1, N_f \quad (4-53)$$

Uniform initial temperature and concentration distributions are initially assumed inside the droplet, as mathematically expressed as follows:

$$T(r, t = 0) = T_{d,0} \quad 0 \leq r \leq R_{d,0} \quad (4-54)$$

$$Y_i(r, t = 0) = Y_{i,0} \quad 0 \leq r \leq R_{d,0} \quad i = 1, N_f \quad (4-55)$$

Assuming ideal equilibrium conditions at the liquid/gas interface, the Raoult's law postulates the proportionality between the gas and the liquid molar fractions at the droplet surface:

$$X_{i,G,S} = X_{i,L,S} \cdot \frac{P_{atm}}{P_{\infty}} \cdot \exp \left[ \frac{\Delta h_{vap,i} \cdot MW_i}{R} \cdot \left( \frac{1}{T_{B,i}} - \frac{1}{T_s} \right) \right] \quad i = 1, N_f \quad (4-56)$$

where 'i' refers to each species in the mixture, composed by  $N_f$  components. The relation between the mass,  $X_i$ , and mole,  $Y_i$ , fractions for each species is given by:

$$X_{i,L} = \frac{Y_{i,L}/MW_{i,L}}{\sum_{j=1}^{N_f} Y_{j,L}/MW_{j,L}} \quad i = 1, N_f \quad (4-57)$$

$$X_{i,G} = \frac{Y_{i,G}/MW_{i,G}}{\sum_{j=1}^{N_f+1} Y_{j,G}/MW_{j,G}} \quad i = 1, N_f \quad (4-58)$$

The modelling of non-equilibrium conditions at the interface using the Langmuir-Knudsen law, equations (4-7) to (4-10), or the investigation of high-pressure effect with the method of fugacity coefficients, equations (4-11) to (4-17), are still valid for multi-component fuel, with a particular attention in the definition of the physical properties for the mixture. They are pressure, temperature and composition dependent and they are calculated using as weighting factors either the vaporised fuel mass or the molar fractions at reference conditions.

According to Sirignano [42], the assumption of equal binary diffusion coefficients is implemented. Consequently, the mass transfer Spalding number, defined in equation (4-22) for single component fuel, is calculated for each species in the mixture:



$$B_M = B_{M_i} = \frac{\sum_{j=1}^{N_f} Y_{j,G,S} - \sum_{j=1}^{N_f} Y_{j,G,\infty}}{1 - \sum_{j=1}^{N_f} Y_{j,g,S}} \quad (4-59)$$

Finally the vaporisation rate for each component is calculated according to the Ranz et al. [51] correlation, extended to the multi-component vaporisation modelling:

$$\dot{m}_i = \dot{m} \cdot \varepsilon_i = 4 \cdot \pi \cdot R_d \cdot \rho_{i,G,\text{ref}} \cdot \text{Diff}_i \cdot \varepsilon_i \cdot \log(1 + B_M) \cdot \left( 1 + \frac{k_{RM} \cdot \text{Sc}^{1/3} \cdot \text{Re}^{1/2}}{2 \cdot F(B_M)} \right) \quad (4-60)$$

The mass of all the vaporising components is calculated at each time step; then the liquid concentrations are updated. They are assumed to be uniform when the investigation does not require detailed liquid-phase solutions; otherwise the standard assumption of radial distribution profiles is imposed. The liquid concentrations transient and spatial profiles are predicted by the ‘finite mass diffusivity model’, FDM, introducing an arbitrary spatial discretisation inside the droplet. The systems of non-linear partial differential equations are calculated using an implicit TDMA method. The droplet is uniformly discretised into  $n$ -intervals ( $\sim 100$ ) and the time step is about  $10^{-6}$  /  $10^{-8}$  s. The mass diffusion equations state that:

$$\frac{\partial \Psi(r, t)}{\partial t} = \frac{\phi_{L,\text{eff}}}{r^2} \frac{\partial}{\partial r} \left( r^2 \frac{\partial \Psi}{\partial r} \right) \quad (4-61)$$

where  $\Psi$  represents the liquid mass fractions and  $\phi_{L,\text{eff}}$  represents the mass diffusivities. They are temperature and concentration dependent. The same procedure deriving the equation in the non-dimensional form according to Abramzon et al. [61], proposed for the ‘finite conductivity model’, is implemented here.

Only  $N_f - 1$  partial differential equations have to be solved to define the transient liquid concentration field, due to the fact that at each radial location the summation of the liquid mass fraction over all the species present is equal to unity.

Finally, similarly to the single component case, the transient liquid-phase temperature distribution is predicted according to the ICM, FCM or ECM algorithms, presented in the previous section. Concentration and temperature distributions in the liquid phase are updated at each time step.

Figure 4-2 describes the general single-droplet evaporation algorithm presented in these sections.



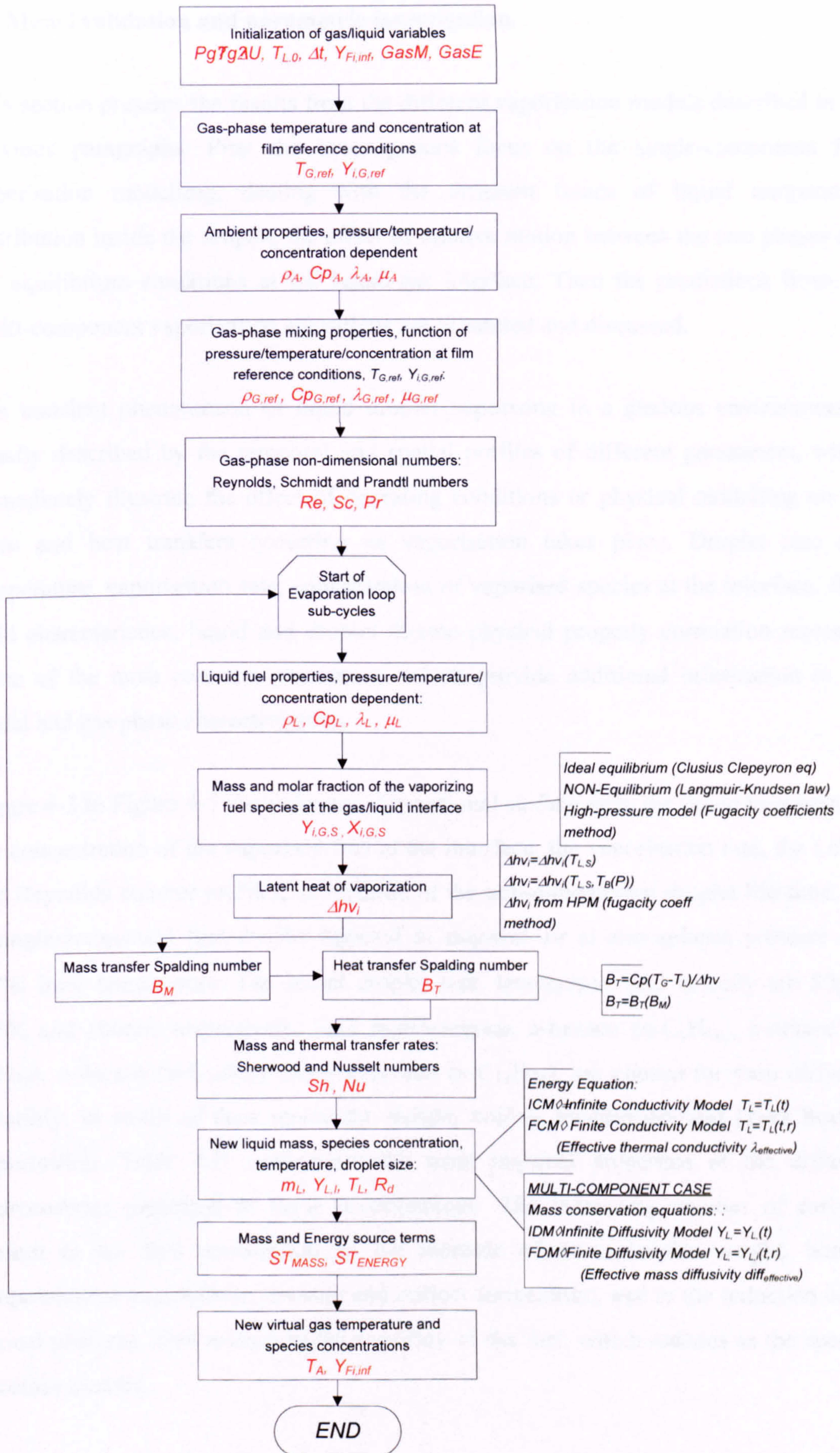


Figure 4-2: Scheme of single-droplet vaporisation algorithm.



### 4.3 Model validation and parametric investigation

This section presents the results from the different vaporisation models described in the previous paragraphs. First the investigations focus on the single-component fuel vaporisation modelling, dealing with the different issues of liquid temperature distribution inside the droplet, the effect of relative motion between the two phases and the equilibrium conditions at the liquid-gas interface. Then the predictions from the multi-component vaporisation algorithms are presented and discussed.

The transient phenomenon of liquid droplet vaporising in a gaseous environment is usually described by the temporal and spatial profiles of different parameters, which immediately illustrate the effect of operating conditions or physical modelling on the mass and heat transfers occurring as vaporisation takes place. Droplet size and temperature, vaporisation rate, concentration of vaporised species at the interface, flow field characteristics, liquid and droplet thermo-physical property correlation represent some of the most common parameters, which provide additional information to the liquid and gas phase characterisation.

Figure 4-3 to Figure 4-5 show the non-dimensional surface area, the liquid temperature, the concentration of the vaporised fuel at the interface, the vaporisation rate, the Lewis and Reynolds number profiles, as function of the non-dimensional droplet life-time, for a single-component fuel droplet injected in stagnant air at atmospheric pressure and 600K back temperature. The initial droplet size, temperature and velocity are 50 $\mu\text{m}$ , 300K and 100m/s respectively. Four hydrocarbons, n-hexane ( $\text{n-C}_6\text{H}_{14}$ ), n-octane ( $\text{n-C}_8\text{H}_{18}$ ), n-decane ( $\text{n-C}_{10}\text{H}_{22}$ ) and n-tridecane ( $\text{n-C}_{13}\text{H}_{28}$ ), are chosen for their different volatility, as result of their molecular weight, boiling temperature and latent heat of vaporisation. Table 4-II summarises the main physical properties of the different hydrocarbons presented in these investigations. The increasing number of carbons present in the fuel corresponds to the increase of its molecular weight, boiling temperature at atmospheric pressure and critical temperature, and to the reduction of its critical pressure. This reflects to the volatility of the fuel, which reduces as the species becomes heavier.

Fuel	Molecular weight (kg/kmol)	$T_{\text{normal boil}}$ (K)	$T_{\text{critical}}$ (K)	$P_{\text{critical}}$ (bar)
n-C <sub>5</sub> H <sub>12</sub>	72.2	309.2	469.7	33.6
n-C <sub>6</sub> H <sub>14</sub>	86.2	341.9	507.1	30.4
n-C <sub>7</sub> H <sub>16</sub>	100.2	371.6	540.2	27.2
n-C <sub>8</sub> H <sub>18</sub>	114.2	398.8	568.7	24.7
n-C <sub>10</sub> H <sub>22</sub>	142.3	447.3	617.7	21.1
n-C <sub>13</sub> H <sub>28</sub>	184.4	508.6	675.	16.8

Table 4-II: Molecular weight, boiling temperature at atmospheric pressure, critical temperature and pressure for six hydrocarbons.

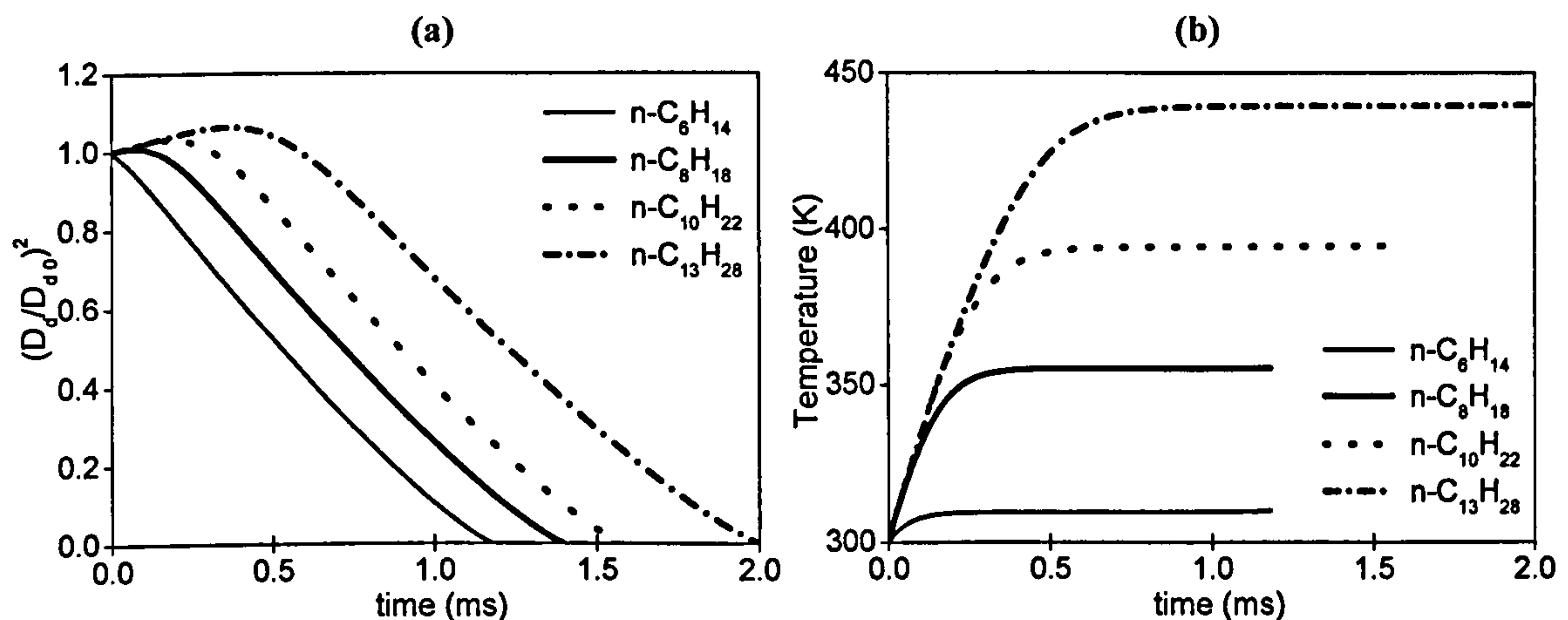


Figure 4-3: Droplet surface (a) non-dimensional area and (b) liquid temperature profiles for four different fuels;  $P_G=1\text{bar}$ ,  $T_G=600\text{K}$ ,  $T_{d,0}=300\text{K}$ ,  $D_{d,0}=50\mu\text{m}$  and  $\Delta U_0=100\text{m/s}$ .

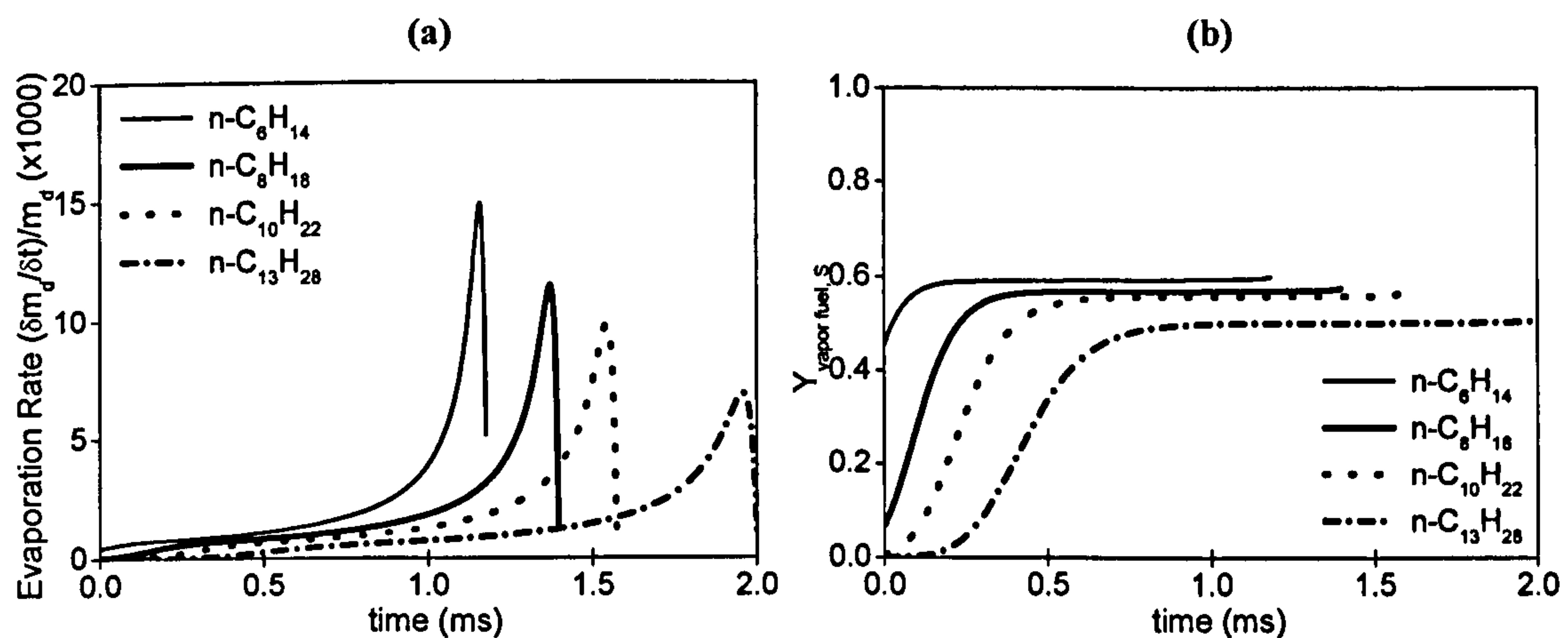


Figure 4-4: (a) Vaporisation rate and (b) vapour mass fraction at the liquid/gas interface profiles for four different fuels;  $P_G=1\text{bar}$ ,  $T_G=600\text{K}$ ,  $T_{d,0}=300\text{K}$ ,  $D_{d,0}=50\mu\text{m}$  and  $\Delta U_0=100\text{m/s}$ .



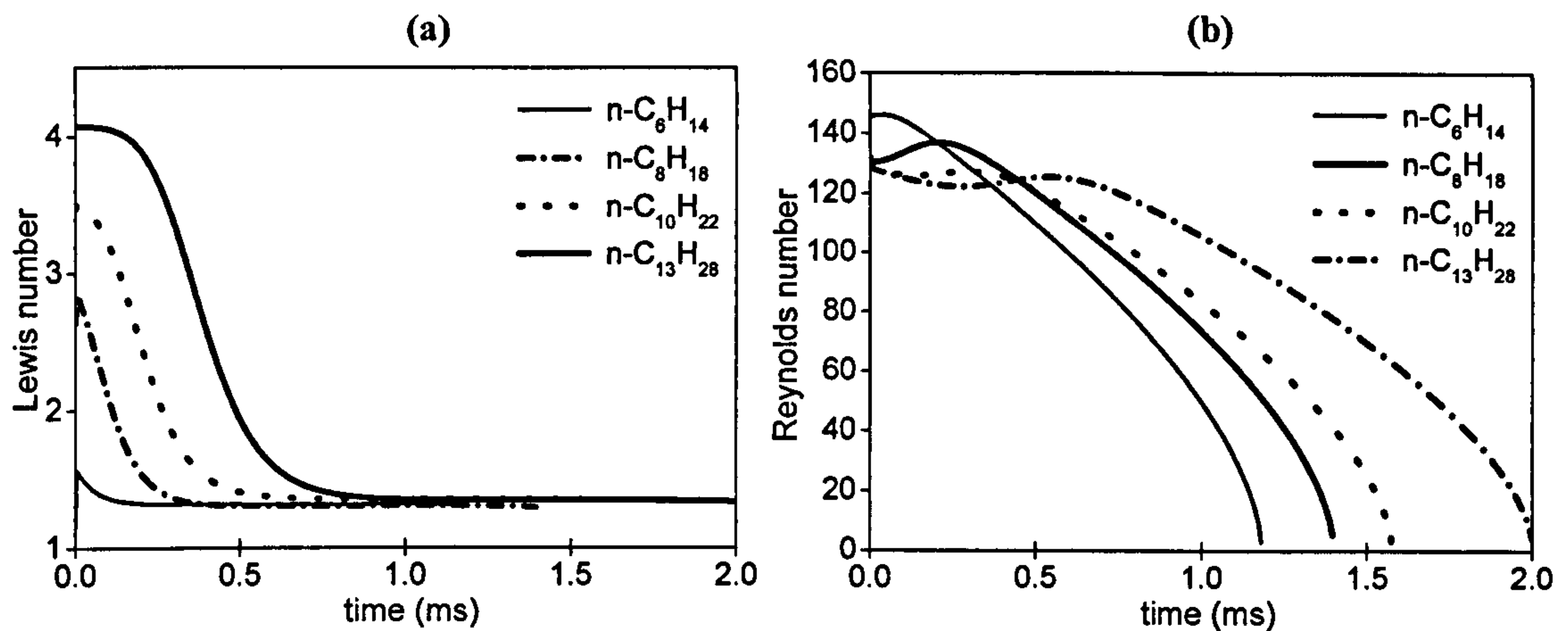


Figure 4-5: Gas-phase (a) Lewis and (b) Reynolds number profiles for four different fuels;  $P_G=1\text{bar}$ ,  $T_G=600\text{K}$ ,  $T_{d,0}=300\text{K}$ ,  $D_{d,0}=50\mu\text{m}$  and  $\Delta U_0=100\text{m/s}$ .

The results are obtained implementing the single-component model with ideal equilibrium at the liquid-gas interface and uniform temperature distribution inside the droplet. The drag force model, described in the Chapter 3, predicts the variation of the droplet velocity, which reflects on the Reynolds number and vaporisation rate profiles. The graphs show that as vaporisation takes place, the droplet size progressively reduces, Figure 4-3(a), its temperature increases reaching an asymptotic value that corresponds to the liquid bulk temperature, Figure 4-3(b), while the vaporisation rate increases up to a maximum and then collapses in the last few instants of the droplet lifetime, Figure 4-4(a). Figure 4-4(b) show that the predicted vapour mass fraction at the interface has similar trend compared to the transient liquid temperature profiles, as suggested by the Clausius-Clapeyron equation implemented, equation (4-6). Finally the Lewis and Reynolds numbers, which approximate the ratio between the mass and thermal liquid diffusivity and between inertial and viscous forces on the droplet, respectively, decrease to an asymptotic value and to zero correspondingly, Figure 4-5. This conclusion suggests that as vaporisation takes place, the mass diffusivity equals the thermal diffusivity by a constant factor; moreover the Reynolds number can be interpreted as one of the most important parameters for the vaporisation modelling, since it describes the initial volumetric expansion, due to the rapid increase of liquid temperature, and the subsequent droplet surface area and relative velocity reduction due to the vaporisation and drag force effect. The graphs also reveal that the model can predict the faster vaporisation of lighter fuels, with higher volatility; this effect will play a fundamental role in the modelling of multi-component fuel vaporisation.

Several studies on single droplet vaporisation modelling reveal that the predictions are quite sensitive on the correlation to estimate the thermo-physical properties and the heat-mass transfer conditions. An example is proposed in Figure 4-6, which show the mass and heat Spalding transfer number profiles defined by equation (4-22) and equation (4-24) or (4-26), corresponding to the theoretical definition,  $B_{T,1}(\Delta T, \Delta H_v)$ , or the Abramzon et al. [61] correlation,  $B_{T,2}(B_M)$ , respectively.

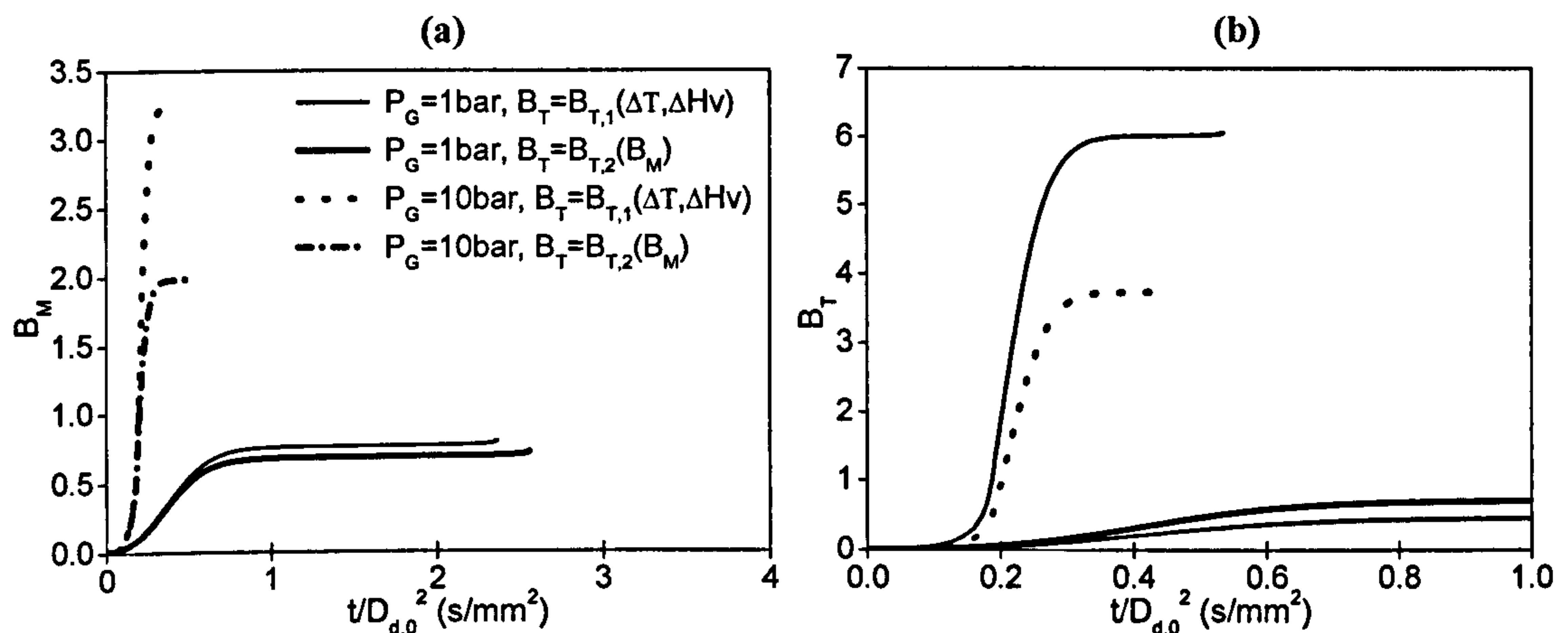


Figure 4-6: (a) Mass and (b) heat transfer Spalding number profiles as function of the operating conditions and the vaporisation model correlation; n-decane,  $P_G=1/10\text{bar}$ ,  $T_G=500/1000\text{K}$ ,  $T_{d,0}=300\text{K}$ ,  $D_{d,0}=50\mu\text{m}$  and  $\Delta U_0=100\text{m/s}$ .

N-decane liquid droplet, with initial diameter and temperature equal to  $50\mu\text{m}$  and  $300\text{K}$  respectively, is injected at  $100\text{m/s}$  in stagnant air at low ( $1\text{bar}$ - $500\text{K}$ ) and high ( $10\text{bar}$ - $1000\text{K}$ ) back pressure-temperature conditions. The effect of Spalding transfer number correlation on the droplet life-time, surface area regression and liquid temperature is shown in Figure 4-7. The results show that the sensitivity of the results on the Spalding transfer number correlation is evident only under high pressure-temperature conditions, when the use of the Abramzon et al. [61] correlation over-predicts the droplet lifetime of about 20% and over-predicts the liquid bulk temperature of about 4%, compared to the theoretical correlation. It's important to mention that these results have been predicted implementing the ideal equilibrium model at the liquid/gas interface, which validity under high-pressure conditions will be discussed later.



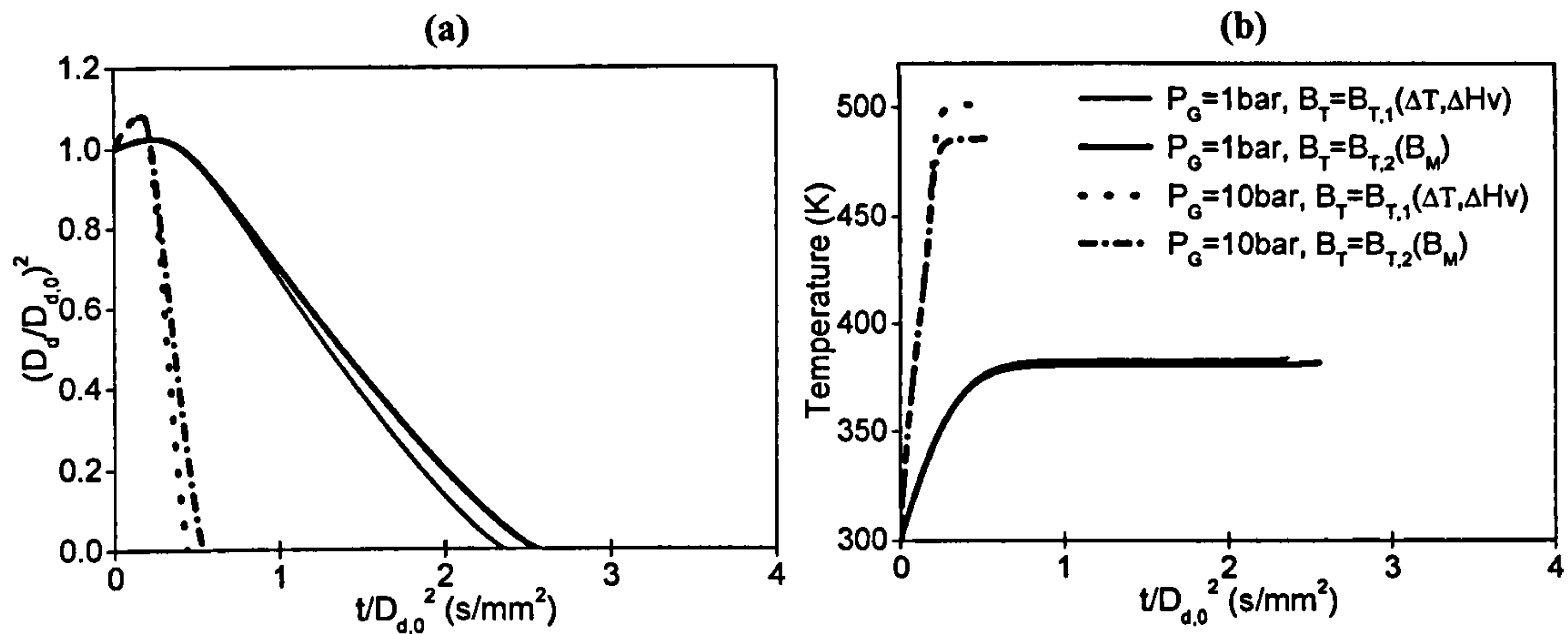


Figure 4-7: Effect of calculation of heat transfer Spalding number on the droplet (a) non-dimensional surface area and (b) temperature profiles; n-decane,  $P_G=1/10\text{bar}$ ,  $T_G=500/1000\text{K}$ ,  $T_{d,0}=300\text{K}$ ,  $D_{d,0}=50\mu\text{m}$  and  $\Delta U_0=100\text{m/s}$ .

The solution of the energy equation (4-2) requires a particular attention in the instantaneous prediction of the new droplet temperature, the heat transfer source term, which estimates the interaction between the two phases, and in the evaluation of the gas-phase temperature affected by vaporisation and heating processes. The following results present the droplet size, temperature and lifetime profiles under different vaporisation rates and gas/liquid temperature gradients at the interface. Unless specified, the operating conditions correspond to n-heptane droplet, with an initial diameter of  $50\mu\text{m}$ , injected at  $100\text{m/s}$  in a gaseous quiescent environment. The gas/liquid temperature and pressure conditions are selected according to the particular case.

‘CASE 1’  $\dot{m}_{\text{vap}} = 0$ .

The vaporisation rate is neglected. Figure 4-8 show the droplet surface area and temperature profiles, under four gas-phase environments, corresponding to 290, 400, 500 and  $800\text{K}$  and atmospheric pressure. The convective heat transfer to or from the liquid phase with the surrounding gas results in the progressive reduction of the liquid/gas temperature gradients, while the droplet surface expansion or regression is a consequence of the density variation, due only to the temperature increase or decrease respectively, since the liquid vaporisation process has been deactivated in the modelling. The results show that when the flow field temperature exceeds the fuel critical temperature the model freezes the liquid temperature at a value of few percents of degree lower than the critical one, in order to avoid numerical issues in the calculation of the thermo-physical fuel properties.

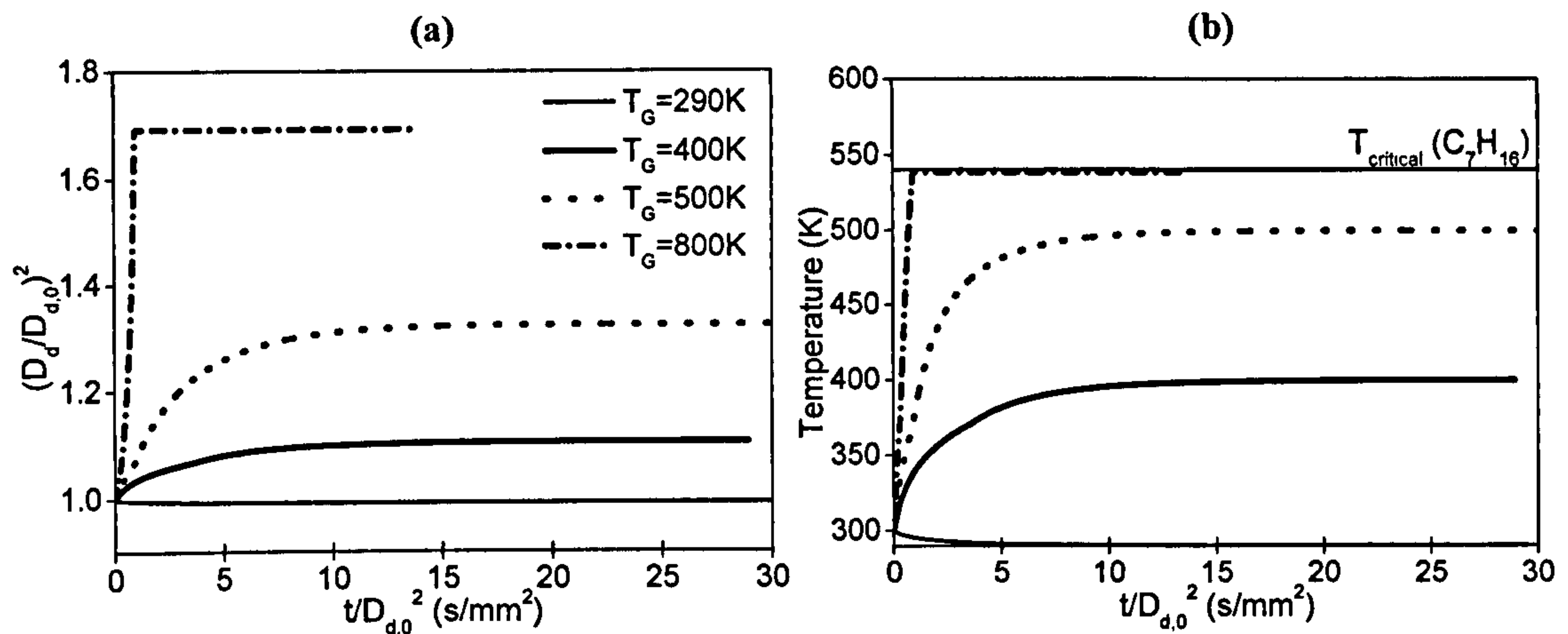


Figure 4-8: Zero droplet vaporisation rate: effect of back temperature on droplet (a) non-dimensional surface area and (b) liquid temperature profiles; n-heptane,  $P_G=1\text{bar}$ ,  $T_G=290/400/500/800\text{K}$ ,  $T_{d,0}=300\text{K}$ ,  $D_{d,0}=50\mu\text{m}$  and  $\Delta U_0=100\text{m/s}$ .

‘CASE 2’:  $T_{\text{Liquid}} = T_{\infty} \Rightarrow \dot{q}_c = 0$ .

Zero temperature gradient at the liquid-gas interface is assumed, resulting in null convective heat transfer. The energy for vaporisation is simultaneously taken from the two phases and no temperature gradients are predicted during the droplet lifetime. Figure 4-9 shows the effect of back temperature and pressure condition on the droplet lifetime, revealing that low temperature environments reduce the vaporisation rate, particularly at high pressure conditions, however the pressure effect becomes negligible as temperature increases. The consideration done for Figure 4-7 about the use of ideal equilibrium model under high-pressure conditions is valid also for this case, although these results are useful to illustrate the general trend of the main vaporisation parameters under a variety of operating conditions.

‘CASE 3’:  $T_{\text{Liquid}} < T_{\infty} \Rightarrow \dot{q}_c > 0$ .

This case describes the ‘classical’ droplet vaporisation conditions, when positive heat transfer from the surroundings to the droplet surface occurs during the droplet lifetime. The main issue is related to the calculation of mass and energy source terms and consequently the proper estimation of the far flow field temperature due to the coupling between the two phases. The initial liquid/gas mass ratio is an important parameter to decide if the flow field would be affected by the heat and mass transfers. Only when the initial liquid/gas mass ratio is negligible, the gas temperature is not influenced by the vaporisation phenomenon. Figure 4-10 show the effect of the initial liquid/gas mass ratio on the droplet surface area and on the liquid and gas phase temperature profiles.



The results predict slower vaporisation when the initial liquid mass is comparable with the gas mass, due to the gas temperature reduction as a consequence of the heat transfer.

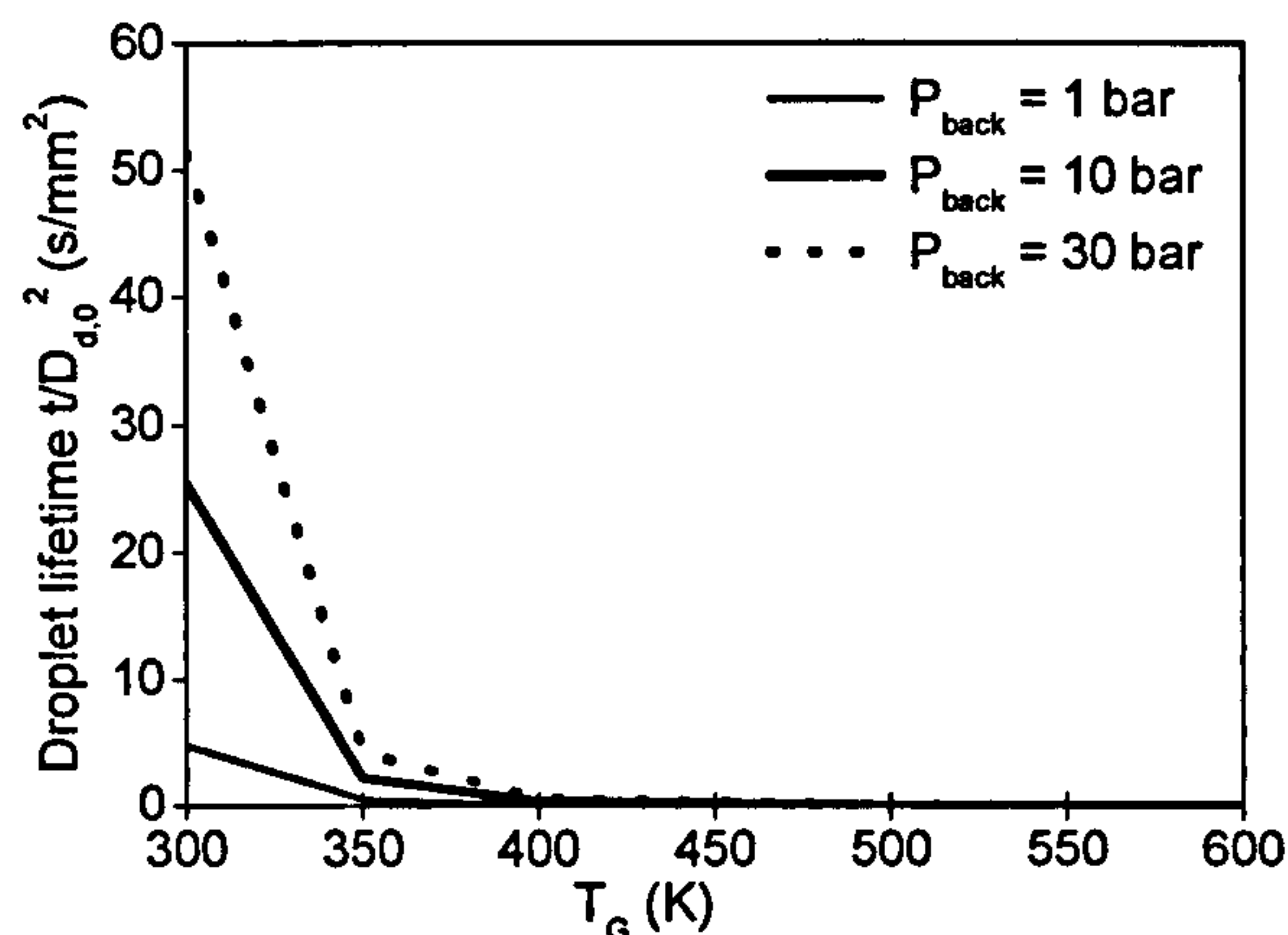


Figure 4-9: Zero temperature gradient at the gas-liquid interface: effect of back temperature on droplet lifetime under low-medium-high back pressure conditions; n-heptane,  $P_G=1/10/30\text{bar}$ ,  $T_{d,0}=T_G$ ,  $D_{d,0}=50\mu\text{m}$  and  $\Delta U_0=100\text{m/s}$ .

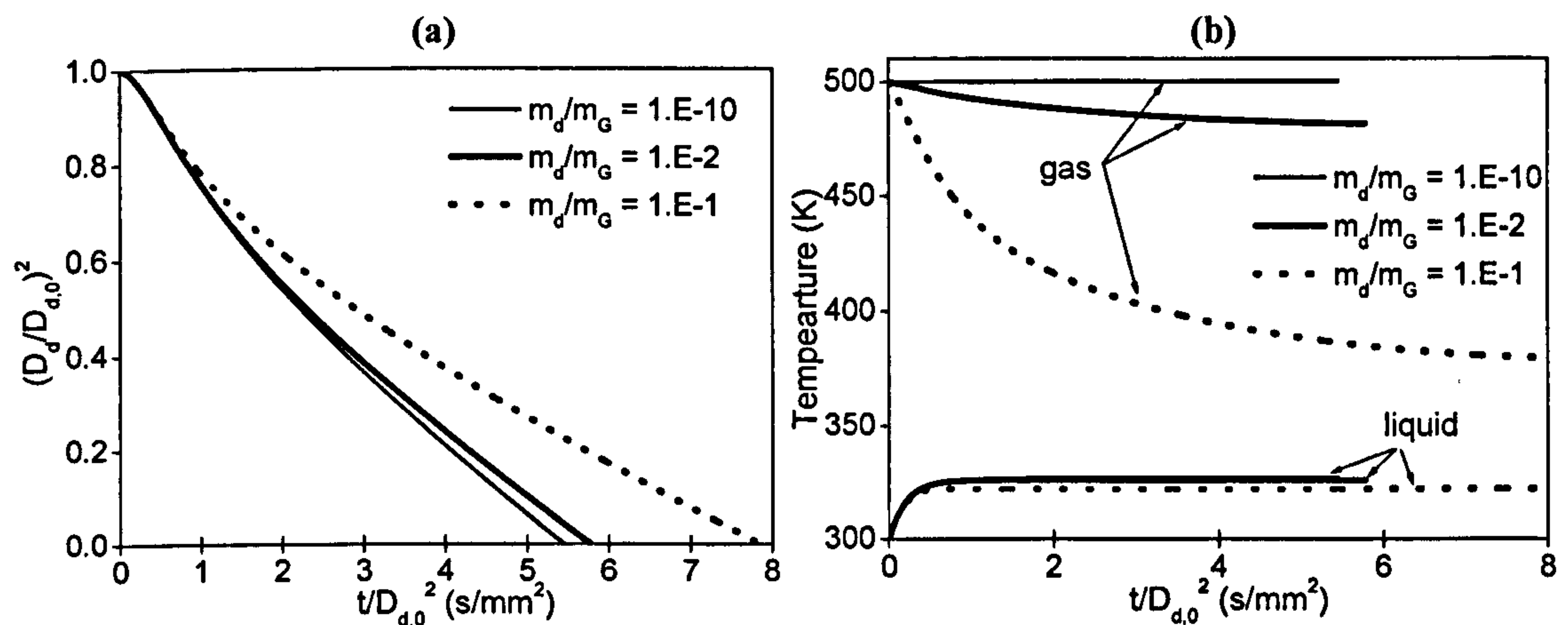
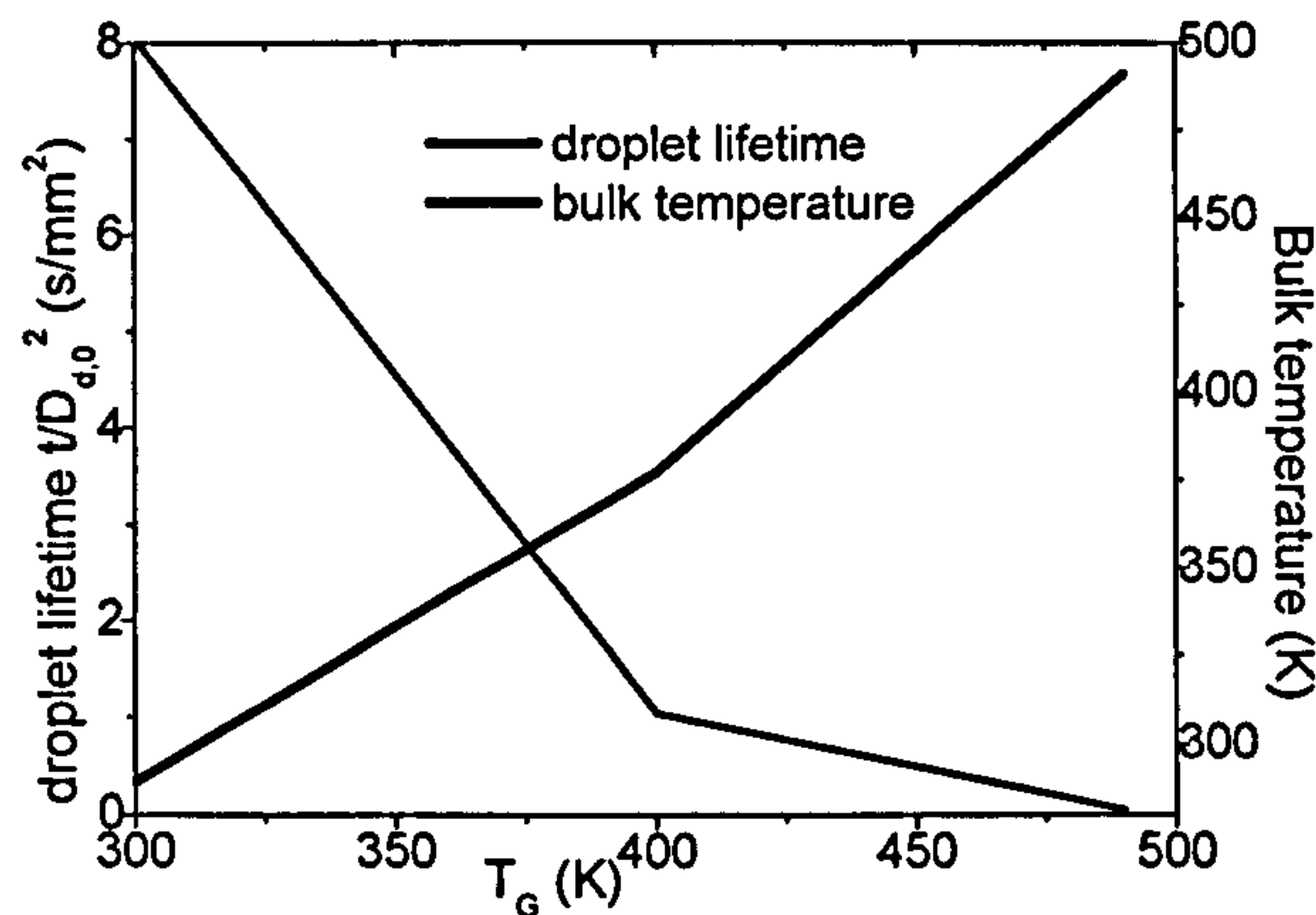


Figure 4-10: Positive gas-liquid temperature gradient at the interface: effect of back temperature on droplet (a) non-dimensional surface area and (b) liquid temperature profiles; n-heptane,  $P_G=1\text{bar}$ ,  $T_{G,0}=500\text{K}$ ,  $T_{d,0}=300\text{K}$ ,  $D_{d,0}=50\mu\text{m}$  and  $\Delta U_0=100\text{m/s}$ .

‘CASE 4’:  $T_{\text{Liquid}} > T_{\infty} \Rightarrow \dot{q}_c < 0$ .

Finally the last scenario sees the liquid temperature exceeding the gas temperature. This results in positive heat transfer from the droplet surface to the surrounding gas. The energy for vaporisation is supplied from the liquid, and the gas phase is influenced by the source term represented by the internal energy of the vaporized masses and the convective heat from the droplet. The droplet lifetime and bulk temperature as function of initial gas temperature are presented in Figure 4-11, for n-decane droplet with initial diameter and temperature of  $50\mu\text{m}$  and  $300\text{K}$  respectively injected at  $100\text{m/s}$  in stagnant air at atmospheric pressure and back-temperature varying from  $300\text{K}$  up to  $490\text{K}$ .

The results predict faster vaporisation at higher gas temperature even if the convective heat decreases because of the temperature gradient reduction; this is due to the lower limit imposed to the liquid phase temperature, which value cannot become smaller than the gas phase one. The investigations (not shown) on the effect of initial liquid/gas mass ratio show a similar behaviour even when the liquid mass is comparable with the gas mass, suggesting that the liquid bulk temperature can be used as one of the most representative vaporisation parameter.



**Figure 4-11: Negative gas-liquid temperature gradient at the interface: effect of back temperature on droplet lifetime and liquid bulk temperature; n-decane,  $P_G=1\text{bar}$ ,  $T_{d,0}=500\text{K}$ ,  $D_{d,0}=50\mu\text{m}$  and  $\Delta U_0=100\text{m/s}$ .**

The first validation of the single-component vaporisation model, predicting uniform liquid temperature profiles and assuming ideal equilibrium condition at the liquid/gas interface, is proposed in Figure 4-12 for relatively low evaporation rate, showing the temporal evolutions of the surface area for a single isolated water droplet ( $D_0=1.1\text{mm}$  and  $T_{d,0}=282\text{K}$ ) evaporating in a quiescent air environment at  $T_G=298\text{K}$  and atmospheric pressure. The model predictions are compared to the experimental results of Ranz et al. [51] obtained under the same conditions. Note that here the droplet Reynolds number is zero and the empirical convective contributions to both the heat and mass transfer numbers are irrelevant, and the Nusselt number is function of the Grashof number, according to equation (4-41). For this relatively low evaporation rate, the model predictions agree nearly well with the experiments.



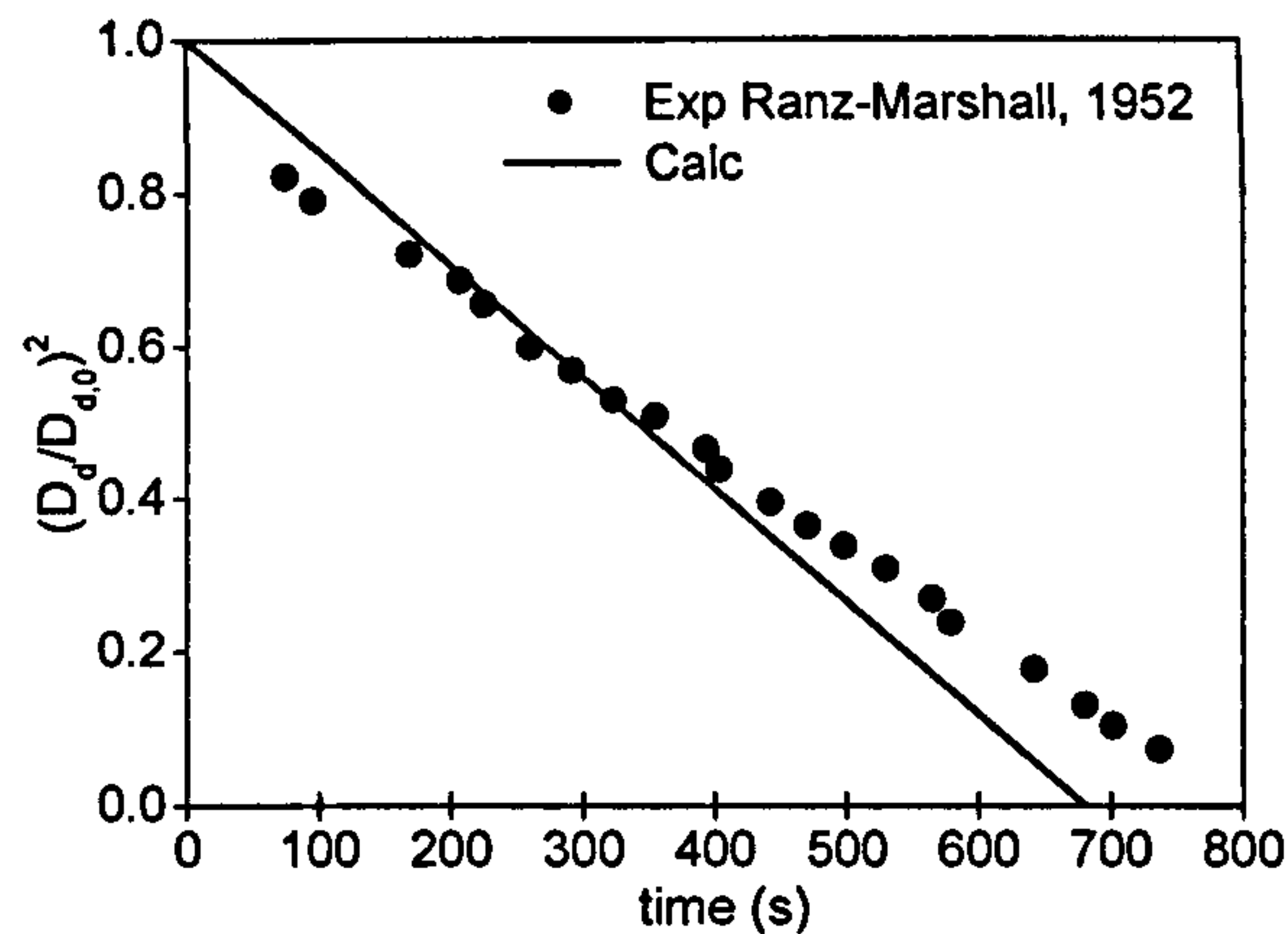


**Figure 4-12: Temporal evolution of the (a) non-dimensional droplet diameter squared for water. The experimental results are from Ranz et al. [51] and the operating conditions are:  $P_G=1\text{bar}$ ,  $T_G=298\text{ K}$ ,  $T_{d,0}=282\text{ K}$ ,  $D_{d,0}=1.1\text{ mm}$  and  $Re_d=0$ .**

Past studies consider that it is sufficient to predict the correct droplet evaporation rate, whereas correct prediction of the droplet temperature is a largely unaddressed issue. Nonetheless, the inaccuracy on the predicted droplet temperature for a spray with a large mass loading may introduce a source of substantial errors in the overall flow predictions because of the large thermal inertia of the dispersed phase [107]. The capability of the model to predict the steady state droplet temperature is shown in Figure 4-13 for n-heptane as a function of the far field gas temperature, comparing computational results with experimental measurements of wet bulb temperatures from Yuen et al. [57]. The steady state droplet temperatures are recorded at a time when the droplet mass has decreased down to 10% of the initial mass. The model simulations do not correspond to the actual experimental conditions, since freely falling droplets of unspecified size were used, specifying that the measured steady state droplet temperatures are equal to the wet-bulb conditions, and they are found to be relatively insensitive to the initial droplet size. The operating conditions correspond to n-heptane liquid droplet with initial droplet size of 1mm, liquid temperature of 300K suspended in quiescent air at atmospheric pressure and back temperature varying in a range from 300 up to 900K. The ideal equilibrium model predicting uniform liquid temperature profiles has been implemented, showing a good agreement between predictions and experimental results. The model under-predicts the bulk temperature of less than 3% under high back temperature conditions. The validated model has been used to predict the effect of back temperature on droplet lifetime and steady-state liquid temperature for smaller droplets, which initial size equal to 50 $\mu\text{m}$  is more realistic in practical spray simulation. The results are shown in Figure 4-14, for n-heptane and n-tridecane fuels, confirming that the droplet lifetime is inversely proportional to the flow field

temperature and the fuel boiling temperature, and on the other hand the liquid bulk temperature does not depend on the initial droplet size, it increases with the gas temperature and it decreases with the fuel volatility.

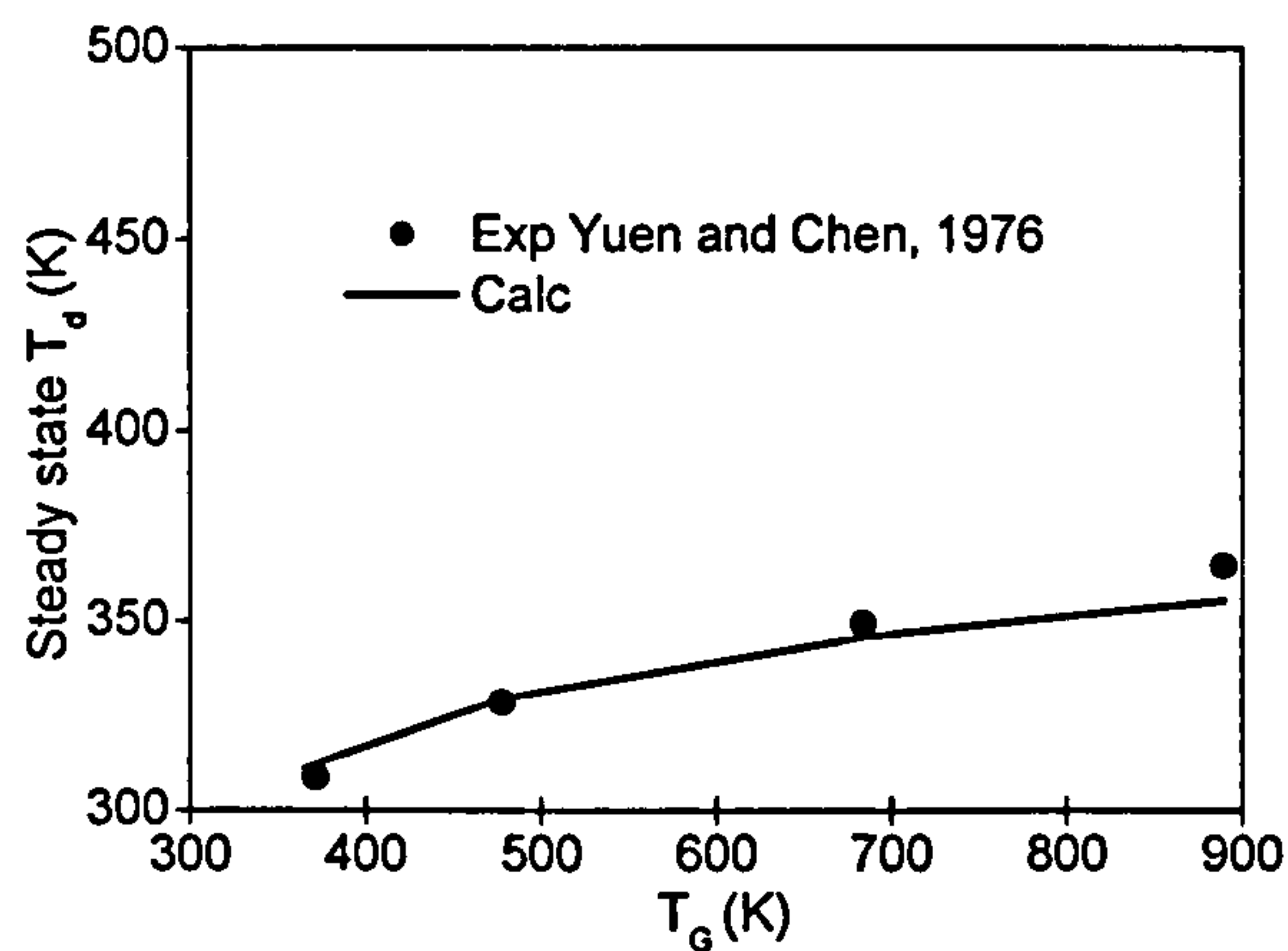


Figure 4-13: Comparison of steady state droplet temperatures (measured when  $m_d=0.1 m_{d,0}$ ) as a function of the free stream temperature predicted by the models with the experimentally measured wet bulb temperatures for: n- heptane [57]. The conditions are:  $P_G=1\text{bar}$ ,  $T_{d,0}=300\text{K}$ ,  $D_{d,0}=1\text{mm}$  and  $Re_d=0$ .

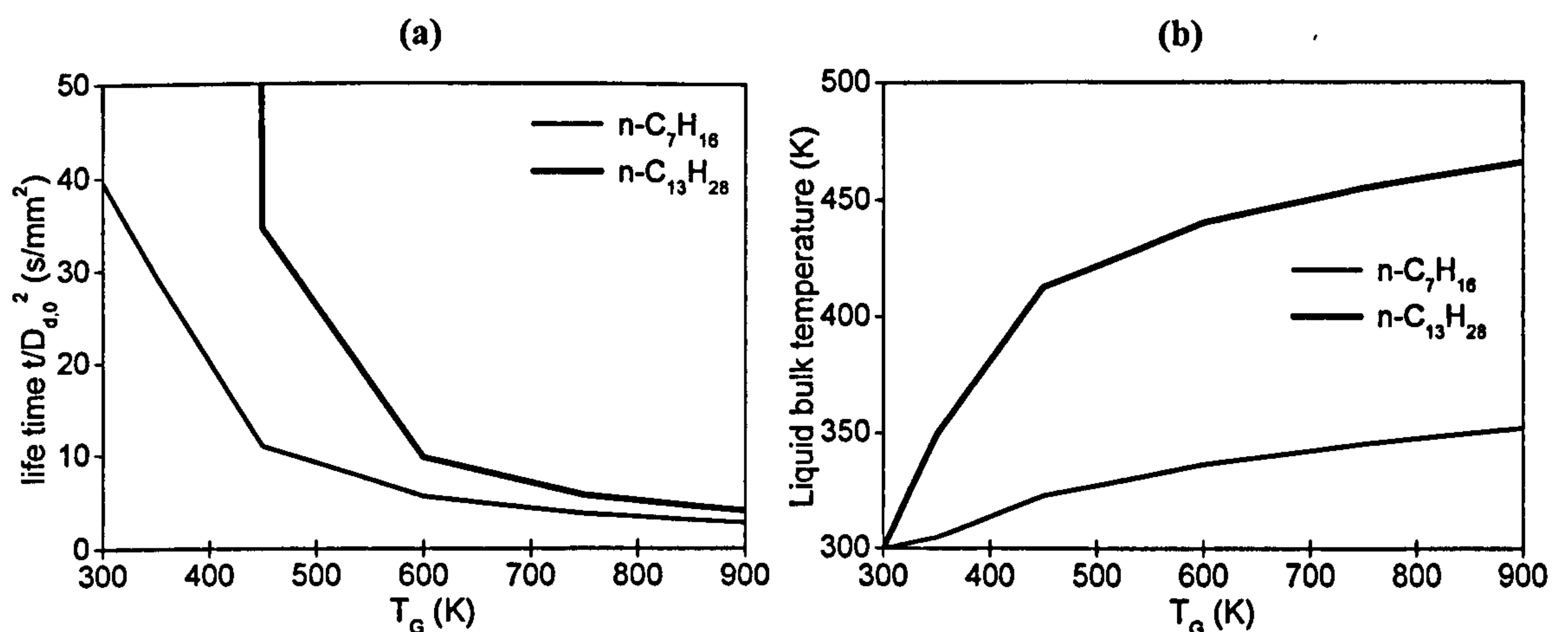


Figure 4-14: Droplet (a) lifetime and (b) liquid bulk temperature as a function of back temperature for n-heptane and n-tridecane fuels;  $P_G=1\text{bar}$ ,  $T_{d,0}=300\text{K}$ ,  $D_{d,0}=50\mu\text{m}$  and  $Re_d=0$ .

The previous results have been obtained assuming an infinite liquid conductivity inside the droplet, which leads the model to predict uniform, transient liquid temperature profiles. This ‘infinite conductivity model’, ICM, has been compared with the ‘classical  $D^2$ -law’, which neglects the initial droplet heat-up assuming that the vaporisation takes place at the fuel constant bulk temperature, and with the more detailed ‘finite conductivity model’, FCM, which predicts the instantaneous radial temperature distribution inside the droplet. The comparison is proposed in Figure 4-15 and Figure 4-16, for the more volatile n-heptane and the heavier n-tridecane fuels. Liquid droplet,



with initial size and temperature of  $50\mu\text{m}$  and  $300\text{K}$  respectively, have been considered to vaporise in air under atmospheric pressure and  $600\text{K}$  back temperature with no relative motion between the two phases. The droplet surface area profiles, shown in Figure 4-15, reveal that the ‘classical  $D^2$ -law’ substantially under-predicts the droplet lifetime from 20% for n-heptane up to 40% for the less volatile n-tridecane, which takes longer to reach the bulk temperature. The results also suggest that, under these operating conditions, the internal liquid temperature distribution does not play any role in predicting the droplet lifetime and its surface area regression.

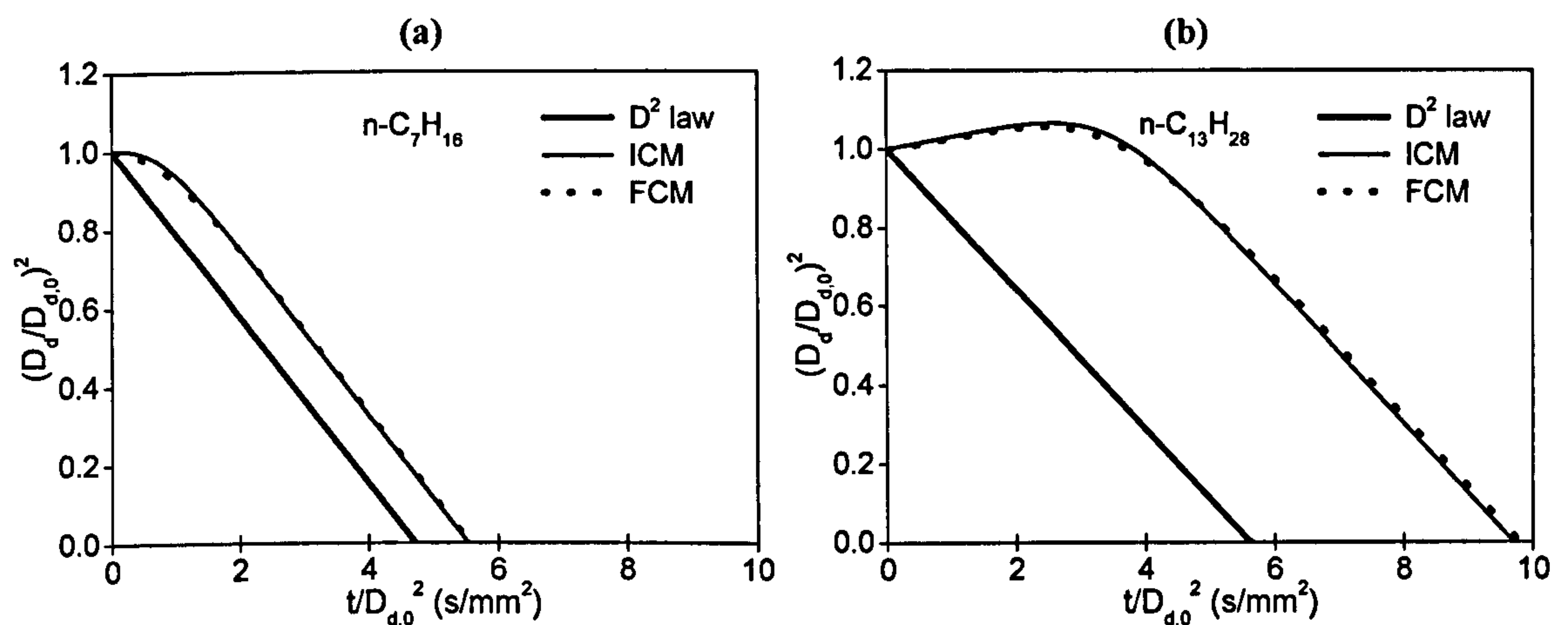


Figure 4-15: Effect of droplet vaporisation model on the droplet non-dimensional surface area profiles for (a) n-heptane and (b) n-tridecane fuels;  $P_G=1\text{bar}$ ,  $T_G=600\text{K}$ ,  $T_{d,0}=300\text{K}$ ,  $D_{d,0}=50\mu\text{m}$  and  $Re_d=0$ .

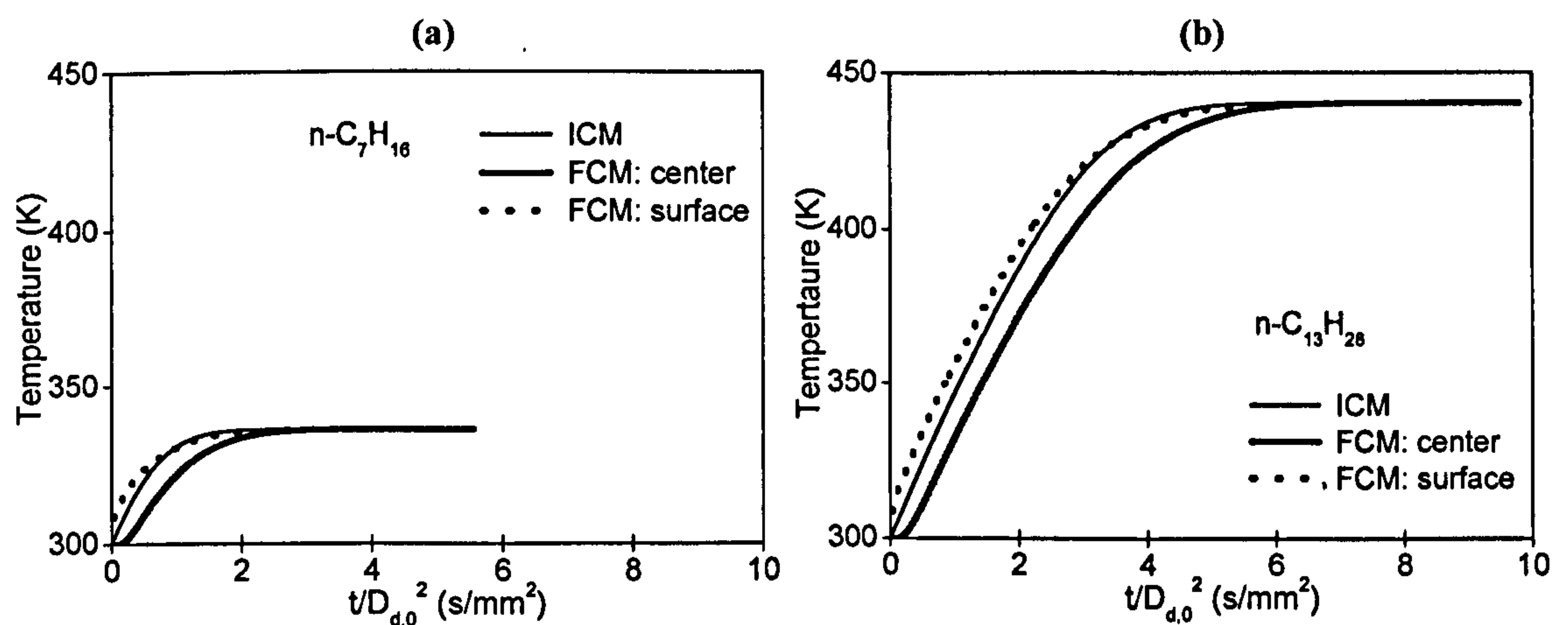
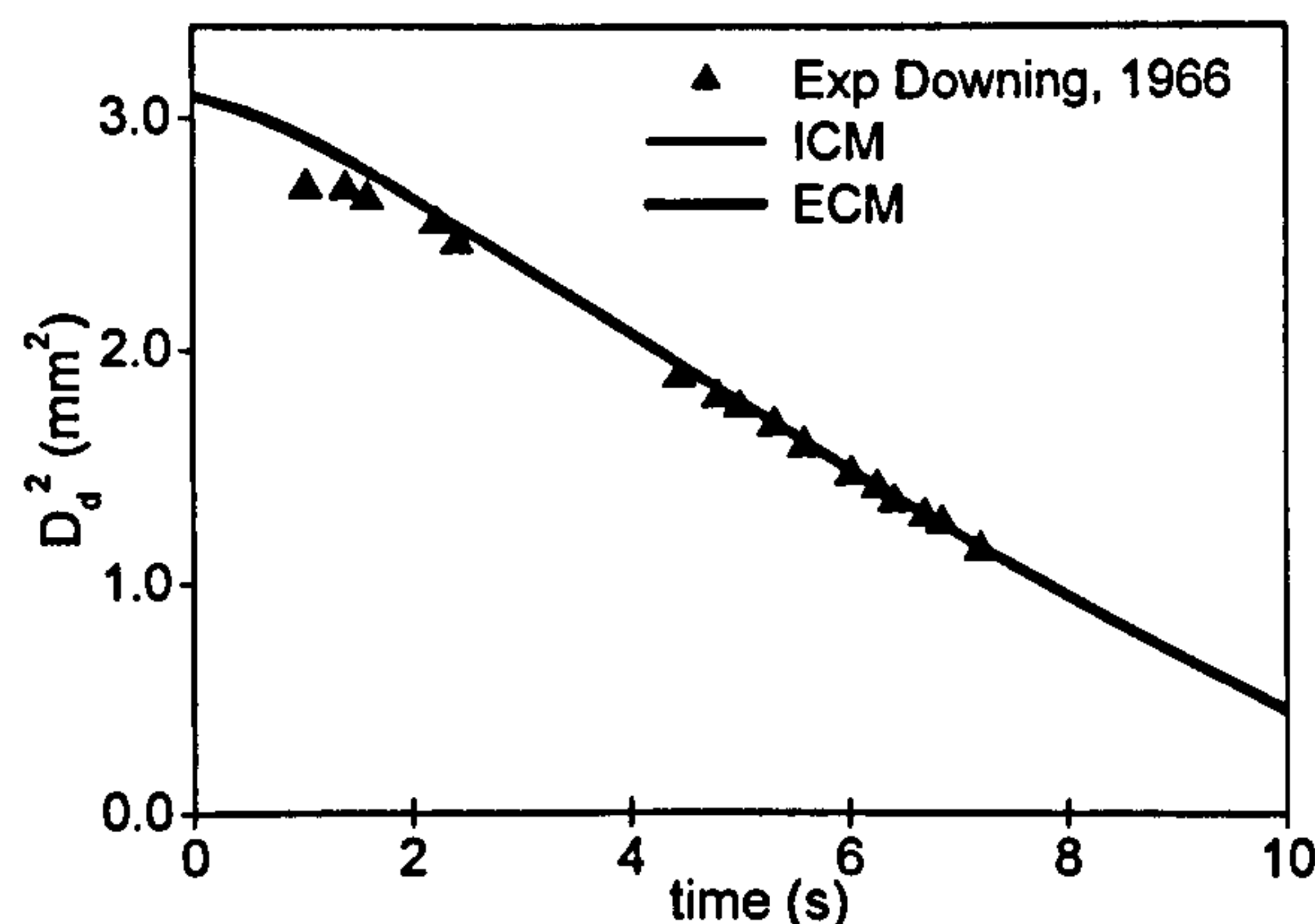


Figure 4-16: Effect of droplet vaporisation model on the liquid temperature profiles for (a) n-heptane and (b) n-tridecane fuels;  $P_G=1\text{bar}$ ,  $T_G=600\text{K}$ ,  $T_{d,0}=300\text{K}$ ,  $D_{d,0}=50\mu\text{m}$  and  $Re_d=0$ .

The liquid temperature profiles calculated by the ICM and the FCM are shown in Figure 4-16 for both fuels investigated, confirming that the two models predict almost identical liquid bulk temperature, and heat-up time interval. The transient temperature gradient

inside the droplet, up to 15 and 25 degrees for the two fuels, doesn't affect the general vaporisation trend.

Convective effect on the droplet vaporisation has been explored in the following investigation. Figure 4-17 shows the comparison between experimental and numerical square diameter for n-hexane droplet evaporating in a convective flow field at atmospheric pressure conditions. Droplet initial temperature and diameter are 1.76mm and 281K respectively; the ambient temperature has been fixed at 473K. The droplet remains stationary (hanging from the end of a thin wire) and the gas phase flow field is defined by the initial Reynolds number equal to 110. The vaporisation model is validated against experimental data from Downing [52] assuming ideal equilibrium conditions at the liquid/gas interface. The effect of the liquid-phase temperature distribution modelling has been investigated, considering either uniform and radial profiles inside the droplet, with the 'infinite conductivity model', ICM, and the 'effective conductivity model', ECM respectively. The effect of liquid internal circulation, due to the relative motion between the liquid and gas phases, has been modelled introducing in the ECM an empirical coefficient, which enhances the liquid thermal conductivity (equation 4-51).



**Figure 4-17:** Temporal evolution of the droplet diameter squared for hexane. The experimental results are from Downing [52] and the operating conditions are:  $P_G=1\text{bar}$ ,  $T_G=298\text{K}$ ,  $T_{d,0}=282\text{K}$ ,  $D_{d,0}=1.1\text{mm}$  and  $Re_d=110$ .

The models predict almost identical profiles in a very good agreement with the experimental data, suggesting that under low/moderate evaporation rate conditions the standard ideal equilibrium model, which assumes uniform temperature profile inside the droplet over the whole evaporation period, is able to capture the vaporisation phenomenon even for large droplets where temperature gradients are more likely to



occur. This conclusion simplifies the calculation under these operating conditions, since this model is the less expensive in terms of computational efforts.

A different conclusion can be drawn under relatively high evaporation rate, as shown in Figure 4-18 for n-decane droplet with initial size of 2mm and temperature of 315K placed in a high temperature, 1000K, convective air flow at 1bar back pressure. Fine thermocouples, put inside the droplet, recorded its temperature at different radial locations. The computational results have been validated against the experimental data from Wong et al. [211] assuming ideal equilibrium conditions at the liquid/gas interface and calculating uniform or radial liquid temperature distribution profiles with the ICM or the ECM respectively. The graphs show that the ‘infinite conductivity model’ predicts an initial droplet volumetric expansion not recorded by the measurements, while the temperature profile better capture the experimental trend. A closer agreement can be achieved assuming radial temperature distribution inside the droplet. Figure 4-18(a) shows the temporal evolution of droplet square diameter, while Figure 4-18(b) presents the liquid temperature transient profiles.

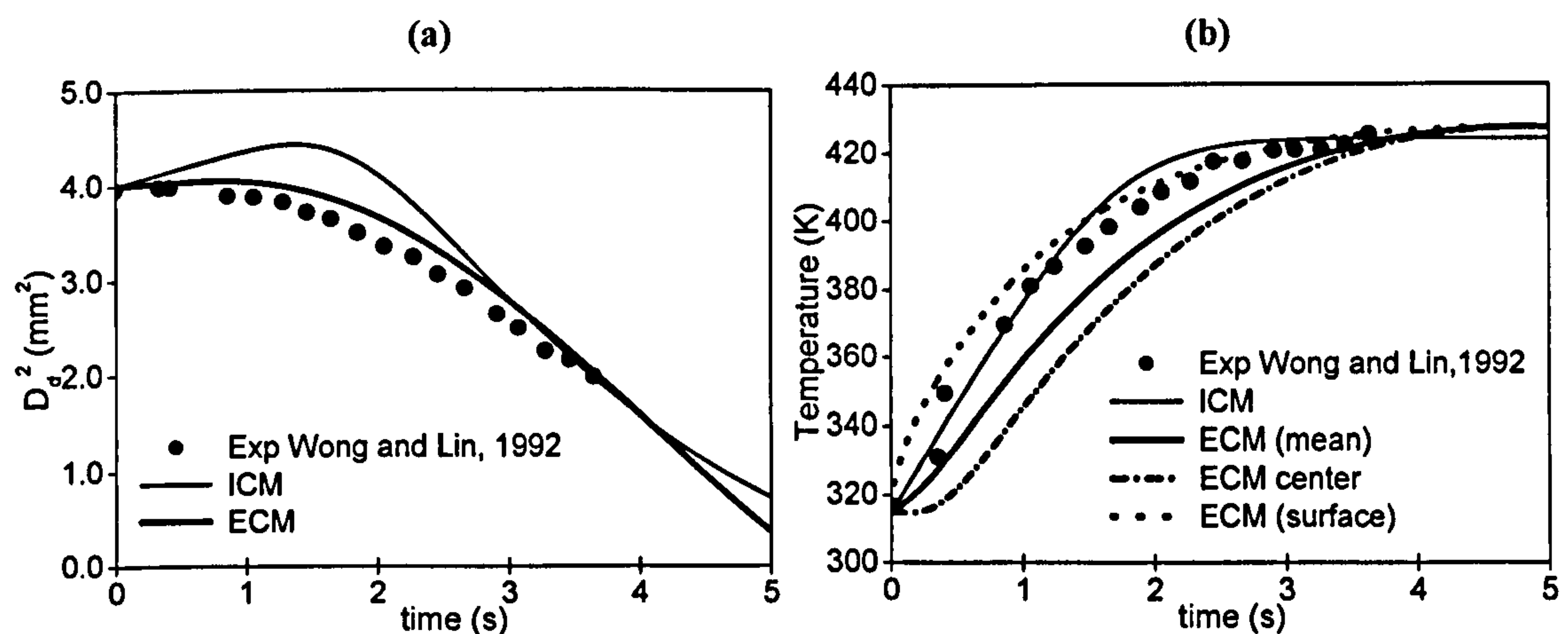


**Figure 4-18: Effect of liquid temperature distribution model on the temporal evolution of the droplet (a) non-dimensional surface area and (b) temperature profiles. The experimental results are from Wong et al. [211] and the operating conditions are: n-decane,  $P_G=1\text{bar}$ ,  $T_G=1000\text{K}$ ,  $T_{d,0}=315\text{K}$ ,  $D_{d,0}=2\text{mm}$  and  $Re_{d,0}=17$ .**

The results from the ECM corresponding to the liquid temperature at the droplet center, at the surface and its mean value have been plotted, in order to reveal the temperature gradient occurring inside the droplet as vaporisation takes place. The ‘effective conductivity model’ predicts a smoother droplet volumetric expansion, compared to the results from the ‘infinite conductivity model’, since the mean temperature calculated by this model is reduced at the initial stages. The liquid temperature distributions at

different time steps before the droplet has reached its bulk temperature are shown in Figure 4-19, comparing the experimental measurements recorded by the thermocouples with the predictions from the ECM. The graph reveal the radial monotonic distribution imposed by the model do not provide the best agreement with the experimental data, since in this case the multi-dimensional vortex model proposed by Sirignano [42] would be preferred, although the general liquid trend has been predicted.

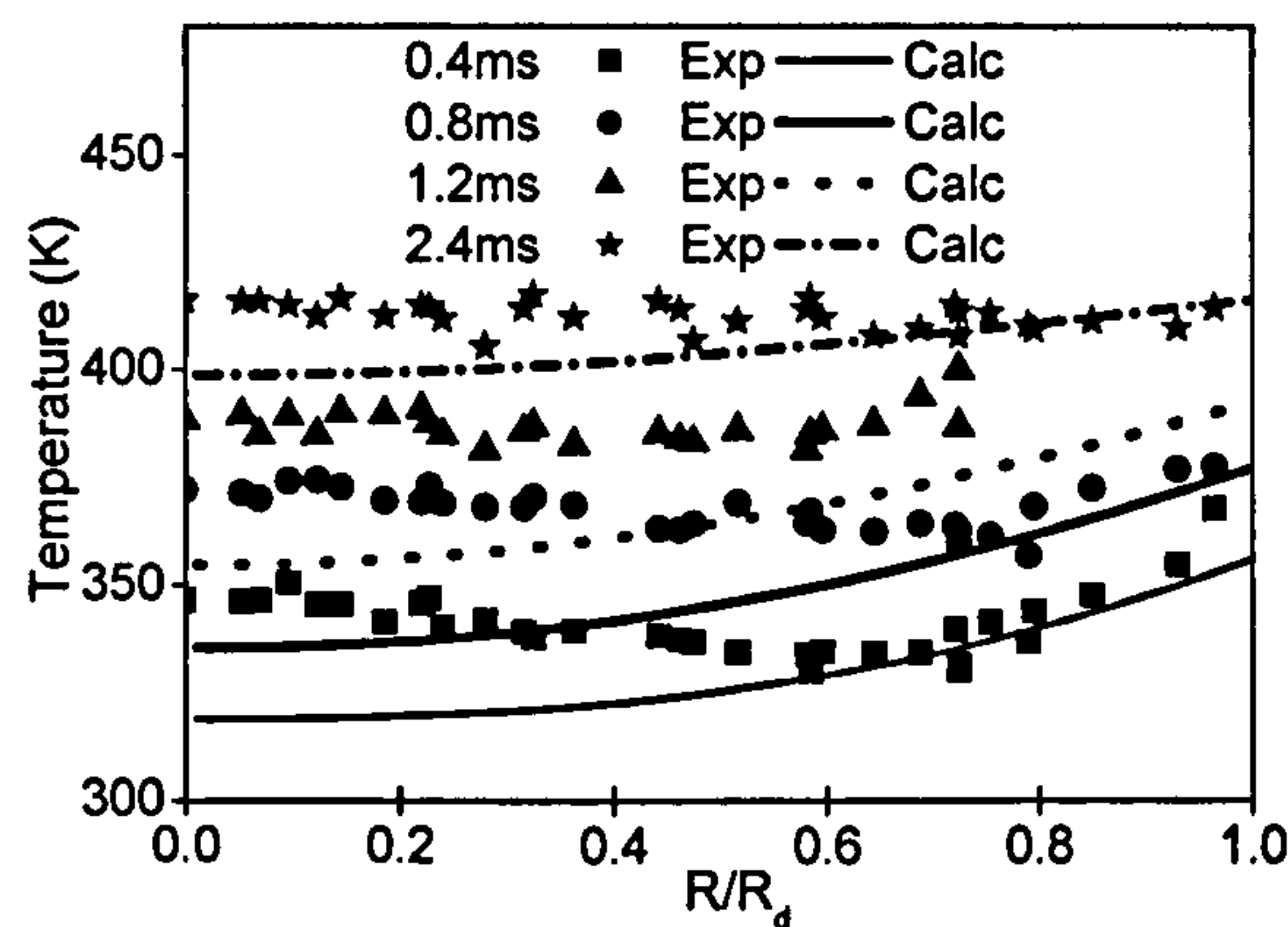


**Figure 4-19: Temperature radial profiles at 0.4, 0.8, 1.2 and 2.4ms after start of injection for n-decane fuel droplet. The operating conditions are:  $P_G=1\text{bar}$ ,  $T_G=1000\text{K}$ ,  $T_{d,0}=315\text{K}$ ,  $D_{d,0}=2\text{mm}$  and  $Re_{d,0}=17$ . The computational results are from the 'effective conductivity model' and experiments from Wong et al. [211].**

The results suggest that for considerably large droplets under low pressure environment, the ideal equilibrium model is able to describe the vaporisation phenomena, while the assumption of uniform temperature distribution is valid at low/moderate vaporisation rate conditions.

The previous investigations have shown the potentialities of the single component vaporisation models under low-pressure conditions, although the majority of the experimental data on single droplet found in literature are limited to relatively large droplet sizes. The following investigations focus on the parametrical analysis of single droplet vaporisation modelling under the operating conditions that characterise more practical spray development in diesel and gasoline engines. Table 4-III summarises the operating conditions, which define the liquid droplet composition, initial size, temperature and velocity relative to the gas phase, the ambient back pressure and temperature, the type of equilibrium model at the gas/liquid interface and the droplet temperature and concentration radial distribution profiles.



Fuel	$P_G$ (bar)	$T_G$ (K)	$T_{d,0}$ (K)	$D_{d,0}$ ( $\mu\text{m}$ )	$\Delta U_0$ (m/s)	Phase equilibrium model	Liquid temperature model
100% $\text{C}_8\text{H}_{18}$ / 20% $\text{C}_6\text{H}_{14}$ - 50% $\text{C}_8\text{H}_{18}$ - 30% $\text{C}_{10}\text{H}_{22}$	1	310	300	20 / 100	100	LPEqM / HPM / NonEqM	ICM / FCM / ECM
	2	350					
	13	450					
	45	850					

**Table 4-III: Operating conditions for the parametric investigation on single droplet evaporation modelling.**

Initially, the effect of liquid phase thermal radial distribution modelling on the transient droplet size and temperature profiles as function of the non-dimensional droplet lifetime is shown in Figure 4-20(a), while Figure 4-20(b) presents the radial distribution of the liquid phase temperature at four time steps after the start of injection, for n-octane droplet of  $20\mu\text{m}$  injected in stagnant air at  $P_G=10\text{bar}$  and  $T_G=450\text{K}$  with an initial relative velocity equal to  $100\text{m/s}$ . The uniform liquid temperature profile, predicted by the ‘infinite conductivity model’, ICM is compared with the predictions obtained with the ‘finite conductivity model’, FCM, assuming radial temperature distributions inside the droplet and the ‘effective conductivity model’, which takes into account the internal liquid motion introducing a correction factor in the calculation of the thermal diffusivity.

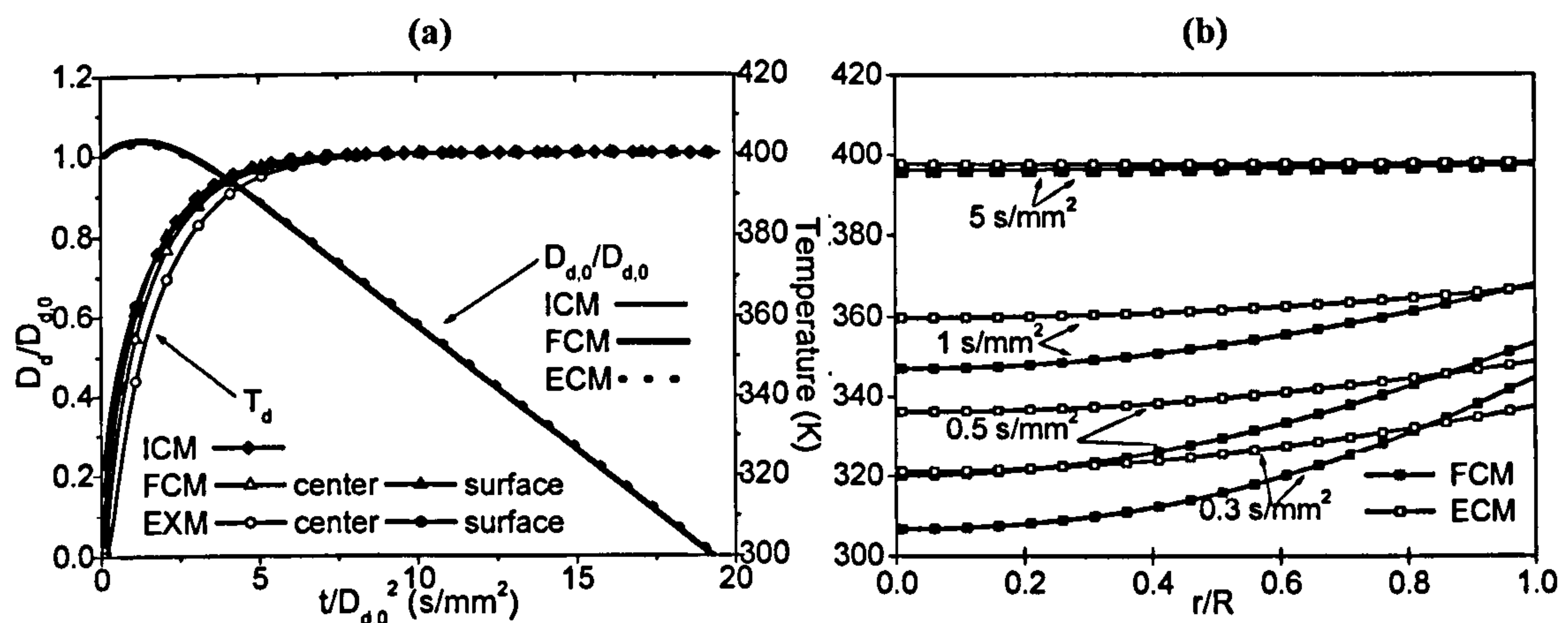


**Figure 4-20: (a) droplet surface area regression and temperature profiles and (b) liquid phase spatial temperature distributions predicted by the ‘infinite conductivity model’, ICM, the ‘finite conductivity model’, FCM, and the ‘effective conductivity model’; n-octane  $T_{\text{back}}=450\text{K}$ ,  $P_{\text{back}}=13\text{bar}$ ,  $D_0=20\mu\text{m}$ ,  $T_0=300\text{K}$ ,  $\Delta U_0=100\text{m/s}$ .**

The drag force contribution on the liquid droplet is modelled, considering the vaporisation effect in the definition of the drag coefficient. The assumption of radial temperature distribution predicts almost identical vaporisation rate compared to the

uniform temperature case and the introduction of effective liquid conductivity, even if it smoothes the liquid temperature gradients, does not calculate appreciably different droplet lifetime for such small droplets.

Figure 4-21 summaries the previous findings predicting the droplet lifetime for single component droplets of 20 $\mu\text{m}$  and 100 $\mu\text{m}$  initial diameter vaporising under five back temperature and pressure conditions, which cover a wide range of operating conditions for fuels injected in the cylinder of an internal combustion engines. The results reveal that the detailed investigation of the liquid temperature distribution does not add any relevant information in terms of droplet life-time. The three models provide almost identical results, predicting the faster fuel vaporisation with the combined increase of back temperature and pressure. These investigations have been performed imposing ideal equilibrium at the liquid-gas interface and implementing the Clausius-Clapeyron equation to calculate the molar fraction of the vaporizing species, according to the ‘low pressure equilibrium model’, LPEqM. Under high pressure conditions the validity of this assumption has to be discussed and the following investigations focused on this issue.

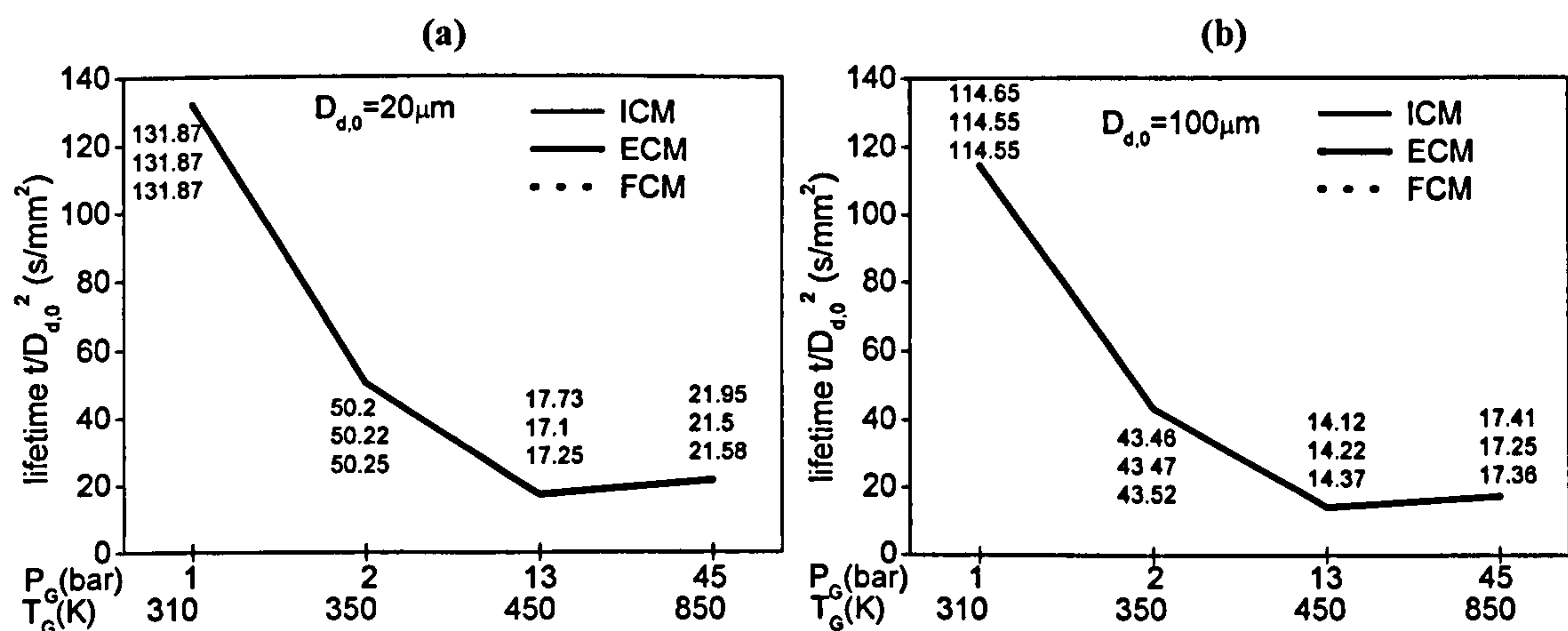
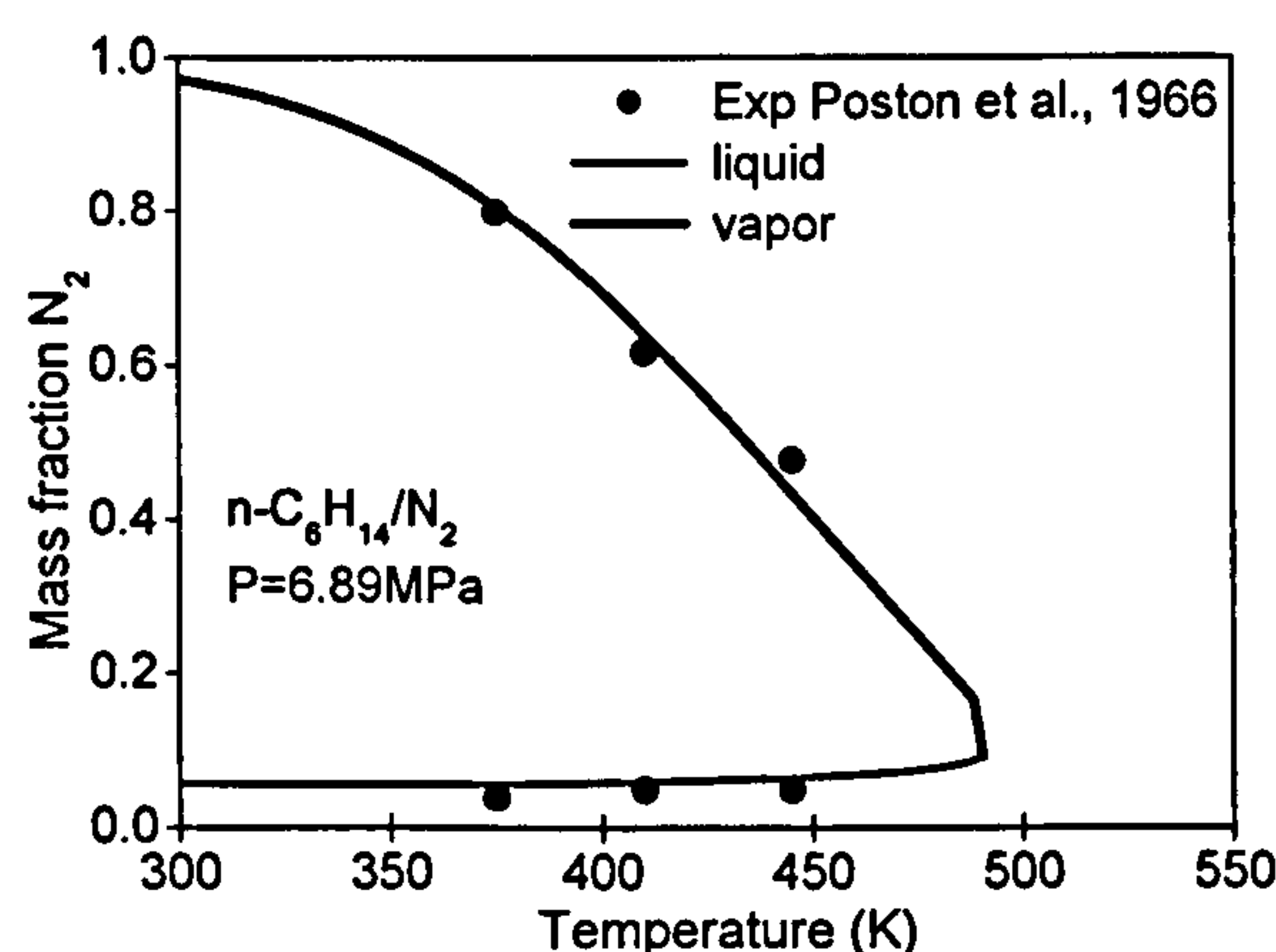


Figure 4-21: Effect of liquid temperature distribution model on the predicted droplet life time under different back conditions, for (a) 20 $\mu\text{m}$  and (b) 100 $\mu\text{m}$  droplet. The operating conditions are: n-octane,  $T_{d,0}=300\text{K}$ ,  $\Delta U_0=100\text{m/s}$ ; LPEqM for liquid-gas interface equilibrium.

The high-pressure model, HPM, which calculates the liquid-gas fugacity coefficients at the interface between the two phases to predict the concentration of the different species in thermo-dynamic equilibrium, has been presented. It assumes the simultaneous vaporisation of the liquid components and the solubility of the gases in the liquid. Several experimental and theoretical studies reveal that for high ambient pressures a



noticeable amount of gas is dissolved at the droplet surface. Figure 4-22 illustrates the high-pressure phase equilibrium of n-hexane and nitrogen for an ambient pressure of 6.89 MPa, corresponding to a reduced pressure  $P_R$  equal to 2. The lower line in this diagram represents the liquid composition, the upper one shows the composition in the gaseous phase which is in equilibrium with the liquid. Both curves approach each other when the critical state is reached. The mass fraction of nitrogen in the gas phase decreases with increasing temperature as the partial pressure of n-hexane rises. It is to mention that the mass fraction of dissolved gas in the liquid is in the order of 5%, nearly independent of temperature. The experimental results from Poston et al. [212], are also plotted, showing a very good agreement between measurements and predictions.



**Figure 4-22:** Phase equilibrium of n-hexane/nitrogen system predicted by the Peng-Robinson equation of state; comparison with data of Poston et al. [212].

Figure 4-23 and Figure 4-24 illustrate the computational results from the fugacity coefficient method implemented in the 'high-pressure model' described by the system of equations (4-11) to (4-17). The high-pressure phase equilibrium of n-octane and nitrogen as function of temperature, under two back-pressure conditions corresponding to n-octane reduced pressure of 0.5 and 2.5 has been solved implementing the Peng-Robinson equation of state. The fugacity coefficients in the liquid and gas phase for the two species in equilibrium are shown in Figure 4-23, revealing that the critical state is reached at higher temperature as back pressure rises, the liquid fugacity of n-octane increases with temperature although it decreases with pressure independently on the phase state, as far as nitrogen its vapour fugacity does not depend on pressure and temperature while its liquid fugacity decreases with temperature and it's significantly reduced at high pressure. Figure 4-24(a) shows the predicted compressibility factor calculated from equation (4-14), suggesting that at moderate back pressure the liquid

compressibility does not depend on pressure and it significantly increases up to 0.5 at higher pressure conditions, the vapour compressibility is monotonically decreasing with increasing temperature, with lower gradient at higher pressure. A similar trend is followed by the nitrogen mole fraction concentration profiles in the liquid and vapour phases. The liquid concentration around 5% at moderate pressure conditions increases up to 25% at higher back pressure close to the critical point, while the vapour concentration decreases from 100% down to 10% and 25% with reduced pressure equal to 0.5 and 2.5 respectively.

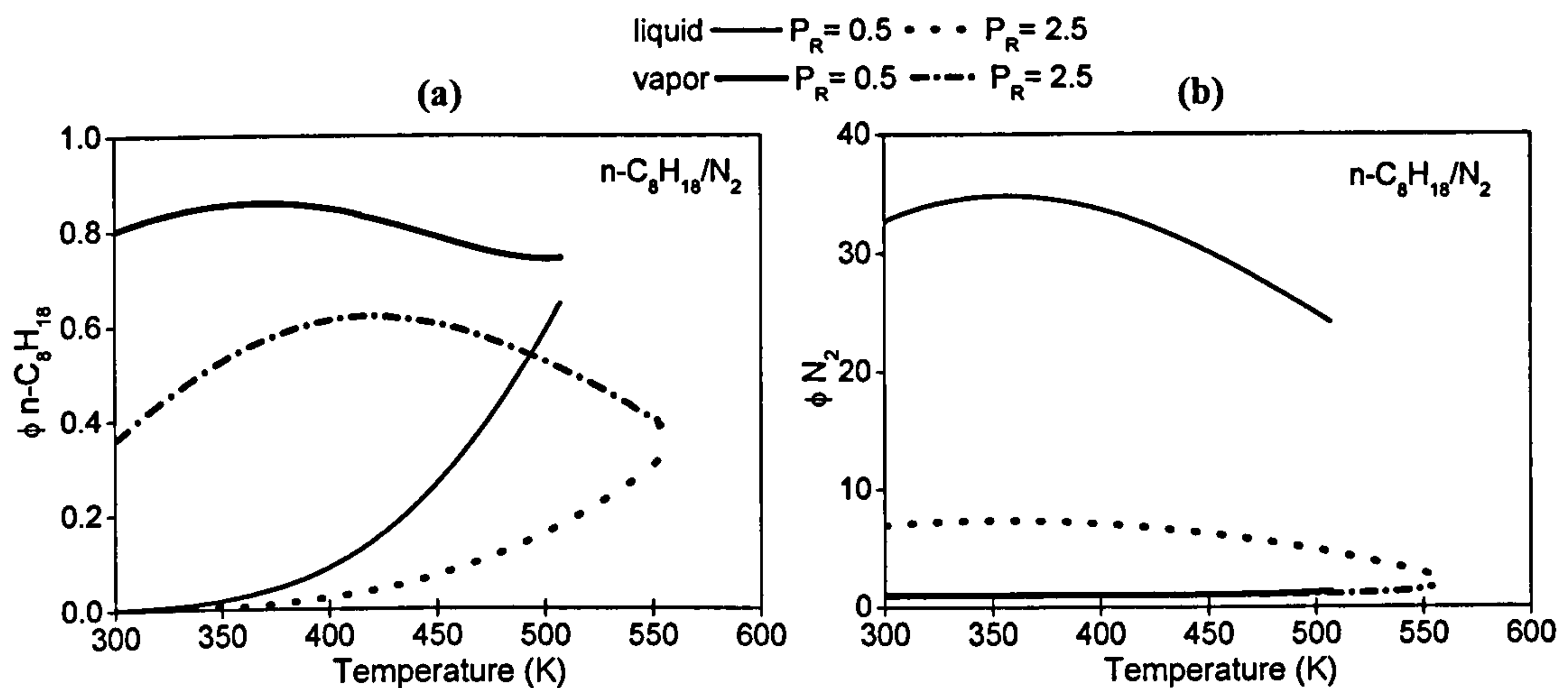


Figure 4-23: (a)  $n\text{-C}_8\text{H}_{18}$  and (b)  $\text{N}_2$  liquid/vapour fugacity coefficients predicted by the P-R EOS for  $n\text{-C}_{10}\text{H}_{22}/\text{N}_2$  system in thermodynamic equilibrium at low and high pressure conditions.

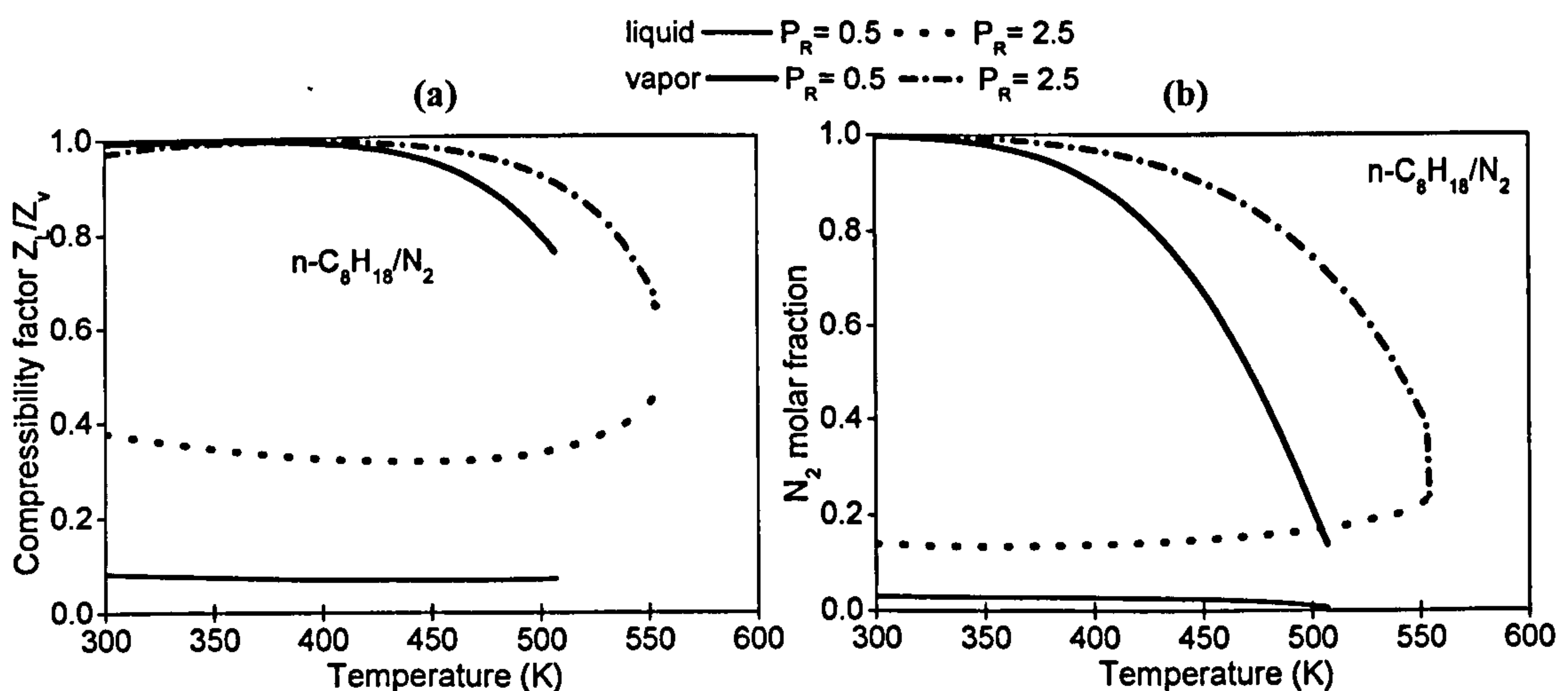
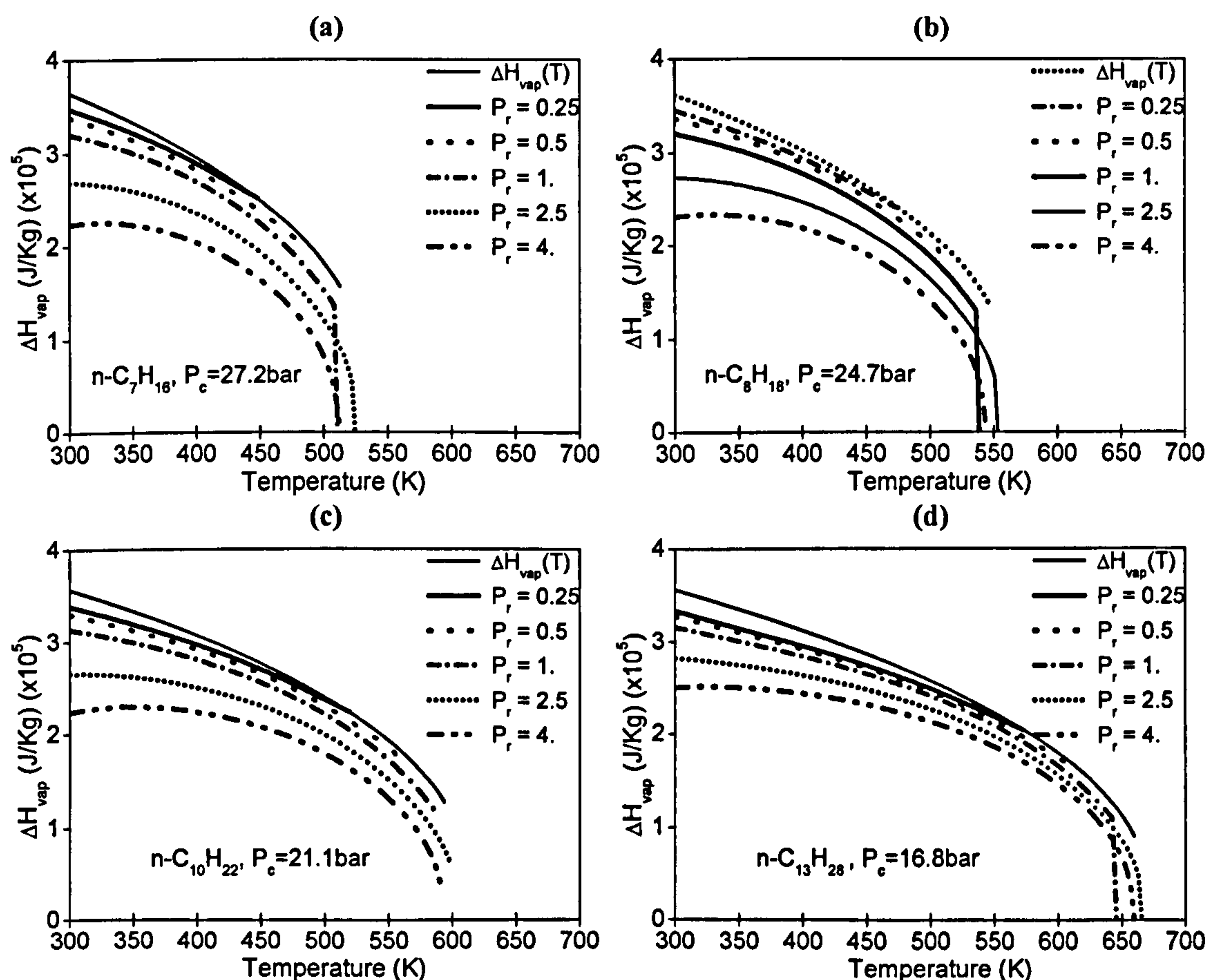


Figure 4-24: Liquid/vapour (a) compressibility factors and (b)  $\text{N}_2$  mole fractions predicted by the P-R EOS for  $n\text{-C}_8\text{H}_{18}/\text{N}_2$  system in thermodynamic equilibrium at low and high pressure conditions.

The fugacity coefficient methodology also includes a correlation to calculate the enthalpy for vaporisation from the molar fraction concentrations and the fugacity



coefficients according to equation (4-17). Figure 4-25 show the heat of vaporisation as function of temperature for four different fuels under five reduced pressure conditions, predicted by the 'high pressure model' solving the Peng-Robinson equation of state and by the 'low pressure ideal equilibrium model', which proposes a correlation from Perris et al., 1999, to calculate the latent heat of vaporisation function only of temperature, equation (4-18). The graphs reveal that the pressure effect on the enthalpy for vaporisation is considerable particularly at low temperatures and they confirm that the heat for vaporisation decreases with increasing temperature and with the fuel volatility.



**Figure 4-25: Effect of back pressure and temperature on the enthalpy of vaporisation profiles for (a) n-heptane, (b) n-octane, (c) n-decane and (d) n-tridecane fuel in thermodynamic equilibrium with  $N_2$ , as predicted by the ideal correlation function of temperature and the Peng-Robinson equation of state (PR-EOS).**

The high-pressure model has been implemented to predict the droplet vaporisation for a wide range of operating conditions and model assumptions. An example is shown in Figure 4-26, which shows the effect of liquid temperature distribution model on the predicted droplet lifetime and mean liquid temperature profiles for n-octane droplet injected in stagnant air at 13bar and 450 back pressure and temperature respectively; the operating conditions are described in Table 4-III. The phase equilibrium at the interface

is calculated according to the fugacity coefficient method, while the radial temperature distribution inside the droplet is solved by the 'finite conductivity model', FCM, and the 'effective conductivity model', ECM, which neglects and considers, respectively, the increase of thermal conductivity due to convective effect. The results reveal that the internal circulation caused by the relative motion between the two phases does not play a substantial role on the overall vaporisation process. The temperature radial distribution profiles, predicted by the two models at four times steps after the start of injection, are shown in Figure 4-27, confirming that the convective empirical factor increasing the thermal conductivity smoothes the temperature gradients, although the droplet lifetime is reduced only of about 3%.

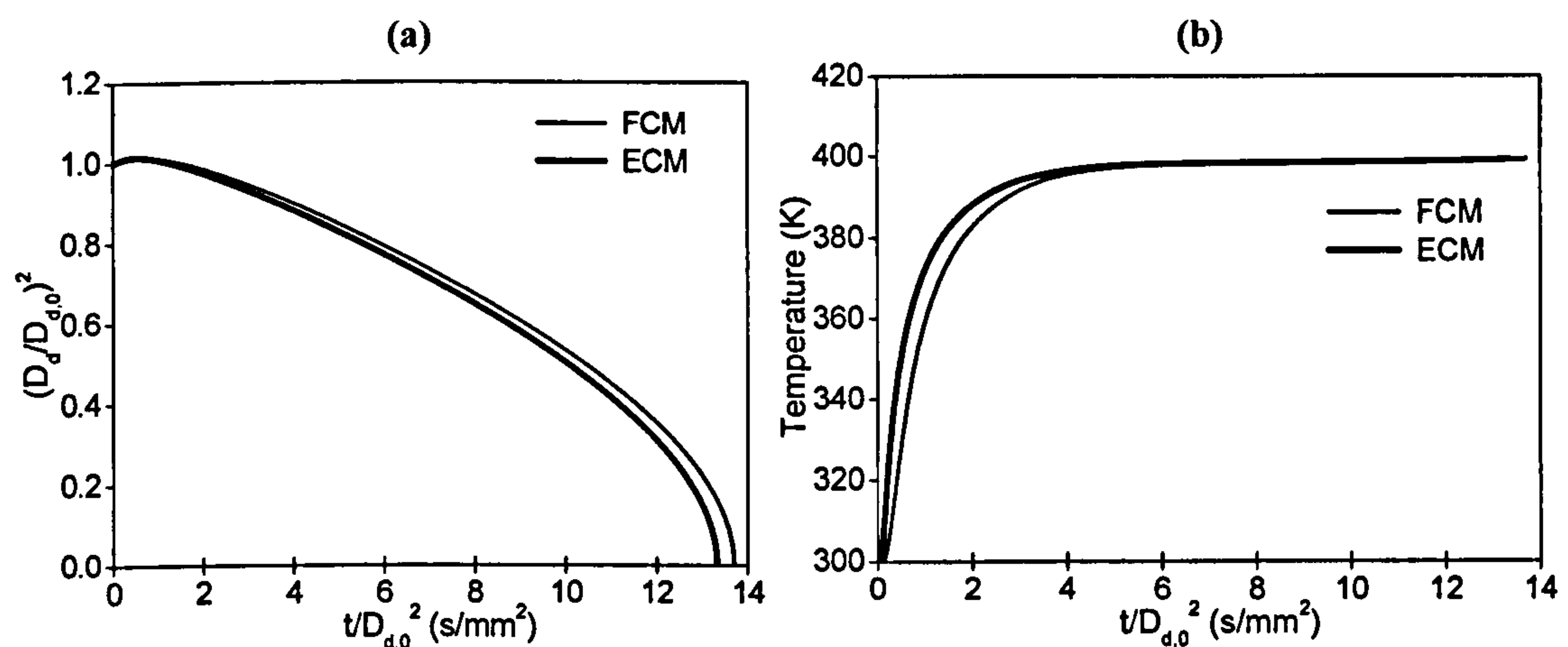


Figure 4-26: Effect of liquid temperature distribution model on the predicted droplet (a) non-dimensional surface area and (b) mean liquid temperature using the HPM for liquid-gas interface equilibrium. The operating conditions are: n-octane,  $P_G=13\text{bar}$ ,  $T_G=450\text{K}$ ,  $D_{d,0}=100\mu\text{m}$ ,  $T_{d,0}=300\text{K}$ ,  $\Delta U_0=100\text{m/s}$ .

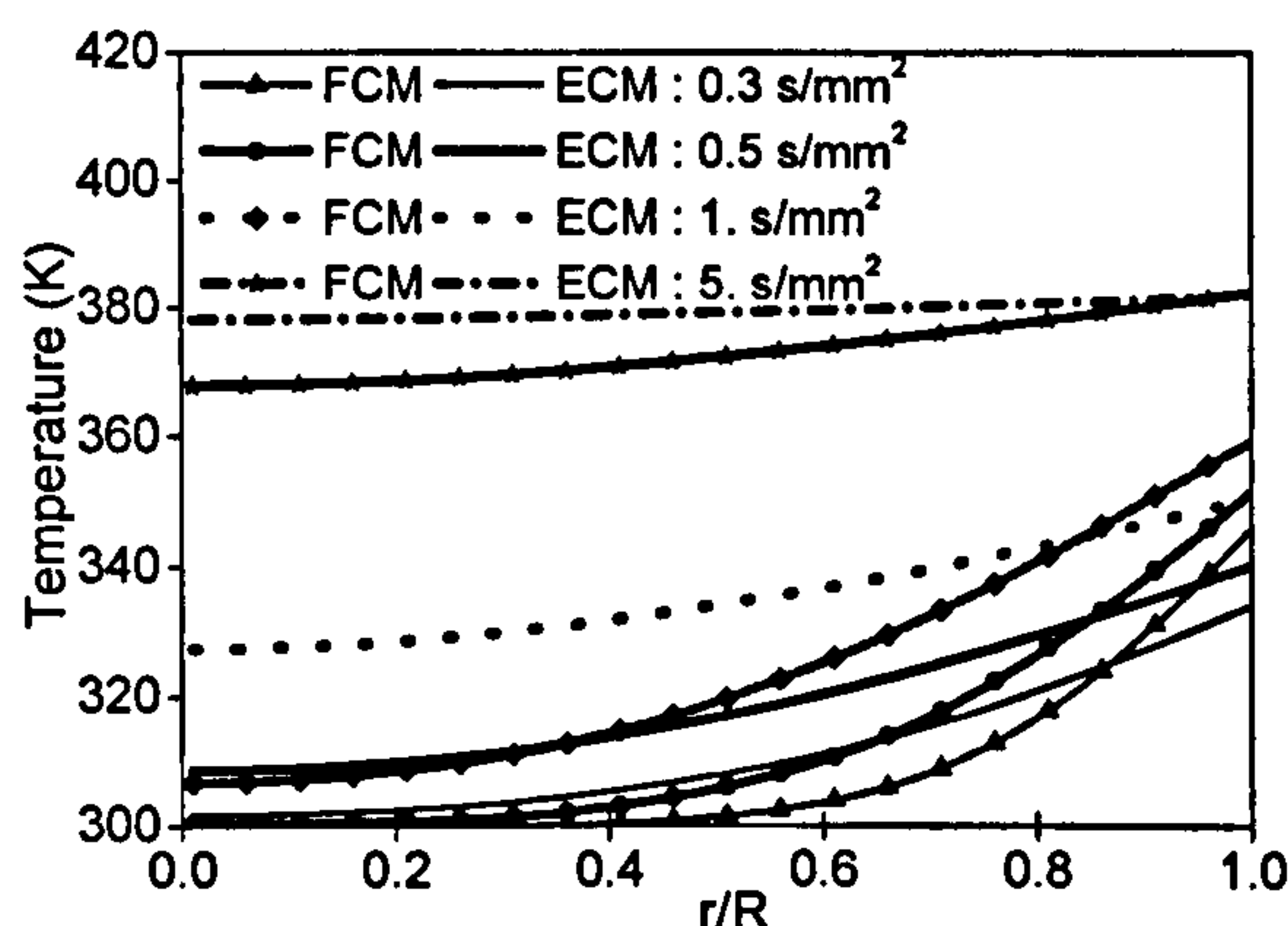


Figure 4-27: Effect of liquid temperature distribution model on the predicted liquid temperature radial profiles at four time steps after start of injection, using the HPM for liquid-gas interface equilibrium. The operating conditions are: n-octane,  $P_G=13\text{bar}$ ,  $T_G=450\text{K}$ ,  $D_{d,0}=100\mu\text{m}$ ,  $T_{d,0}=300\text{K}$ ,  $\Delta U_0=100\text{m/s}$ .



The sensitivity of the droplet lifetime on the liquid temperature distribution model, assuming high pressure equilibrium effect at the liquid-gas interface, has been investigated for the operating conditions presented in Table 4-III and the results are illustrated in Figure 4-28 for n-octane fuel droplet, implementing the ICM, which assumes uniform liquid temperature inside the droplet and two radial distribution models, the FCM and the ECM. The graphs reveal that the high pressure model predicts faster vaporisation increasing back pressure and temperature, independently on the initial droplet size and liquid temperature analysis. The droplet lifetime predictions at high pressure and temperature conditions suggest that more than the choice to implement or not a liquid temperature distribution model, the option to model convective effect can have marked consequences, over-estimating the droplet lifetime up to 40% when its contribution is neglected.

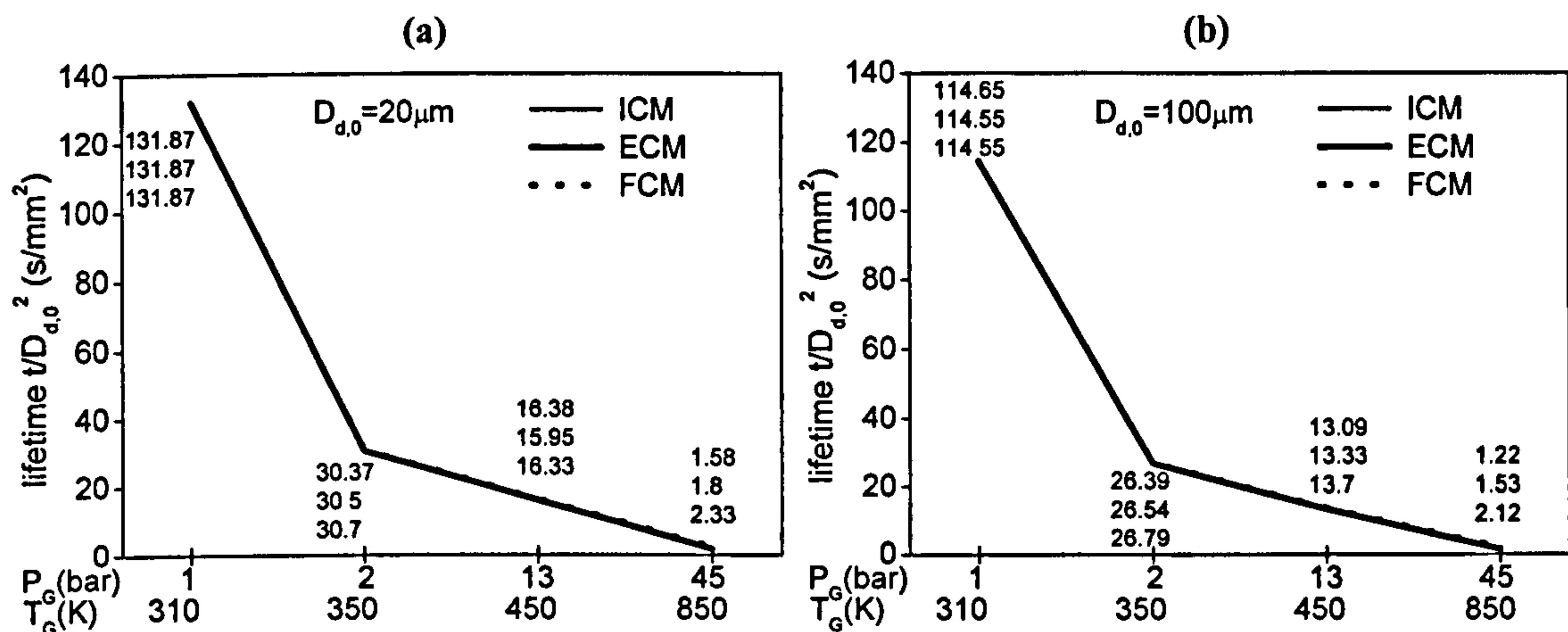
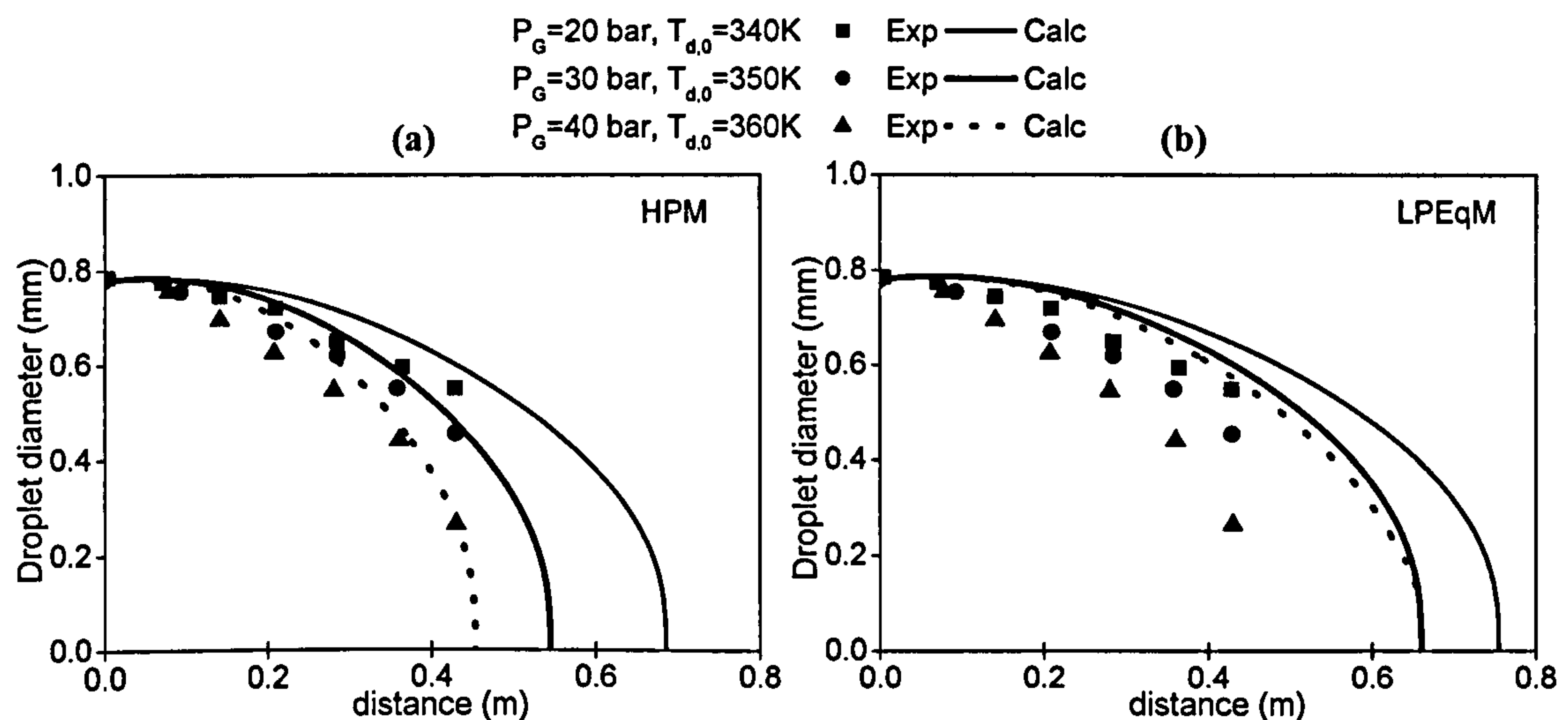


Figure 4-28: Effect of liquid temperature distribution model on the predicted droplet life time under different back conditions, for (a) 20 $\mu\text{m}$  and (b) 100 $\mu\text{m}$  droplet. The operating conditions are: n-octane,  $T_{d,0} = 300$  K,  $\Delta U_0 = 100$  m/s; HPM for liquid-gas interface equilibrium.

The validation of the high-pressure model, HPM, is presented in Figure 4-29, which shows the comparison among model predictions and experimental results from Stengele et al. [213] for a free-falling n-heptane fuel droplet in high-pressure stagnant air at 550K back temperature and pressure varying from 20bar up to 40bar. The initial droplet diameter and velocity are 0.78mm and 0.5m/s, respectively. The initial droplet temperature varies from 340K to 360K, according to the back pressure. Figure 4-29(a) illustrates the droplet diameter regression as function of the travelled distance, for the three pressures and liquid initial temperatures investigated, revealing good agreements between computational and experimental results. Figure 4-29(b) shows the corresponding predictions implementing the ideal equilibrium model, LPEqM, for the

calculation of the fuel vapour mass fraction at the interface. The results reveal that the ideal equilibrium model substantially under-predict the vaporisation rate at high-pressure conditions. Thus, for these cases the HPM should be preferred.

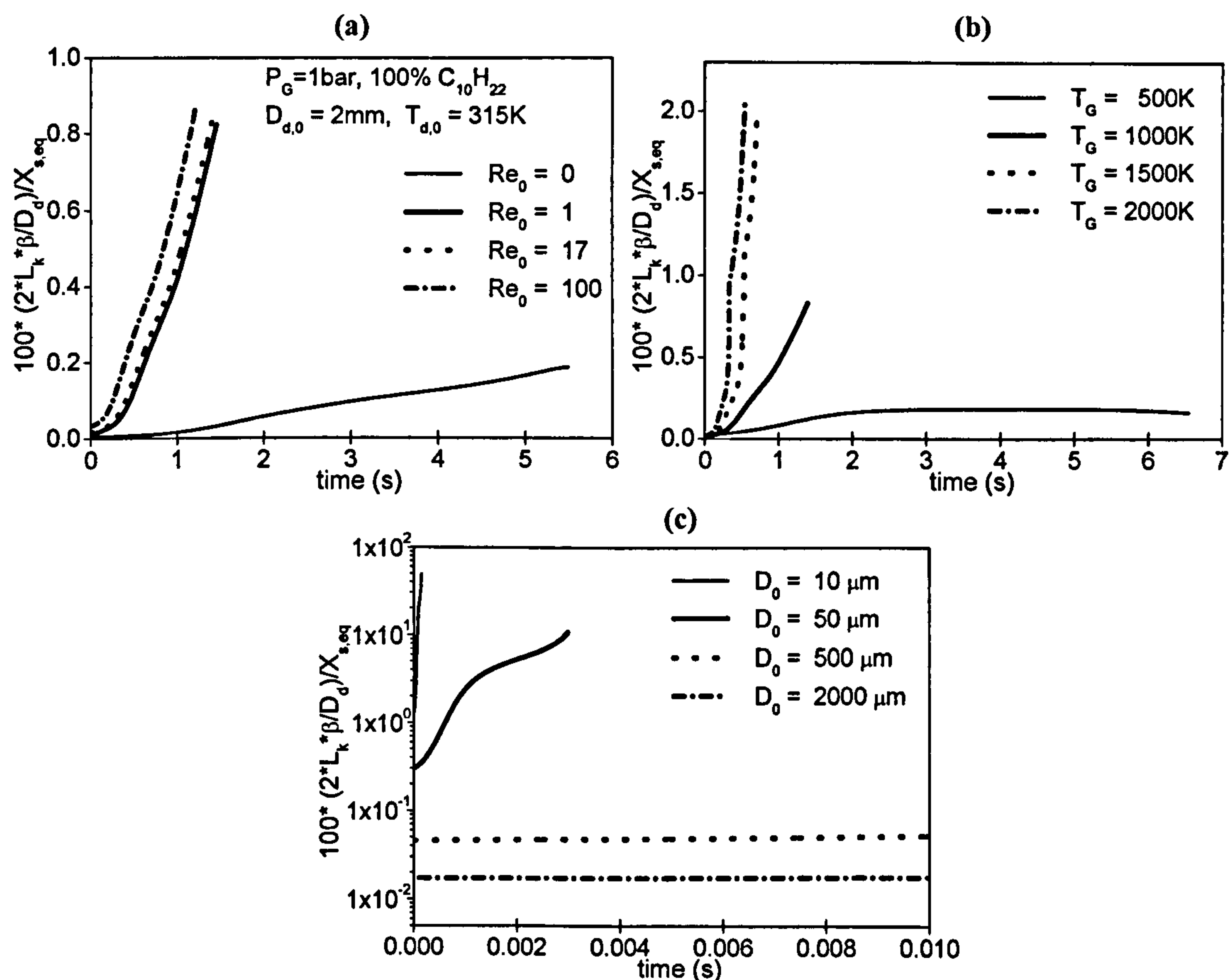


**Figure 4-29: Gas pressure effect on the droplet diameter profile over the evaporation distance for n-heptane fuel droplet predicted by the uniform temperature distribution model considering (a) high-pressure effect (HPM) and (b) ideal equilibrium conditions (LPEqM) at the liquid/gas interface; the experimental results are from Stengele et al. [213] and the operating conditions are:  $P_G=20/30/40\text{bar}$ ,  $T_G=550\text{K}$ ,  $D_{d,0}=0.78\text{mm}$ ,  $T_{d,0}=340/350/360\text{K}$ ,  $\Delta U_0=0.5\text{m/s}$ .**

The third model implemented to calculate the concentration of the vaporising species at the liquid-gas interface, namely the ‘non-equilibrium model’, NON-EqM, introduces a correction to the molar fraction value calculated assuming ideal equilibrium to account for non-equilibrium effect, according to the Langmuir-Knudsen evaporation law, equation (4-7). As proposed in Miller et al. [107], the temporal evolution of the non-equilibrium contribution to the surface mole fraction for n-decane droplets, vaporising in a convective flow field of nitrogen at atmospheric pressure and different back temperatures, and initial droplet size, from  $10\mu\text{m}$  up to  $2\text{mm}$ , has been investigated and the results are illustrated in Figure 4-30. Unless specified the Reynolds number, gas temperature and initial droplet diameter are equal to 17,  $1000\text{K}$  and  $2\text{mm}$ , respectively. The calculations end when the liquid mass reduced down to 1% of its initial value. The predictions confirm the conclusion of Miller et al. [107], that the non-equilibrium effects play a role only for small droplet, with initial diameter lower than  $50\mu\text{m}$ , since with bigger droplets the vapour mass fraction predicted by the Langmuir-Knudsen evaporation law and by the ideal equilibrium model differ less than 2%. It’s worthwhile to remind that the non-equilibrium model has been explored under atmospheric pressure

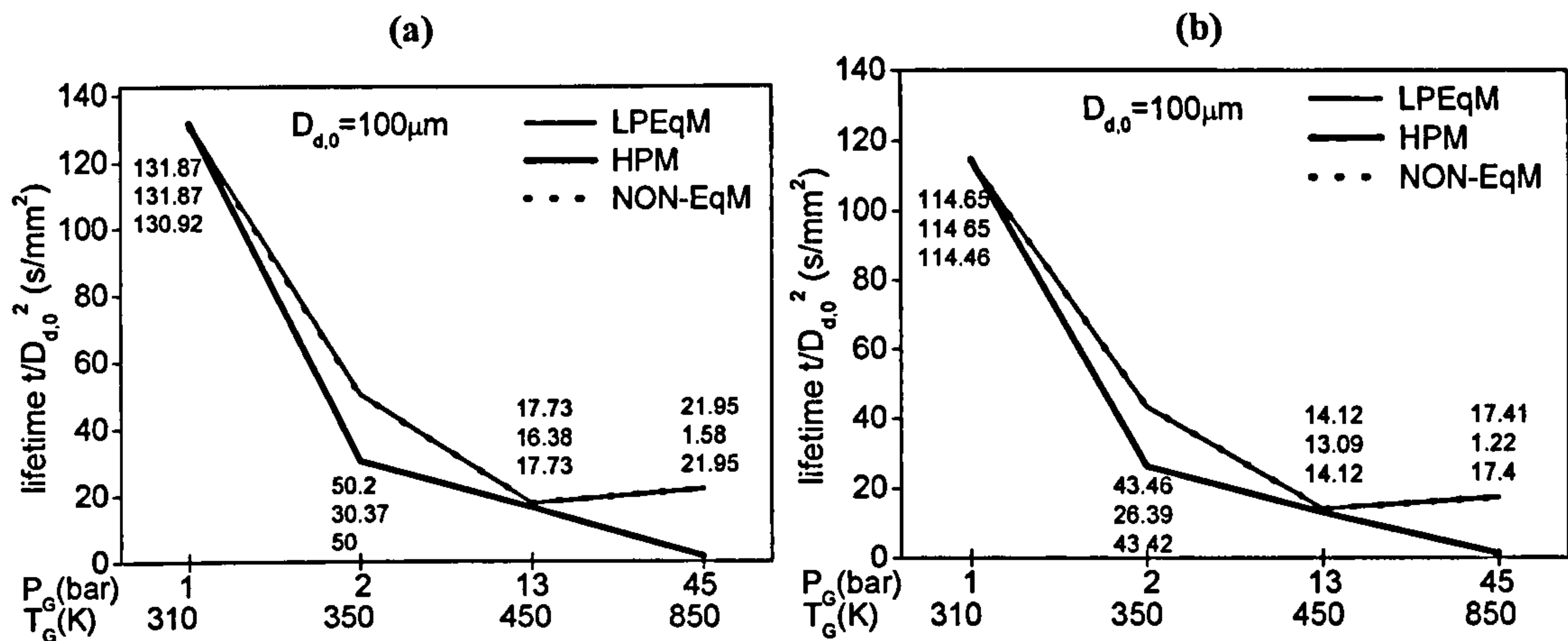


conditions, and further investigation is required to study its contribution in combination with high-pressure effect.



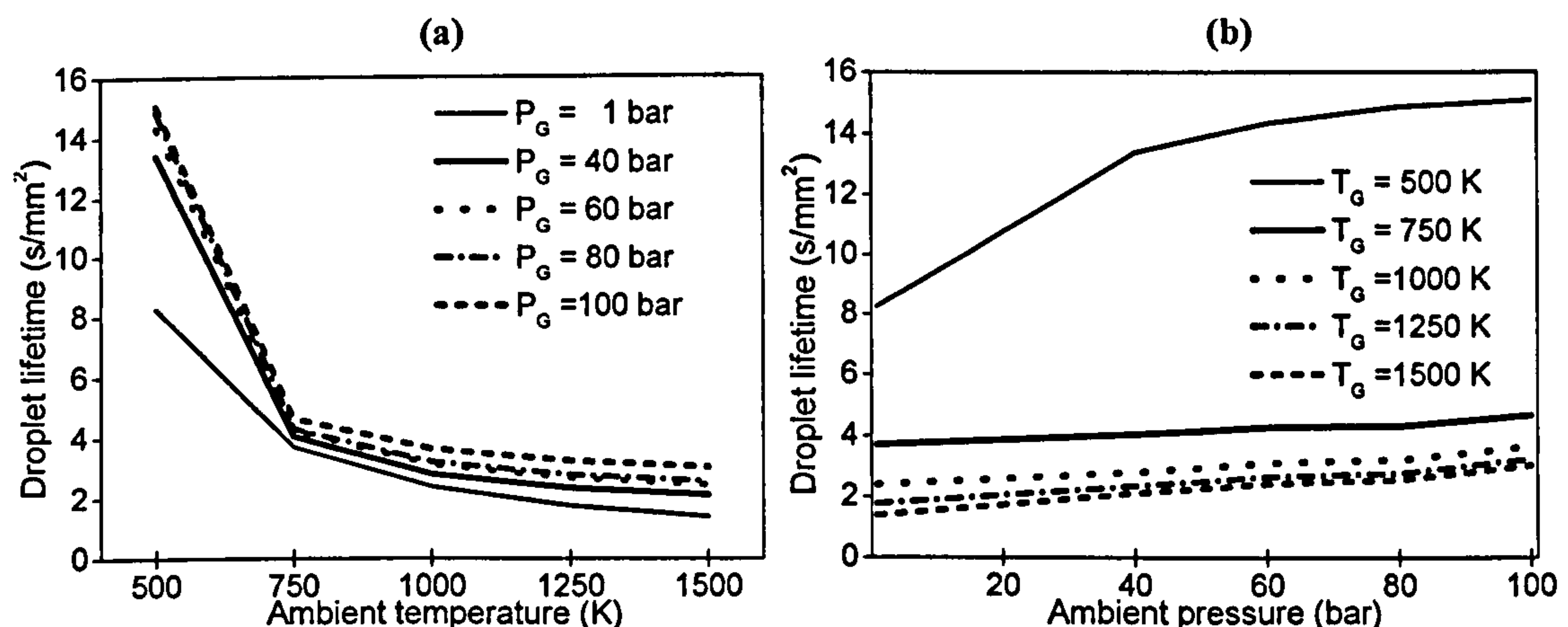
**Figure 4-30: Temporal evolution of the non-equilibrium contribution to the surface mole fraction for Langmuir-Knudsen model; unless specified the operating conditions are: n-decane fuel,  $P_G=1\text{bar}$ ,  $T_G=1000\text{ K}$ ,  $T_{d,0}=315\text{ K}$ ,  $D_0=2\text{ mm}$  and  $Re_{d,0}=17$ ; calculations end when  $m_d=0.01m_{d,0}$ ; effect of (a) initial droplet Reynolds numbers; gas temperatures, and (c) initial droplet diameters.**

Figure 4-31 illustrate the parametrical investigation on the vaporisation equilibrium model, using the operating conditions described in Table 4-III for n-octane fuel droplets, with uniform liquid temperature predicted by the ‘infinite conductivity model’, ICM. The results clearly show that the non-equilibrium contribution is negligible in terms of droplet lifetime, due to the fact at low pressures conditions, which correspond to the operating settings actually investigated for this model, heat-up effect are responsible for the slow vaporisation process. The high pressure model, on the other hand, predicts faster vaporisation with increasing back-pressure and temperature independently on the droplet initial size.



**Figure 4-31:** Effect of evaporation model at the liquid-gas interface on the predicted droplet life time under different back conditions, for (a) 20 μm and (b) 100 μm droplet. The operating conditions are: n-octane fuel,  $T_{d,0}=300\text{K}$ ,  $\Delta U_0=100\text{m/s}$ ; uniform liquid temperature distribution.

Finally the effect of back-pressure and temperature on the lifetime of n-octane droplet vaporising in stagnant environment, with initial droplet size and temperature equal to 50 μm and 300K, respectively, is presented in Figure 4-32. The high-pressure model is used to predict the vaporisation equilibrium conditions at the interface, together with the ‘infinite conductivity model’ for the liquid temperature distribution profiles. The results suggest that vaporisation is accelerated with increasing back temperature, although this effect is reduced when the gas temperature exceeds the fuel critical temperature. High pressure environments increase the droplet lifetime up to 200% with pressure from atmospheric up to 100 bar.



**Figure 4-32:** Droplet lifetime function of ambient temperature and pressure for n-heptane droplet.  $D_{d,0}=50\mu\text{m}$ ,  $T_{d,0}=300\text{K}$ ,  $Re_d=0$ .

The following investigations focus on the effect of liquid phase initial composition for vaporising droplets under a wide range of operating conditions and modelling assumptions. The results will show that the batch distillation type mainly describes the



vaporisation phenomena. This can be explained by the increasing concentration of heavier components in the liquid phase as vaporisation proceeds. These findings underline the importance of implementing a model able to capture the phenomena in terms of droplet lifetime, liquid/gas phase concentrations and temperature distributions in practical applications with diesel and gasoline fuels, which consist of mixtures of hydrocarbons.

Figure 4-33 show the droplet surface area regression, temperature and concentration profiles for n-octane/n-decane droplet vaporising in a convective flow at atmospheric pressure and high temperature conditions. In analogy with the liquid phase internal heat transport, three models have been implemented to solve the mass transport: the ‘infinite diffusivity model’, IDM, which predicts uniform liquid phase concentration profiles, the ‘finite diffusivity model’, FDM, which assumes radial concentration distributions inside the droplet, and the ‘effective diffusivity model, EDM, which includes the effect of liquid mass transport due to internal recirculation, introducing an effective mass diffusivity coefficient in the mass conservation equation. The results reveal that the droplet lifetime is almost independent on the liquid concentration distribution model, Figure 4-33(a). The liquid temperature profile predicted by the ICM suggests the typical distillation curve, while the spatial distribution models predict an almost coincident average value for the bulk temperature of the different species, Figure 4-33(b). Figure 4-33(c) present the temporal profile of the lighter component liquid concentration at the droplet surface and at the center according to the three models, while Figure 4-33(d) shows the total vaporised mass of the two fuels, suggesting that the uniform concentration model predicts faster vaporisation of the lighter component in the mixture. The introduction of the effective mass diffusivity coefficient in the radial concentration distribution models enhanced the liquid mass transport, decreasing the concentration of the lighter component in the liquid phase center, and slightly increasing its concentration at the droplet surface. Finally the radial concentration distribution profiles of n-octane at 4 time steps after start of injection are illustrated in Figure 4-34, comparing the predictions from the FCM and the ECM. The results confirm that the ‘effective conductivity model’ predicts faster mass transport in the liquid phase compared to the ‘finite conductivity model’, with the lighter components preferably diffused towards the droplet surface for their favourite vaporisation.

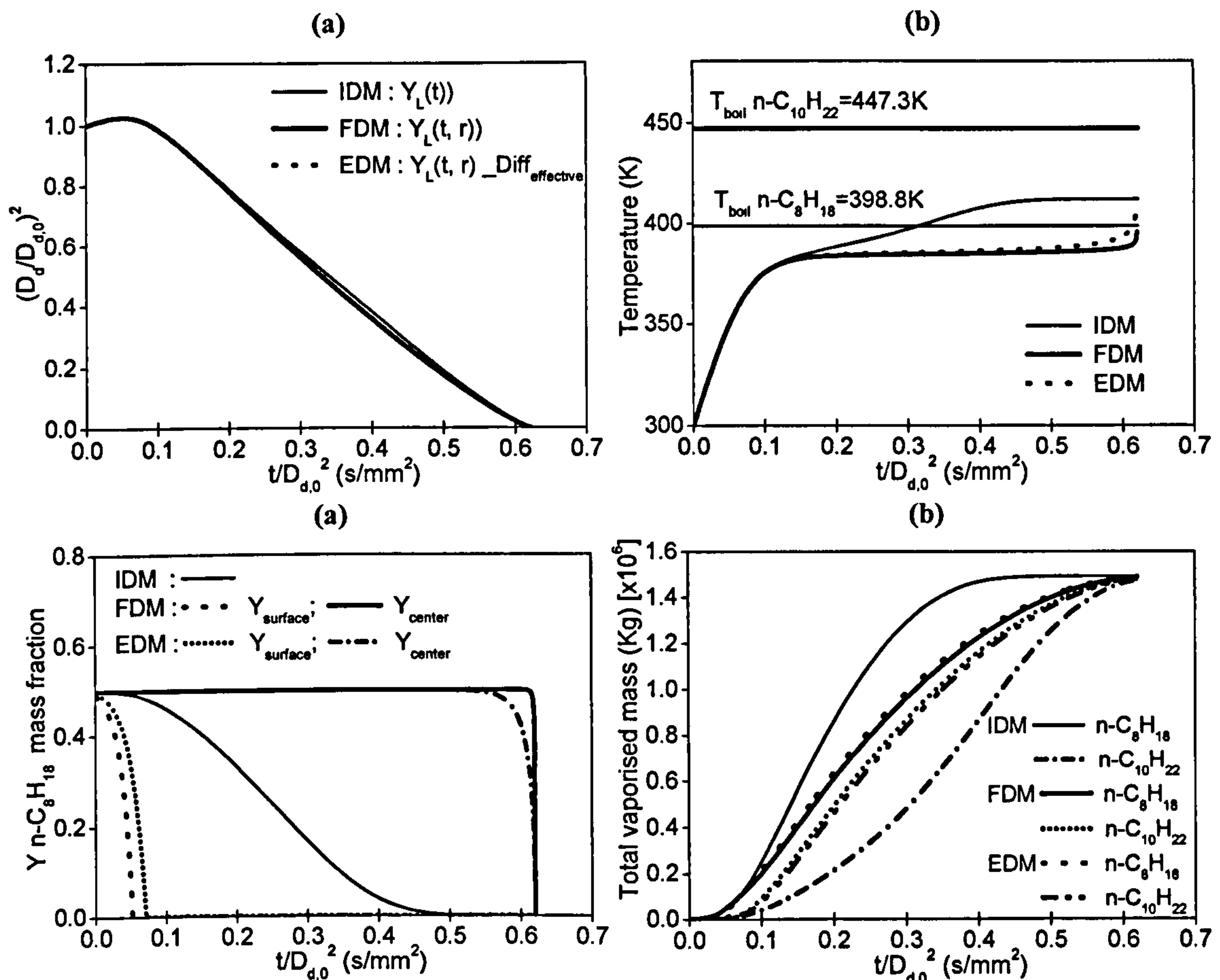


Figure 4-33: n-decane (a) droplet surface area regression, (b) mean temperature, (c) n-octane liquid concentration and (d) n-octane/n-decane total vaporized mass profiles, predicted by the 'infinite diffusivity model', IDM, the 'finite diffusivity model', FDM, and the 'effective diffusivity model', EDM; initial fuel composition 50%n-octane-50%n-decane,  $T_G=1000\text{K}$ ,  $P_G=1\text{bar}$ ,  $D_{d,0}=2\text{mm}$ ,  $T_{d,0}=300\text{K}$ ,  $\text{Re}=110$ .

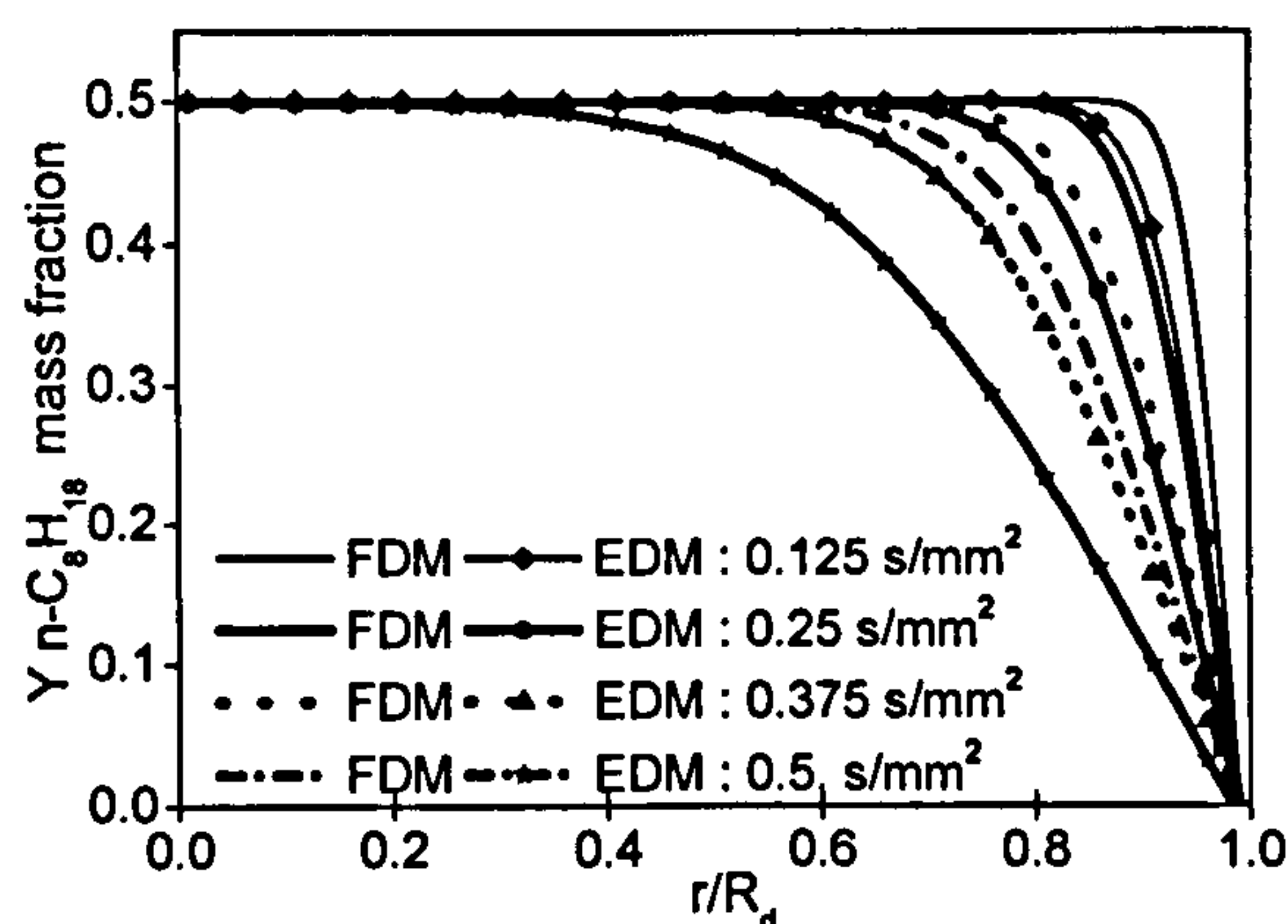
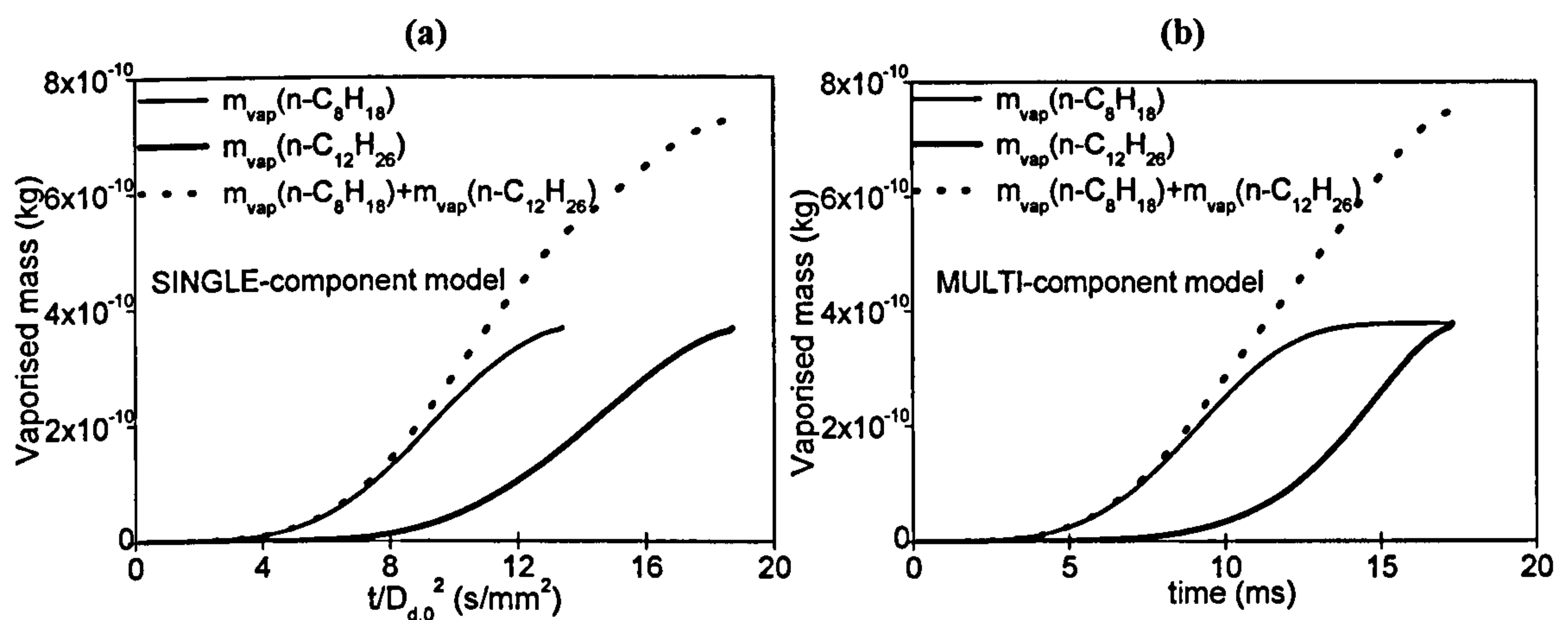


Figure 4-34: n-octane liquid phase spatial concentration distributions at four time steps after start of injection predicted by the 'finite diffusivity model', FDM, and the 'effective diffusivity model', EDM; initial fuel composition 50%n-octane-50%n-decane,  $T_G=1000\text{K}$ ,  $P_G=1\text{bar}$ ,  $D_{d,0}=2\text{mm}$ ,  $T_{d,0}=300\text{K}$ ,  $\text{Re}=110$ .

The vapourisation models assume either single-component fuels or more realistic mixtures of different species. The effect of the different hypothesis on the nature of the fuel composition has been discussed, modelling the evaporation process of a fixed



amount of two fuels, assuming first no-interaction between the two species and then assuming uniform mixing conditions. Single-component model predicts the first case, while the multi-component model analyses the second case assuming uniform liquid phase temperature and concentration distributions. The vaporised fuel masses are doubled, for a correct comparison with the first case. The results are shown in Figure 4-35 in terms of the total vaporised masses, suggesting that the single-component model, assuming not interaction between the species, predicts faster vaporisation of the lighter component, although the droplet lifetime increases up to 8% compared to the multi-component model results, due to the neglected interaction between the two species.



**Figure 4-35: n-octane/n-dodecane vaporised mass profiles, assuming not interaction (a) and uniform mixing (b) between the two species;  $T_{\text{back}}=1000\text{K}$ ,  $P_{\text{back}}=5\text{bar}$ ,  $m_0(\text{C}_8\text{H}_{18}/\text{C}_{12}\text{H}_{26})=3.65\text{E}-5\text{Kg}$ ,  $T_{d,0}=300\text{K}$ ,  $\text{Re}=0$ .**

Figure 4-36 shows the prediction of the droplet lifetime for single and multi-component mixture under the operating conditions described in Table 4-III, assuming uniform temperature inside the droplet and high-pressure effect at the liquid-gas interface. The single component fuel is represented by n-octane, while the multi-component fuel by a mixture of 20% of lighter n-hexane, 30% by heavier n-decane and the remaining 50% by n-octane. The results show that the multi-component effects are evident particularly at low pressure and temperature conditions, when the less volatile species dramatically reduced the droplet vaporisation and increases its lifetime. As pressure and temperature increase, the vaporisation time of single- and multi-component fuels differs of about 30%.

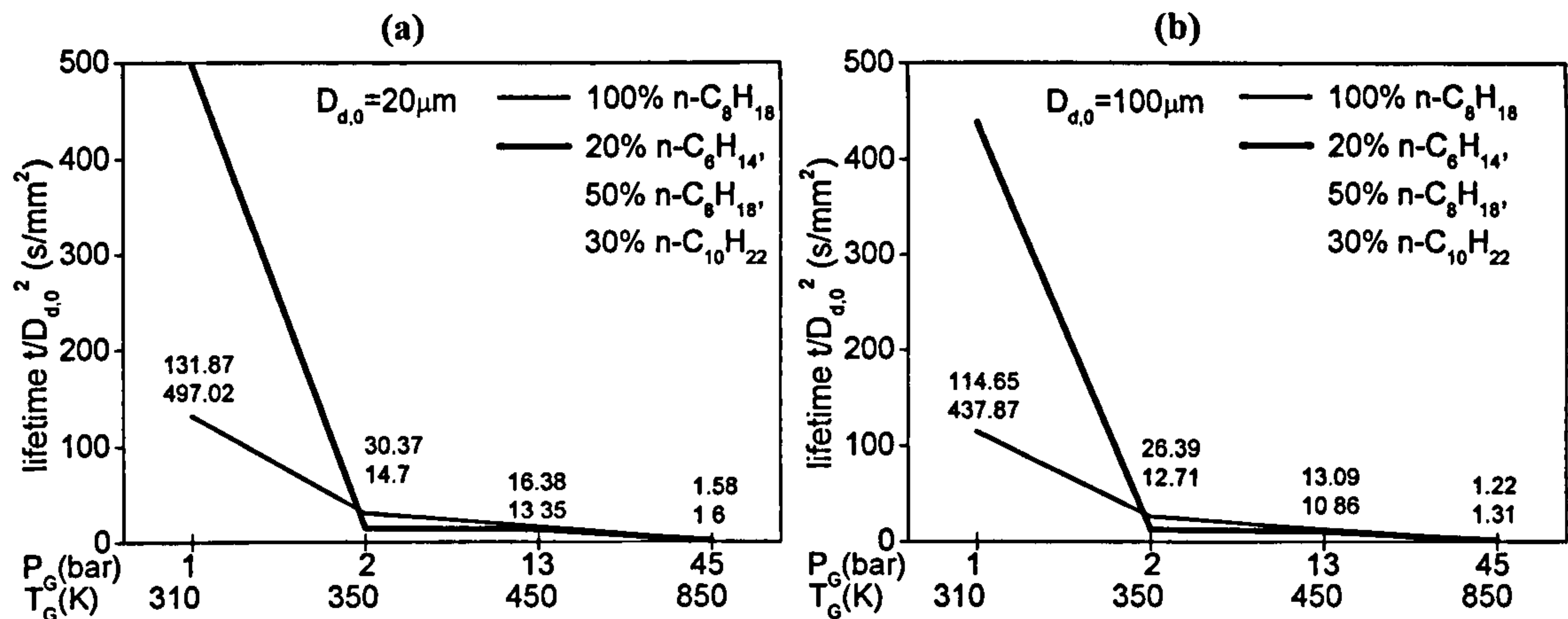


Figure 4-36: Effect of fuel composition on the predicted droplet life time under different back conditions, for (a) 20mm and (b) 100mm droplet. n-octane,  $T_{d,0}=300$  K,  $\Delta U_0=100$ m/s, uniform liquid temperature distribution, and HPM to solve the liquid-gas interface equilibrium.

The following investigations focus on the validation of the vaporisation models considering multi-component and high-pressure effect. As concluded by previous investigations, the type of the liquid temperature and concentration distributions doesn't have considerably influence on the droplet temporal evolutions, and uniform profiles are assumed. The results are presented in terms of droplet diameter and velocity profiles over the vaporisation distance. Figure 4-37 to Figure 4-41 show the comparison among the experimental data found in Stengele et al. [109] and the predictions from the models assuming ideal equilibrium conditions (LPEqM) and high-pressure effect at the liquid/gas interface (HPM). The first one predicts the molar fraction of the vaporising species at the liquid/gas interface using the Clausius-Clapeyron equation with the Raoult's law in case of multi-component mixtures, while the high-pressure model implements an equation of state to calculate the liquid/gas concentrations at the droplet surface, the fugacity coefficients and the enthalpy of vaporisation. The vaporisation phenomena of a free falling droplet have been investigated focusing on the effect of droplet initial composition (different pentane-nonane concentrations), size ( $D_{d,0}=0.63$ - $0.82$ mm), temperature ( $T_{d,0}=370$ - $400$ K), velocity ( $V_{d,0}=0.45$ - $0.6$ m/s), gas pressure ( $P_G=20/30/40$ bar) and temperature ( $T_G=550$ - $650$ K). Figure 4-37 and Figure 4-38 present the gas pressure effect on the droplet size and velocity, respectively, predicted by the 'low pressure ideal equilibrium model', LPEqM, and by the 'high pressure model, HPM, revealing that the first one remarkably over-predicts the droplet lifetime since it simulates low vaporisation rate when the droplet has reached higher temperature estimating higher latent heat of vaporisation. As a consequence, the assumption of high pressure effect is chosen for the following validation cases.



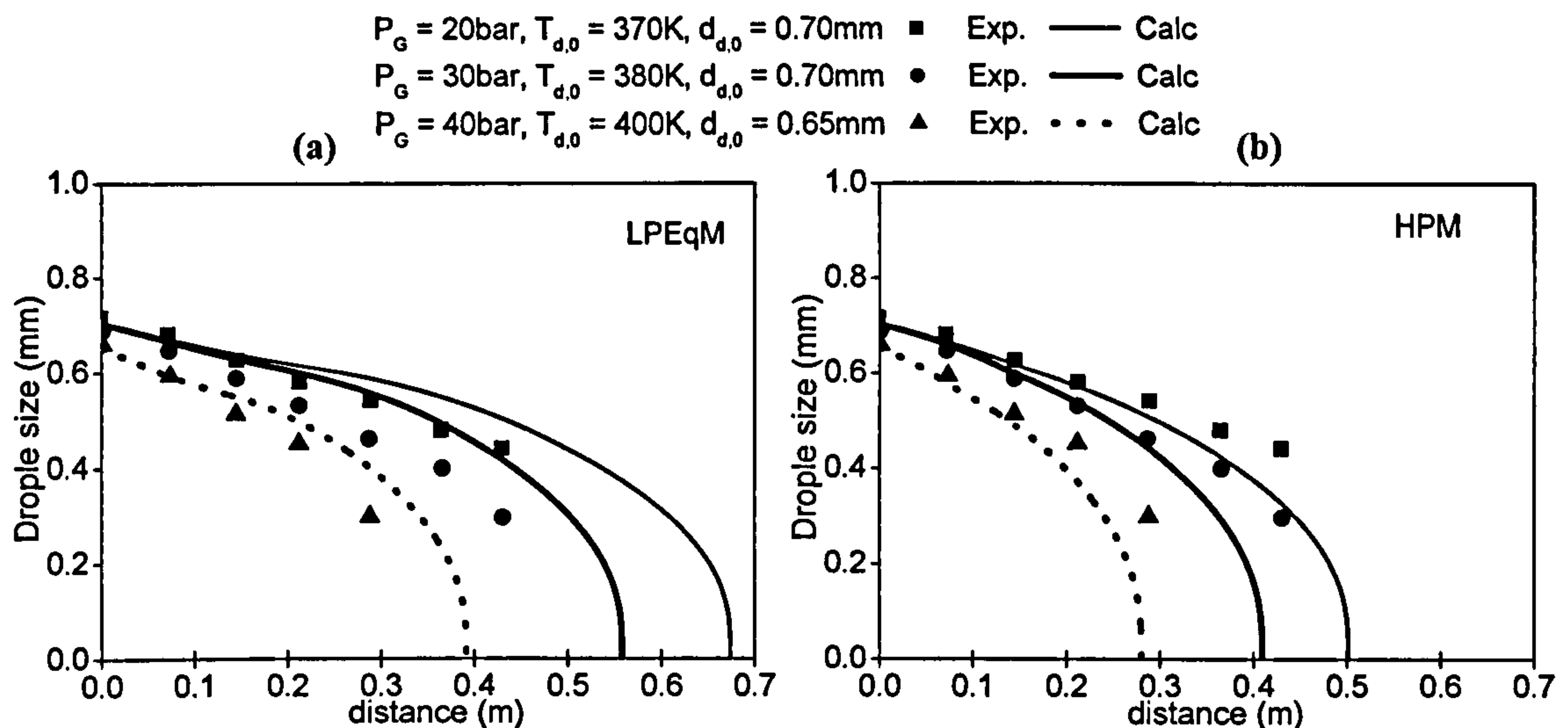


Figure 4-37: Gas pressure effect on the droplet diameter profile over the evaporation distance for two-components fuel droplet predicted by the multi-component model considering (a) ideal equilibrium conditions (LPEqM) and (b) high-pressure effect (HPM) at the liquid/gas interface; the experimental results are from Stengele et al. [109] and the operating conditions are:  $P_G=20/30/40\text{bar}$ ,  $T_G=550\text{K}$ , fuel initial composition 30% pentane and 70% nonane,  $D_{d,0}=0.7/0.65\text{mm}$ ,  $T_{d,0}=370/380/400\text{K}$ ,  $\Delta U_0=0.5\text{m/s}$ .

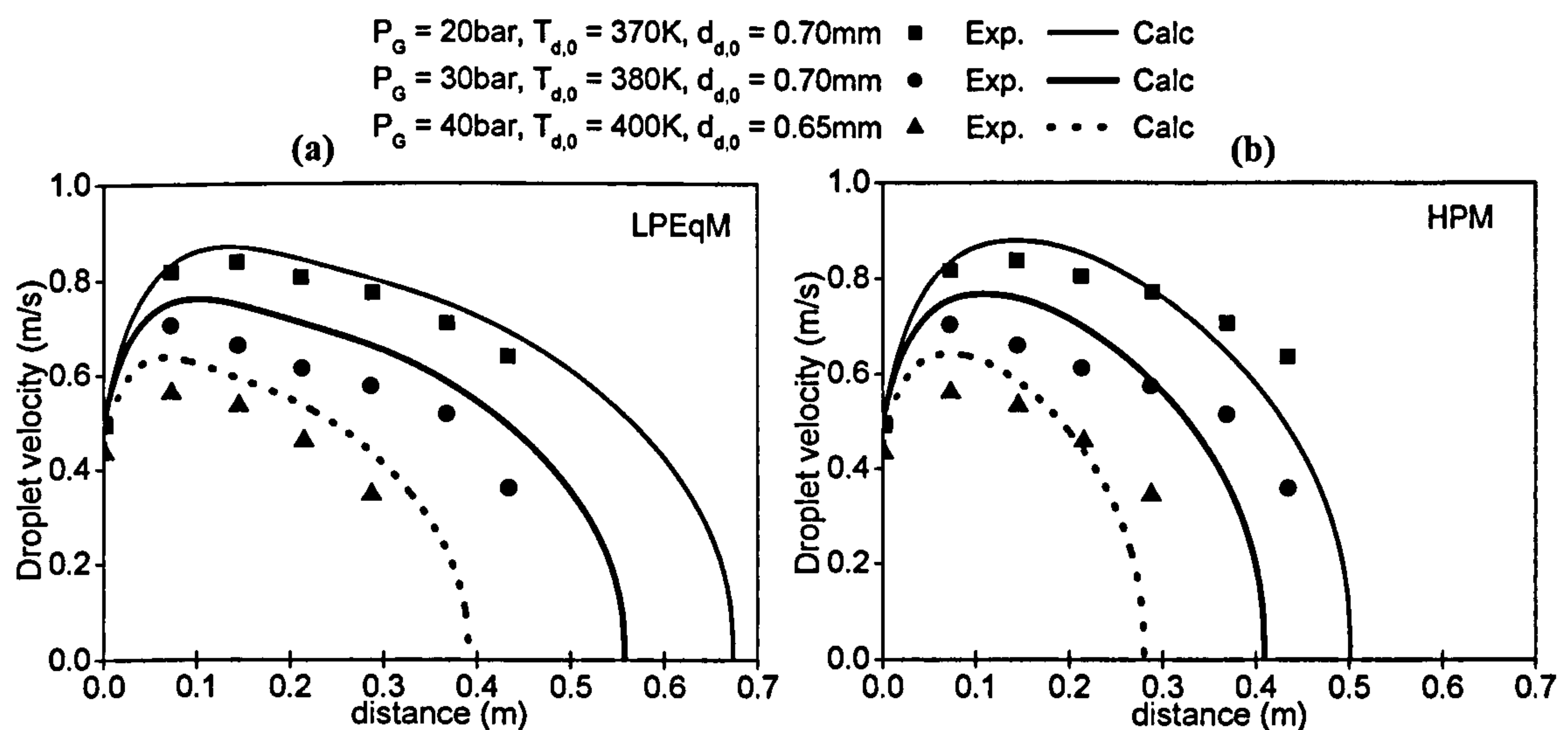


Figure 4-38: Gas pressure effect on the droplet velocity profile over the evaporation distance for two-components fuel droplet predicted by the multi-component model considering (a) ideal equilibrium conditions (LPEqM) and (b) high-pressure effect (HPM) at the liquid/gas interface; the experimental results are from Stengele et al. [109] and the operating conditions are:  $P_G=20/30/40\text{bar}$ ,  $T_G=550\text{K}$ , fuel initial composition 30% pentane and 70% nonane,  $D_{d,0}=0.7/0.65\text{mm}$ ,  $T_{d,0}=370/380/400\text{K}$ ,  $\Delta U_0=0.5\text{m/s}$ .

Figure 4-39 presents the gas temperature influence and Figure 4-40 the initial droplet size effect on the droplet size and velocity profiles over the vaporisation distance, showing a good agreement with the experimental data.

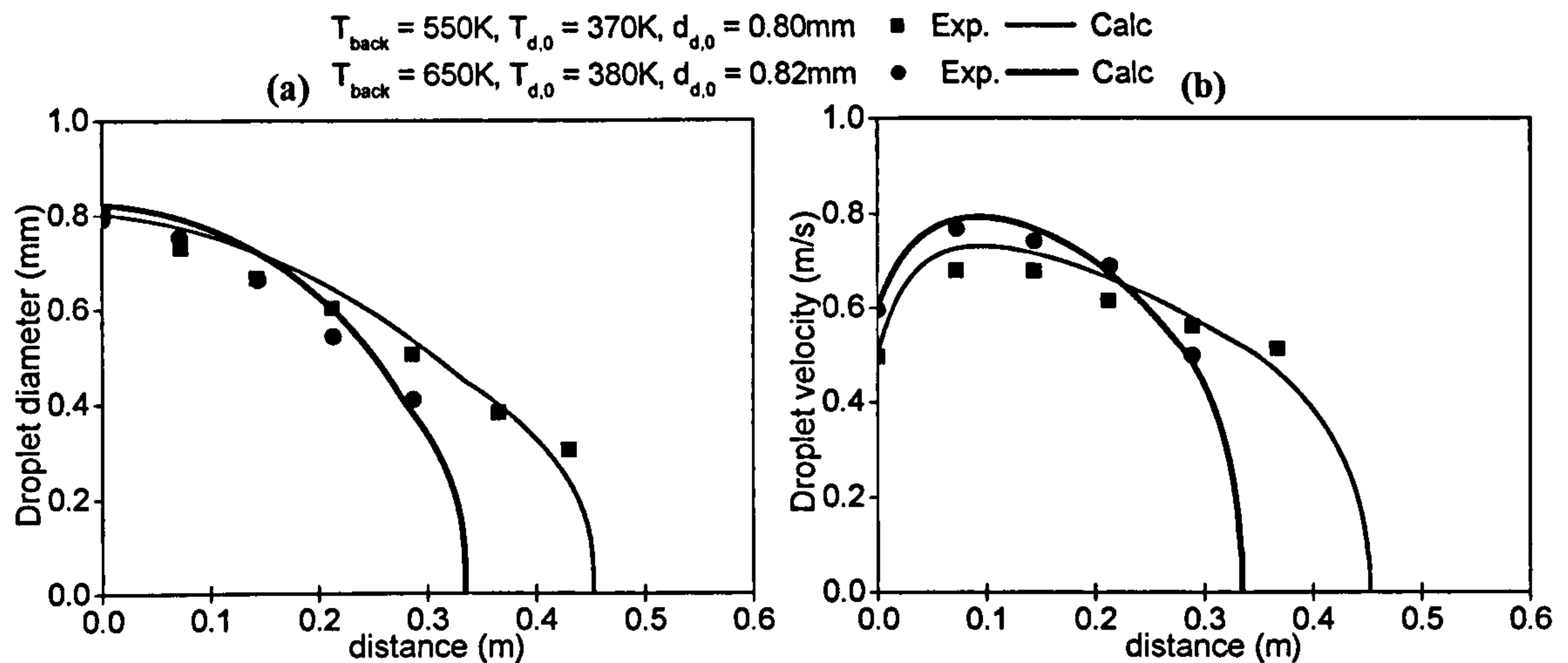


Figure 4-39: Gas temperature effect on the droplet (a) diameter and (b) velocity profiles over the evaporation distance for two-components fuel droplet predicted by the multi-component model considering high-pressure effect (HPM) at the liquid/gas interface; the experimental results are from Stengele et al. [109] and the operating conditions are:  $P_G=30bar$ ,  $T_G=550/650K$ , fuel initial composition 70% pentane and 30% nonane,  $D_{d,0}=0.8/0.82mm$ ,  $T_{d,0}=370/380K$ ,  $\Delta U_0=0.5m/s$ .

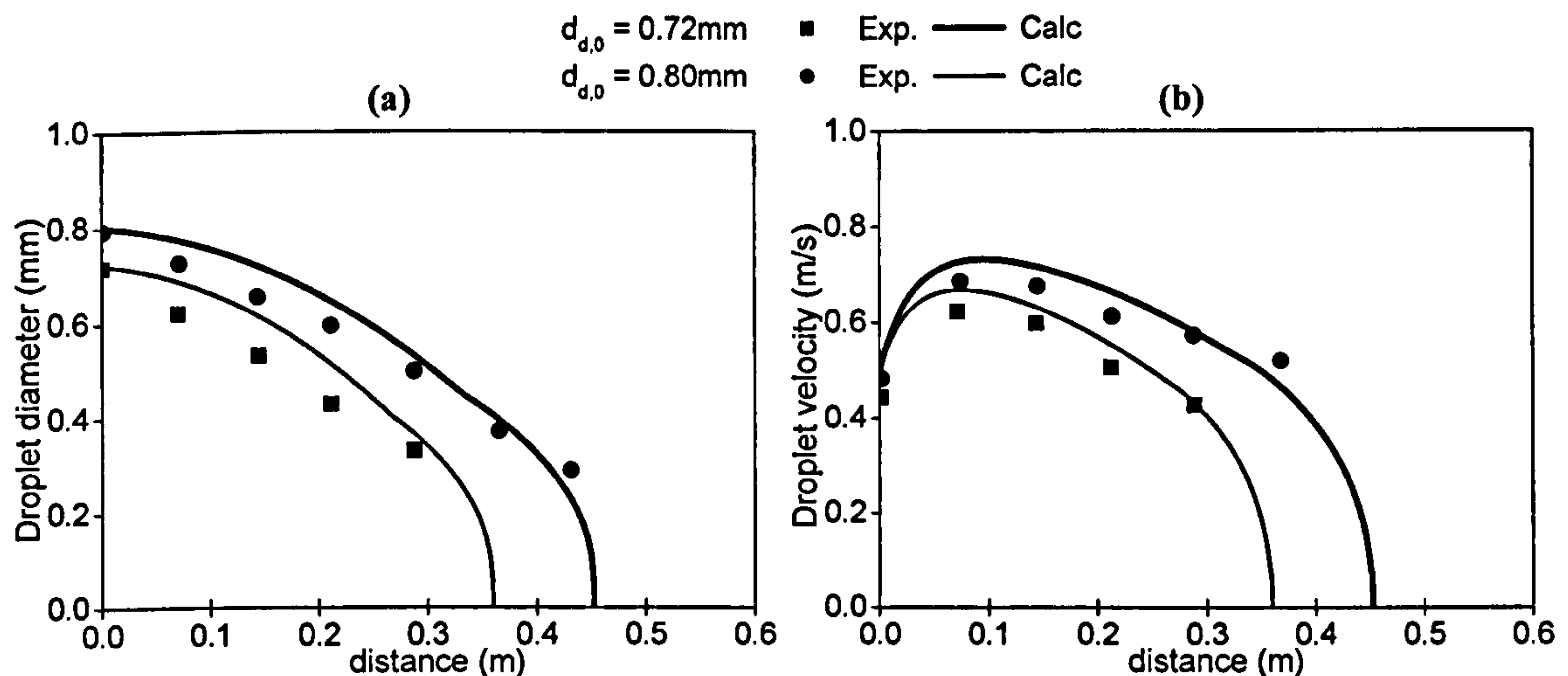
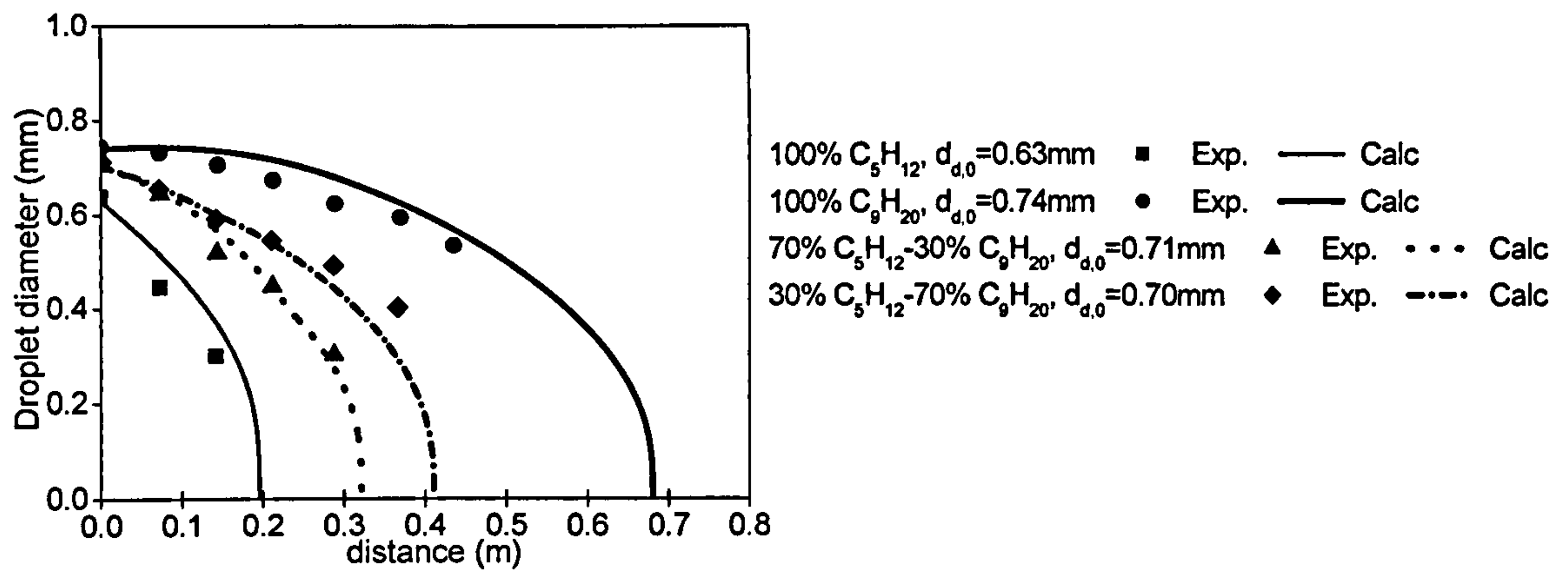


Figure 4-40: Initial droplet size effect on the droplet (a) diameter and (b) velocity profiles over the evaporation distance for two-components fuel droplet predicted by the multi-component model considering high-pressure effect (HPM) at the liquid/gas interface; the experimental results are from Stengele et al. [109] and the operating conditions are:  $P_G=30bar$ ,  $T_G=550K$ , fuel initial composition 70% pentane and 30% nonane,  $D_{d,0}=0.72/0.80mm$ ,  $T_{d,0}=370K$ ,  $\Delta U_0=0.5m/s$ .

Finally, Figure 4-41 presents the droplet size evolution for different initial liquid concentration of n-pentane/n-nonane fuel droplet revealing the preferably batch distillation type followed by the vaporisation phenomenon.





**Figure 4-41: Fuel composition effect on the droplet diameter profiles over the evaporation distance for single and two-components fuel droplets predicted by the multi-component model considering high-pressure effect (HPM) at the liquid/gas interface; the experimental results are from Stengele et al. [109] and the operating conditions are:  $P_G=30\text{bar}$ ,  $T_G=550\text{K}$ ,  $D_{d,0}=0.63/0.70/0.71/0.74\text{mm}$ ,  $T_{d,0}=380\text{K}$ ,  $\Delta U_0=0.5\text{m/s}$ .**

#### 4.4 Conclusions

This chapter focuses on the discussion of single-droplet vaporisation modelling, investigating a wide range of operating conditions and model assumptions. The results illustrate the sensitivity of vaporisation predictions on liquid temperature distribution model, internal liquid circulation due to the relative motion between the two phases, equilibrium conditions at the interface, solubility of the gases in the liquid phase, pressure-temperature-composition dependent physical properties correlation and fuel composition. The different models proposed have been validated against an extensive data-base of experimental measurements, showing a reasonable good agreement among predictions and experiments. The results confirm that ideal equilibrium assumption is valid only under sub-critical vaporisation conditions, while pressure effect should be considered at high pressure and temperature environments. Moreover detailed spatial distribution of liquid temperature and species concentrations adds significant information only in case of large droplets under moderately high evaporating rate conditions. Finally, investigations on the vaporisation behaviour of multi-component fuels under a wide range of operating environment reveal that the process preferably follows the batch-type behaviour, with lighter components vaporising first and less volatile components determining the droplet lifetime.

# Chapter 5

All truths are easy to understand once they are discovered;  
the point is to discover them.

Galileo Galilei

## VALIDATION & NUMERICAL INVESTIGATION OF DIESEL SPRAY MODELLING

### 5.1 Introduction

In this chapter the discussion focuses on numerical investigation and experimental validation of the diesel spray CFD model described in Chapter 3. Predictions are extensively validated against experimental data, which have included spray tip penetration, spray CCD images and PDA measurements obtained for single- and multi-hole nozzle designs and a wide range of operating conditions. First the spray velocity and size, predicted by the CFD model have been validated against the experimental measurements of Chang [214], Cutter [215] and Choi [216] for two types of multi-hole nozzles under non-evaporating and moderate evaporating conditions. Successively, the experimental data obtained as part of the I-LEVEL EU project by König et al. [217] for the liquid and vapour penetration are used to assess the physical and numerical effect of the various spray sub-models, for cavitating and non-cavitating nozzles under non-evaporating and evaporating conditions. Finally, the calibrated model is validated against the data base of Siebers [218] for single-hole injectors under a variety of injection pressures, back pressures and temperatures, injection hole diameters and fuel initial temperatures and composition. Many of the fundamental physical processes assumed to take place during the spray development are incorporated in the model. These include link with the internal nozzle flow conditions, fuel atomisation, liquid droplet aerodynamic break-up, turbulent dispersion and liquid droplet vaporisation. The liquid initial properties are determined by solving for the flow conditions inside and at the exit of the injector nozzle. The cavitating nozzle flow model of Giannadakis [148] is used to estimate the injection velocity of the liquid while its effect on the spray formation is considered through specific atomisation models. These predict the initial droplet size and velocity, assuming turbulence-induced or cavitation-induced atomisation for liquid ligaments exiting from non-cavitating or cavitating nozzle hole,



respectively. Different droplet break-up and droplet aerodynamic drag models are used to assess the predicted results. In particular, the increased surface area of the droplets associated with their fragmentation process is found to play a major role on the exchange of heat and mass between the evaporating liquid and the surrounding air. Various vaporisation models have been tested, including high-pressure and non-equilibrium effects. This has allowed for calculation of liquid penetration length independent of the injection pressure. The numerical methodology introduced in order to estimate the source terms expressing the mass, momentum and energy exchange between the liquid and the gas phases and the interpolation of the continuous phase variables at the parcel location is assessed. This is based on the assumption that the region of influence between the two phases should be independent of the cell size, as it is done in the majority of the commercial CFD codes, and it is defined according to specific physical criteria. The cells found within this region of interest are identified while a combination of distance, cell volume and internal energy-based weighting factor is used for the distribution of the source terms to those cells. Additionally, local grid refinement at the area where the spray evolves allows the use of Eulerian grids with cell size comparable to that of the droplets. Figure 5-1 shows the 2-D axis-symmetric computational domains used in all the simulations presented, except otherwise specified.

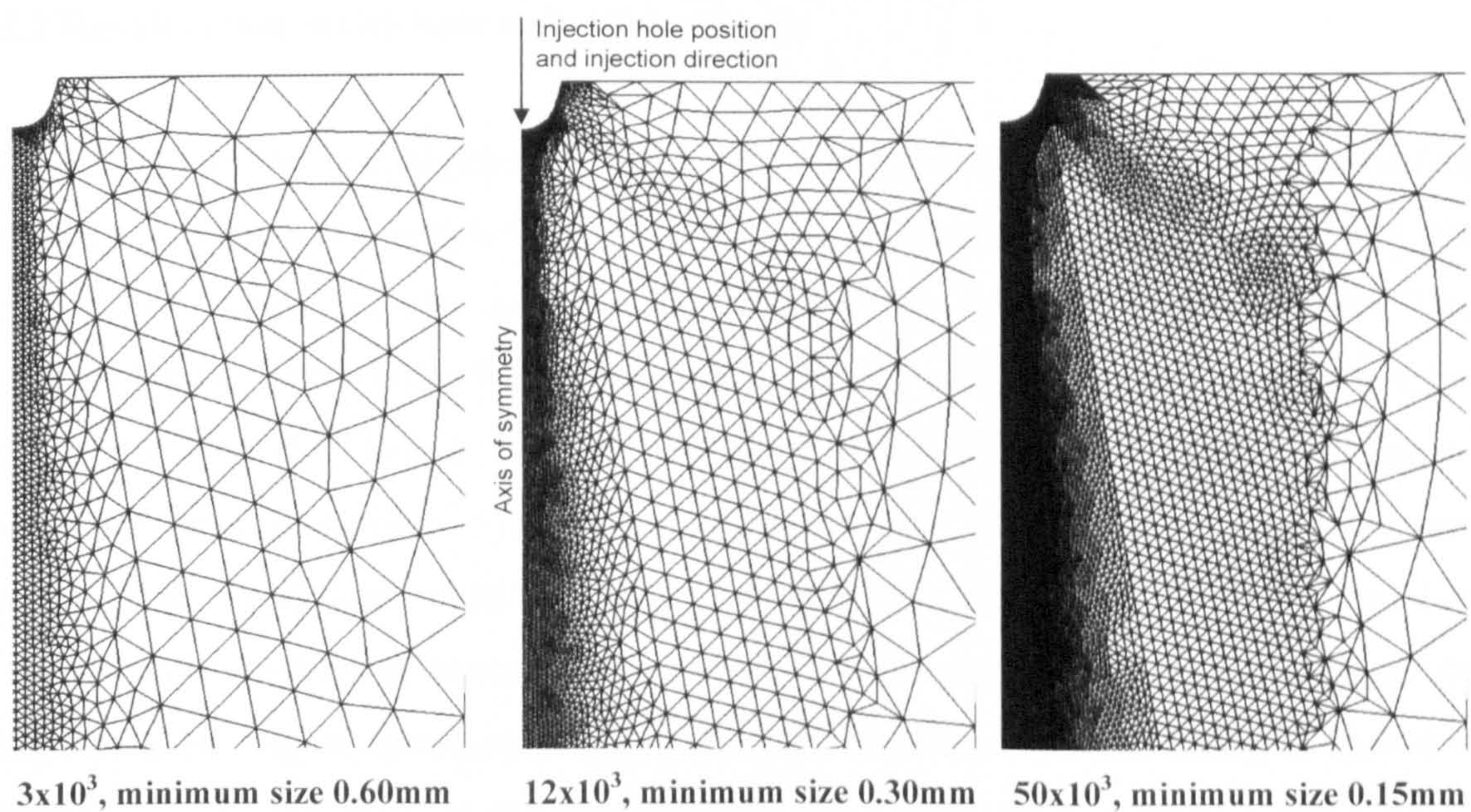


**Figure 5-1:** Sub-domain of the computational grids used, 2D-s1, 2D-s2 and 2D-s3. The minimum cell length on the axial direction is also indicated.



The coarse one is comprised by 3,000 cells and has a minimum cell spacing of 0.6mm in the direction of fuel injection. The fine one is comprised by 50,000 cells and has a minimum cell size of 0.15mm. This cell size was considered small enough to demonstrate the ability of the developed model to couple the Lagrangian spray model with the Eulerian flow solver at fine meshes, where the local void fraction may take values close to zero. The time step used for the Lagrangian tracking of the liquid droplets was  $0.5 \times 10^{-6}$ s, while the time step for the Eulerian gas phase solver was approximately  $2.0 \times 10^{-5}$ s. For simulating the time step of the evaporation process, an adaptive time step has been used, defined by the local liquid droplets properties and the specific cell size containing it at every time step, as described in section 4.2.1. This methodology has allowed for grid-independent interaction between the Eulerian and the Lagrangian phases to be reached.

The specific contribution of physical and numerical parameters to the computational results is extensively discussed in sections 5.3.4 and 5.3.5, with the scope to determine the role of each sub-model in the prediction of high-pressure diesel sprays injected in high-density environments at room and high back temperatures. Then, the assessed model has provided a practical and encouraging tool to estimate the spray characteristics under a variety of operating conditions.

## 5.2 Results from multi-hole cavitating nozzles

In this section the investigation of the spray characteristics from multi-hole cavitating nozzles is presented through the CFD modelling validation for the spray velocity and size against phase Doppler anemometry measurements and CCD spray images. Two different multi-hole nozzles have been used for model validation, a sac-type and a valve covered orifice (VCO) one. Both nozzles have a sharp inlet and cylindrical holes, so they are both cavitating. Free spray injection takes place either under quiescent atmospheric conditions or in a constant volume high pressure/temperature chamber. Those types of nozzle geometries have their main difference in the way they seal off the high pressure region upstream of the needle seat from the injection holes, as shown in Figure 5-2. In the case of the conical mini-sac nozzle there is only a line contact between the needle and the needle seat, which causes a relatively large amount of fuel to remain in the 'dead volume' of the nozzle tip after the end of injection. In the VCO



nozzle there is virtually no sac volume left to be filled with fuel, since the needle is in surface contact with the needle seat and covers the injection holes completely.

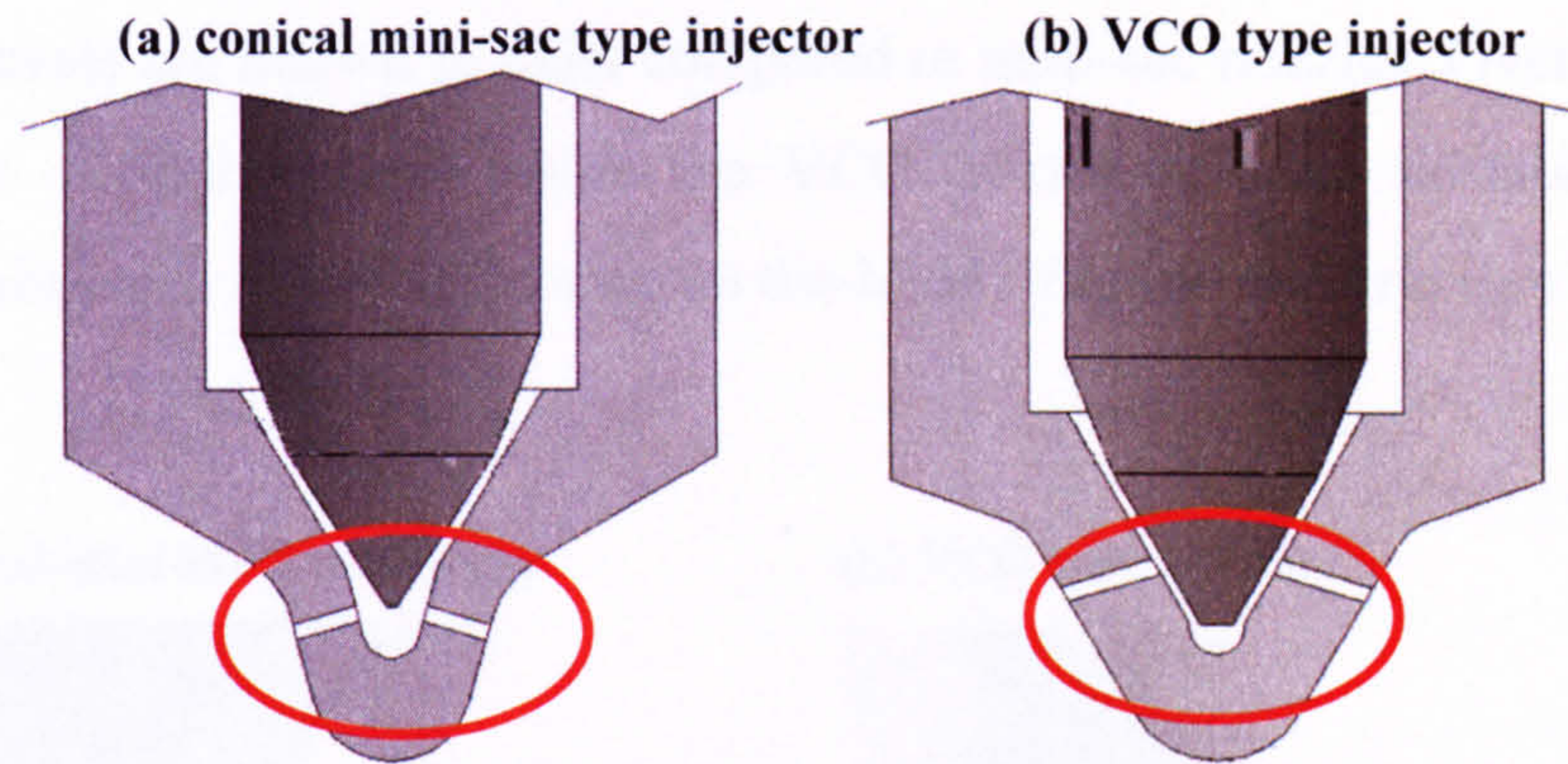


**Figure 5-2: Tip geometry of (a) the conical mini-sac type and (b) VCO type injectors [219].**

The internal nozzle flow in those multi-hole nozzles has been found to be rather complicated. Figure 5-3 shows two examples of the internal flow structure inside the sac volume and the injection hole of the conical mini-sac type multi-hole nozzle and the VCO nozzle at 300 $\mu$ m needle lift, predicted using the two-phase cavitating model of Giannadakis [148]. The model predicts that inside the mini-sac type multi-hole nozzle different cavitation regimes occur. Initially, the so-called incipient cavitation regime is realised, mainly consisting of dispersed bubbles formed at the low-pressure region present to the entrance of the injection holes. With increasing cavitation number, the bubbles become larger and more vapour volume is formed inside the hole; for fully developed cavitating flow regime, the highest amount of vapour is attached to the top of the hole while it diffuses towards the exit, as shown in Figure 5-3(a). At the same time, the predictions show a double-vortex structure formed on the upper part of the hole. These vortices originate from the hole inlet and may extend up to the hole exit. The streamlines inside the sac volume suggest that the flow entering into the sac volume is forced to turn sharply inside the sac volume, reverse its direction and enter into the injection hole from the bottom side of the hole-entrance. As a result, the flow inside the sac volume is always rotating and highly unsteady, as model predictions have confirmed [220]. Moreover, Figure 5-3(b) shows that, as the flow enters into the dead volume below the needle of the VCO nozzle, it forms two counter-rotating structures. One of them is constantly rotating without contributing to the flow entering into the injection hole, while the other one turns upwards and enters into the injection hole from its lower part. The main cavitation area is formed at the hole top inlet, where representative



cavitating bubbles used to simulate the cavitating flow are plotted. The volume fraction distribution at the hole exit exhibits a non-uniform profile leaving a space with less cavitation at the hole centre. According to Roth et al. [219] in VCO nozzles higher turbulence levels are known to exist compared to mini-sac nozzles. Overall, it is fair to say that the cavitating flow inside the VCO nozzle is more unstable, due to the increased turbulence levels, reflecting on the highly fluctuating structure of the injected sprays.

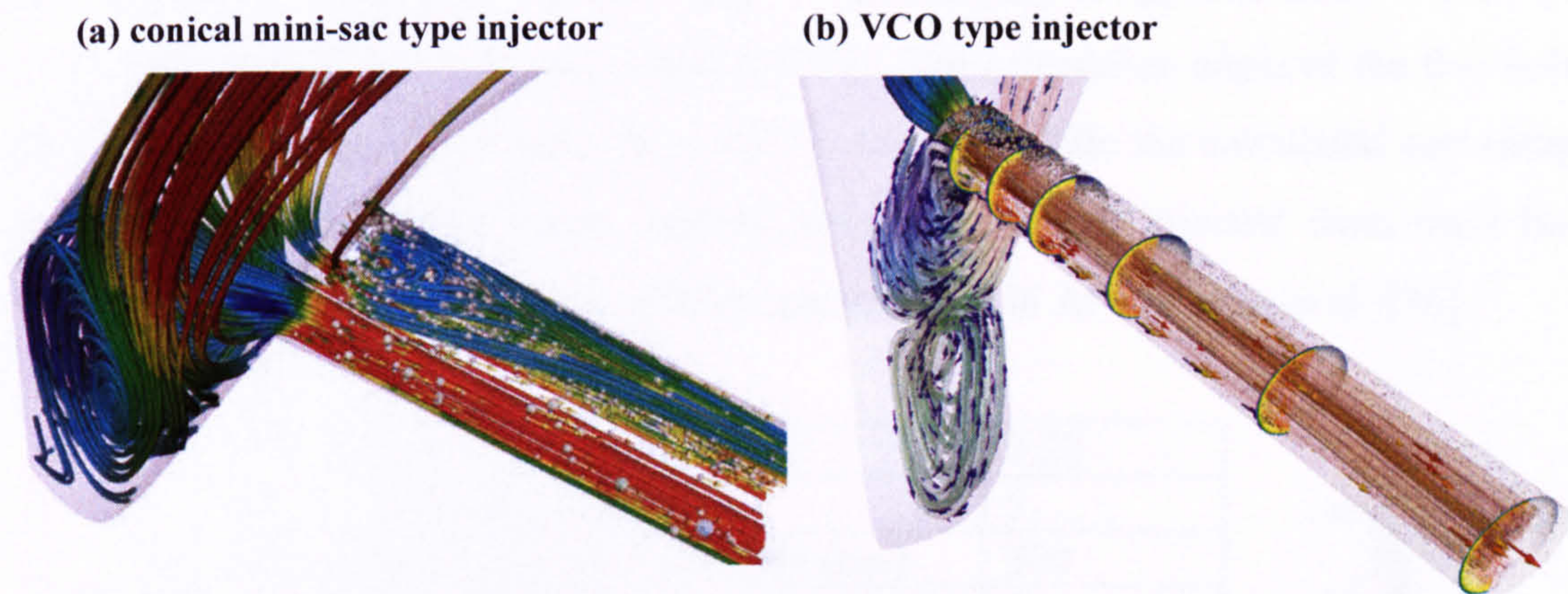


**Figure 5-3: Predicted internal nozzle flow structure for (a) the sac volume and the injection hole of a conical mini-sac type 6-hole nozzle and for (b) the 6-hole VCO nozzle operating at 1200bar at 350 $\mu$ m needle lift, as predicted using the two-phase cavitating model of Giannadakis [148].**

In the next section of this chapter a brief description of the test cases investigated is given, focusing on the injection characteristics as identified from the internal nozzle flow modelling, performed by other members of the research group [4, 76, 148]. Then the spray modelling validation against experimental measurements and the sensitivity of the spray characteristics on the computational grid are presented and discussed.

### 5.2.1 Overview of the test cases

Free spray injected under atmospheric quiescent conditions from the sac-type 5-hole nozzle.

For injection under atmospheric conditions, the fuel injection system used consists of a Bosh VE distributor-type pump, connected to Stanadyne pencil-type nozzles (5X0.22mm in hole diameter). The injection conditions (flow rate per injection hole for inclined multiple injectors, effective hole area, hole turbulent kinetic energy and its dissipation rate, volume of cavitation bubbles) are the inputs required by the fuel



injection simulation model developed by Arcoumanis et al. [76]. Extensive experimental investigation has been reported on the characteristics of free sprays injected in either quiescent or cross flowing air environment under atmospheric conditions with this fuel injection equipment. Experiments at Imperial College [214, 215] provided information about the temporal and spatial droplet velocity and size distributions, obtained with a phase Doppler anemometer (PDA). Comparison between computational and experimental results is presented for injection conditions corresponding to a pump speed of 600rpm. The fuelling is approximately 4 mm<sup>3</sup> per hole, while the injection duration is about 0.8ms. The orientation angle of the five holes relative to the needle seat ranges from 63° up to 101°, while the calculated percentage difference from the above mean fuelling value of the fuel injected from each hole ranges from -9% up to +4%. More details can be found in Arcoumanis et al. [76].

Orifice diameter (mm)	0.22
Number of holes	5
Peak injection pressure (bar)	300
Fuel delivery (mm <sup>3</sup> /injection)	20
Chamber pressure (bar)	1
Chamber temperature (K)	300
T <sub>fluid</sub> (K)	300
Fuel	n-C <sub>12</sub> H <sub>26</sub>

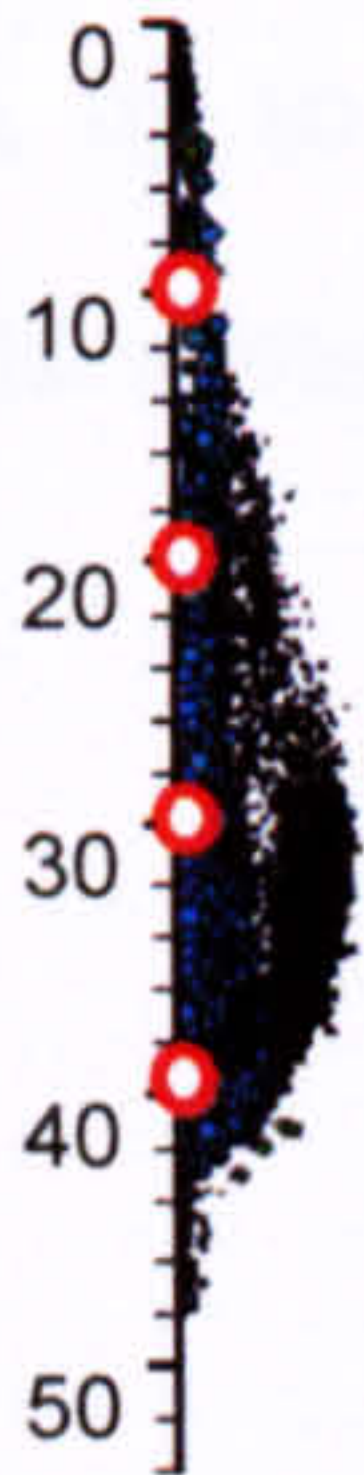


**Table 5-I: Table with operating conditions for the PLN injection system and schematic showing the PDA measurement points where droplet velocity has been obtained at 10, 20, 30 and 40mm from the nozzle hole exit on the centreline.**

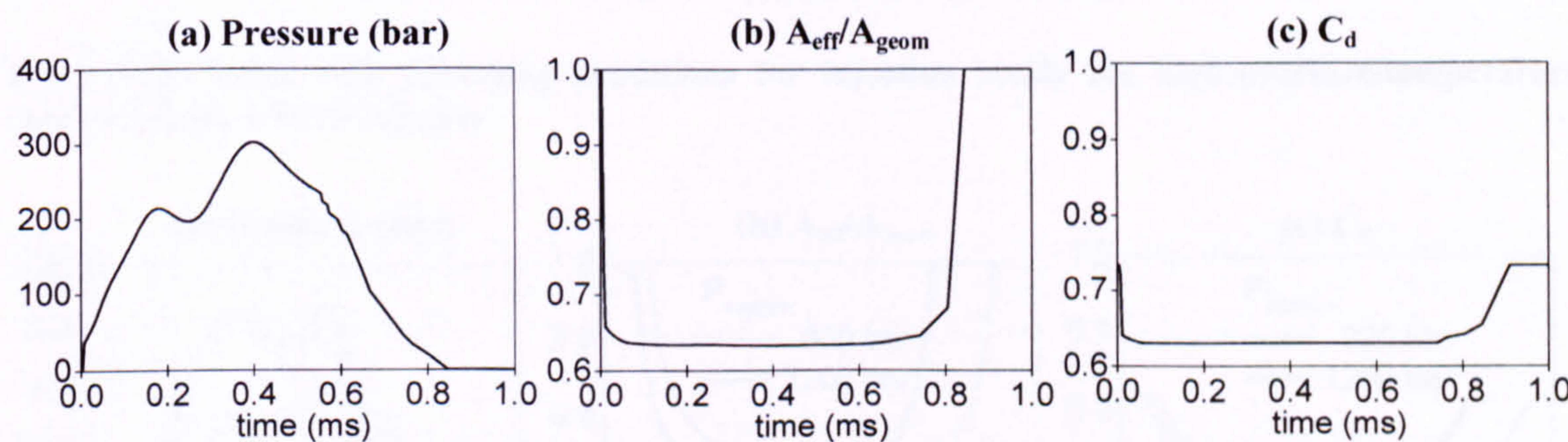


**Figure 5-4: Predicted (a) injection pressure, (b) hole exit contraction area and (c) nozzle discharge coefficient as function of the measured needle lift signal for nominal rail pressure of 300bar, for the VE distributor-type pump, connected to Stanadyne pencil-type nozzle; injection of diesel spray under atmospheric conditions.**

Here the investigation on the spray characteristics of the hole 4 is presented, which has an inclination angle of 63° and the total fuel injected from this hole differs -9% from the mean value. Table 5-I presents the operating conditions investigated and a schematic of



the PDA measurements points where droplet velocity have been obtained at 10, 20, 30 and 40mm from the nozzle hole exit on the spray centreline, while Figure 5-4 presents the temporal profiles of the injection pressure, hole exit contraction area and nozzle discharge coefficient used as injection input data in the spray model. The diesel fuel is modelled using the physical properties of n-dodecane.

#### Spray injected in high-pressure/temperature chamber from 6-hole VCO injector

The operating conditions for injection inside the high-pressure/temperature chamber from the VCO 6-hole nozzle, with orifice diameter equal to 0.172mm, are presented in Table 5-II and in Figure 5-5. The VCO injector was connected to a first-generation Bosch common-rail system operating at nominal rail pressures equal to 800 and 1200bar, while the total fuelling was 20mm<sup>3</sup> per injection. Chamber back pressure is fixed equal to 17.2bar, while the back temperature is varied from 300K up to 500K in order to reproduce non-evaporating and evaporating environments. The diesel fuel is modelled using the physical properties of n-dodecane.

Orifice diameter (mm)	0.172
Rail pressure (bar)	800/1200
Fuel delivery (mm <sup>3</sup> /injection)	20
Chamber pressure (bar)	17.2
Chamber temperature (K)	300, 500
T <sub>fluid</sub> (K)	300
Fuel	n-C <sub>12</sub> H <sub>26</sub>

**Table 5-II:** Table with operating conditions for injection inside the high-pressure/temperature chamber from a VCO injector.

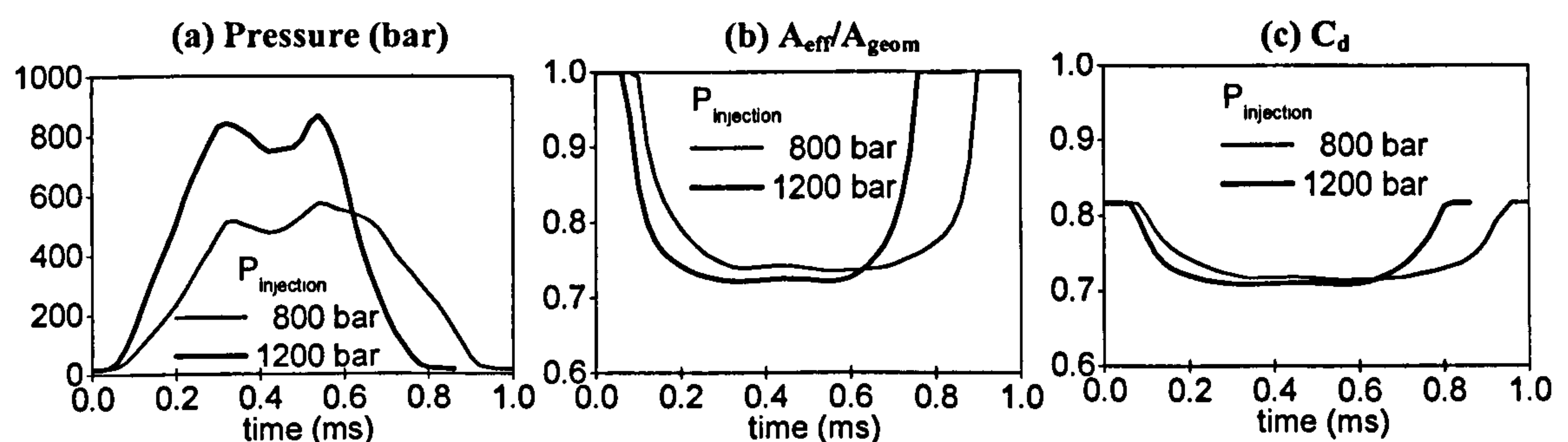


**Figure 5-5:** Predicted (a) injection (sac volume) pressure (b) hole exit effective area and (c) nozzle discharge coefficient as function of the measured needle lift signal for nominal rail pressure of 800 and 1200 bar for the 6-hole VCO nozzle.



### 5.2.2 Spray velocity and size prediction

Figure 5-6 shows the comparison between PDA measurements and model predictions for the temporal profile of droplet mean axial velocities at 10, 20, 30 and 40mm from the nozzle exit along the spray axis. The operating conditions for non-evaporating spray injected from mini-sac 5-hole nozzle under atmospheric conditions are described in Table 5-I and Figure 5-4.

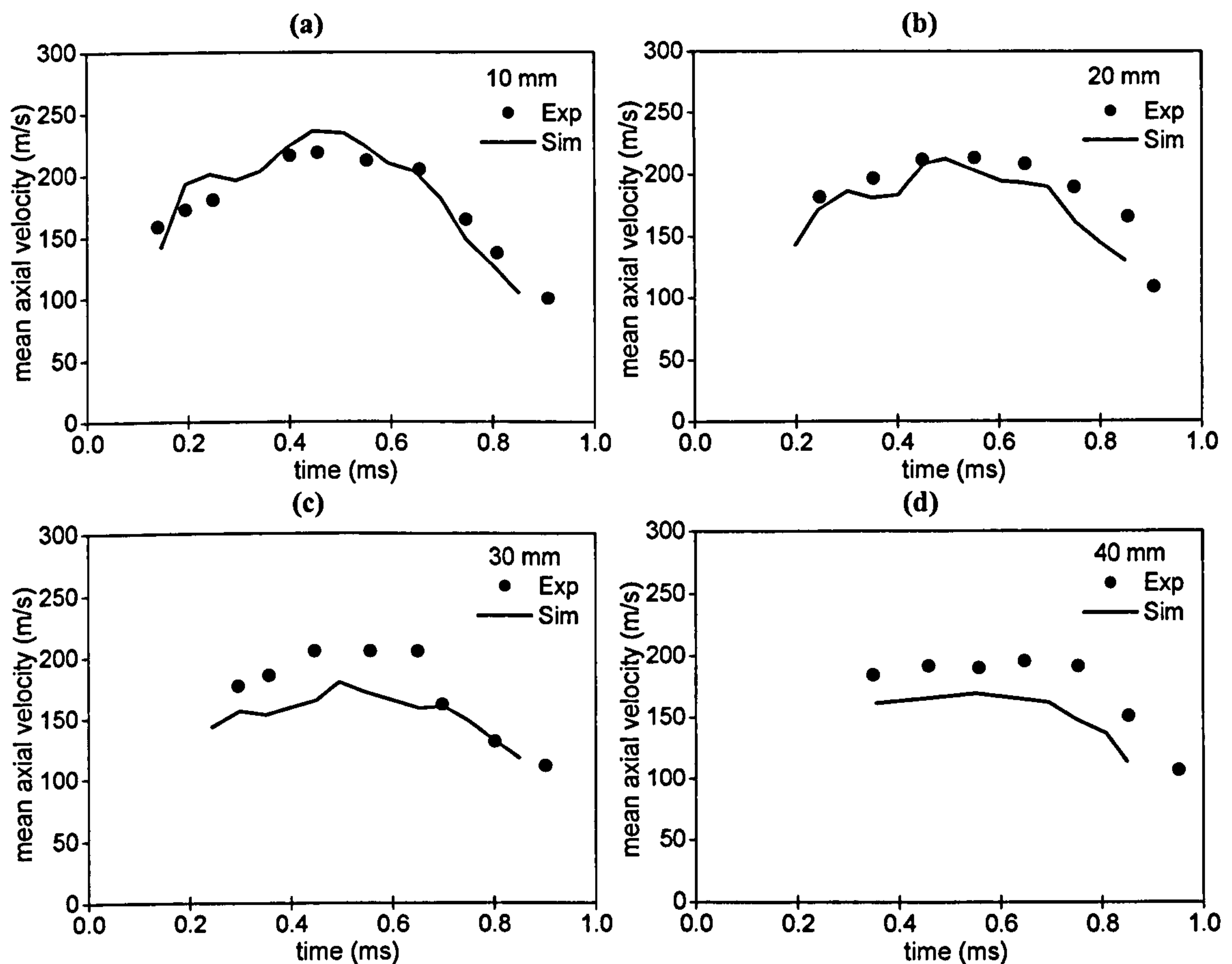


**Figure 5-6: Comparison between PDA droplet velocity measurements and model predictions using one and two levels of cell refinement at (a) 10, (b) 20, (c) 30 and (d) 40mm from the nozzle exit for non-evaporating spray under atmospheric conditions and nominal rail pressure of 300bar.**

The computational simulations have been performed using grids obtained with one levels of dynamic cell refinement in the region of spray development from the original computational domain shown in Figure 5-1. The graphs show good agreement between the experiments and the computations, revealing that the model is able to predict the experimental trend of spray velocity initially increasing up to about 0.4ms after start of injection, which coincides with the maximum injected flow rate (Figure 5-4(a)), and

then successively decreasing following an almost linear profile. The pick of velocity reduces from 250m/s down to 200m/s at increasing distance from the hole exit.

The following set of results corresponds to the investigation on the spray characteristics from the VCO-type multi-hole nozzle in a high pressure-temperature chamber, according to the operating conditions specified in Table 5-II and Figure 5-5.

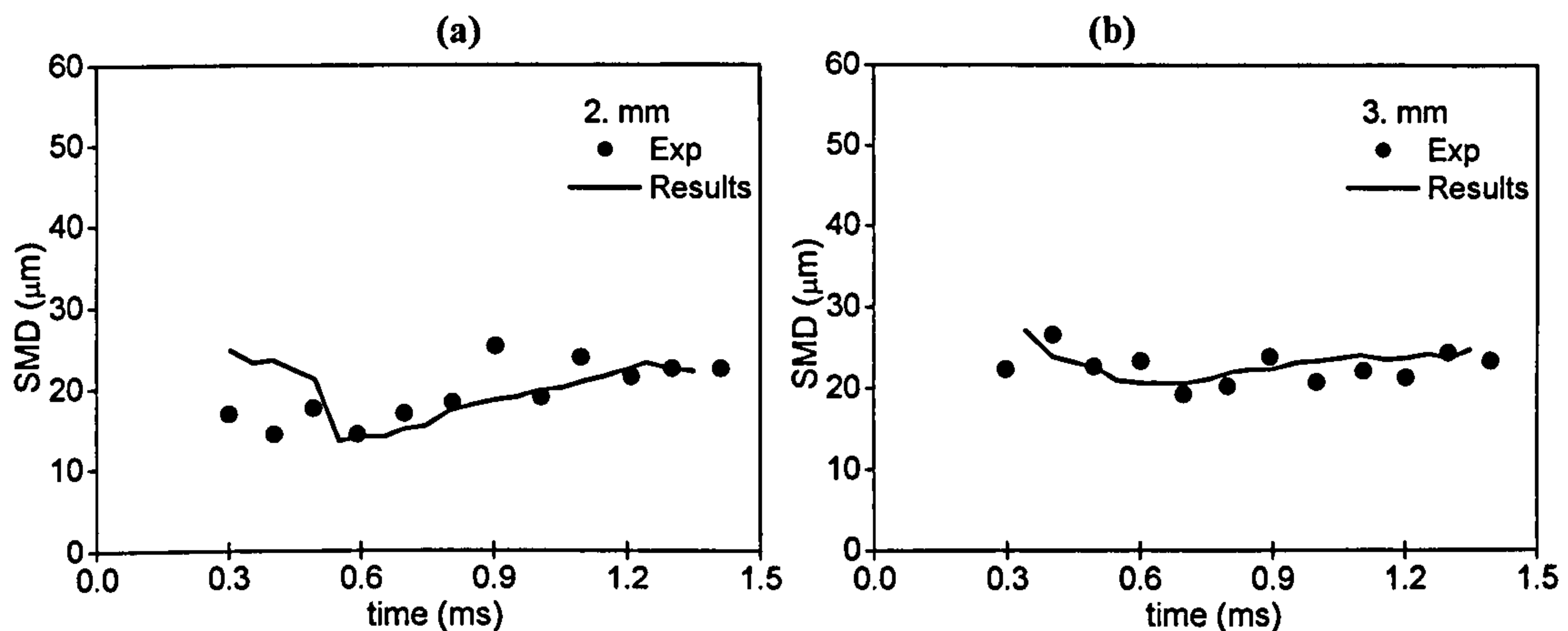


**Figure 5-7: Comparison between PDA droplet diameter measurements [216] and model predictions at different points across the spray, located 2 and 3mm from the centreline and at 12.5mm from the nozzle hole exit for evaporating spray, with nominal rail pressure of 800bar, 500K back temperature and 17.2bar back pressure.**

Two different back temperatures equal to 300 and 500K have been selected, corresponding to non-evaporating and moderate evaporating environments, respectively. The computational results have been validated against PDA data and CCD images [216]. Figure 5-7 present the temporal profiles of the spray SMD under evaporating conditions at different points across the spray, located 2 and 3mm from the centreline and at 12.5mm axial distance from the nozzle hole exit, which is the nearest distance from the hole location where measurements are available. The simulations have been performed using the original computational domain shown in Figure 5-1. The graphs show reasonable agreement between PDA measurements and calculations, in the area where liquid core atomisation has been already completed and the secondary droplet break-up is the most important spray processes taking place. The model is capable to predict the almost constant profile of the droplets located close to the periphery of the spray, which SMD is about 20μm.

The sensitivity of the model predictions on the computational domain has been investigated, performing one and two levels of cell refinement in the region of spray



development from the original grid shown in Figure 5-1. The injection conditions correspond to the high nominal rail pressure of 1200bar under room temperature, according to Table 5-II and Figure 5-5. The comparison between CCD images [216] and model predictions is shown in Figure 5-8.

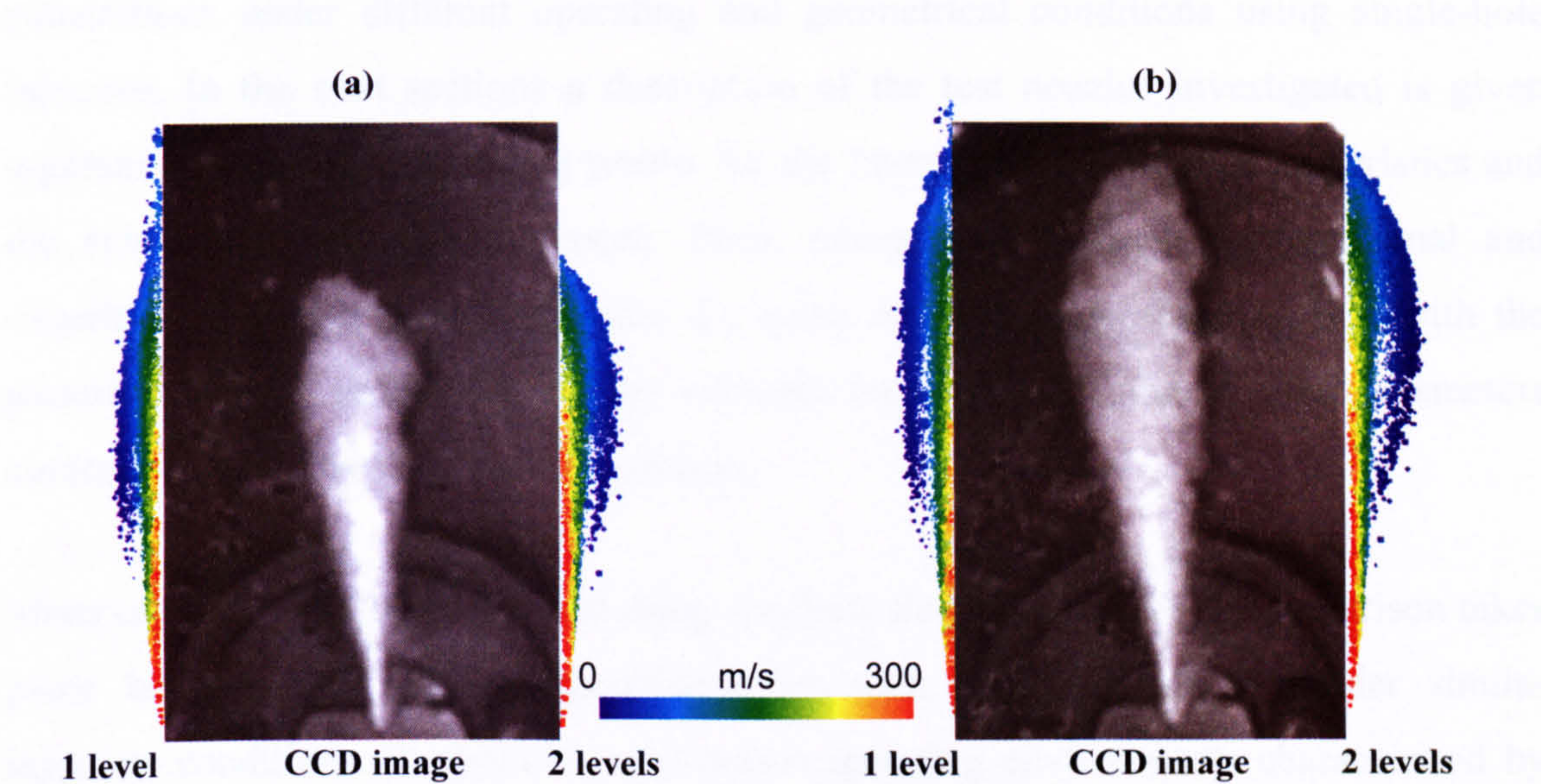


Figure 5-8: CCD spray images [216] and model predictions at (a) 0.3 and (b) 0.5ms after start of injection using one and two levels of local refinement [ $T_{AIR}=300K$ ,  $P_{BACK}=17.2bar$ ,  $P_{INJ}=1200bar$ ].

This figure shows the spray development at 0.3 and 0.5ms after start of injection. The results clearly indicate that local grid refinement offers an improvement to the predicted spray structure, particularly during the initial stages of the injection period, although the temporal profiles of spray penetration, calculated according to the 95% of total liquid mass, do not catch that sensitivity of the results on the computational domain, as shown in Figure 5-9, suggesting that this parameter gives a good estimation of the spray development characteristics, relatively free from numerical implementation issues.

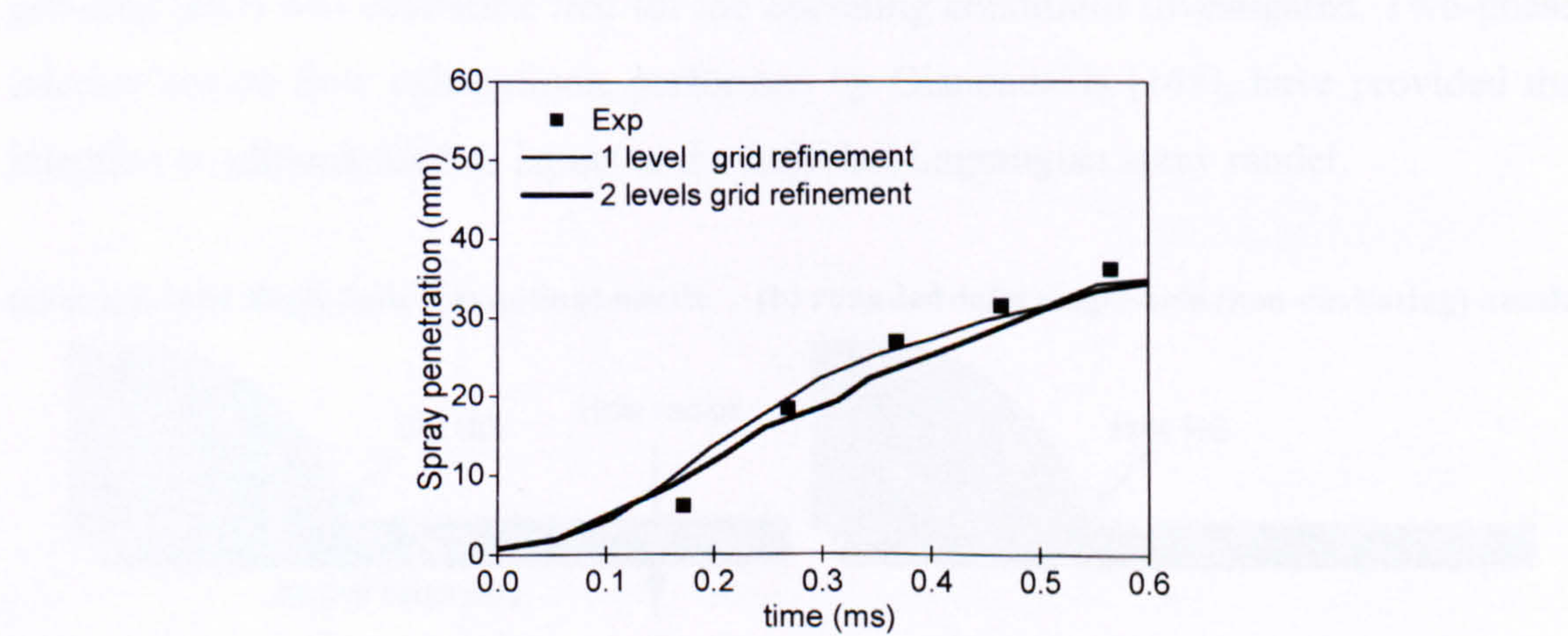


Figure 5-9: Comparison between experimental data [216] and model predictions obtained using grids with one and two levels of dynamic local refinement for the liquid penetration temporal profiles [ $T_{AIR}=300K$ ,  $P_{BACK}=17.2bar$ ,  $P_{INJ}=1200bar$ ].



### 5.3 Results from the 2-D axis-symmetric single-hole nozzles

Having validated the model against droplet size and velocity measurements, the discussion focuses on the prediction of the spray structure and liquid and vapour penetrations under different operating and geometrical conditions using single-hole injectors. In the next sections a description of the test nozzles investigated is given together with the corresponding results for the internal nozzle flow characteristics and the subsequent spray development. Then, comparison between computational and experimental results used to validate the spray model is presented, together with the parametric cases used to assess the relevant importance of the various parameters controlling the spray development process.

Since cavitation can be eliminated using specially designed nozzles, a comparison takes place between the spray characteristics for such nozzles operating under similar injection conditions. Evaporating and non-evaporating environments characterised by high back pressure conditions are also investigated. Once the model has been validated against experimental measurements, the study addresses the sensitivity of the spray sub-models and the numerical parameters on the computational results.

#### 5.3.1 Overview of the test cases

The two axis-symmetric single-hole nozzles used for the spray investigations presented in this section are shown in Figure 5-10. As can be seen, a sharp inlet nozzle was used to produce fully cavitating conditions while a rounded-inlet nozzle with 18% hydro-grinding (HG) was cavitation free for the operating conditions investigated. Two-phase internal nozzle flow calculations, performed by Giannadakis [148], have provided the injection conditions used as inputs to the Eulerian-Lagrangian spray model.

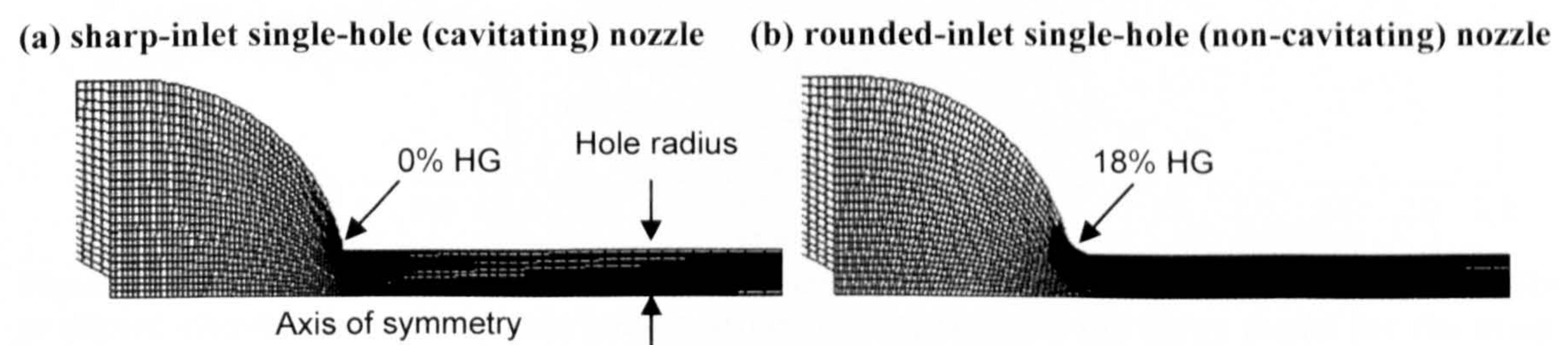


**Figure 5-10:** Numerical grid of the (a) sharp-inlet (cavitating) nozzle and (b) rounded-inlet (non-cavitating) nozzle [148].



Injection was taking place against pressurised  $N_2$  at 20bar and 54bar while the nominal rail pressure values used were 500, 800 and 1200bar. The actual injection rate for cavitating and non-cavitating nozzles for the three nominal rail pressure conditions is shown in Figure 5-11(a) and Figure 5-11(b) respectively. Knowledge of the discharge coefficient of each nozzle at a given range of operating conditions is an important prerequisite for the design and the optimised performance of modern injection systems. Effectively, one has to know at a given combination of injection and cylinder pressures how much fuel is actually injected into the cylinder; this information is obviously critical for optimising fuel consumption and controlling the formation of pollutants during combustion. Since the discharge coefficient of the cavitating nozzle was around 0.7, as shown in Figure 5-11(c) for the three nominal rail pressures, which is much smaller compared to the 0.85 value of the non-cavitating nozzle, in order to match the same fuel injection quantity, the cavitating nozzle had a hole diameter  $D_{0\%HE} = 209\mu m$  while the non-cavitating nozzle  $D_{18\%HE} = 184\mu m$ . The maximum needle lift for both cases was  $250\mu m$  while the injection duration was approximately 2.5ms. Actual rail pressure measurements were used as input for the calculations, and this is reflected on the predicted fuel injection rate profiles of Figure 5-11 (a-b). Looking to the profiles in Figure 5-11 (a), a relatively high-frequency oscillations can be seen, which are mainly attributed to the development of the cavitating structures inside the nozzle. Various test cases have been selected for calibrating and validating the spray model. The set of experimental data selected have been obtained as part of the I-LEVEL EU research programme, and have been reported in König et al. [217]. Both non-evaporating and vaporising conditions have been tested; Table 5-III summarises the nozzle flow and operating characteristics to be presented here.

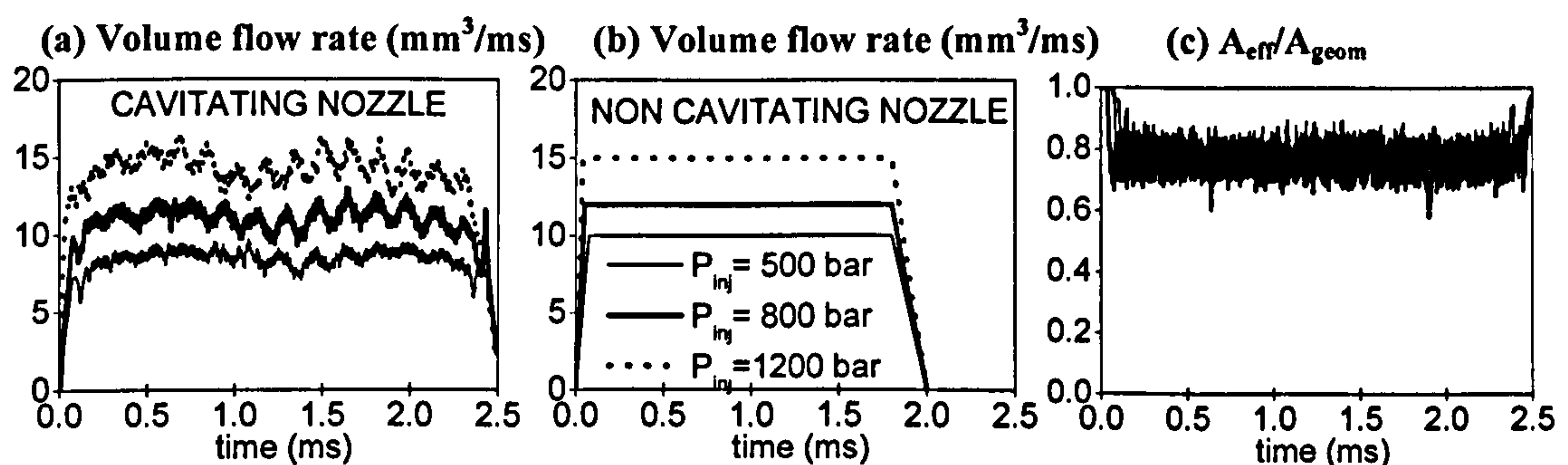


Figure 5-11: Fuel injection rate of the (a) sharp-inlet nozzle and (b) rounded-inlet nozzle and (c) predicted effective area of the sharp-inlet nozzle used as input to the spray model for the three nominal rail pressures investigated.



As can be seen, two back pressures and temperatures have been tested. The 20bar-273K cases correspond to the non-evaporating spray while the 54bar-900K case corresponds to the evaporating conditions. These operating points have been selected to have the same back density, which is one of the main parameter controlling fuel penetration. For all calculations performed, the fuel injection rate and the cavitation level at the nozzle hole exit have been estimated from the nozzle cavitation model developed by Giannadakis [148], which uses as input the measured rail pressure.

Orifice diameter (mm)	0.209, 0.184
Discharge coefficient for rounded-inlet nozzle	0.9
Injection pressure (bar)	500, 800, 1200
$T_{\text{ambient}}$ (K)	273, 900
$P_{\text{ambient}}$ (bar)	20, 54
$T_{\text{fluid}}$ (K)	300
Fuel	n-C <sub>8</sub> H <sub>18</sub> , n-C <sub>13</sub> H <sub>28</sub>

**Table 5-III: Injector geometric and flow parameters and operating conditions.**

Furthermore, the occurrence of cavitation has also a profound effect on the injection velocity, as shown in Figure 5-12, for two nominal rail pressure values of 500 and 1200bar respectively. The time scale is shorten to 1.0ms in order to be more clear both the initial stage of velocity increase and also the fluctuating behaviour of the cavitating nozzle relative to the steady-state value of the cavitation-free nozzle. The thin and dot symbol lines correspond to the cavitating nozzle injection velocity predictions obtained using the geometric hole area, as well as the effective hole area. The latter is the percentage of the geometric one occupied by liquid only, while the remaining part represents the hole exit cross sectional area blockage due to the presence of cavitation. It can be seen that the effective injection velocity is about 15% to 20% higher than the geometric one. It can be also seen that the actual injection velocity of the non-cavitating but smaller hole size nozzle (approximately 30% smaller cross sectional hole exit area) has a mean velocity relatively higher than the cavitating nozzle. The difference in the hole exit cross sectional area is reflected to the mean injection velocity, which is higher in the case of nozzle with smaller hole diameter. However, the actual difference in the injection velocity between the two nozzles is smaller due the increase of the actual (effective) velocity in the cavitating nozzle. The graphs show that, although the nominal rail pressure is fixed at a constant value, the cavitating nozzle exhibits fluctuations due



to the transient nature of cavitation itself, which has the tendency to appear-cease as function of the pressure recovery process with vapour production at the nozzle hole inlet.

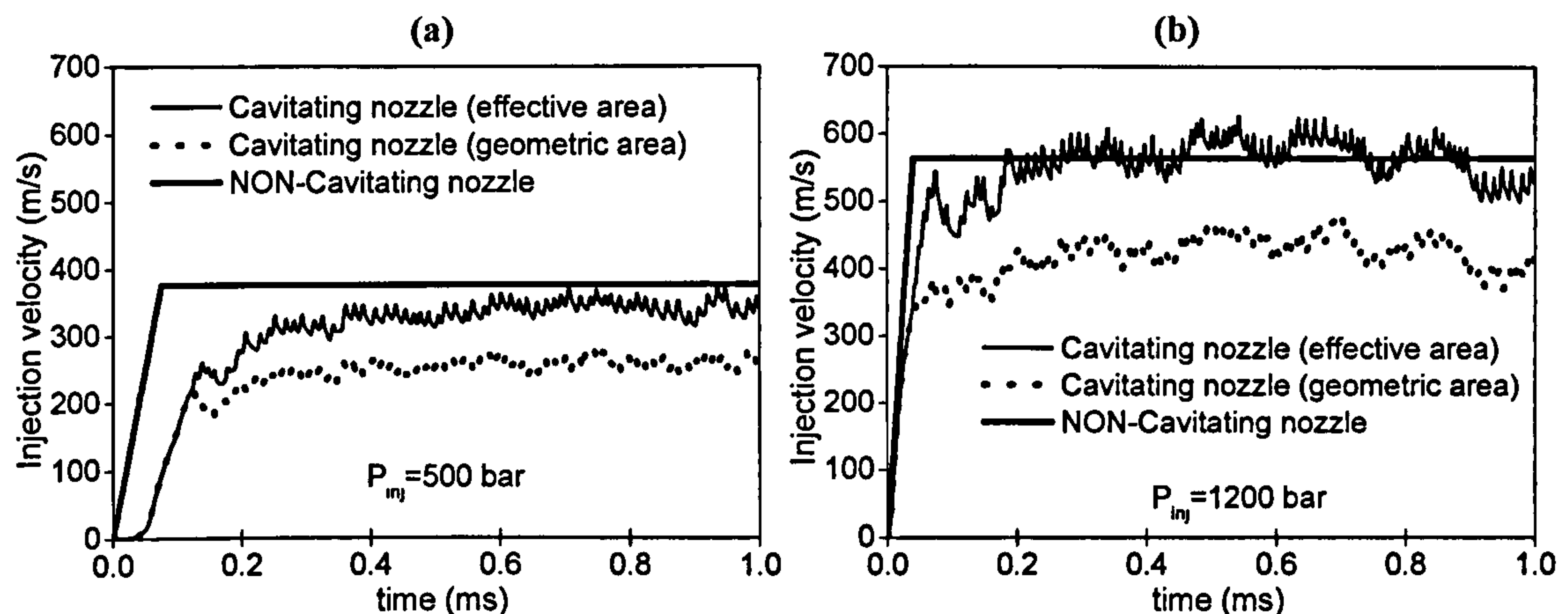


**Figure 5-12:** Predicted effective and geometric injection velocity for the cavitating and the non-cavitating nozzle for nominal rail pressures of (a) 500bar and (b) 1200bar. The non-cavitating and the cavitating nozzles have the same volumetric capacity.

The onset and development of cavitation has been found to also affect on the predicted spray atomisation cone angle, shown in Figure 5-13, for two nominal rail pressures of 500 and 1200bar respectively. This is calculated according to the cavitation-induced and turbulence-induced atomisation model parameters described in Chapter 3.

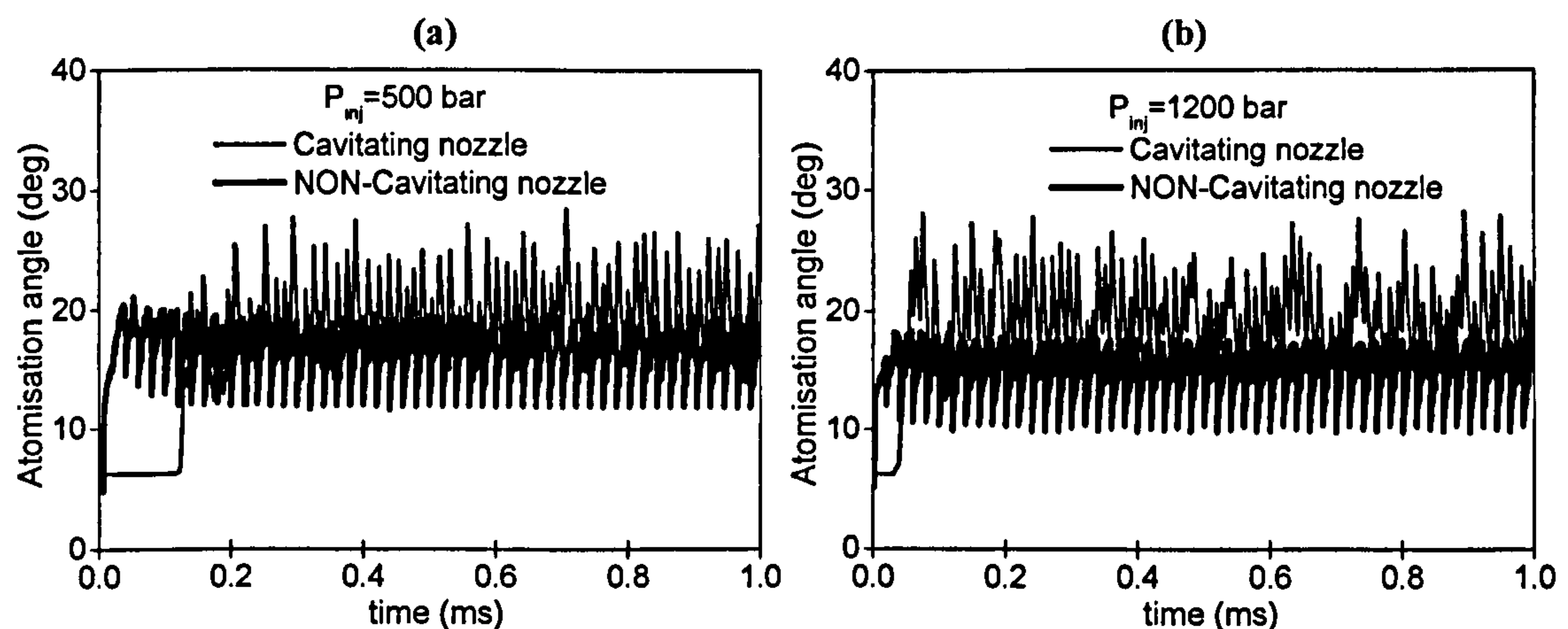


**Figure 5-13:** Predicted near-nozzle spray cone angle for the cavitating and the non-cavitating nozzle during the injection period for rail pressures of (a) 500bar and (b) 1200bar.

As can be seen, the cavitating nozzle exhibits higher frequency fluctuations of the near-nozzle angle that estimate the deviation from the injector axis of the liquid parcels exiting from the nozzle hole. The comparison between the low and the high nominal rail pressure cases reveals that the fluctuating behaviour of the spray cone angle has a mean



value equal to 20 and 16 for the 500bar and 1200bar cases, respectively, for both the cavitating and the non-cavitating nozzles.

The difficulty to perform experimental measurements near the very dense spray area close to the injector location reflects to the necessity to develop sophisticated computational models able to resolve the unknown phenomena taking place in this region. Extensive experimental and computational investigation suggest that the fuel atomisation process significantly affects the performance of direct injection diesel engines, since it determines the spray velocity, cone angle and the size of the droplets formed from the fragmentation of the injected liquid ligaments. Figure 5-14(a) and Figure 5-14(b) present the temporal profiles of the spray Sauter mean diameter (SMD), predicted using the cavitation-induced atomisation model and the liquid turbulence-induced atomisation model for cavitating and non-cavitating nozzle designs respectively, for the three nominal rail pressures investigated under room temperature conditions. The results for the cavitating injector show that as the injection velocity increases, smaller droplets are formed, reaching an asymptotic value, which ranges from 23 to 15 $\mu\text{m}$  as the nominal rail pressure is varied from 500 to 1200bar. The size of the droplet formed from fragmentation of the liquid ligaments exiting from the nozzle is almost independent on the injection pressure, since it is a function of the effective area. On the other hand the injection velocity is proportional to the square root of the injection pressure. This has a direct effect on the secondary break-up, which increases with higher droplet velocity. The droplet SMD predicted using the turbulence-induced atomisation model for the cavitation-free nozzle design results to be independent on the nominal rail pressure. The value of the SMD predicted by the model is around 15 $\mu\text{m}$ . The injection pressure is directly proportional to the droplet velocity, which has an effect in increasing the secondary break-up, resulting in smaller droplets. On the other hand, the turbulence-induced atomisation model predicts a droplet size, which increases with the injection pressure. This is due to the fact that the droplet size estimated by the model decreases with higher turbulence time scale, which is inversely proportional to the injection velocity (i.e. injection pressure). This combined effect explains the almost constant profile predicted using that model. The smaller value of 15 $\mu\text{m}$ , compared to the average one from the cavitation induced atomisation model is related also to the smaller hole dimension of the non-cavitating nozzle. The maximum droplet size after the fragmentation of the liquid ligament predicted by the turbulence-induced



atomisation model is around  $70\mu\text{m}$  for injection pressure of 1200bar, which is smaller compared to the minimum droplet size predicted by the cavitation-induced atomisation model, which is around  $80\mu\text{m}$ .

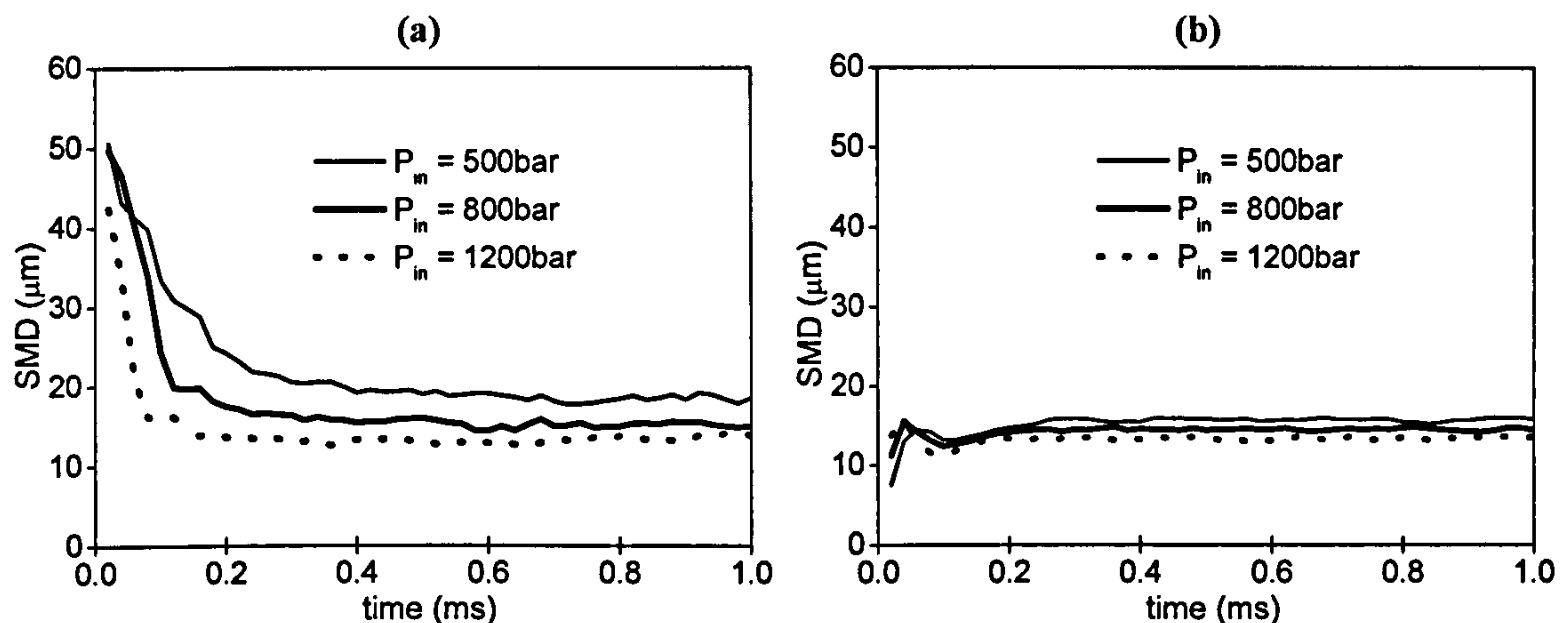


**Figure 5-14: Effect of initial conditions and atomisation model on predicted droplet SMD for the three nominal rail pressures investigated (a) cavitating nozzle and (b) non-cavitating nozzle.**

These parameters have been used as input for the modelling of the subsequent spray development, which will be discussed in details in the following sections. Before presenting the model predictions, Figure 5-15 and Figure 5-16 has been selected for presentation in order to demonstrate typical results of the calculation model. Figure 5-15 show the liquid penetration and induced flow field under non-evaporating conditions at 0.2, 0.4, 0.6 and 0.8ms after start of injection using as injection conditions those derived from the cavitating nozzle internal flow simulations. The scatter plots represent the liquid parcels, while the vectors describe the air-flow motion, coloured according to their total velocity magnitude. It can be concluded that as the liquid penetrates, it loses momentum which is transferred to the surrounding gas, forming a recirculation zone on the spray periphery. Figure 5-16 shows the vapour and liquid penetrations and induced flow field under evaporating conditions at the same time steps presented in Figure 5-15 during the spray development from the same nozzle design. As can be seen, liquid penetration freezes after some time from the start of injection, while the air motion induced by the spray, continues to develop, convecting vapour further downstream from the injection point. The liquid parcels are plotted on the right hand side of each picture in black together with the flow field velocity vectors, coloured according to their total velocity normalised with its maximum value, while on the left



hand side the contours of the vapour concentration are plotted, coloured according to a scale normalised with the maximum vapour concentration.

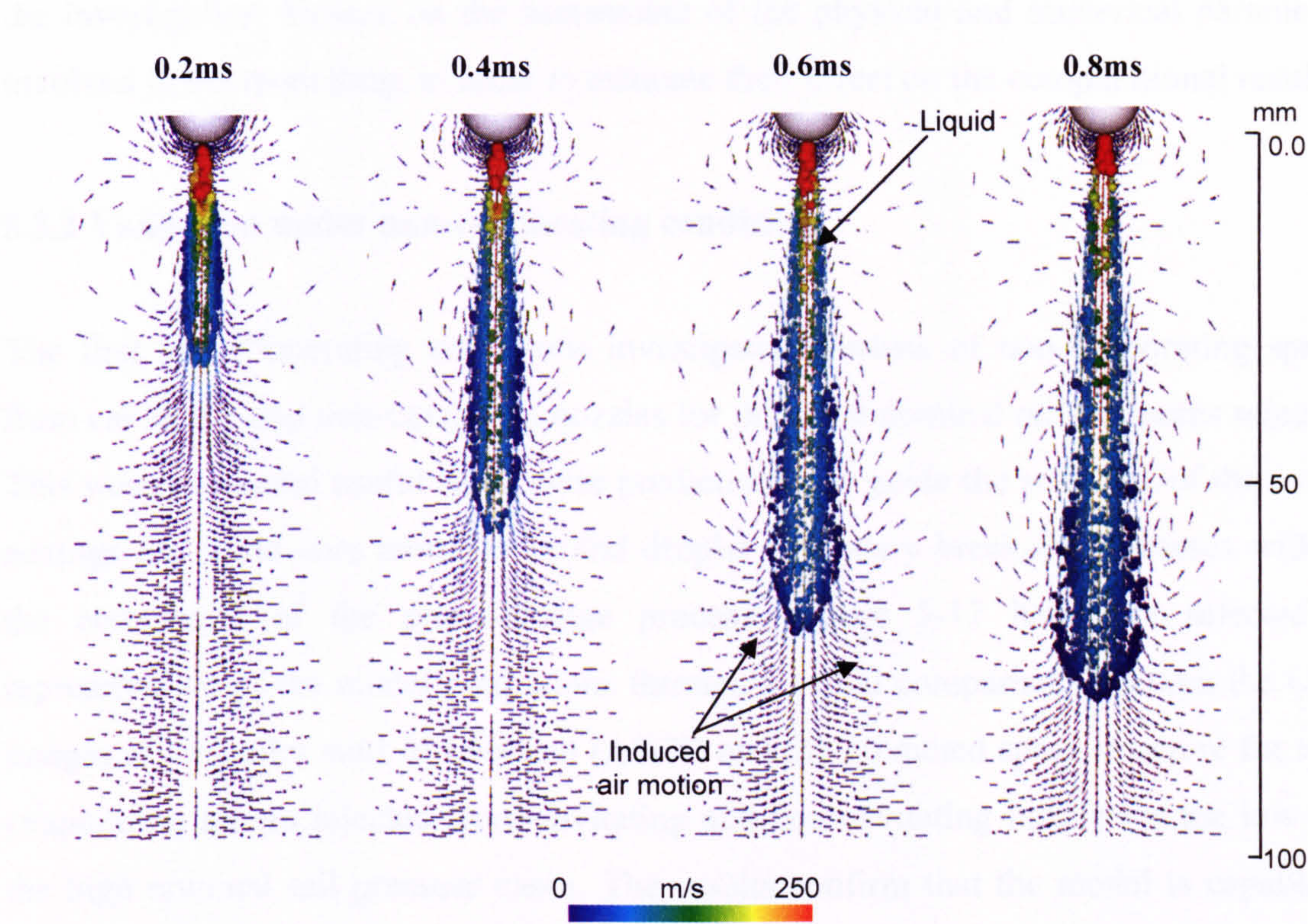


**Figure 5-15:** Predicted non-evaporating spray development at 0.2, 0.4, 0.6 and 0.8ms after start of injection. Liquid penetration and induced flow field are shown [ $P_{INJ}$ =1200bar,  $P_{BACK}$ =54bar,  $T$ =900K]. Scatter plots and air flow vectors are coloured according to their total velocity.

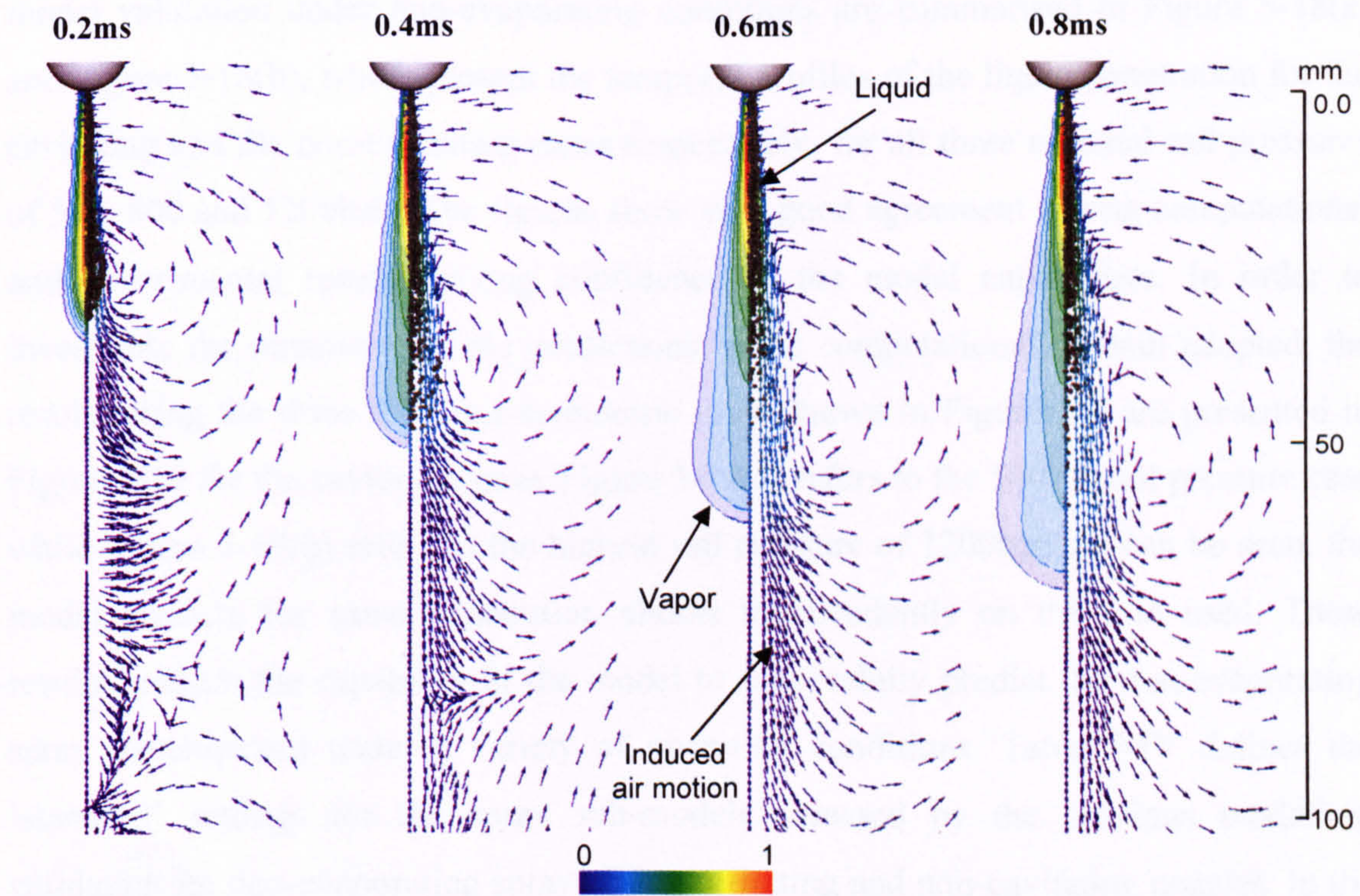


**Figure 5-16:** Predicted evaporating spray development at 0.2, 0.4, 0.6 and 0.8ms after start of injection. Liquid penetration (right), vapour penetration (left) and induced flow field (right) are shown [ $P_{INJ}$ =1200bar,  $P_{BACK}$ =54bar,  $T$ =900K]. The colour scales for the vapour concentration and the flow velocity vector distributions are normalised with their maximum values.



In the following section the spray model has been first validated against the experimental data base for non-evaporating and evaporating conditions; successively the investigation focuses on the assessment of the physical and numerical parameters involved in the modelling, in order to estimate their effect on the computational results.

### 5.3.2 Validation under non-evaporating conditions

The first set of operating conditions investigated consists of non-evaporating sprays from cavitating and non-cavitating nozzles for the three nominal rail pressures selected. This was considered useful since these predictions can guide the selection of the model settings for liquid core atomisation and droplet secondary break-up processes without the complexity of the phase-change process. Figure 5-17 has been selected as representative of the model predictions through a visual comparison between the CCD images at 1ms after start of injection (ASOI) and the predicted spray structure for non-evaporating sprays injected from cavitating and non-cavitating nozzle for the low and the high nominal rail pressure cases. The results confirm that the model is capable to capture the increase of penetration with injection pressure and to predict the experimental spray shape for all conditions investigated. The results from the complete model validation under non-evaporating conditions are summarised in Figure 5-18(a) and Figure 5-18(b), which present the temporal profiles of the liquid penetration for the cavitating and the non-cavitating cases respectively, for all three nominal rail pressures of 500, 800 and 1200bar. The figures show very good agreement among computational and experimental results, giving confidence to the model capabilities. In order to investigate the sensitivity of the predictions to the computational domain adopted, the results using the three 2-D axis-symmetric grids shown in Figure 5-1 are presented in Figure 5-19 for the cavitating case. Figure 5-19(a) refers to the 500bar rail pressure case while Figure 5-19(b) refers to the highest rail pressure of 1200bar. As can be seen, the model predicts the same penetration almost independently on the grid used. These results confirm the capability of the model to successfully predict the non-evaporating spray development under a variety of operating conditions. Table 5-IV defines the ‘standard’ settings for the spray sub-models assessed by the previous modelling validation for non-evaporating sprays from cavitating and non-cavitating nozzles. In the following section, investigation of more complex evaporating spray cases in high pressure and temperature environments are presented.



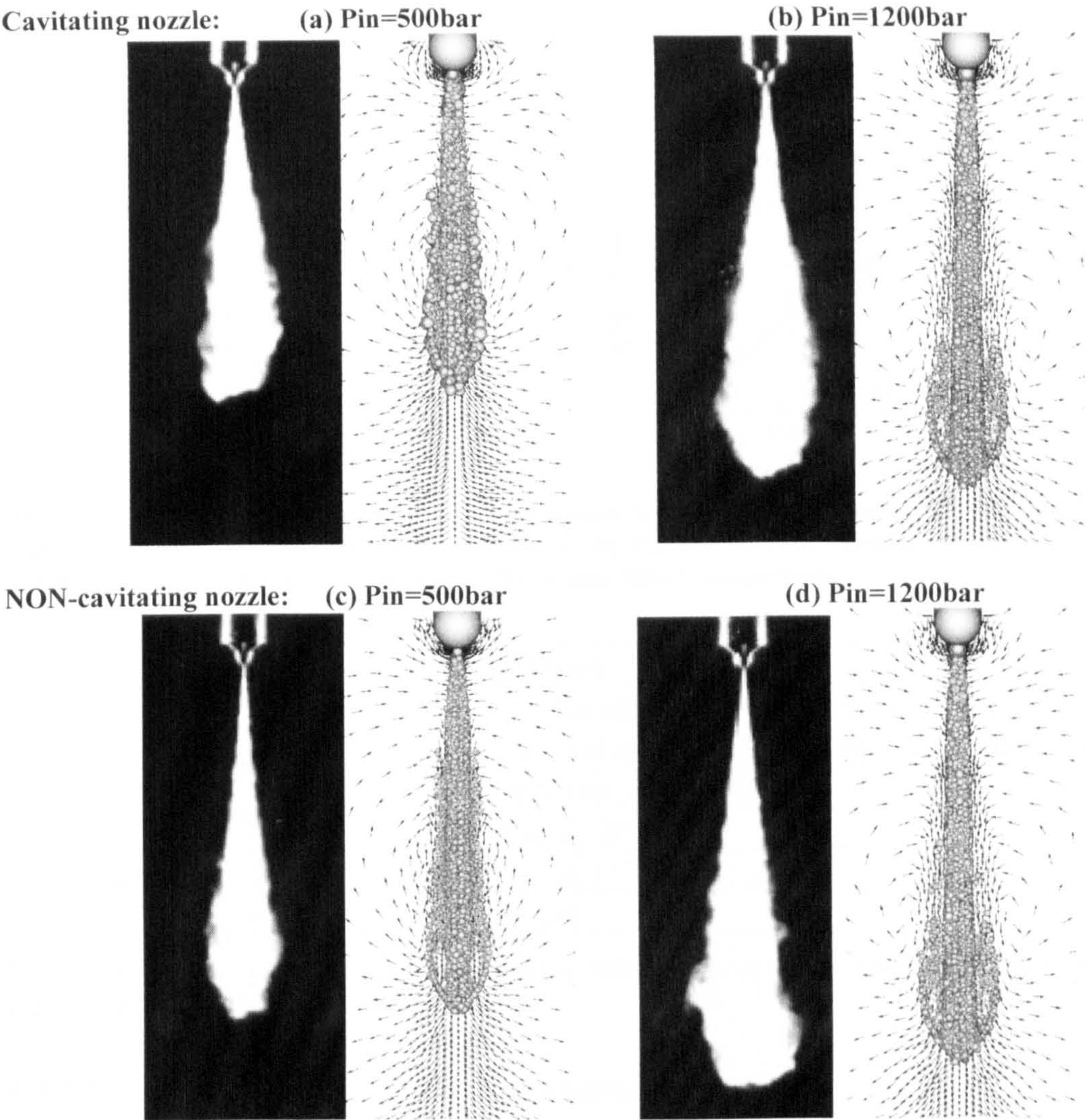


Figure 5-17: Comparison between CCD images and predicted spray structures at 1ms ASOI for the (a,b) cavitating and the (c,d) non-cavitating nozzles for rail pressures of 500bar and 1200bar, under non-evaporating conditions.

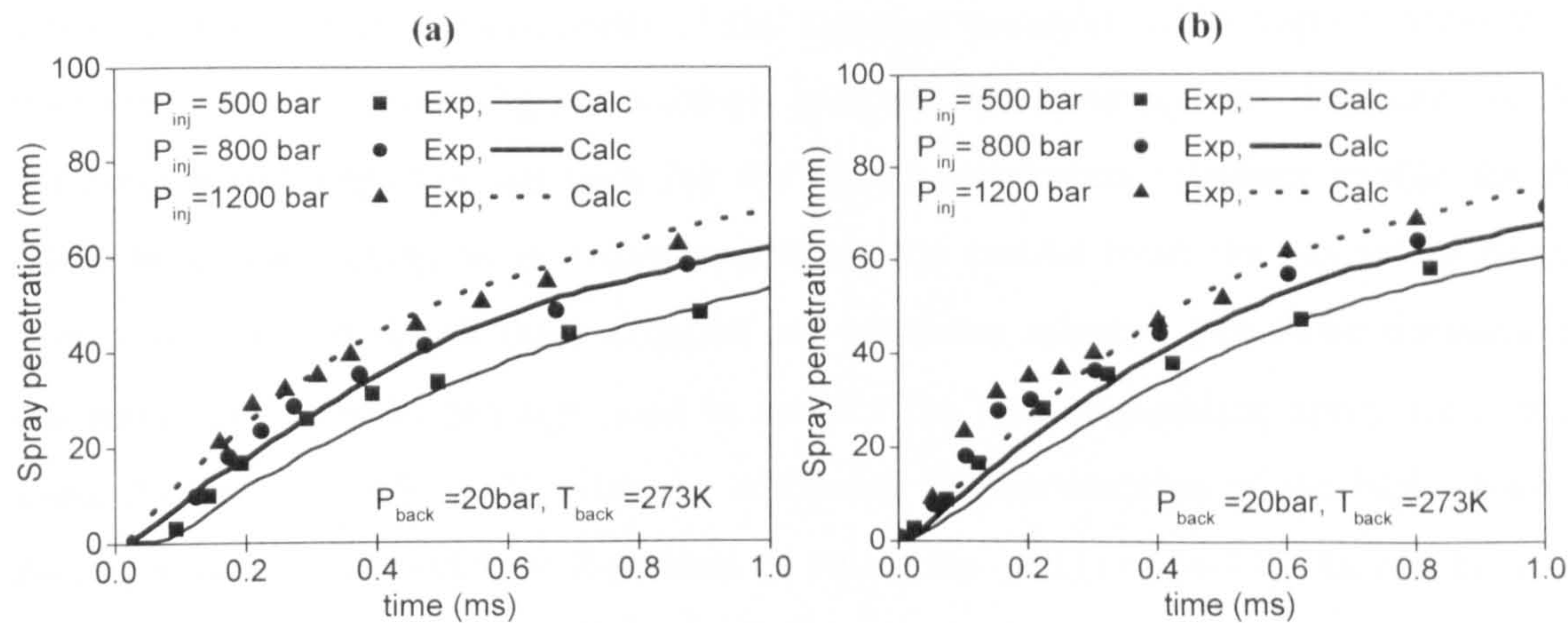


Figure 5-18: Effect of initial conditions and atomisation model on predicted non-evaporating spray tip penetration for the three nominal rail pressures investigated of the (a) sharp-inlet nozzle and (b) rounded-inlet nozzle.



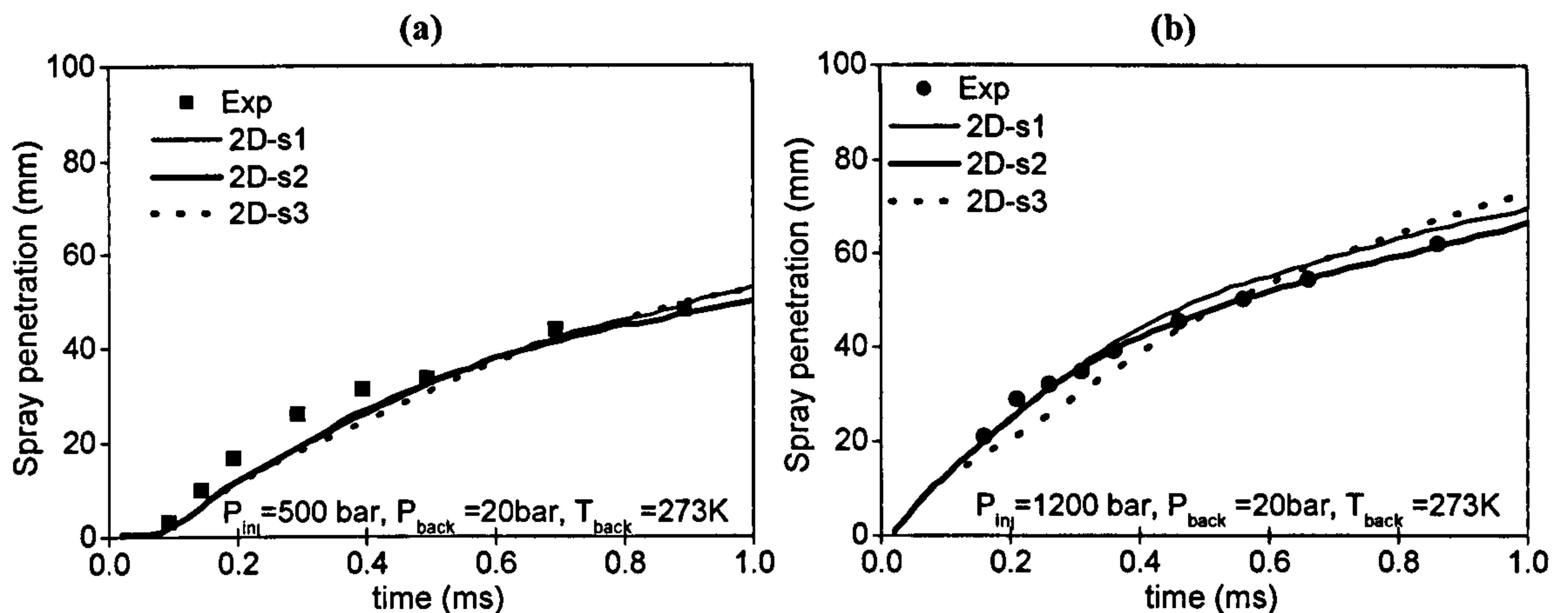


Figure 5-19: Grid effect on predicted non-evaporating spray tip penetration of the sharp-inlet nozzle for nominal rail pressures of (a) 500bar and (b) 1200bar. Minimum cell lengths are 0.6, 0.3 and 0.15mm for grid 2D-s1, 2D-s2 and 2D-s3 respectively.

Spray sub-model	Description
Atomisation	( <sup>1</sup> ) Cavitation-induced with radial distribution ( <sup>2</sup> ) Turbulence-induced without radial distribution
Secondary break-up	Arcoumanis et al. [76]
Drag	Feng et al. [185]
Turbulence dispersion	O'Rourke [197]
Droplet shape	Spherical

Table 5-IV: 'Standard' settings for the spray sub-models used for non-evaporating sprays from cavitating (<sup>1</sup>) and non-cavitating (<sup>2</sup>) nozzles.

### 5.3.3 Validation under evaporating conditions

As known from experimental observations, the main conclusion regarding evaporating sprays at relatively high temperatures is that liquid penetration stops at some distance from the nozzle hole independently of the injection pressure, while vapour penetration continues to increase. Figure 5-20(a) presents the comparison between model predictions and experimental data for the liquid penetration transient profile for the 54bar-900K case using as injection conditions the results from the cavitating nozzle flow investigations for all three nominal rail pressures selected. For those simulations, the same spray model settings used to predict the non-evaporating spray have been used, defined in Table 5-IV, with the additional implementation of the high-pressure droplet evaporation model, as described in equations (4-11) to (4-17). As can be seen, those predictions fail dramatically not only to capture the experimental data but also the trend of having liquid penetration independent of injection pressure. Figure 5-20(b) shows the predicted temporal evolution of spray SMD for those conditions. As can be seen, the calculated spray size is of the order of 15 $\mu$ m, which is a reasonable value,



according to numerous experimental data available for similar operating conditions [128]. The model predicts a small decrease of the spray SMD with increasing injection pressure, which, again is an expected result. The initial increase of the spray SMD, followed by its slightly decrease is due to the turbulence-induced atomisation model, which is implemented in the first instants after the start of injection, when the effective area is approximately equal to 1 (Figure 5-11(c)). As the flow rate increases, the predicted droplet size increases, up to 0.03ms, then the cavitation-induced atomisation model is used to estimate the size of the particles formed by the fragmentation of the liquid ligaments. The predicted droplet size results now to be proportional to the effective area, which decreases asymptotically to a value around 0.85.

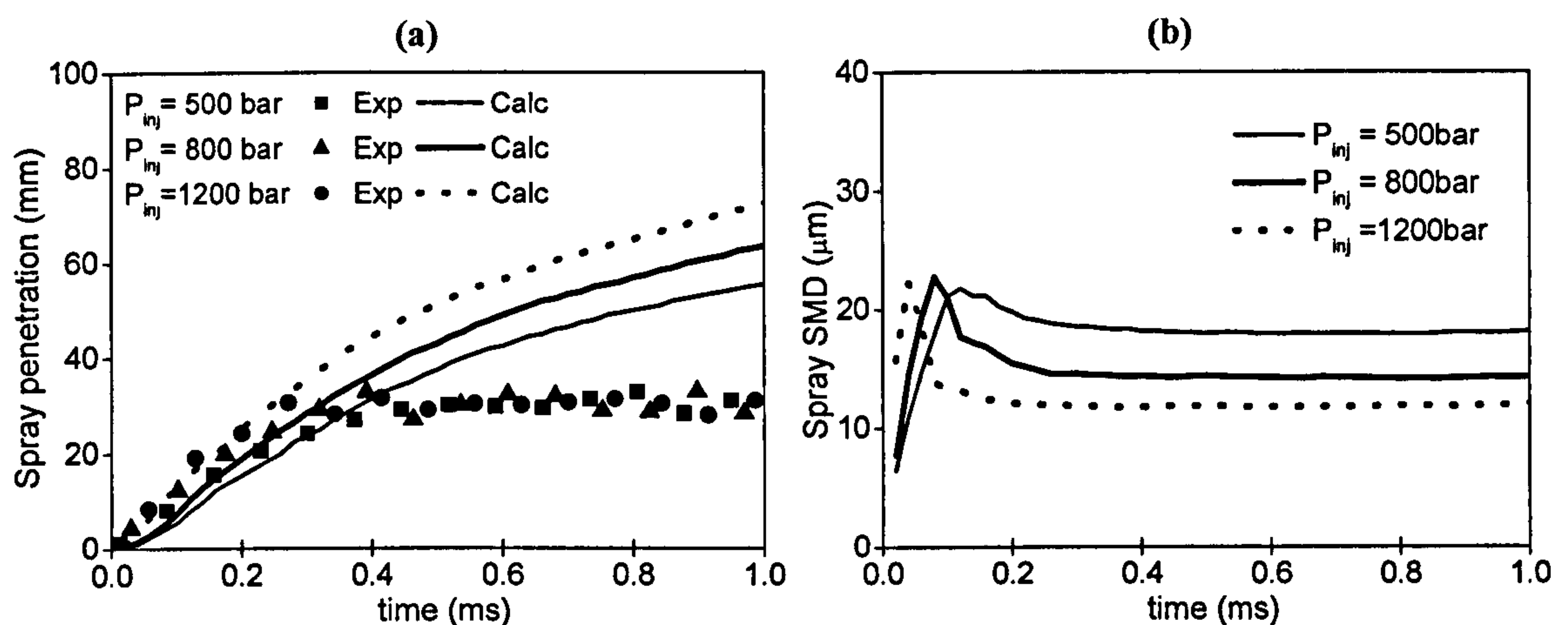
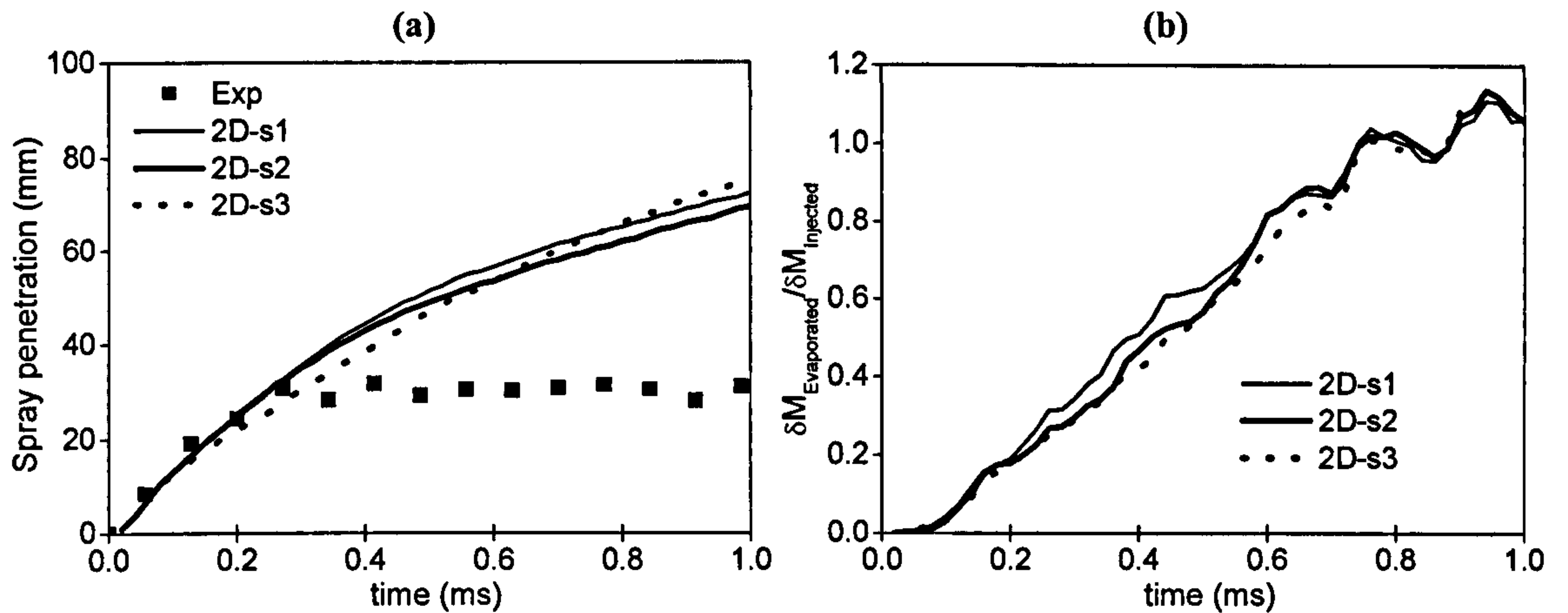


Figure 5-20: (a) Comparison between experimental data and model predictions for the temporal variation of liquid penetration and (b) predicted spray SMD, using the 'Standard' spray model settings, defined in Table 5-IV, with the high-pressure droplet evaporation model, for the three nominal rail pressures tested.

To understand the failure of the model to predict those data, numerous parametric studies have been performed and the results are presented below. The first parameter tested was the influence of the numerical grid on the calculation of liquid penetration. Figure 5-21(a) presents the same set of predictions for the 1200bar case using the three numerical grids shown in Figure 5-1. As can be seen, the results are almost independent from the mesh in terms of both the liquid penetration and the spray evaporation rate transient profiles. This parameter is normalised with the instantaneous injection rate and it is presented in Figure 5-21(b). The fluctuations in the evaporation rate are related to the fluctuation in the injection flow rate, shown in Figure 5-11(a).





**Figure 5-21: Effect of numerical grid on temporal variation of (a) liquid penetration and (b) non-dimensional evaporation rate, using the ‘Standard’ spray model settings [ $P_{\text{INJ}}=1200\text{bar}$ ]. Minimum cell lengths are 0.6, 0.3 and 0.15mm for grid 2D-s1, 2D-s2 and 2D-s3 respectively.**

As clear, this ratio becomes almost one after about 0.7ms after start of injection. This implies that after that time, the fuel vaporising will be equal to the fuel injected, and thus, it is expected that after a short delay, liquid penetration will stop. Thus, one parameter that becomes of significant importance is the time until the vaporisation rate becomes equal to the injection rate. If this is long enough, then liquid will penetrate far enough, leading to overestimation of the measured values.

One parameter that can affect the predictions is the selection of the evaporation model itself. As already presented in Chapter 4, three different models have been implemented in the GFS code, the ideal equilibrium, the high-pressure and the non-equilibrium evaporation models. The corresponding results are proposed in Figure 5-22. In particular, Figure 5-22(a) shows the effect of the evaporation model used on liquid penetration transient profiles. As clear, no major change is predicted in the predicted liquid penetration. This is due to the fact that liquid penetration is controlled by the largest droplets, which are not much affected by the evaporation model. However, by looking to Figure 5-22(b), showing the normalised evaporation rate as calculated by the three models, it can be concluded that the high pressure model predicts a value 20% higher than the other two models. Still, the vaporisation rate is still not fast enough to freeze the penetration of the liquid at values close to the experimental one. Figure 5-22(c) and Figure 5-22(d) show the predicted temporal variation of the spray SMD and temperature using the three models. As can be seen, the predicted droplet size is of the order of 10 to 15 $\mu\text{m}$ , which is within the expected range, and the vaporisation takes place under sub-critical conditions, since the liquid temperature is far below the critical



point of the n-tridecane fuel used. Moreover, use of different vaporisation models seems to have no major effect on the spray SMD, while the mean liquid temperature predicted by the high pressure model is 20% lower compared the other two models, suggesting that the high pressure model predicts higher vaporisation even for slightly cooler liquid droplets.

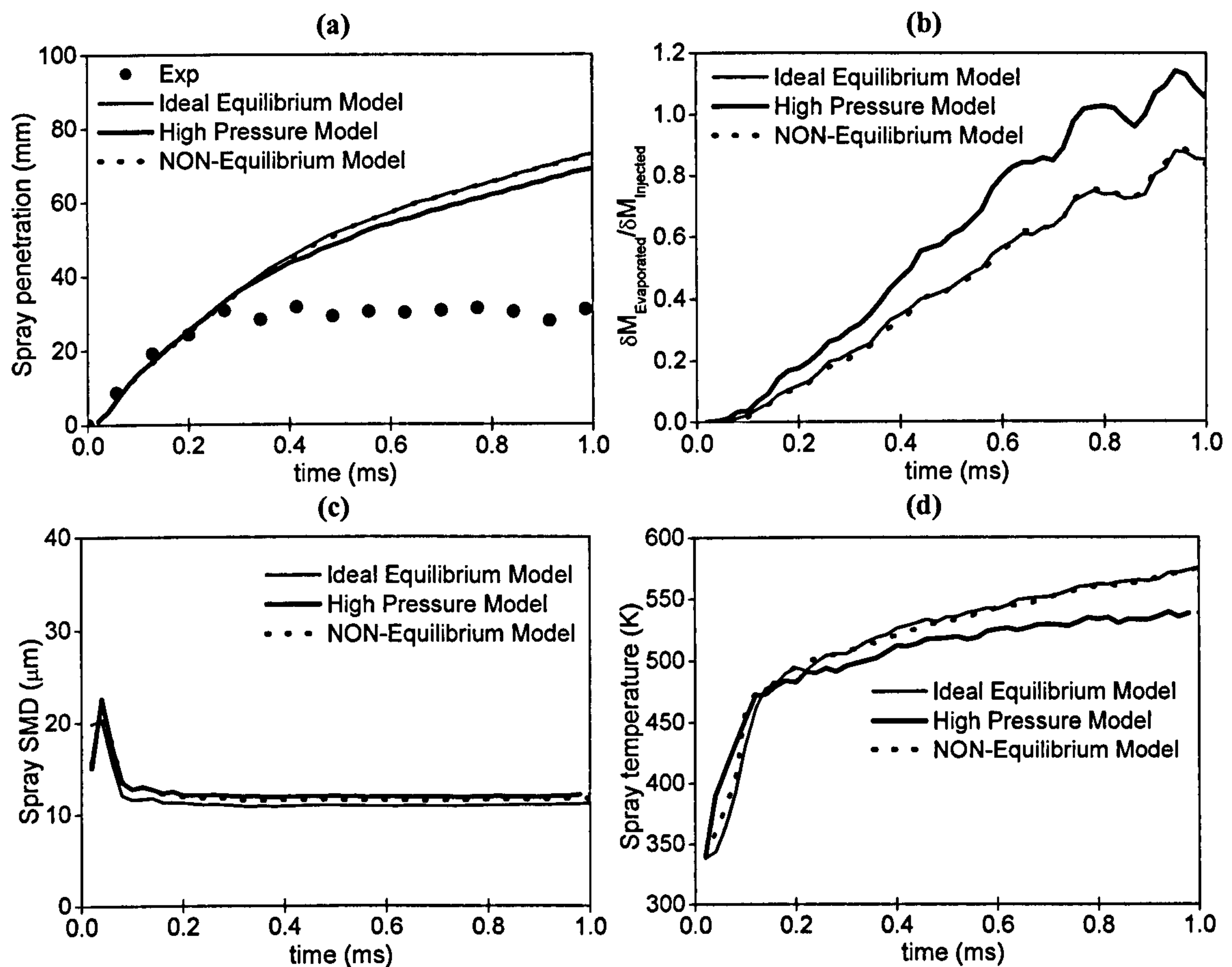


**Figure 5-22:** Effect of evaporation model on temporal variation of (a) liquid penetration, (b) non-dimensional vaporization rate, (c) spray SMD and spray temperature using the ‘Standard’ spray model settings [ $P_{\text{INJ}}=1200\text{bar}$ ].

The next parameter that has been tested is the empirical correlation for the droplet drag coefficient. As already mentioned in Chapter 3, different relationships have been used. Figure 5-23 shows the effect of those correlations on the liquid penetration. Those correspond to the classical correlation of solid spheres (Model 1), a correlation taking into account the flow circulation inside the liquid droplets (Model 2), a correlation correcting the drag law in the presence of other droplets (Model 3) and a correlation taking into account the fact that during the break-up process of the liquid droplets those can be highly deformed (Model 4), which leads to increased drag. Again, it can be seen that even for the case of significantly increased drag relative to that of spherical



droplets, which is of the order of 2, liquid penetration is not stopping at the experimental value. This can be explained from the fact that reduced droplet velocity decreases vaporisation rate, and thus, the overall effect on liquid penetration is not enough to explain the observed differences between model predictions and experiments.

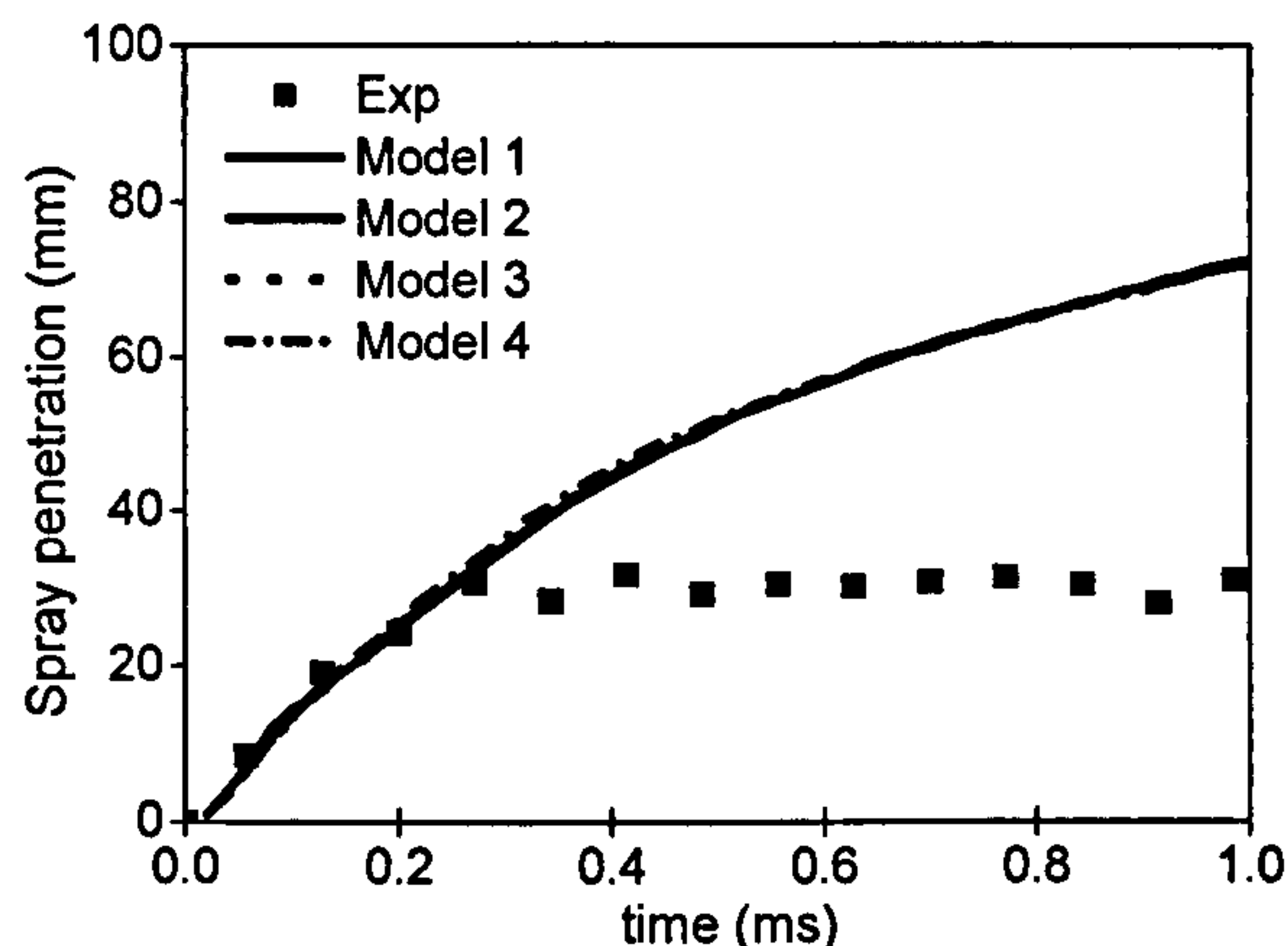


**Figure 5-23:** Effect of drag coefficient model on temporal variation of liquid penetration, using the ‘Standard’ spray model settings [ $P_{INJ}=1200\text{bar}$ ].

At this point it is evident that different models for two of the most important processes taking place during the development of sprays, the aerodynamic drag and the evaporation of the liquid droplets fail to predict the observed liquid penetration. The other two major spray sub-models used are the liquid core atomisation and the droplet secondary break-up. Although these sub-models have been validated under non-evaporating conditions, it was considered useful to de-activate them and perform spray simulations with a pre-defined droplet size. In particular, three cases have been investigated, assuming a droplet size distribution of the spray with SMD values of 5, 10 and  $20\mu\text{m}$  and double value for the maximum possible droplet size. The corresponding predictions for the liquid penetration, the normalised evaporation rate and the spray mean total velocity are presented in Figure 5-24. As can be seen, if the initial droplet SMD is equal to  $5\mu\text{m}$ , then the liquid penetration can be actually predicted reasonably well, Figure 5-24(a). Figure 5-24(b) shows that the vaporisation rate of those small droplets becomes equal to the injection rate shortly after the start of injection, at about 0.2ms. This allows for the liquid penetration to stop at about the same time as the experimental observation. Figure 5-24(c) confirms that the liquid for the  $5\mu\text{m}$  droplet case vaporises before it stops due to the drag forces acting on the small droplets in the spray, since the spray tip velocity has a value above 100m/s. However, this droplet size is believed to be rather small and it is not expected to reflect the real mean droplet size.



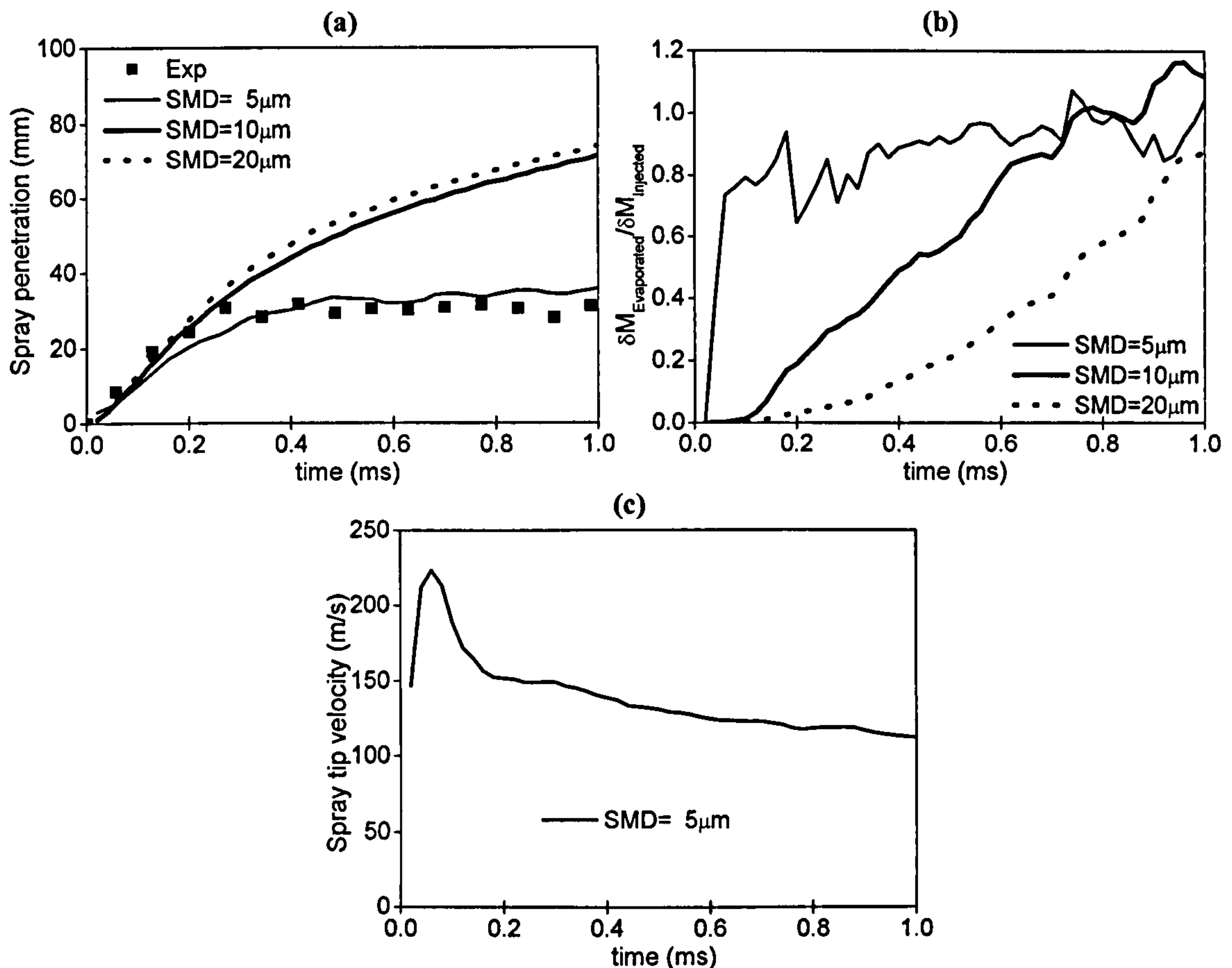


**Figure 5-24:** Effect of injected droplet size on temporal variation of (a) liquid penetration and (b) non-dimensional vaporization rate. (c) Spray tip total velocity for 5μm droplet case. Liquid core atomisation, droplet secondary break-up and droplet collisions models are de-activated [ $P_{\text{INJ}}=1200\text{bar}$ ].

To further investigate the mechanism of fuel vaporisation and energy exchange between the liquid and air for those pre-assumed droplet size cases, Figure 5-25 are included. This figure shows for the three cases investigated the temporal evolution of the mean droplet heat transfer number, the normalised mean temperature difference between the liquid and the surrounding gas, the non-dimensional total spray surface area, normalised with the spray surface area corresponding to the 20μm droplet case, and the total convection energy exchange between the two phases normalised with the enthalpy of the surrounding air. As shown, decreasing droplet size on one hand increases the mean droplet heat transfer coefficient but on the other it results to a decrease of the mean temperature difference between the two phases. Those two effects actually cancel with each other and contribute equally to the heat convection rate between the liquid droplets and the surrounding air for the different droplet sizes. However, decreasing droplet size has a substantial effect on the spray surface area available for heat and mass exchange between the two phases in the first period after start of injection, when the total spray surface area for 5μm droplets is up to 4 to 5 times bigger than the one corresponding to



20 $\mu$ m droplets, as shown in Figure 5-25(c). This results to a significant increase to the heat convection between the liquid and the air, as shown in Figure 5-25(d). Thus, it can be concluded that in order to increase the evaporation rate of the spray at the initial stages of injection, the heat convection must be transferred fast enough to vaporise the droplets. This can be achieved if the surface area between the two phases is sufficiently large. Assuming that the predicted droplet size of 10 $\mu$ m is representing the actual droplet size while the surface area of the 10 to 15 $\mu$ m droplets is the close to the experimental one, it is concluded that predictions with the calculated droplet size can actually lead to full fuel vaporisation at the observed time and length only if the area available for heat exchange is about 4 to 10 times larger than that of the 10-15 $\mu$ m spherical droplets. That increased surface area may be considered if the computational parcels are assumed to be highly deformed, as a result of the break-up process [180].

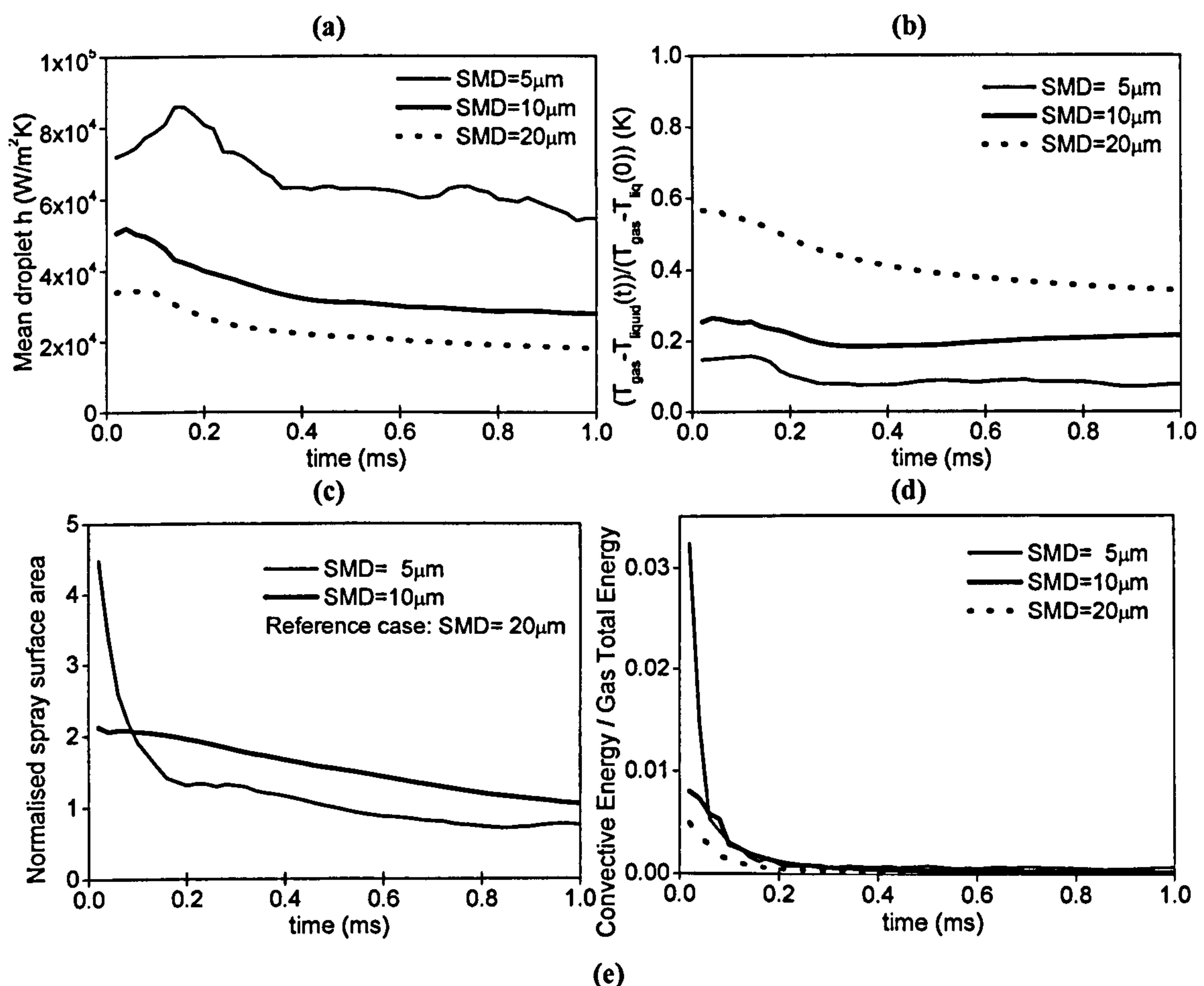


**Figure 5-25: Effect of initial droplet size on temporal variation of (a) mean droplet heat transfer number, (b) normalised mean temperature difference between liquid and gaseous phases, (c) total spray surface area and (d) normalised energy exchange between liquid and gaseous phases. Liquid core atomisation, droplet secondary break-up and droplet collisions models are de-activated [ $P_{INJ}$ =1200bar].**



Before presenting such predictions, another possible mechanism leading to faster vaporisation rates was also investigated. According to Yanagihara [222], when hydrocarbon fuel is injected into hot air, thermal fuel decomposition has been observed. Unfortunately, at present there is no model available for accounting such effects. Nevertheless, an effort can be made to simulate a case where instead of having the fuel properties of  $C_{13}H_{28}$ , it is assumed that the fuel physical properties correspond to those of a much lighter component, for example  $C_6H_{14}$ . Two cases have been tested. In the first one, a pre-assumed droplet size with SMD equal to  $20\mu m$  has been used and the corresponding results are presented in Figure 5-26. The droplet fragmentation processes have been freeze for these calculations. As can be seen in Figure 5-26 (b), the vaporisation rate of the  $C_6H_{14}$  is faster than that of the  $C_{13}H_{28}$ , although this difference is not enough to result to a reasonable prediction of the liquid penetration, Figure 5-26 (a). The second case refers to a simulation again with  $C_6H_{14}$  but this time considering the effect of droplet fragmentation; the corresponding liquid penetration profiles are presented in Figure 5-27. This time, the experimentally observed trend of liquid penetration can be predicted reasonably well by the model. However, by looking to Figure 5-28, which presents the predicted droplet size, it can be concluded that this result is effectively driven by the very small droplet size resulting from the break-up mechanism of this light fuel. As can be seen, the model predicts a droplet size of the order of 4 to  $8\mu m$ .

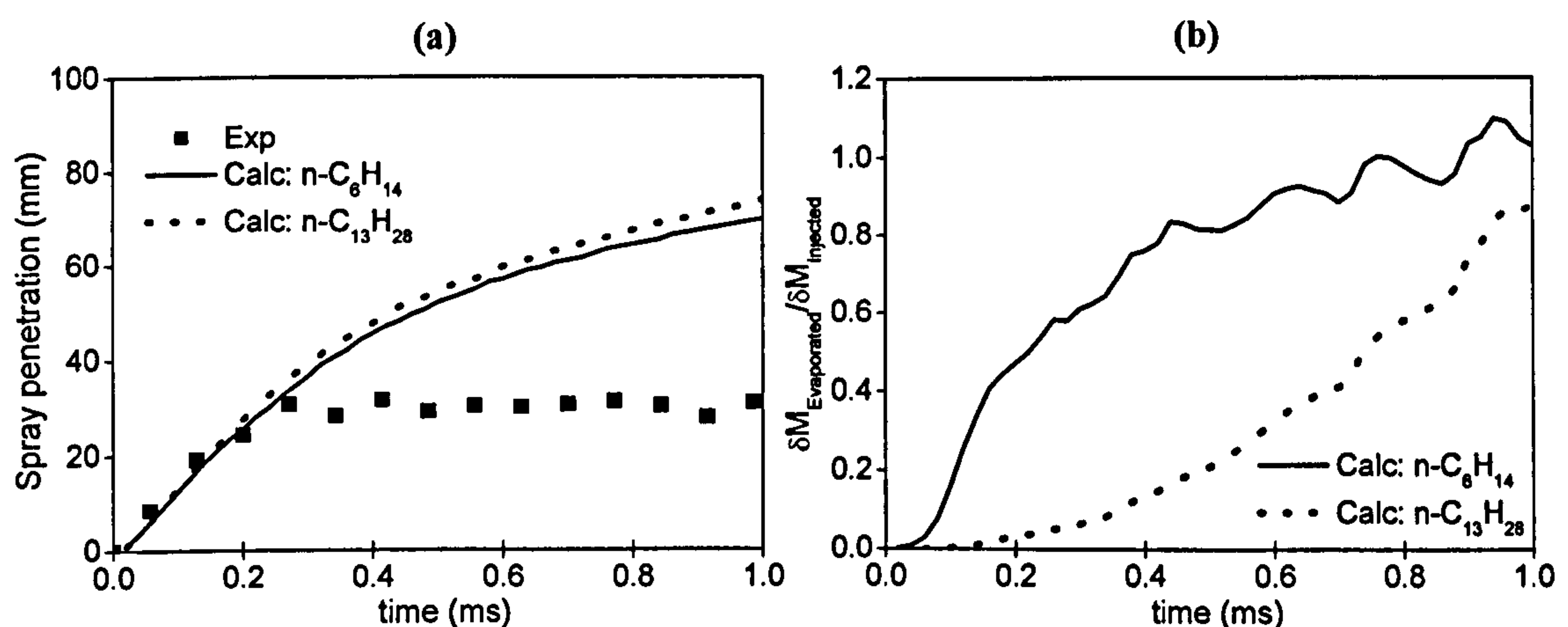


**Figure 5-26: Effect of fuel physical properties on temporal variation of (a) liquid penetration and (b) non-dimensional vaporization rate. Liquid core atomisation, droplet secondary break-up and droplet collisions models are de-activated [ $P_{INJ}=1200bar$ ].**

As explained before, this droplet size is rather small and no experimental evidence exists to confirm diesel spray mean droplet sizes around that small value. At the same



time, the scenario tested here was the more severe one where all fuel has been converted into a lighter component. In reality, one would expect that such effects may take place after some time and only if the fuel temperature increases above some physical limits associated with thermal decomposition. Thus, it can be concluded that even this possible explanation for the sufficient high evaporation rate leading to freezing of the liquid penetration is not adequate.

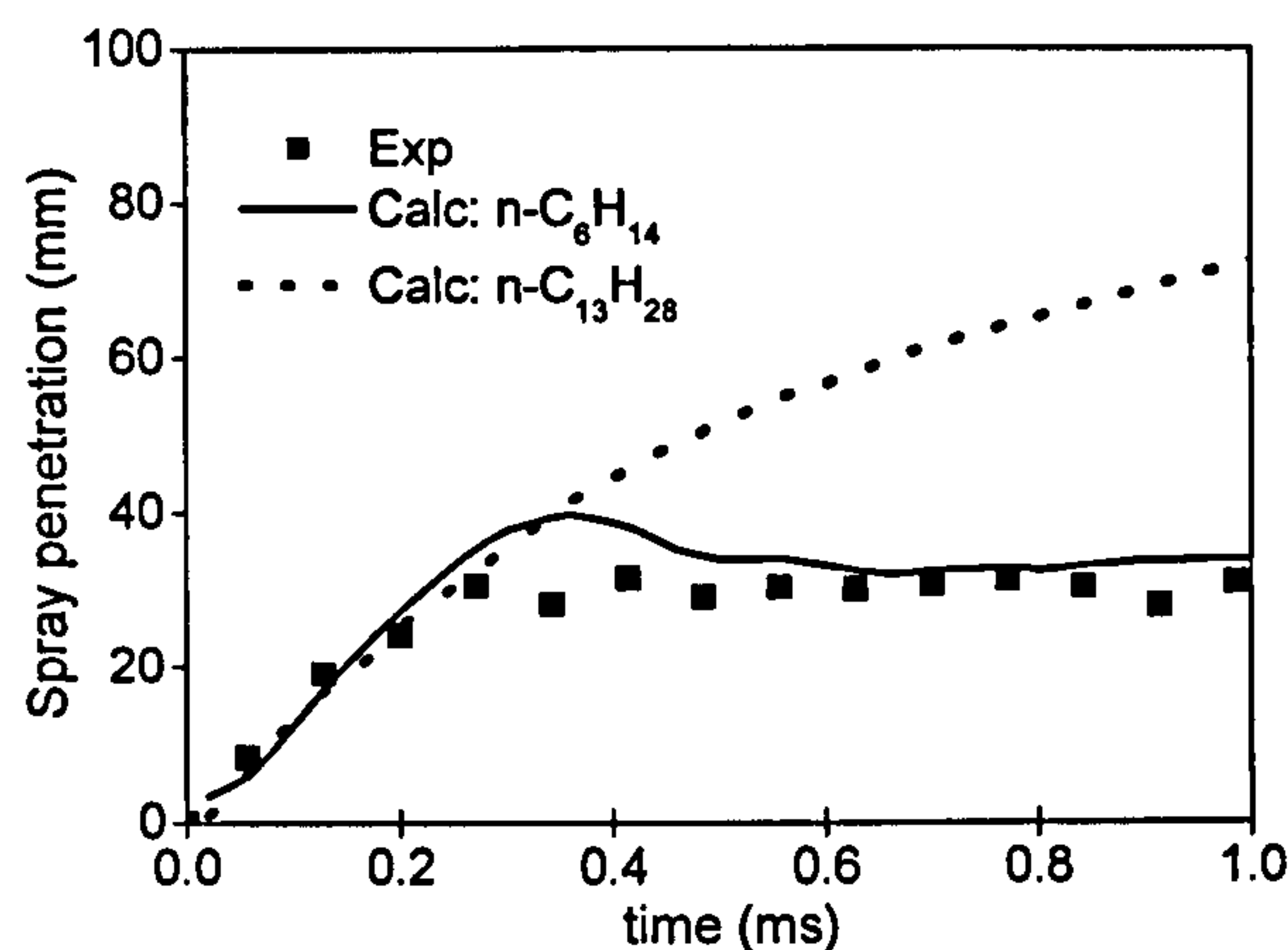


Figure 5-27: Effect of fuel physical properties on temporal variation of (a) liquid penetration and (b) spray SMD, using the 'Standard' spray model settings [ $P_{INJ}=1200\text{bar}$ ].

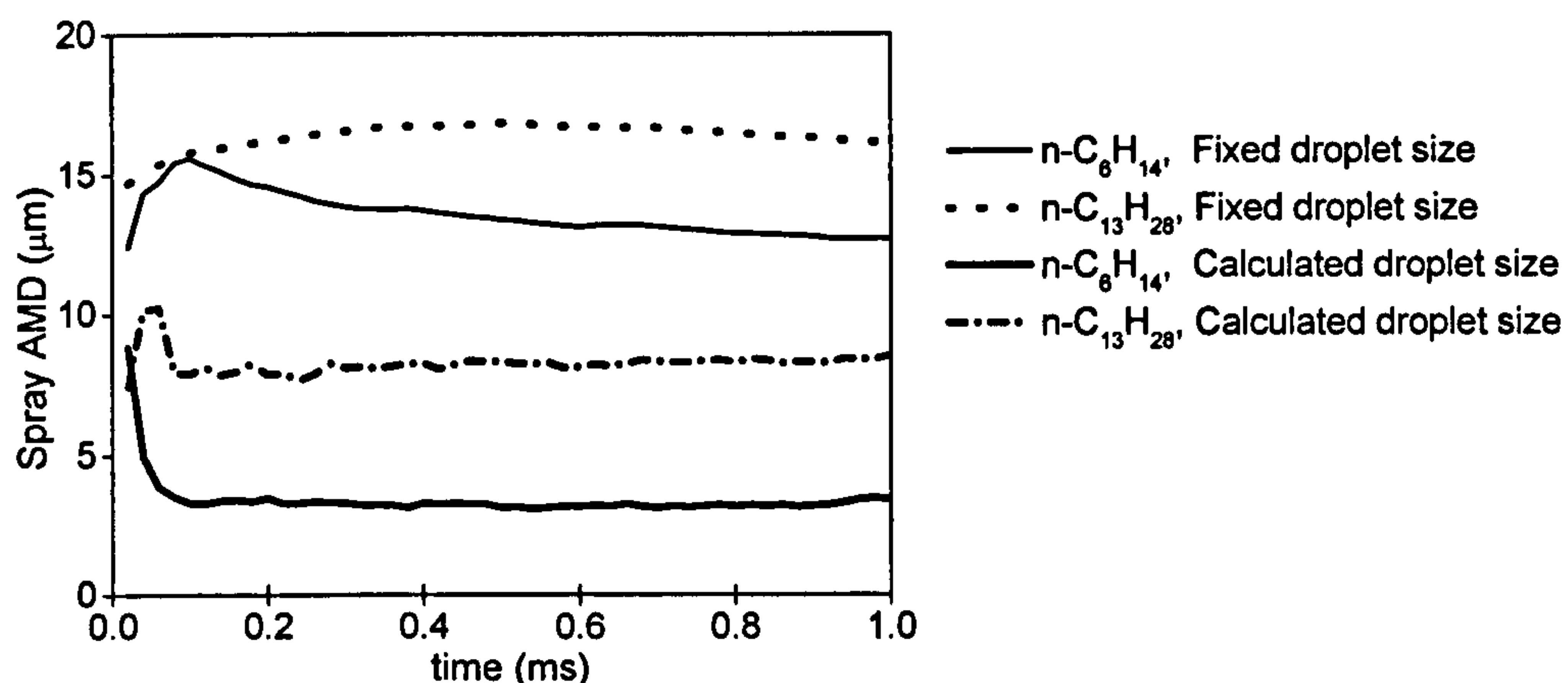
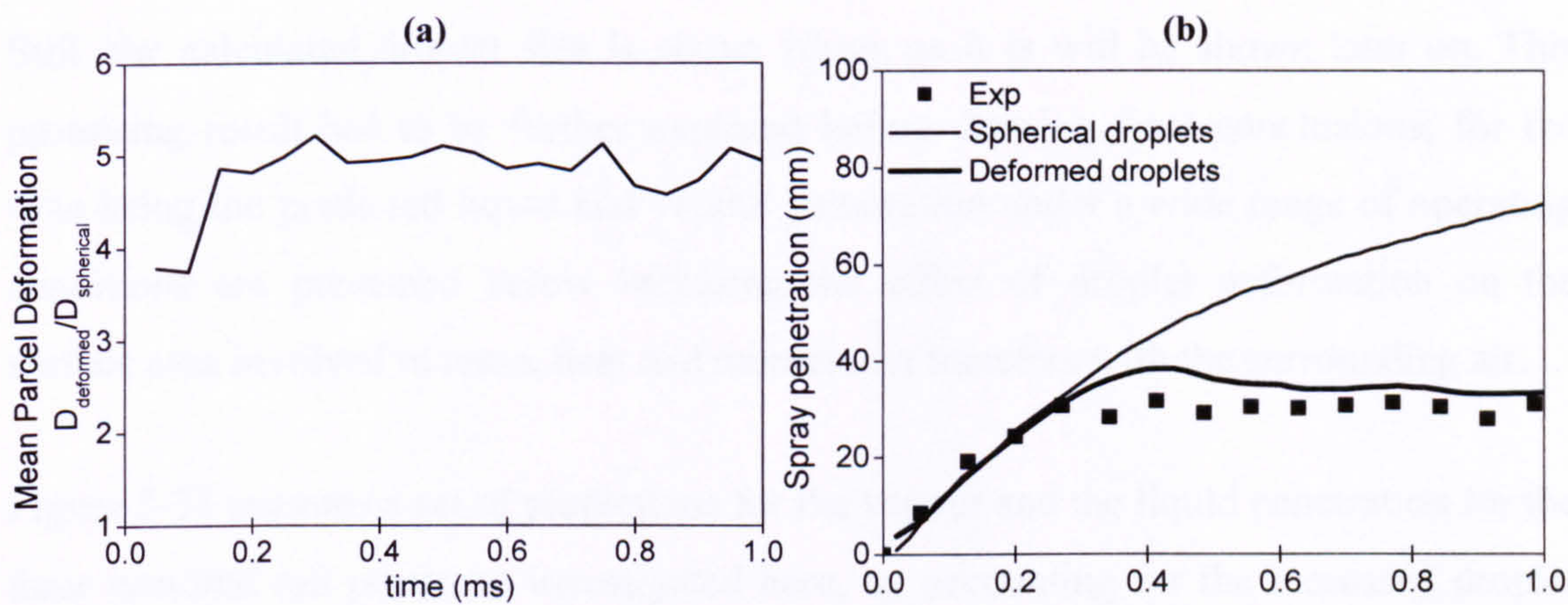


Figure 5-28: Predicted arithmetic mean diameter of the whole spray using different fuels and activating/de-activating droplet secondary break-up [ $P_{INJ}=1200\text{bar}$ ].

As already mentioned, a possible reason for increasing the vaporisation rate of the injected liquid is to consider that the surface area available for heat convection between the liquid and the surrounding air is not that of the spherical droplets but a sufficiently increased one. Experimental data on the break-up process of liquid droplets [180] suggest that during the time scales of those events droplets are actually at a highly deformed state, and empirical correlations exist for accounting those effects. Figure 5-29(a) shows the temporal variation of the predicted mean droplet deformation,



according to the break-up correlation described in Chapter 3. As can be seen, the mean of this distribution is around 5, which implies that the maximum surface area of the droplets available for heat and mass transfer with the surrounding air is of the order of 25 times higher than that of the spherical droplets. The liquid penetration profiles predicted assuming spherical particles and including the effect of droplet deformation are plotted in Figure 5-29(b). The graph confirms that the deformation contribution on the droplet surface area involved in the heat and mass transfers plays a remarkable role, since the corresponding results validate with a reasonably approximation the experimental data.



**Figure 5-29: Predicted (a) mean droplet deformation and (b) liquid penetration temporal profile, using the ‘Standard’ spray model settings and including the droplet deformation effect [ $P_{INJ}$ =1200bar].**

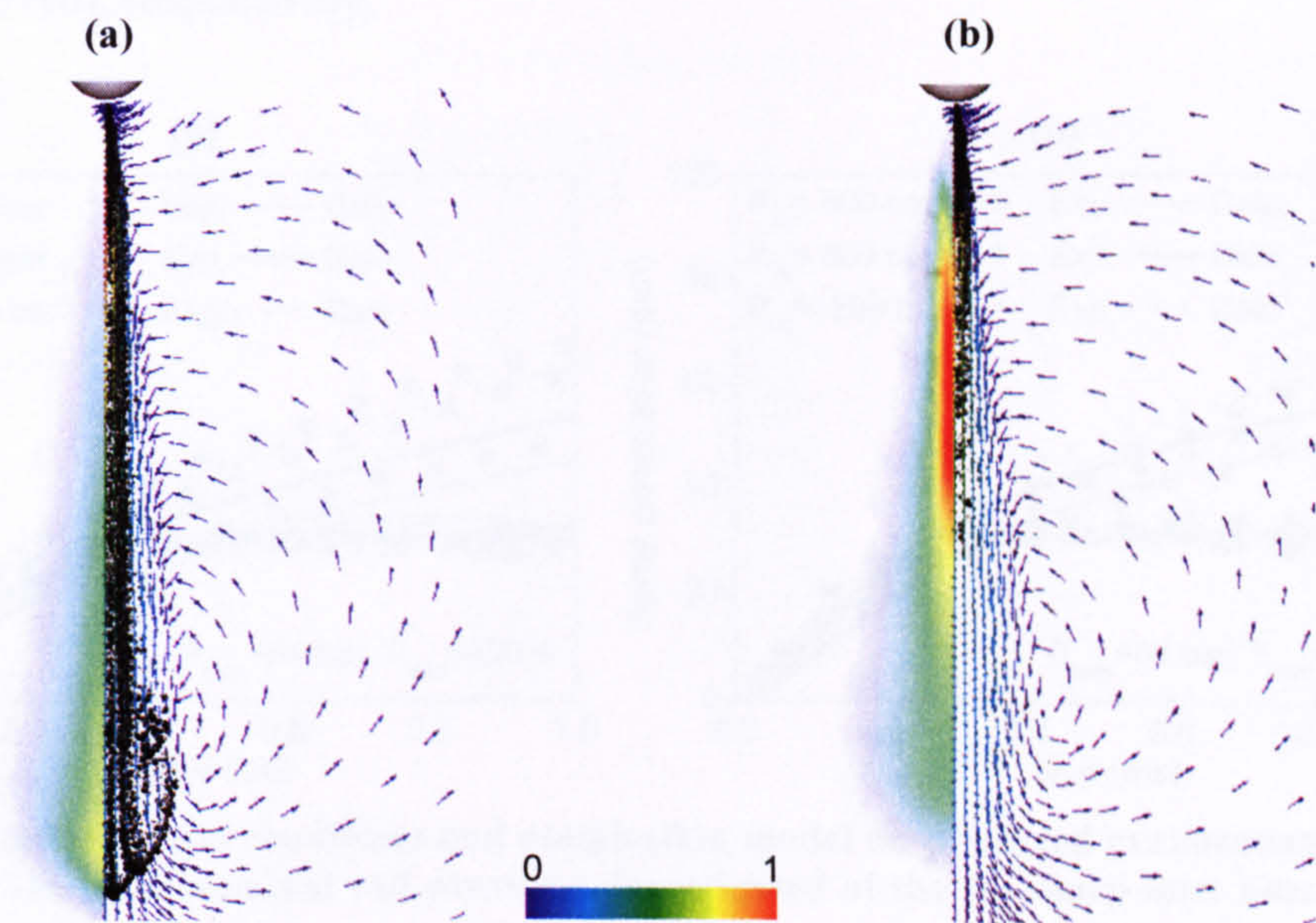


**Figure 5-30: Predicted liquid penetration (right), vapour penetration (left) and induced flow field (right) at 1ms ASOI (a) using the ‘Standard’ spray model settings and (b) including the droplet deformation effect [ $P_{INJ}$ =1200bar].**



Figure 5-30(a) and Figure 5-30(b) show the liquid and vapour distribution at 1ms after start of injection predicted by the model neglecting and including the effect of droplet deformation, respectively. The liquid phase scatter plots are presented on the right side of each picture together with the flow field vector distribution coloured according to the axial velocity, while the fuel vapour concentration is plotted on the left side. In case of spherical droplets the liquid and vapour penetration almost coincide, since the liquid penetrating in the gas phase convects the vaporised fuel further down. The graphs clearly show that the particle deformation dramatically affects the results, confirming that the liquid stops at a certain distance from the injector hole, where the maximum vapour concentration is present corresponding to the maximum vaporisation rate region. Still, the calculated droplet size is above  $10\mu\text{m}$ , as it will be shown later on. This promising result has to be further explored before drawing final conclusions; for the time being the predicted liquid and vapour penetration under a wide range of operating conditions are presented below including the effect of droplet deformation on the surface area involved in mass, heat and momentum transfers with the surrounding air.

Figure 5-31 presents a set of predictions for the vapour and the liquid penetration for the three nominal rail pressures investigated here, by accounting for the increased droplet surface area during the break-up process of the liquid. The injection conditions corresponding to cavitating and non-cavitating nozzle cases are shown in Figure 5-31(a) and Figure 5-31(b), respectively.

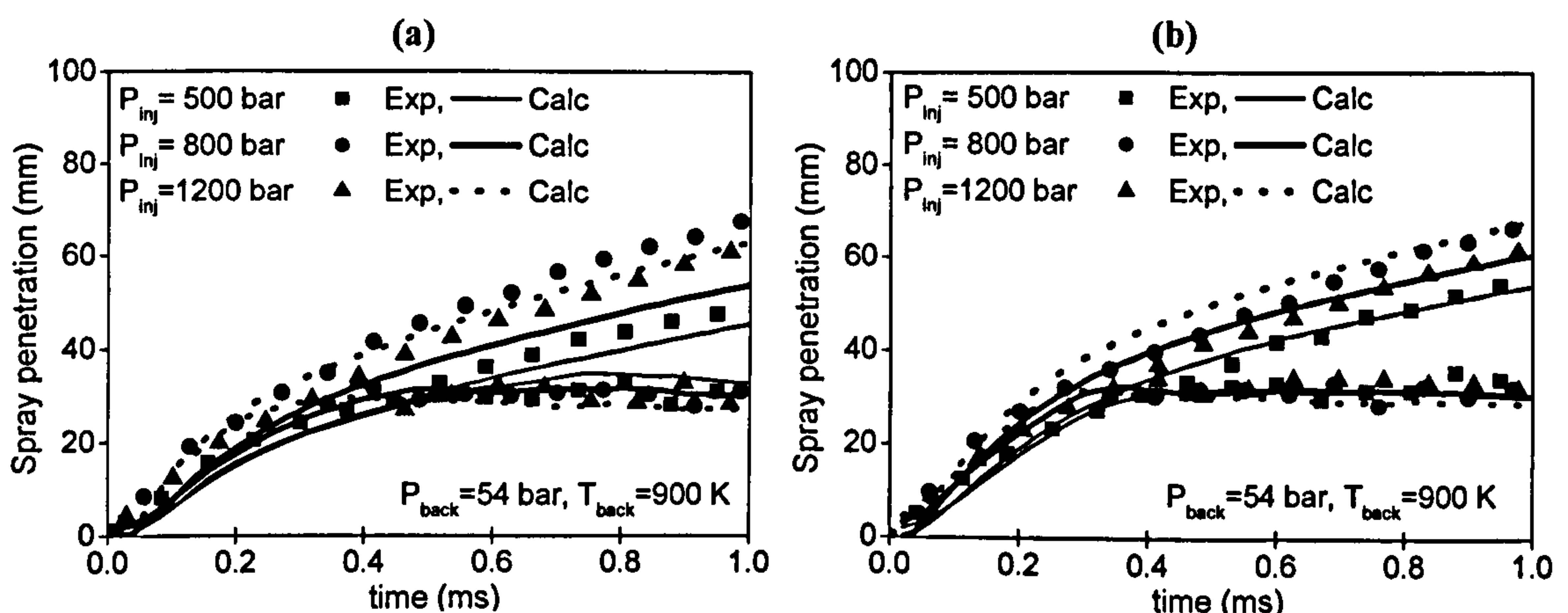


Figure 5-31: Effect of initial conditions and atomisation model on predicted evaporating spray tip penetration for the three nominal rail pressures investigated of the (a) sharp-inlet nozzle and (b) rounded-inlet nozzle.

As can be seen, the predicted liquid penetration actually stops at about the same time and at the same level as the experimental one and it is independent of the injection



pressure while the vapour penetration continuously increases with time. The predicted vapour penetration is higher with increased injection pressure, in agreement with the experimental observations.

Finally the comparison of the predicted spray shape against CCD images is presented in Figure 5-32, for the cavitating and the non-cavitating nozzle cases at 1.6ms after start of injection for the three nominal rail pressures considered. The results show a very good agreement between the simulations and the experiments in terms of spray structure and liquid-vapour penetrations and confirming the capability of the model to predict evaporating spray development under a wide range of operating conditions.

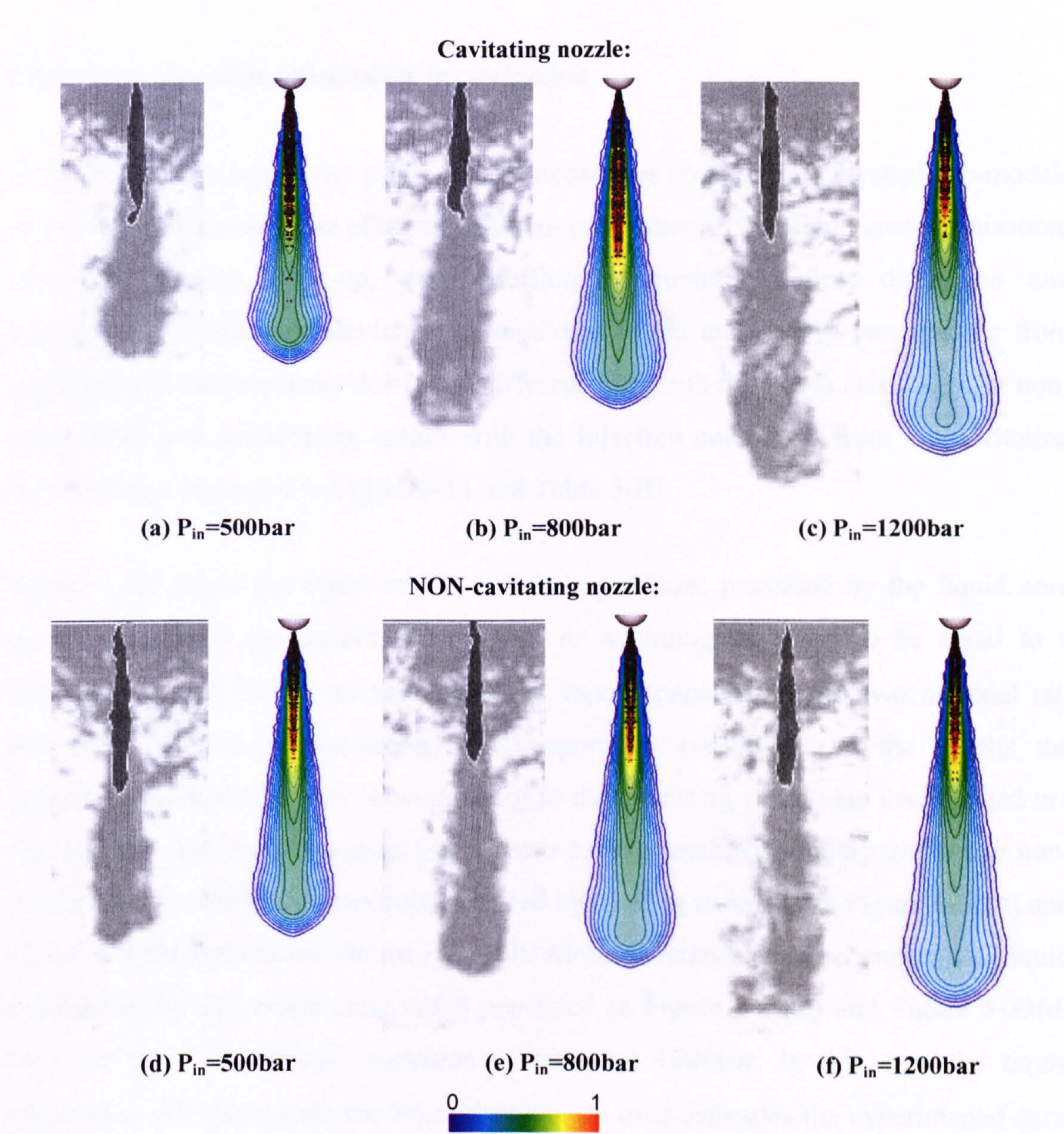


**Figure 5-32: Comparison between CCD images and predicted spray structures at 1.6ms ASOI for the (a,b,c) cavitating and the (d,e,f) non-cavitating nozzles for rail pressures of 500bar, 800bar and 1200bar under evaporating conditions.**



In the following two sections, the effect of the main sub-models used to resolve the spray development is investigated, in a similar way followed so far for the so called ‘standard’ spray model settings. Those include the effect of liquid core atomisation, secondary droplet break-up, drag coefficient, droplet turbulence dispersion and fuel evaporation models. Finally the sensitivity of the model predictions on the various numerical parameters is investigated focusing on the effect of the computational grid, the distribution of the source terms expressing the interaction between the liquid and gas phases, the interpolation of the continuous phase variables at the parcel location, the time step for the continuous and the dispersed phase numerical solution algorithms and the temporal/spatial discretisation schemes implemented in the code.

#### 5.3.4 Spray physical sub-models investigation

In this section the sensitivity of the model predictions on the spray physical sub-models is presented, discussing the effect of different correlation in the liquid core atomisation, secondary droplet break-up, drag coefficient, droplet turbulent dispersion and evaporation models. The deviation of predicted liquid and vapour penetrations from experimental measurements due to the different spray sub-models is calculated for non-evaporating and evaporating sprays with the injection conditions from the cavitating nozzle design presented in Figure 5-11 and Table 5-III.

Figure 5-33 shows the effect of the initial droplet size, predicted by the liquid core cavitation-induced atomisation model [76] or assuming its SMD to be equal to a constant value of  $50\mu\text{m}$ , on the liquid and vapour penetrations for two nominal rail pressures, under non-evaporating and evaporating conditions. In the graphs the experimental measurements corresponding to the operating conditions investigated are also plotted. The results suggest that the two models predict a similar trend under non-evaporating conditions, as can be deduced by looking to results in Figure 5-33(a) and Figure 5-33(b), which are almost identical. More differences can be seen in the liquid penetration for the evaporating cases presented in Figure 5-33(c) and Figure 5-33(d) with the two nominal rail pressures of 500 and 1200bar. In this case the liquid penetration calculated with the  $50\mu\text{m}$  droplet size over-estimates the experimental data, while the cavitation induced atomisation model is capable to predict the right penetration. A possible explanation is related to the effect of droplet secondary break-



up. The droplet size estimated by the break-up model without the contribution of the atomisation modelling is 20% bigger than the value predicted implementing the cavitation-induced atomisation model, as shown in Figure 5-34 for the nominal rail pressure of 500 and 1200bar. These differences do not affect the liquid penetration under non-evaporating conditions, possibly because the drag effect is similar for the range of droplet size present, while they play a major role in the vaporisation modelling.

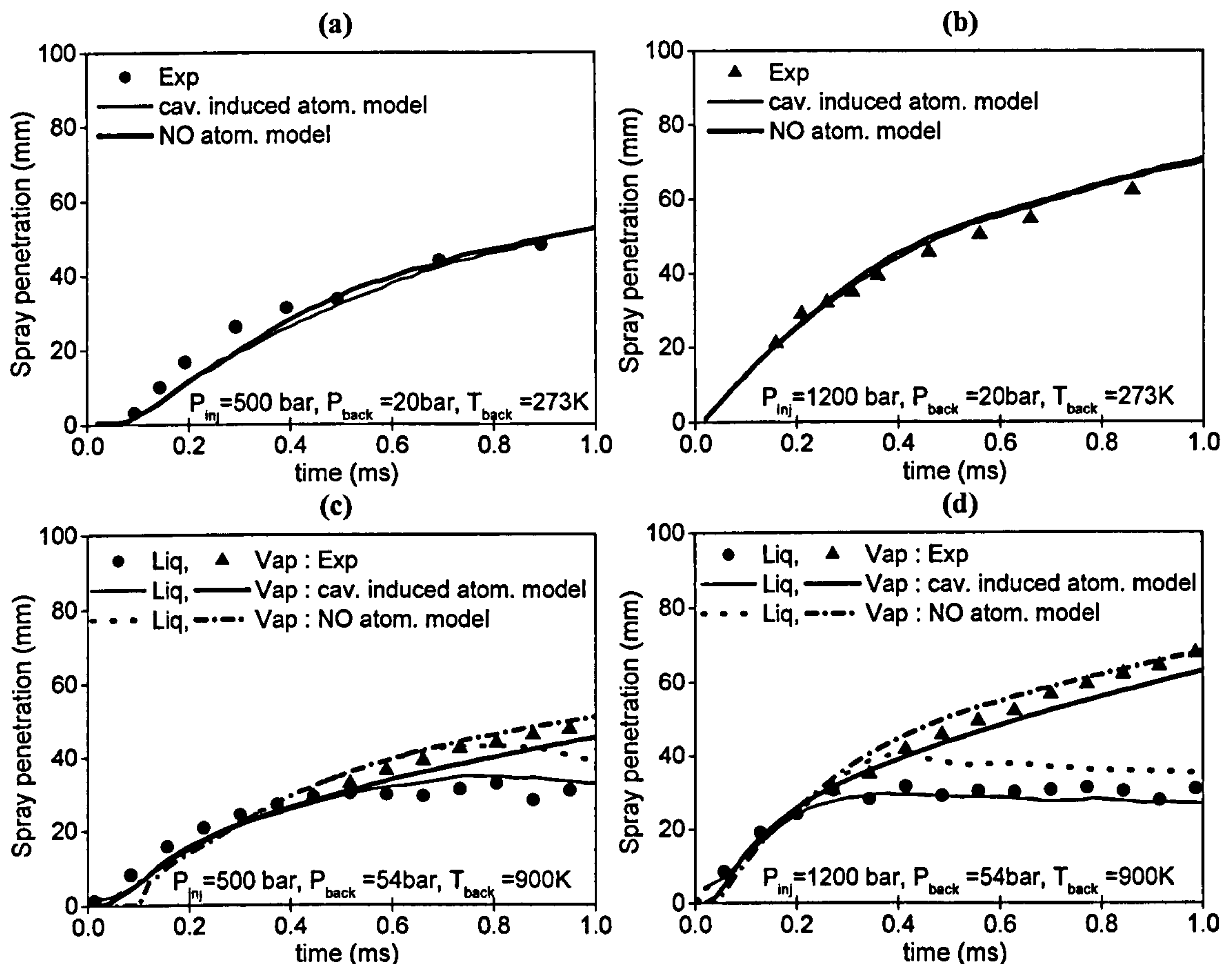


Figure 5-33: Effect of atomisation model on liquid and vapour penetration for non-evaporating sprays with (a)  $P_{INJ}=500$ bar and (b)  $P_{INJ}=1200$ bar and for evaporating sprays with (c)  $P_{INJ}=500$ bar and (d)  $P_{INJ}=1200$ bar.

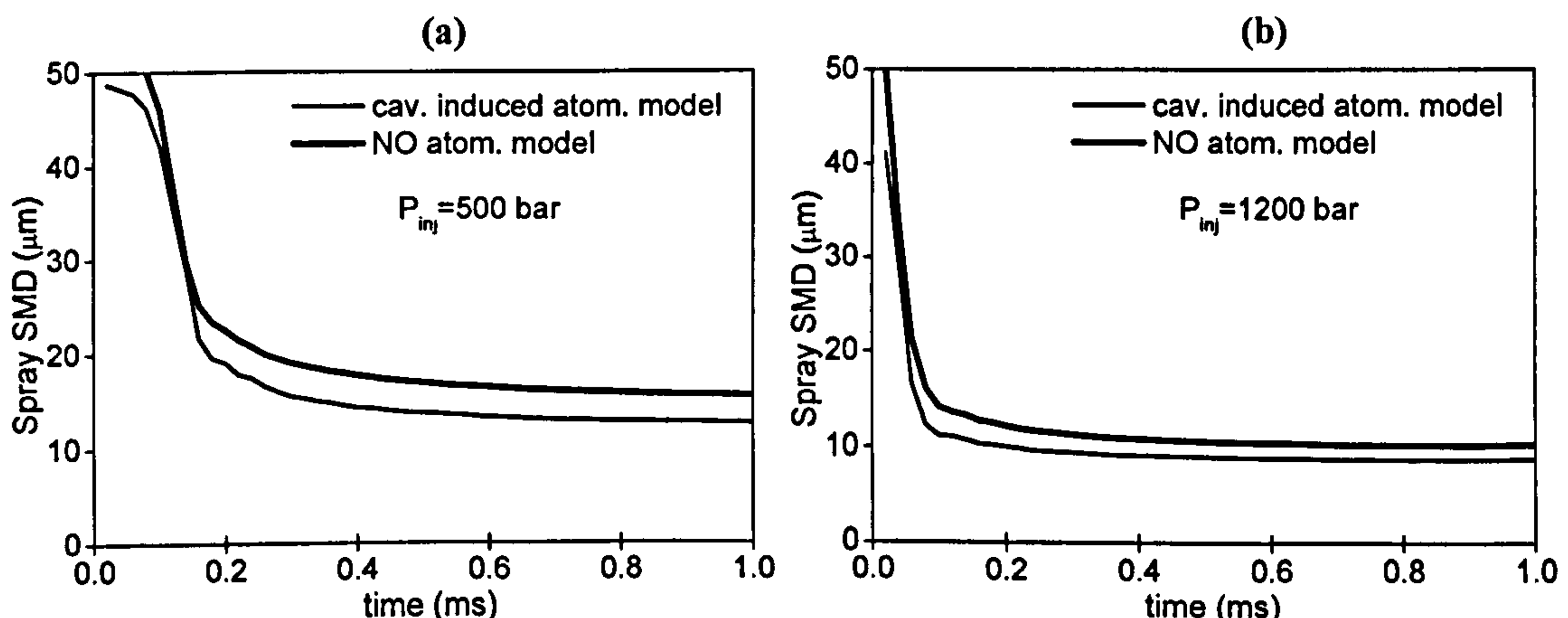
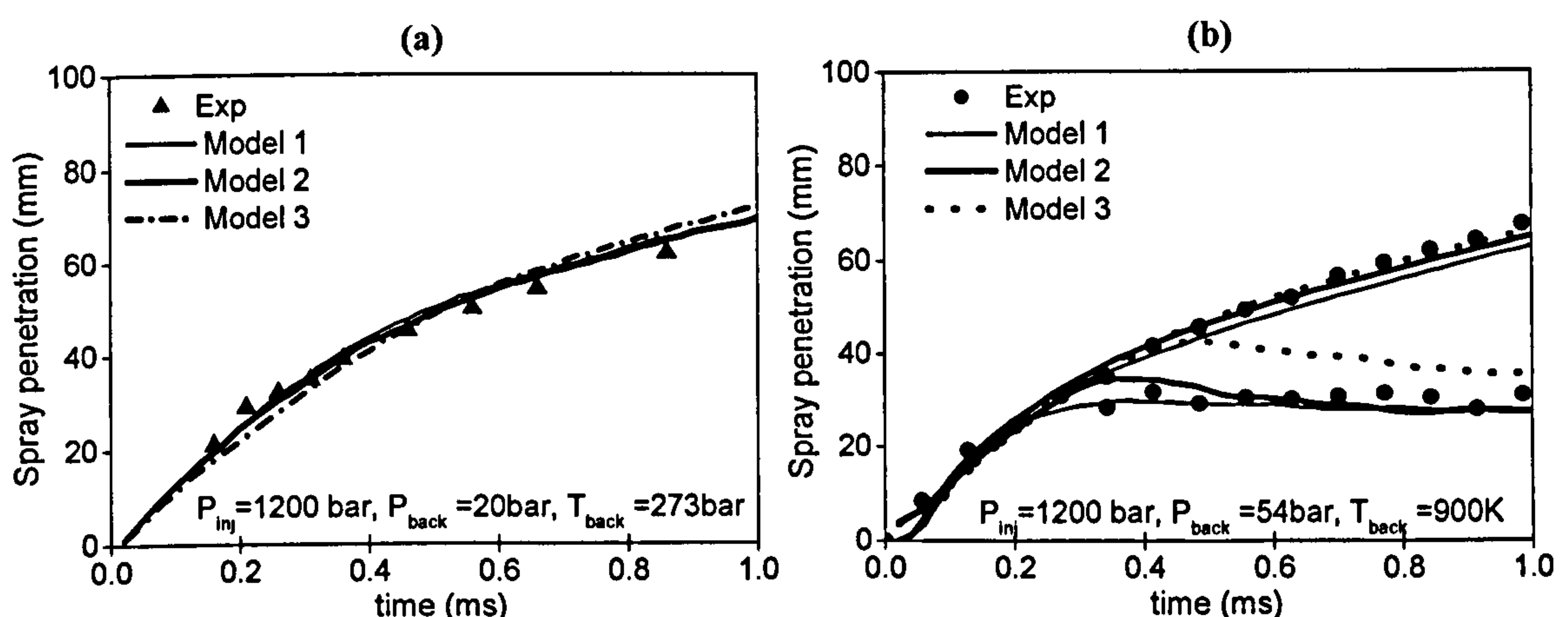


Figure 5-34: Effect of atomisation model on the spray SMD predicted by the droplet secondary break-up for (a)  $P_{INJ}=500$ bar and (b)  $P_{INJ}=1200$ bar.



Atomisation is known to be the first physical process taking place following the injection of the fuel from the nozzle. Unfortunately, at present only limited quantitative experimental information exist for the spray structure very near to the injector hole exit. Thus, models can be used to provide evidence for the characteristics of the droplets formed during that process. Figure 5-35(a) and Figure 5-35(b) present the effect of two atomisation models and two different ways of distributing the liquid mass within the spray cone angle on the liquid penetration, for non-evaporating and evaporating conditions, respectively, with the nominal rail pressure of 1200bar. The first model, Model 1 in the legend, implements the cavitation-induced atomisation, reported in Arcoumanis et al. [76]. In this model, the liquid droplets have been non-uniformly distributed within the spray cone angle. In particular, it has been assumed that the probability to find a liquid droplet close to the spray axis of symmetry is proportional to its size. In this way, relatively larger droplets are found closer to the core of the spray and smaller ones at the periphery. The second model, Model 2, uses the same cavitation-induced atomisation model, but this time the liquid droplets are uniformly distributed within the spray cone angle independently on their size. Finally, the third model, Model 3, used is the turbulence-induced atomisation for all the injection period with the liquid droplets non uniformly distributed within the spray cone angle independently of their size.



**Figure 5-35: Effect of atomisation model and atomisation angle on temporal variation of liquid and vapor penetration of (a) non-evaporating and (b) evaporating spray from the sharp-inlet nozzle [ $P_{INJ}=1200$ bar].**

As can be seen, there is no noticeable difference between the two cavitation-induced atomisation models, while the turbulence-induced atomisation model substantially over-predicts the liquid penetration and it is not recommended for predicting sprays from



cavitating nozzles. Looking at the liquid penetration under evaporating conditions estimated by the liquid cavitation-induced atomisation model assuming uniform distribution of liquid within the spray cone, Model 2 in Figure 5-35(b), it shows a slightly higher penetration in the interval between 0.3 and 0.5ms after start of injection compared to the profile predicted by the Model 1. This is due to the fact that the spray velocity calculated assuming a radial distribution of liquid within the spray cone is higher close to the spray axis, which leads to slightly higher vaporisation rate during the early time steps after start of injection as confirmed by the following figures.

The normalised vaporisation rate for the evaporating case is presented in Figure 5-36(a); it shows that this becomes equal to the injection rate at about 0.25ms after start of injection, with a small delay in case of uniformly distributed liquid droplets within the spray cone angle independently of their size. Following that time, it takes about 0.2ms until the liquid penetration stops. The evaporation rate equals the injection rate only after 0.4ms after start of injection when the turbulence-induced atomisation model is implemented and this explain the over-predicted liquid penetration shown in Figure 5-35(b). Finally, Figure 5-36(b) shows that the spray SMD is of the order of  $13\mu\text{m}$ , implementing the two cavitation-induced atomisation models, while a value around  $18\mu\text{m}$  is predicted using the third model. It has to be noted that the spray droplet size is mainly determined by droplet secondary break-up and vaporisation effects rather than by the liquid atomisation, since this is completed within a distance less than 0.5mm from the nozzle hole exit according to model predictions [282].

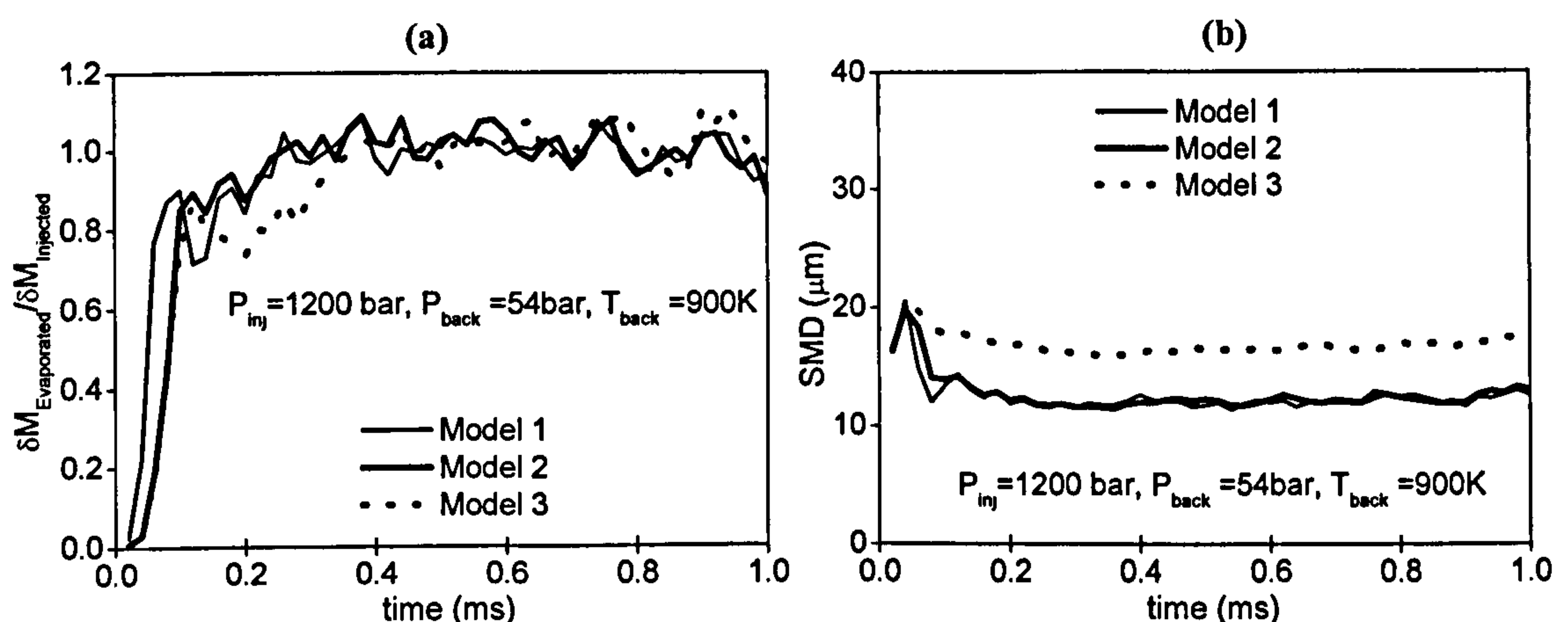


**Figure 5-36: Effect of atomisation model and atomization angle on temporal variation of (a) non-dimensional vaporization rate and (b) spray SMD of evaporating spray from the sharp-inlet nozzle [ $P_{INJ}=1200\text{bar}$ ].**



The structure of the spray predicted deactivating or including the secondary droplet break-up model of Arcoumanis et al. [76] is shown in Figure 5-37, for non-evaporating and evaporating sprays with 1200bar nominal rail pressure at 1ms after start of injection. The graphs show the liquid scatter plots, coloured in black with size proportional to the droplet diameter, the gas-phase velocity for the non-evaporating cases and fuel vapour concentration for the evaporating ones and the flow field vectors. Figure 5-37(a/c) show the results of the predictions without the break-up model, while Figure 5-37(b/d) include the break-up contribution. The colour scale is normalised with the maximum value of the corresponding variable plotted. The results show that the break-up model plays a dramatic role in the simulation of the spray, predicting smaller droplets, which penetrate less and vaporise faster. In particular the sensitivity on the liquid and vapour penetration of the implementation of the droplet secondary break-up model [76] is presented in Figure 5-38(a) and Figure 5-38(b) for the non-evaporating and the evaporating cases, respectively. The graphs present the comparison between the predictions obtained with the selected break-up model [76] and the liquid and vapour penetrations calculated deactivating the model.

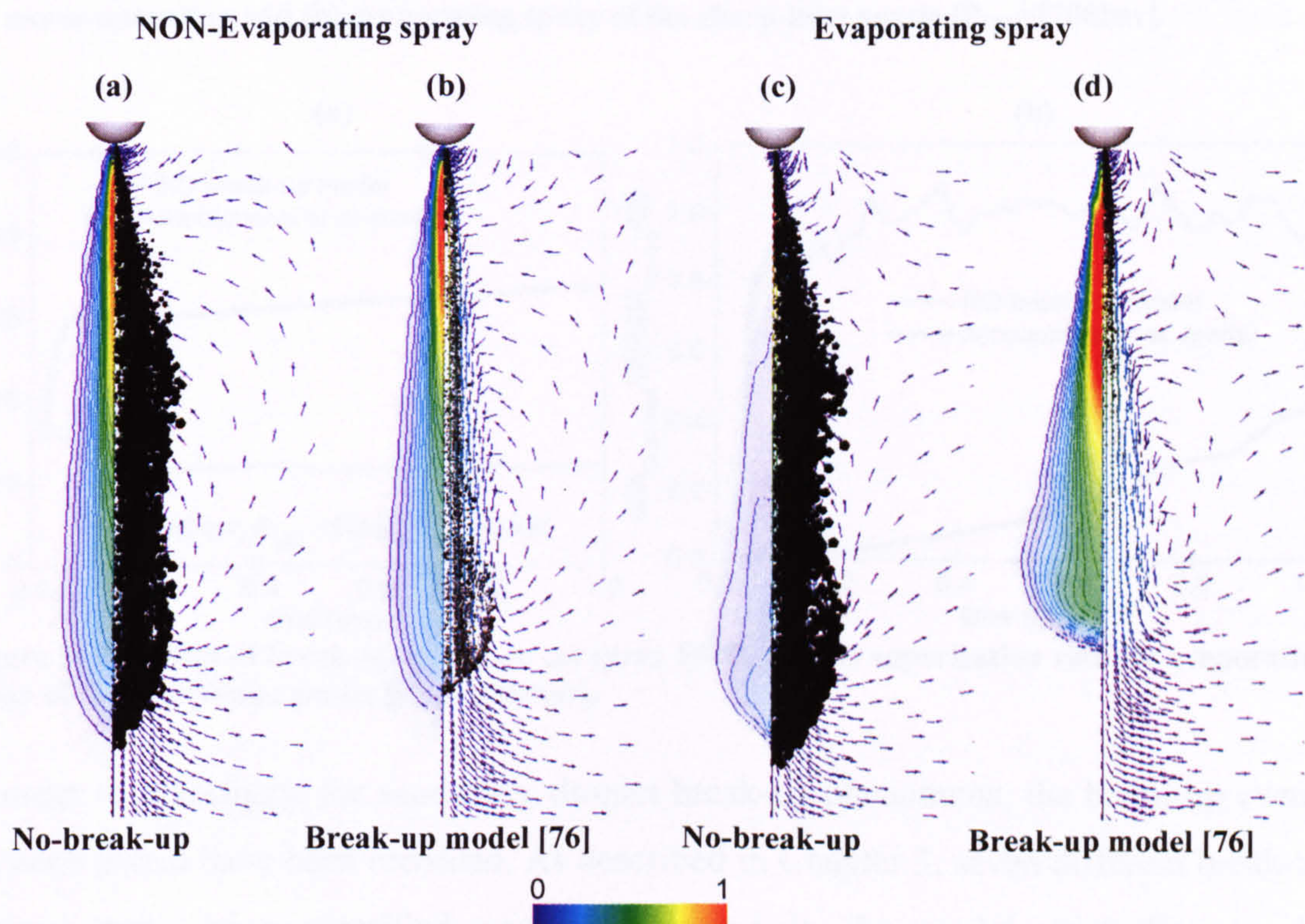


**Figure 5-37:** Predicted liquid penetration (right), (a/b) flow field axial velocity or (c/d) vapour penetration (left) and induced flow field (right) (a/c) at 1ms ASOI, deactivating and (b/d) including the droplet secondary break-up model of Arcoumanis et al. [76], for (a/b) non-evaporating and (c/d) evaporating spray [ $P_{INJ}=1200\text{bar}$ ].



The results suggest that the secondary break-up process has significant effect on the liquid and vapour penetration particularly under evaporating conditions. Figure 5-38(b) shows that the liquid penetration predicted without the contribution of droplet secondary break-up doesn't freeze at a constant value as the experimental data confirm. This trend can be explained by the presence of large liquid droplets, as shown by the spray SMD profiles in Figure 5-39(a), which do not undergo successive fragmentation and are characterised by very low vaporisation rate, according to Figure 5-39(b).

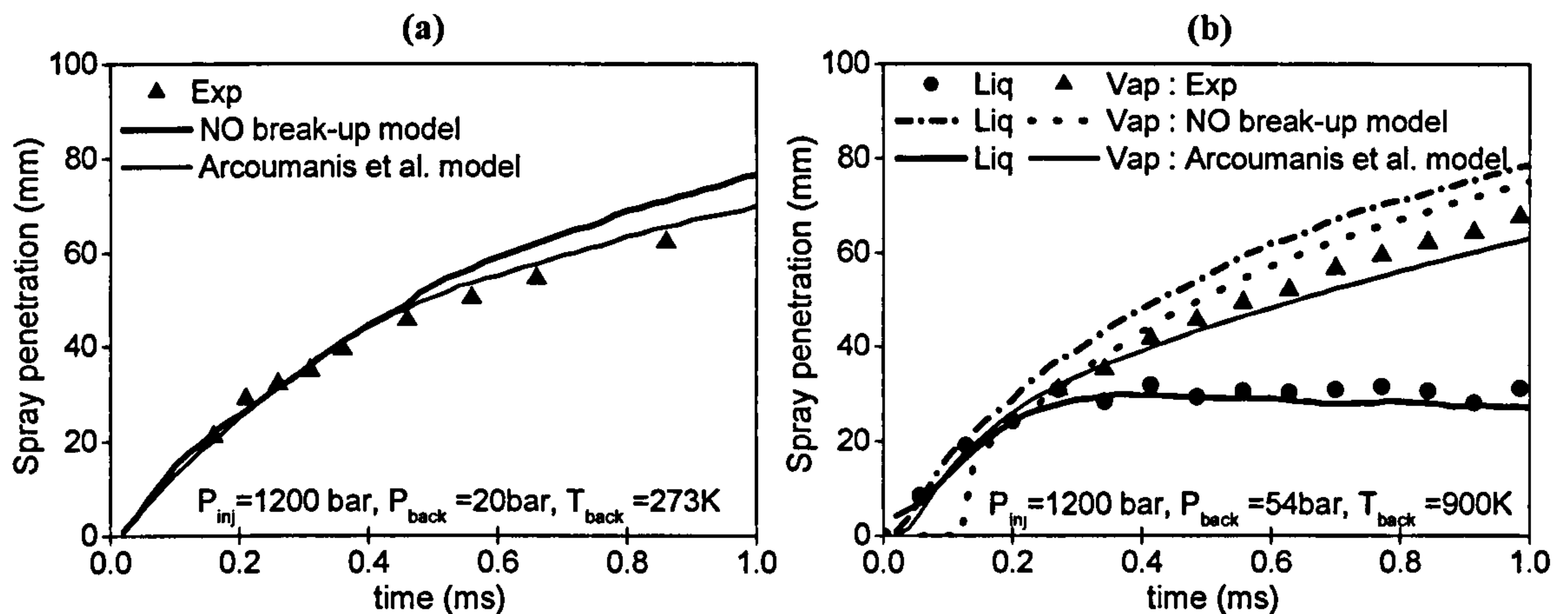


Figure 5-38: Effect of break-up model on temporal variation of liquid and vapour penetration of (a) non-evaporating and (b) evaporating spray of the sharp-inlet nozzle [ $P_{INJ}=1200\text{bar}$ ].

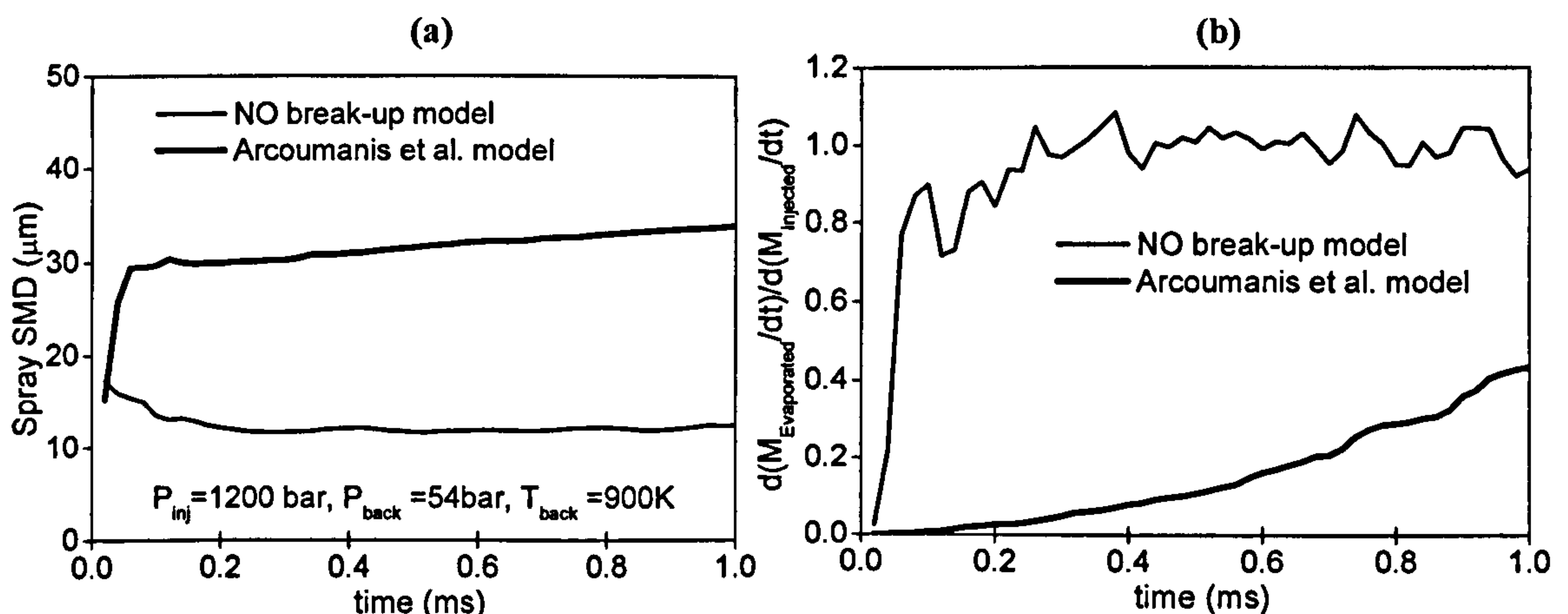
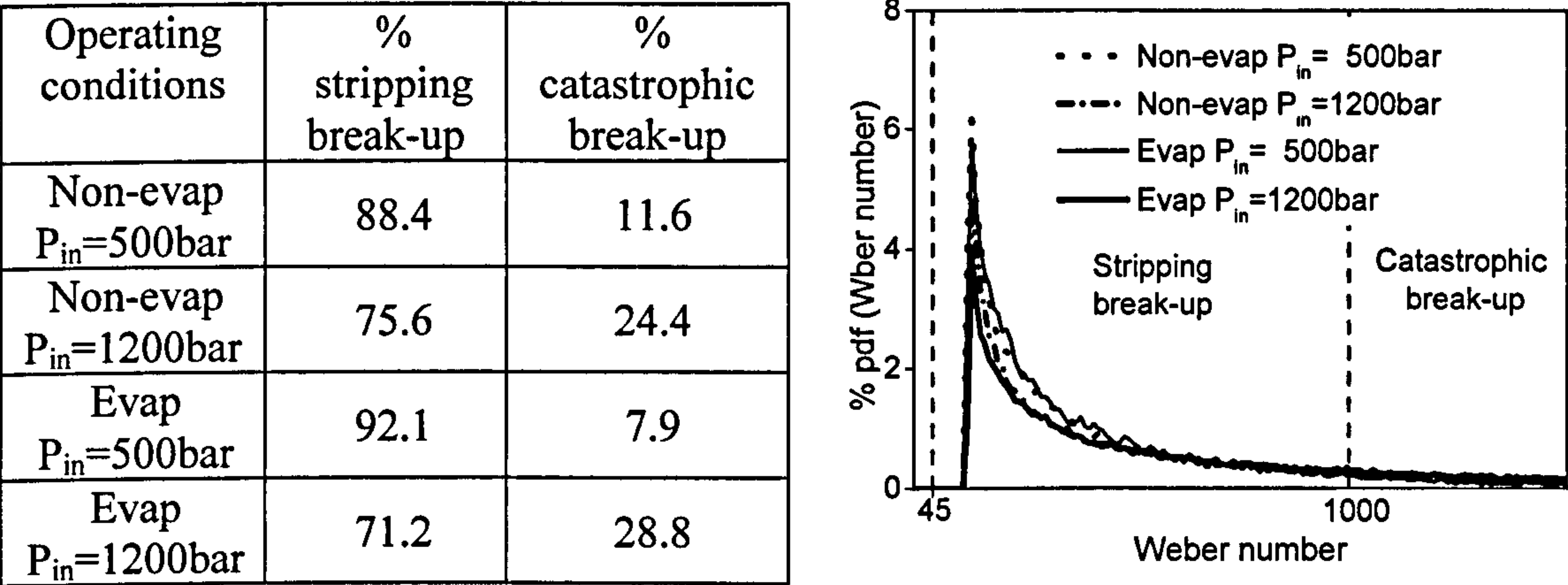


Figure 5-39: Effect of break-up model on (a) spray SMD and (b) vaporisation rate for evaporating spray of the sharp-inlet nozzle [ $P_{INJ}=1200\text{bar}$ ].

In order to investigate the secondary droplet break-up phenomena, the break-up events for each parcel have been recorded. As described in Chapter 3, seven different break-up regimes have been classified and implemented in the model, according to the instantaneous droplet Weber number; for purposes of simplicity the first four regimes, vibrational, bag, bag and steamer and chaotic, have been grouped under the 'chaotic mode', which occurs in droplets with Weber number less than 45, the sheet stripping



and wave crest stripping are grouped under the ‘stripping mode’, occurring with Weber number from 45 up to 1000 and the catastrophic regime when Weber number is above 1000. Figure 5-40 shows the percentage of the occurring of droplet secondary break-up events according to the different regimes and the droplet Weber number distributions along the injection period for the non-evaporating and evaporating sprays with low and high nominal rail pressures of 500 and 1200bar. As can be seen from the graphs, only stripping and catastrophic regimes are recorded for all the operating conditions investigated and this is confirmed by the minimum calculated Weber number, equal to 100. The results suggest that the majority of the break-up events occur according to the stripping mode, particularly for low injection flow rate conditions.



**Figure 5-40: (left) Percentage of occurring of different secondary droplet break-up events and (right) droplet Weber number distribution along the injection period for non-evaporating and evaporating sprays with nominal rail pressure of 500 and 1200 bar.**

Further investigations on the distance from the injector hole where break-up occurs reveal that independently of the operating and evaporating conditions, the droplets fragment within a distance of 20mm, with a pick at 10mm from the injector, as shown in Figure 5-41(a). In particular the percentage of occurring of the break-up events according to the specific mode is presented in Figure 5-41(b) for non-evaporating and evaporating sprays with 1200bar nominal rail pressure. The graphs show that the catastrophic regime takes place within 15mm from the injector, with a pick at 8mm, while the stripping regime occurs even further down, up to 20mm distance from the hole exit.



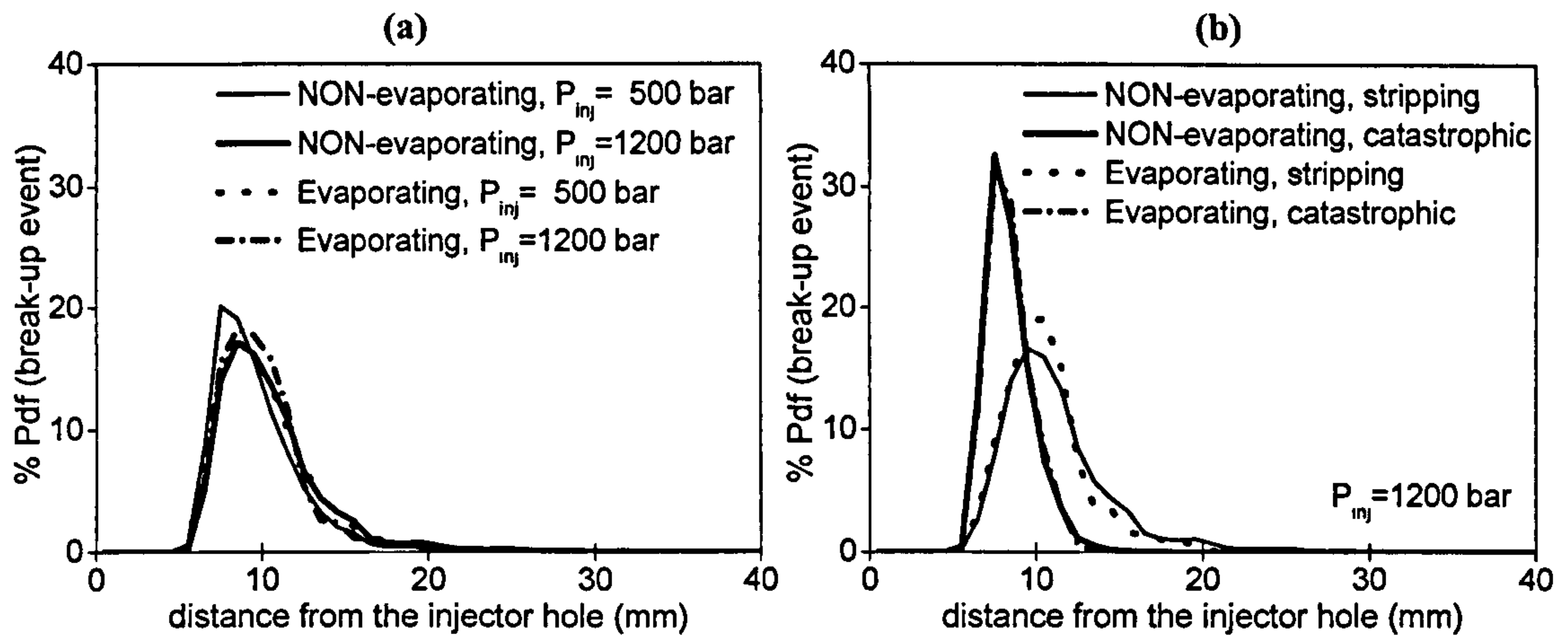


Figure 5-41: Percentage of break-up event as function of the distance from the injector (a) for non-evaporating and evaporating sprays and (b) for different break-up mode and evaporating conditions [ $P_{INJ}=1200$ bar].

Successive investigations focus on the role of the drag coefficient model on the temporal liquid and vapour penetration of non-evaporating and evaporating diesel sprays. Its effect is shown in Figure 5-42 for the nominal rail pressure of 1200bar. Four models have been implemented for the purposes of the present investigation. Similarly to Figure 5-23, where the drag model effect has been investigated for evaporating case without the contribution of droplet deformation on the vaporisation rate, the ‘Model 1’ corresponds to the classical correlation for solid particle, the ‘Model 2’ takes into account the flow circulation inside the spherical liquid droplet, the ‘Model 3’ corrects the drag coefficient calculated by the ‘Model 2’ considering the presence of other droplets, while ‘Model 4’ simulates the effect of highly distorted droplet on the mass, momentum and heat transfers with the surrounding air.

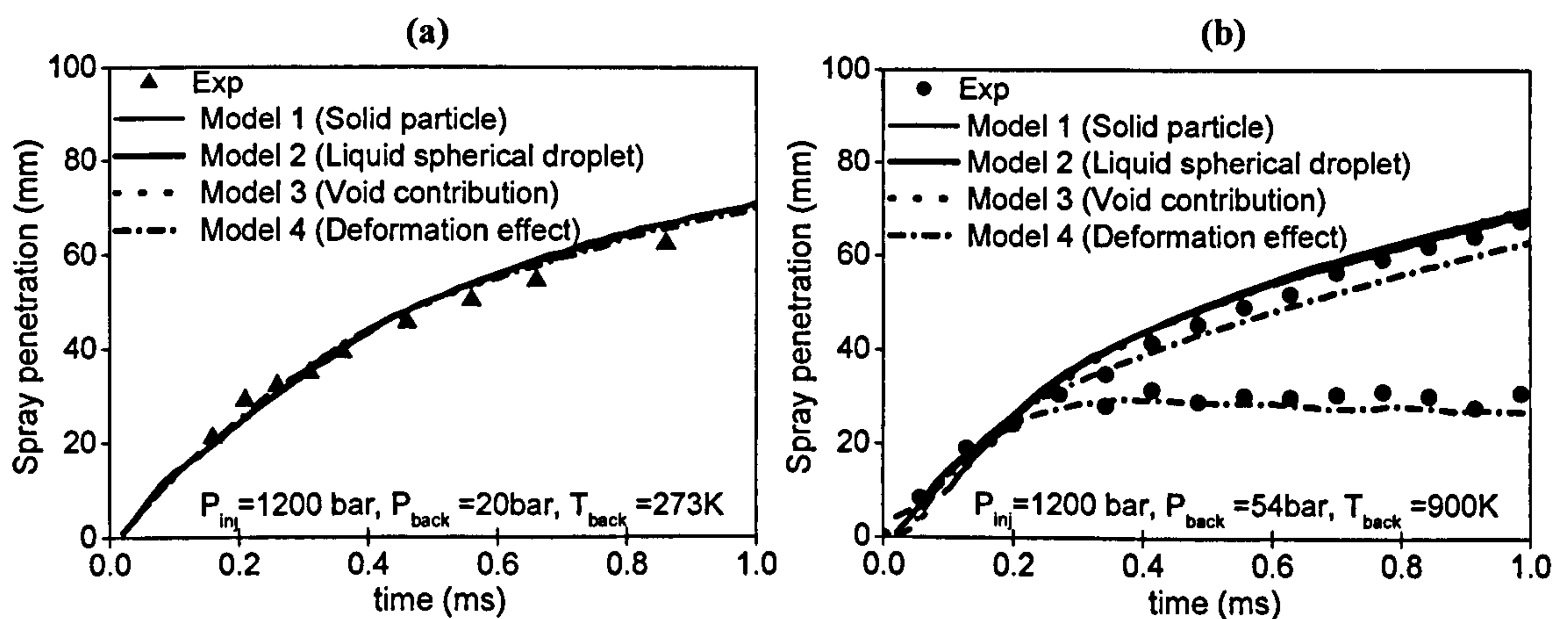


Figure 5-42: Effect of drag coefficient model on liquid and vapor penetration profiles of (a) non-evaporating and (b) evaporating spray of the sharp-inlet nozzle [ $P_{INJ}=1200$ bar].



Clearly any noticeable differences can be appreciated in the temporal profiles of non-evaporating sprays using the four different correlations for the drag model, as shown in Figure 5-42(a), on the other hand the results presented in Figure 5-42(b) for the evaporating case suggest that only the 'Model 4', which includes the contribution of liquid droplet deformation, can predict the correct trend for the liquid penetration. The other three models fail in the calculation of the vaporisation rate, which is severely under-estimated, resulting in almost indistinguishable liquid and vapour penetrations.

The turbulent nature of the gas flow may have a strong influence on the droplet movement and the spray development. Different models have been published to account for the interaction of the liquid droplets with the turbulent characteristics of the continuum phase. Three of them have been selected for investigation here, and the corresponding results are presented in Figure 5-43 for the evaporating spray model with nominal rail pressure of 1200bar. The results from the models of O'Rourke [197], Langevin [198] and Gosman et al. [195] are presented together with the predictions obtained without the contribution of the turbulent dispersion, suggesting that the phenomenon seems to have no remarkable effect on the liquid and vapour penetrations for diesel spray evaporating in high pressure and temperature environments.

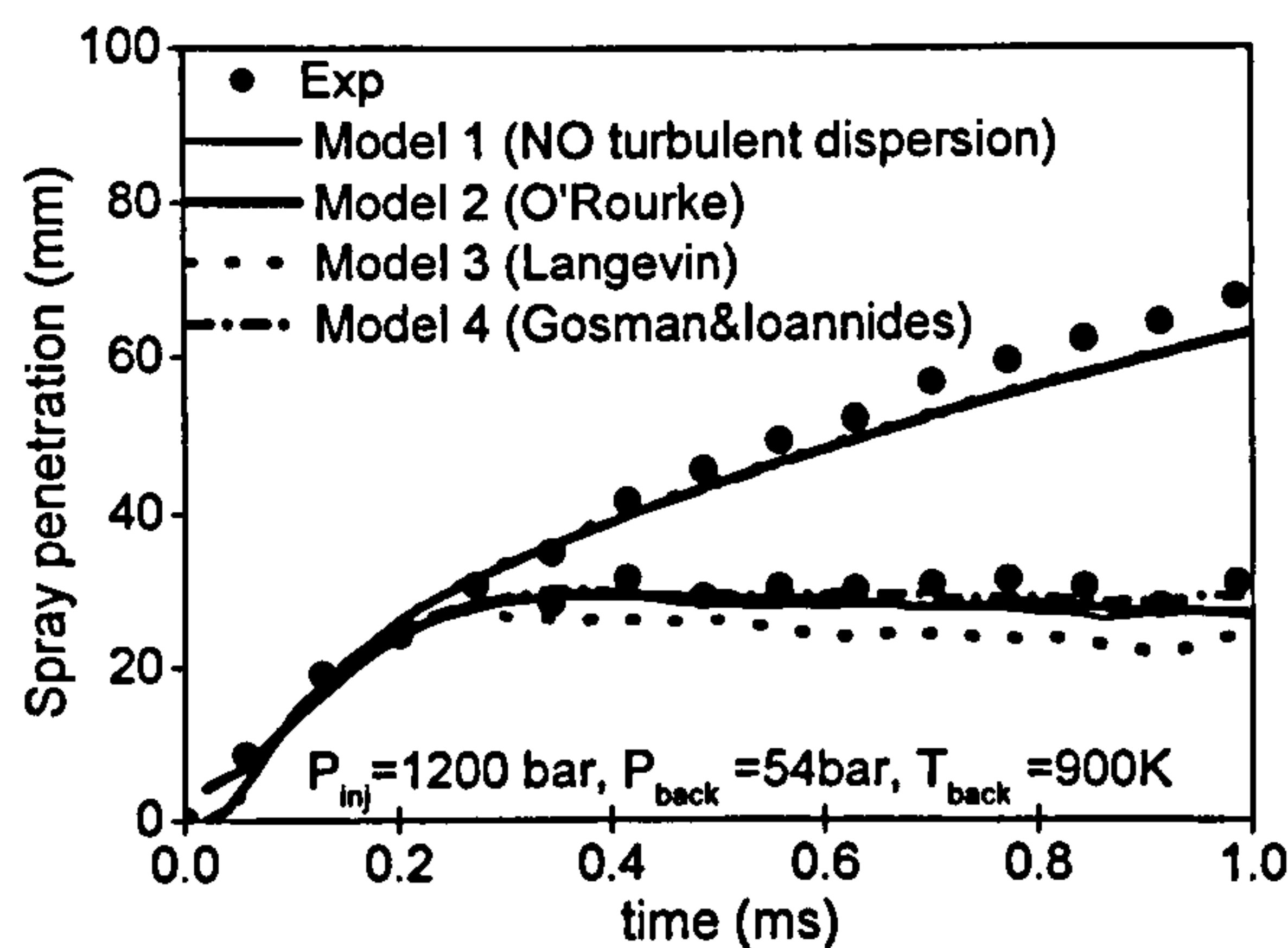


Figure 5-43: Effect of droplet turbulent dispersion model on temporal variation of liquid and vapour penetration of the sharp-inlet nozzle [ $P_{INJ}=1200\text{bar}$ ].

As already mentioned in the previous sections of the chapter, after the disintegration of the liquid jet emerging from the injection nozzle, the formed droplets may further break-up as they move into the surrounding gas. Meanwhile, the non-uniform pressure distribution developing around the liquid droplets resulting from the relative velocity between them and the gas and the enhanced motion within the droplet may lead to



droplet distortion and finally to break-up into small droplets. The liquid deformation effect should be properly modelled, in order to investigate the spray development particularly in case of high mass, momentum and heat exchanges with the surrounding gas. Figure 5-44 shows the temporal profile of the mean parcel deformation experienced by the evaporating sprays for nominal rail pressures of 500 and 1200bar. The results confirm that the liquid deformation starts increasing according to the increase of the injection velocity, reaching a value around 5 for both cases.

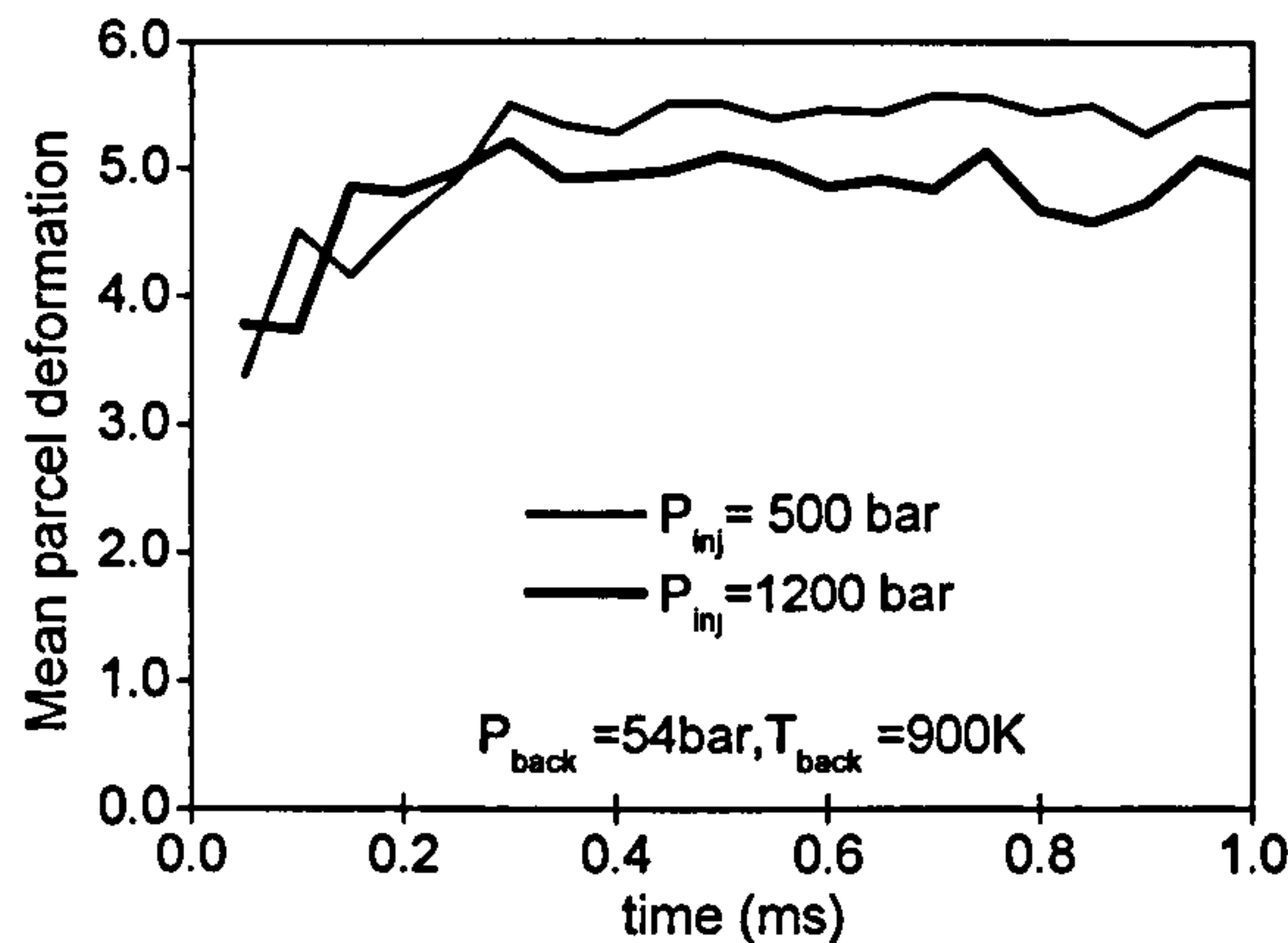


Figure 5-44: Temporal variation of parcel deformation, for evaporating sprays with two nominal injection pressures injected from the sharp-inlet nozzle.

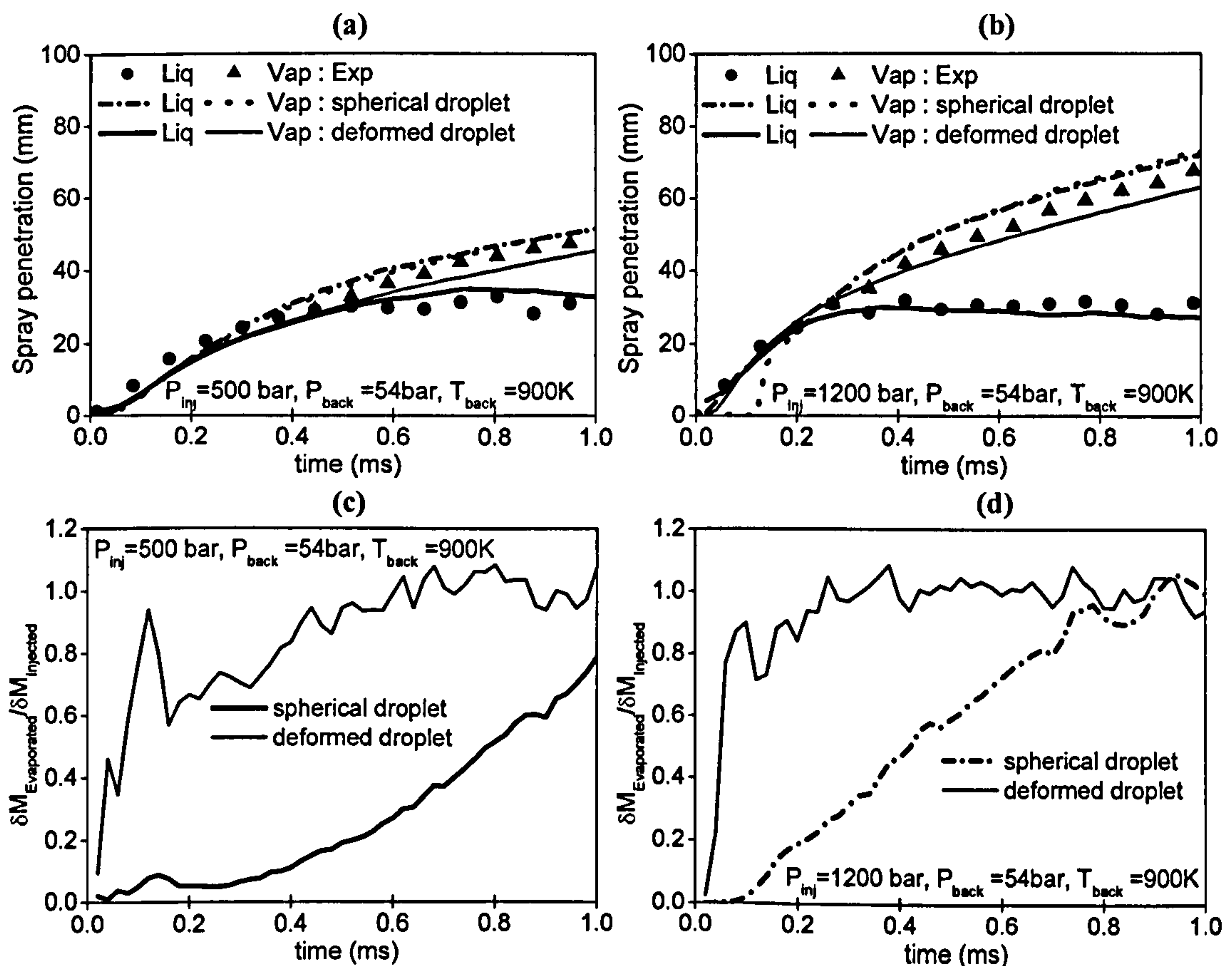


Figure 5-45: Effect of droplet shape on the temporal variation of liquid and vapour penetration with (a)  $P_{INJ}=500$ bar and (b)  $P_{INJ}=1200$ bar, and corresponding non-dimensional evaporation rate for (c)  $P_{INJ}=500$ bar and (d)  $P_{INJ}=1200$ bar.



In order to summarise the effect of droplet deformation for highly evaporating sprays, the comparison between the liquid and vapour penetration and the non-dimensional vaporisation rate assuming spherical or deformed liquid droplets is presented in Figure 5-45. The results confirm that liquid droplet distortion plays a remarkable role on the spray development and only with the assumption of deformed droplet the correct trend of the liquid penetrations can be predicted, as presented in Figure 5-45(a) and Figure 5-45(b) for the low and high injection pressure cases respectively, as a consequence of the higher non-dimensional vaporisation rates, shown in Figure 5-45(c) and Figure 5-45(d), compared to that of spherical droplets.

Finally, the effect on the spray development of the three different vaporisation models, discussed in Chapter 4 for a single evaporating droplet, is also investigated here. Figure 5-46(a) compares model predictions with experimental data for the liquid and vapour penetrations using the high pressure, the ideal equilibrium and the non-equilibrium vaporisation models, including in all three the effect of droplet deformation on the vaporisation rate. Under these assumptions, the liquid penetration predicted by the three models depends on the empirical coefficient  $C_{DEF}$ , which corrects the inter-phase area, according to equation (4-35). Since no experimental information exists for the actual value of this coefficient, numerical predictions suggest to use a value equal to 0.3, although further investigation have to be done on this issue. Figure 5-46(b) shows the effect of the vaporisation model on the non-dimensional evaporation rate, confirming that the high pressure correlations predict slightly faster vaporisation, compared to the other two models, which reflects on the liquid penetration trend.

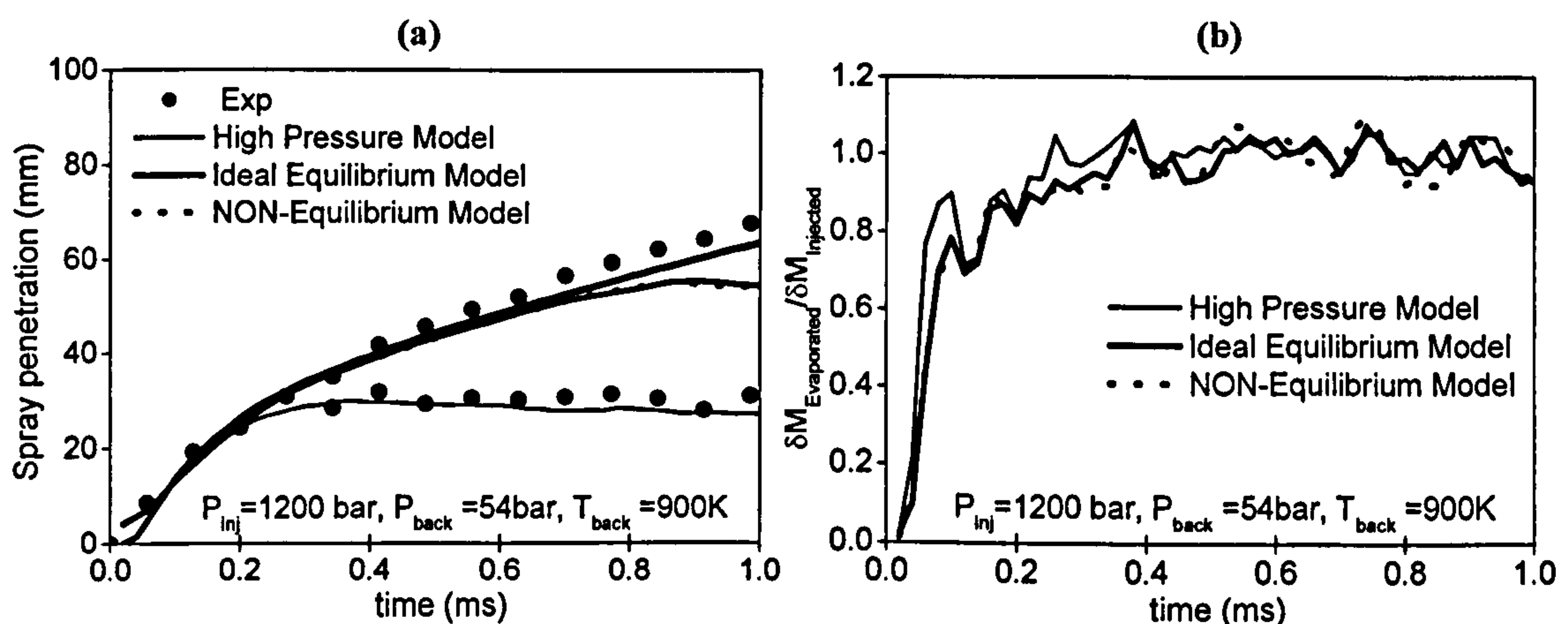


Figure 5-46: Effect of evaporation model on (a) temporal variation of liquid and vapour penetration and (b) non-dimensional evaporation rate for the sharp-inlet nozzle [ $P_{INJ}=1200$ bar].



Table 5-V and Figure 5-47 summarise the results of the cases presented in this section, showing the standard deviation of the predicted liquid and vapour penetrations from the experimental measurements, averaged over an interval up to 1ms after start of injection, for non-evaporating and evaporating sprays with nominal rail pressure of 1200bar. This is calculated according to the equation:

$$\sigma_y = \sqrt{\frac{1}{N_{\Delta t}} \sum_{i=1}^{N_{\Delta t}} (y_i(t) - \bar{y}(t))^2} \quad (5-1)$$

where  $y_i(t)$  is the predicted spray penetration at the time-step  $t$  and  $\bar{y}(t)$  the corresponding experimental value.

Spray sub-model	Description	Case	non-Evap	Evap	
			$\sigma_{liq}$	$\sigma_{liq}$	$\sigma_{vap}$
Standard settings	cavitation induced atomisation model with radial distribution, Arcoumanis et al. [76] break-up model, Feng et al. [185] drag model, O'Rourke [197] turbulent dispersion model, high pressure vaporisation model, droplet deformation	A <sub>1</sub>	2.8	2.3	3.4
Atomisation model	NO atomisation model (SMD <sub>inj</sub> =50 $\mu$ m)	B <sub>1</sub>	6.6	7.3	3.2
	calculated atomisation angle, NO radial distribution	B <sub>2</sub>	5.8	3.0	1.8
	Turbulence induced atomisation model	B <sub>3</sub>	3.8	8.8	1.1
Break-up model	NO break-up model	C <sub>1</sub>	8.9	34.2	5.6
Drag model	Model 1 (Solid particle)	D <sub>1</sub>	6.9	26.5	3.2
	Model 2 (Liquid spherical droplet)	D <sub>2</sub>	6.6	26.8	3.2
	Model 3 (Void contribution)	D <sub>3</sub>	6.8	26.7	2.9
Turbulent dispersion model	Model 1 (NO Turbulent dispersion)	E <sub>1</sub>	-	2.8	3.5
	Model 3 (Langevin [198])	E <sub>2</sub>	-	5.9	3.2
	Model 4 (Gossman et al. [195])	E <sub>3</sub>	-	1.5	3.5
Evaporation model	Ideal Equilibrium Model	F <sub>1</sub>	-	18.7	3.1
	NON-Equilibrium Model	F <sub>2</sub>	-	18.6	3.1
Deformation model	Spherical droplet	G <sub>1</sub>	-	26.6	2.8

**Table 5-V: Summary of the effect of spray physical sub-models on the predicted liquid and vapor penetration under non-evaporating and evaporating conditions for the sharp-inlet nozzle. [P<sub>inj</sub>=1200bar].**



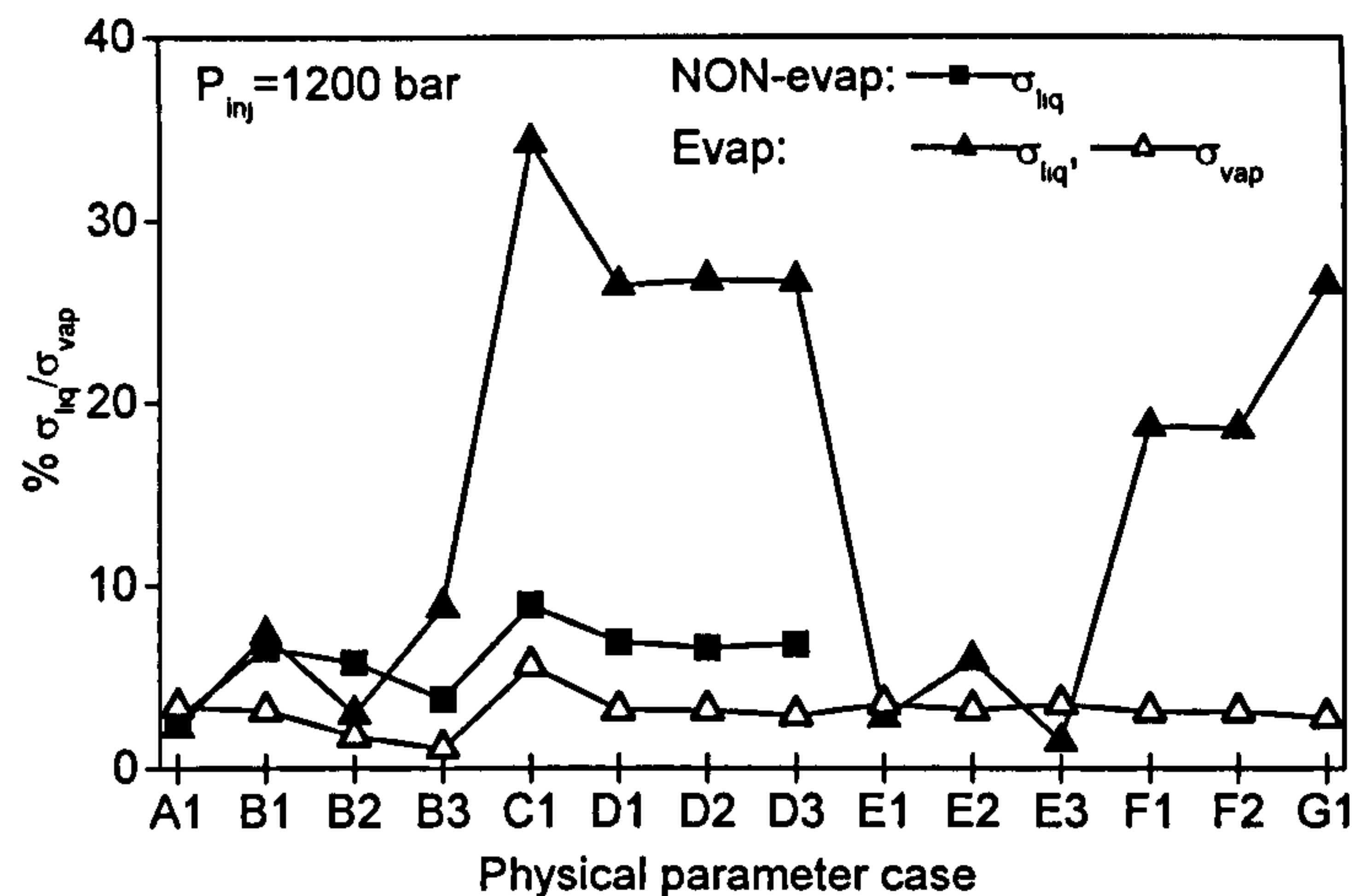


**Figure 5-47: Summary of the effect of spray physical sub-models on the predicted liquid and vapour penetration under non-evaporating and evaporating conditions for the sharp-inlet nozzle. [ $P_{INJ}=1200\text{bar}$ ].**

It can be concluded that remarkable deviations of the simulations from the experiments are calculated mainly for the liquid penetration under evaporating conditions deactivating the break-up model, assuming spherical droplets in the momentum, mass and heat transfers with the surroundings, or solving the vaporisation rate without the contribution of high pressure effect. These parameters seem to play an important role in the dense spray modelling under high back pressure and temperature environments and they should be properly taken into account.

Finally, another important aspect involved in the computational investigation of such sprays is related to the sensitivity of the results on different numerical parameters; these will be presented in details in the next section of the chapter.

### 5.3.5 Numerical parameters investigation

This section focuses on the investigation of the numerical parameters involved in the simultaneous solution of the continuous and dispersed phases according to the Eulerian-Lagrangian methodology described in Chapter 3. The sensitivity of the predictions on the computational domain, the interpolation of the continuous phase variables at the parcel location, the distribution of mass, momentum and heat source terms from interaction of the liquid spray with the surrounding gas, the selection of the time step for the continuous and dispersed phase solution and the implementation of the spatial and temporal discretisation schemes according to the Eulerian frame of reference is



presented for the non-evaporating and evaporating sprays from the cavitating nozzle design.

Particular emphasis has been given in the last decades to the influence of the temporal and spatial resolution on the spray computational models. The stochastic particle method of Dukowicz [3], usually implemented to model the dispersed phase according to a Lagrangian methodology, has been found by many authors to predict a strong dependence of the global spray structure on the grid resolution. The reason for such grid-dependence is that, on one hand, the cell volume in the computational domain used for the solution of the gas phase should be much larger than the maximum size of the droplets contained in the cell itself, according to the assumption made by the Eulerian-Lagrangian formulation for the two-phase flow, and on the other hand, the grid size should be small enough to resolve the gas phase distribution near the nozzle. The finer the grid, the more detailed and exact the solution is. Furthermore, the computational time represents one of the main constraints, leading to the awareness that a reasonable compromise has to be achieved between the accuracy of the results and the time to predict them.

The important issue related to the sensitivity of the model on the spatial discretisation is described in Figure 5-48, which present the development of a liquid fuel spray injected into a gaseous environment using structured grids with homogeneous and variable cell density and cell size from 2mm down to 0.5mm. The images present the spray development at 0.6ms after start of injection; liquid droplets with initial size calculated from a distribution function according to the maximum entropy formalism model are injected in a constant volume domain occupied by stagnant air at 30bar pressure and 800K back temperature. 'Case I' in Table 5-VI summaries the injection conditions used as input for the simulations. In order to isolate the computational domain effect, the liquid core atomisation, droplet secondary break-up, coalescence, turbulent dispersion and evaporation models have been deactivated. The results show the remarkable effect of the spatial resolution on the spray structure: the finer the grid is, the more the spray penetrates, as seen in Figure 5-48(a,b,c). Figure 5-48(d) summaries the previous conclusion showing the spray development under the same operating conditions, using a non uniform computational grid. Two sprays, using identical injection conditions, have been simulated; the first spray penetrates in the homogeneous fine region, while the second spray develops from the fine towards the coarse grid area. The spray shape, which should have been identical in these two cases, is considerably influenced by the



injection direction, due to the non-homogeneous grid cell density. The results confirm the previous findings, which state that the higher momentum exchange calculated with coarser grids induces faster deceleration of the spray and consequently its reduced penetration.

Operating conditions	Case I	Case II
$SMD_{injection} (\mu m)$	15	20
$D_{MAX}_{injection} (\mu m)$	30	40
Injection flow rate ( $mm^3/ms$ )	7.5	5.8
Area contraction coefficient	0.8	0.9
Discharge coefficient	0.7	0.7
$T_{ambient} (K)$	800	273
$P_{ambient} (bar)$	30	20
$T_{fluid} (K)$	300	300
Fuel	$C_{12}H_{26}$	$C_{13}H_{28}$

**Table 5-VI:** Table with operating conditions for two cases of liquid droplet injection in a constant volume domain with variable cell density.

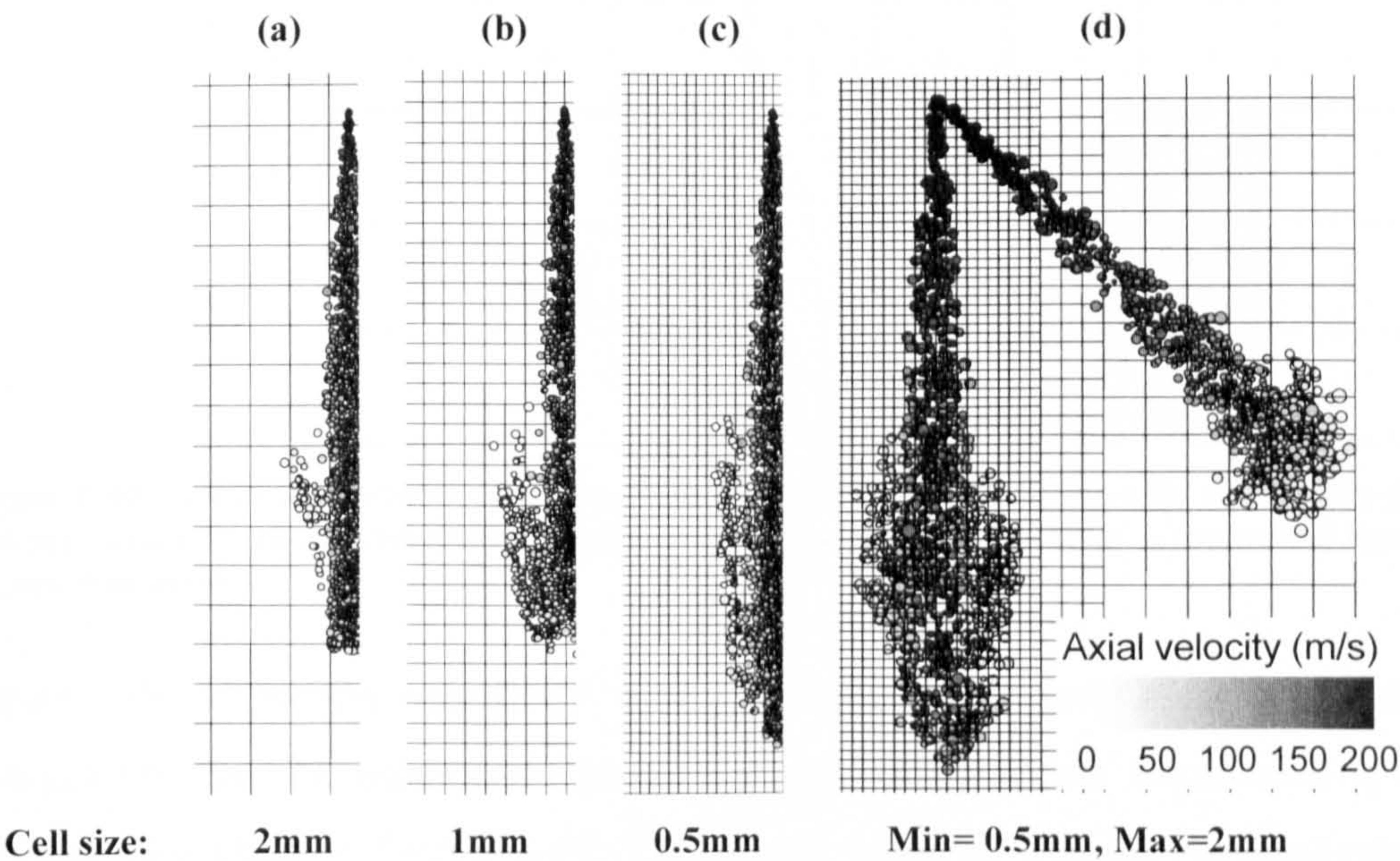


**Figure 5-48:** Effect of grid cell size on predicted spray structure at 0.6ms ASOI in homogeneous grids with (a) 2mm, (b) 1mm (c) 0.5mm cell size and (d) in a grid with variable cell size. Source terms are given to the cell-of-parcel. [Injection of liquid droplets according to the operating conditions described in Table 5-VI, Case II].

Another important aspect taken into account in the model is related to the numerical treatment of the source terms expressing the mass, momentum and energy exchanges between the liquid and the gas phases and the interpolation of the continuous phase properties (temperature, pressure, velocity, density, viscosity, heat capacity, turbulence



variables and void fraction) at the parcel location. Two different approaches have been presented and discussed for the purposes of the present investigation: in the first ‘standard method’ the source terms are added to the cell of the parcel location independently on the cell size and the continuous phase variables ‘seen’ by the parcels are those of the cell; the second approach, named here ‘solution method’ since it provides improvements to the grid dependence issue, is based on the assumption that the region of influence between the two phases should be independent on the cell size, but should be rather based on a predefined distance,  $r$ . The cells found within this distance are then identified and a weighting factor, function of this distance, rather than the cell volume or its internal energy, is used for the continuous phase interpolation and the distribution of the source terms to those cells, according to equation (3-99) to (3-101). Figure 5-49 describes the scheme of the two implemented methods, showing the parcel in the cell  $C_i$  and the region of influence within a radius  $r$  from the parcel centre.

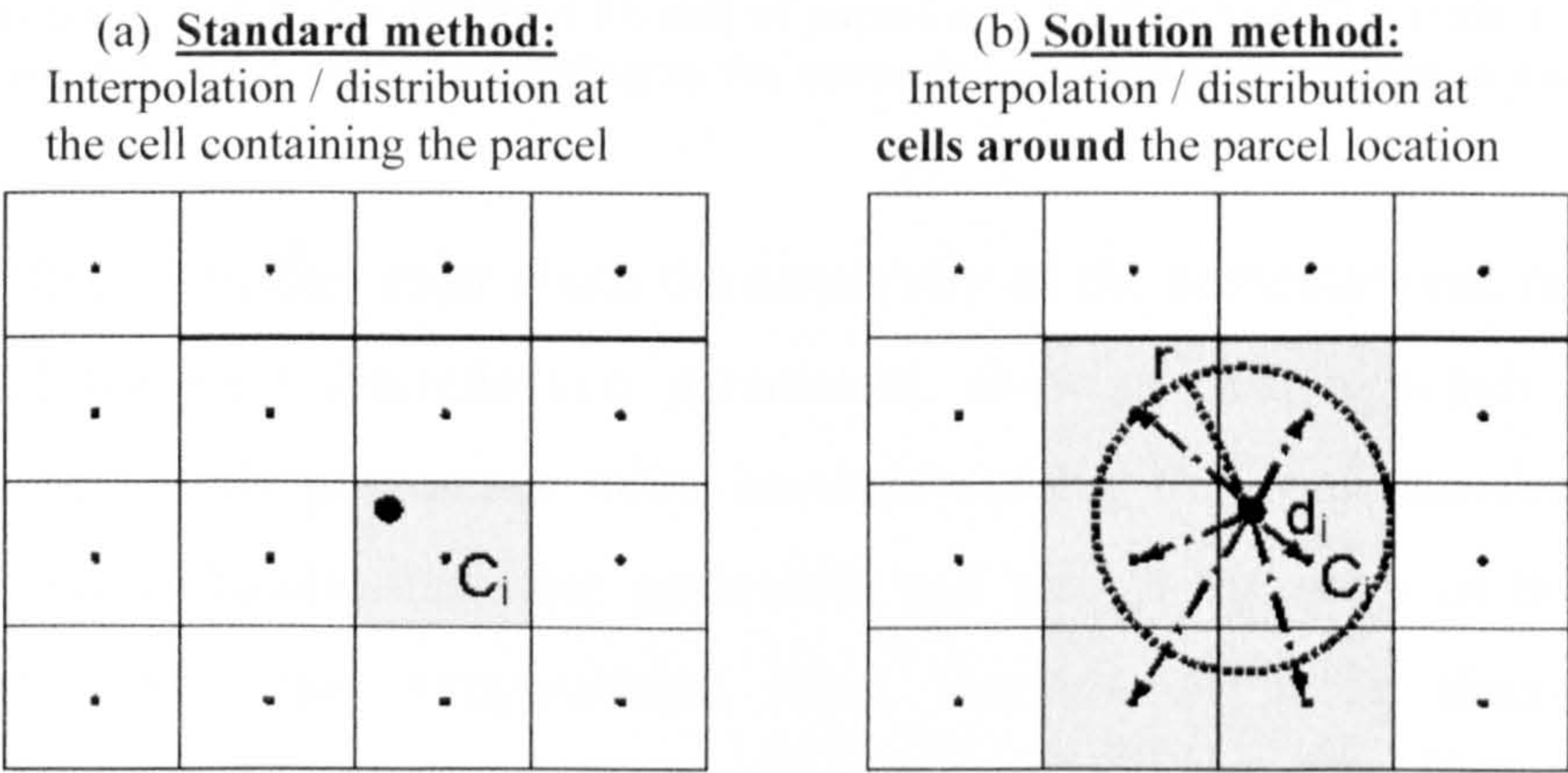


**Figure 5-49:** Schematic showing how source terms are distributed to the cells around the parcel and the continuos phase variables at the parcel location are interpolated; (a) standard method and (b) solution method.

Figure 5-50 show the sensitivity of the computational results on the source term distribution and the continuous phase variable interpolation implementing the two methods described in Figure 5-49. The scatter plots on a plane perpendicular to the injection direction at 15mm from the injection point, 0.6ms after the start of injection, using the injection conditions of Case I described in Table 5-VI, are presented, revealing the significant role of the method for the source term distribution and the continuous phase interpolation. If the ‘standard method’ is selected, the spray splits in four parts, due to the fact that a parcel takes longer time to ‘travel’ a cell on a direction along the cell diagonal, thus the parcels concentrate in these four areas. On the other



hand, the ‘solution method’ gives a more realistic uniform distribution of the liquid droplets on that plane.

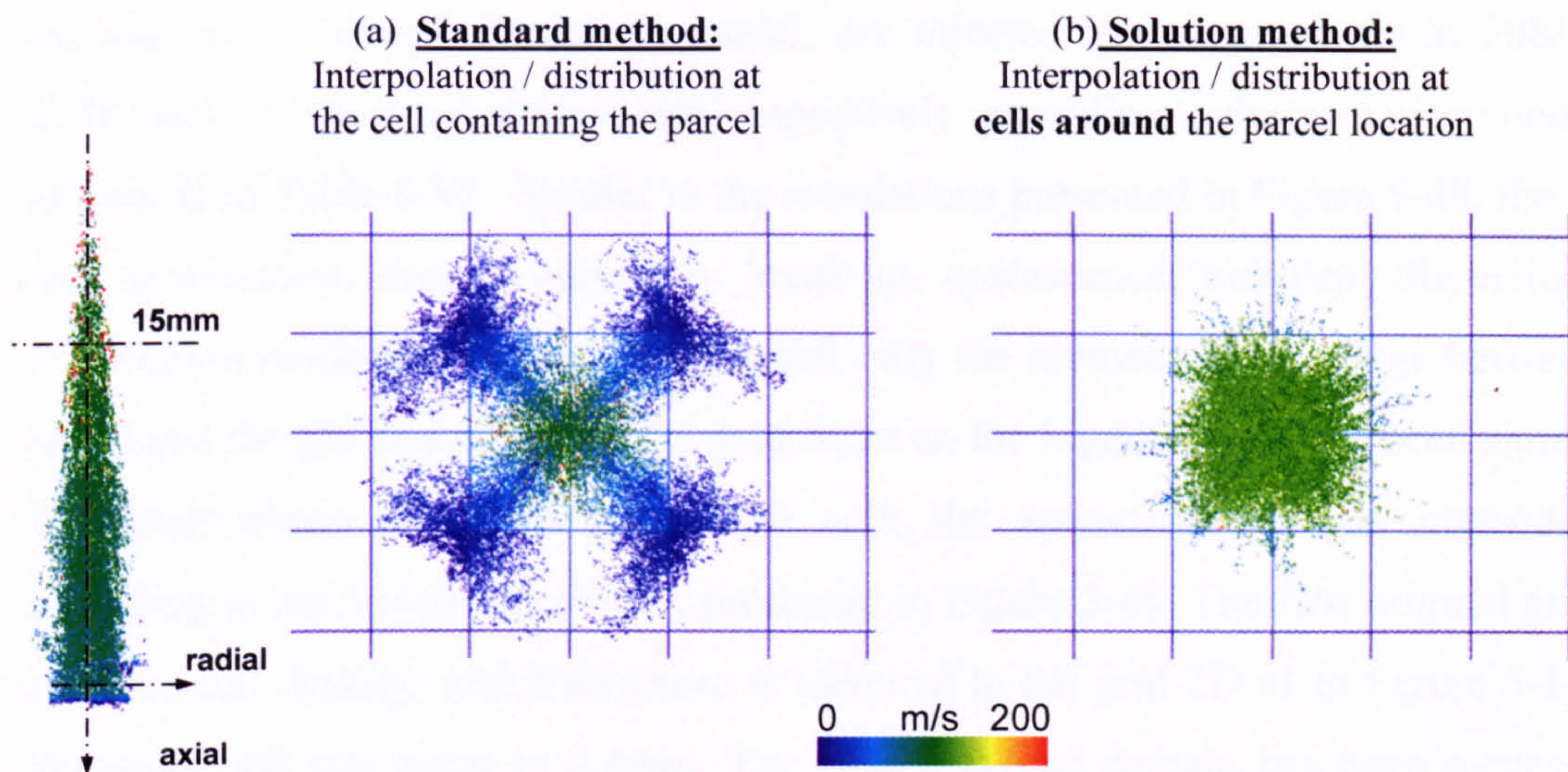


**Figure 5-50: Effect of source term distribution and continuous phase variable interpolation on calculated spray structure on a plane perpendicular to the injection axis at 15mm from the injection hole, at 0.6ms ASOI. (a) ‘Method 1’: cell of parcel and (b) ‘Method 2’: within a region of 0.4mm. [Injection of liquid droplets according to the operating conditions described in Table 5-III, Case I].**

In literature different studies exist about the sensitivity of the computational results on the spatial and temporal discretisation parameters, showing that, although the cell refinement of fine grids guarantees more accurate results, the computational codes might not be able to handle very fine grids with cell size of the order of the parcel dimension. Moreover, the computational time, function of these discretisation parameters, represents one of the main numerical constraints to be taken into account during the simulations. These contradictory issues suggest the idea to implement a procedure for automatic local refinement in selected regions of the computational domain where and when it is needed. This idea has a practical application on the numerical investigation of the flow field in internal combustion engines. The spray development, which modelling preferably requires fine grids, occurs in a short interval of time, generally few crank angles, of the total engine cycle. Then the dynamic local refinement restricted in this period of time represents an alternative to the use of a dense static computational domain over the whole simulation time. Having introduced the issue of the spray model sensitivity on the computational grid and one possible solution, implementing in the GFS code the spatial distribution method for the inter-phase interaction modelling, the next step is to demonstrate that the code can handle cells size



comparable to the parcel volume. Figure 5-51 shows the effect of grid refinement on the spray penetration temporal profile and its development at 0.6ms after start of injection. Liquid droplets, which initial size is calculated from a distribution function according to the maximum entropy formalism model, are injected into stagnant air at 20bar and 273K back pressure and temperature, respectively, according to the operating conditions of Case II in Table 5-VI. Similar to the simulations presented in Figure 5-48, the liquid core atomisation, droplet secondary break-up, coalescence, turbulent dispersion and evaporation models have been deactivated; only the momentum exchange between the liquid and the gas phases due to the drag force on the liquid parcels has been simulated. The multi-phase interaction is solved with the spatial distribution methodology, according to the ‘solution method’, presented in Figure 5-49. The first original grid has a coarse cell density, which structure is identical to the grid 2D-s1 in Figure 5-1, with minimum cell size equal to 2.4mm. The computational domain has been successively refined in the region of the spray development, splitting each selected cell in three cells, and then creating four new grids with minimum cell size down to 0.15mm. According to the liquid penetration profiles, presented in Figure 5-51(a), the model predicts considerably higher penetration reducing the cell size, although the differences decrease when the cell size approaches a value of the order of the parcel dimension. This result suggests that at this point further grid refinement wouldn’t add any remarkable improvements to the solution, however it would have a dramatic effect on the computational time due to the increased number of cells. Figure 5-51(b.1-5) show the scatter plots and the induced flow field at 0.6ms after start of injection using the five grids. The images reveal that the use of grid refinement results in more realistic spray structure reaching a sort of ‘good compromise’ between accuracy and computational efforts. The percentage standard deviation  $\% \sigma_y$  of the liquid penetration, predicted using the different numerical domains, from the value obtained with the finest grid, taken as reference case, is calculated according to the equation (5-1) where  $y_i(t)$  represents the spray penetration at the time  $t$  calculated using the grid  $i$  and  $\bar{y}(t)$  the corresponding value for the reference grid. The values are plotted in Figure 5-51(b), below the corresponding spray images, underlying the previous conclusion that the sensitivity of the predictions on the computational grid is reduced decreasing the cell size, and that a degree of considerable accuracy can be reached, beyond which further grid refinement wouldn’t add any improvements to the predictions.



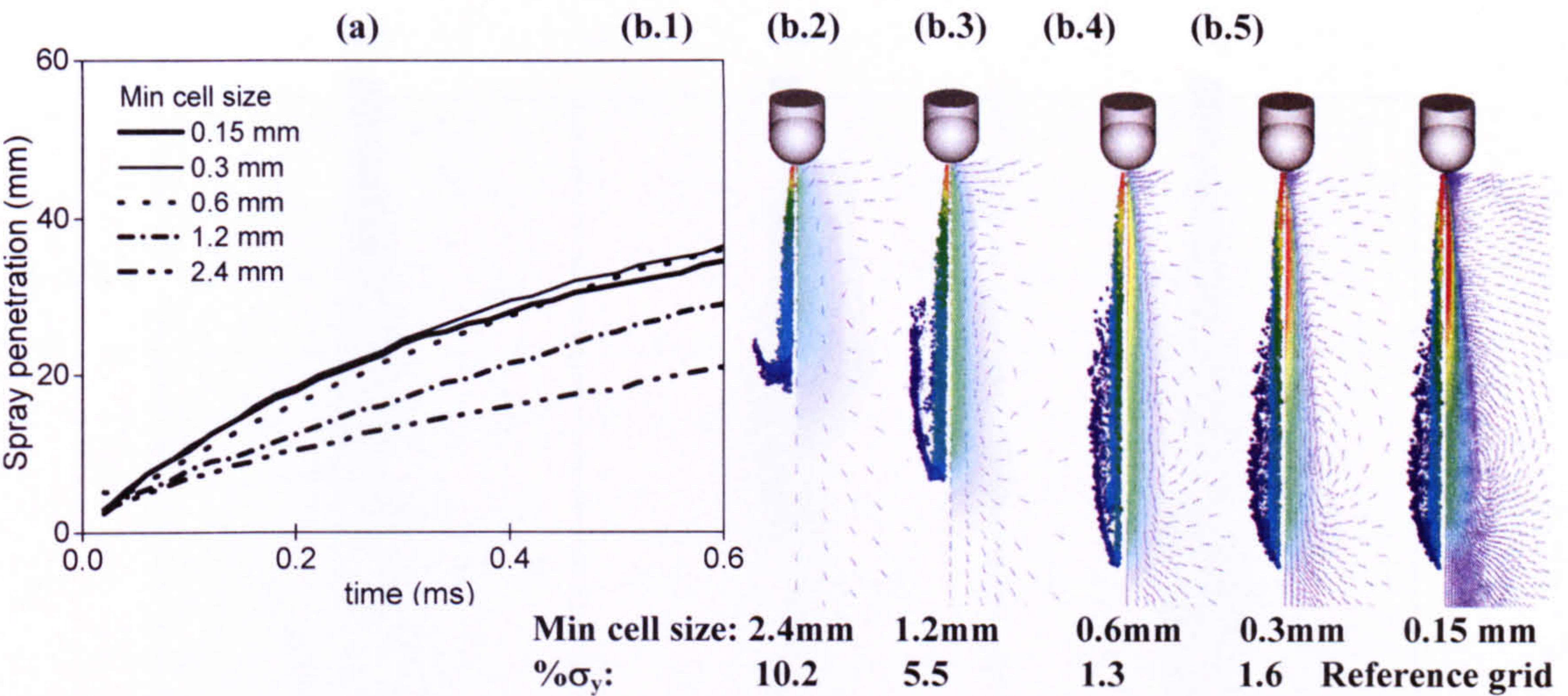


**Figure 5-51:** Effect of dynamic grid refinement on predicted (a) liquid penetration and (b) spray development, using five 2-D axis-symmetric grids with minimum cell size from 2.4mm down to 0.15mm, obtained with four successive levels of dynamic grid refinement from the coarse grid (b.1) [Injection of liquid droplets according to the operating conditions described in Table 5-VI, Case II].

The remaining part of this section focuses on the investigation of the numerical parameters involved in the spatial and discretisation methodology used to predict the non-evaporating and evaporating diesel sprays from the cavitating nozzle design described in the section 5.3.1, and using the operating conditions specified in Table 5-III. This time, the liquid atomisation, droplet break-up, turbulent dispersion, drag force, distortion and evaporation models are activated according to the final settings discussed in the section 5.3.4.

The first numerical issue considered is the sensitivity of the results on the computational domain.

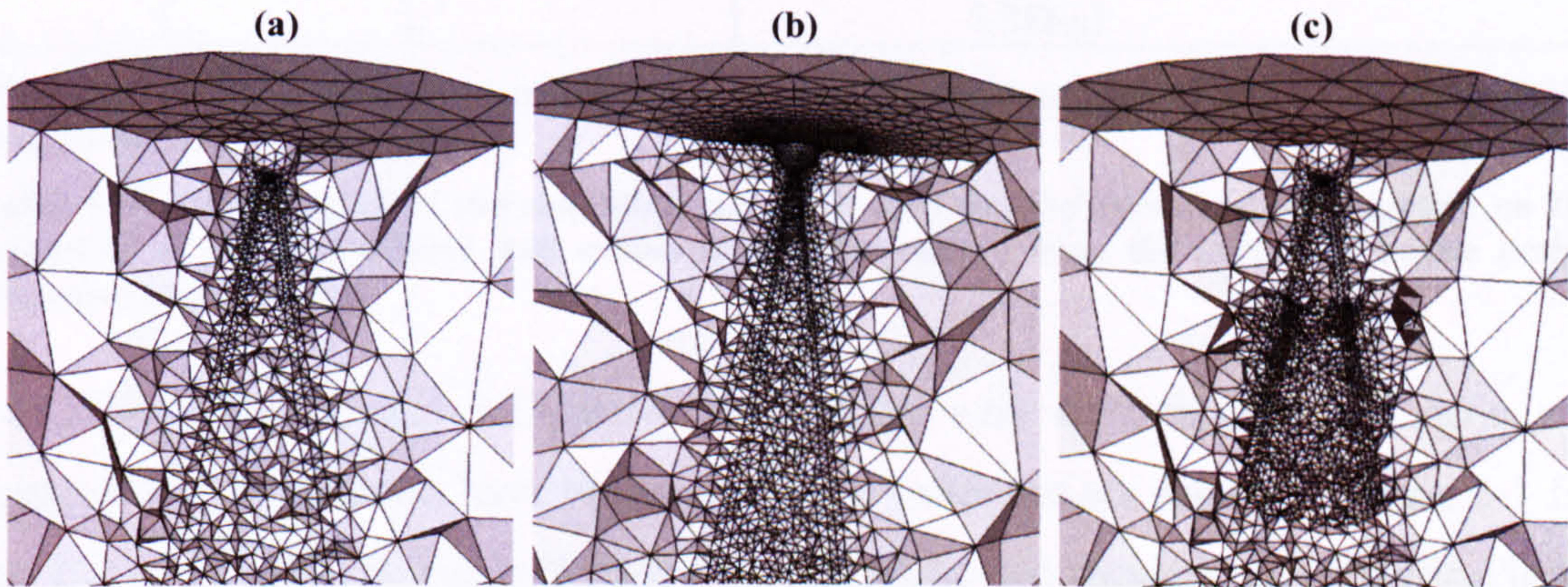


**Figure 5-52:** 3-D static and adaptive numerical grids used for the simulation of the spray development (a)  $50 \times 10^3$  cells, (b)  $240 \times 10^3$  cells, (c)  $50 \times 10^3$  cells with automatic local refinement at the spray tip.



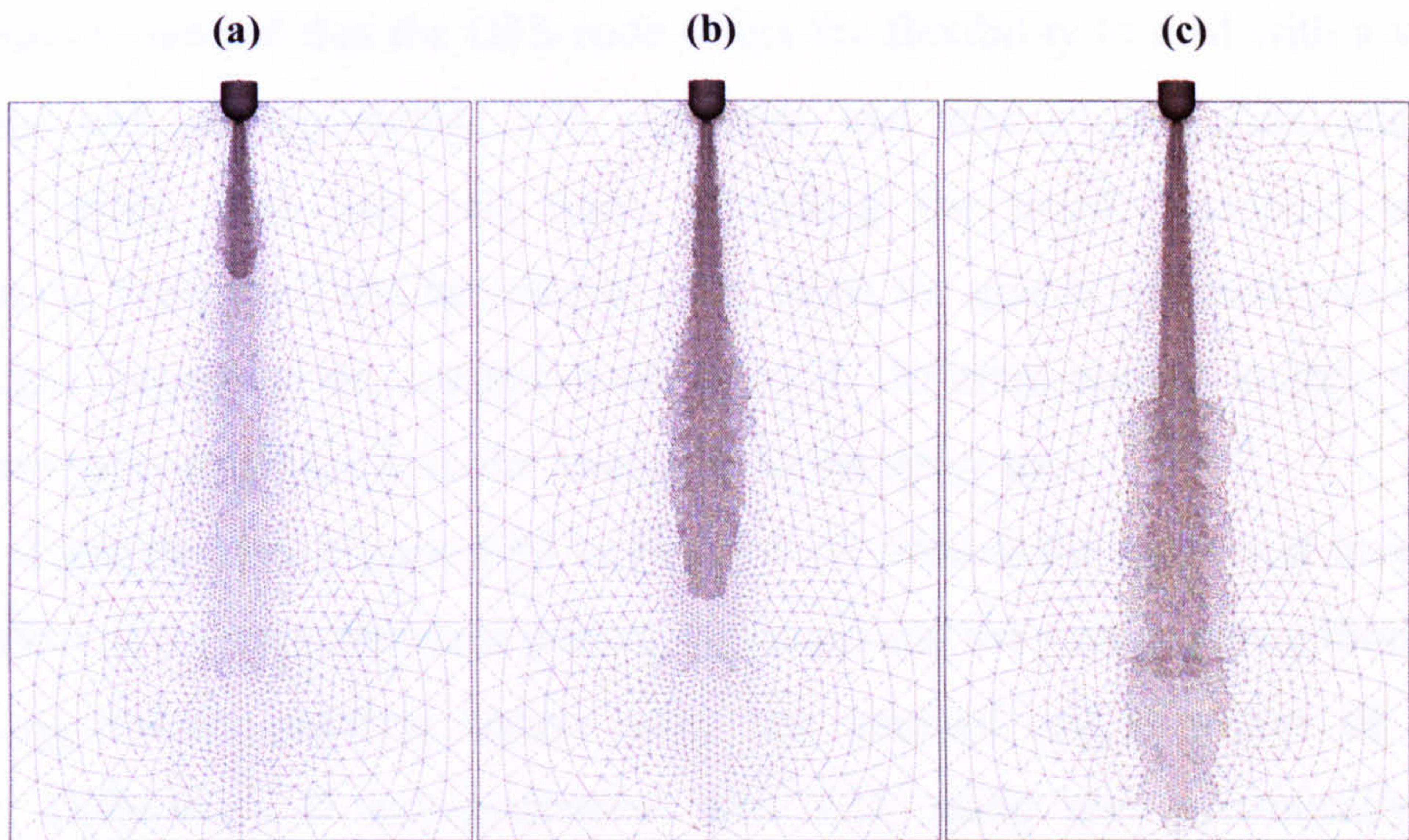


**Figure 5-53: 2-D axis-symmetric adaptive numerical grid at three time instances calculated during the spray development at (a) 0.2ms, (b) 0.5ms and (c) 1.0ms.**

Grid	Min cell size (mm)	Max cell number	Cell type	Description
2D-s1	0.6	$3\times10^3$	triangular	2D static grid
2D-s2	0.3	$12\times10^3$		
2D-s3	0.15	$50\times10^3$		
2D-a1	0.3	$6.3\times10^3 - 7.5\times10^3 (*)$		2D adaptive grid; -a1 and -a2 correspond to 1 and 2 levels of dynamic cell refinement from original grid 2D-s1
2D-a2	0.15	$17\times10^3 - 25\times10^3 (*)$		
3D-s1	0.30	$50\times10^3$	tetrahedral and pyramids	3D static grid
3D-s2	0.15	$1.4\times10^5 - 1.6\times10^5 (*)$		
3D-a1	0.15	$1.4\times10^5 - 1.6\times10^5 (*)$		3D adaptive grid, obtained with 1 level of dynamic cell refinement from original grid 3D-s1

(\*) at 1ms ASOI, the first value refers to the evaporating cases and the second value to the NON-evaporating ones.

**Table 5-VII: Description of the computational grids used for the numerical investigation on the modelling of non-evaporating and evaporating diesel sprays from the cavitating nozzle design presented in section 5.3.**

2-D axis-symmetric and 3-D unstructured grids, with different level of static and dynamic cell refinements have been used. Some examples are shown in Figure 5-1 for the 2-D static grids, in Figure 5-52 for the 3-D static and dynamic grids and in Figure 5-53 for the 2-D grids with automatic cell refinement in the region of the spray development. The complete description of the different grids used for the numerical investigation presented in the remaining part of this section is shown in Table 5-VII. It



is important to remind that the GFS code offers the flexibility to deal with a variety of 2-D planar and axis-symmetric, 3-D, structured and unstructured, static and moving numerical grids, with any cell types, including the usually adopted triangular, quadrilateral, tetrahedral and hexahedral cells. Here, the grid is automatically refined in pre-selected sections of the computational domain. Different options include the whole area where spray develops or in the area close to the spray tip.

The set of graphs from Figure 5-54 to Figure 5-58 present the numerical investigation on the effect of the computational grid on the liquid and the vapour penetration for non-evaporating and evaporating sprays using the nominal rail pressures of 500 and 1200bar. Different 2-D axis-symmetric and 3-D, static and dynamically refined numerical grids, with minimum cell spacing down to 0.15mm, have been used. Figure 5-54 show the comparison between model predictions and experimental data for the low-injection pressure case using static 2-D grids, revealing that as the cell volume decreases, the predicted liquid penetration converges to the experimental data, although not remarkable differences can be really appreciated among the profiles corresponding to different grids. Particularly for the non-evaporating case, the results confirm that even the coarser computational domain allows for predictions with reasonable accuracy. On the other hand, more visible differences exist between the model predictions for the vapour penetration. This is an expected result, since the penetration of the vapour is mainly due to the air motion induced by the spray injection. Calculation of that motion is performed on the Eulerian grid, and thus, different cell sizes and discretisation methods are expected to play a role on the convection of the vapour far downstream from the injection point. Figure 5-55 presents a similar comparison for the high-pressure injection cases, but this time also the results from the simulations performed introducing one and two-levels of dynamic grid refinement are also included. The graphs confirm the previous conclusion about the degree of validation reached with finer grids. It reveals that dynamically refined domains guarantee the accuracy of static grid with the same cell density in the region of spray development, but obviously at reduced computational cost.



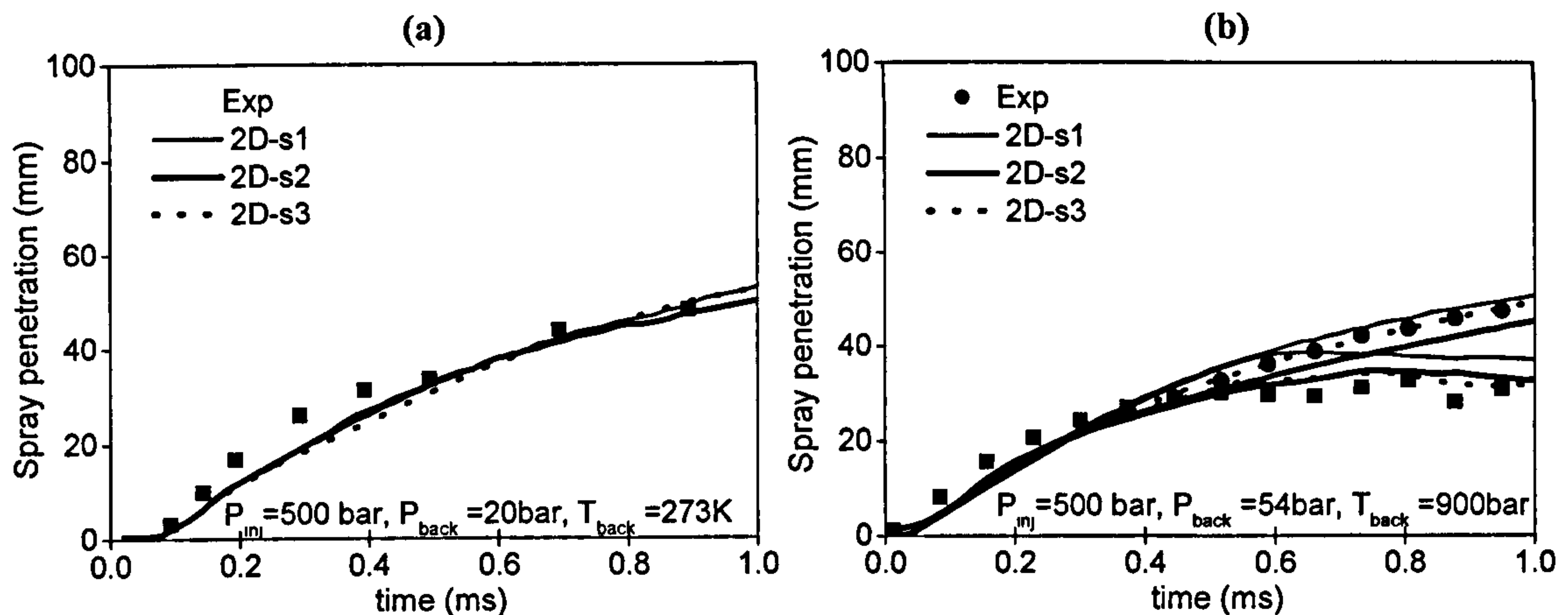


Figure 5-54: Effect of numerical grid on the predicted liquid and vapor spray penetration of the (a) non-evaporating and (b) evaporating sprays for nominal rail pressure of 500bar, using 2-D static grids.

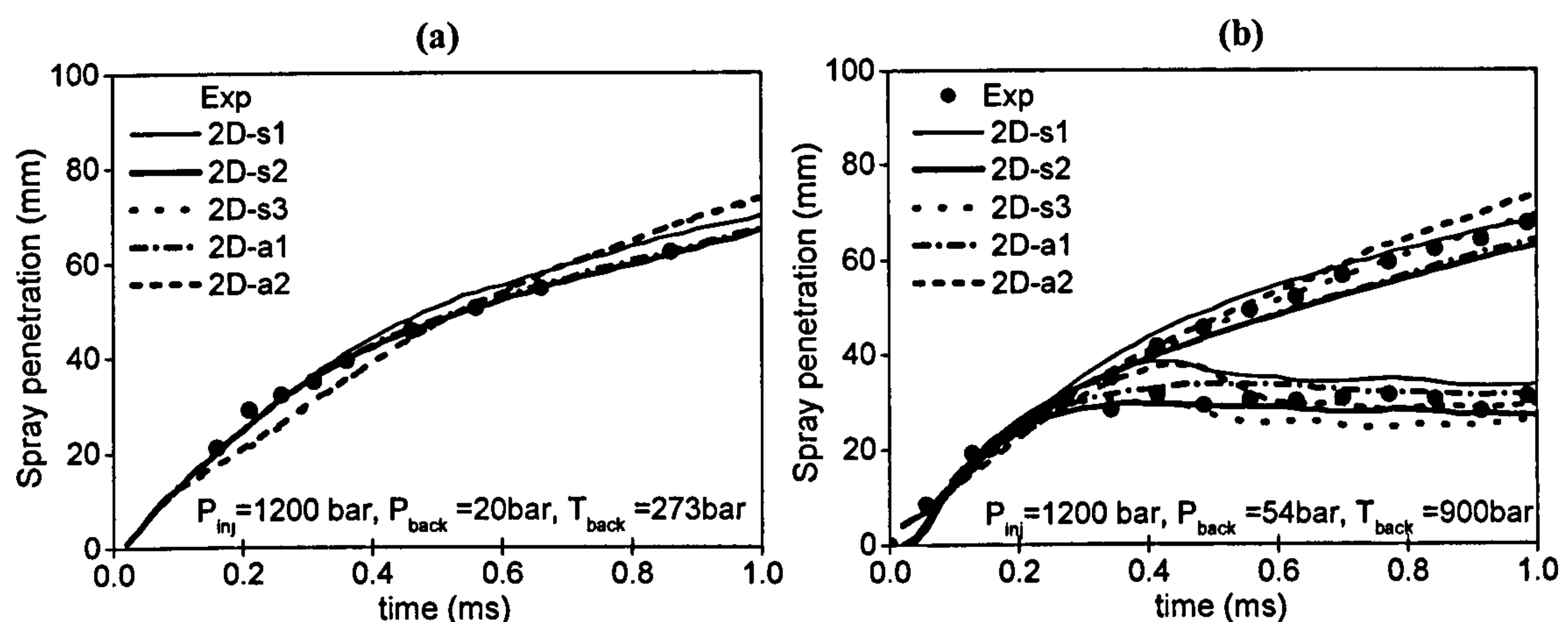


Figure 5-55: Effect of numerical grid on the predicted liquid and vapor spray of the (a) non-evaporating and (b) evaporating sprays for nominal rail pressure of 1200bar, using static and adaptive 2-D grids.

Figure 5-56 enlightens the grid effect for the same conditions of Figure 5-55, using 3-D computational domains. The first simulation have been performed using the reference coarse grid, with 50,000 cells, successively a second simulation activating one level of dynamic cell refinement in the region of spray development has been done. The grid automatically created by the code at 1ms after start of injection has been used for the last simulation, which has been performed with a static fine grid. It consists of about 140,000 and 160,000 cells for the evaporating and non-evaporating cases, respectively. This difference is a consequence of the larger area occupied by the non-evaporating spray, compared to the evaporating one.



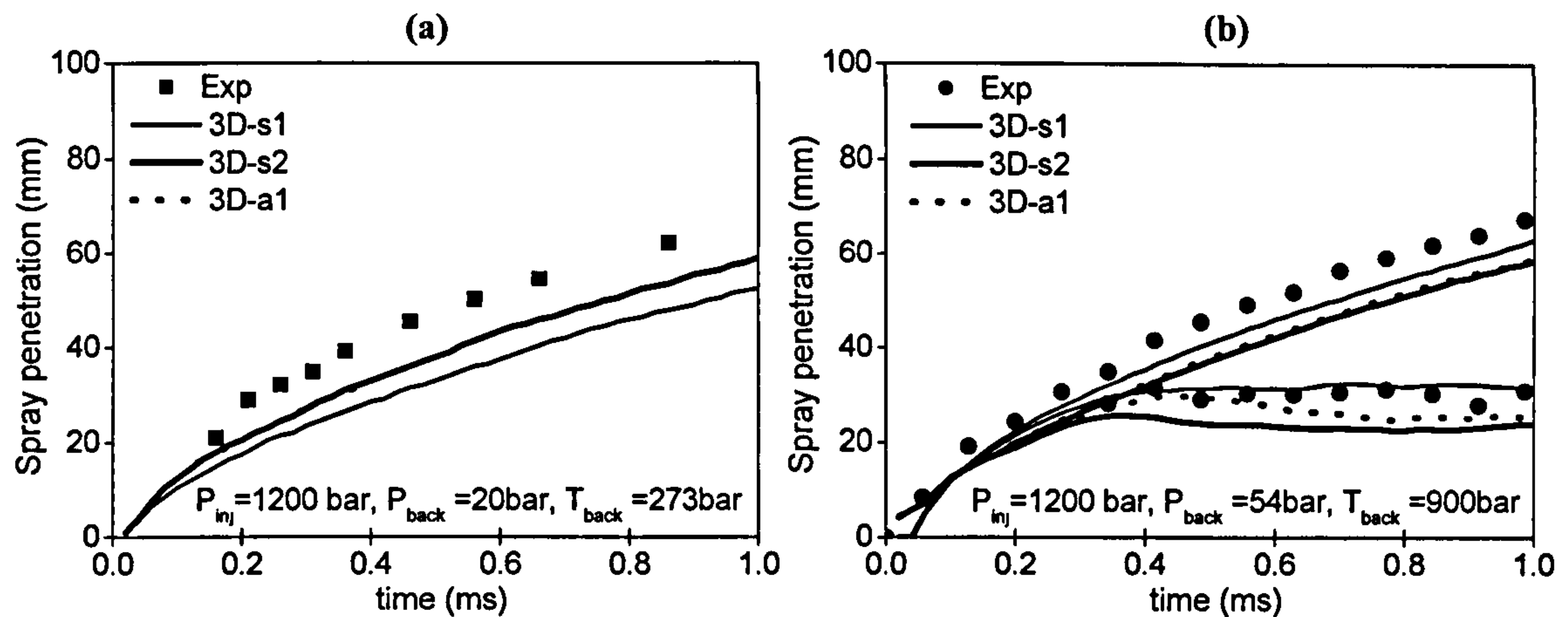


Figure 5-56: Effect of numerical grid on the predicted liquid and vapour spray penetration of the (a) non-evaporating and (b) evaporating sprays for nominal rail pressure of 1200bar, using static and adaptive 3-D grids.

The results reveal that the increase of cell density leads to higher liquid penetration for non-evaporating sprays. A different trend is observed in case of evaporation. The liquid stops at a lower distance from the nozzle hole, due to the increased evaporation rate predicted with finer grids at the initial stage of the injection period. Again, similar accuracy is predicted with dynamically refined and static grids, provided that the cell density is the same.

A summary of the main conclusions drawn from the results presented in Figure 5-55 and Figure 5-56 is presented in Figure 5-57, in terms of the ensemble standard deviation, up to 1ms after start of injection, of the predicted liquid and vapour penetrations from the experimental values, calculated according to the formula (5-1), with  $y_i(t)$  representing the predicted spray penetration at the time  $t$  using the grid  $i$  and  $\bar{y}(t)$  the corresponding experimental value.

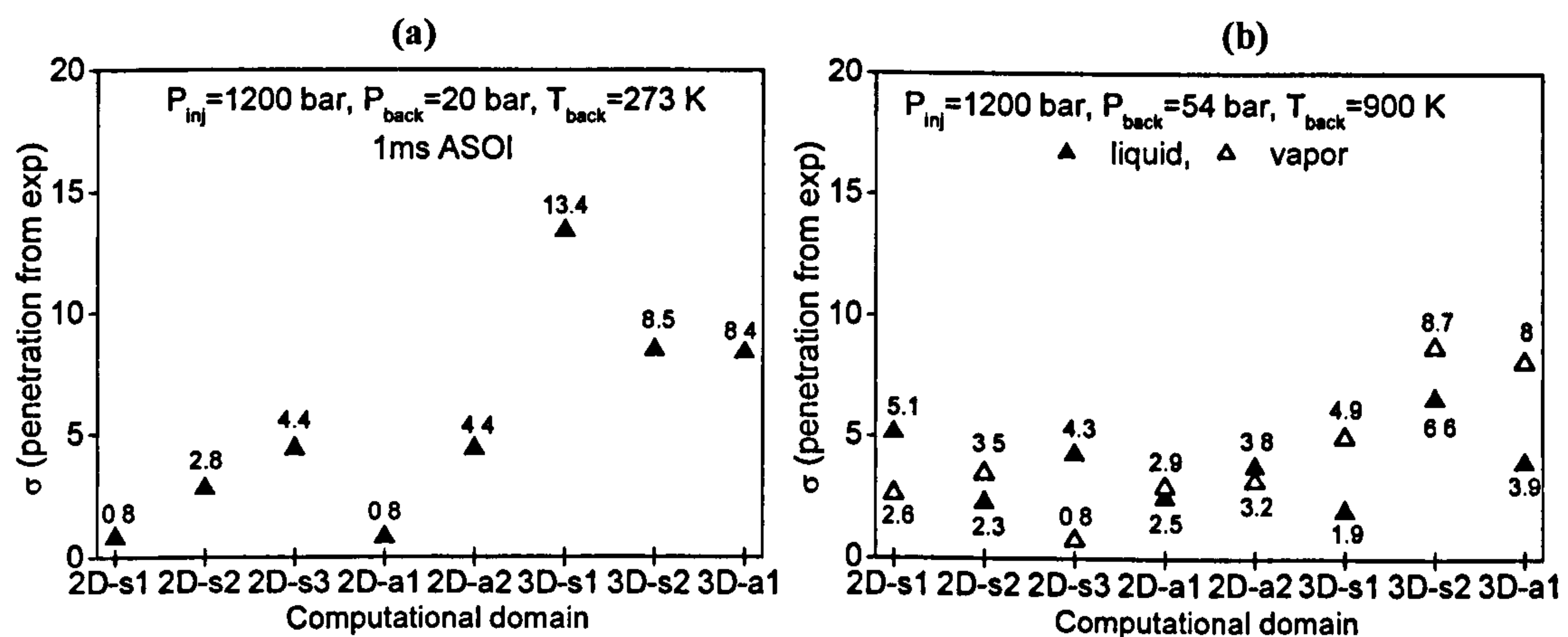


Figure 5-57: Computational domain effect on the standard deviation of the predicted liquid and vapour penetration from the experimental measurements, using static and adaptive 2D and 3D numerical grids with nominal rail pressure of 1200bar, for (a) non-evaporating and (b) evaporating sprays.



The results show that the standard deviation for all the conditions investigated is of the order of 5% for 2-D calculations, and about 8.5% for refined 3-D grids under non evaporating conditions; the initial 3-D grid results to predictions that substantially deviate from the experiments more than 13%. Generally the use of grid refinement does not significantly increase the precision of the simulations, particularly using 2-D computational domains. Differences are smaller for the evaporating sprays and do not exceed 4% for the 2-D calculations and 4-8% for the 3-D cases.

The implementation of adaptive grid refinement is expected to reduce the computational time required for the simulation. This has been investigated in Figure 5-58, showing the normalised CPU time for all the simulations presented in Figure 5-57, assuming as reference value the 2D-s2 grid, which provides the best agreement against the experiments under evaporating spray conditions, and the coarse 3D-s1 grid for the 3-D. The results show that the CPU time for 2-D computational domain reduces down to 40% relative to the reference case using the coarse 2D-s1 grid and down to 60% using one level of dynamic local refinement instead of the static one. Moreover the computational time increases up to 390-440% introducing a second level of static local refinement, and up to 150-160% with dynamic refinement. In case of 3-D domain, the CPU time increases up to 280-300% and up to 200-260% introducing one level of grid refinement statically and dynamically, respectively. These conclusions are valid for both non-evaporating and evaporating conditions.

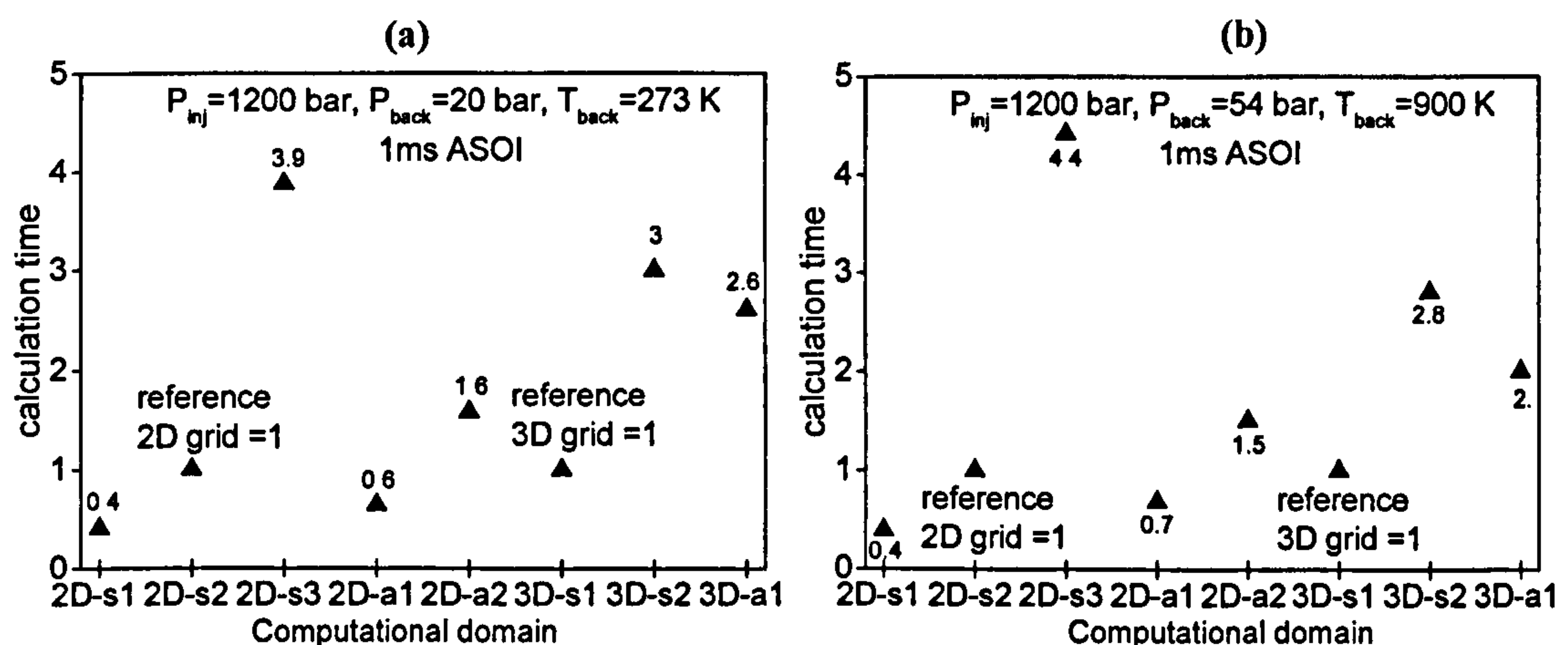


Figure 5-58: Computational domain effect on the normalised calculation time relative to the reference-case, using static and adaptive 2D and 3D numerical grids with nominal rail pressure of 1200bar, for (a) non-evaporating and (b) evaporating sprays.



These results confirm that the option to implement adaptive cell refinement in the region of interest, achieving the same accuracy of statically refined grid and, on the same time, reducing the time required for the simulation, represents an interesting solution in order to realise a good compromise between numerical precision and computational effort.

The following investigation focuses on the implementation of the spatial distribution method for the multi-phase interaction modelling previously described in Figure 5-49. The effect of different interpolation/distribution distance on the temporal profiles of liquid and vapour penetrations are presented for non-evaporating and evaporating sprays for nominal rail pressure of 1200bar case. The results are shown in Figure 5-59 selecting two interpolation/distribution distances; the first one is equal to a constant value of 0.4mm and the second one is proportional to the ‘equivalent’ parcel diameter, estimated from the following correlation:

$$R_{\text{interp/distr,P}} = \gamma D_P = \gamma \sqrt[3]{N_{\text{droplet,P}} \left( \frac{D_{\text{droplet,P}}}{2} \right)^3} \quad (5-2)$$

where  $R_{\text{interp/distr,P}}$  represents the interpolation/distribution distance for the parcel P,  $\gamma$  is a constant selected equal to 2 and  $D_{\text{parcel,P}}$  stands for the diameter of the parcel P, containing a number equal to  $N_{\text{droplet,P}}$  of identical droplets with diameter  $D_{\text{droplet}}$ . Looking to the graph of Figure 5-59(a), the sensitivity of the predicted liquid and vapour penetration on the calculated variable  $R_{\text{interp/distr,P}}$  seems to be negligible for non-evaporating sprays, while it seems to affect the liquid penetration under evaporating conditions, Figure 5-59(b). The use of an interpolation/distribution distance proportional to the ‘equivalent’ parcel size slightly over-predicts the experimental liquid penetration, although the percentage standard deviation of the predicted results from the corresponding experimental data is below 5.5%, which represents an acceptable interval of tolerance for model validation. Moreover an interpolation/distribution distance proportional to the ‘equivalent’ parcel size rather than equal to a fixed value represents a more physically-based approach. In particular, the sensitivity of the liquid and vapour penetration on the choice of the constant of proportionality  $\gamma$  in equation (5-2), which controls the region of influence surrounding the parcel, is shown in Figure 5-60. The value of  $\gamma$  has been varied from 1 up to 4, which means that the radius of the region of influence for each parcel increases from one up to four times the radius of the selected parcel. The results reveal that this parameter seems not to affect the solution.



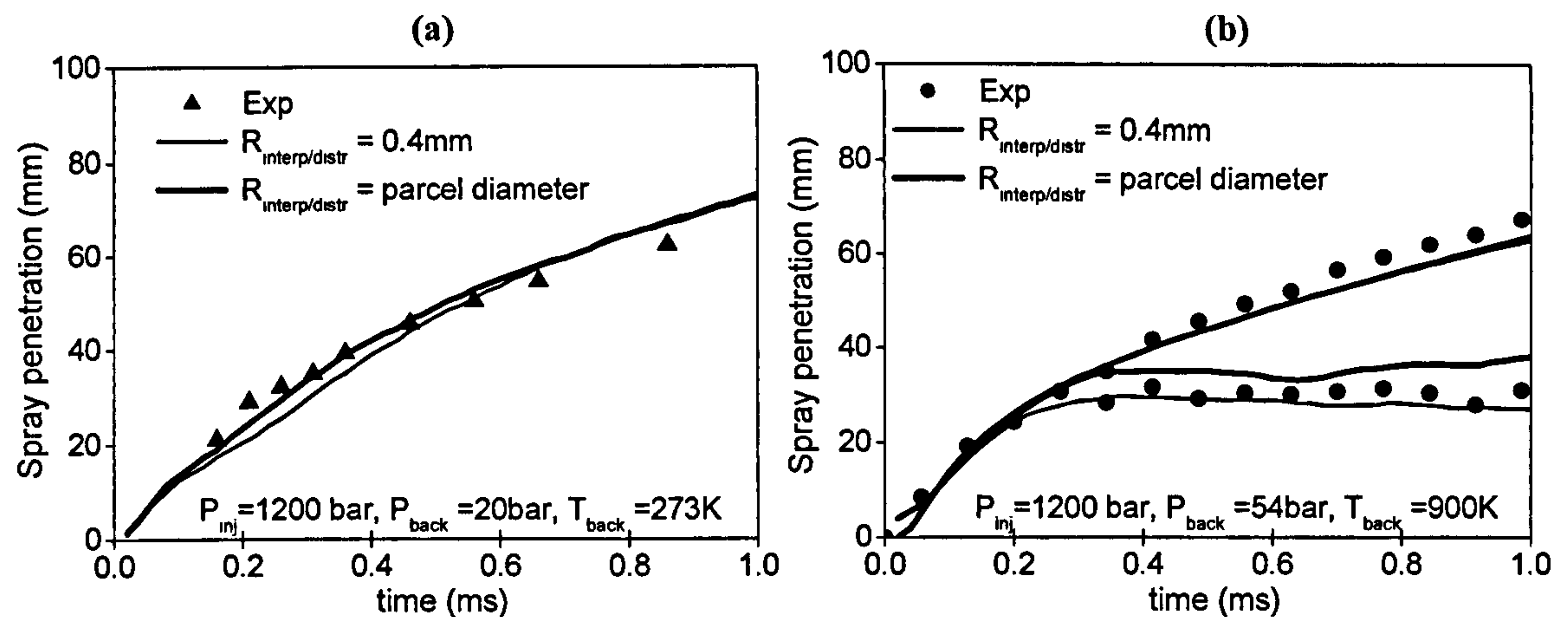


Figure 5-59: Effect of interpolation/distribution distance on predicted liquid and vapour spray penetration of the (a) non-evaporating and (b) evaporating spray (fixed distance, proportional to the 'equivalent' parcel diameter). [ $P_{INJ}=1200\text{bar}$ ].

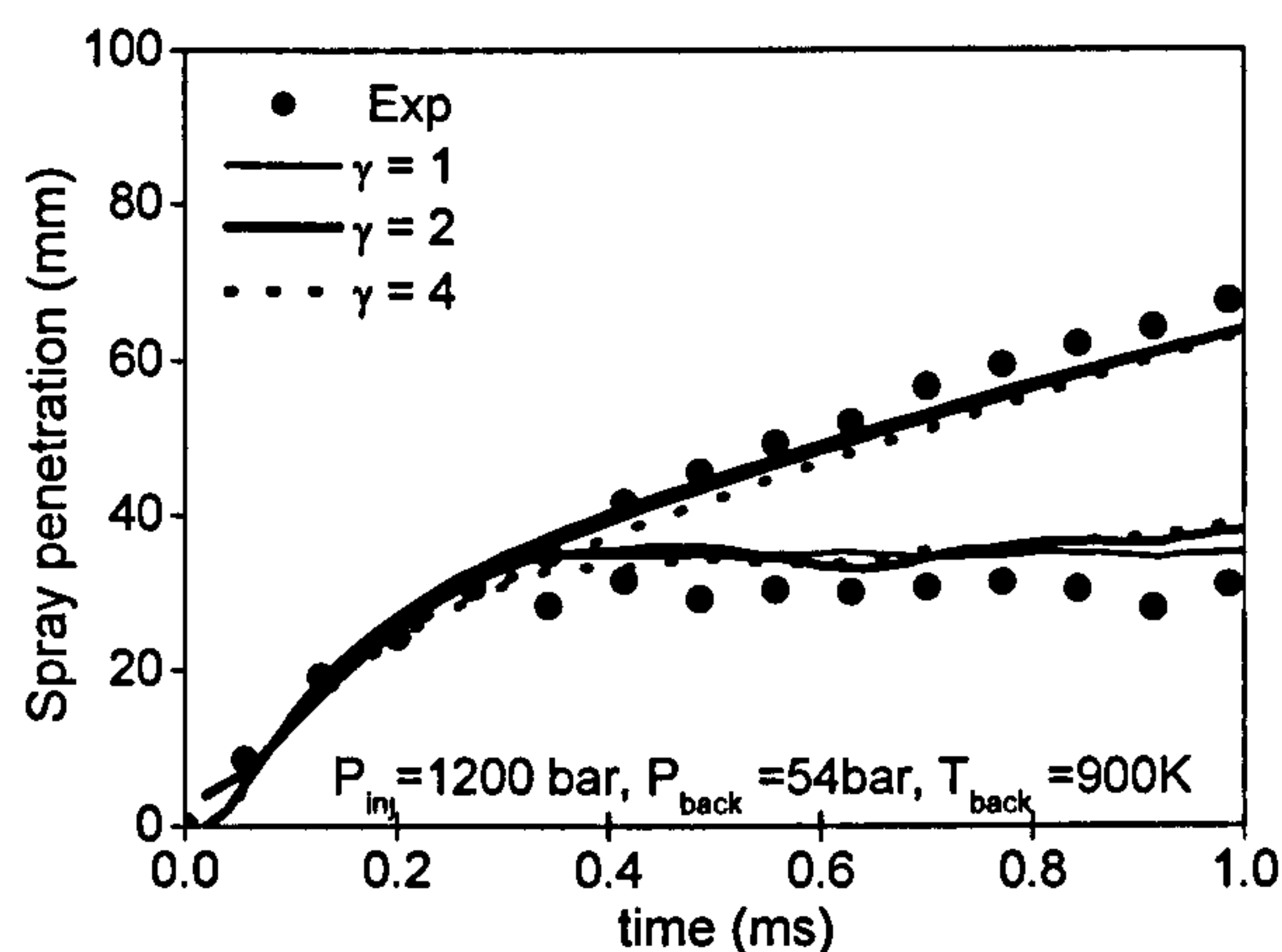
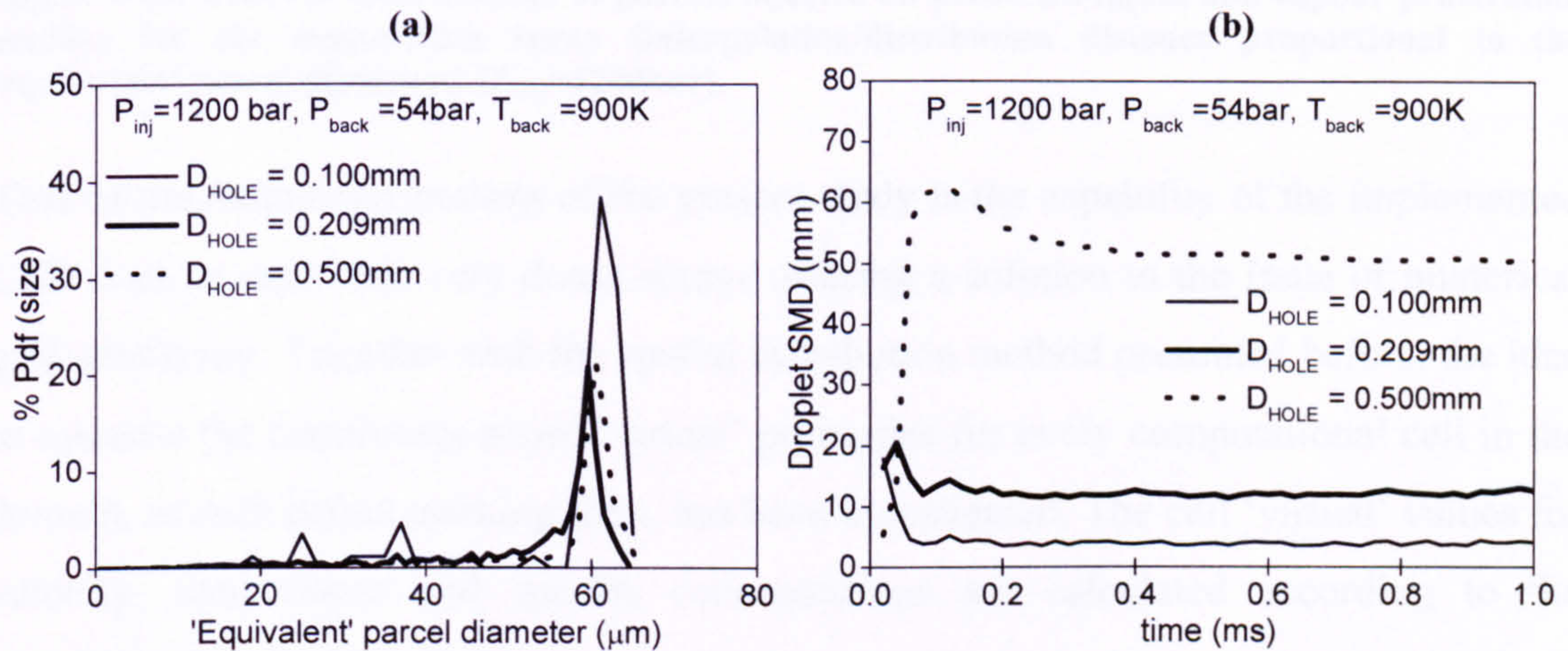


Figure 5-60: Effect of constant factor, in the interpolation/distribution distance proportional to the 'equivalent' parcel diameter, on predicted liquid and vapour spray penetration for the evaporating spray [ $P_{INJ}=1200\text{bar}$ ].

The interpolation/distribution method based on the distance proportional to the parcel effective diameter has been implemented to simulate the spray development from three nozzles with hole diameter equal to 0.1, 0.209 and 0.5mm. Figure 5-61(a) shows the percentage probability distribution function of the 'equivalent' parcel diameter, defined according to the volume occupied by the particles in each parcel, for the three sprays. The results reveal that the 'equivalent parcel size' is almost independent on the nozzle hole exit area. This can be explained by the fact that the parcel size is a function of the droplet dimension, which is actually proportional to the hole size as shown in Figure 5-61(b), but also to the number of particles contained in each parcel, which decreases as the hole size increases in order to conserve the total injected mass. The temporal profiles of the liquid and vapour penetrations, black and red lines respectively, for the three sprays are presented in Figure 5-62(a) showing that as the hole size reduces, the liquid vaporises faster and it reaches earlier the maximum asymptotic distance from the



injector exit. The corresponding increased vaporisation, as shown in Figure 5-62(b), due to the smaller droplets present in the spray, results in higher vapour penetration. Finally, the size of the interpolation/distribution region, function of the ‘equivalent’ parcel size, is inversely proportional to the total number of parcel injected during the whole injection period. Figure 5-63 shows that the liquid and vapour penetrations are not considerably affected by the total number of parcels injected, which is varied from 10,000 up to 1000,000.



**Figure 5-61: Effect of initial injector hole size on predicted (a) ‘equivalent’ parcel size percentage distribution and (a) droplet SMD for the evaporating spray (interpolation/distribution distance proportional to the ‘equivalent’ parcel diameter). [ $P_{INJ}=1200\text{bar}$ ].**

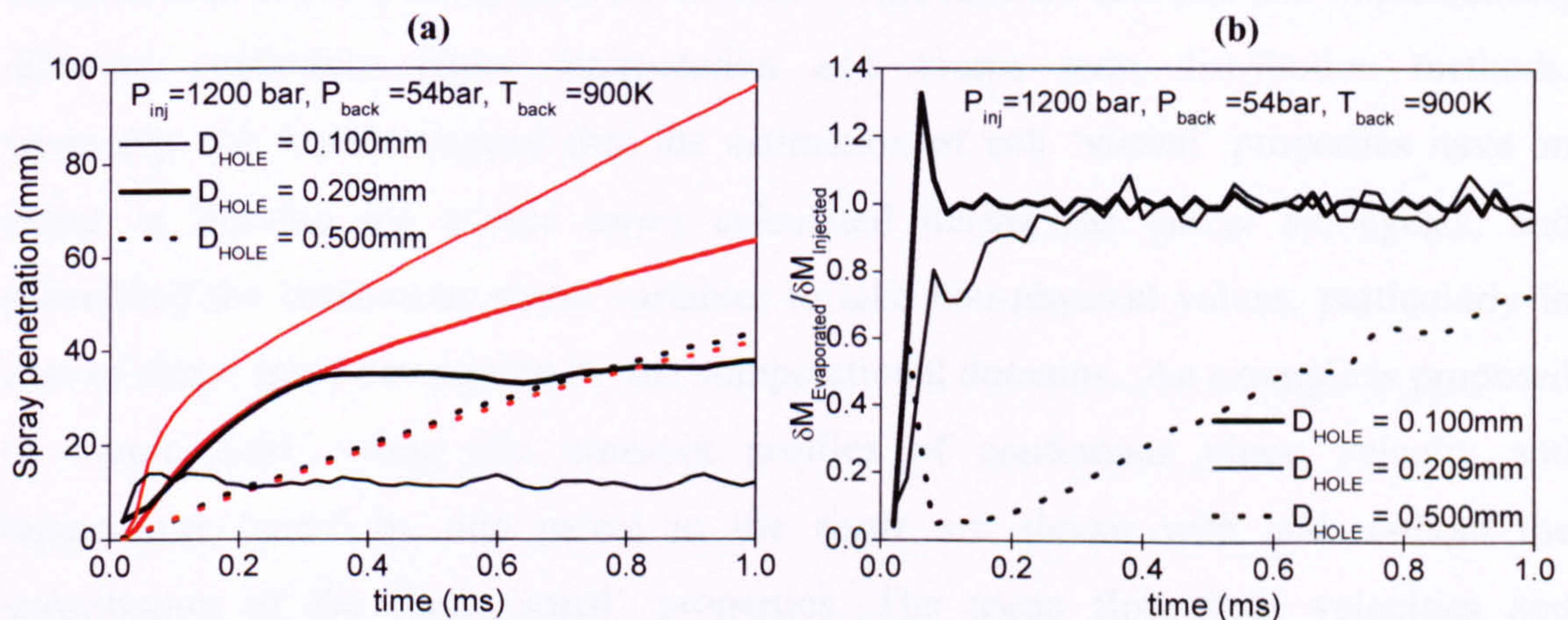


**Figure 5-62: Effect of initial injector hole size on predicted (a) liquid (black lines) and vapour (red lines) penetrations and (b) non-dimensional vaporisation rate of the evaporating spray (interpolation/distribution distance proportional to the ‘equivalent’ parcel diameter). [ $P_{INJ}=1200\text{bar}$ ].**



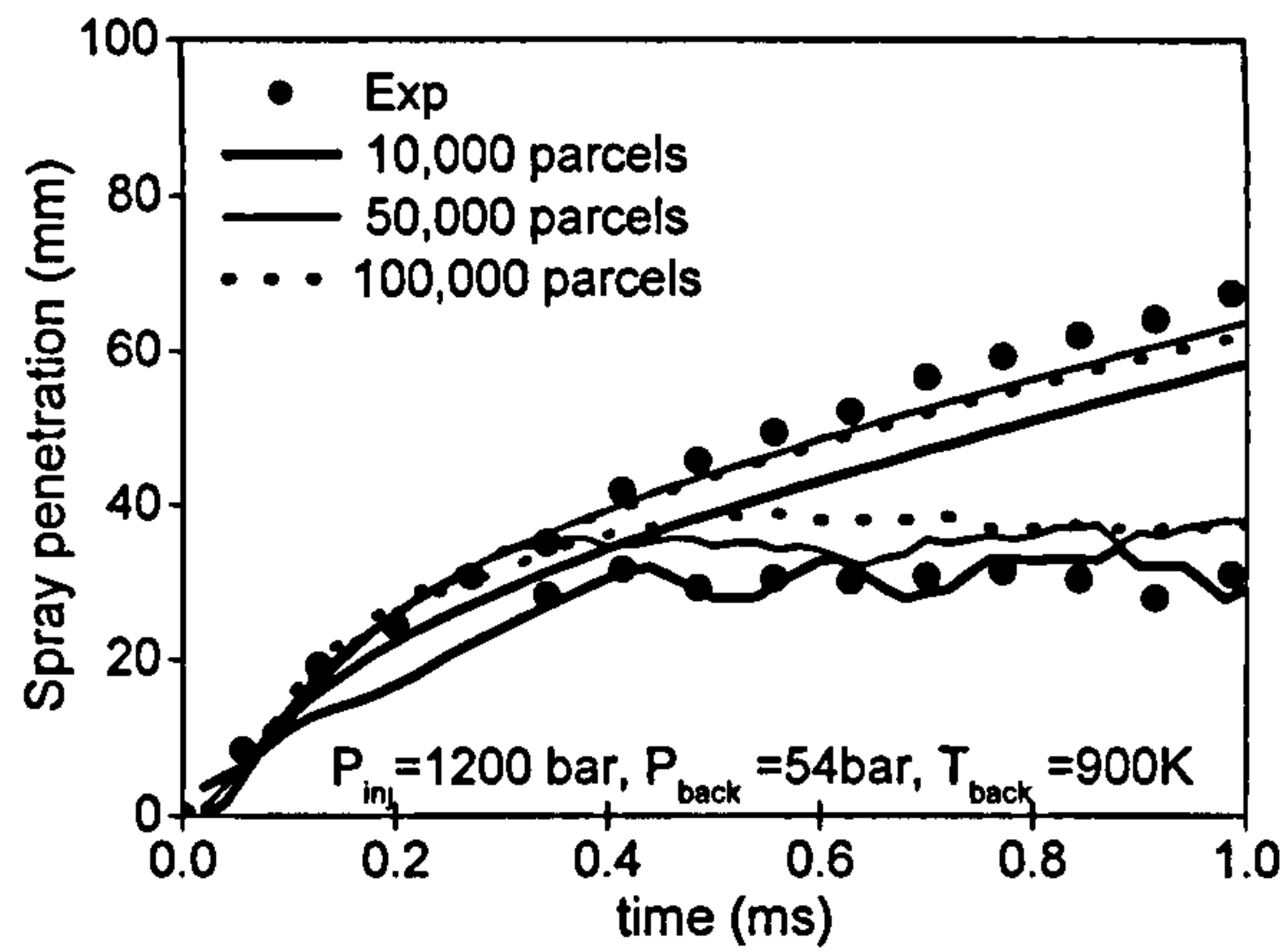


**Figure 5-63: Effect of total number of parcels injected on predicted liquid and vapour penetration profiles for the evaporating spray (interpolation/distribution distance proportional to the ‘equivalent’ parcel diameter). [ $P_{INJ}=1200\text{bar}$ ].**

One of the main contributions of the present study is the capability of the implemented CFD code to deal with very dense sprays offering a solution to the issue of numerical grid sensitivity. Together with the spatial distribution method presented before, the idea to estimate the continuous phase ‘virtual’ properties for every computational cell in the domain, at each parcel tracking time, has been investigated. The cell ‘virtual’ values for velocity, temperature and species concentrations are calculated according to the equations (3-113) to (3-116).

Several tests have been done to investigate the effect of cell ‘virtual’ properties calculation over a variety of physical and geometrical operating conditions, using different 2-D and 3-D computational domains with variable cell size and implementing different continuous phase interpolation and source term distribution methods. Generally, the results suggest that the estimation of cell ‘virtual’ properties have an effect in limiting the source terms calculated during the parcel sub-cycles, and preventing the continuous phase variables to take non-physical values, particularly in case of dense spray developing in fine computational domains. An example is proposed in Figure 5-64, where the transient profiles of continuous phase velocity and temperature ‘seen’ by one parcel in the spray are shown with and without the contribution of the ‘cell virtual’ properties. The mean flow field velocities and temperatures, calculated solving the corresponding conservation equations, are also plotted. The simulations have been done using the fine 2D-s3 grid shown in Figure 5-1 implementing the first interpolation/distribution method presented in Figure 5-49, according to the cell of the parcel location, in order to emphasis the role of the ‘virtual cell’ properties calculation. The time step for the solution of the flow field variables and the tracking time step for the parcel have been fixed equal to 1.E-5s and 5.E-7s,



respectively. The results from the simulation without the contribution of the 'cell virtual' properties take non-physical values at 0.02ms after start of injection, for both the flow field axial velocity and temperature, which decrease down to -1600m/s and -200K, respectively. In this case the continuous phase properties 'seen' by each parcel at their location are not affected by the multi-phase interaction and they vary during the tracking time only due to the fact that the parcel travels in different cells. On the other hand, the contribution of the 'cell virtual' properties, limiting the source terms exchanged between the two phases, guaranties more realistic results. This is more evident after few time steps after the start of injection, when a large number of parcels are present and interact with the flow field. In this case the continuous phase properties, re-calculated at each tracking time step, change because the parcel travels in different cells and because they are interpolated among new up-dated 'virtual' cell properties.

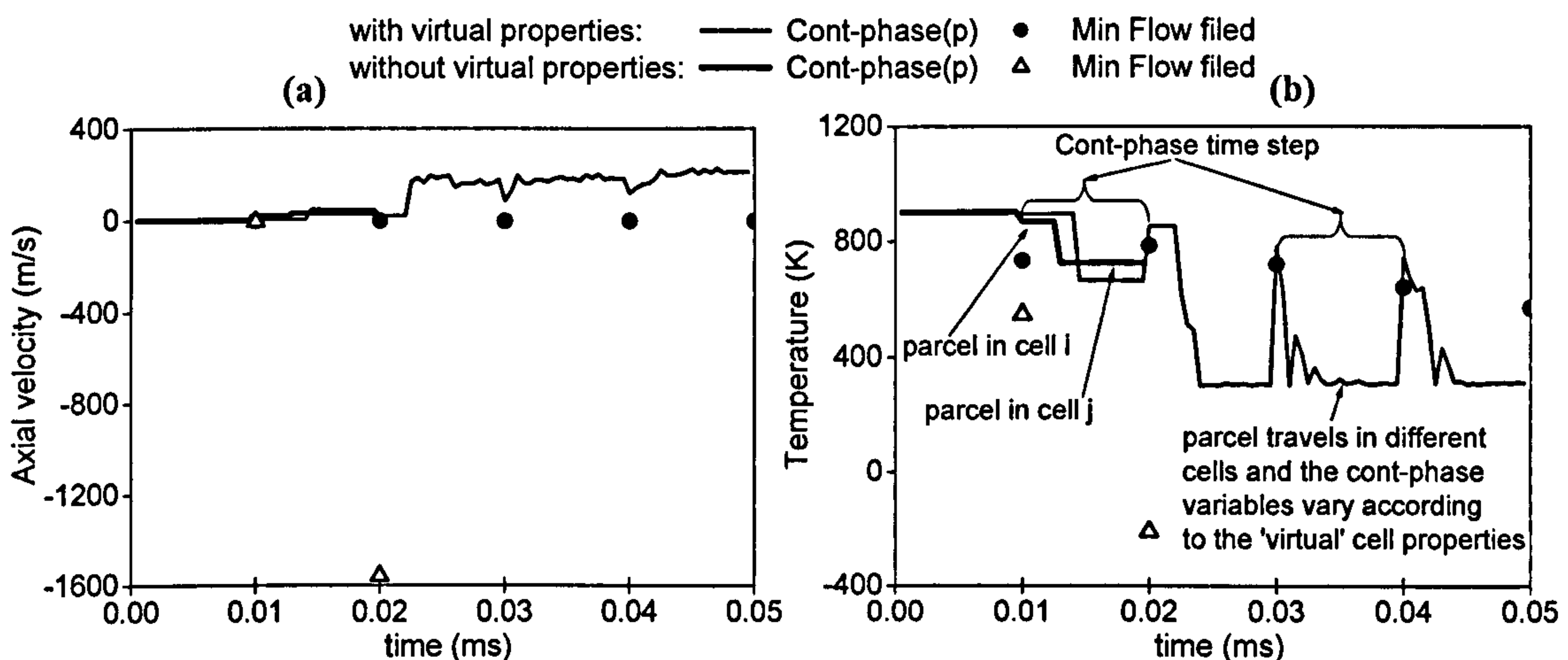


**Figure 5-64:** Effect of 'cell' virtual' velocity calculation on the prediction of the continuous phase (Cont-phase(p)) and mean flow field (a) velocity and (b) temperature; evaporating spray  $P_{INJ}=1200\text{bar}$ .

A second sample is presented in Figure 5-65, for non evaporating and evaporating conditions with high injection pressure. In this case the 2D-s2 grid was used and the interpolation/distribution scheme adopted was according to the spatial distribution method described in Figure 5-49. The graphs show that the liquid penetration for both evaporating and non-evaporating sprays is over-predicted without the calculation of the cell 'virtual' properties. This can be explained by the fact that, in this case, the source terms are over-predicted during the first time steps of the simulation, since the parcels 'see' continuous phase properties not affected by the multi-phase interaction, and consequently the spray can penetrate further down. Moreover, the results suggest that the calculation of cell 'virtual' variables seem to be more important especially in the



dense spray region close to the injection point, where high gradients of velocity, temperature and species concentration exist. The graph in Figure 5-65(b) shows that the vapour penetration seems to be less sensitive to the cell ‘virtual’ properties calculation, suggesting that this is due to its opposite effect on liquid velocity and vaporisation rate. When the cell ‘virtual’ variables are not estimated the liquid velocity is over-predicted increasing the spray penetration, since the vaporisation rate is considerably underestimated.

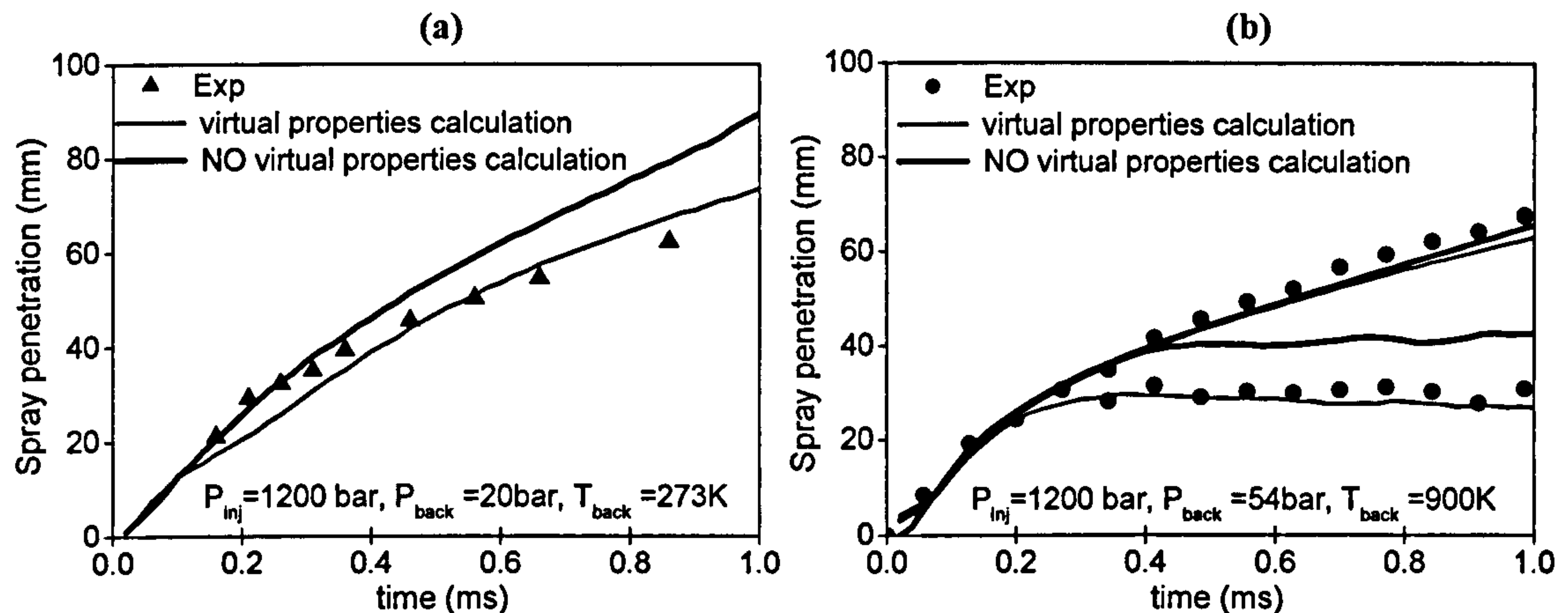


Figure 5-65: Effect of virtual properties on predicted liquid and vapour spray penetration of (a) non-evaporating and (b) evaporating spray. [ $P_{INJ}=1200\text{bar}$ ].

The next numerical parameter investigated is presented in Figure 5-66, and show the sensitivity of the model prediction on the selection of the time step used for the solution of the continuous and dispersed phases. The operating conditions correspond to the previous case of Figure 5-59. Four combinations of continuous and dispersed phase time steps have been used. In the first three cases the time step for the dispersed phase was set equal to  $5.E-7\text{s}$ ,  $2.5E-6\text{s}$  and  $5.E-6\text{s}$ , while the time step for the continuous phase was fixed at  $2.E-5\text{s}$ . In the last case the time step for the dispersed and continuous phase have been set equal to  $5.E-7\text{s}$  and  $2.E-6\text{s}$ , respectively. The results show that the smaller tracking time step allows more accurate results, while the use of continuous phase time step equal to  $2.E-5\text{s}$  or  $2.E-6\text{s}$  does not affect the predictions. This is according to the Courant number restriction:

$$C_p = \frac{|\vec{u}_p| \Delta t}{\Delta l} \leq C_{MAX} < 1 \quad (5-3)$$

where  $C_p$  and  $C_{MAX}$  are the cell and the maximum allowed Courant numbers, typically in the range of  $0.1 \sim 0.3$ ,  $\Delta t$  is the parcel tracking time step and  $\Delta l$  is a typical length, which is characteristic of the control volume of the parcel location. Moreover the parcel tracking time step should be smaller than the residence time of the parcel in the



computational cell (i.e. the time interval spent by the parcel to travel through the selected cell), in order to guarantee the correct interpolation/distribution of the multi-phase coupling. Finer grids required smaller time steps. This is particularly important in case of dynamically refined grids, which need variable time steps, in order to predict the same results.

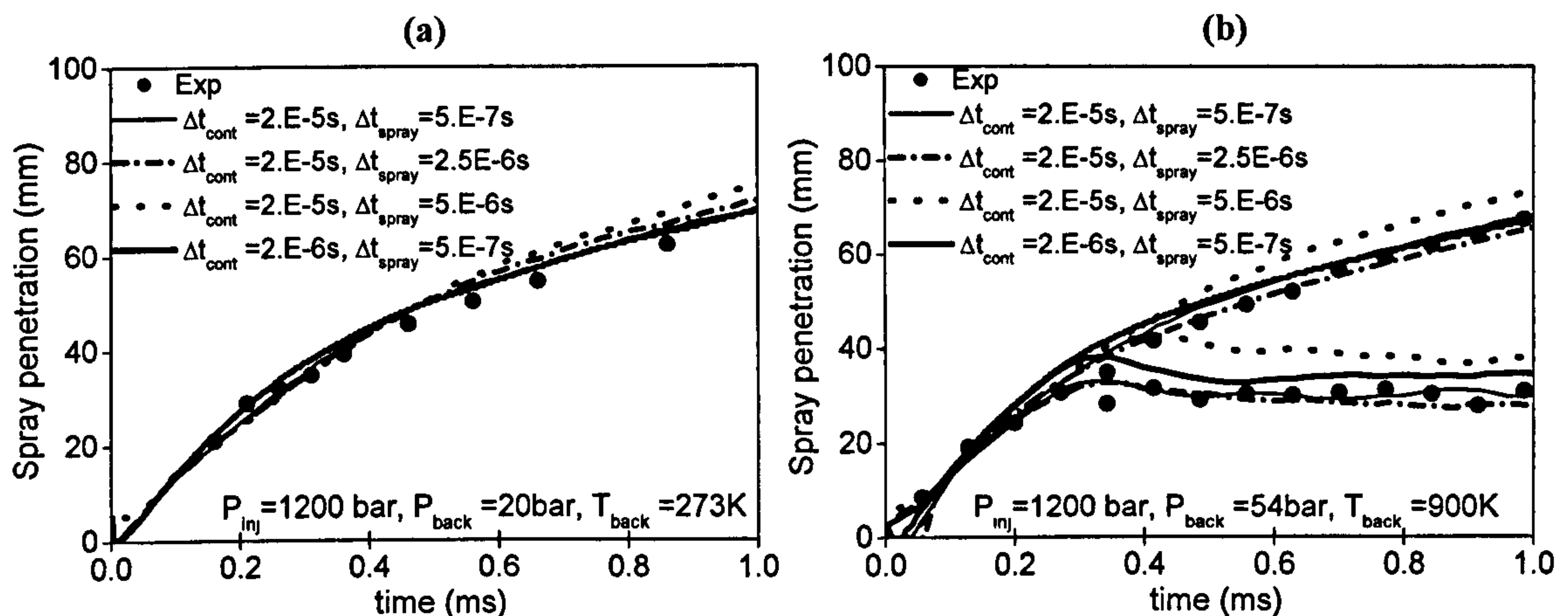
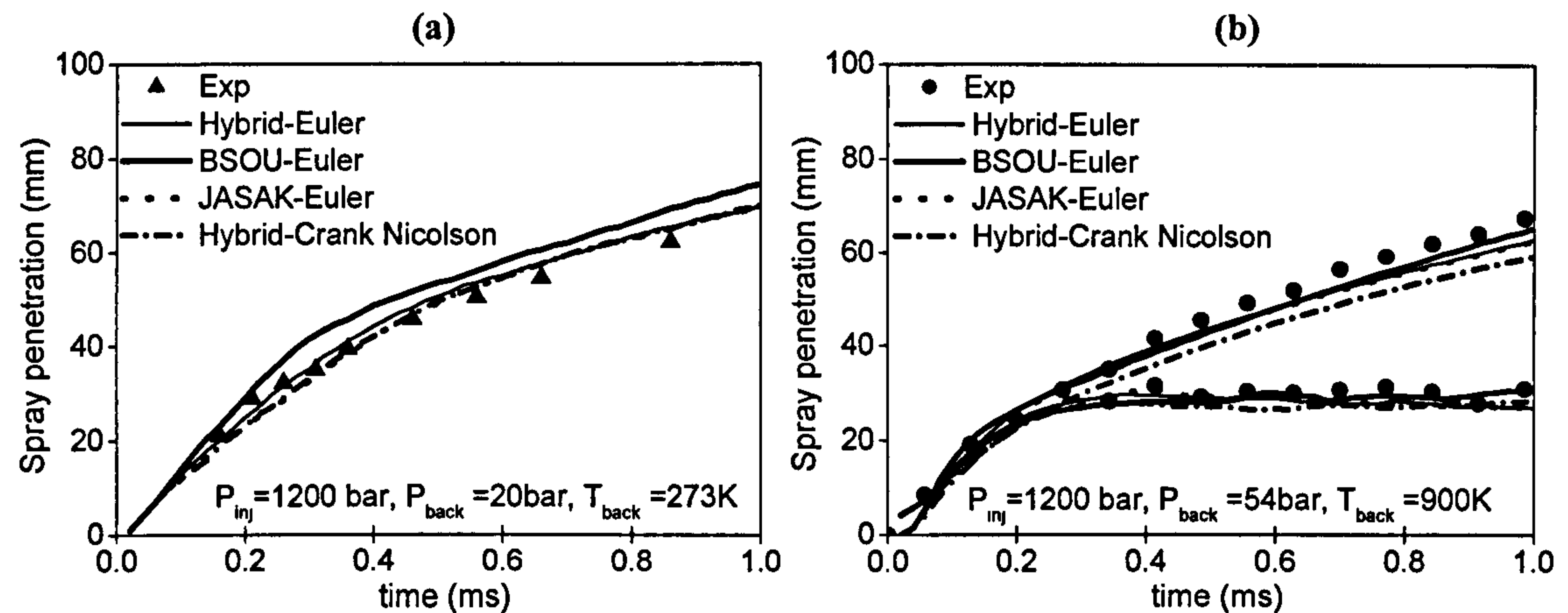


**Figure 5-66: Effect of time step on liquid and vapour spray penetration of (a) non-evaporating and (b) evaporating spray. [ $P_{INJ}=1200\text{bar}$ ].**

Finally the sensitivity of the model predictions on the temporal and spatial discretisation schemes implemented in the GFS code for the solution of the continuous phase flow according to the Eulerian frame of reference has been investigated and proposed in Figure 5-67, for the non-evaporating and evaporating cases with nominal rail pressure of 1200bar. According to the mathematical formulation described in Chapter 3, the code solves the governing equations for the conservation of mass, momentum, energy and other scalar variables, such as turbulent kinetic energy, its dissipation rate and vapour species concentrations, using the finite volume methodology. The convection term, in the general form of the conservation equation for the generic flow quantity  $\phi$  with reference to the control volume, can be discretised using different differencing schemes according to specific linear factors in the numerical algorithm. The effect of three schemes, named ‘Hybrid’, ‘BSOU’ and ‘Jasak’ (equations 3-15, 3-20), is discussed for the purposes of the present investigation. As far as the temporal discretisation of the term representing the rate of change per unit volume of the generic flow quantity  $\phi$ , the explicit Euler as well as the fully implicit and unconditionally stable Crank-Nicolson schemes have been tested. The results presented in Figure 5-67 reveal that the method is not significantly affected by different discretisation schemes. This is mainly due to the fact that the flow is driven by the momentum exchange between the two phases while



velocity components in the direction of the spray are two orders of magnitude greater compared to the other two. Thus, numerical diffusion effects are playing only a minor role. This is only evident in the vapour penetration during the later stages of the spray injection.



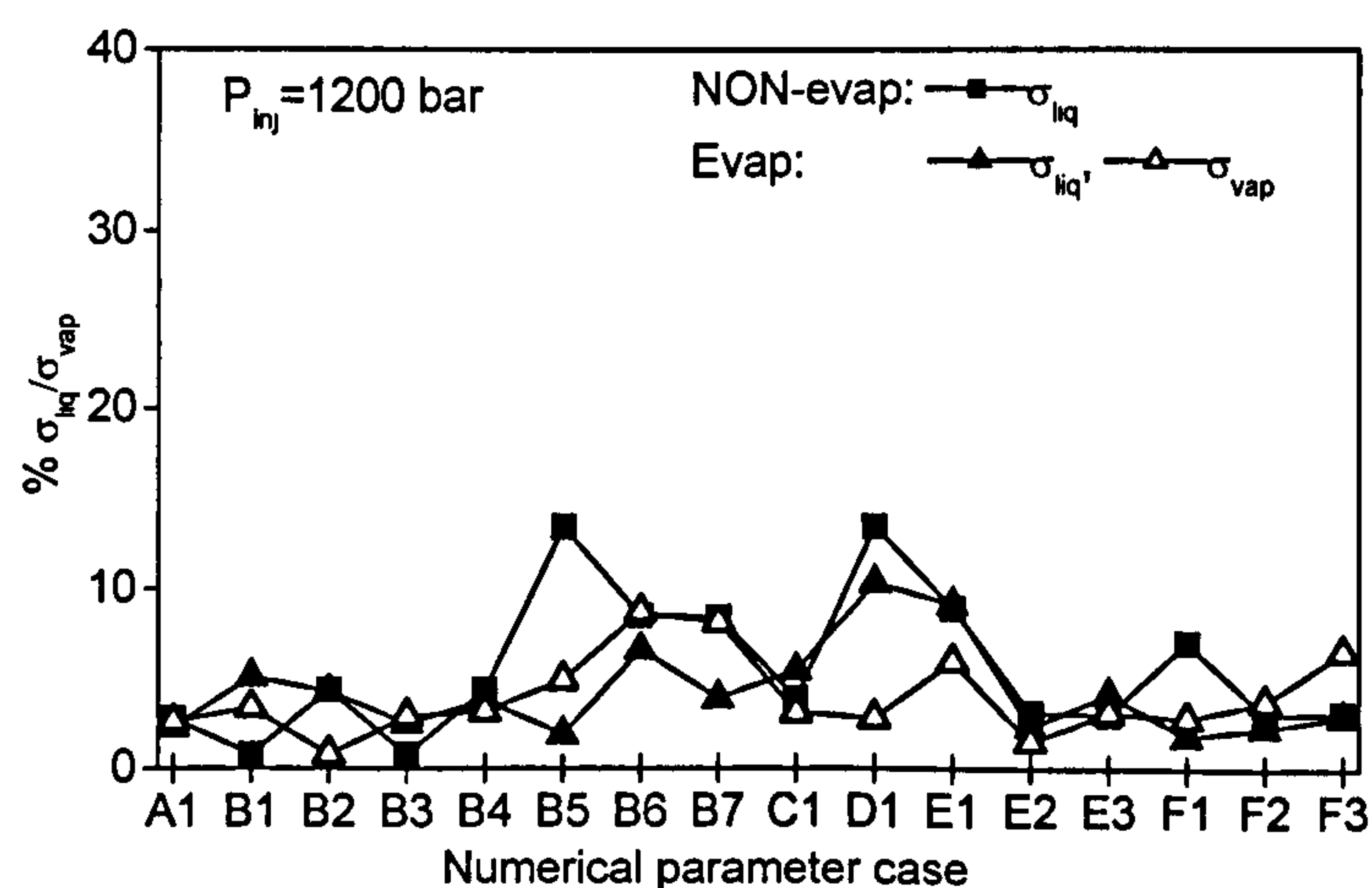
**Figure 5-67: Effect of discretisation method of the gas-phase equations on spray tip penetration of (a) non-evaporating and (b) evaporating spray (HYBRID, JASAC, BSOU for space, EULER, CRANK NICOLSON for time) [ $P_{INJ}=1200\text{bar}$ ].**

Table 5-VIII and Figure 5-68 summarises the results from the numerical investigation performed in this section, using as operating conditions the parameters presented in Table 5-V for non-evaporating and evaporating sprays injected from the cavitating nozzle design with nominal rail pressure of 1200bar. The percentage standard deviation of the predicted liquid and vapour penetrations from the experimental measurements is shown. Deviation above 10% is calculated only for 3-D non-evaporating spray simulation using the coarse grid, suggesting the necessity to refine the computational domain. Moreover, when the cell ‘virtual’ properties are not considered during the parcel sub-cycles, the results over-predict the source terms and consequently over-estimate the liquid penetration.



Numerical parameter	Description	Case	non-Evap	Evap	
			$\sigma_{liq}$	$\sigma_{liq}$	$\sigma_{vap}$
Standard settings	Grid: 2d-s2; $R_{interp/distr} = 0.4mm$ ; with virtual properties; $\Delta t_{cont} = 2.E-5s$ , $\Delta t_{spray} = 5.E-7s$ ; discretisation method: Hybrid-Euler	A <sub>1</sub>	2.8	2.3	2.6
Grid effect	2d-s1	B <sub>1</sub>	0.8	5.1	3.4
	2d-s3	B <sub>2</sub>	4.4	4.3	0.8
	2d-a1	B <sub>3</sub>	0.8	2.5	2.9
	2d-a2	B <sub>4</sub>	4.4	3.8	3.2
	3d-s1	B <sub>5</sub>	13.4	1.9	4.9
	3d-s2	B <sub>6</sub>	8.5	6.6	8.7
	3d-a1	B <sub>7</sub>	8.4	3.9	8.1
Effect of distribution distance	$R_{interp/distr} = \text{parcel diameter}$	C <sub>1</sub>	3.9	5.4	3.1
Effect of virtual properties	NO virtual properties	D <sub>1</sub>	13.4	10.3	2.8
Effect of time step	$\Delta t_{cont} = 2.E-5s$ , $\Delta t_{spray} = 5.E-6s$	E <sub>1</sub>	8.9	9.1	5.9
	$\Delta t_{cont} = 2.E-5s$ , $\Delta t_{spray} = 2.5E-6s$	E <sub>2</sub>	3.1	2.3	1.5
	$\Delta t_{cont} = 2.E-6s$ , $\Delta t_{spray} = 5.E-7s$	E <sub>3</sub>	3.0	4.1	3.1
Effect of discretisation method	BSOU-Euler	F <sub>1</sub>	7.0	1.8	2.8
	JASAK-Euler	F <sub>2</sub>	3.0	2.3	3.7
	Hybrid-Crank Nicholson	F <sub>3</sub>	3.1	2.9	6.5

**Table 5-VIII: Summary of the numerical parameters effect on the predicted liquid and vapour penetration under non-evaporating and evaporating conditions for the sharp-inlet nozzle. [ $P_{inj}=1200bar$ ].**



**Figure 5-68: Summary of the numerical parameters effect on the predicted liquid and vapour penetration under non-evaporating and evaporating conditions for the sharp-inlet nozzle. [ $P_{inj}=1200bar$ ].**



## 5.4 Results from the Sandia experimental measurements (Siebers [218])

This section focuses on the validation of the simulation spray model against the set of experimental data reported by Siebers [218]. The parameters tested include combination of injection pressure, back temperature and density, nozzle orifice diameter, injected liquid temperature and fuel physical properties.

### 5.4.1 Overview of the test cases

The wide range of conditions investigated in this section are summarised in Table 5-IX, while Table 5-X refers to the different fuel physical properties investigated. Finally, in the absence of a detailed injection profile for the nozzle flow rate, a fixed flow rate has been assumed. Its value has been calculated from the given pressure drop, hole orifice diameter and discharge coefficient. Similarly, a fixed injection velocity has been used, as estimated from the mass flow rate and the given contraction coefficient.

Orifice diameter (mm)	0.100, 0.246, 0.498
Area contraction coefficient	0.86, 0.81, 0.88
Discharge coefficient	0.80, 0.78, 0.84
$T_{\text{ambient}}$ (K)	696, 700, 1000, 1007, 1295, 1300
$T_{\text{fluid}}$ (K)	375, 410, 438
$\rho_{\text{ambient}}$ (Kg/m <sup>3</sup> )	3.6, 14.7, 30.2, 59
$\Delta P$ (Mpa)	65, 110, 135, 136, 137
Fuel	HMN, C <sub>16</sub> H <sub>34</sub> , DF2

**Table 5-IX: Summary of variation of the various parameters investigated. Those include the injector nozzle hole geometric and flow characteristics, the ambient pressure and temperature, the fuel temperature, the injection pressure and fuel physical properties.**

Table 5-X shows the fuels used in the experiments. In the absence of a complete data base for their physical properties, the HMN fuel has been simulated with the properties of C<sub>14</sub>H<sub>30</sub> and the cetane with those of C<sub>16</sub>H<sub>34</sub>. Finally, for the DF2 the distillation curve was given, together with the remaining fuel properties as function of temperature.

HMN →  $T_{\text{Bn}} = 520\text{K}$  (close to n-C<sub>14</sub>H<sub>30</sub>),

Cetane →  $T_{\text{Bn}} = 560\text{K}$  (close to n-C<sub>16</sub>H<sub>34</sub>)

DF2 → Distillation curve:	IBP	10%	30%	50%	70%	90%	EBP
	472K	499K	518K	534K	550K	576K	599K

**Table 5-X: Fuel boiling temperatures and distillation curves.**



### 5.4.2 Effect of physical and geometrical parameters

The simulations have been performed using the same model settings assessed in the previous section, while the 2D-s2 grid, shown in Figure 5-1, has been adopted. Again, the same definition of liquid penetration length as in the previous section is used here.

Before presenting the detailed validation cases, Figure 5-69 and Figure 5-70 present in a visual form the effect of injection pressure and air density on the vapour penetration, liquid penetration and induced flow field at 1.0ms after start of injection. The operating conditions selected for presentation here are those used for the validation cases of Table 5-IX. From Figure 5-69 it can be interpreted that increase of injection pressure leaves the liquid penetration unaffected, since all liquid vaporises shortly after its injection, within a distance of 25mm. Liquid penetration is increasing but not significantly. It has to be noted that the same scale for the plotted vapour mass fraction has been used in all four plots, implying a similar total amount of vaporised liquid. Figure 5-70 shows the effect of air density for fixed injection conditions. This time it is evident that huge differences are expected with increasing density. Both liquid and vapour penetration are significantly reduced, as expected.

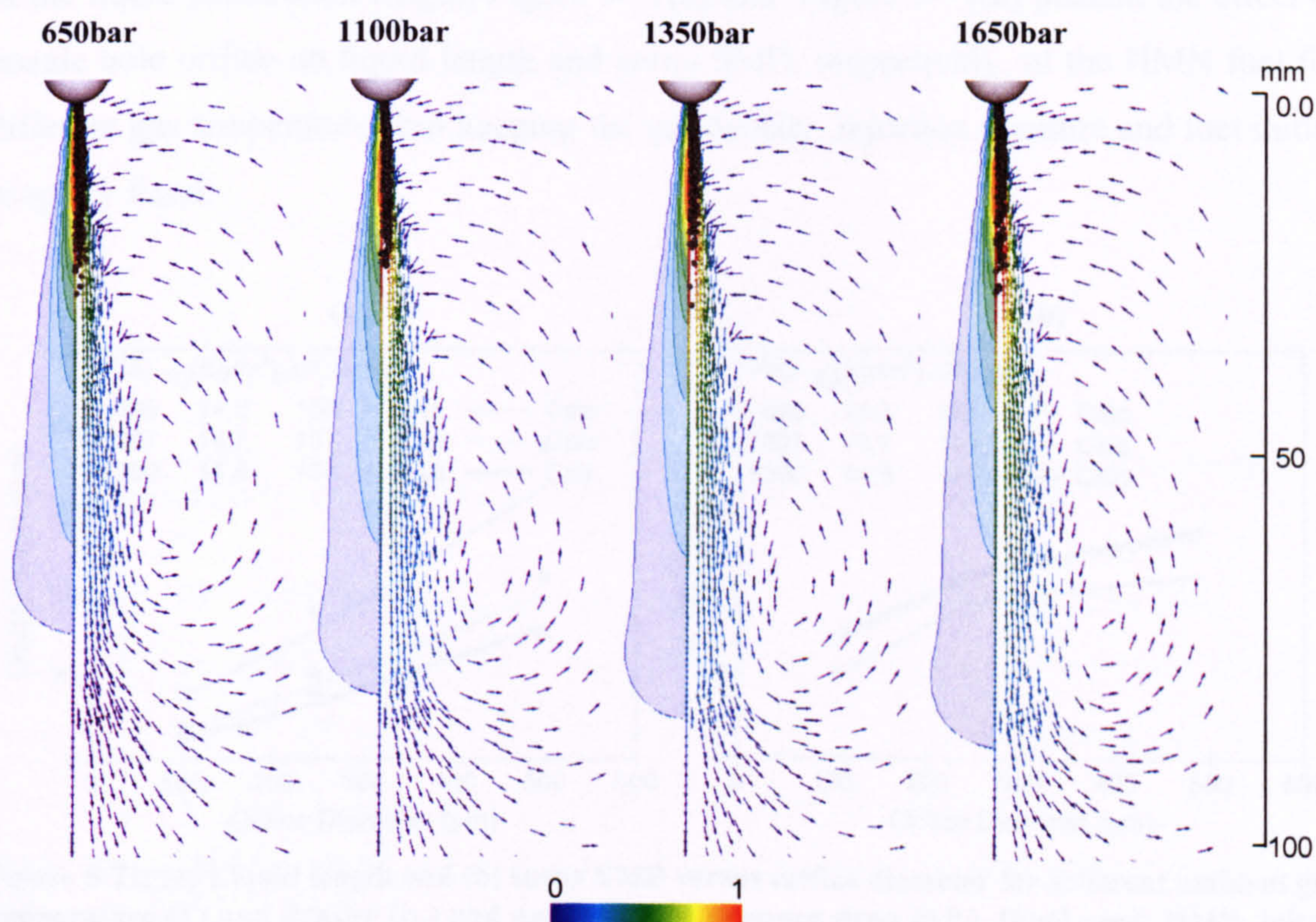


**Figure 5-69:** Effect of injection pressure on predicted spray structure 1.0ms after start of injection for four nominal rail pressures [ $T_{\text{BACK}}=1000\text{K}$ ,  $\rho_{\text{BACK}}=14.8\text{kg/m}^3$ ]. The colour scale of the vapour penetration is normalised with its maximum value.



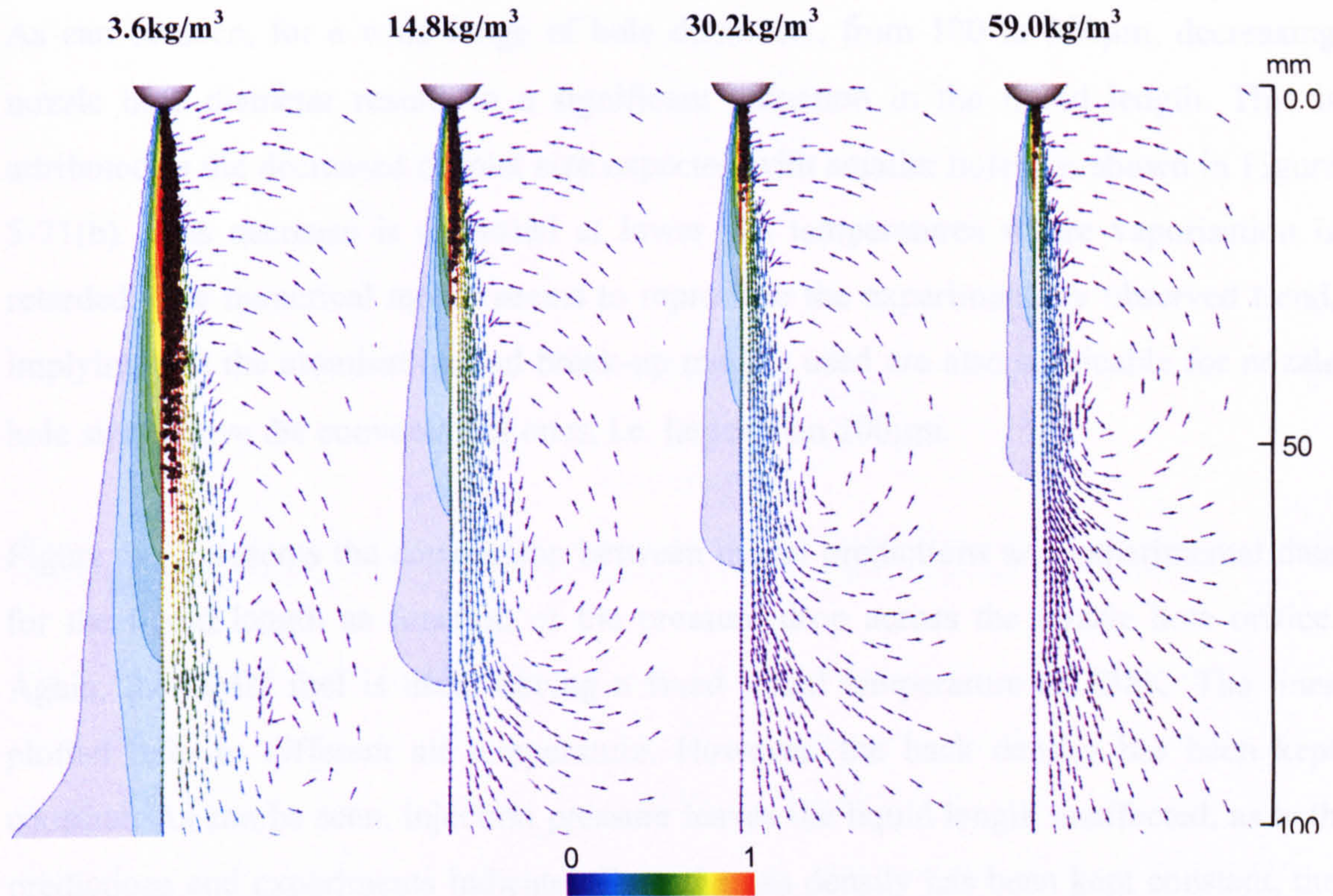


**Figure 5-70: Effect of back density on predicted spray structure 1.0ms after start of injection for four nominal rail pressures [ $T_{\text{BACK}}=1000\text{K}$ ,  $P_{\text{INJ}}=1350\text{bar}$ ]. The color scale of the vapour penetration is normalised with its maximum value.**

In the remaining part of this section, validation of the model is performed on the basis of the liquid penetration length. Figure 5-71(a) and Figure 5-71(b) present the effect of nozzle hole orifice on liquid length and spray SMD, respectively, of the HMN fuel for different gas temperatures but keeping the gas density, injection pressure and fuel initial property fixed.

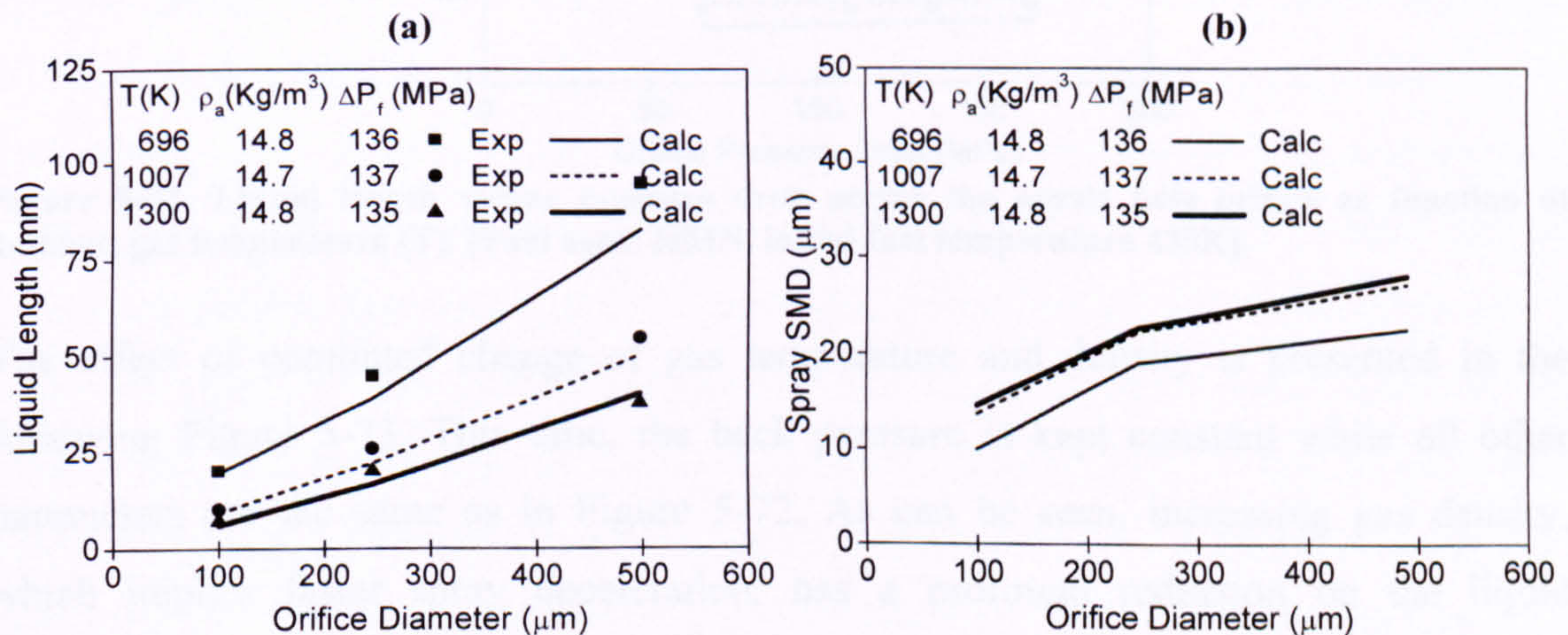


**Figure 5-71: (a) Liquid length and (b) spray SMD versus orifice diameter for different ambient gas temperature ( $T$ ) and density ( $\rho_a$ ) and nozzle orifice pressure drop ( $\Delta P_f$ ). [Fuel used: HMN, initial fuel temperature 438K].**



As can be seen, for a wide range of hole diameters, from 100 to 500 $\mu\text{m}$ , decreasing nozzle hole diameter results to a significant reduction in the liquid length. This is attributed to the decreased droplet size expected with smaller holes, as shown in Figure 5-71(b). This decrease is enhanced at lower gas temperatures where vaporisation is retarded. The numerical model seems to reproduce the experimentally observed trend, implying that the atomisation and break-up models used are also applicable for nozzle hole sizes above the conventional ones, i.e. larger than 200 $\mu\text{m}$ .

Figure 5-72 presents the comparison between model predictions and experimental data for the liquid length as function of the pressure drop across the nozzle hole orifice. Again, the HMN fuel is used, having a fixed initial temperature of 438K. The lines plotted refer to different air temperature. However, the back density has been kept constant. As can be seen, injection pressure leaves the liquid length unaffected, as both predictions and experiments indicate. Since the gas density has been kept constant, the decrease of the liquid length with increasing air temperature reveals the effect of faster fuel vaporisation rather than a different spray deceleration.

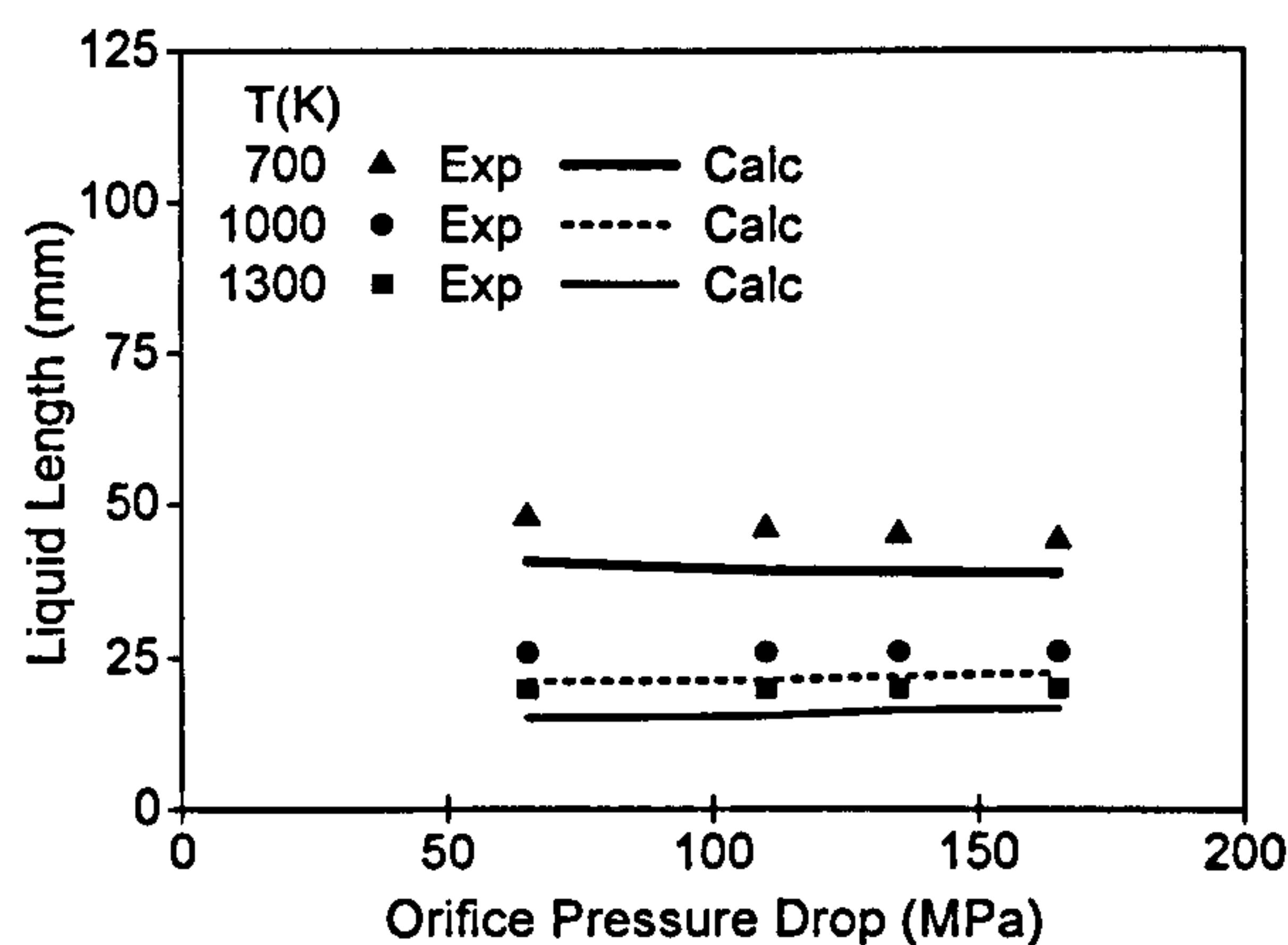


**Figure 5-72: Liquid length versus pressure drop across the nozzle hole orifice as function of ambient gas temperature (T). [Fuel used: HMN, initial fuel temperature 438K].**

The effect of combined change of gas temperature and density is presented in the following Figure 5-73. This time, the back pressure is kept constant while all other parameters are the same as in Figure 5-72. As can be seen, increasing gas density, which implies faster spray deceleration, has a profound reduction on the liquid penetration length. Again, the numerical model predicts reasonably the experimental values and trend.



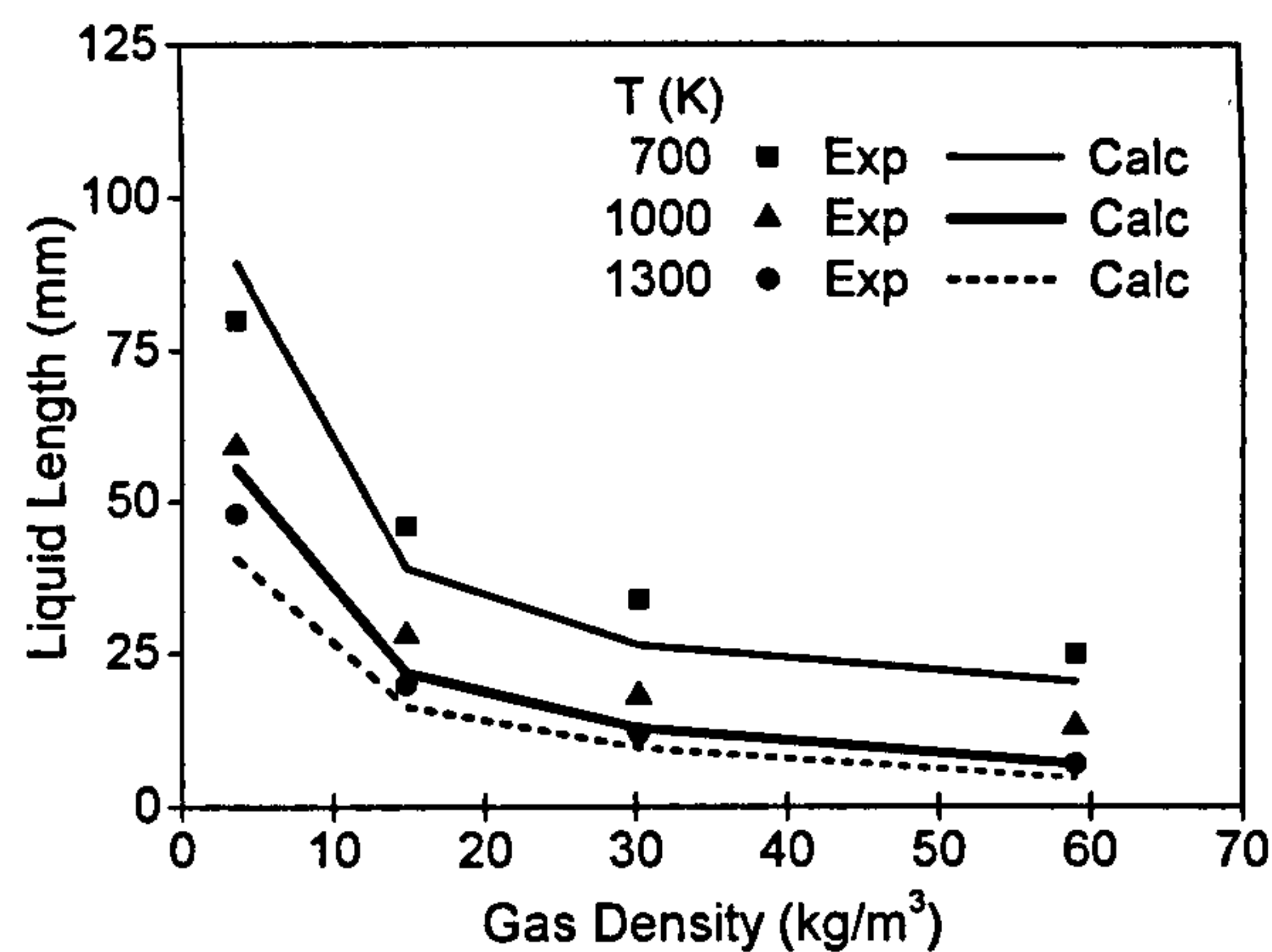


**Figure 5-73: (a) Liquid length as a function of gas density for different gas temperatures. [Nozzle hole diameter 0.246mm, HMN fuel, initial fuel temperature 438K, pressure drop 136MPa].**

The remaining studies address the effect of fuel initial temperature and its physical properties on liquid length rather than injection and chamber thermodynamic conditions. As already mentioned, three different fuels have been tested, HMN, cetane and DF2. At this point it should be mentioned that since the actual physical properties of the test fuel were not properly modelled, it is expected that model predictions may deviate from the real ones. Thus, those calculations can be interpreted as providing the correct trend with change of fuel rather than predicting the actual experimental values. Figure 5-74 shows the predicted and measured liquid penetration for those three fuels as function of the air density and temperature. It can be seen that for the low temperature case of 700K, the heavier fuel penetrates more, while the much lighter HMN fuel exhibits a significantly reduced penetration length compared to the other two. For those cases the model predictions underestimate the experimental values of the heavy fuels by approximately 25%. This was the largest deviation between experiments and predictions from all studies performed. They are possibly attributed to the differences in the actual fuel properties and the assumed ones. Increasing gas temperature, vaporisation is significantly enhanced and liquid penetration decreases. In this case, the model predictions are quite close to the experimental values, since fast evaporation hides the effect of fuel physical properties. The effect of initial temperature of the cetane and DF2 fuels on liquid length is shown in Figure 5-75. It can be seen that, within the range tested (380 to 440K), liquid penetration is not significantly affected, especially at higher gas temperatures. As in the previous Figure 5-74, for the lower gas temperature case, the assumed fuel properties of the model result to much lower liquid length compared to the measured one.



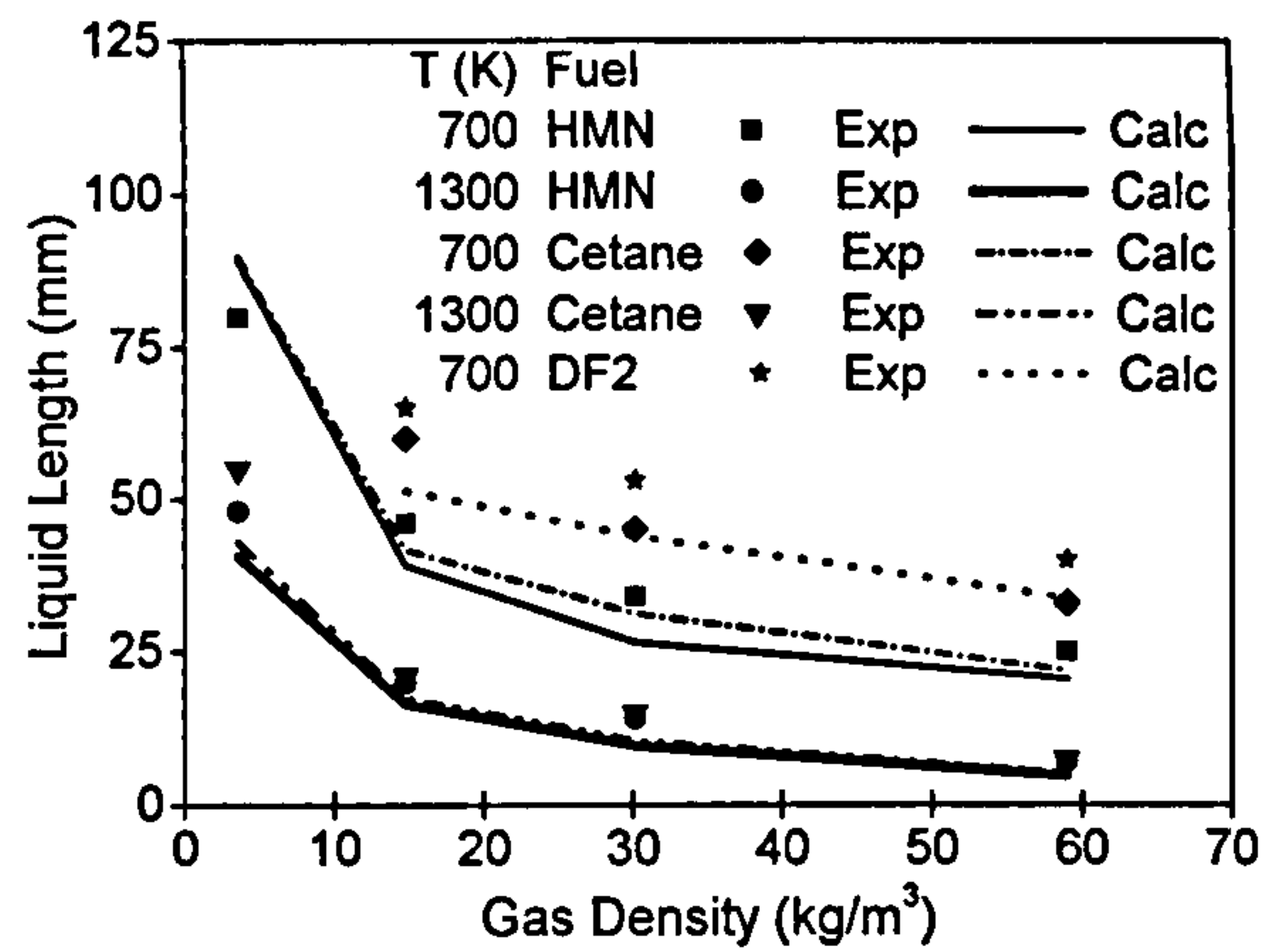


Figure 5-74: Effect of fuel on liquid length (HMN/ $n\text{-C}_{14}\text{H}_{30}$  versus Cetane/ $n\text{-C}_{16}\text{H}_{34}$ ). [Nozzle hole diameter 0.246mm, HMN fuel, initial fuel temperature 438K, pressure drop 136MPa].

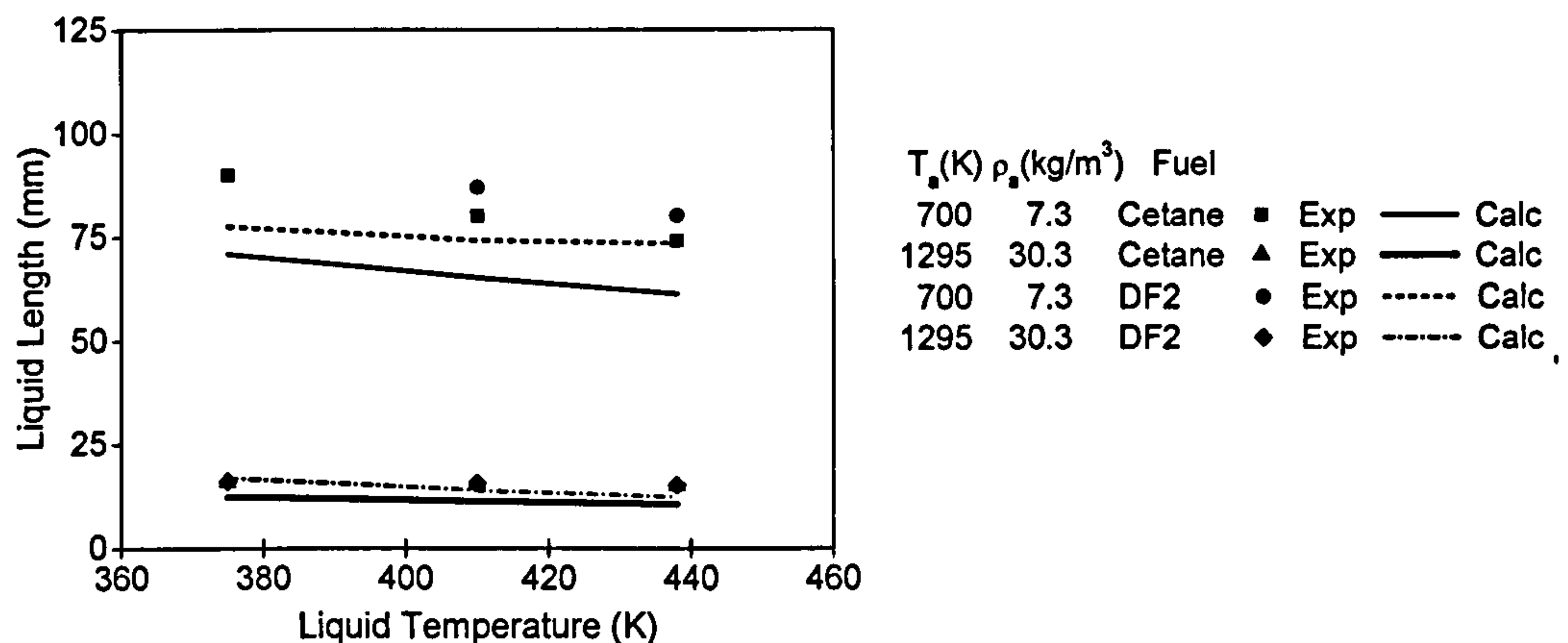


Figure 5-75: Liquid length as function of initial fuel temperature for different ambient conditions. [Nozzle hole diameter 0.246mm, HMN fuel, pressure drop 135MPa].

Overall, it can be concluded that the computational model reproduces the experimental values for the liquid penetration length over a wide range of operating conditions. In most cases, the differences were less than 10% while the trend of the different parameters investigated was reasonably predicted.

Finally, in order to investigate the effect of multi-component vaporisation in high pressure and temperature environment, typical of diesel sprays injected near TDC, the spray development of a mixture, initially composed by 50% dodecane and 50% hexadecane, has been simulated in an environment at 1295K and 30.3kg/m<sup>3</sup> back temperature and density, respectively. Under these highly evaporating conditions, the vaporisation rate equals the injection rate at 0.03ms after start of injection, as shown in Figure 5-76(a). This has a sudden effect on the liquid penetration, which stops, almost immediately, at a distance of 10mm from the injector hole exit, as presented in Figure 5-76(b). The same graph also shows the vapour penetration of the two fuels initially



present in the mixture. The results reveal that the vaporisation of these two components is almost identical, and this can be explained by the rapid vaporisation occurring under these operating conditions. The same conclusion can be drawn looking to the Figure 5-77, which show the liquid mixture and vapour distribution of dodecane and hexadecane fuels at 0.5 and 1.0ms after start of injection. Clearly the vapour penetrations for the two components are nearly the same, suggesting that the composition of diesel fuel seems not to play a crucial role under high pressure and temperature conditions. This was also confirmed by the previous investigations, where small differences were estimated in the liquid penetration of HMN, Cetane and DF2 at the same operating conditions, according to Figure 5-74 and Figure 5-75.

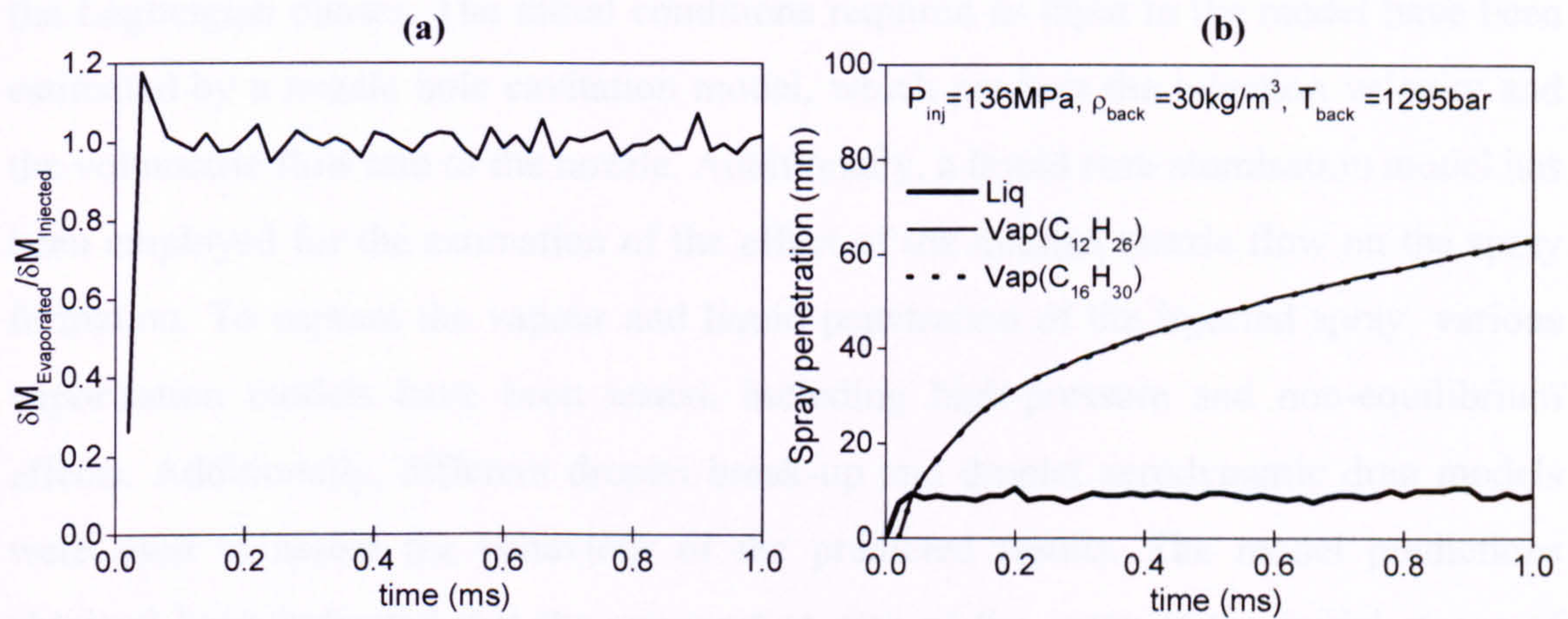


**Figure 5-76: (a) Non-dimensional vaporization rate and (b) liquid and vapour penetration temporal profiles for a mixture of 50% dodecane and 50% hexadecane [Nozzle hole diameter 0.246mm, HMN fuel, pressure drop 135MPa, 1295K gas temperature, 30.3kg/m<sup>3</sup> gas density].**

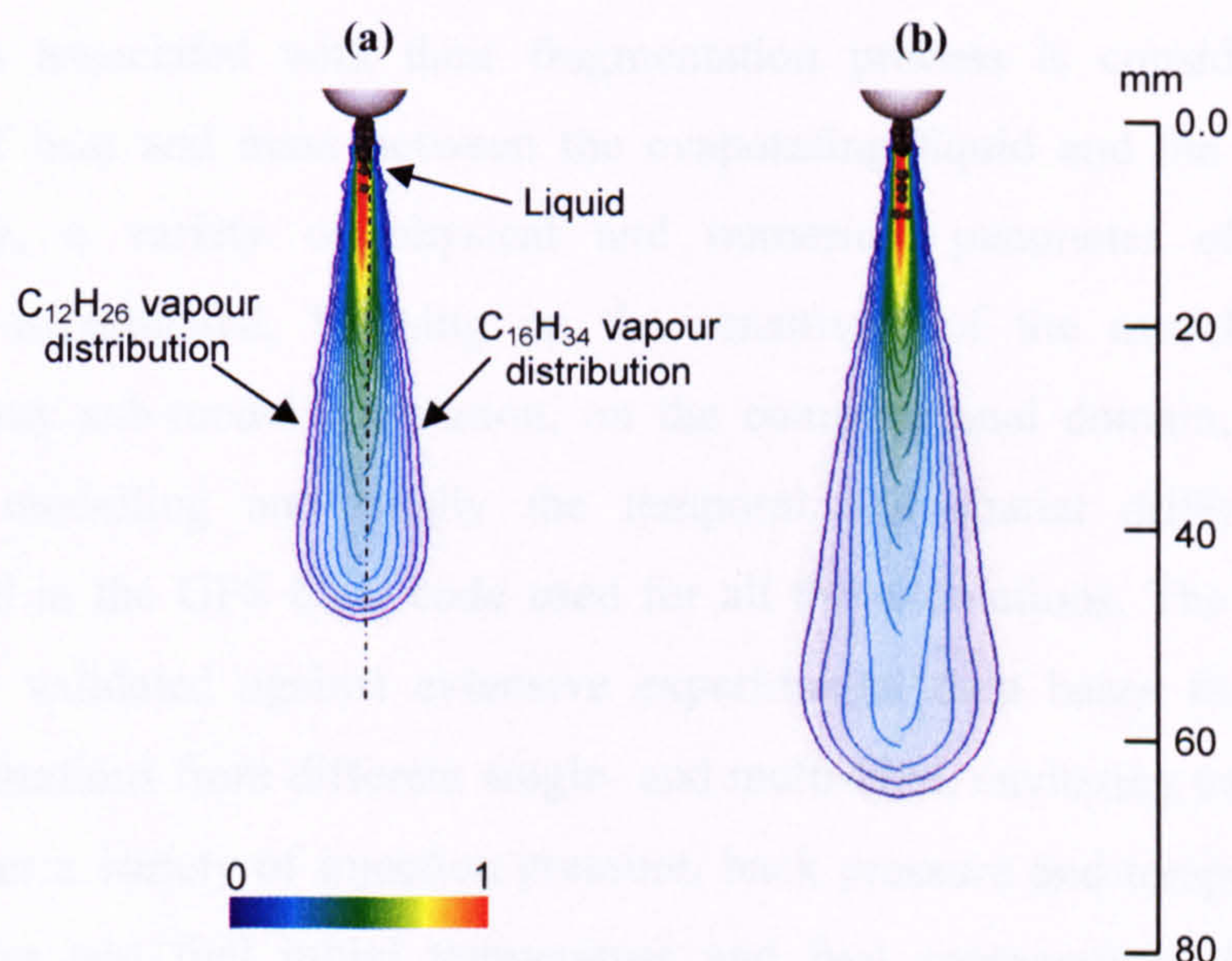


**Figure 5-77: Liquid mixture and vapor distribution of (left) dodecane and (right) hexadecane fuels at (a) 0.5ms and (b) 1.0ms after start of injection [Nozzle hole diameter 0.246mm, HMN fuel, pressure drop 135MPa, 1295K gas temperature, 30.3kg/m<sup>3</sup> gas density].**



## 5.5 Conclusions

The effect of different physical mechanisms taking place during the injection and further development of diesel sprays has been investigated. To minimise grid errors, a dense-particle Eulerian-Lagrangian stochastic methodology has been employed. This is able to resolve the dense spray formed at the nozzle exit using local grid refinement and resulting to cells with volume comparable to that of the dispersed droplets. Results obtained using cell with minimum spacing down to 0.15mm have shown that it plays minor role on model predictions, if appropriate spatial distribution functions for the liquid volume fraction and the fuel vapour mass, momentum and energy exchange source terms are implemented for modelling the interaction between the Eulerian and the Lagrangian phases. The initial conditions required as input to the model have been estimated by a nozzle hole cavitation model, which predicts the injection velocity and the volumetric flow rate of the nozzle. Additionally, a liquid core atomisation model has been employed for the estimation of the effect of the internal nozzle flow on the spray formation. To capture the vapour and liquid penetration of the injected spray, various vaporisation models have been tested, including high-pressure and non-equilibrium effects. Additionally, different droplet break-up and droplet aerodynamic drag models were used to assess the behaviour of the predicted results. The model predictions obtained have indicated that the evaporation rate of the spray at the initial stages of injection plays a crucial role in accurately calculating the liquid penetration as function of the injection pressure. Correct trends can be predicted if the increased surface area of the droplets associated with their fragmentation process is considered during the exchange of heat and mass between the evaporating liquid and the surrounding air. Successively, a variety of physical and numerical parameter effect have been extensively investigated, focusing on the sensitivity of the model predictions on different spray sub-model correlation, on the computational domain, the multi-phase interaction modelling and finally the temporal and spatial differencing schemes implemented in the GFS CFD code used for all the simulations. The model was then successfully validated against extensive experimental data bases for the liquid and vapour penetrations from different single- and multi-hole, cavitating and non-cavitating nozzles under a variety of injection pressure, back pressure and temperature, injection hole diameter and fuel initial temperature and fuel composition. The results have confirmed that liquid penetration under high vaporisation rate conditions is nearly



independent on injection pressure, while vapour penetration is higher with increased injection pressure and continuously increases with time. Liquid and vapour penetrations are significantly reduced with increasing back temperature and density. Liquid penetration is linearly decreasing with nozzle hole diameter and this effect is enhanced at lower gas temperatures where vaporisation is retarded. The composition of the fuel results to play a role under moderately low ambient temperature and density, where the liquid penetration has been estimated to be inversely proportional to the fuel volatility, while it seems to have minor effect under highly evaporating environment, characterised by high temperature and density conditions. Finally, the liquid penetration is not significantly affected by the initial liquid temperature at higher gas temperature conditions, while it linearly decreases with increasing liquid temperature at low temperature environments.



## Chapter 6

Never discourage anyone...who continually makes progress,  
no matter how slow.

Plato

# APPLICATIONS TO HIGH-PRESSURE INJECTION SYSTEMS FOR GDI ENGINES

### 6.1 Introduction

The main target for engine developers of small- and mid-size displacement spark-ignition engines, which typically power more than 50% of European passenger cars, remains the best compromise between fuel economy, emissions and power output/drivability. In the recent years, a number of automotive manufacturers have introduced gasoline direct-injection (GDI) engines, which are found to offer significant fuel-economy advantages over conventional port-fuel-injection engines, satisfying the conflicting requirements of mixture preparation during high-load (homogeneous stoichiometric/lean) and part-load (stratified overall lean) conditions. The fuel injection system in a gasoline direct injection (GDI) engine is a key component that must be carefully matched with the in cylinder flow field to provide the desired mixture cloud over the entire operating range of the engine, producing a well-atomised fuel spray. For the efficient combustion of a stratified mixture, stable and compact spray structure is necessary. The combustion system designs for GDI can be divided into three main types, classified according to the relative position of the injector towards the spark plug and the piston crown and according to the mixture preparation approach. The first production solutions have adopted either wall-guided or air-guided concepts, as shown in Figure 6-1.

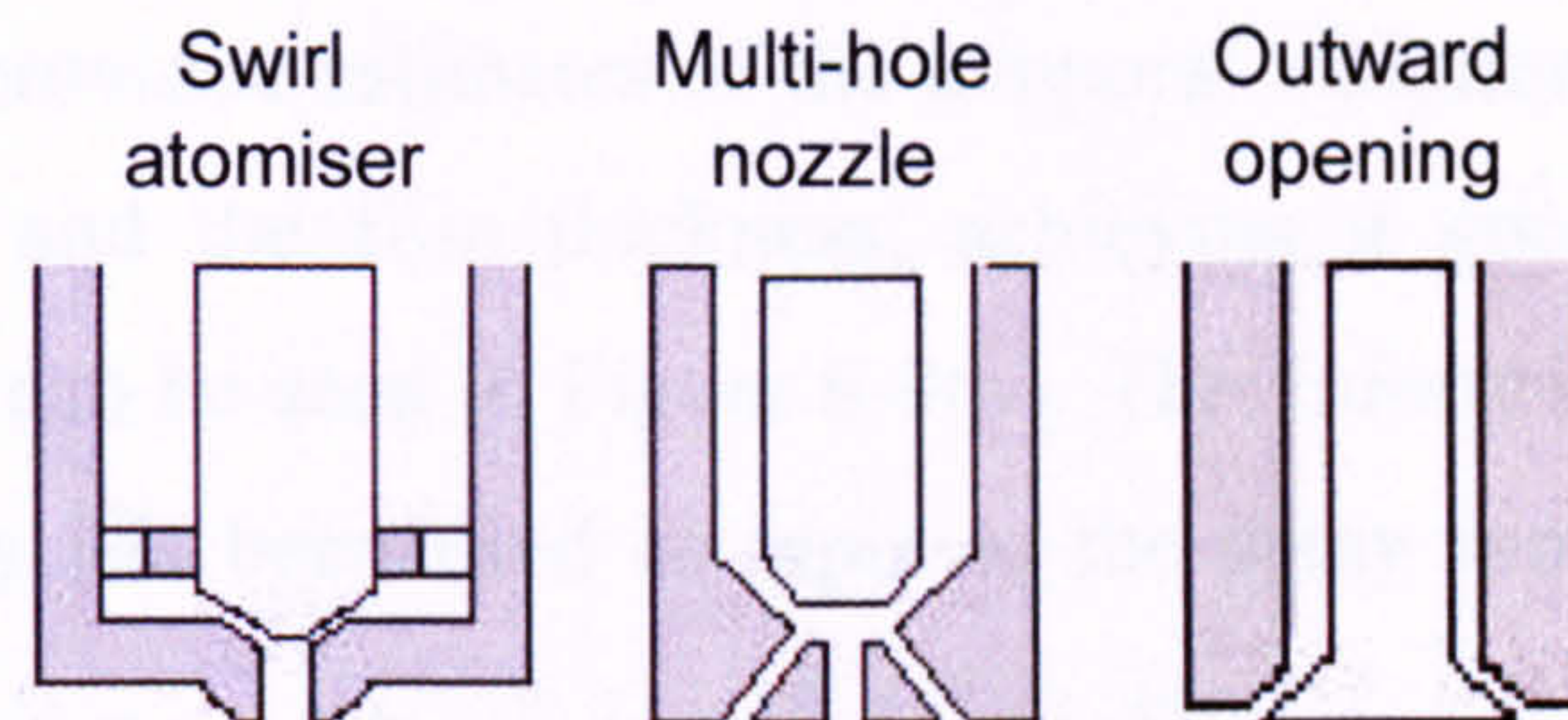


Figure 6-1: GDI combustion systems [2].



The second-generation of GDI engines is using a spray-guided concept with a centrally mounted fuel injector spraying along the cylinder axis towards the spark plug with electrodes located near the edge of the spray.

Spark location, fuel injection quantity and timing represent crucial factors. High pressure injection systems for GDI engines are investigated to inject a well-atomised fuel into the cylinder during the induction or compression stroke (early or late injection strategy, respectively) since they are capable of generating spray patterns that fulfil the conflicting injection demands during the two engine strokes [117]. There are presently two different mixture preparation principles under development for spray-guided systems, based on the multi-hole nozzle and the outwards-opening pintle injector, as schematically illustrated in Figure 6-2. The swirl-pressure atomiser, used with wall-guided systems as well for injection during induction, is also shown for comparison.



**Figure 6-2: Three different injector designs for spray-guided concept with central-mounted injector: swirl atomizer, multi-hole nozzle and outward opening injector [2].**

Modelling of the flow processes inside the fuel injection system and the injection nozzle has provided better understanding of the near-nozzle spray formation. Fuel atomisation process is controlled by the nozzle geometry, the characteristics of the fuel supply system, and the liquid-gas aerodynamic interaction. For these reasons, efforts are concentrated in using both experiments and calculations in an attempt to gain better understanding of these phenomena and their effect on performance and durability of emerging gasoline high-pressure fuel injection systems and their application to direct injection spark-ignition engines.

This chapter presents the results obtained from the computational investigations on the three different high-pressure GDI systems currently available for the new generation of direct-injection spark-ignition engines. The results to be presented highlight the importance of linking the internal nozzle flow characteristics to the subsequent spray development.



## 6.2 Swirl-pressure atomiser

The swirl-pressure atomiser represents the first fuel injection system investigated for spray-guided GDI applications. Previous computational and experimental studies of the flow development inside the hole of pressure swirl atomisers employing the VOF (Volume Of Fluid) methodology [117, 128] have revealed that a liquid film is formed inside the discharge hole, due to the fuel swirling motion as shown in Figure 6-3(a) for a nominal injection pressure of 70bar. That, in turn, leads to the formation of a hollow cone spray. The computational results have confirmed that it is the two-phase flow dynamics that controls the film formation process and its thickness during the injection period. Validation of the predicted flow distribution against experimental data using the GFS code has been done through comparison with CCD images obtained on a purpose-build transparent hole extension attached to the nozzle exit [117]. Post-processing of the obtained images has provided estimates of the temporal variation of the axial and swirl velocity components and the film thickness, achieving a good agreement with the experimental data, as can be seen in Figure 6-3(b). This information for the liquid film thickness and velocity has been used as input to the spray model for the subsequent spray investigation.

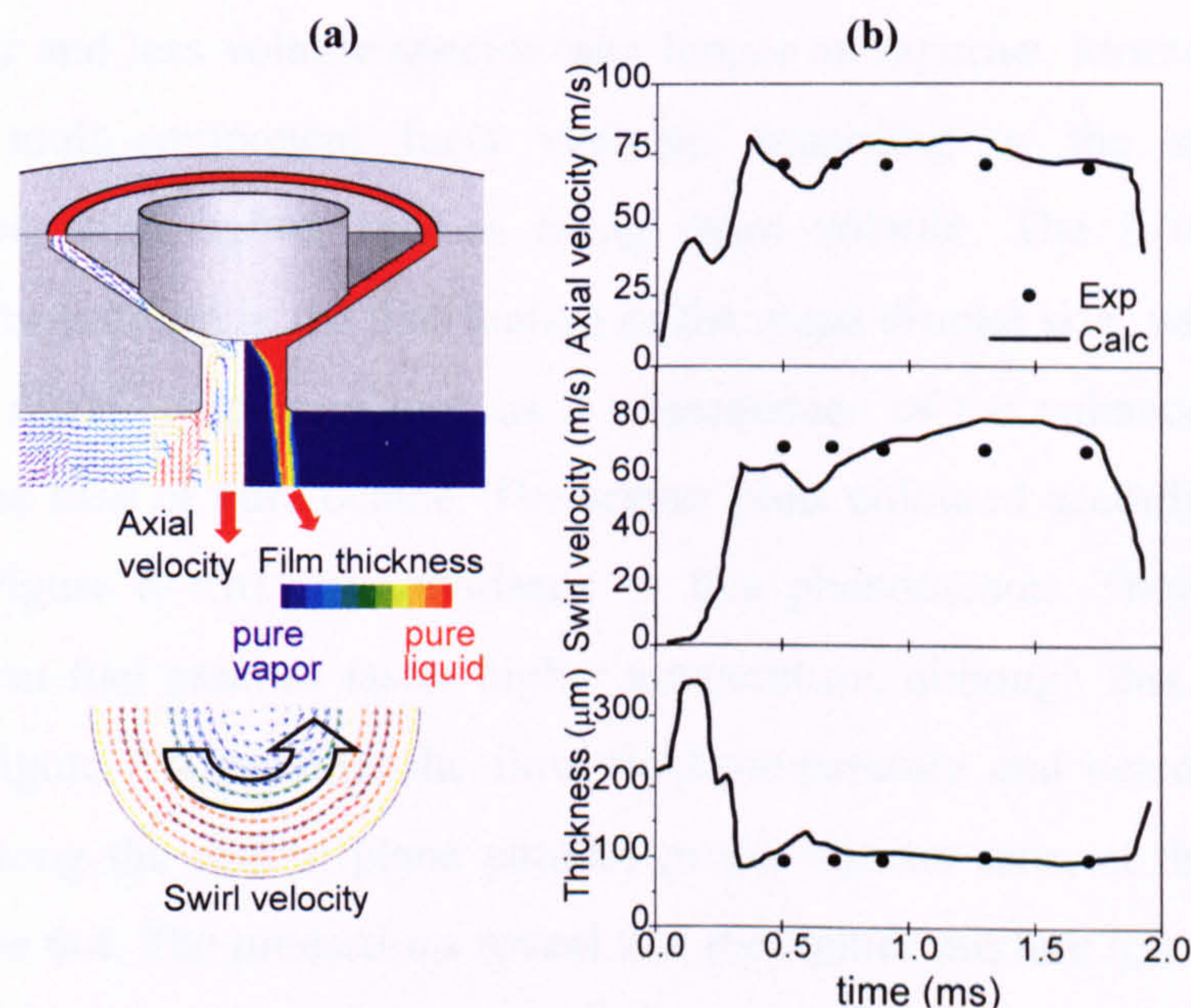


**Figure 6-3: (a) Schematic of the pressure swirl atomiser. (b) Calculated and measured temporal variation of the spatially averaged (mean) nozzle flow exit conditions: axial velocity, swirl velocity and film thickness [117].**



### 6.2.1 Multi-component fuel vaporization in a constant volume chamber

The first application presented in this thesis of the spray model using a GDI system is the injection of fuel from a swirl-pressure atomizer inside a constant volume chamber at 10bar back pressure and 600K temperature, respectively. The effect of fuel composition on the liquid and gas phase characteristics is presented in Figure 6-4 and Figure 6-5. It shows the dispersed and continuous phase distributions, as predicted implementing the multi-component vaporisation model, described in Chapter 4. Two different initial fuel compositions have been assumed: the first one consists of pure octane, while the second fuel is represented by a lighter mixture of 50% pentane and 50% octane. For the purposes of clarity and thanks to the symmetry of the problem, half of the whole cylindrical domain is represented in the graphs. Figure 6-4(a) shows the scatter plots of the dispersed phase coloured according to the droplet diameter, at 0.5, 1.5 and 3.5ms after the start of injection, corresponding to the start, middle and end of injection, which lasts 3ms. The comparison between single (right) and multi (left) component fuel cases is presented, highlighting how liquid vaporisation takes place as the spray develops inside the chamber. The first conclusion that can be derived from the predictions is that the composition of the fuel does not affect the spray shape, during the injection period, although bigger droplets are present in the chamber in case of pure octane, confirming that the heavier and less volatile species take longer to vaporise. Moreover, the graphs confirm that multi-component fuels vaporise according to the so-called batch-distillation type, with lighter species being more volatile. The first effect of this behaviour can be realised in the distribution of the mean droplet size, which has smaller values for the multi-component fuel, as a consequence of the enhanced vaporisation, compared to the case of pure octane. The scatter plots coloured according to the liquid temperature, Figure 6-4(b), give evidence to this phenomenon. They show that the multi-component fuel reaches faster higher temperature, although this effect is not so pronounced. Figure 6-5 presents the flow field temperature and octane concentration distributions along the central plane parallel to the injector axis, at the same instants shown in Figure 6-4. The predictions reveal that the lighter mixture (on the left) absorbs faster the energy necessary to heat-up and successively vaporise the liquid, compared to the single-component fuel, with the consequence that the low temperature region is confined in a more limited area.



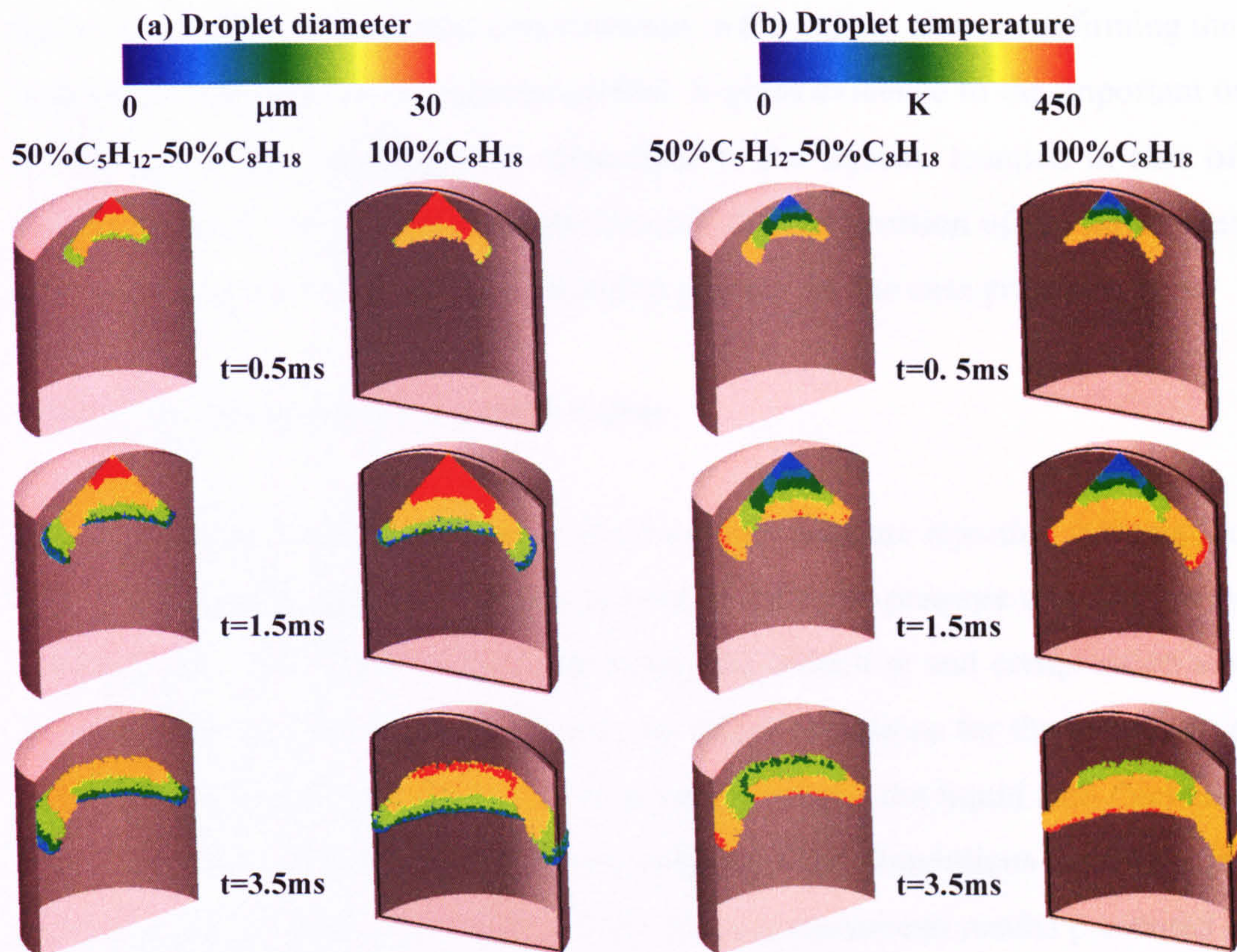


Figure 6-4: Effect of fuel composition on the liquid dispersed phase (a) size and (b) temperature distributions at 0.5, 2.5 and 4.5ms ASOI. Scatter plots are coloured according to the droplet (a) diameter and (b) temperature.  $P_{\text{back}}=10\text{bar}$  and  $T_{\text{back}}=600\text{K}$ .

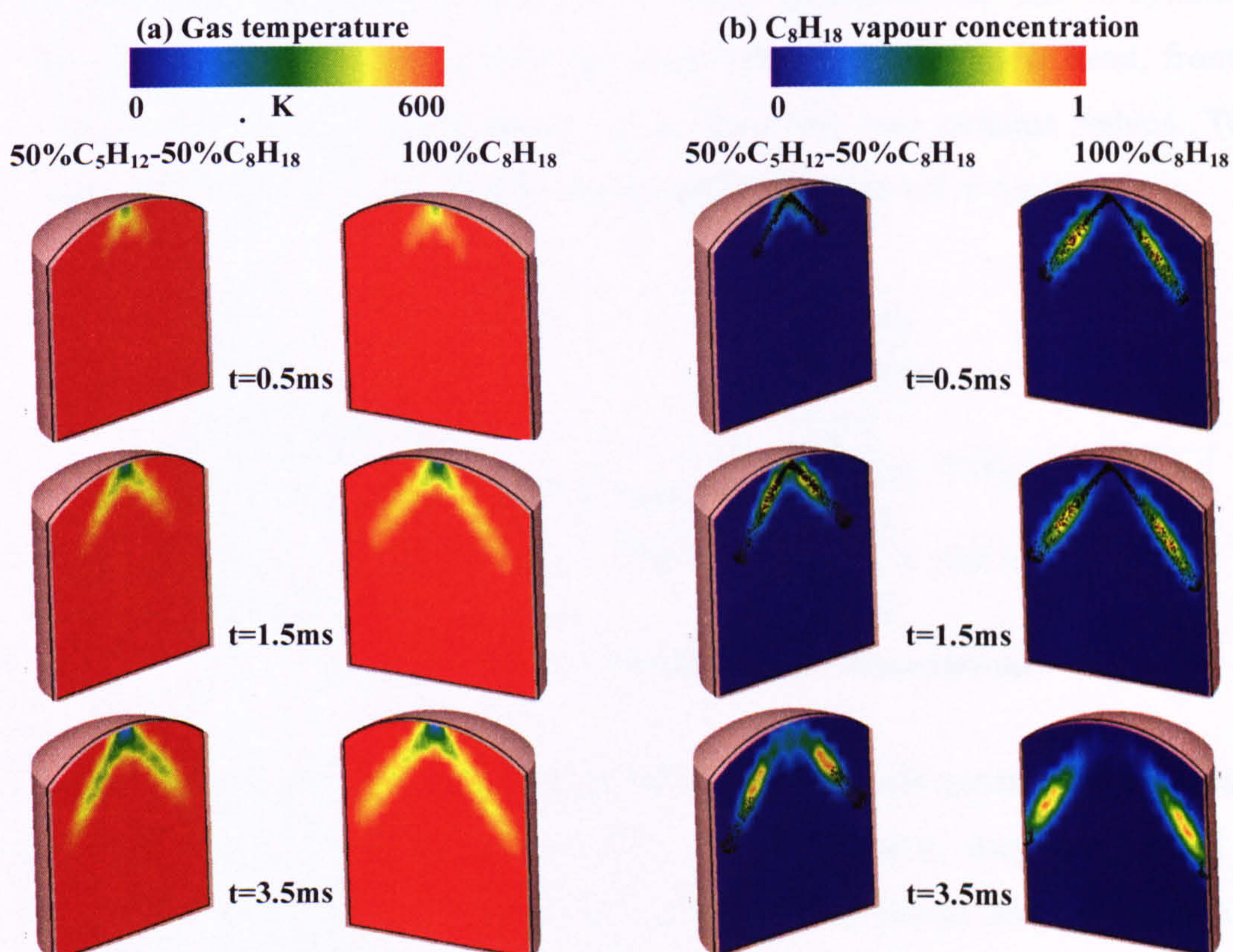


Figure 6-5: Effect of fuel composition on the continuous phase (a) temperature and (b) octane concentration distributions at 0.5, 2.5 and 4.5ms ASOI.  $P_{\text{back}}=10\text{bar}$  and  $T_{\text{back}}=600\text{K}$ .



Figure 6-5(b) shows the octane concentration in the vapour phase, confirming the batch-distillation behaviour of the vaporising fuel. It gives evidence to the important outcome of the vapour being concentrated more close to the injector location in case of multi-component fuel. The results show that overall the composition of the liquid fuel seems not to play a crucial role in the vaporisation process for the case presented here.

### 6.2.2 Spray development in a GDI engine

The second application of the spray model on high pressure injection systems for spark-ignition engines focuses on the development of the swirl-pressure atomiser spray inside a transparent multi-valve GDI engine during the induction and compression strokes of the engine cycle. As already mentioned, the initial conditions for the temporal variation of the axial and swirl injection velocity components and the liquid film thickness at the exit of the injection hole have been calculated by flow simulations inside the pressure-swirl atomizer, as shown in Figure 6-3(b). The computational results presented here are supported by LDV measurements for the air-charge-motion obtained on a mass-produced single-cylinder motorcycle crank case with an elongated cylinder block to accommodate the optical piston [223], while validation for the in-cylinder spray development is performed using CCD spray images. The cylinder head, from a four-cylinder engine, was incorporating three inlet and two exhaust valves. Table 6-I specifies the main geometrical dimensions and the engine valve timing.

Bore	73 mm
Stroke	59.6 mm
Compression Ratio	9.5:1
Inlet Valve: Open (IVO) / Close(ICV)	31° CA BTDC / 61° CA ABDC
Exhaust Valve: Open (EVO) / Close(ECV)	61° CA BBDC / 31° CA ATDC

**Table 6-I: Optical multi-valve engine characteristics.**

Figure 6-6 shows the five blocks of the numerical sub-grids constructed for meshing the whole engine at top-dead-centre (TDC). As can be seen, they are formed using a combination of cell types. The moving parts (engine piston and valves) are meshed using hexahedral cells while the non-moving parts (inlet/exhaust ports around the valves and piston pockets) using tetrahedral cells [224].



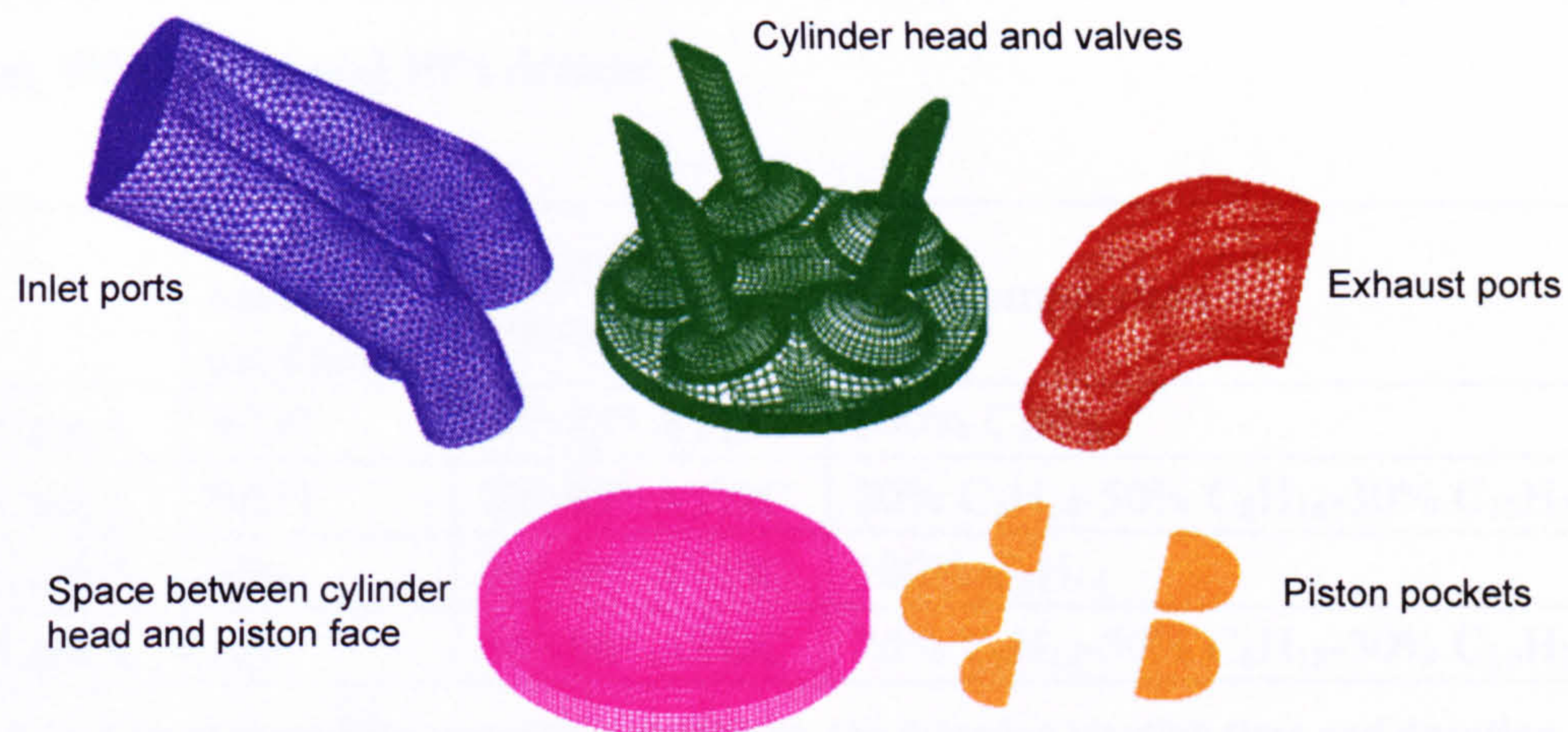


**Figure 6-6:** Outline of the numerical grids of the five blocks constructed for meshing the DI gasoline engine; a combination of tetrahedrals and hexahedrals cells has been used.

The flow field inside the cylinder is shown in Figure 6-7, which presents the streamlines coloured according to the axial velocity at three crank angles corresponding to the start, end of induction and end of compression strokes, for wide-open throttle conditions at an engine speed of 1500rpm.

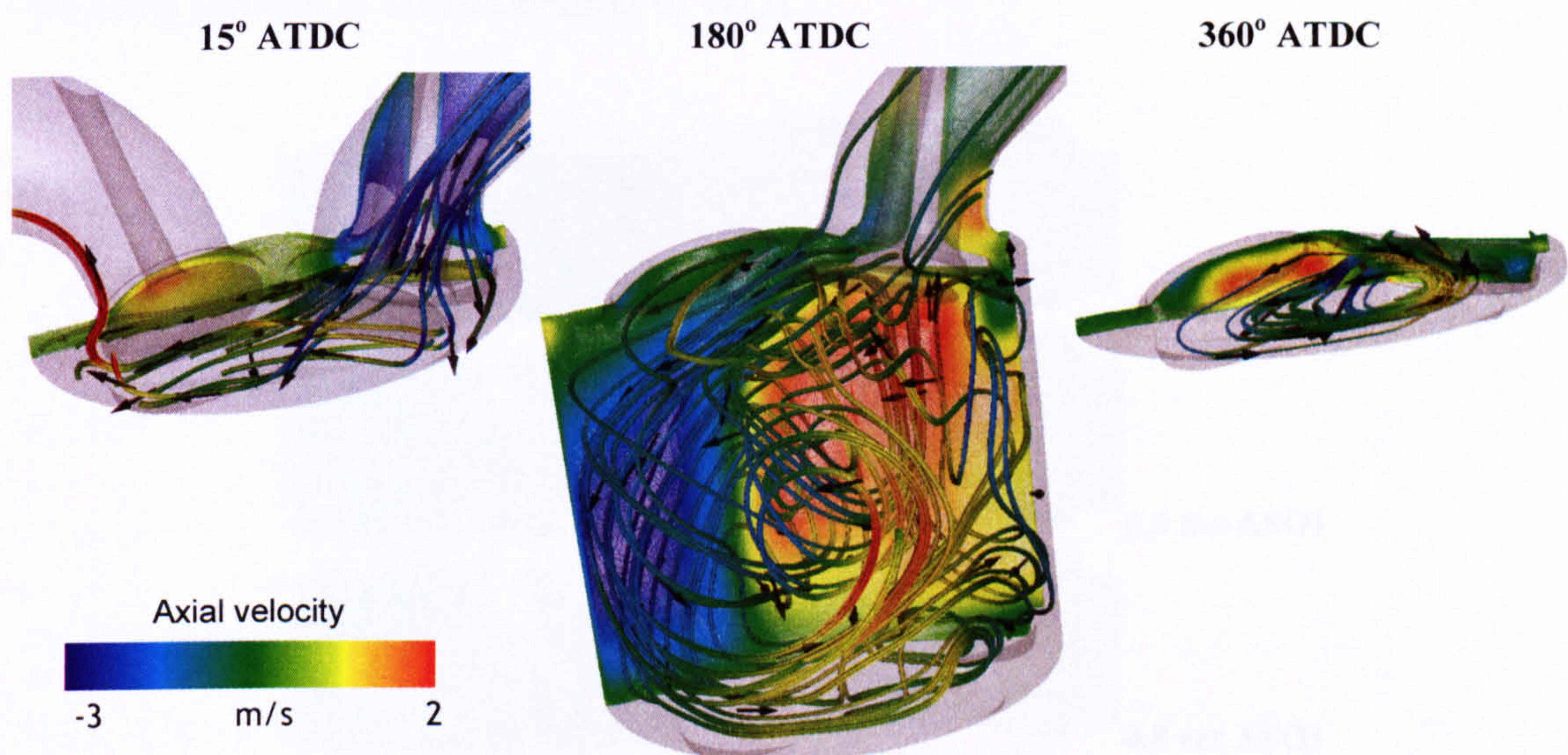


**Figure 6-7:** Predicted flow field inside the engine cylinder on the symmetry plane at three crank angles ATDC for WOT conditions, with engine rotational speed of 1500rpm.

Various calculations were performed, aiming to characterise the spray development, and in particular the effect of multi-component fuel evaporation modelling under different engine operating conditions. Table 6-II summarises the main parameters defining the four cases investigated. As can be seen, they correspond to two engine operating conditions (wide-open throttle (WOT) and idle), while injection takes place during the induction stroke. Two different fuel compositions were tested, the standard single-



component of octane and a mixture of three-components, initially composed by 20% hexane, 50% octane and 30% decane.

	Engine operating conditions	Injection timing	Fuel composition
Case 1	WOT	70°-85° ATDC	100% C <sub>8</sub> H <sub>18</sub>
Case 2	WOT	70°-85° ATDC	20% C <sub>6</sub> H <sub>14</sub> -50% C <sub>8</sub> H <sub>18</sub> -30% C <sub>10</sub> H <sub>22</sub>
Case 3	Idle	80°-90° ATDC	100% C <sub>8</sub> H <sub>18</sub>
Case 4	Idle	80°-90° ATDC	20% C <sub>6</sub> H <sub>14</sub> -50% C <sub>8</sub> H <sub>18</sub> -30% C <sub>10</sub> H <sub>22</sub>

**Table 6-II: List of the engine operating conditions, the injection starting time and duration and the fuel composition for the four cases proposed as part of the parametric investigation.**

The spray development inside the cylinder engine and its interaction with the air-flow during the whole engine cycle has been simulated, using the computational modelling described in Chapter 3. Initially, the characterisation of the spray structure during the injection period is described. Model predictions have been compared against Mie spray images [225], as shown in Figure 6-8 for the three-component fuel spray under operating conditions corresponding to WOT.

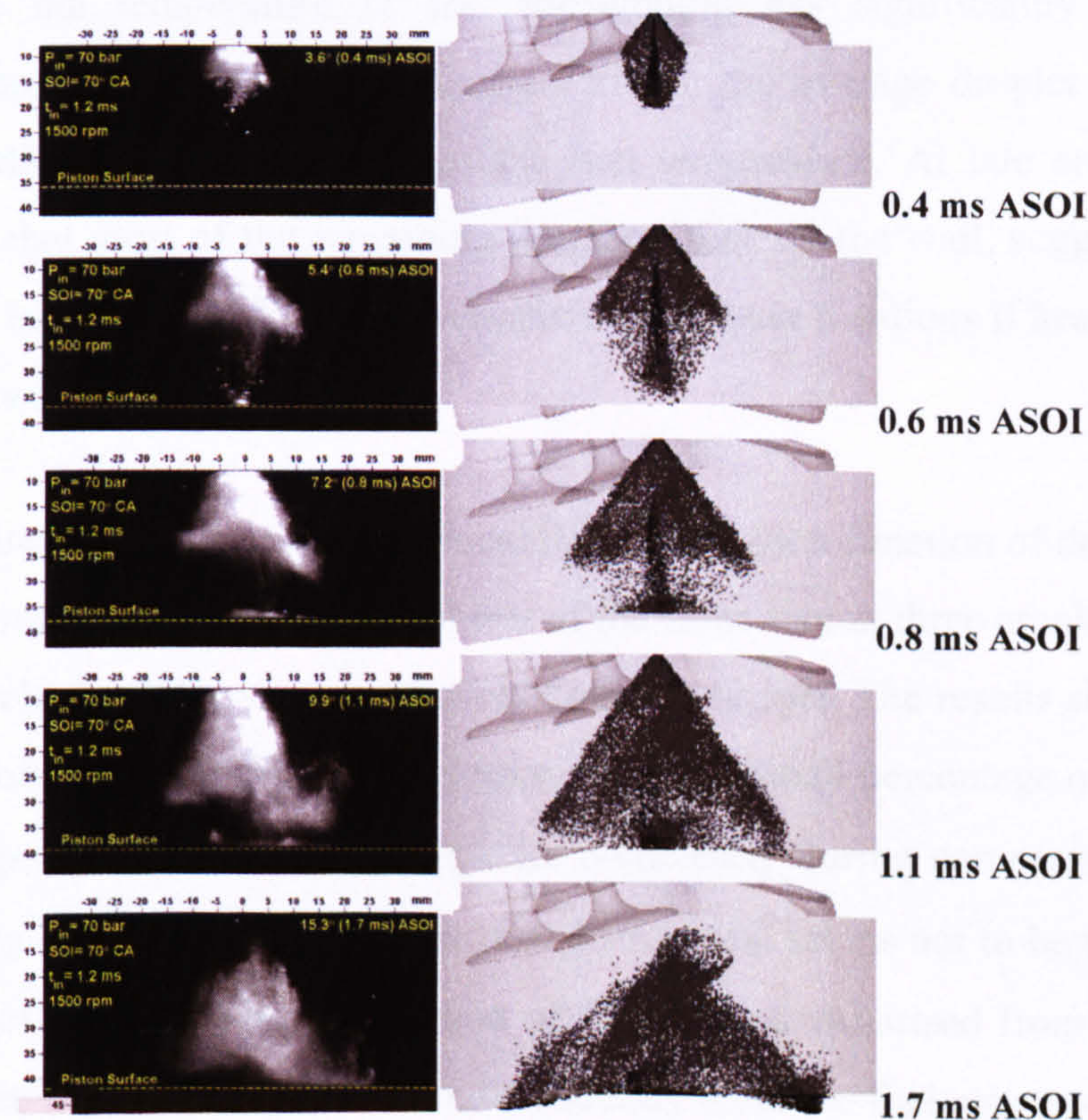


**Figure 6-8: Comparison between CCD spray images [225] and model predictions during the injection period; multi-component fuel injected from a high pressure swirl atomiser during induction into the moving cylinder of the multi-valve GDI engine.**



The first stages during the injection period are presented, showing a good agreement among the experiments and the computational results. The pre-spray development, the shape of the overall-spray at different time steps, the impingement of the liquid fuel on the piston surface and the spray deformation due to the air motion during the induction stroke can be reasonably well predicted.

The effect of in-cylinder air motion on the spray development during the induction and compression strokes is visually presented by the scatter plots of the liquid droplets shown in the collection of images of Figure 6-9. The scatter plots are coloured according to the droplet temperature while their size is proportional to droplet diameter. Flow field streamlines are also presented. Bigger droplets are present in the centre of the spray during the injection period, forming the pre-spray that first impinges on the piston wall. Those are relatively low temperature and less volatile droplets. It is necessary to remind that the cylinder engine surfaces are assumed to be adiabatic, so the heat transfer from the hot walls is not considered in the simulations. The air motion and air-entrainment inside the cylinder drastically deform the conical shape of the spray injected from the pressure-swirl atomizer. During the compression stroke, when the pressure and the temperature of the surrounding gas significantly increase, the evaporation process starts showing its main effect: the average droplet size is visibly reduced, together with the increase of the fuel temperature. At late compression the images show that most of the remaining droplets stuck on the wall, suggesting that the model would have predicted the fuel vaporisation at those locations if heat transfer from the hot walls was properly simulated.

Figure 6-10 presents the percentage probability distribution function of droplet diameter and of liquid mass vaporised from droplets of the same size at three crank angles during the engine cycles both for single and multi-component fuel. The results show that at the end of injection, during the induction stroke, there is a small percentage of droplets with diameter bigger than  $40\mu\text{m}$ , which vaporise completely during compression, when the droplet mean size is around  $20\mu\text{m}$ . The size distribution seems not to be affected by the composition of the fuel. The distribution of liquid mass vaporised from droplet of the same class size follow similar trends independently from the fuel composition, although it is slightly shifted towards bigger droplets.



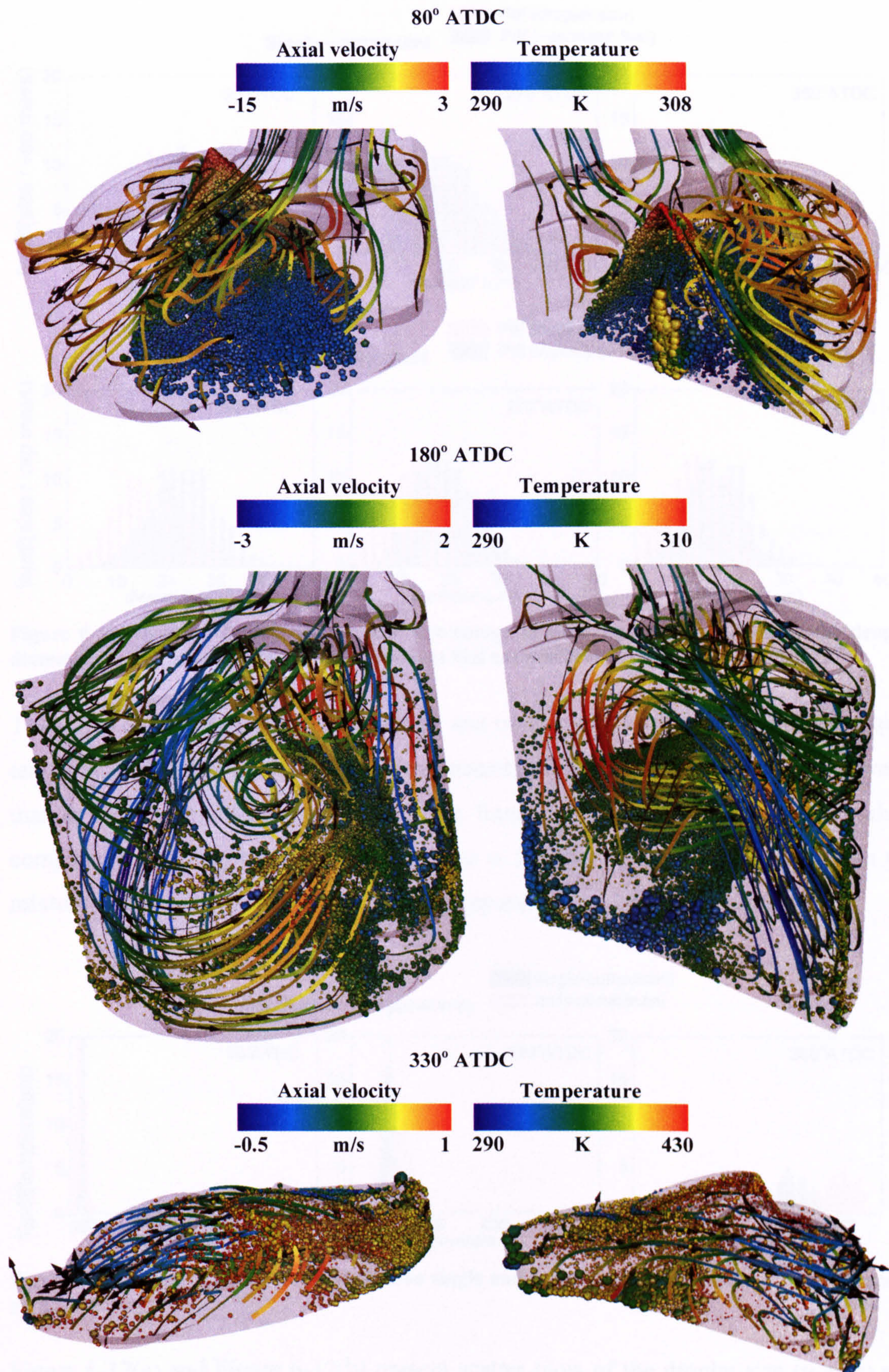


**Figure 6-9:** Scatter plots at three crank-angles ATDC of liquid droplet coloured according to the liquid temperature and flow field streamlines coloured according to the gas axial velocity from two different views; operating conditions correspond to the WOT 3-components case.



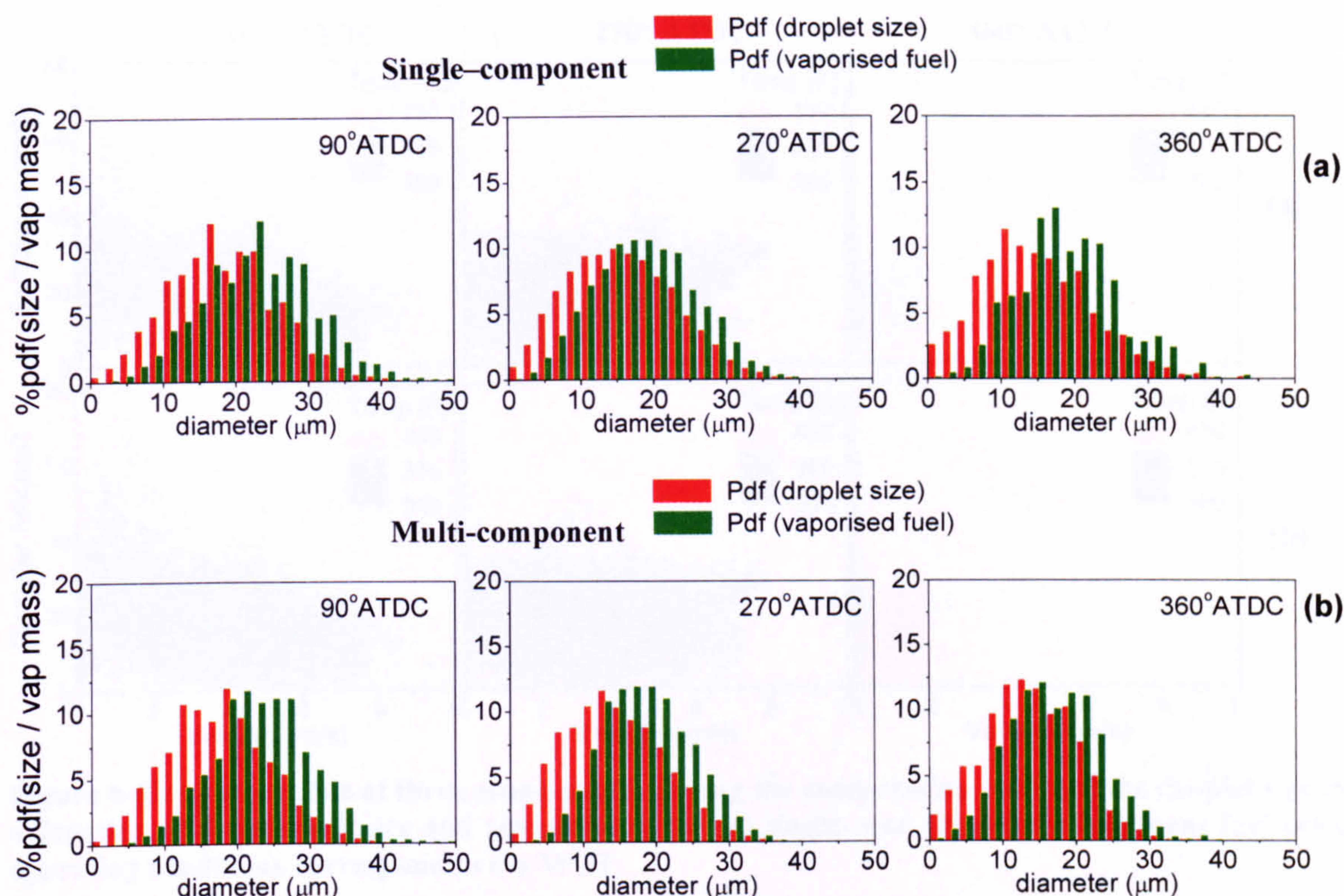


**Figure 6-10: Droplet size distribution and percentage of vaporized fuel according to the droplet diameter for (a) single and (b) multi-component fuel cases at three crank angles ATDC.**

The direct comparison between the single and multi-component fuels in terms of liquid temperature distribution at the same time instants is presented in Figure 6-11. It reveals that in case of multi-component fuel, the liquid temperature reaches higher values compared to the single-component case, due to the less volatile species present in the mixture which need to heat-up at a higher temperature before to start vaporising.

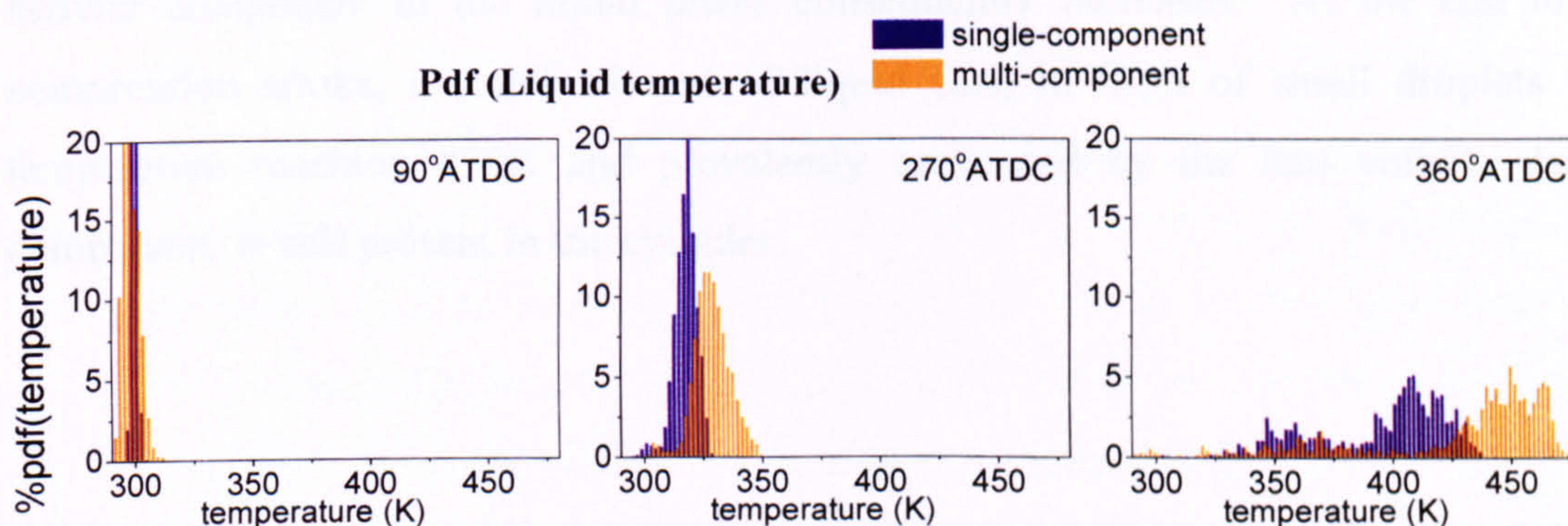


**Figure 6-11: Liquid temperature distribution single and multi-component fuel cases at three crank angles ATDC.**

Figure 6-12(a) and Figure 6-12(b) present scatter plots of the droplet size (y-axis) and velocity (x-axis) at 180, 270 and 360° ATDC, for the single and multi-component fuel, respectively. The symbols plotted are coloured according to the liquid temperature. As time advances, droplet size and velocity decrease while liquid temperature increases.



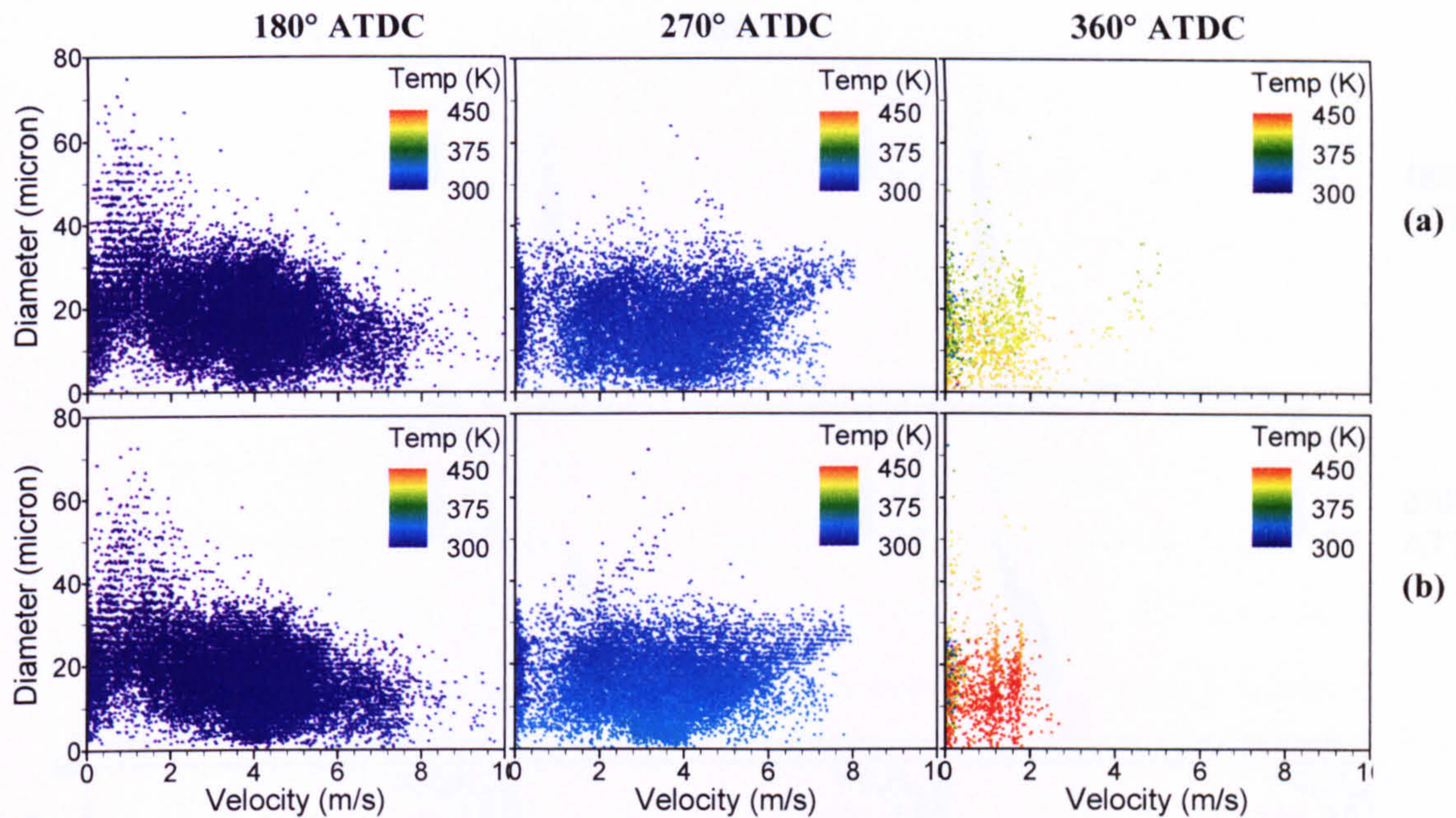


**Figure 6-12: Scatter plots at three crank angles during the compression stroke of the droplet size as a function of droplet velocity and temperature for (a) single- and (b) multi-component fuel case; operating conditions correspond to the WOT.**

This trend is enhanced in case of multi-component fuel, which vaporises faster due to the lighter component present in the mixture. This behaviour is confirmed by the results presented in Figure 6-13, which show the droplet size (y-axis) as function of the liquid temperature (x-axis) for the multi-component case. This time, the symbols plotted are coloured according to the mass fraction of the three components present in the mixture. The results reveal that from early compression stroke the lighter component in the fuel mixture is already vaporised due to its high volatility, and the mass fraction of the heavier component in the liquid phase consequently increases. At the end of the compression stroke, a small amount of liquid fuel, in form of small droplets with temperature reaching 450K and prevalently composed by the less volatile decane component, is still present in the cylinder.



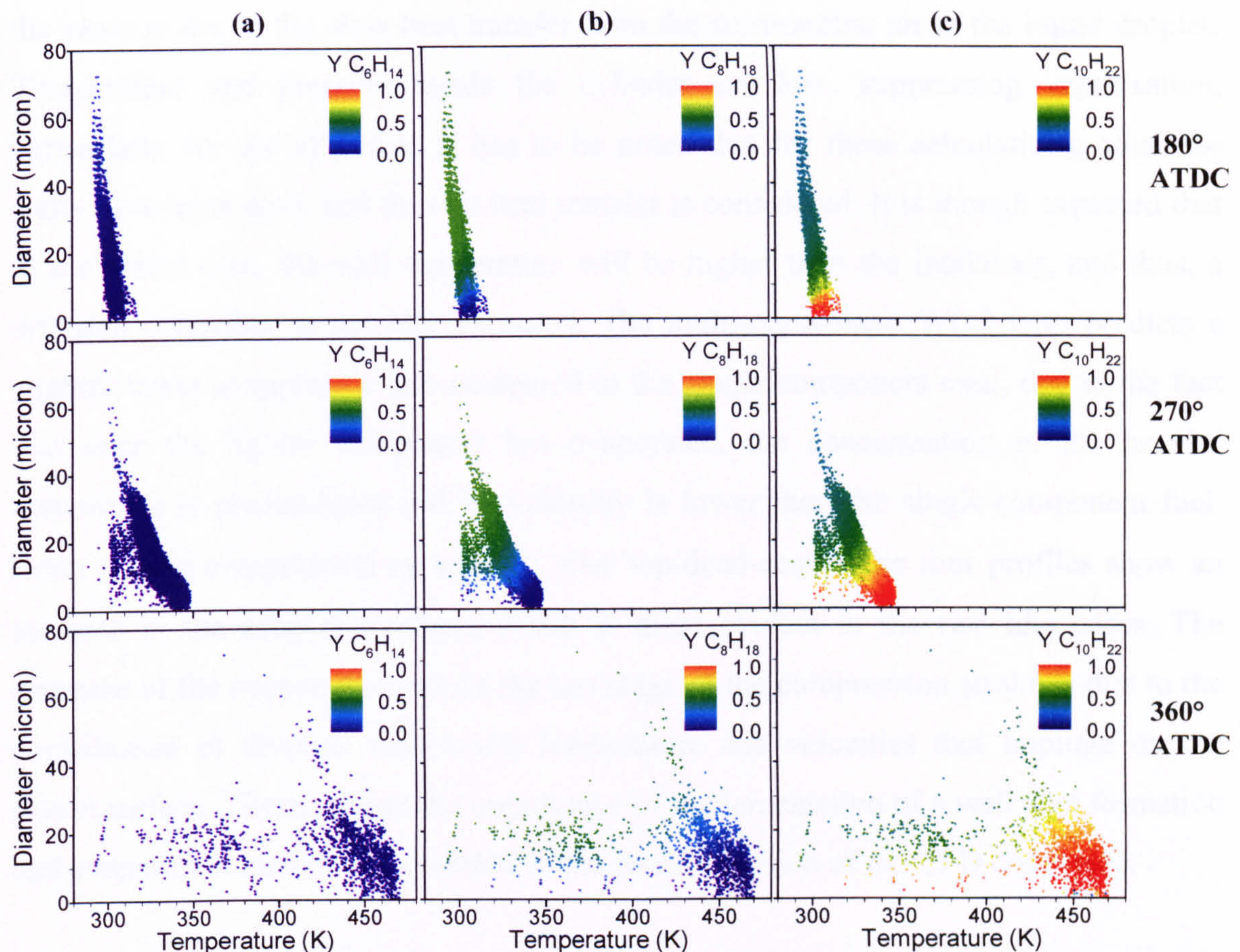


**Figure 6-13: Droplet scatter plots at three crank angles during the compression stroke of the droplet size as a function of droplet temperature and fuel mass fraction of (a)  $C_6H_{14}$ , (b)  $C_8H_{18}$  and (c)  $C_{10}H_{22}$ ; operating conditions correspond to the WOT and 3-components fuel.**

The temporal variation of the instantaneous liquid composition of the multi-component fuel, normalised with the whole amount of injected fuel, for the WOT case is presented in Figure 6-14(a), during the induction and compression strokes. The lighter component completely vaporises at the early stages of compression, when the evaporation of the octane starts showing the first effect, and the percentage of its concentration starts decreasing. This picture clearly describes the distillation process of multi-component fuel evaporation when the effect of heat and mass diffusion inside the liquid droplet are negligible, the liquid temperature and species concentrations are assumed to be uniform, and the volatility of the components forming the mixture represents the key factor controlling the preferential evaporation process. The effect of the engine operating condition and the injected fuel composition, on the evaporation rate during the induction and compression strokes are summarised in Figure 6-14(b). The higher volatility of the lighter component present in the multi-component fuel explains the peaks in the profile at the early stages of injection, both for the idle and the WOT case. The reduction of the evaporation rate during late induction and early compression for all



the cases is due to the slow heat transfer from the surrounding air to the liquid droplet. Temperature and pressure inside the cylinder are low, suppressing vaporisation, particularly for the idle case. It has to be noted that for these calculations, adiabatic walls have been used, and thus no heat transfer is considered. It is though expected that in the actual case, the wall temperature will be higher than the intake air, and thus, a different behaviour is actually expected. The multi-component WOT case predicts a slightly lower evaporation rate compared to the single-component case, due to the fact that once the lighter component has evaporated, the concentration of the heavier component is predominant and its volatility is lower than the single-component fuel. From middle compression up to  $330^\circ$  after top-dead-centre, the four profiles show an increase in the evaporation rate, which is more evident in the two idle cases. The decrease of the evaporation rate in the last stage of the compression stroke is due to the contribution of droplets with lower temperature and velocities that impinge on the piston surface. These remind the importance of implementation of a wall film formation and evaporation model, not available in the present version of the CFD code used.

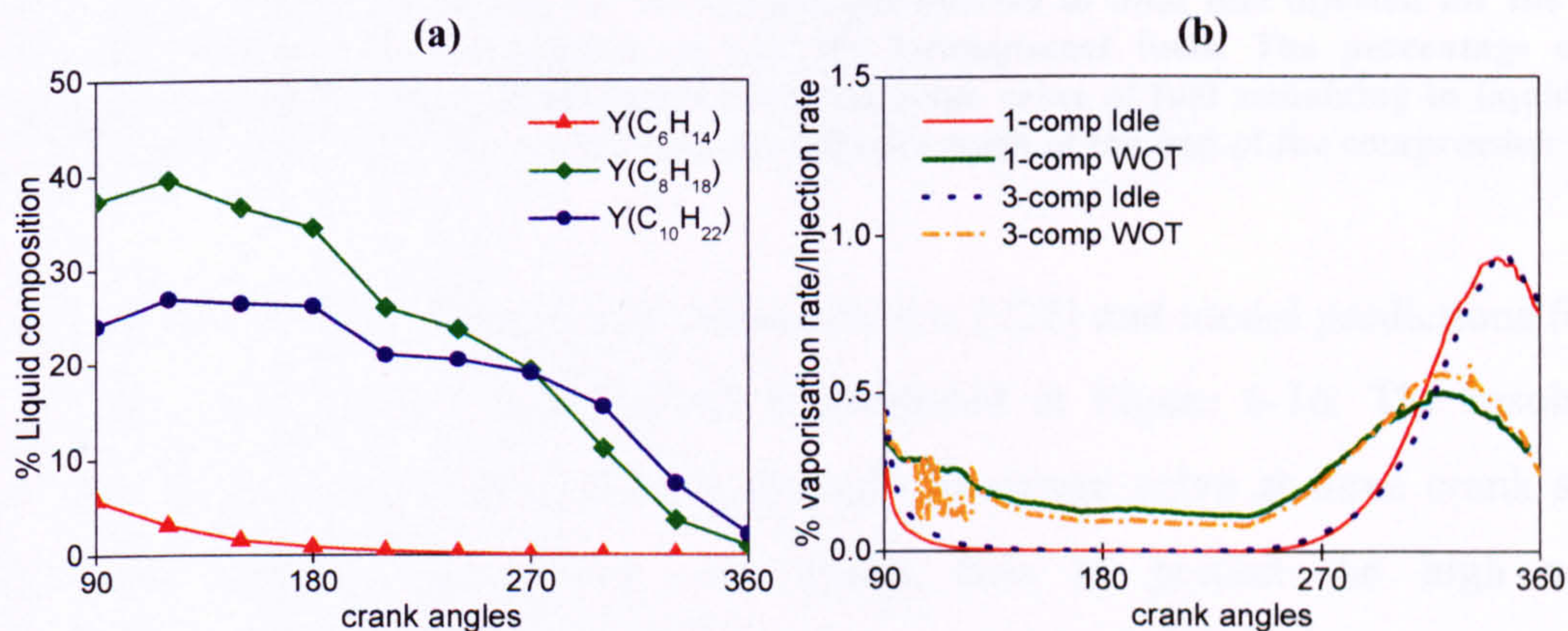


**Figure 6-14: (a) Fuel composition during the induction and the compression strokes for the WOT 3-components case. (b) Calculated fuel evaporation rate for all four injection cases investigated.**

Figure 6-15 presents for the two WOT cases the temporal variation of the liquid fuel present in the cylinder relative to the total fuel injected. At the same time, the percentage of fuel impinging and sticking on the cylinder walls and that in non-evaporated droplets is also shown. When a mixture of different species is used, Figure 6-15(b), the model predicts lower values for the remaining fuel in the cylinder and on the walls, suggesting that the evaporation is enhanced in this case. The percentage concentrations of the different species forming the mixture are also shown at three times



(end of injection, early compression and end of compression), highlighting the effect of the fuel evaporation according to their volatility.

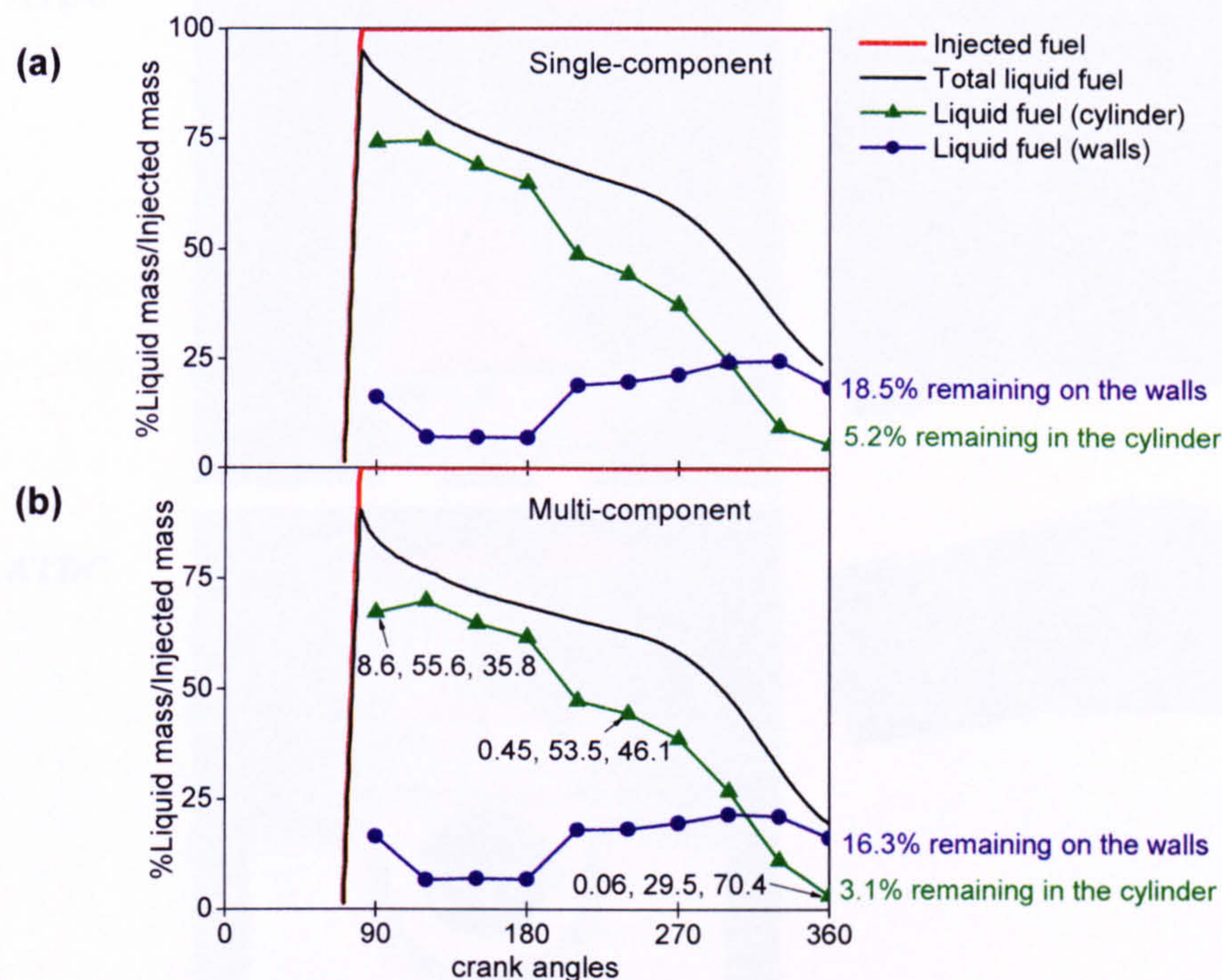


**Figure 6-15: Predicted percentage of fuel evaporated relative to total fuel injected for the WOT cases investigated for (a) one-component and (b) 3-component fuels. The percentage of fuel remaining on the wall is also shown, while the percentage value of fuel remaining in liquid form both inside the engine cylinder as well as on the cylinder walls at the end of the compression stroke is specified.**

Finally the comparison between LIF measurements [225] and model predictions for the vapour fuel concentration distributions is presented in Figure 6-16. The results are shown on the symmetry plane passing through the centre valve at three crank angles during the compression strokes. The model fails to predict the high vapour concentration in the centre of the cylinder. It calculates more vapour concentrated to the side of the cylinder, due to its convection by the air motion. This suggests that the assumption of adiabatic wall imposed in the simulations may have an important role. Thus, the introduction of more realistic boundary conditions, with the implementation of a wall film model, represents a major recommendation for further investigations.



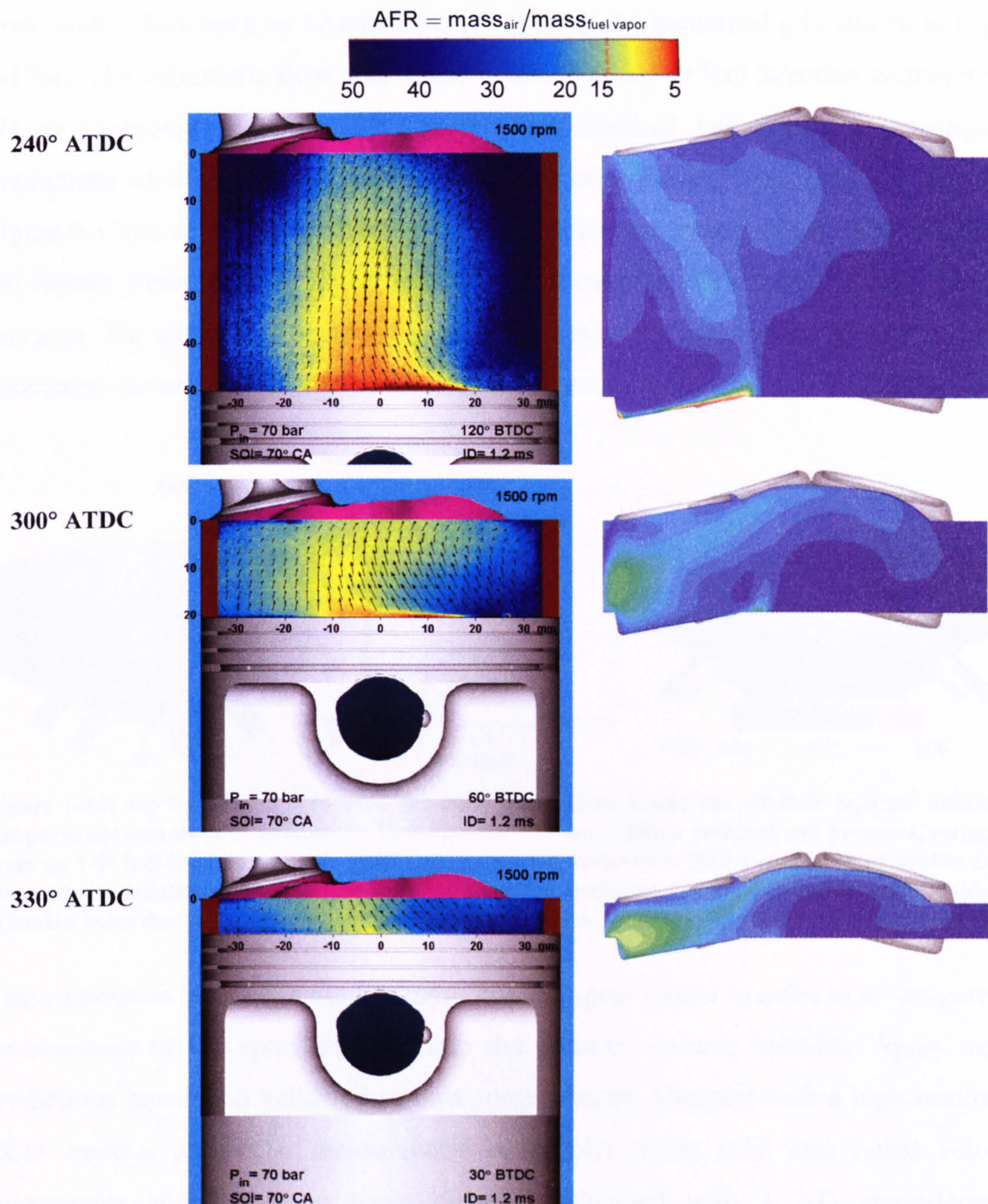


**Figure 6-16: Comparison between (left) LIF [225] and (right) model predictions for the vapour fuel concentration distribution in terms of air fuel mass ratio (AFR) at three crank angles during the compression stroke.**

### 6.3 Multi-hole gasoline injector

The second high-pressure injection system investigated is a prototype six-hole injector, with symmetric hole arrangement, nominal cone angle of  $90^\circ$  and maximum operating pressure of 200bar. Tests have been carried out injecting iso-octane at two injection pressures of 120 and 200bar, at two chamber pressures of 1 and 12bar, under room temperature. The duration of the injection triggering signal was kept constant at 1.5ms. The flow conditions at the injector hole exit are predicted by the two-phase cavitation



flow model, developed by Giannadakis [148] using the numerical grid shown in Figure 6-17(a). The volumetric flow rate, as calculated from a 1-D fuel injection system model [4], is illustrated in Figure 6-17(b) for both nominal rail pressures investigated. Predictions of the cavitation volume fraction inside the injection hole are shown in Figure 6-17(c). At the entrance of the injection holes, the local pressure falls well below the vapour pressure of the liquid, indicating that cavitation is expected to take place in this area. The cavitation model estimates a hole exit effective area of about 90% of the geometric one and a discharge coefficient value around 0.7.

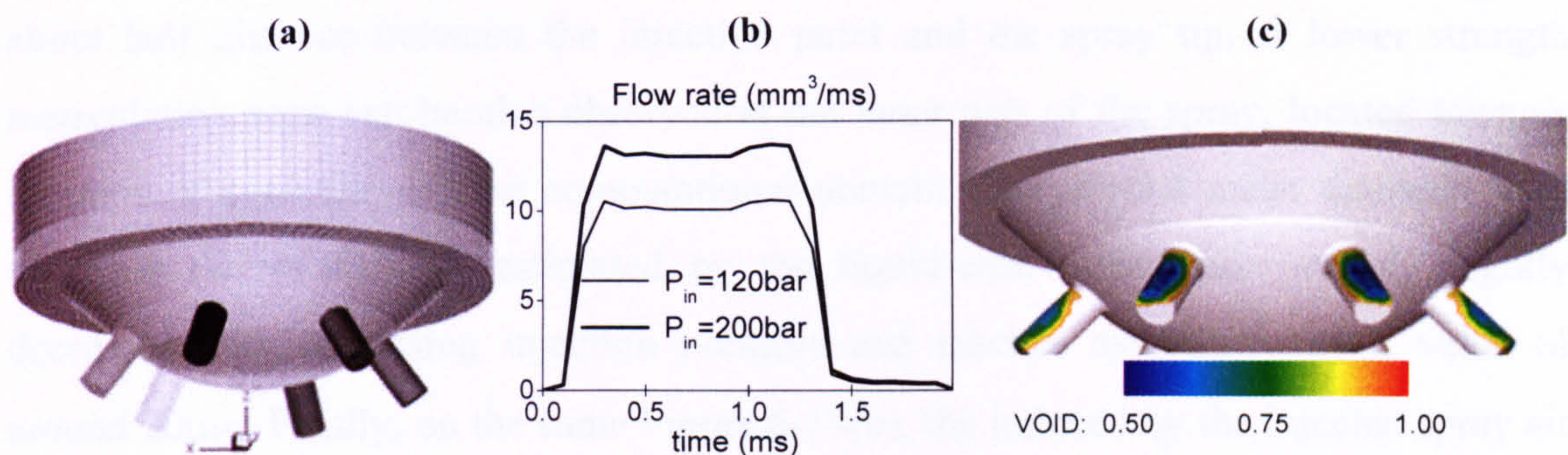


**Figure 6-17: (a) Numerical grid used for flow simulations inside the six-hole injector nozzle (b) temporal development of volumetric flow-rate for 120 and 200 bar nominal rail pressure, estimated from an 1-D fuel injection system model, (b) predicted volumetric flow-rate transient profile under atmospheric conditions for 120 and 200 bar injection pressure and (c) volume fraction inside the injection holes due to onset and development of cavitation, at 200 bar nominal rail pressure [129].**

These estimates have been used as input into the spray model in order to investigate the development of the spray injected into the constant volume chamber. Spray model predictions have been validated against spray images, obtained with a high-resolution CCD camera, and PDA measurement of droplet mean axial and radial velocity components and arithmetic mean diameter, obtained with a 2-D phase-Doppler anemometry system [129]. The PDA measurement points are shown in Figure 6-18. As can be seen, these are concentrated on two horizontal planes located at 10 and 30 mm below the nozzle exit.

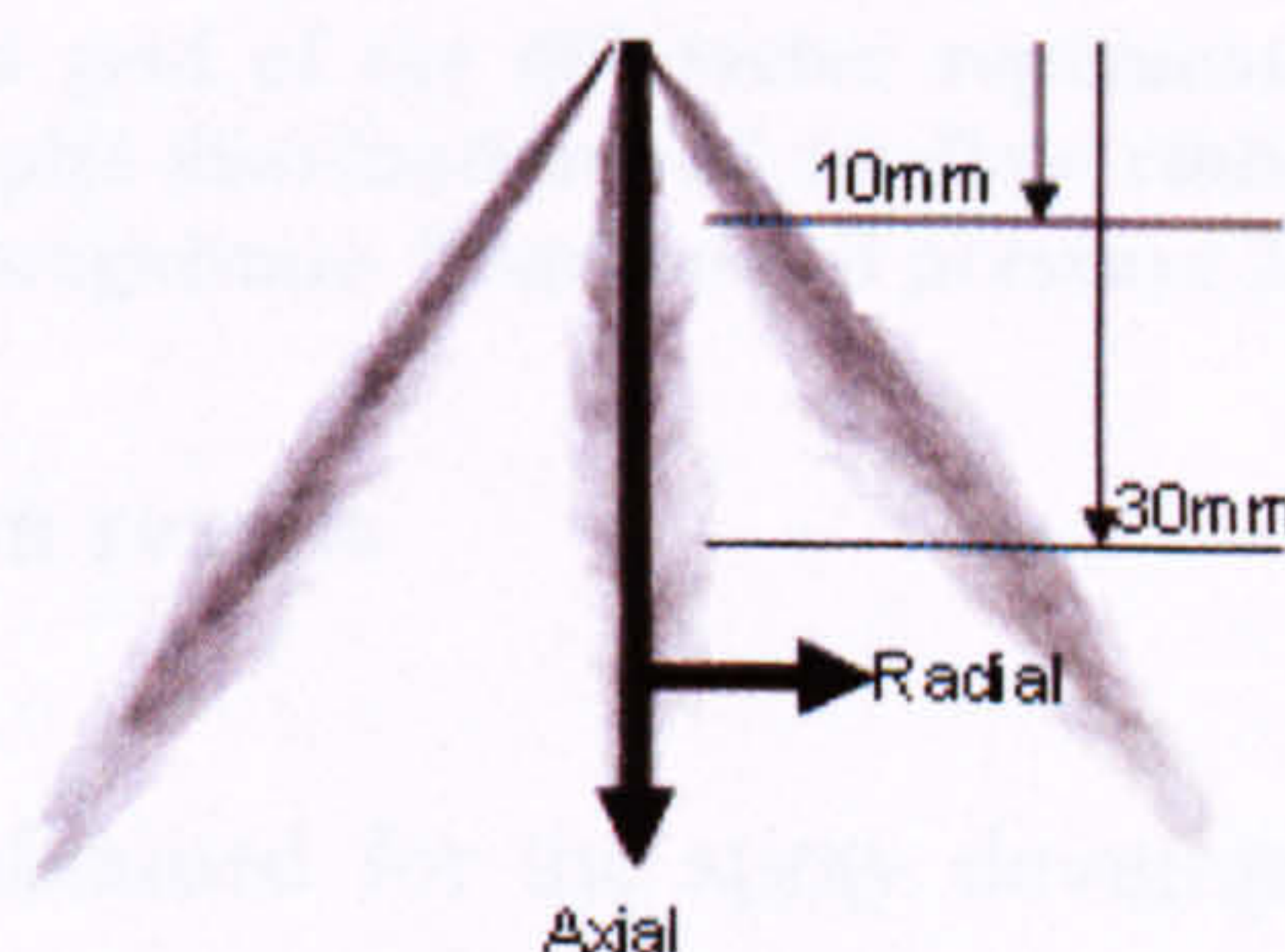


**Figure 6-18: PDA measurement grid points.**



Figure 6-19(a) shows the 3-D numerical grid initially used for the spray simulations. This is a 60degrees sector with symmetric boundary conditions, representing the 1/6 of the constant volume chamber. Two different grids have been used. The initial grid consists of approximately 100,000 tetrahedral cells, while the second one is refined automatically in the area of spray development and reaching up to 250,000cells at the end of injection. Figure 6-19(b) shows the predicted spray structure 1.0ms after start of injection (ASOI) and the corresponding induced by the spray air motion, for the 200bar nominal rail pressure case and for injection under atmospheric conditions. As can be seen, there is a recirculation zone formed at the upper part of the spray and extending about half distance between the injection point and the spray tip. A lower strength recirculation zone can be also observed at the inner part of the spray, located towards the axis of symmetry of the computational domain. The droplet mean diameter very near the nozzle exit, as estimated by the liquid-core atomisation model, slightly decreases with increasing injection pressure and reaches asymptotically a value of around  $20\mu\text{m}$ . Finally, on the same Figure 6-19(b), the induced by the injected spray air velocity magnitude can be observed. Induced air-velocity can reach velocities almost 80-90% of those of the injected droplets near the nozzle exit when injecting under atmospheric conditions, but much lower values for injection against increased air pressure and density.

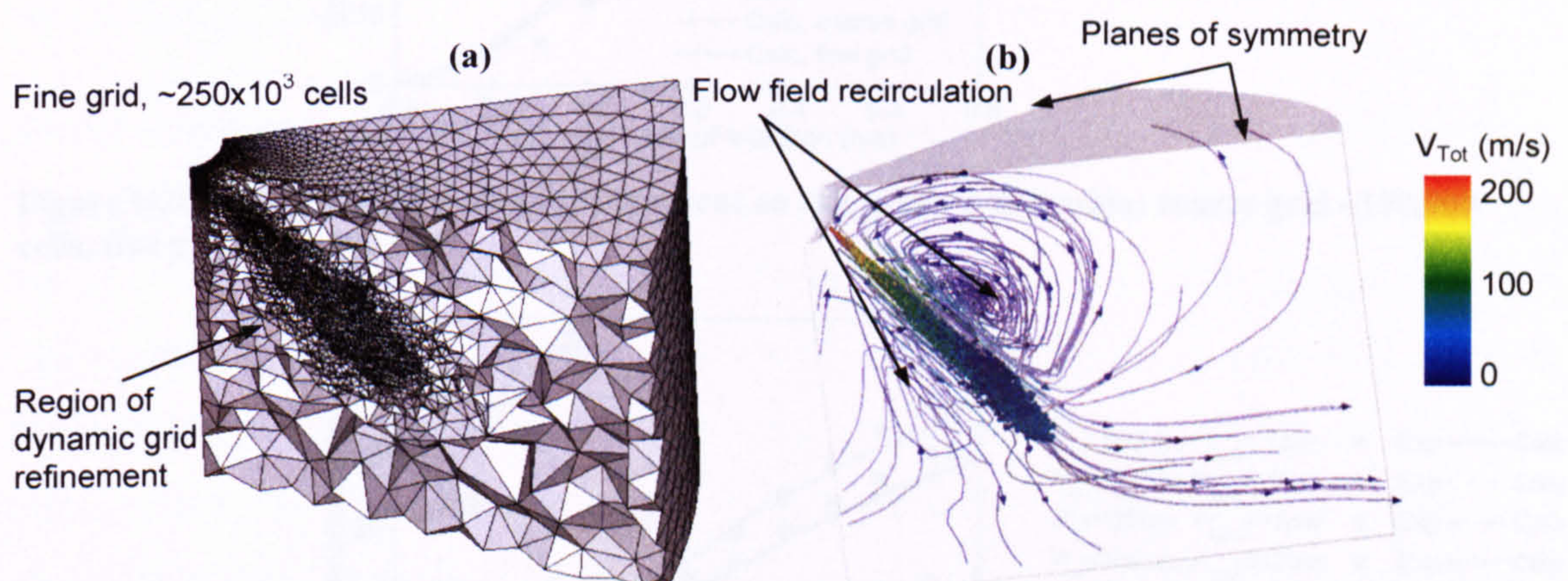


**Figure 6-19: (a) Half numerical grid of the 60° sector representing 1/6 of the constant volume chamber and (b) fuel spray droplet distribution and air-flow ribbons 1.0ms after ASOI, coloured according to their total velocity magnitude. Nominal rail pressure 200bar, back-pressure 1bar.**

### 6.3.1 Spray model validation results

In this section, the results obtained for the spray development are discussed in more details. Initially, sample validation cases against the experimental data published by



Mitroglou et al. [129] are presented, followed by examples of spray injection conditions investigating the effect of different nozzle hole arrangement configuration and the effect of fuel vaporisation on the predicted spray structure. Figure 6-20 presents a comparison between model predictions and experimental results for the spray tip penetration for the two 3-D grids adopted, with different levels of local grid refinement. This calculation corresponds to the 200bar-1bar nominal rail pressure and back pressure case. As can be seen, results obtained with the finer grid are in better agreement with the measured values, especially at distances far from the injection hole. Spray tip penetration seems to follow an almost linear variation during the early injection period, lasting up to 0.5ms. A summary of them can be seen in Figure 6-21, which presents the model validation against experimental data for the liquid penetration for all four operating conditions investigated. Model predictions are close to the experimental observations, and as expected, they both confirm that spray tip penetration increases with injection pressure and substantially decreases with increasing back pressure.

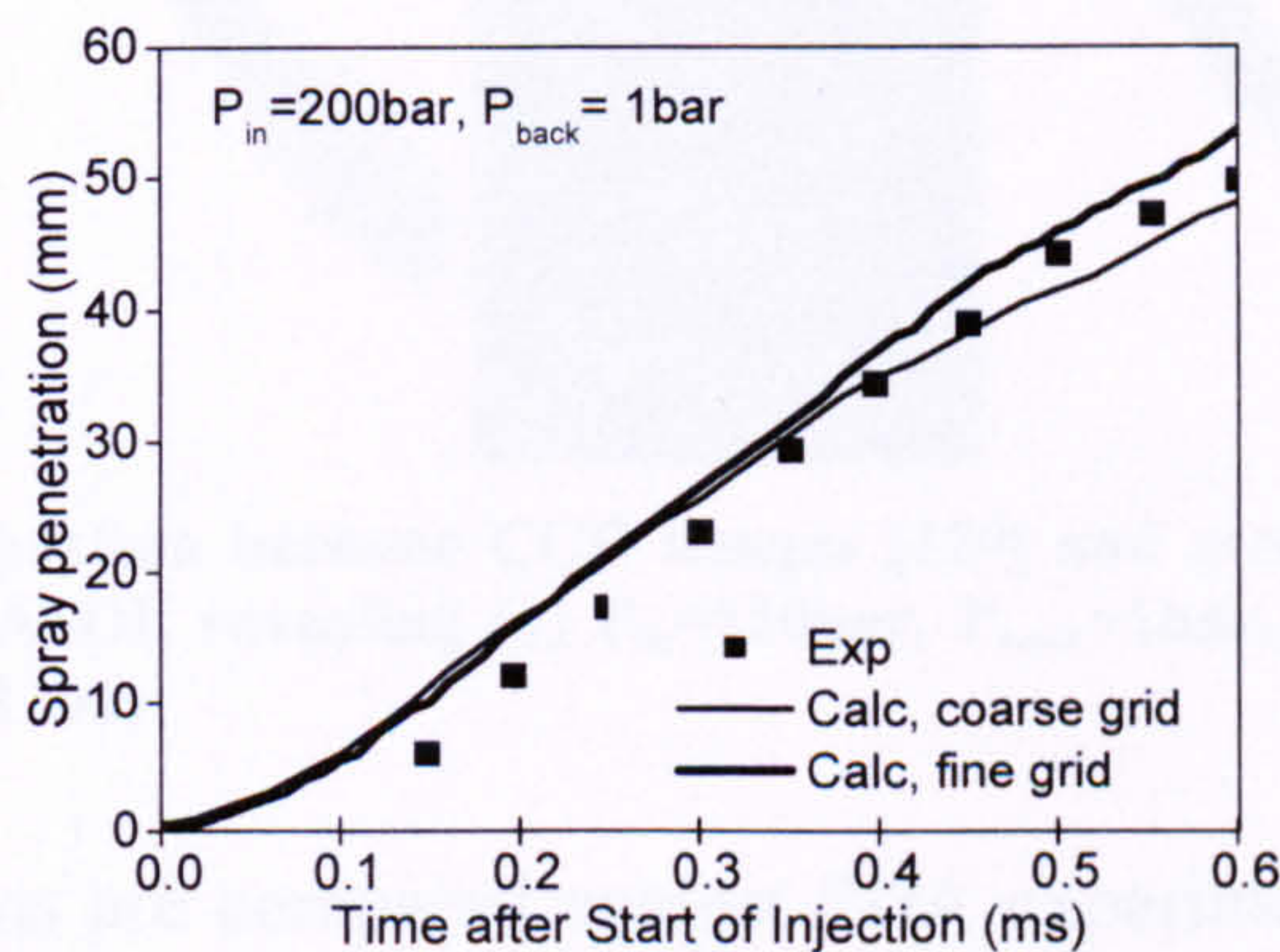


**Figure 6-20: Effect of grid dynamic refinement on the spray penetration; coarse grid ~100,000 cells, fine grid ~250,000 cells.**

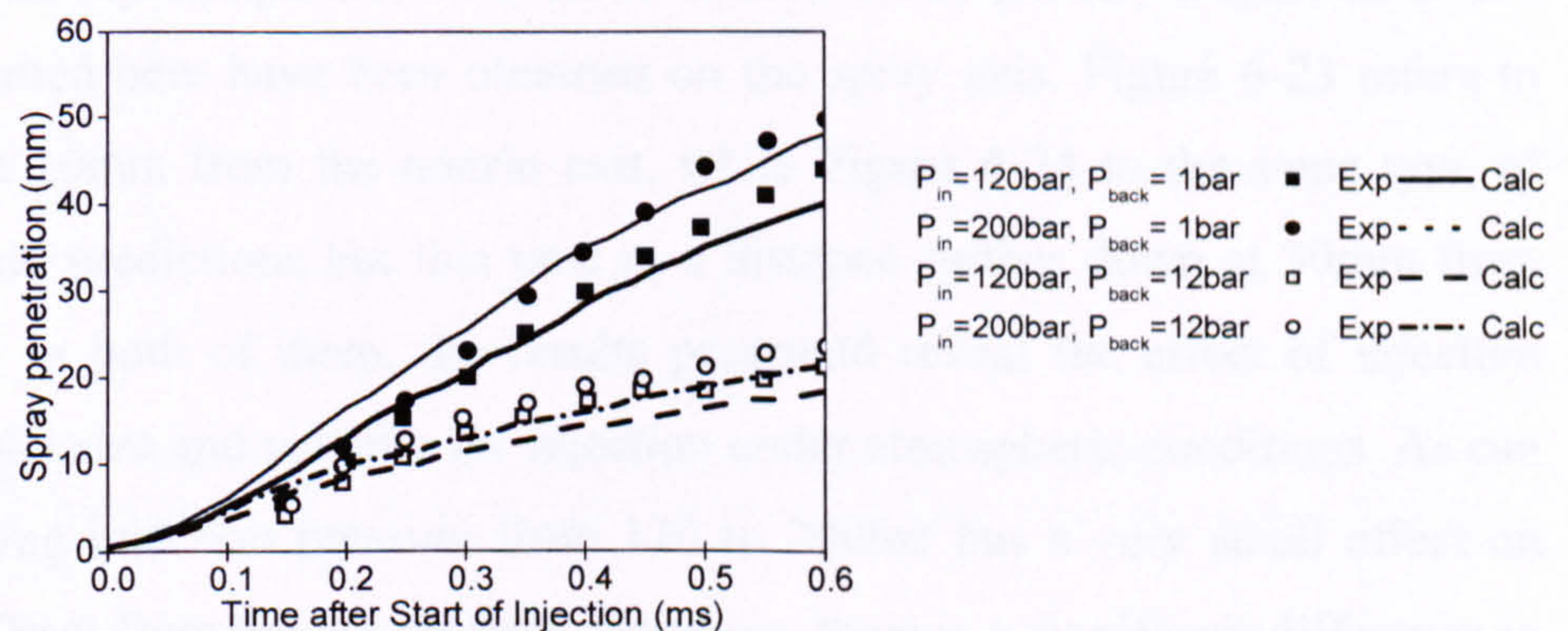


**Figure 6-21: Comparison between model predictions and experimental data of spray tip penetration for two different nominal injection and back pressure conditions.**



The comparison between CCD images [129] and computational results 0.5ms after the start of injection is presented in Figure 6-22. Figure 6-22(a) corresponds to the lower injection pressure case of 120bar with injection under atmospheric conditions, while Figure 6-22(b) corresponds to the higher injection case of 200bar keeping the same back pressure. Finally, Figure 6-22(c) corresponds to the same high rail pressure case, but with injection at elevated back pressure of 12bar. It is clear that increasing back pressure results to a significant reduction of the spray penetration. However, the spray shape remains similar in terms of spray cone and deflection angles, independently of the injection and back pressures used. This characteristic of the multi-hole injector is a clear advantage compared to the pressure-swirl atomiser for spray-guided combustion systems [117, 127].

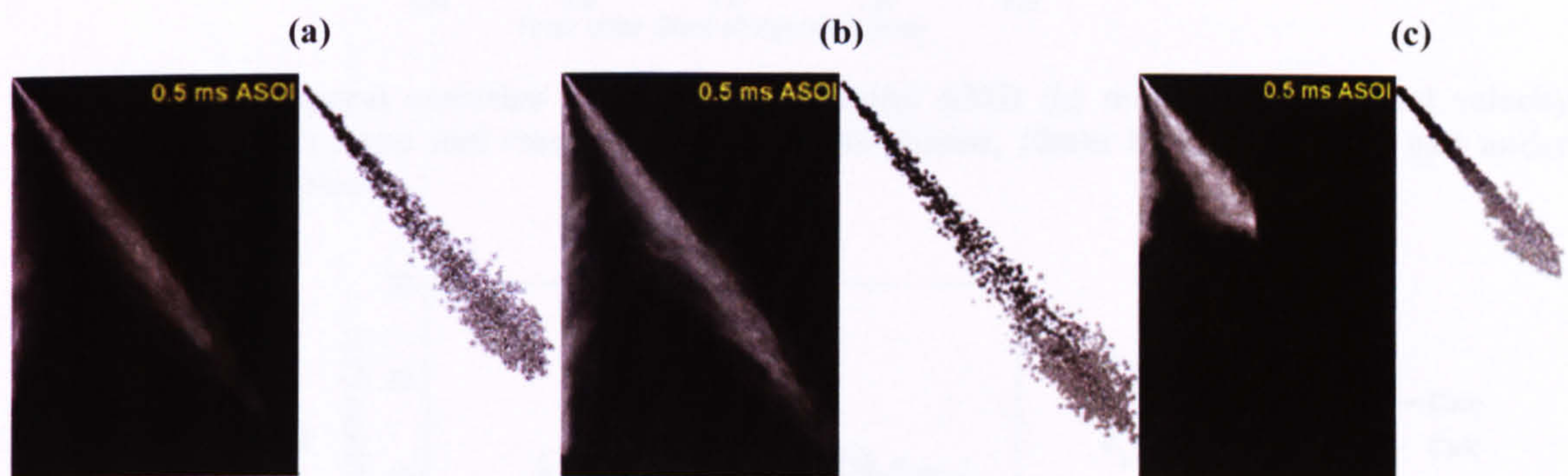


**Figure 6-22: Comparison between CCD images [129] and model predictions from the multi-hole injector at 0.5ms ASOI, revealing (a)  $P_{in}=120\text{bar}$ ,  $P_{back}=1\text{bar}$ , (b)  $P_{in}=200\text{bar}$ ,  $P_{back}=1\text{bar}$  and (c)  $P_{in}=200\text{bar}$ ,  $P_{back}=12\text{bar}$ .**

Model predictions are compared against PDA experimental data [129] in Figure 6-23, Figure 6-24 and Figure 6-25 for the temporal variation of the ensemble averaged droplet mean and rms velocity components and the arithmetic mean (AMD) droplet diameter. All results presented here have been obtained on the spray axis. Figure 6-23 refers to measurements at 10mm from the nozzle exit, while Figure 6-24 to the same type of measurements and predictions but this time at a distance further down at 30mm from the nozzle hole. In both of them, the results presented reveal the effect of injection pressure on droplet size and velocity for injection under atmospheric conditions. As can be seen, increasing injection pressure from 120 to 200bar has a very small effect on droplet size at 10mm from the nozzle hole. However, there is a significant difference in the injection velocity.



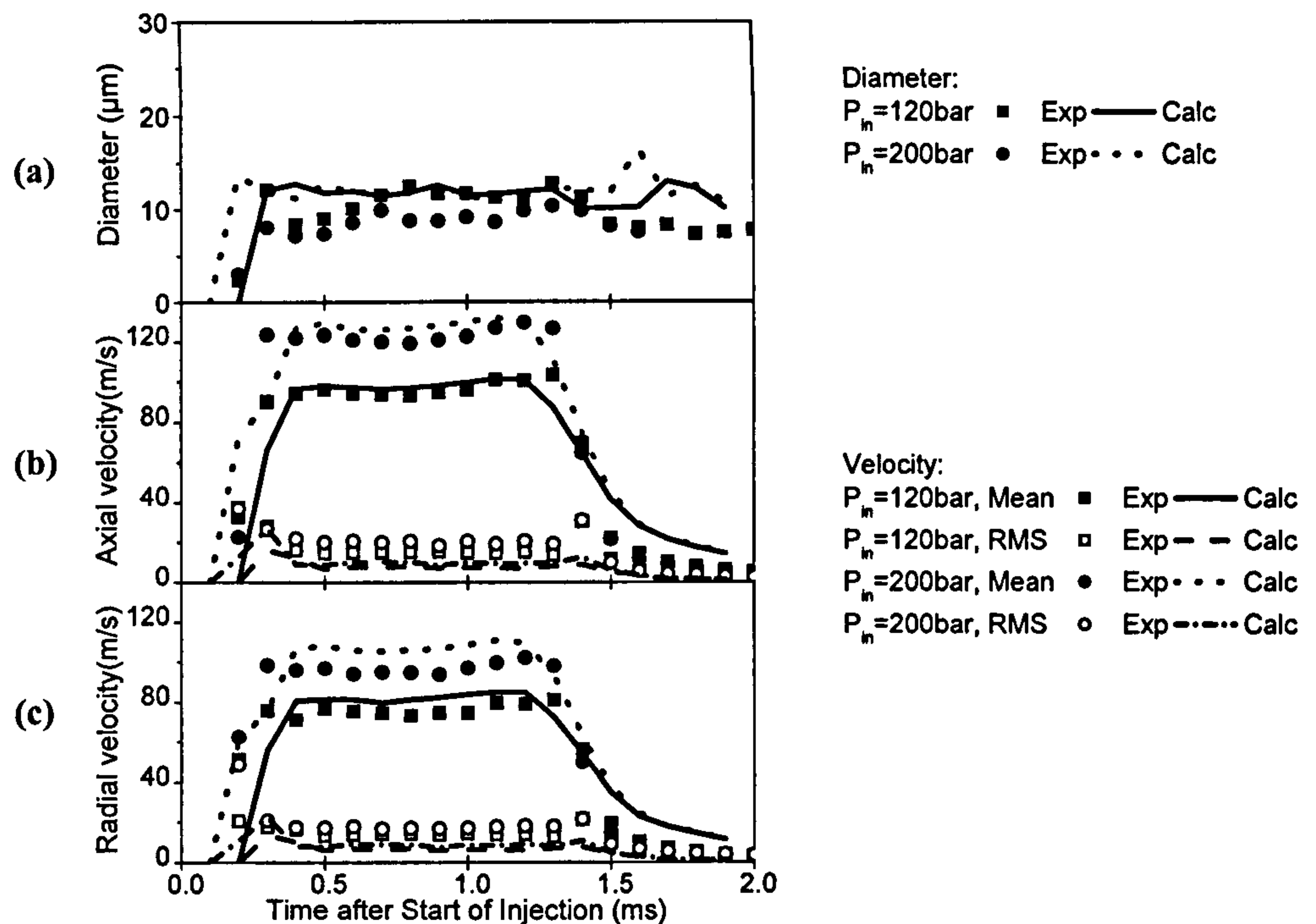


**Figure 6-23:** Temporal variation of droplet (a) droplet AMD (b) mean and rms axial velocity component and (c) mean and rms radial velocity component, 10mm below the nozzle exit under atmospheric conditions.

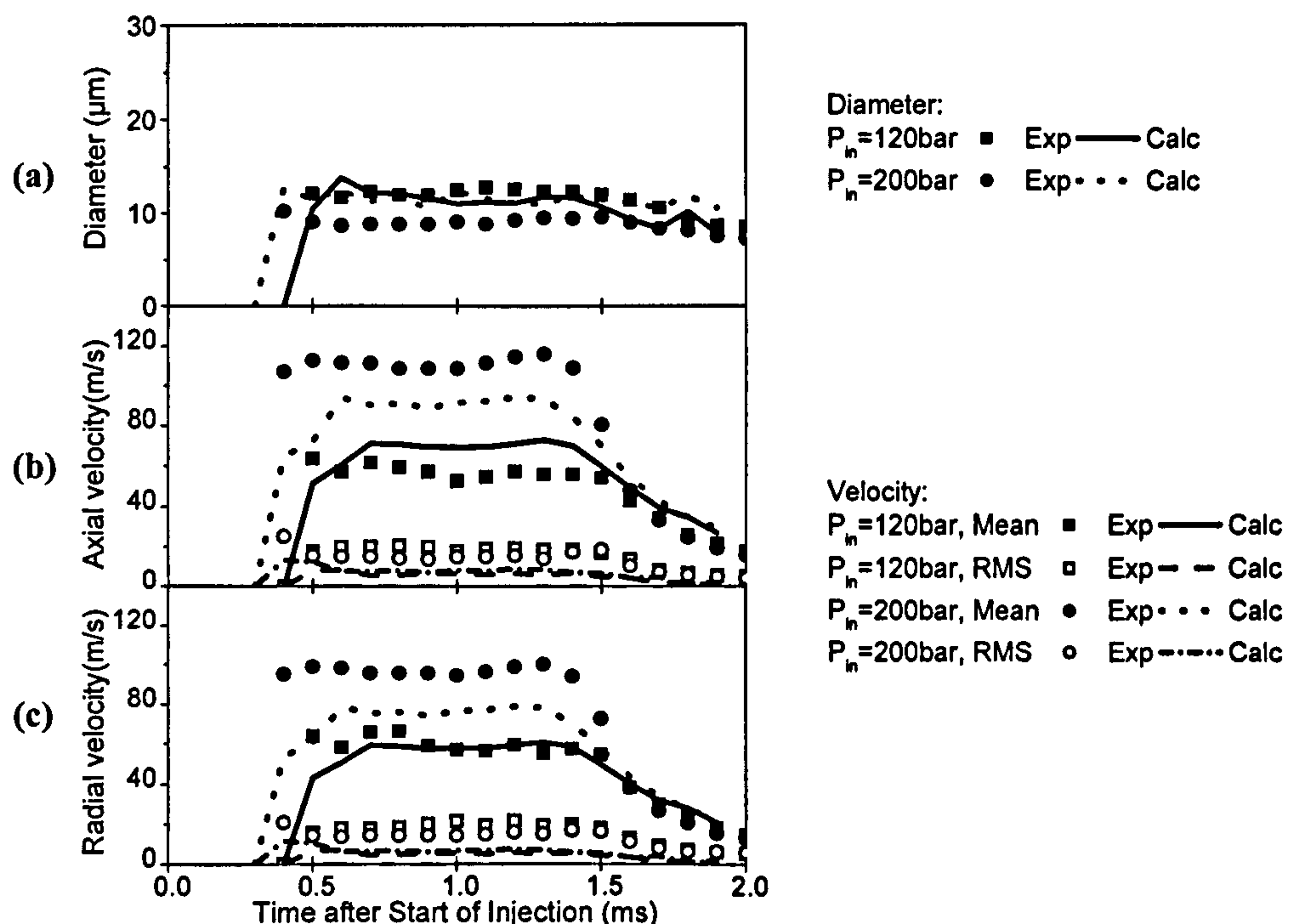


**Figure 6-24:** Temporal variation of droplet (a) droplet AMD (b) mean and rms axial velocity component and (c) mean and rms radial velocity component, 30mm below the nozzle exit under atmospheric conditions.

At 30mm from the injection hole, the droplet size between the two different injection cases is also different, with the lower injection case exhibiting larger droplet sizes. This is attributed not to the liquid atomisation process but rather to the droplet secondary



break-up, which seems to be enhanced with increasing injection pressure. Model predictions suggest that these processes are completed about 15mm from the nozzle exit, and thus, can be only realised at the 30mm measurement plane. Figure 6-25 reveals the effect of increasing back pressure on the predicted droplet characteristics at 30mm below the nozzle exit, for the 200bar nominal rail pressure case.

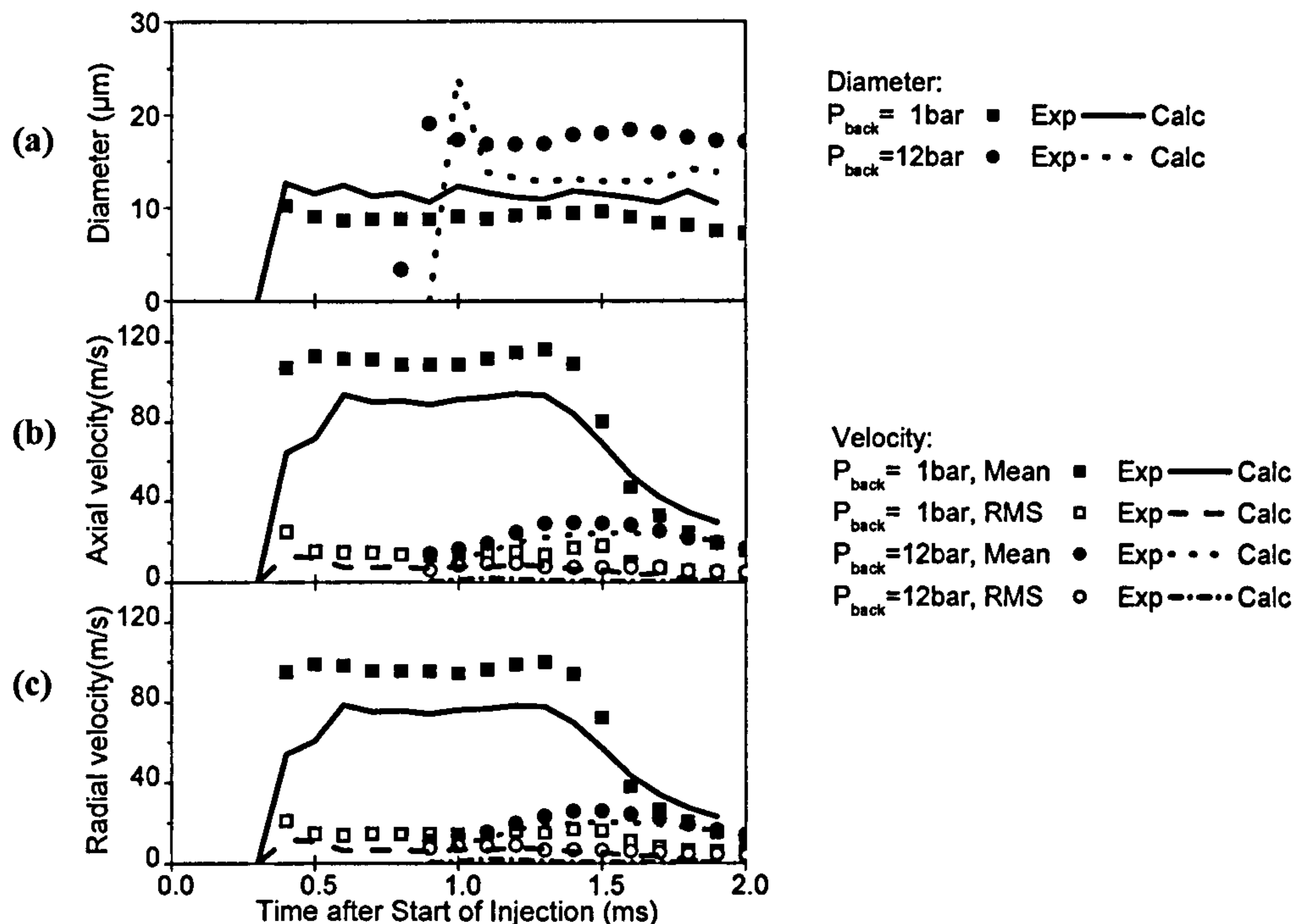


**Figure 6-25: Temporal variation of droplet (a) AMD, (b) mean and rms axial velocity component and (c) mean and rms radial velocity component, for nominal injection pressures of 200bar, chamber pressures of 1 and 12bar, at 30mm below the nozzle exit.**

As can be seen, both experimental data and model predictions suggest that increasing the back pressure not only results to significant droplet deceleration due to increased drag, but also to much larger droplets. It seems that the fast droplet deceleration takes place at time scales shorter than those required for droplet aerodynamic break-up, resulting to the observed and calculated increase in the droplet size far downstream of the injection point.

### 6.3.2 Parametrical investigation

Since model predictions seem to reproduce reasonably well the measured spray characteristics for both injection and back pressure conditions investigated, it was considered useful to employ the computational model in order to investigate the effect of parameters related to the nozzle design and operating conditions. A sample of the



simulation cases performed is presented in this section, starting from the predictions for a '6+1' multi-hole nozzle arrangement and then proceeding with a parametrical investigation of injection from the 6-hole symmetric nozzle under increased back temperature conditions, which correspond to injection during the late compression stroke of a GDI engine. Combination of different hole arrangements and injector positioning relative to the spark plug can offer flexibility in obtaining the desired air-fuel vapour distribution at the time of ignition, since the air motion induced from the interaction between the injected sprays affects the fuel vapour distribution. Figure 6-26 demonstrates such an example. It refers to injection from an injector having a central hole in addition to the six side holes. The presence of this central hole aims to produce vapour in the area between the six symmetrically located sprays of the original design. As can be seen, this configuration enhances the formation of a recirculation zone located at the inner part of the side spray, Figure 6-26(a). This recirculation zone has been found to be relatively unstable, not only because the central hole spray never develops in a perfectly symmetric way, but mainly because the cavitation structures of internal flow of the central hole has been found to develop in a more unstable fashion compared to the side holes. As a result, the spray injected from the central hole can be over-penetrating compared to the rest, leading to undesirable wall impingement and also exhibiting significant cycle-to-cycle variations. The instability of the central hole, detected by experimental observations, has been further investigated by computational predictions, simulating the effect of the atomisation cone angle, predicted by the cavitation induced atomisation model as function of the hole effective area, on the liquid spray penetration. The central hole effective area fluctuations during the injection period predicted by the multi-phase cavitation model developed by Giannadakis [148] have been introduced as input in the spray model, which calculates the atomisation cone angle varying in the range between 9 and 25 degrees. This has an effect on the subsequent spray development, as shown in Figure 6-26 (b), which presents the central spray liquid penetration calculated assuming constant and variable atomisation cone angles. The results reveal that the spray penetration, as expected, substantially increases with smaller cone angle, confirming the dependence of the spray development from the internal nozzle flow characteristics. This is a case that the computational model has provided insight to the reasons leading to the observed undesirable central-hole spray characteristics.



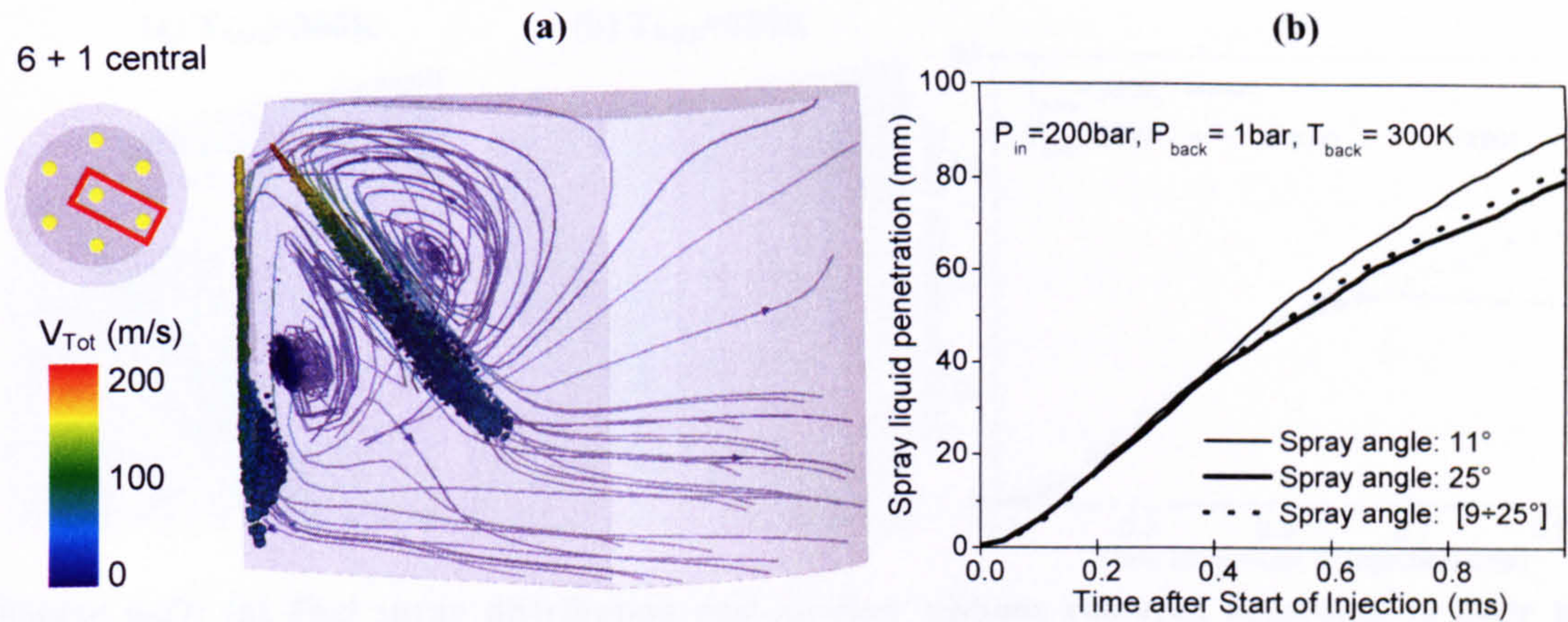


**Figure 6-26: (a) Fuel spray distribution and air-flow ribbons from the '6+1' central hole nozzle configuration showing the over-penetration of the central hole spray relative to the side ones. Droplets and air-flow ribbons are coloured according to their total velocity magnitude. (b) Atomisation cone angle effect on the temporal profile of liquid penetration for the central spray under non-evaporating conditions.**

The second set of parametrical investigation cases presented refers to spray injection from the 6-hole symmetric nozzle under elevated back temperature. Figure 6-27(a) and Figure 6-27(b) show the comparison between the non-evaporating spray previously examined and the evaporating one at 388K back temperature. In addition to the air-flow ribbons and the liquid droplets plotted, the fuel vapour mass fraction distribution is plotted for the evaporating case. As can be seen, the iso-octane fuel is vaporising relatively fast, leading to relatively weaker induced air motion recirculation zones. At the same time, the liquid phase seems to penetrate significantly less compared to the non-evaporating one. This can be seen more clearly in Figure 6-27(c), which presents the calculated spray penetration for both cases. As can be seen, when evaporation takes place, liquid penetration stops at a distance downstream of the injection hole, although there is no significant difference during the initial part of the spray penetration curve. At this liquid-length distance, the total spray evaporation rate becomes equal to the fuel injection rate. Clearly, this flow characteristics, being a function of the injector geometric characteristics and back chamber thermodynamic conditions, but less dependent on injection pressure in a way similar to that observed for diesel sprays, can greatly affect the design of the combustion system and the selection of the appropriate injection nozzle. In Figure 6-27(c), in addition to the liquid phase penetration plotted, the vapour phase penetration is also plotted. As can be seen, vapour continues to penetrate even after the liquid phase penetration stops, due to the momentum transfer from the injected liquid to the surrounding air.



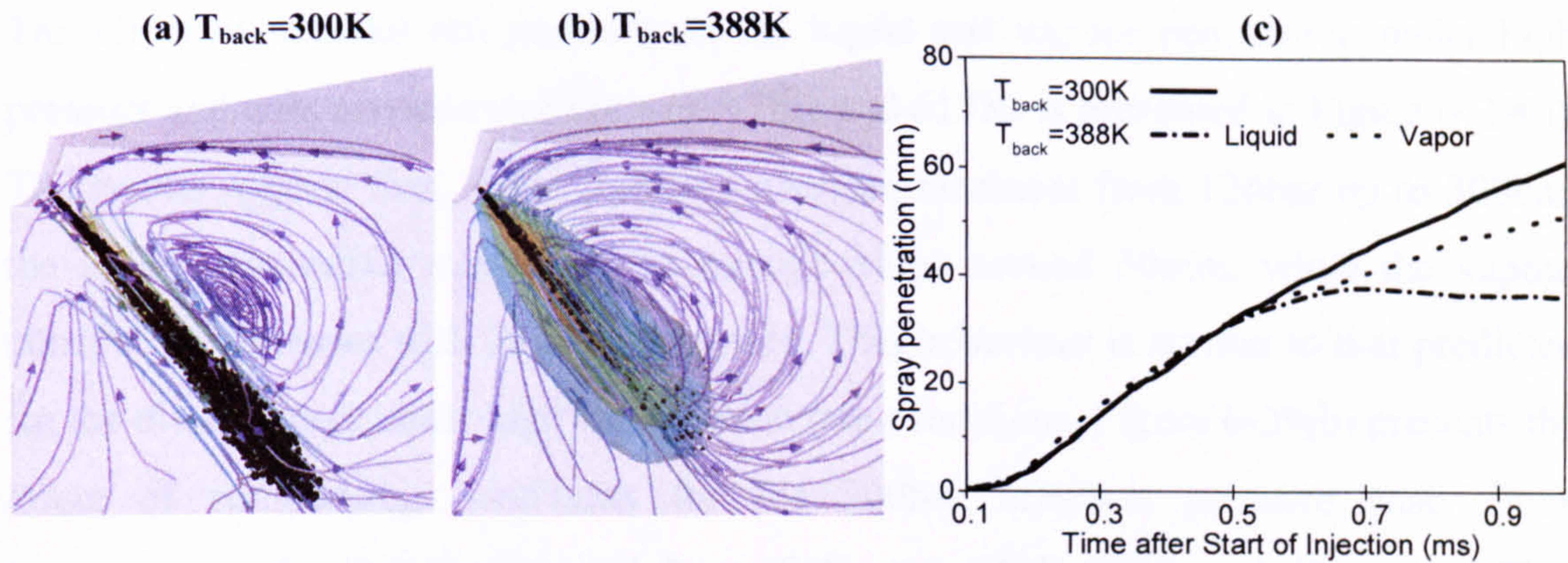


**Figure 6-27:** (a) Fuel spray distribution and air-flow ribbons coloured according to their total velocity magnitude, (b) fuel vapour mass fraction iso-surfaces for evaporating ( $T_{back}=388K$ ) conditions superimposed to liquid droplets distribution and air-flow ribbons coloured according to their total velocity magnitude, at 1.0ms ASOI, and (c) liquid and vapour spray penetration for non-evaporating and evaporating cases;  $P_{back}=1bar$ .

Finally, a parametrical study has been performed to investigate the effect of operating and geometric conditions on the liquid and vapour penetrations, similar to the one proposed for diesel sprays in Chapter 5. In order to reduce the computational time and due to the symmetry of the problem, 2-D axis-symmetric grids have been used. First the grid dependency issue was addressed. Figure 6-28 shows the liquid and vapour penetration under atmospheric pressure and room temperature and under elevated back pressure and temperature conditions, equal to 6.7bar and 617K respectively, for the three grids described in Figure 5-1. The results prove that the sensitivity of the predictions to the computational domain becomes almost negligible with successive levels of cell refinement, suggesting that the ‘Grid 2’, with 12,000 cells and minimum cell size of 0.3mm, represents the best compromise between computational efforts and numerical accuracy and thus it has been used for the successive simulations.

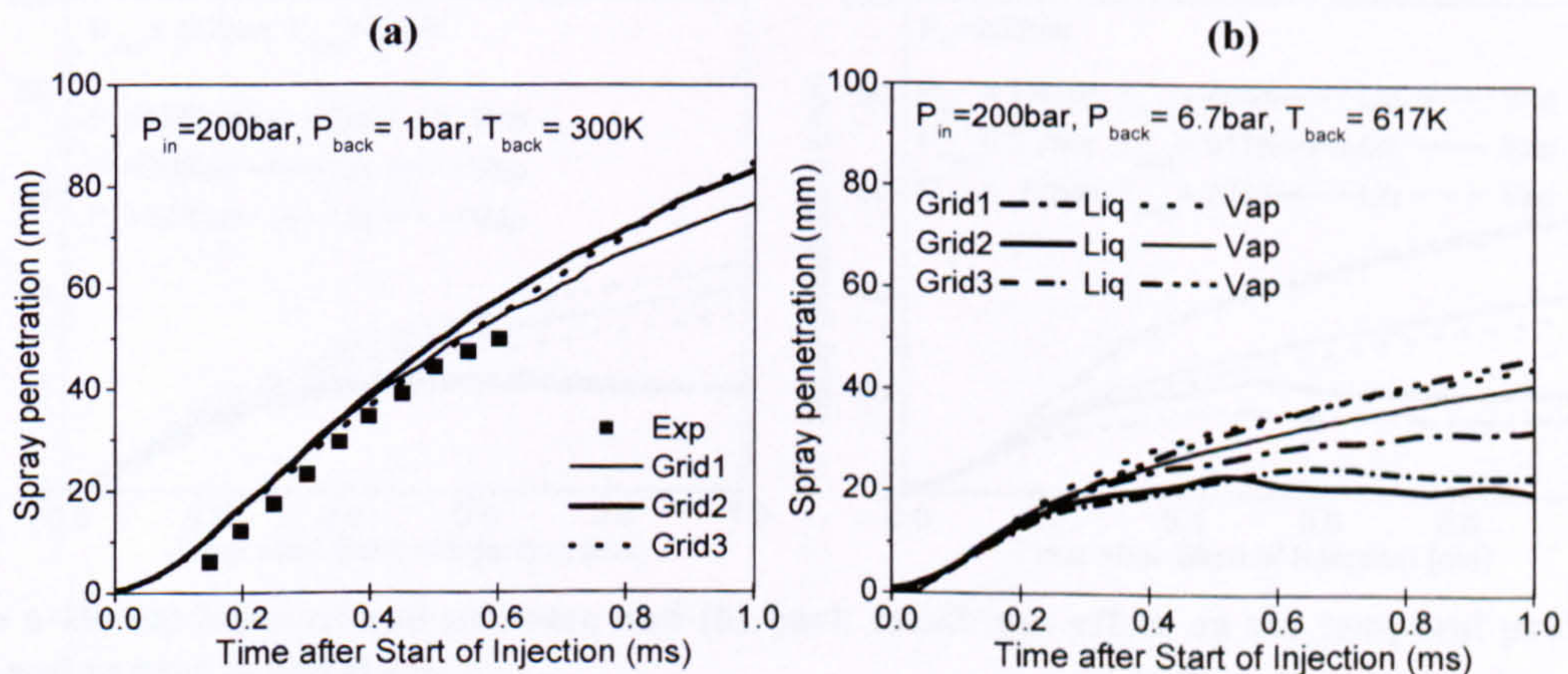


**Figure 6-28:** Grid effect on the temporal profiles of liquid and vapour penetration for (a) atmospheric back-pressure conditions under room temperature and (b) high-back pressure and temperature conditions. Grid 1, Grid 2 and Grid 3 correspond to the computational domains described in Figure 5-3.



The effect of nominal rail pressure on the liquid and vapour penetration under high pressure and temperature conditions of 6.7bar and 617K, is presented in Figure 6-29(a). The results suggest that, as the injection pressure increases from 120bar up to 300bar, the liquid penetration reaches an asymptotic value around 30mm, while the vapour penetration increases with injection pressure. This behaviour is similar to that predicted for the diesel sprays under high vaporisation rate conditions. Figure 6-29(b) presents the effect of surrounding conditions for the 200bar injection pressure case. Back temperature and pressure are varied, from 408K up to 722K and from 1.4bar up to 12bar respectively, in order to increase the gas density from 1.4 up to 5.8kg/m<sup>3</sup>; the model predicts that the liquid and vapor penetrations are substantially reduced with increasing gas density, due to the increased vaporisation rate and drag. The effect of injected fuel temperature is shown in Figure 6-30(a), suggesting that the liquid vaporisation is accelerated with increasing fuel temperature, due to the reduced heat-up period needed to reach the bulk-temperature condition. This results to reduced liquid penetration as the injection temperature increases, while the vapour penetration, which is more sensitive to the back temperature and pressure conditions, seems to be unaffected by the liquid temperature variation. Figure 6-30(b) shows the dependence of the spray penetration on the hole size, which directly affects the dimension of the injected liquid ligaments. The predictions reveal that, similarly to the diesel spray cases, the liquid penetration linearly decreases with the dimension of the hole cross sectional area, while the vapour penetration increases due to the higher vaporisation rate generated by smaller droplets with bigger relative velocity.

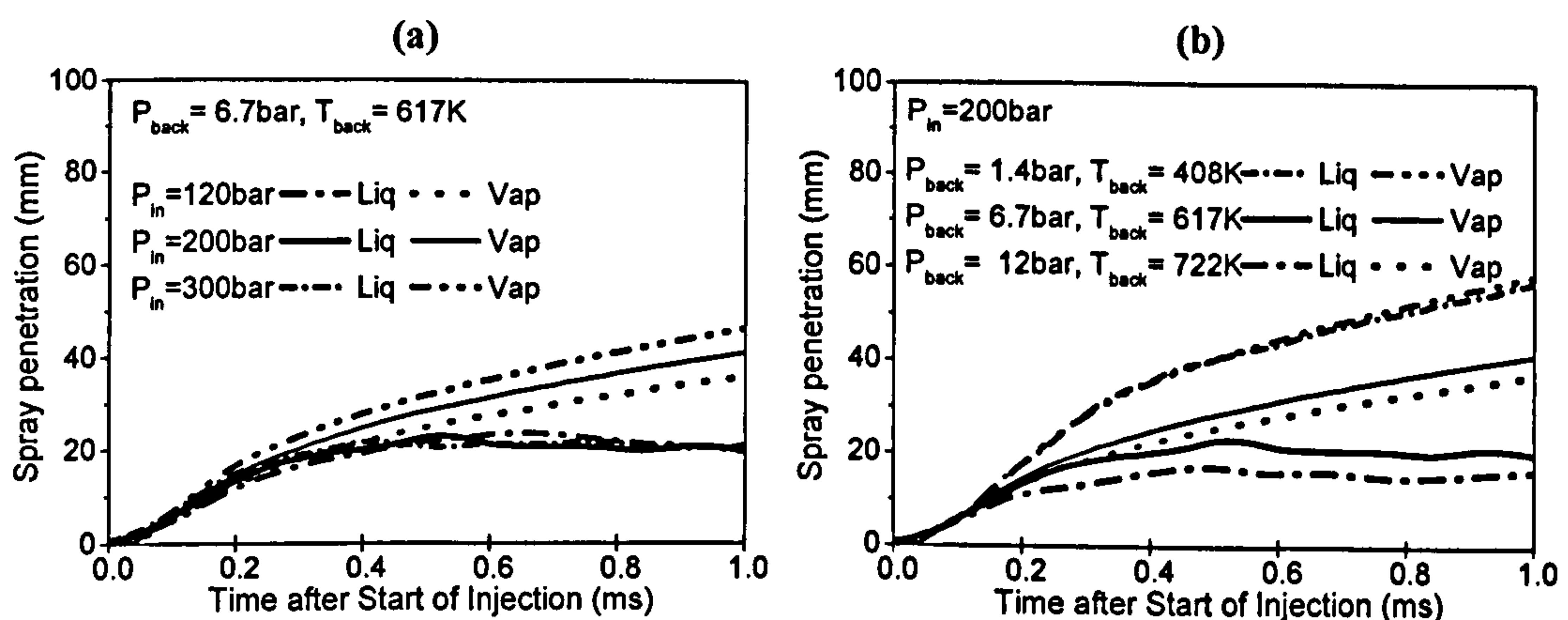
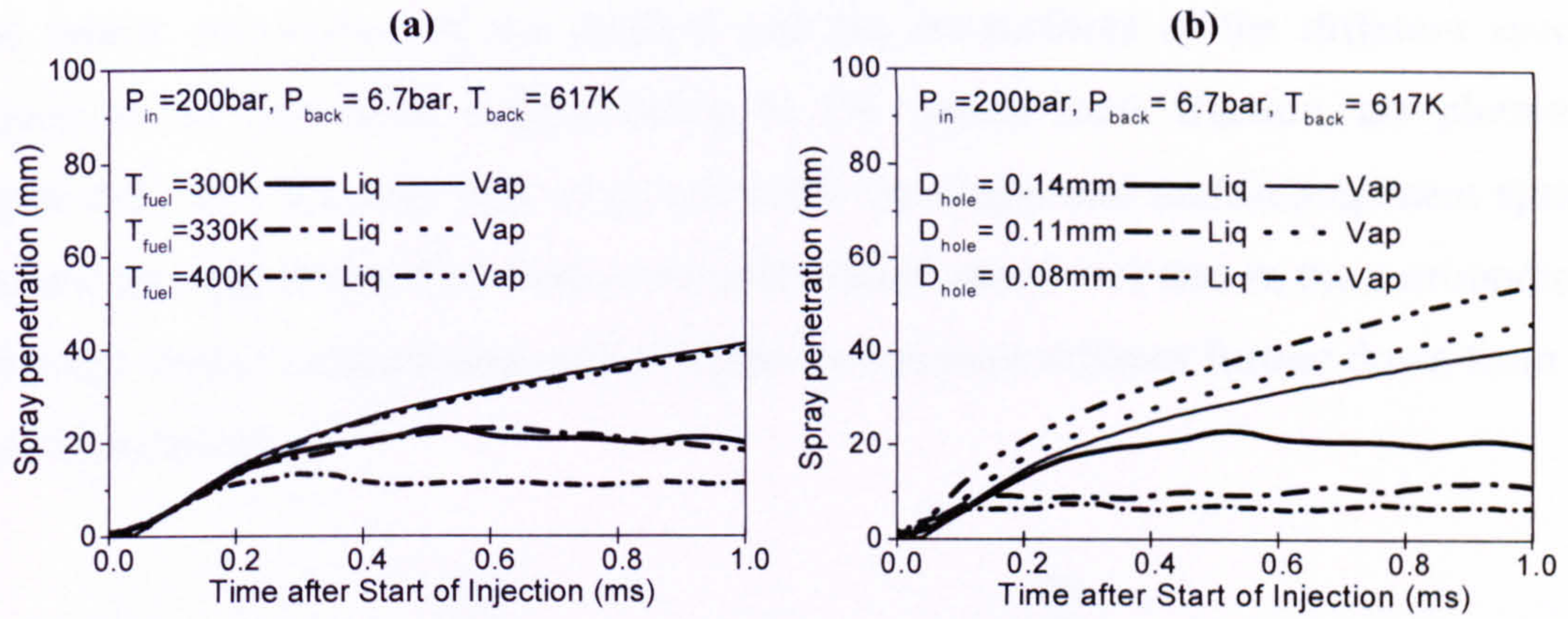


Figure 6-29: (a) Nominal rail pressure and (b) back conditions effect on the temporal profiles of liquid and vapour penetration.





**Figure 6-30: (a) Initial fuel temperature and (b) hole size effect on the temporal profiles of liquid and vapour penetration.**

The last case to be presented in this section focuses on the multi-component fuel vaporisation effect on the spray development, as predicted by the vaporisation model described in Chapter 4. A mixture initially composed by 20% hexane, 50% octane and 30% decane has been used. The previously examined 200bar injection pressure, 12bar back pressure and 600K gas temperature case has been adopted, while additional inputs correspond to 300K injected fuel temperature and 0.14mm injector hole diameter. Figure 6-31(a) shows the effect of liquid composition on the liquid and vapour penetration temporal development. It suggests that the multi-component fuel, which contains a lighter and thus more volatile species, initially has higher vaporisation rate compared to the single component case. This results to the lighter liquid component reaching faster the asymptotic liquid penetration value while the vapour penetration increases. Figure 6-31(b) shows the temporal variation of the vapour penetration for each species presented in the two fuels, remarking that the heavier component (decane) vaporises slower compared to the other two species.

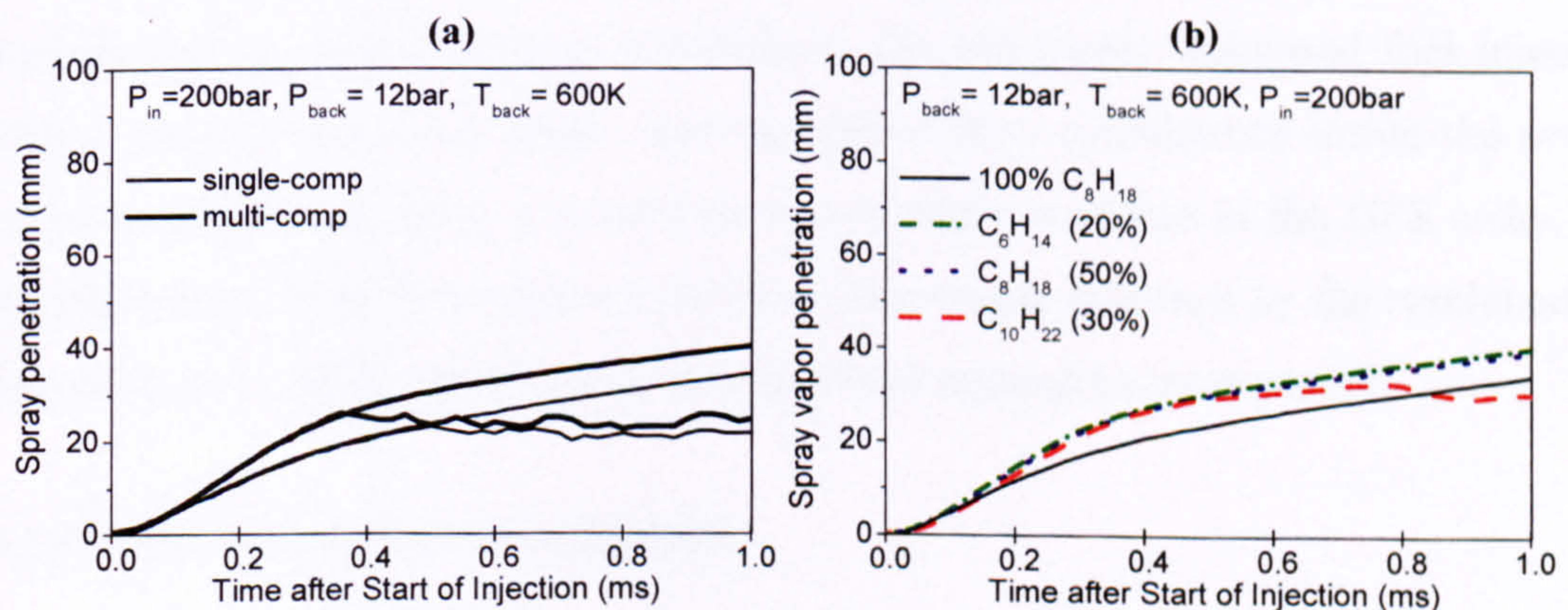


**Figure 6-31: Temporal variation of (a) liquid and vapour penetrations and of (b) vapour penetration for each species present in the single component (100%  $C_8H_{18}$ ) and in the multi-component (20%  $C_6H_{14}$ -50%  $C_8H_{18}$ -30%  $C_{10}H_{22}$ ) fuels.**



The spatial distribution of the droplets and the iso-surfaces of the different species present in the two fuels, corresponding to 1% vapour mass fraction, are plotted in Figure 6-32 at 1.ms after start of injection for the single and multi-component sprays. The results suggest that the multi-component liquid penetrates less in the surroundings, while the vapour concentration of the lighter component diffuses further down from the injector location.

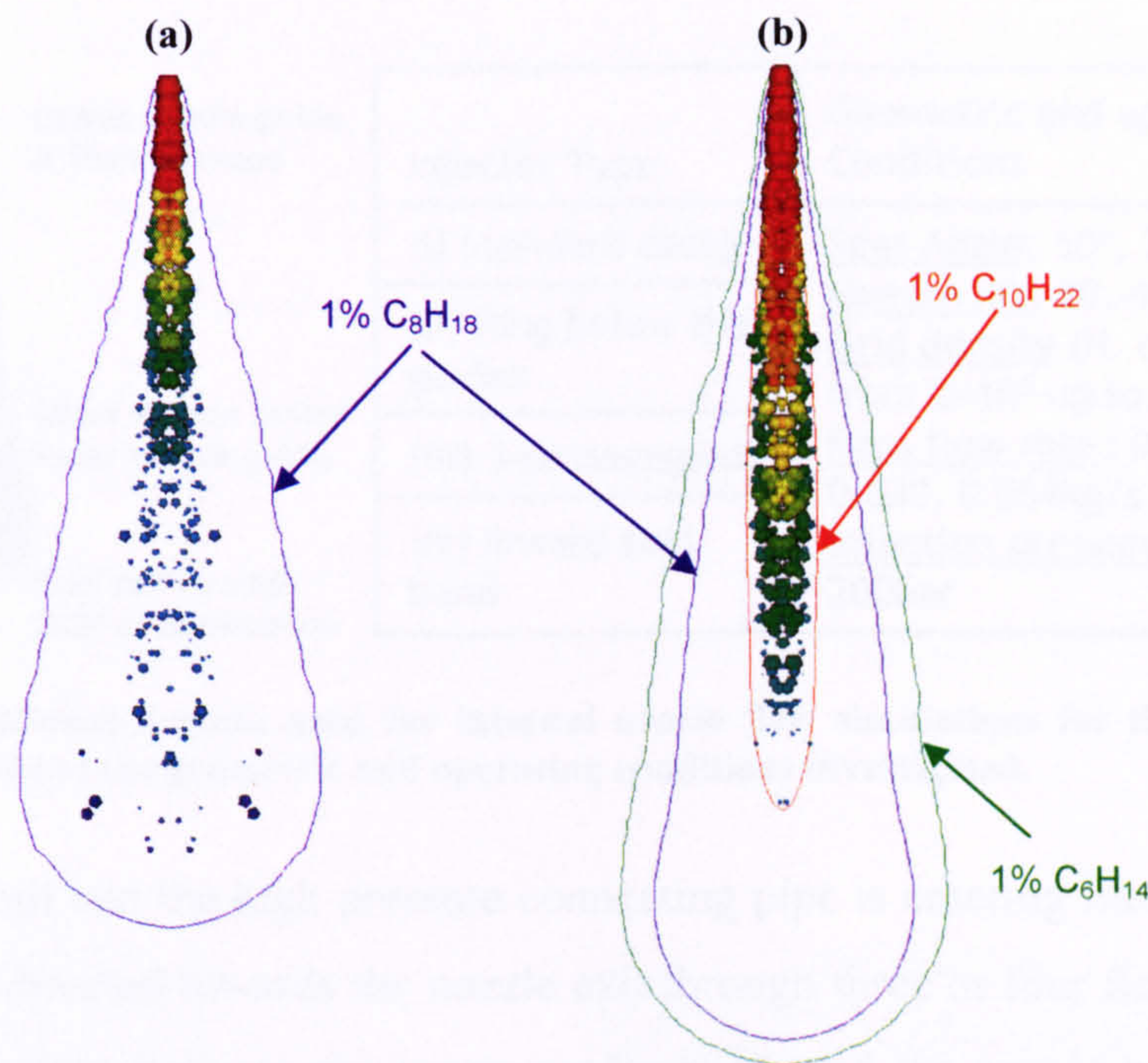


**Figure 6-32: Parcel scatter plots colored according the total velocity and vapour fuel concentration iso-surfaces corresponding to 1% vapour mass fraction for the (a) single component (100%  $C_8H_{18}$ ) and the (b) multi-component (20%  $C_6H_{14}$ -50%  $C_8H_{18}$ -30%  $C_{10}H_{22}$ ) fuels at 1ms ASOI.**

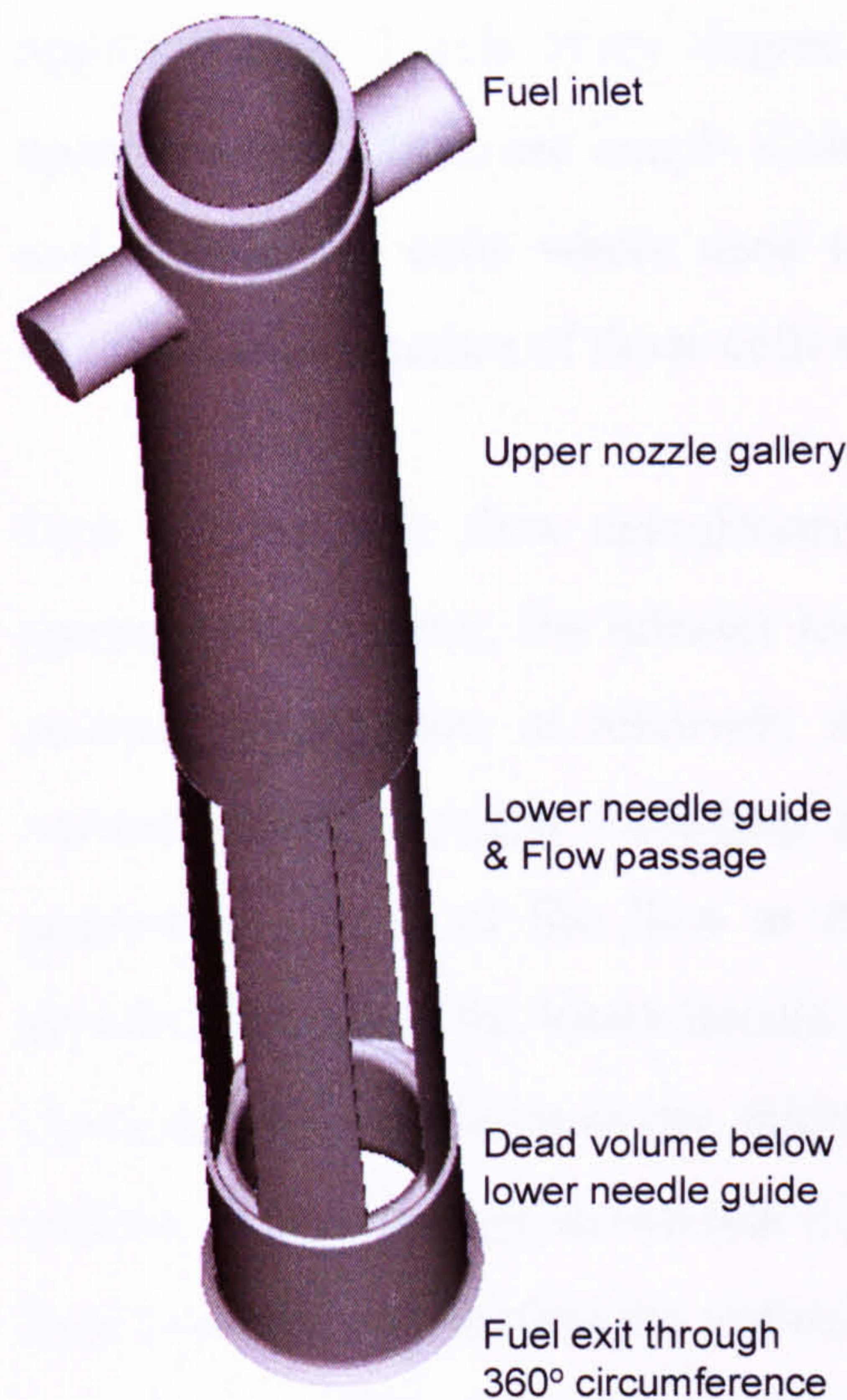
## 6.4 Outwards-opening pintle-type injector

The last high-pressure nozzle investigated for spray-guided GDI applications is the outwards-opening pintle injector. Similarly to the previously discussed fuel injection systems, multi-dimensional single- and two-phase flow calculations inside the nozzle have been performed, using a combination of models available in the GFS code. The most important nozzle flow characteristics are discussed, followed by the results on the subsequent spray development using the Eulerian-Lagrangian spray model.

### 6.4.1 Internal nozzle flow investigation

This section focuses on the internal nozzle flow investigation inside the outwards-opening pintle-type piezo-driven injector.





Injector Type	Geometric and operating Conditions
(i) Standard design	<u>Seat Angle</u> : 50°, 70°, 90° <u>Needle lift</u> : 20, 40, 60 $\mu$ m <u>Grid density</u> (N. cells): from $2 \times 10^5$ up to $9 \times 10^5$ <u>Mass flow rate</u> : 0.018, 0.030, 0.054kg/s <u>Injection pressure</u> : 100, 200bar
(ii) Ring below the guides	
(iii) 3-passageguide	
(iv) Inward seal band	

**Table 6-III: Computational domain used for internal nozzle flow simulations for the outwards-opening injector and list of the geometric and operating conditions investigated.**

The fuel from the rail and the high pressure connecting pipe is entering into the nozzle gallery and then is directed towards the nozzle exit through three or four flow passages located at the free-space between the lower needle guide and the nozzle body. Below the lower needle guide there is a dead volume where the four high speed flow jets entering from the flow passages are mixing before the fuel exits from the injector. The spray direction is mainly determined by the seat angle of the pintle-type needle. During the injection period, the needle is pushed down (entering into the combustion chamber), and fuel is exiting from the seal area, forming a hollow-cone spray. Table 6-III shows the basic nozzle geometry simulated and summarises the main geometric and operating conditions investigated. For all cases simulated, iso-octane was used as the working liquid fuel. The nozzle geometry was meshed with unstructured grids combining tetrahedral and hexahedral cells. The total cell number varied from  $2 \times 10^5$  up to  $9 \times 10^5$ , with up to two levels of local refinement at the needle seat area in order to test the grid dependency of the results. Additionally, for a particular nozzle design having 90 degrees symmetry, a grid sector with symmetry boundary conditions was also constructed, allowing use of cells with an aspect ratio at the needle seat area to be  $\sim 1$ . This was considered important since the standard grids were constructed with



approximately 1 cell every degree of circumferential angle, which corresponds to approximately  $70\mu\text{m}$  arc length. Considering that the needle lift is approximately  $40\mu\text{m}$  and at least 20 cells were used to resolve the flow within this flow passage, the resulting aspect ratio of those cells was 1/35.

First single-phase flow calculations at fixed needle positions and fixed flow rates (pressure drop along the nozzle) have been performed. They provide evidence of the internal nozzle flow at relatively short times and highlight the differences between various nozzle designs including identification of possible cavitation sites. Before presenting details of the flow at the nozzle exit, a general description of the flow distribution below the lower needle guide is given. Figure 6-33 explains the main flow characteristics inside those two injectors for a needle lift of  $40\mu\text{m}$  and a pressure drop of 200bar. Figure 6-33(a) shows that the flow mainly exits from the area directly below the flow passages connecting the volume below the lower guide to the upstream geometry. At the same time, as shown in Figure 6-33(b), below the needle guide two counter-rotating recirculation zones are observed.

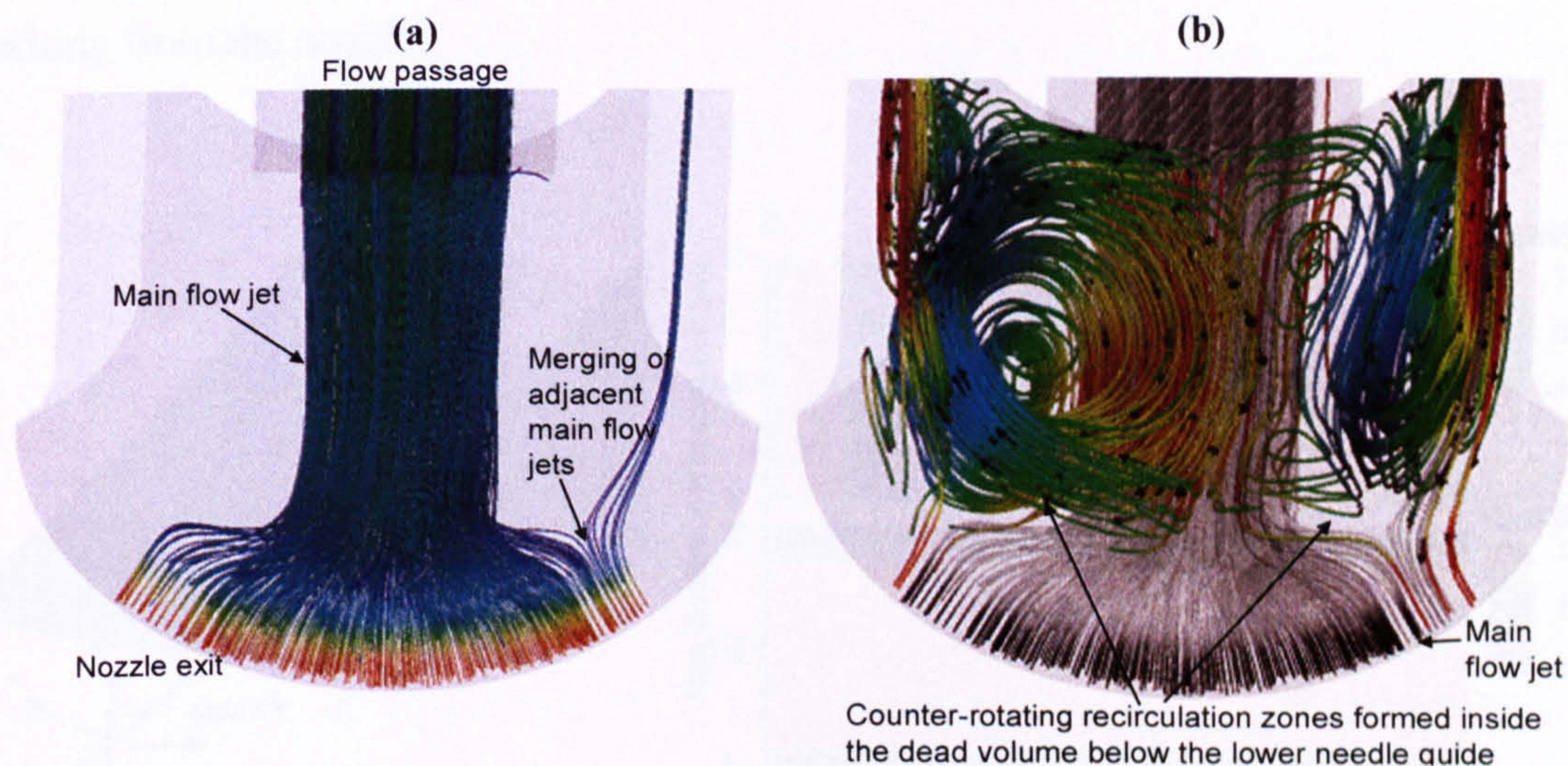


**Figure 6-33: (a) Main flow path inside the nozzle and (b) recirculation zones formed below the needle guides (in colour scale); on the black-white scale the stream lines of the main flow path are superimposed.**

In this plot, the colour scale represents the velocity component in the direction of the needle guide, while the main flow path is also superimposed, but this time coloured on a grey scale in order to separate those two distinguishable flow paths. Another important flow characteristic can be seen at the nozzle exit area located directly below the lower needle guide. In this location the exiting flow is the result of the merging of two



adjacent main flow paths, which enter to this location from the edges of the upstream recirculation zones. This flow distribution is responsible for the so-called ‘snake’ type motion that has been observed during the spray development. Focusing on the nozzle exit, it can be seen that the flow distribution exhibits more pronounced areas of higher velocity, which are found at locations below the eight recirculation zones. It is thus clear that the details of the nozzle design affect to a large extent the flow distribution of the exiting fluid.

To highlight those difference between different designs, the axial (in the direction of the needle seat) and circumferential velocity component at the nozzle exit gap, as defined in Figure 6-34(a), are presented. Figure 6-34(b) show the spatial distributions around the nozzle exit plane of those two velocity components for the standard design. The x-axis on those graphs corresponds to the  $360^\circ$  of the circular nozzle circumference, while the y-axis coincides with the needle lift gap. As can be seen, the flow of the standard design exhibits four high-peak and four low velocity areas. As also explained, four more, but with lower intensity peaks, are observed at the area located directly below the lower guide, where the two flow streams forming the recirculation zones merge again before exiting from the nozzle.

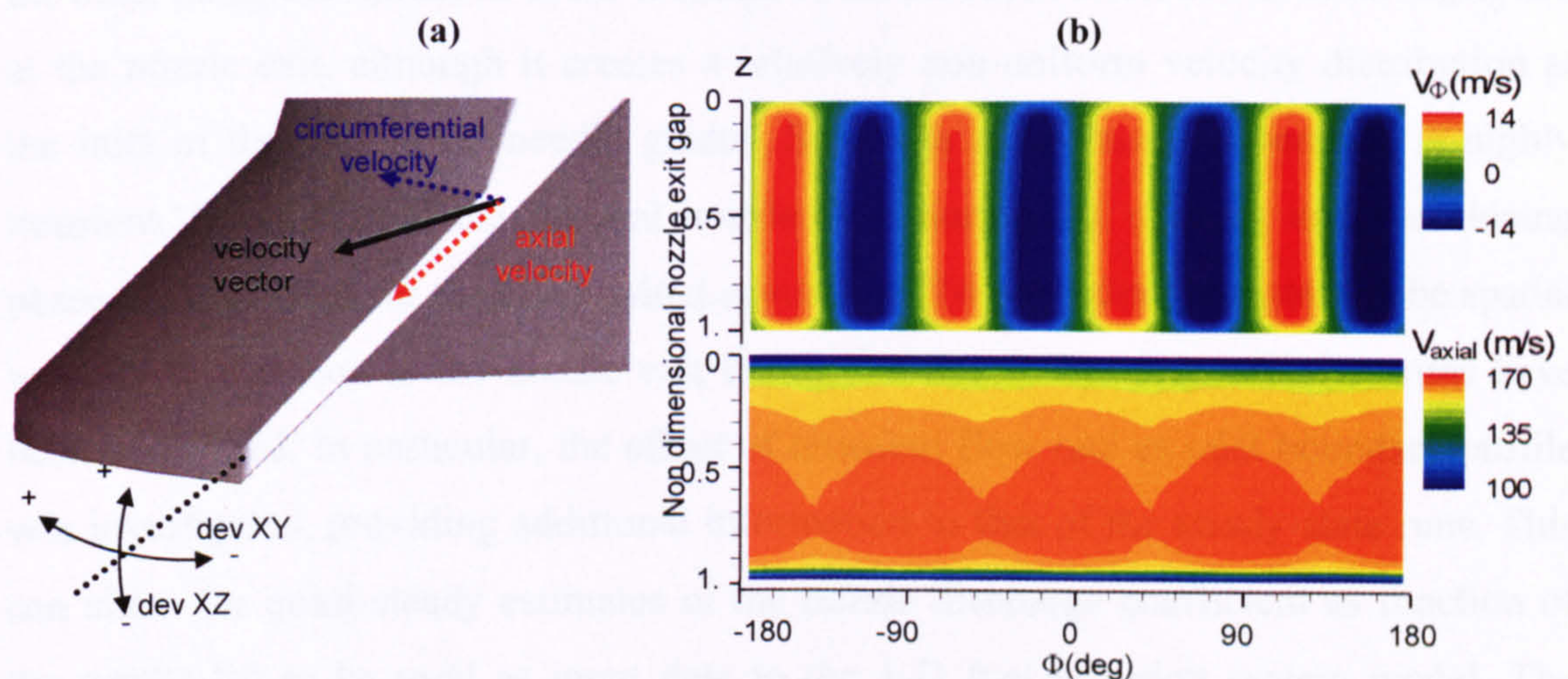


**Figure 6-34: (a) Schematic showing the definition of axial and circumferential velocity components and the corresponding deviation angles. (b) Circumferential and axial velocity component distributions at the nozzle exit gap around the  $360^\circ$  circumference at the nozzle exit plane [Standard design,  $50\mu\text{m}$  needle lift,  $m_{FR} = 0.048 \text{ kg/s}$ ].**

This non-uniformity of the flow at the exit of the nozzle can be also seen in Figure 6-35. This graph presents the spatially averaged along the needle lift gap, mean axial and circumferential velocity components for the designs of Table 6-III, i.e. the standard, the



‘ring’, the inward seal band and the three-guide nozzles. On the same graph, the corresponding flow deviation angles from the mean value along the X-Y and X-Z planes around the 360° nozzle periphery, as defined in Figure 6-34(a), are also plotted. The simulations predict up to  $\pm 10^\circ$  peak-to-peak flow deviation angle in the circumferential direction while much smaller values, of the order  $\pm 1^\circ$  degrees are predicted on the X-Z plane. In some cases, not presented here, values as low as 1-2% in the circumferential direction have been calculated, implying a more uniform flow at the nozzle exit plane. This deviation angle has been found to play an important role on the spray development, as spray calculations, to be presented on a following section of the chapter, have indicated. The effect of needle lift has also been investigated. The results have indicated that the magnitude of the tangential velocity variation is independent on the needle lift at fixed flow rates, but the axial velocity is more uniform for smaller lifts. The velocity deviation angle in the X-Y plane is larger at higher needle lifts, which implies a better mixing of the flow at the nozzle exit. Generally the details of the internal nozzle geometry seem to affect the non-uniformity of the velocity profile at the exit. Out of the various geometries investigated, those allowing a smoother entry of the flow into the volume below the lower needle guide (i.e. nozzle with larger guide area or bigger ‘dead’ volume) seem to produce more uniform velocity profiles at the exit. On the other hand, the influence of the location of the fuel feed inlets seems to be negligible at the nozzle exit, although it creates a relatively non-uniform velocity distribution at the inlet of the four lower needle guides. Since the actual nozzle operation is highly transient, the details of the internal nozzle flow during the opening and the closing phase are important for the spray initial conditions. To get better estimates of the spatial velocity distribution at the nozzle exit during the nozzle opening, transient runs have been performed. In particular, the effect of transient flow rate as inlet boundary profile was investigated, providing additional information to that of the steady-state runs. This can allow for quasi-steady estimates of the nozzle discharge coefficient as function of the needle lift to be used as input data to the 1-D fuel injection system model. The model described in Arcoumanis et al. [163], using as input the measured rail pressure and needle lift signals and the predicted (or measured) nozzle seat area discharge coefficient, provides the transient flow rate and the mean flow velocity through the nozzle during the injection period. For the particular nozzles investigated here, rail pressure and needle lift measurements for two injection pulses of 0.3 and 0.5ms have been used as input to the model. That information allows estimates of the actual flow



rate and injection velocity components. Figure 6-36 presents the result of such calculations for the two injection pulses and shows a double-peak profile with the injection fuel velocity which follows the variation of the line pressure. This is in good agreement with experimental data presented in Nouri et al. [141], which shows similar double-peak velocity profiles, at 2.5mm from the injector location. These values have been used as initial conditions for the successive spray calculations.

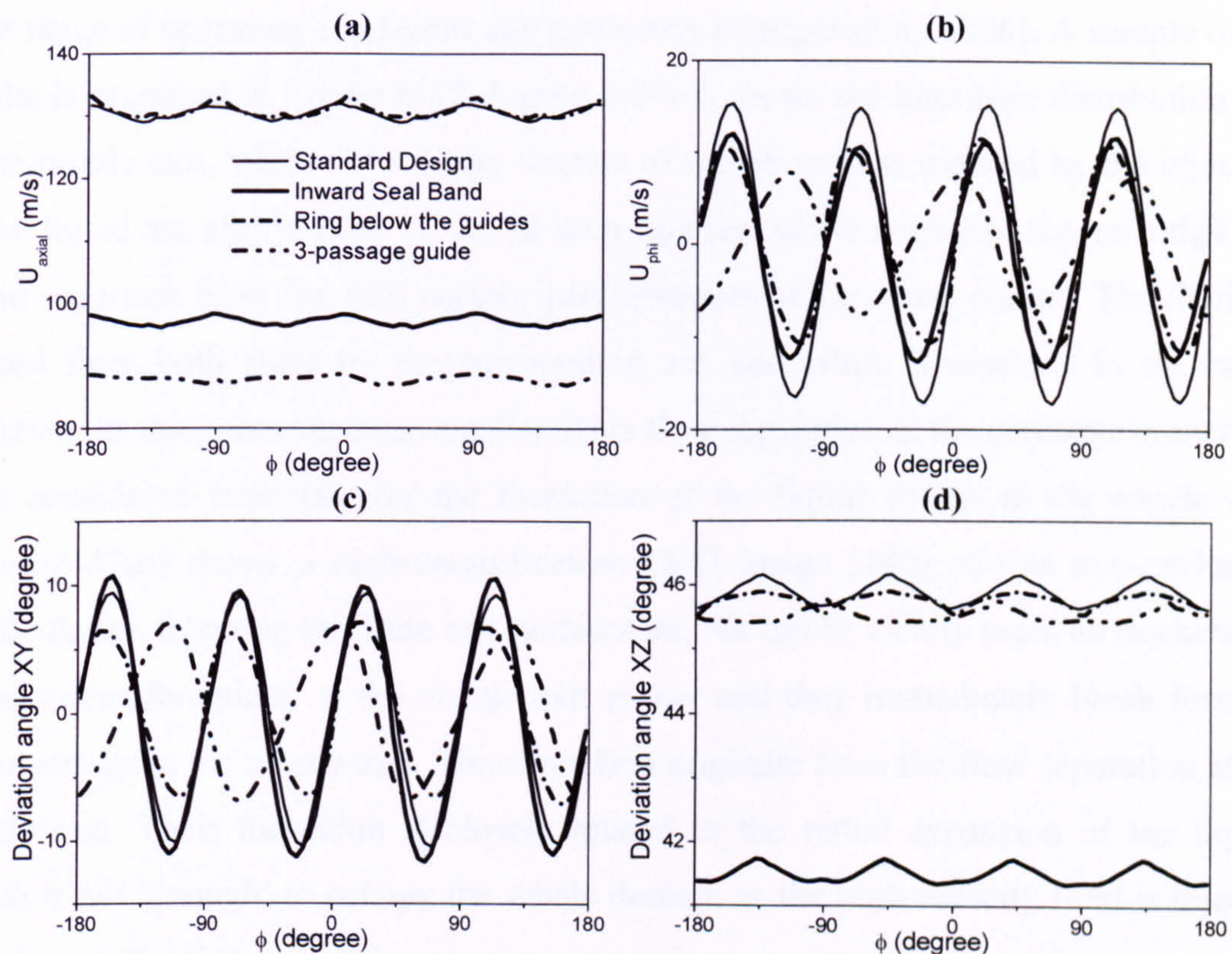


**Figure 6-35:** Spatially averaged along the needle lift gap (a) axial (b) circumferential velocity component and resulting deviation angles on the (c) X-Y and (d) X-Z planes around the 360° circumference of the nozzle exit plane for the designs listed in Table 6-III [50 $\mu$ m needle lift,  $m_{FR} = 0.036$  kg/s].

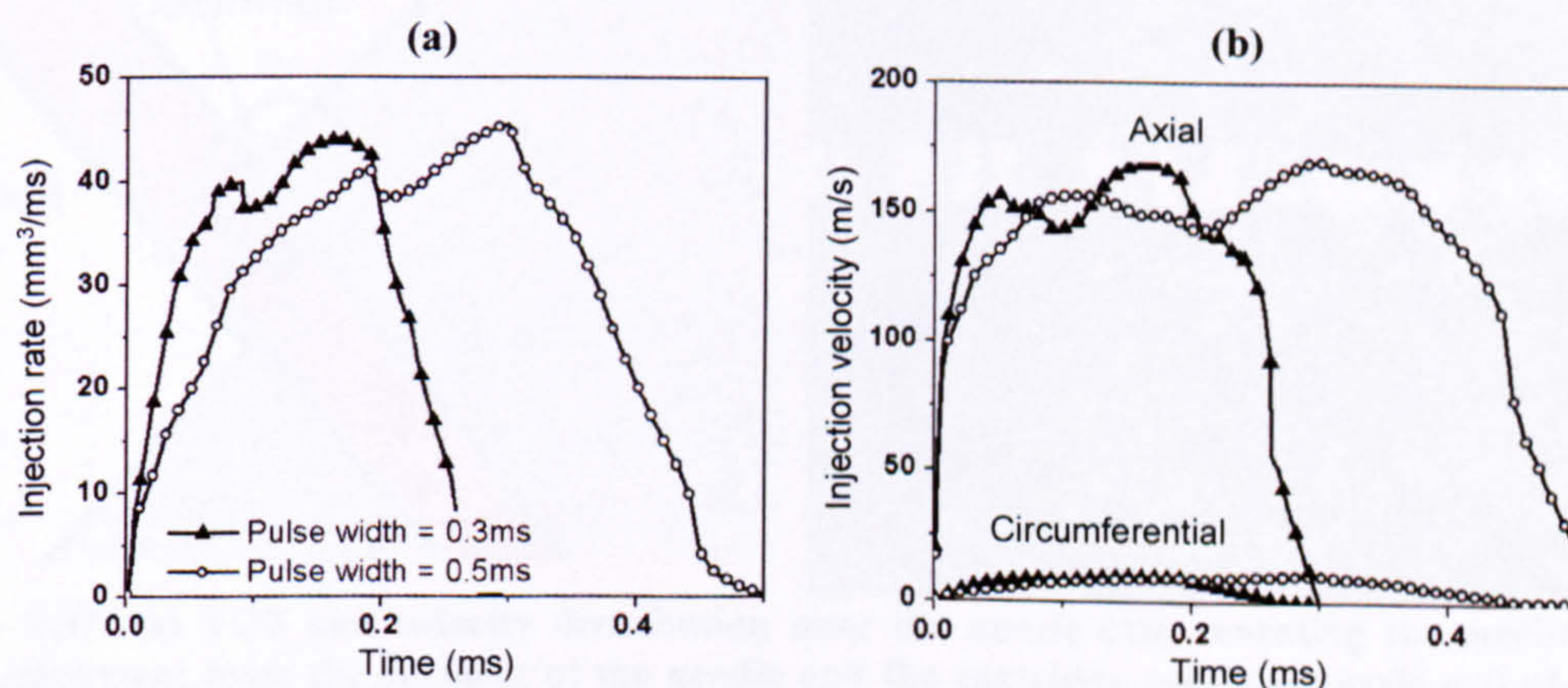


**Figure 6-36:** Predicted temporal profiles (a) flow rate and (b) mean injection velocity for two nominal injection pulse widths of 0.3 and 0.5 ms.



### 6.4.2 Near-nozzle flow and spray simulations

The results from the internal nozzle flow simulations described in the previous section provided the injection conditions for the subsequent near nozzle flow and spray investigation. The mechanism of string formation, which have been observed both in real-size and large-scale injectors [140, 141] with the scope to define their correlation to the spray characteristics, was investigated performing 2-D VOF calculations under a wide range of operating conditions and geometric configurations [226]. A sample of the results is proposed in Figure 6-37. Figure 6-37(a) shows the liquid-air distribution just at the nozzle exit, while the velocity vectors of the air motion induced by the injection of the liquid are also plotted. It can be seen that just at the corner of the cartridge, the liquid separates from the wall surface just upstream of the sharp corner. The liquid is pushed from both sides by the surrounding air, and while it expands in the radial direction, its thickness becomes smaller. This flow separation at the cartridge corner has been considered important for the formation of the liquid strings at the nozzle exit. Figure 6-37(b) shows a high-magnification CCD image [140] of this non-cavitating nozzle design injecting this time into ambient air. As can be clearly seen, air pockets are found circumferentially at the nozzle exit corner and they immediately break forming liquid strings at the nozzle exit. Those pockets originate from the flow separation at the nozzle exit. Their formation is closely related to the radial expansion of the liquid, which is not ‘enough’ to occupy the whole domain as the high velocity fluid is injected into the surrounding air.

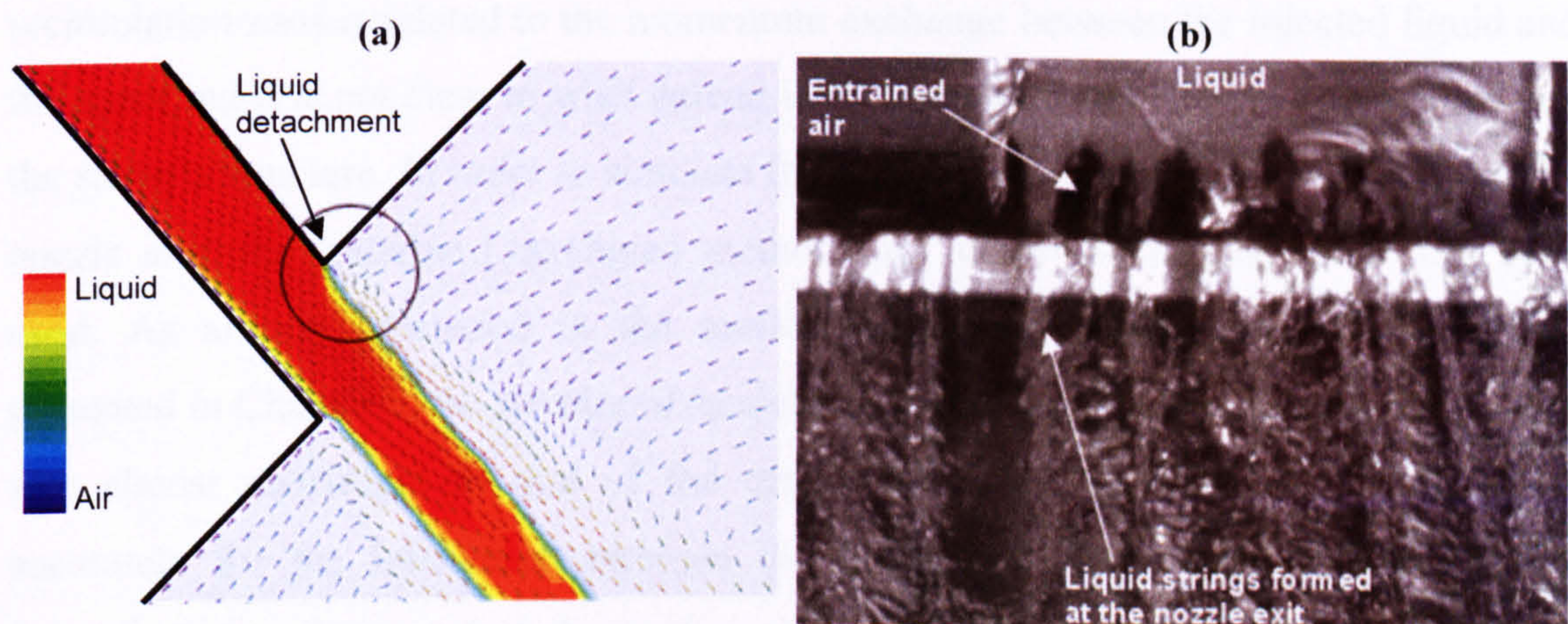


**Figure 6-37: (a) VOF and velocity distribution near the nozzle exit, revealing the mechanism of flow detachment from the surfaces of the needle and the cartridge near the nozzle exit plane, as a result of the induced air velocity (b) CCD image taken from a non-cavitating large-scale transparent nozzle [140], showing flow separation at the nozzle exit along the nozzle circumference. The formation of the liquid strings is connected to those air pockets formed at the nozzle exit.**



That information provided a detailed data base of injection parameters useful to predict the spray structure far from the nozzle exit. Model predictions have been validated against CCD images obtained during the parallel experimental programme performed by the research group [141]. A typical spray image obtained during the development of the spray with a high-speed camera is shown in Figure 6-38(a) [141].

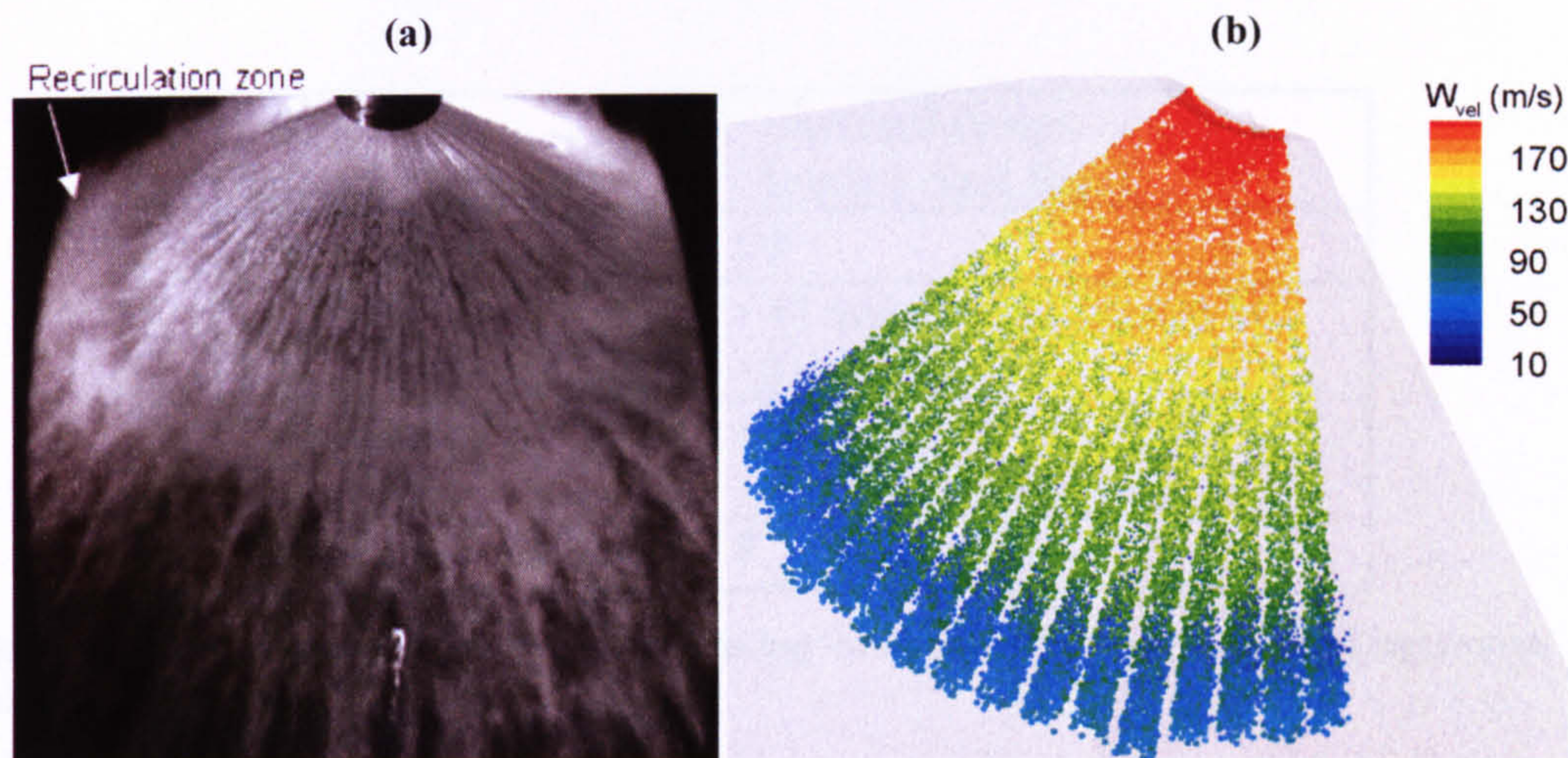


**Figure 6-38: (a) Mie spray image taken at the end of injection and (b) calculated sample droplet scatter plots coloured according to their velocity, for nominal rail pressure of 200bar, at  $P_{back}=4$ bar and room temperature.**

From this picture it can be seen that as the liquid strings penetrate into the surrounding air, a recirculation zone is formed around the spray but not at its tip, as one would expect but at about mid-way distance from the most penetrating liquid part. Liquid droplets are captured by this recirculation zone and serve as traces of its formation and development without any additional flow traces. The mechanism of formation of this recirculation zone is related to the momentum exchange between the injected liquid and the spray but it is not clear to what extent it is affected by the internal nozzle flow and the string's structure. In order to simulate the spray development further away from the nozzle exit, the Eulerian-Lagrangian methodology described in Chapter 3, has been used. As already discussed in the section on numerical parameters investigation presented in Chapter 5, the developed model allows for very dense cells to be used, with size almost equivalent to that of the droplet diameter, in order to account more accurately for the interaction between the liquid and the surrounding gas, which determines to a large extent the spray penetration. In the absence of an atomisation model suitable for such type of nozzles, the injection location of the liquid droplet parcels was distributed at various discrete points along the nozzle exit circumferential



area and the initial size distribution of the droplets was an input to the model. Initial conditions for the injection velocity and direction were taken from the internal nozzle flow simulation cases. Simulations have been performed under non-evaporating, but realistic back pressure conditions, for two different nozzle designs (the standard 90° seal angle design and one of the inward-seal-band injectors); Table 6-IV summarises the geometric and operating conditions investigated.

Injector Geometry	<ul style="list-style-type: none"> <li>• Standard design</li> <li>• Inward Seal Band</li> </ul>
Seat Angle	90°
Flow rate	<ul style="list-style-type: none"> <li>• 47 ml/s (40µm needle lift)</li> <li>• Transient</li> </ul>
Circumferential angle for the cross section	<ul style="list-style-type: none"> <li>• 0° (below lower guide)</li> <li>• 45° (in-between guides)</li> </ul>
Boundary Conditions	$P_{\text{back}} = 15 \text{ bar}, 11.98$

**Table 6-IV:** List of the geometric and operating conditions for the Eulerian-Lagrangian spray simulations.

A typical spray droplet structure at 0.3ms after the start of injection is shown in Figure 6-38(b) where the colour scale is according to the liquid velocity. It can be seen that the injected droplets follow trajectories resembling those of the observed liquid strings. Thus, the assumption of initialising droplets, rather than a continuous film, at the nozzle exit seems to be reasonable. However, the capturing of droplets in the recirculation zone, as shown in the experimental image of Figure 6-38(a), is not properly captured. The few droplets actually shown on the side of the spray are predicted close to the tip of the spray.

To further investigate that point, 2-D calculations have been performed on very fine grids, as shown in Figure 6-39(a). For this calculation, the cell spacing was approximately 25µm near the nozzle and the grid was selected to be denser in the whole region of the spray development. The initial droplet size was set equal to the experimentally measured needle lift, while the internal nozzle flow has provided the required injection velocity magnitude and deviation angle (Figure 6-34). In particular, two simulation cases have been performed, corresponding to the liquid injected from two different locations. The first one is selected directly below the flow passage ( $\Phi=0^\circ$  plane) and the second one below the lower needle guide ( $\Phi=45^\circ$  plane).



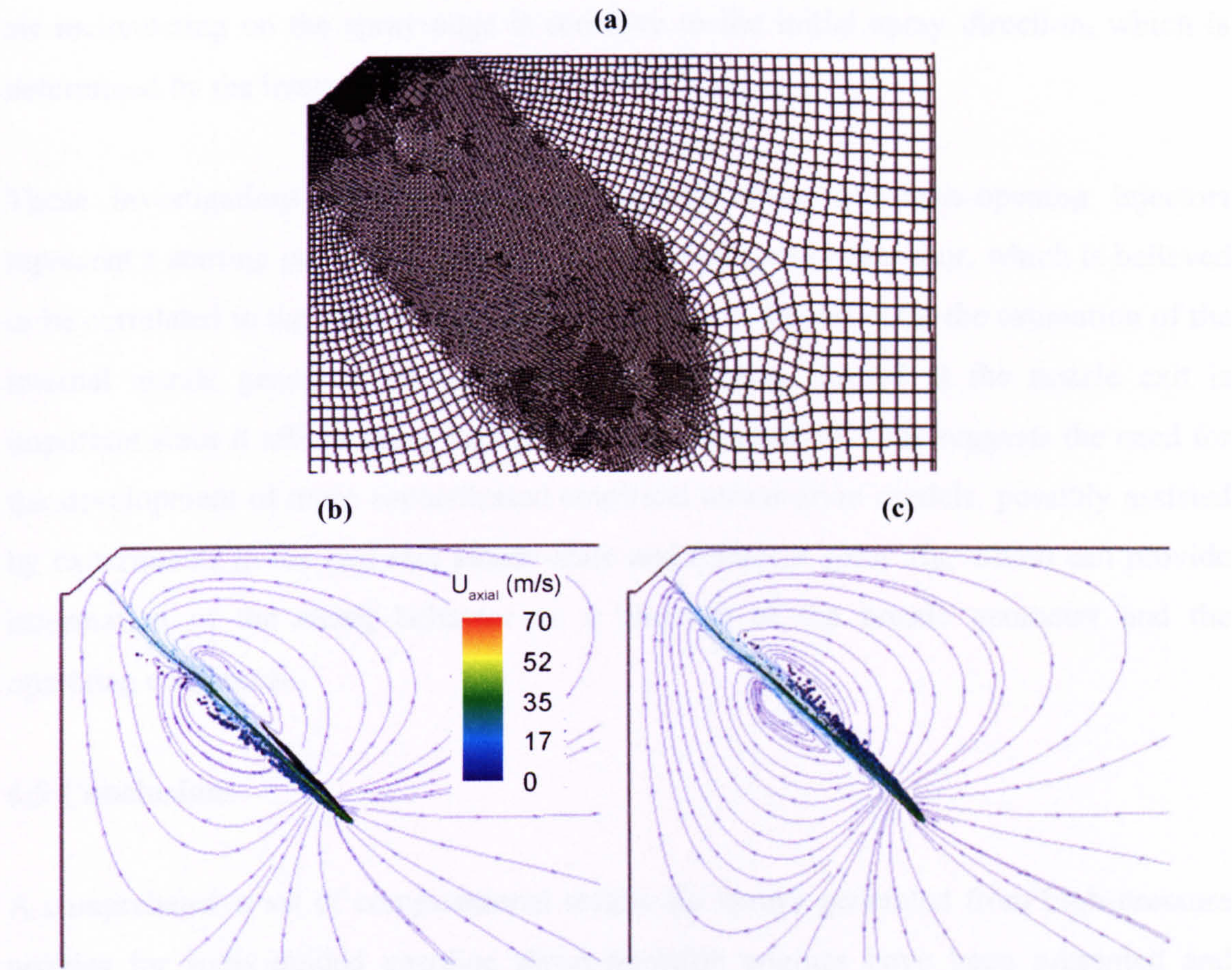


**Figure 6-39: (a) Numerical grid used for the Lagrangian spray calculations. Sample droplet scatter plots along two planes corresponding to (b) the middle of the flow passage ( $\Phi=0^\circ$ ) and (c) below the lower guides ( $\Phi=45^\circ$ ) at 0.4ms ASOI. Droplets are coloured according to their axial velocity component [Standard design].**

As already shown, the flow deviation angle corresponding to those two locations is different. These predictions at 0.3ms after start of injection are presented in Figure 6-39(b) and Figure 6-39(c) for the two planes, respectively. On the same plots, the stream-lines of the air motion are also indicated, showing the formation of the inner and outer recirculation zones around the hollow cone spray. It is evident this time that the predicted flow shows the formation of the experimentally observed recirculation at locations not close to the spray tip, but at about mid-distance between the injection point and the spray tip. At the same time, small liquid droplets are trapped inside them. Since the initial spray dispersion angle depends on the circumferential location, the calculations on those two planes result in a different dispersion of the smaller droplets relative to the mean injection direction. As can be seen, droplets at the  $\Phi=0^\circ$  plane are found inside the inner recirculation zone while droplets on the  $\Phi=45^\circ$  plane are found on the outer recirculation zone. It can be thus concluded that not only the grid resolution affects such predictions, but the dispersion of the droplets and their capturing into the



air recirculating on the spray edge is sensitive to the initial spray direction, which is determined by the internal nozzle configuration.

These investigations on the spray development from outwards-opening injectors represent a starting point to understand the complex spray behaviour, which is believed to be correlated to the mechanism of string formation. In particular the estimation of the internal nozzle geometry on the size of the droplets formed at the nozzle exit is important since it affects spray vaporisation and penetration. This suggests the need for the development of more sophisticated empirical atomisation models, possibly assisted by experiments in the real-size steady-state and transient spray rig, which can provide information of the string behavior as a function of the nozzle geometry and the operating conditions.

## 6.5 Conclusions

A comprehensive set of computational results for sprays generated from high-pressure nozzles for spray-guided gasoline direct-injection engines have been presented and discussed. These have included the swirl-pressure atomiser, the multi-hole nozzle and the outwards-opening pintle injector. Model predictions are validated against experimental data of high resolution CCD and high-speed spray images and phase Doppler anemometry measurements of the droplet size and velocity. Measurements have provided information both for the internal flow characteristics and the subsequent spray development. Different multi-phase computational models have been employed for estimating the two-phase flow usually forming inside the injector nozzle. The Eulerian VOF methodology has been employed for the simulation of the liquid film forming inside the hole of the pressure-swirl atomiser, while a cavitation model has been used for estimating the vapour volume fraction, present at the multi-hole nozzle and the outwards-opening pintle nozzle. These results provide the necessary information required to investigate the effect of the fuel injection system design on the subsequent spray characteristics. The model incorporates validated sub-models for the droplet secondary break-up, turbulent dispersion, wall impingement, droplet trajectory (as a result of the forces acting on the moving droplets including drag, turbulent dispersion, collision and coalescence). Validated atomisation models exist currently for pressure-swirl atomisers (linear instability model) and for hole-type nozzle. The



advanced points of the existing model relative to other codes are related to the fact that it can handle very fine meshes at the area of spray injection, thus resolving more accurately the mass, momentum and energy exchange between the liquid and the surrounding gas. Thus, it can take advantage of all the existing information about the 3-D distribution of the flow at the nozzle exit of the geometries already investigated, which is required as initial condition and it can account for the evaporation process of multi-component fuels. Spray model predictions have resulted to reasonable predictions of the spray structure for all three nozzles investigated and for a wide range of operating conditions.



# Chapter 7

Do not turn back when you are just at the goal.  
Publilius Syrus [Maxims]

## CONCLUSIONS AND RECOMMENDATIONS FOR FUTURE WORK

### 7.1 Overview

The research work presented in this thesis has focused on the implementation of the spray modelling in the ‘GFS’ code, the ‘General Fluid Solver’ developed by our research group over the last decade. The present study offers some new insights on the physical processes involved in evaporating sprays under a wide range of operating conditions typical of modern diesel and gasoline direct injection engines. Particular emphasis has been given to the development of a new methodology for the interaction between the Eulerian and the Lagrangian phases which, rather than being treated on the cell-to-parcel basis, is using spatial distribution functions. This allows to handle numerical grids irrespective of the volume of the Lagrangian phase introduced, thus offering considerable advantages to Lagrangian spray calculations.

The droplet vaporisation modelling, validated against extensive experimental data bases, has been implemented in the GFS code in combination with a variety of physical sub-models, which have been thoroughly assessed in order to predict the effect of thermodynamic, operating and physical parameters on the spray development for diesel fuels. Furthermore, the analysis of the numerical parameters playing the most crucial role in the simulations have been presented and discussed, focusing on the sensitivity of the modelling on the computational domain, the interpolation and the source terms distribution methodologies, the ‘virtual’ cell properties estimation and the temporal and discretisation schemes implemented in the solver. The validated code has been successively used to investigate the flow processes from three high-pressure injection systems for new generation direct injection spark-ignition engines. These have included the pressure swirl atomiser, the multi-hole injector and the outwards-opening pintle nozzle.



The next two sections summarise the main conclusions drawn from the investigation presented in this thesis and offer recommendations for further work.

## 7.2 Conclusions

Initially the single droplet vaporization modelling has been implemented and validated against experimental data followed by a parametric investigation. The main conclusions from this study are summarised as follows:

- The vaporisation model results seem to be very sensitive to the estimation of transient and variable thermo-physical properties in the gas and liquid phases.
- The model predicts the correct trend of droplet lifetime that is inversely proportional to the flow field temperature and the fuel volatility, while the liquid bulk temperature does not depend on the initial droplet size but it increases with gas temperature and decreases with fuel volatility.
- Under low/moderate evaporation rate conditions the standard ideal equilibrium model, with the assumption of uniform liquid temperature profile over the whole evaporation period, is able to capture the vaporisation phenomenon for small droplets where temperature gradients are negligible.
- Investigations of the droplet vaporisation behaviour at the high pressures and temperatures typical of modern diesel and gasoline engines revealed that under such conditions the phenomenon of super-critical vaporisation is likely to occur, questioning the validity of common assumptions like the gas-phase quasi-steadiness, the ideal gas behaviour and the solubility of gases in the liquid-phase.
- The composition of the fuel in diesel and gasoline engines has a remarkable effect on the flame propagation, which is also a function of the vapour fuel/air mixture ratio. Consequently, the prediction of the fuel vapour concentration, the equivalence ratio and the correct initial composition of the fuel to be injected have to be correctly estimated. The implemented multi-component vaporisation model predicts the faster vaporisation of lighter fuels with higher volatility and the less volatile components determining the droplet lifetime.

The major conclusions drawn from the investigation on the spray development from different high pressure diesel injection systems, followed by the detailed investigation



of the main physical and numerical parameters involved in the modelling, are summarised as follows:

- The model predicts that the size of the droplet formed from fragmentation of the liquid ligaments exiting from the nozzle and the fluctuating behaviour of the spray cone angle are almost independent of the injection pressure.
- Numerical investigation on the spray development suggests that as the liquid penetrates, it loses momentum, which is transferred to the surrounding gas, forming a recirculation zone on the spray periphery. Under evaporating conditions, liquid penetration freezes after some time from the start of injection, while the air motion induced by the spray, continues to develop, convecting vapour further downstream from the injection point. The model predictions have indicated that the evaporation rate of the spray at the initial stages of injection plays a crucial role in accurately calculating the liquid penetration as function of the injection pressure. Correct trends can be predicted if the increased surface area of the droplets associated with their fragmentation process is considered during the exchange of heat and mass between the evaporating liquid and the surrounding air.
- Results obtained using cells of the same order of magnitude to the droplet size have shown that the computational domain plays a minor role on model predictions, if appropriate spatial distribution functions for the interpolation and source term distribution, combined with the estimation of 'virtual' cell properties, are implemented for modelling the interaction between the Eulerian and the Lagrangian phases.
- In order to combine the requirements of increased numerical accuracy and reduced computational effort, a procedure is implemented in the code for automatic local refinement in selected regions of the computational domain where and when it is needed. Moreover, dynamically refined domains guarantee the accuracy of static grid with the same cell density in the region of spray development, but obviously at reduced computational cost.
- Overall the model predictions agree reasonably well with the experimental data from different single- and multi-hole, cavitating and non-cavitating nozzles under a variety of injection pressures, back-pressure and temperature, injection hole diameter, fuel initial temperature and composition.



The investigation of the internal nozzle flow and subsequent spray development from three high-pressure injection systems for direct injection gasoline engines (the pressure swirl atomiser, the multi-hole injector and the outward-opening nozzle) allows to derive the following conclusions:

- The model predicts bigger droplets in the centre of the spray during the injection period from a pressure swirl atomiser, forming the pre-spray that first impinges on the piston wall. Those are relatively low temperature and less volatile droplets. On the other hand, the model fails to predict the high vapor concentration in the centre of the cylinder, calculating the fuel vapor more concentrated in the side of the bore, as convected by the air motion, suggesting that the assumption of adiabatic wall imposed in the simulations may have a crucial role.
- Increasing back-pressure results to a significant reduction of the spray penetration from multi-hole nozzles. However, the spray shape remains similar, in terms of spray cone and deflection angles, independently of the injection and back pressures used. This characteristic of the multi-hole injector is a clear advantage compared to the pressure-swirl atomiser.
- The presence of a central hole in multi-hole nozzles aims to produce vapour in the area between the six symmetrically located sprays of the original design. This configuration enhances the formation of a recirculation zone located at the inner part of the side spray, although this recirculation zone has been found to be relatively unstable. The spray penetration substantially increases with smaller cone angle, confirming the dependence of the spray development from the internal nozzle flow characteristics.
- Results from a multi-component fuel case reveal that the heavier species in the liquid mixture take longer to vaporise, while the vapour concentrations of the lighter components present a more significant diffusion further down from the injection location, revealing crucial information of the spray development inside the combustion chamber of GDI engines.
- The exiting flow from the nozzle of an outwards-opening injector has been found to vary considerably around the nozzle periphery, both in terms of actual velocity magnitude but also in flow direction. This, in turn, has been found to affect the dispersion of the injected droplets in the inner and outer recirculation zones formed at the two sides of the developing spray. The injected droplets, predicted by the model, follow trajectories resembling those of the experimentally observed



liquid strings. Thus, in the absence of an atomisation model suitable for such type of nozzles, the assumption of initialising droplets, rather than a continuous film, at the nozzle exit has been found to be quite reasonable.

Overall, the GFS code has reached a promising level of accuracy in predicting the spray development under the wide range of operating conditions investigated. The results have demonstrated that simulation of the internal nozzle flow and its link with the spray is critical for accurate prediction of the characteristics of the developing sprays as a function of the design of the fuel injection system used.

### **7.3 Recommendations for further work**

In this section the main recommendations for future work on the improvement and extension of the developed spray modelling are presented:

- In order to accurately predict the spray characteristics under high back-pressure conditions, the droplet vaporisation model implemented in the code requires further development, investigating the sensitivity of multi-phase equilibrium assumption at their interface, which has been currently explored under only atmospheric pressure conditions. Different equations of state should be tested to predict the fugacity of the two phases at their interface. Moreover, the multi-component nature of real diesel and gasoline fuels should be thoroughly investigated implementing for example the ‘continuous thermodynamics’ model, which describes some macroscopic aspects of the components in the mixture with continuous distribution functions. The comparison between this model and the discrete one already implemented in the code will add further insight on the validity of the different assumptions made by the two methodologies.
- The main issues related to fuel forming a liquid film on the cylinder surfaces in direct injection diesel and gasoline engines need to be accurately assessed. This suggests the development and implementation of a specific model predicting the wall film characteristics, including the heating-up and evaporation phenomena. Furthermore, the assumption of adiabatic walls in spray simulations inside the cylinder should be removed and the heat transfer from the surface to the liquid impinging on it has to be properly modeled.



- The link between the internal nozzle flow characteristics and the subsequent formation of liquid droplets exiting from the injector has been found to be a crucial issue in spray modelling. The methodology that has been suggested in the present thesis to estimate the injection boundary conditions from the interpolation of the continuous distribution properties at the nozzle exit requires further development, particularly in remapping the different variables in a general form, independently on the computational domain used for the simulations.
- This also suggests the development of a two-phase flow solver, combining the ‘Volume of Fluid’ method, which provides the near-nozzle fuel atomisation and droplet formation characteristics, with a Lagrangian approach being effective for each droplet after its formation. This method may be also be used to simulate the whole injection process without the need of a phenomenological atomisation model, while taking into account all the detailed geometric characteristics of the nozzle. Moreover, this concept can be extended, implementing a new ‘hybrid’ model, which allows to switch from the Eulerian to the Lagrangian methodology according to specific physical and numerical criteria such as the fraction of the volume occupied by the liquid in each computational cell. This method would require special attention particularly in the definition of the interaction between the two phases in terms of variable interpolation and source terms distribution and it may add further complexity to the modelling. Nevertheless, it is expected to improve the capabilities of the code in the prediction of very dense spray regions close to the injector or in areas where large droplets collide, when the Lagrangian approximation of dilute spray ceases to be valid.
- The development of specific empirical and phenomenological atomisation models predicting the formation of liquid droplet from emerging high pressure diesel and gasoline injectors, supported by experimental measurements in the crucial region close to the nozzle exit, could provide additional computational tools for the prediction of the spray development. Furthermore, the modelling of droplet secondary break-up has to be improved in order to take into account high back-pressure effects, which are likely to occur under trans- and super-critical conditions, when the interface between the liquid and gas phases cannot be clearly distinguished.
- Another important issue that could add further information to the spray characterisation is related to the investigation of the turbulence dispersion of



droplets trapped in the gaseous recirculation zones and of those that simply travel through them, estimating the turbulence time and length scales using different turbulence models.

- Finally the topic of thermal decomposition, which has been briefly treated in this investigation, is thought to explain some unknown phenomena in the development of sprays under high back-pressure and temperature conditions. This suggests further investigation of the chemical issues related to it and their successive modelling.

Overall, the above recommendations should be seen as the natural step towards the definition of an advanced CFD code able to deal with the variety of operating and geometric conditions characterising the fuel injection systems in modern diesel and gasoline engines. It's hoped that this investigation would provide further insights in the development of computational tools that may have a wider range of applications outside the automotive sector.



# References

1. Gosman A.D., State of the art of multi-dimensional modelling of engine reacting flows, Oil&Gas Science and Technology, Vol. 54, No. 2, pp. 149-159, 1999.
2. Wirth M., Zimmermann D., Friedfeldt R., Caine J., Schamel A., Davies M., Peirce G., Storch A., Ries-Müller K., Gansert K.-P., Pilgram G., Ortmann R., Würfel G. and Gerhardt J., A cost optimised gasoline spray guided direct injection system for improved fuel economy, Seminar on Fuel Economy and Engine Downsizing, Institution of Mechanical Engineers, UK, 13 May, 2004.
3. Dukowicz J.K., A particle-fluid numerical model for Liquid Sprays, J. of Computational Physics, Vol. 35, pp. 229-253, 1980.
4. Gavaises M., Modelling of diesel fuel injection processes, PhD Thesis, Imperial College, University of London, 1997.
5. Gold M., Li G., Sapsford S. and Stokes J., Application of optical techniques to the study of mixture preparation in direct injection gasoline engines and validation of a CFD model, SAE Technical Paper 2000-01-0538, 2000.
6. Fan L. and Reitz R.D., Development of an ignition and combustion model for spark-ignition engines, SAE Technical Paper 2000-01-2809, 2000.
7. Alsemgeest R., Shaw C.T., Richardson S.H. and Pierson S., Modelling the time-dependent flow through a throttle valve, SAE Technical Paper 2000-01-0659, 2000.
8. Patterson M.A. and Reitz R.D., Modelling the effect of fuel spray characteristics on diesel engine combustion and emission, SAE Paper 980131, 1998.
9. Bauman S.D., A spray model for an adaptive mesh refinement code, PhD thesis, University of Wisconsin, 2001.
10. Tanner F.X. and Reitz R.D., Scaling aspects of the characteristic time combustion model in the simulation of diesel engines, SAE Technical Paper 1999-01-1175, 1999.
11. Lippert A.M., Chang S., Are S. and Schmidt D.P., Mesh independence and adaptive mesh refinement for advanced engine spray simulations, SAE 2005-01-0207, 2005.



12. Tatschl R., v. Kunsberg Sarre C. and v. Berg E., IC-engine spray modelling - status and outlook, International Multidimensional Engine Modelling User's Group Meeting at the SAE Congress, 2002.
13. Versaevel P., Motte P. and Wieser K., A new 3D model for vaporizing diesel sprays based on mixing-limited vaporization, SAE Technical Paper 2000-01-0949, 2000.
14. Subramaniam S., O'Rourke P.J., Numerical convergence of the KIVA-3 code for sprays and its implications for modelling, Los Alamos Unclassified Report LAUR 98-5465, 1998.
15. Aneja R. and Abraham J., How far does the liquid penetrate in a diesel engine: computed results vs. measurements?, Combust. Sci. Tech., Vol. 138, pp. 233–255, 1998.
16. Beard P., Duclos, J.M., Habchi C., Bruneaux G., Mekkadem K. and Baritaud T., Extension of Lagrangian-Eulerian spray modelling: application to high pressure evaporating diesel sprays, SAE Paper 2000-01-1893, 2000.
17. Nordin N., Complex chemistry modelling of diesel spray combustion, PhD thesis, Chalmers University of Technology, 2001.
18. Barroso G., Schneider B. and Boulouchos K., An extensive parametric study on diesel spray simulation and verification with experimental data", SAE Technical Paper 2003-01-3230, 2003.
19. Larimi M., Rantanen P., Tiainen J., Kiijärvi J., Tanner F.X. and Stalsberg-Zarling K., Simulation of non-evaporating diesel sprays and verification with experimental data, SAE Technical Paper 2002-01-0946, 2002.
20. Hieber S.E., An investigation of the mesh dependence of the stochastic discrete droplet model applied to dense liquid sprays, Master of Science in Mathematics thesis, Michigan Technological University, 2001.
21. Bensler H., Bühren F., Samson E. and Vervisch L., 3-D CFD Analysis of the combustion process in a DI diesel engine using a flamelet model, SAE Technical Paper 2000-01-0662, 2000.
22. Rodatz P., Weisser G. and Tanner F.X., Assessment of CFD methods for large diesel engines equipped with a common rail injection system, SAE Technical Paper 2000-01-0948, 2000.
23. Tristano J.R., Chen Z., Hancq D. A. and Kwok W., Fully automatic adaptive mesh refinement integrated into the solution process, Proceedings, 12th International Meshing Roundtable, Sandia National Laboratories, pp. 307-314, September 14-17, 2003.



24. Wan J., Kocak S. and Shephard M.S., Automated adaptive forming simulations, proceedings, 12<sup>th</sup> International Meshing Roundtable, Sandia National Laboratories, pp. 323-334, September 14-17, 2003.
25. Malik M., Volume tracking with adaptive refinement, Master of Applied Science, University of Toronto, 2004.
26. Steiner R., 3D-combustion simulation: potentials, modelling and application Issues, 10<sup>th</sup> Diesel Engine Emissions Reduction Conference Coronado, California, August 29 – September 02, 2004.
27. Krüger Ch., Validierung eines 1D-spraymodells zur simulation der gemischbildung in direkteinspritzenden dieselmotoren, Dissertation RWTH Aachen, 2001.
28. Abraham J., What is adequate resolution in the numerical computation of transient jets?, SAE Paper 970051, 1997.
29. v. Berg E., Alajbegovic A., Tatschl R., Krüger Ch. and Michels U., Multiphase modelling of diesel sprays with the Eulerian/Eulerian approach, 17<sup>th</sup> ILASS Europe Conference, Zürich, 2001.
30. Tomiyama A., Some attempts for the improvement of computational bubble dynamics, 10th Workshop on Two-Phase Flow Predictions, Merseburg, Germany, pp. 125-136, April 9-12, 2002.
31. Alajbegovic A., Drew D.A. and Lahey R.T., An analysis of Phase Distribution and Turbulence in Dispersed Particle/Liquid Flows, Chem. Eng. Comm., Vol. 174, pp. 85-133, 1999.
32. Platzer E. and Sommerfeld M., Modelling of turbulent atomisation with a combined Euler/Lagrangian approach: starting with a two-fluid model in the dense spray region, ILASS-Europe 2002, Zaragoza, Spain, September 9 –11, 2002.
33. Lebas R., Blokkeel G., Beau P.-A. and Demoulin F.-X., Coupling vaporization model with Eulerian-Lagrangian spray atomization (ELSA) model in diesel engine conditions, SAE Paper 2005-01-0213, 2005.
34. Beau P.-A., Funk M., Lebas R. and Blokkeel G., Applying quasi-multiphase model to simulate atomization processes in diesel engines: modelling of the slip velocity, SAE Paper 2005-01-0220, 2005.
35. Sazhin S.S., Advanced models of fuel droplet heating and evaporation, Progress in Energy and Combustion Science, Vol. 32, pp.162–214, 2006.



36. Schrage R.W., A theoretical study of interphase mass transfer, New York, Columbia University Press, 1953.
37. Fuchs N.A., Evaporation and droplet growth in gaseous media, London, Pergamon Press, 1959.
38. Spalding D.B., Convective mass transfer; an introduction, London, Edward Arnold, 1963.
39. Clift R., Grace J.R. and Weber M.E., Bubbles, drops and particles, New York, Academic Press, 1978.
40. Faeth G.M., Evaporation and combustion of sprays, Prog. Energy Combust. Sci., pp. 1-76, 1983.
41. Givler S.D. and Abraham J., Supercritical droplet vaporization and combustion studies, Prog. Energy Combust Sci., Vol. 22, pp. 1-28, 1996.
42. Sirignano W.A., Fluid Dynamics and Transport of Droplets and Sprays, Cambridge University Press, 1999.
43. Bellan J., Supercritical (and subcritical) fluid behavior and modelling: drops, steams, shear and mixing layers, jets and sprays, Prog. Energy Combust Sci., Vol. 26, pp. 329-66, 2000.
44. Bird R.B, Stewart W.E. and Lightfoot E.N., Transport phenomena, Chichester, Wiley, 2002.
45. Godsave G.A.E., Burning of Fuel Droplets , Fourth Symposium (International) on Combustion, The Combustion Institute, Pittsburgh, pp. 818-830, 1953.
46. Spalding D.B., The Combustion of Liquid Fuels, Fourth Symposium (International) on Combustion, The Combustion Institute, Pittsburgh, pp. 847-864, 1953.
47. Soret Ch., Sur l'e'tat d'e'quilibre que prend au point de vue de sa concentration une dissolution saline primitivement homogene dont deux parties sont porte'es a des tempe'ratures diffe'rentes, Arch Sci Physiques Nat., Vol. 2, pp. 48-61, 1879.
48. Postelnicu A., Influence of a magnetic field on heat and mass transfer by natural convection from vertical surfaces in porous media considering Soret and Dufour effects, Int. J. Heat Mass Transfer, Vol. 47, pp.1467-1472, 2004.
49. Hubbard G.L., Denny V.E. and Mills A.F., Droplet evaporation: effects of transient and variable properties, International Journal of Heat and Mass Transfer, Vol. 18, pp. 1003-1008, 1975.



50. Frössling N., Evaporation of falling drops, *Gerlands Beitr. Geophys.*, Vol. 52, pp. 170–216, 1938.
51. Ranz W.E. and Marshall W.R., Evaporation from drops, *Chem. Eng. Prog.*, Vol. 48, pp. 141-146 and 173-180, 1952.
52. Downing C.G., The evaporation of drops of pure liquids at elevated temperatures: rates of evaporation and wet-bulb temperatures, *AIChE J.*, Vol. 12, No.4, pp. 760-766, 1966.
53. Beard K.V. and Pruppacher H.R., A wind tunnel investigation of the rate of evaporation of small water drops falling at terminal velocity in air, *J. Atmos. Sci.*, Vol. 28, pp. 1455–1464, 1971.
54. Sirignano W.A. and Law C.K., Transient heating and liquid phase mass diffusion in droplet vaporization, Zung JT, editor, *Evaporation–combustion of fuels*, Advances in chemistry series, Vol. 166, Washington, DC: American Chemical Society, pp. 1–26, 1978.
55. Prakash S. and Sirignano W.A., Theory of convective droplet vaporization with unsteady heat transfer in the circulating liquid phase, *International Journal of Heat and Mass Transfer*, Vol. 23, pp. 253-268, 1980.
56. Tong A.Y. and Sirignano W. A., Analysis of vaporising droplet with slip, internal circulation and unsteady liquid-phase and quasi-steady gas-phase heat transfer, *ASME-JSME Thermal Joint Engineering Conference*, 1983.
57. Yuen M.C. and Chen L.W., On the drag of evaporating droplet, *Combust. Sci. Technol.*, Vol. 14, pp. 145-154, 1976.
58. Renksizbulut M. and Yuen M.C., Numerical study of droplet evaporation in a high-temperature air stream, *Journal of Heat Transfer-Transactions of the Asme*, Vol. 105, pp. 389-397, 1983.
59. Chiang C.H., Raju M.S. and Sirignano W.A., Numerical analysis of convecting, vaporizing fuel droplet with variable properties, *Int. J. Heat Mass Transfer*, Vol. 35, pp. 1307–24, 1992.
60. Aggarwal S.K., Tong, A.Y. and Sirignano W.A., A comparison of vaporization models in spray calculations, *AIAA Journal*, pp. 1448-1457, 1984.
61. Abramzon B. and Sirignano W.A., Droplet vaporization model for spray combustion calculations, *International Journal of Heat and Mass Transfer*, Vol. 32(9), pp. 1605-1618, 1989.



62. Wu J.-S., Liu Y.-J. and Sheen H.-J., Effects of ambient turbulence and fuel properties on the evaporation rate of single droplets, *Int. J. Heat Mass Transfer*, Vol. 44. pp. 4593–4603, 2001.
63. Gokalp I., Chauveau C., Simon O. and Chesneau X., Mass transfer from liquid fuel droplets in turbulent flow, *Combust. Flame*, Vol. 89, 1992.
64. Birouk M., Gokalp I., A new correlation for turbulent mass transfer from liquid droplets, *Int. J. Heat Mass Transfer*, Vol. 45, pp. 37–45, 2002.
65. Wu J.-S., Hsu K.-H., Kuo P.-M. and Sheen H.-J., Evaporation model of a single hydrocarbon fuel droplet due to ambient turbulence at intermediate Reynolds numbers, *Int. J. Heat Mass Transfer*, Vol. 46. pp. 4741–5, 2003.
66. Harpole G.B., Radiative absorption by evaporating droplets, *Int. J. Heat Mass Transfer*, Vol. 23, pp. 17–26, 1980.
67. Lage P.L.C. and Rangel R.H., Total thermal radiation absorption by a single spherical droplet. *J. Thermophys. Heat Transfer*, Vol. 7(1), pp. 101–9, 1993.
68. Lage P.L.C. and Rangel R.H., Single droplet vaporization including thermal radiation absorption, *J. Thermophys. Heat Transfer*, Vol. 7(3), pp. 502–9, 1993.
69. Dombrovsky L.A., *Radiation heat transfer in disperse systems*, New York, Begell House, 1996.
70. Dombrovsky L.A., Sazhin S.S., Sazhina E.M., Feng G., Heikal M.R., Bardsley M.E.A., Mikhalovsky S.V., Heating and evaporation of semitransparent diesel fuel droplets in the presence of thermal radiation, *Fuel*, Vol. 80, pp. 1535–44, 2001.
71. Dombrovsky L.A., Sazhin S.S., Absorption of thermal radiation in a semi-transparent spherical droplet: a simplified model, *Int. J. Heat Fluid Flow*, Vol. 24, pp. 919–27, 2003.
72. Sazhin S.S., Abdelghaffar W.A., Sazhina E.M., Mikhalovsky S.V., Meikle S.T. and Bai C., Radiative heating of semi-transparent diesel fuel droplets, *ASME J. Heat Transfer*, Vol. 126, pp. 490–501, 2004.
73. Abramzon B. and Sazhin S., Convective vaporization of fuel droplets with thermal radiation absorption, *Fuel*, Vol. 85, pp. 32–46, 2006.
74. Dombrovsky L.A. and Sazhin S.S., A parabolic temperature profile model for heating of droplets, *ASME J. Heat Transfer*, Vol. 125, pp. 535–7, 2003.



75. Dai M., Perot J.B. and Schmidt D.P., Heat transfer within deforming droplets, Proceedings of ASME: Internal Combustion Engine Division, New Orleans, September, 2002.
76. Arcoumanis C., Gavaises M. and French B., Effect of fuel injection processes on the structure of diesel sprays, SAE Paper 970799, 1997.
77. Haywood R.J., Renksizbulut M. and Raithby G.B., Transient deformation and evaporation of droplets at intermediate Reynolds numbers, Int. J. Heat Mass Transfer, Vol. 37, pp.1401–1409, 1994.
78. Renksizbulut M. and Yuen M.C., Experimental study of droplet evaporation in a high temperature air stream. Journal of Heat Transfer, Vol. 105, pp. 384-388, 1983.
79. Mashayek F., Dynamics of evaporating drops. Part 1: formulation and evaporation model, Int. J. Heat Mass Transfer, Vol. 44, pp. 1517–1526, 2001.
80. Muckhopadhyay A. and Sanyal D., A study of thin-flame quasi-steady spherically symmetric combustion of multicomponent fuel droplets, Part I: Modelling for droplet surface regression and non unity gas-phase Lewis number, Int. J. Energy Res., Vol. 23, pp. 963-977, 1999.
81. Law C.K., Multicomponent droplet combustion with rapid internal mixing, Combust. Flame, Vol. 26, pp. 219-233, 1976.
82. Law C.K., Internal boiling and superheating in vaporizing multicomponent droplets, A.I.Ch.E.J., Vol. 24 (4), pp. 626-632., 1978.
83. Law C.K. and Law H.K., A  $d^2$ -law for multicomponent droplet vaporization and combustion, AIAA Journal, Vol. 20(4), pp. 522-527, 1982.
84. Aggarwal S.K., Modelling of a dilute vaporising multicomponent fuel spray, Int. J. Heat & Mass Trans, Vol. 30, pp. 1949-1961, 1987.
85. Megaridis, C.M. and Sirignano W.A., Numerical modelling of a vaporizing multicomponent droplet., 23<sup>rd</sup> Symposium (International) on Combustion/The Combustion Institute, pp. 1413-1421, 1990.
86. Kneer R. and M. Schneider, Diffusion controlled evaporation of a multicomponent droplet: theoretical studies on the importance of variable liquid properties, International Journal of Heat and Mass Transfer, Vol. 36(9), pp. 2403-2415, 1993.
87. Tamim J. and Hallett W.L.H., A continuous thermodynamics model for multicomponent droplet vaporization, Chem. Eng. Science, Vol. 50, pp. 2933, 1995.



88. Lippert A.M., Modelling of multicomponent fuels with application to sprays and simulation of diesel engine cold start, PhD Thesis at the University of Wisconsin-Madison, 1999.
89. Harstad K. and Bellan J., Modelling evaporation of Jet A, JP-7, and RP-1 drops at 1 to 15 bars, *Combust Flame*, Vol. 137, pp. 163–77, 2004.
90. Abdel-Qader Z. and Hallett W.L.H., The role of liquid mixing in evaporation of complex multi-component mixtures: modelling using continuous thermodynamics, *Chem. Eng. Science*, Vol. 60, pp. 1629-1640, 2005.
91. Burger M., Schmehl R., Prommersberger K., Schäfer O., Koch R. and Wittig S., Droplet evaporation modelling by the distillation curve model: accounting for kerosene fuel and elevated pressures, *Int. J. Heat Mass Transfer*, Vol. 46, pp. 4403–4412, 2003.
92. Zhu G. S. and Aggarwal S. K., Transient supercritical droplet evaporation with emphasis on the effects of equation of state, *International Journal of Heat and Mass Transfer* 43(7), pp. 1157-1171, 2000.
93. Peng D. and Robinson D.B., A new two-constant equation of state, *Indust. Eng. Chem. Fund*, Vol. 15, pp. 59-64, 1976.
94. Redlich, O., and J. N. S. Kwong, On the thermodynamics of solutions. V: an equation of state. Fugacities of gaseous solutions, *Chem. Rev.*, Vol. 44, pp. 233, 1949.
95. Graboski M.S. and Daubert T.E., A modified Soave equation of state for phase equilibrium calculations. Part I: Hydrocarbon systems, *Industrial and Engineering Chemistry Process Design and Development*, Vol. 17, pp. 337-443, 1987.
96. Prausnitz J.M., Lichtenthaler R.N. and Gomes de Azevedo E., *Molecular thermodynamics of fluid-phase equilibria*, Prentice Hall International Series in the physical and chemical engineering sciences, ISBN: 0-13-977745-8, 1999.
97. Patankar, S.V., *Numerical Heat Transfer and Fluid Flow*, Taylor & Francis Inc., 1980.
98. Cotterman R.L. and Prausnitz J.M., Flash calculations for continuous and semicontinuous mixtures using an equation of state, *Ind. Eng. Chem. Process Des. Dev*, Vol. 24, pp. 434-443, 1985.
99. Wei Y.S. and Sadus R.J., *Equations of State for the Calculation of Fluid Phase Equilibria*, *AIChE J.*, Vol. 46, pp. 169-196, 2000.
100. Jin J.D. and Borman G.L., A model for multicomponent droplet vaporization at high ambient pressures, *SAE Paper 850264*, pp. 2483-2493, 1985.



101. Delplanque J.P. and Sirignano W.A., Numerical study of the transient vaporization of an oxygen droplet at sub- and super-critical conditions, *J. Heat Mass Transfer*, Vol. 36, No. 2, pp. 303-314, 1993.
102. Jia H. and Gogos G., High pressure vaporization; effects of liquid-phase gas solubility, *International Journal of Heat and Mass Transfer*, Vol. 36(18), pp. 4419-4431, 1993.
103. Nomura H., Ujhe Y., Rath H.J., Sato J. and Kono M., Experimental study on high-pressure droplet evaporation using microgravity conditions, 26<sup>th</sup> Symposium on Combustion, pp. 1267–1273, 1996.
104. Zhu G.S. and Aggarwal S.K., Fuel droplet evaporation in a supercritical environment, *Journal of Engineering for Gas Turbines and Power-Transactions of the Asm*, Vol. 124(4), pp. 762-770, 2002.
105. Hohmann S., Klingsporn M. and Renz U., An improved model to describe spray evaporation under diesel-like conditions, SAE Paper 960603, 1996.
106. Gradinger T.B. and Boulouchos C., A zero-dimensional model for spray development vaporization at high pressures and temperatures, *Int. J. of Heat and Mass Transfer*, No. 41, pp. 2947-2959, 1998.
107. Miller R.S., Harstad K. and Bellan J., Evaluation of equilibrium and non-equilibrium evaporation models for many-droplet gas-liquid flow simulations." *International Journal of Multiphase Flow*, Vol. 24, pp. 1025-1055, 1998.
108. Bellan J. and Summerfield M., Theoretical examination of assumptions commonly used for the gas phase surrounding a burning droplet, *Combustion and Flame*, No. 33, pp. 107-122, 1978.
109. Stengele J., Prommersberger K., Willmann M. and Wittig S., Experimental and theoretical study of one- and two- component droplet vaporization in a high pressure environment, *International Journal of Heat and Mass Transfer*, Vol. 42, pp. 2683-2694, 1999.
110. Aggarwal S.K. and H. Mongia C., Multicomponent and high-pressure effects on droplet vaporization, *Journal of Engineering for Gas Turbines and Power-Transactions of the Asme*, Vol. 124(2), pp. 248-255, 2002.
111. Hohmann S. and Renz U., Numerical simulation of fuel sprays at high ambient pressure: the influence of real gas effects and gas solubility on droplet vaporisation, *Int. J. Heat Mass Transfer*, Vol. 46, pp. 3017–3028, 2003.
112. Kim H. and Sung N., The effect of ambient pressure on the evaporation of a single droplet and a spray, *Combustion and Flame*, Vol. 135, pp. 261-270, 2003.



113. Sazhin S.S., Modelling of heating, evaporation and ignition of fuel droplets: combined analytical, asymptotic and numerical analysis, *Progress in Energy and Combustion Science*, Vol. 32, pp. 162–214, 2006.
114. Zhao F., Lai M.-C. and Harrington D.L., Automotive spark-ignited direct-injection gasoline engines, *Progress in Energy and Combustion Sciences*, No. 25, pp. 437-562, 1999.
115. Lippert A.M., El Tahry S.H., Huebler M.S., Parrish S.E., Inoue H., Noyori T., Najama K. and Abe T., Development and optimization of a small-displacement spark-ignition direct-injection engine-stratified operation, SAE Paper 2004-01-0033, 2004.
116. Pontoppidan M., Gaviani G., Bella G., De Maio A., Optimization by CFD simulation of spray formation parameters to adapt direct injection high-pressure fuel injectors to high-speed SI-engines, SAE Paper 2004-01-0539, 2004.
117. Gavaises M. and Arcoumanis C., Modelling of sprays from high-pressure swirl atomisers, *Int. J. Engine Research*, Vol. 2, No 2, pp. 95-117, 2001.
118. Landenfeld T., Kufferath A., Gerhardt J., Gasoline direct injection SULEV emission concept, SAE Paper 2004-01-0041, 2004.
119. Mitroglou N., Arcoumanis C., Mori K. and Motoyama Y., Mixture distribution in a multi-valve twin-spark ignition engine equipped with high-pressure multi-hole injectors, ICOLAD London, 2005.
120. Drake M.C., Fansler T.D. and Lippert A.M., Stratified-charge combustion: modelling and imaging of a spray-guided direct-injection spark-ignition engine, *Proceedings of the Combustion Institute*, Vol. 30, Issue 2, pp. 2683-2691, 2005.
121. Allen J., Hargrave G. and Khoo Y., In-nozzle and spray diagnostic techniques for real sized pressure swirl and plain orifice gasoline direct injectors, SAE Paper 2003-01-3151, 2003.
122. Shelby M.H., VanDerWege B.A. and Hochgreb S., Early spray development in gasoline direct-injection spark-ignition engines, SAE Paper 980160, 1998.
123. Ipp W., Wagner H.K., Wensing M., Leipertz A., Arndt S. and Jain A.K., Spray formation of high-pressure swirl gasoline injectors investigated by two-dimensional Mie and LIEF techniques, SAE 1999-01-0498, 1999.
124. Nouri J.M. and Whitelaw J.H., Spray characteristics of a GDI injector with short injection duration, *Exp. Fluids*, 2001.
125. Abo-Serie E., Arcoumanis C., Gavaises M., Argueyrolles B. and Galzin F., Structure of sprays generated by pressure swirl injectors for direct-injection



- gasoline engines, 15<sup>th</sup> Annual Conference on Liquid Atomisation and Spray Systems (ILASS-Europe), Toulouse, France, July 5-7, 1999.
126. Arcoumanis C. and Gavaises M., Pressure-swirl atomizers for DISI engines: further modelling and experiments, SAE Paper 2000-01-1044, SAE Transactions, 2000.
  127. Abo-Serie E., Arcoumanis C. and Gavaises M., Spray characteristics of pressure-swirl atomisers for G-DI engines: phase Doppler measurements, 16<sup>th</sup> Annual Conference on Liquid Atomisation and Spray Systems (ILASS-Europe, Germany), September, 2000.
  128. Gavaises M., Abdul-Wahab E. and Arcoumanis C., Nozzle hole film formation and its link to spray characteristics in swirl-pressure atomisers for direct injection gasoline engines, SAE Paper 2002-01-1136, 2002.
  129. Mitroglou N., Nouri J. M., Gavaises M. and Arcoumanis C., Spray characteristics of a multi-hole injector for direct-injection gasoline engines, accepted for publication to Int. J. Engine Research, 2006.
  130. AboSerie E., Gavaises M. and Arcoumanis C., Spray/wall interaction in direct-injection spark-ignition engines equipped with multi-hole injectors, Proc. 9<sup>th</sup> Int. Conf. on Liquid Atomisation and Spray Systems (ICLASS), Sorrento, Italy, July, 2003.
  131. Pontoppidan M, Gaviani G., Bella G. and De Maio A., Direct injection for future SI-engines – stand alone combustion layout or integrated part of multi-function fuel/air management approach?, SAE 2003-01-0540, 2003.
  132. Ortmann R., Arndt S., Raimann J., Grzeszik R. and Wuerfel G., Methods and Analysis of Fuel Injection, Mixture Preparation and Charge Stratification in Different Direct Injected SI Engines, SAE 2001-01-0970, 2001.
  133. Arndt S., Gartung K. and Brueggemann D., Spray Structure of High Pressure Gasoline Injectors: Analysis of Transient Spray Propagation and Spray-Gas Momentum Transfer, ILASS Europe, Zurich, September 2-6, 2001.
  134. Skogsberg M., Dahlander P., Lindgren R. and Denbratt I., Effects of Injector Parameters on Mixture Formation for Multi-Hole Nozzles in a Spray-Guided Gasoline DI Engine, SAE 2005-01-0097, 2005.
  135. Kawamoto M., Honda T., Katashiba H., Sumida M., Fukutomi N. and Kawajiri K., A Study of Centre and Side Injection in Spray Guided DISI Concept, SAE Paper 2005-01-0106, 2005.
  136. Das S. and VanBrocklin P.G., Effect of design and operating parameters on the spray characteristics of an outward opening injector, 13<sup>th</sup> International



- Multidimensional Engine Modelling User's Group Meeting, Detroit, MI., pp. 1-6, March 2, 2003.
137. Stan C. and Tröger R., Direct injection of variable gasoline/methanol mixtures: injection and spray characteristics, SAE Paper 2001-01-0966, 2001.
  138. Zeng Y. and Strauss S., Modelling of Air-Fuel Mixing in a Two-Stroke Direct Injection Engine, SAE Paper 2003-01-3103, 2003.
  139. VanDerWege B.A., Han Z., Iyer C. O., Muñoz R. H. and Yi J., Development and analysis of a spray-guided DISI combustion system concept, SAE Paper 2003-01-3105, 2003.
  140. Nouri J. M., Abo-Serie E., Marchi A., Mitroglou N. and Arcoumanis C., Internal and near nozzle flow characteristics from an enlarge model of an outward opening gasoline direct injector, ICOLAD 2005, London, UK, September 12-14, 2005.
  141. Nouri J. M., Hamid M. A., Yan Y. and Arcoumanis C., Spray characterization of a piezo pintle-type injector for gasoline direct injection engines, ICOLAD 2005, London, UK, September 12-14, 2005.
  142. Theodorakakos A., Numerical simulation of flow processes in IC engines, PhD Thesis, National Technical University of Athens, Greece, 1998.
  143. Ferziger J.H. and Peric M., Computational methods for fluid dynamics, 2<sup>nd</sup> ed. Berlin Heidelberg: Springer-Verlag, 1996.
  144. Jasak H., Error analysis and estimation for the finite volume method with applications to fluid flows, PhD Thesis, Imperial College, University of London, 1996.
  145. Caretto L.S., Gosman A.D., Patankar S.V. and Spalding D.B., Two calculation procedures for steady, three-dimensional flows with recirculation, in Proc. Third International Conference on Numerical Methods in Fluid Dynamics, Paris, France, 1972.
  146. Rhie C.M. and Chow W.L., A numerical study of the turbulent flow past an isolated airfoil with trailing edge separation, AIAA Journal, Vol. 21, pp. 1525-1532, 1983.
  147. Ramos J.I., Internal combustion engine modelling, Hemisphere Publishing Corporation, 1989.
  148. Giannadakis E., Modelling of cavitation in automotive fuel injector nozzles, PhD Thesis, Imperial College, University of London, 2005.



149. Launder B.E. and Spalding D.B., Lectures in Mathematical Models of Turbulence, London: Academic Press. 1972.
150. SLAP Sparse Linear Algebra Package. Netlib Repository - <http://www.netlib.org/>.
151. Papadakis G. and Bergeles G., A locally modified second order upwind scheme for convection terms discretisation, International Journal of Numerical Methods in Heat and Fluid Flow, Vol. 5, pp. 49–62, 1995.
152. Jasak H., Weller H.G., and Gosman A.D., High resolution NVD differencing scheme for arbitrarily unstructured meshes, International Journal for Numerical Methods in Fluids, Vol. 31(2), pp. 431-449, 1999.
153. Ubbink O., Numerical prediction of two fluid systems with sharp interfaces, PhD Thesis, Imperial College, University of London, 1997.
154. Ubbink O. and Issa R.I., A method for capturing sharp fluid interfaces on arbitrary meshes, Journal of Computational Physics, Vol. 153, pp. 26–50, 1999.
155. Poling B.E., Prausnitz J.M. and O'Connell J.P., The Properties of Liquids and Gases, 5<sup>th</sup> ed., New York, McGraw-Hill, 2000.
156. Perry R.H., Green D.W., Perry's Chemical Engineers' Handbook, 7<sup>th</sup> ed., McGraw-Hill, 1997.
157. O'Rourke P.J. and Amsden A.A., The TAB method for numerical calculation of spray droplet break up, SAE Paper No 872089, 1987.
158. Amsden A.A., O'Rourke P.J. and Butler T.D., KIVA II - A computer program for chemically reactive flows with sprays, Los Alamos Labs, report LS 11560 MS, 1989.
159. Lee and Bracco F.V., Comparisons of computed and measured hollow-cone sprays in an engine, SAE Paper 950284, 1995.
160. Han Z., Fan Li and Reitz D., Multidimensional modelling of spray atomization and air-fuel mixing in a direct injection spark-ignition engine, SAE Paper 970884, 1997.
161. Travis J.R., Harlow F.H. and Amsden A.A., Numerical calculations of two-phase flows', Nuclear Science and Engineering, Vol. 6, pp. 1-10, 1976.
162. Williams F.A., Combustion theory, The Benjamin/Cummings Publishing Company, Inc., 1985.



163. Arcoumanis C., Gavaises M., Abdul-Wahab E. and Moser V., Modelling of advanced high-pressure fuel injection systems for passenger car diesel engines, SAE Paper 1999-01-0910, 1999.
164. Arcoumanis C. and Gavaises M., Linking the nozzle flow with spray characteristics in a diesel fuel injection system, *Atomization and Sprays*, vol.8, pp. 179-197, 1998.
165. Chaves H., Knapp M., Kubitzek A., Obermeier F. and Schneider T., Experimental study of cavitation in the nozzle hole of diesel injectors using transparent nozzles, SAE Paper 950290, 1995.
166. Ahmadi M. and Sellens R.W., A simplified maximum-entropy-based drop size Distribution, *Atomization and Sprays*, Vol. 3, pp. 291-310, 1993.
167. Tanner F.X. and Weisser G., Simulation of liquid jet atomization for fuel sprays by means of a cascade drop break-up model, SAE Technical paper 980808, 1998.
168. Taskinen P., Modelling of spray combustion, emission formation and heat transfer in medium speed diesel engine, Doctor of Technology degree Thesis, Tampere University of Technology, 2005.
169. Reitz R.D. and Bracco F.V. Mechanism of atomisation of a liquid jet, *Phys. Fluids*, Vol. 25, No 2, pp. 1730-1741, 1982.
170. Huh K.Y. and Gosman A.D., A phenomenological model of diesel spray atomisation, *Proc. Int. Conf. Multiphase Flows*, Tsukuba, Japan, September 24-27, 1991.
171. Brennen E.C., *Cavitation and bubble dynamics*, Oxford University Press, 1995.
172. Hiroyasu H., Arai M., and Shimizu M., Breakup length of a liquid jet and internal flow in nozzle, *ICLASS-91*, Gaithersburg, MD, USA, July, 1991.
173. Su T.F. and Farrell P.V., Characterization of high-injection pressure diesel spray with relation to particulate and NO<sub>x</sub> emissions, *Atomisation and Sprays*, Vol. 8, pp. 83-107, 1998.
174. Faeth G.M. and Hsiang L.-P., Drop deformation and breakup sue to shock wave and steady disturbances, *Int. J. Multiphase Flow*, Vol. 21, No. 4, pp. 545-560, 1995.
175. Faeth G.M., Hsiang L.-P. and Wu P.-K., Structure and breakup properties of sprays, *Int. J. Multiphase Flow*, Vol. 21, Suppl., pp. 99-127, 1995.
176. Chryssakis C.A. and Assanis D.N., A Secondary atomization model for liquid droplet deformation and breakup under high Weber number conditions, *ILASS*



- Americas, 18th Annual Conference on Liquid Atomization and Spray Systems, Irvine, CA, May, 2005.
177. Reitz R.D. and Diwakar R., Structure of high-pressure fuel sprays, SAE report 870598, 1987.
  178. Pilch M. and Erdman C.A., Use of breakup time data and velocity history data to predict the maximum size of stable fragments for acceleration-induced breakup of a liquid drop, *Int. J. Multiphase Flow*, Vol. 13, pp. 741–757, 1987.
  179. Nigmatulin R.I., *Dynamics of Multiphase Media*, Hemisphere Publishing Corp., Washington D.C., Vol. 1, 1991.
  180. Hsiang L.-P. and Faeth G.M., Near limit drop deformation and secondary breakup, *Int. J. Multiphase Flow*, Vol. 18, pp. 635-652, 1992.
  181. Hsiang L.-P. and Faeth G.M., Drop properties after secondary breakup, *Int. J. Multiphase Flow*, Vol. 19, No. 5, pp. 721-735, 1993.
  182. Bayvel L. and Orzechowski Z., *Liquid Atomization*, Taylor and Francis, 1993.
  183. Azzopardi, B.J., Drops in annular two-phase flow, *International Journal of Multiphase Flow*, vol. 23, supplement, pp. 1-53, 1997.
  184. Ranger A.A. and Nicholls T.A., Aerodynamic shattering of liquid drops, *AIAA Journal*, Vol. 7, No. 2, 1969.
  185. Feng Z.G. and Michaelides E.E., Drag coefficients of viscous spheres at intermediate and high Reynolds numbers, *Journal of Fluids Engineering-Transactions of the ASME*, 123(4), pp. 841-849, 2001.
  186. Lefebvre A.H., *Atomization and Sprays*, Hemisphere, Washington, DC, 1989.
  187. Eisenklam P., Arunachlaman S.A., Weston J.A., Evaporation rates and drag resistance of burning drops, 11<sup>th</sup> Symposium (International) on combustion, The Combustion Institute, pp. 715-728, 1967.
  188. Rusche H. and Issa R., The Effect of Voidage on the Drag Force on Particles, Droplets and Bubbles in Dispersed Two-Phase Flow, in *Proc. 2<sup>nd</sup> Japanese-European Two-Phase Flow Group Meeting*, Tsukuba, Japan, 2000.
  189. Schmidt D.P. and Rutland C.J., A New Droplet Collision Algorithm, *Journal of Computational Physics* 164, pp. 62–80, 2000.
  190. Gavaises M., Theodorakakos A., Bergeles G. and G. Brenn, Evaluation of the effect of droplet collisions on spray mixing, *Proc. Inst. Mech. Eng.* 210, pp. 465-475, 1996.



191. O'Rourke P.J. and Bracco F.V., Modelling of drop interactions in thick sprays and a comparison with experiments, IMechE C404/80, Conference on Stratified charge automotive engines, November, 1980.
192. O'Rourke P.J., Collective Drop Effects on Vaporizing Liquid Sprays, PhD Thesis, Princeton University, 1981.
193. Orme M., Experiments on droplet collisions, bounce, coalescence and disruption, Progress in Energy and Combustion Science, Vol. 23, pp. 65, 1997.
194. Andrews M.J. and O'Rourke P.J., The multiphase particle-in-cell (MP-PIC) method for dense particulate flows, Int. J. Multiphase Flow, Vol. 22, pp. 379-402, 1996.
195. Gosman A.D. and Ioannides E., Aspects of computer simulation of liquid-fuelled combustors, Paper AIAA-81-0323, AIAA 19<sup>th</sup> Aerospace Science Meeting, St. Louis, MO, 1981.
196. Graham D.I., An improved eddy interaction model for prediction of turbulent particle, J. Fluids Eng. (Trans. ASME), Vol. 118, pp. 819-823, 1996.
197. O'Rourke P.J., Statistical Properties and Numerical Implementation of a Model for Droplet Dispersion in Turbulent Gas, Journal of Computational Physics, Vol. 83, pp. 345-360, 1989.
198. Stohl A. and Thomson D.J., A density correction for Lagrangian particle dispersion models, Bound.-Layer Met., Vol. 90, pp. 155-167, 1999.
199. Stanton D.W., Lippert A.M., Reitz R.D. and Rutland C.J., Influence of Spray-Wall Interaction and Fuel Films on Cold Starting in Direct Injection Diesel Engines, SAE Technical paper series, No. 982584, 1998.
200. Bai C. and Gosman A. D., Development of methodology for spray impingement simulation, SAE Technical paper series, No. 950283, 1995.
201. Mundo C., Sommerfield M. and Tropea C., Numerical and experimental investigation of spray characteristics in the vicinity of a rigid wall, ICLASS Conference, 1995.
202. Naber J., Enright B. and Farrell P., Fuel impingement in a direct injection diesel engine, SAE Technical paper series, No. 881316, 1988.
203. Senda J., Kobayashi M., Iwashita S. and Fujimoto H., Modelling of diesel spray impingement on a flat wall, SAE Technical paper series, No. 941894, 1994.
204. Nagaoka M., Kawazoe H. and Nomura N., Modelling fuel spray impingement on a hot wall for gasoline engine, SAE Technical paper series, No. 940525, 1994.



- 
205. Williams F. A., Combustion Theory, Addison Wesley, Reading, MA, 1965.
  206. Chigier N.A., Energy, combustion, and environment, McGraw-Hill, New York, 1981.
  207. Aggarwal S. K., Shu Z., Mongia H. and Hura H., Multicomponent fuel effects on the vaporization of a surrogate single-component fuel droplet, Paper 98-0157, 36<sup>th</sup> Aerospace Sciences Meeting, Reno, NV, Jan. 12–15, 1998.
  208. Schlichting H., Boundary Layer Theory, McGraw-Hill, 7<sup>th</sup> Edition, 1979.
  209. Sirignano W.A., Fuel droplet vaporization and combustion theory, Prog. Energy Combust. Sci., No. 9, pp. 291-322, 1983.
  210. Johns L.E. and Beckmann R.B., Mechanism of dispersed-phase mass transfer in viscous, single-drop extraction system, AIChE J., Vol. 12, pp. 10-16, 1996.
  211. Wong S.C and Lin A.C., Internal temperature distributions of droplets vaporizing in high-temperature convective flows, J. Fluid Mechanics, pp. 671-687, 1992.
  212. Poston R.S. and McKetta J.J., Vapor-liquid equilibrium in the n-hexane-nitrogen system, J. Chem. Eng. Data, 11, 362, 1966.
  213. Stengele J., Willmann M. and Wittig S., Experimental and theoretical study of droplet vaporization in a high pressure environment, ASME-97-GT-151, 1997.
  214. Chang J.-C., Diesel spray characteristics and spray/wall heat transfer, PhD thesis, University of London, Imperial College, 1994.
  215. Cutter P., Diesel spray characteristics, spray/wall interactions and heat transfer, PhD thesis, University of London, Imperial College, 1997.
  216. Choi Y.S., Diesel spray characterisation in a high-pressure chamber and in a single-cylinder engine, PhD Thesis, Imperial College of Science, London, 1999.
  217. König G. and Blessing M., Database on spray characteristics, I-LEVEL Confidential report Daimlerchrysler AG, 2003.
  218. Siebers D.L., Liquid-Phase Fuel Penetration in Diesel Sprays, SAE Paper 980809, 1998.
  219. Roth H., Gavaises M. and Arcoumanis C., Cavitation initiation, its development and link with flow turbulence in diesel injector nozzles, SAE Paper 2002-01-0214, SAE Transactions, 2002.



220. Gavaises M., Arcoumanis C., Roth H., Choi Y.S. and Theodorakakos A., Nozzle flow and spray characteristics from VCO diesel injector nozzles, THIESEL 2002 Conference on Thermo- and Fluid-Dynamic Processes in Diesel Engines, Valencia, Spain, 2002.
221. Giannadakis E., Gavaises M., Roth H. and Arcoumanis C., Cavitation modelling in single-hole diesel injector based on Eulerian-Lagrangian approach, THIESEL 2004 Conference on Thermo- and Fluid-Dynamic Processes in Diesel Engines, Valencia, Spain, 2004.
222. Yanagihara H., A Study on combustion structure of premixed compression ignition diesel engines, THIESEL 2002 Conference on Thermo- and Fluid-Dynamic Processes in Diesel Engines, Valencia, September 11-15, 2002.
223. Kampanis N., Arcoumanis C., Kato R. and Kometani S., Flow, Combustion and emissions in a five-valve research gasoline engine, SAE Paper 2001-01-3556, 2001.
224. Gavaises M., Tonini S., Arcoumanis C., Kometani S. and Theodorakakos A., Multi-component fuel vaporization and its effect on spray development and air-fuel mixing in gasoline direct injection engines, 5<sup>th</sup> International Conference ICE2003 Internal Combustion Engines: Experiments and Modelling, Italy, September 15-18, 2003.
225. Kampanis N., Flow, mixture distribution and combustion in five-valve gasoline engines, PhD Thesis, Imperial College, University of London, 2003.
226. Gavaises M., Tonini S., Marchi A., Theodorakakos A. and Bouris D., Modelling of internal and near-nozzle flow of a pintle-type outward opening gasoline piezo-injector, accepted for publication in Int. J. Engine Research, 2006.